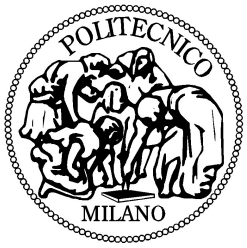

Politecnico di Milano
School of Civil, Environmental and Land Engineering

Graduate Program in Civil Engineering

Master Thesis

Beam Finite Element for Nonlinear Analysis of Floating Structures

Author:
Eduard Bargués Junyent

Advisor:
Prof. Fabio Biondini
Co-Advisor:
Dr. Andrea Titi

December 2, 2014

Eduard Bargués
Beam Finite Element for Nonlinear Analysis of Floating Structures
© December 2, 2014
eduardbargues@gmail.com

School of Civil, Environmental and Land Engineering
Politecnico di Milano

Dedicat a la meva mare i el meu germà

Abstract

This thesis deals with the static analysis of floating structures, with emphasis on floating breakwaters and floating bridges anchored by cable systems to the seabed. The formulation of a beam finite element on elastic foundation is developed by taking into account the nonlinearities associated with both the fluid-structure interaction and the large displacements due to the change of configurations of the anchoring cables. The effects of the nonlinear fluid structure-interaction are evaluated at the cross-sectional level by considering arbitrary geometry and loading conditions. The cross-sectional formulation is extended at the structural level based on the principle of virtual displacements to obtain the stiffness matrices and the equivalent nodal force vectors of both the beam finite element on elastic foundation and the cable finite element under large displacements. The characteristics of a contact element are also formulated to consider the interaction between the cables and the seabed. The accuracy of the proposed formulation is validated by means of several benchmarks and applicative examples. The effectiveness and applicability in engineering practice of the presented approach is demonstrated through the structural analysis of an existing anchored floating bridge under different loading conditions.

The thesis includes an introductory chapter, a first part consisting of three chapters devoted to nonlinear analysis of frame and cable structures, and a second part subdivided into six chapters focusing on floating structures.

General concepts related to structural typology, construction procedures and use of floating structures in civil engineering are discussed in Chapter 1. A state of the art is also presented, with emphasis on the limitations of current approaches based on beam elements on linear elastic foundation. Therefore, the scope and objectives of the thesis are presented and discussed.

In Part I, Chapter 2 recalls basic concepts of nonlinear mechanics. For the sake of synthesis and to make this chapter self-contained, only the concepts used in the thesis are reported and explained. Chapter 3 is devoted to the classical formulation of nonlinear analysis of beam and cable structures, and the numerical methods used to solve the nonlinear problem are presented in Chapter 4. Concepts such as prediction and correction phases, arc-length techniques and work control procedures are presented and discussed. Special emphasis is given to techniques and procedures for computer programming and numerical implementation of the presented approaches.

In Part II, Chapter 5 presents the cross-sectional formulation of the equilibrium equations and the fluid-structure interaction model. The proposed formulation is applied to a number of applicative examples related to typical box-girdercross-sections with different shape and geometry. The cross-sectional model is extended at the structural level in Chapter 6 for the basic formulation of a beam finite element on nonlinear elastic foundation. This model is validated through several numerical benchmarks. In Chapter 7, the formulation of the nonlinear structural analysis of floating structures is generalized to include large displacements based on the formulation of a corotational beam finite element and a cable finite element. The characteristics of a contact element are also formulated to consider the interaction between the cables and the seabed. In Chapter 8, the sectional model, the corotational beam finite element and the cable finite elements are validated by comparison with several case studies from literature. Therefore, chapter 9 presents the nonlinear structural analysis of an existing floating box-girder bridge anchored by a system of cables to the seabed under different loading conditions. Finally, Chapter 10 summarizes the conclusions drawn by the proposed approaches and provides recommendations for future research.

Acknowledgements

When I first came to Milan, I would never have expected to experience as many things as I have done. The expectation was so high: new university, new people, new challenges, ... a new world was opening in front of me. I have met some incredible people which I will certainly fight to mantain them in my life. I can barely believe this adventure is coming to an end.

The work I present in this document is one of the biggest achievements in my life. The dedication and hard work invested have let to this thesis that I feel humbly proud of. Although there have been some difficult moments when my forces almost fail me, I am happy about the conclusion of this thesis.

This thesis would not have been possible without the constant guidance of my advisor professor Fabio Biondini, who proposed me the subject of this research and from whom I have had the honor to learn a lot.

I would like to express my sincere gratitude to my co-advisor Andrea Titi. His constant support and dedication have given me the strength to keep going in the development of this thesis. He is one of the persons who have made possible this thesis.

I am also grateful to Manuel Quagliaroli from Politecnico di Milano for providing me with many fruitful advices and suggestions.

Also, a special thanks goes to Ulric Celada from Universitat Politècnica de Catalunya for his friendship. Our constant and challenging conversations about many topics have certainly increased the value of this work and they encourage me to give my best.

I would like to dedicate this work to my mother Ernes for helping me since I was born and being always there to protect me. Her dedication and love to his soons is an inspiration for me. Also, I dedicate this work to my brother Víctor, one of the persons I love most in this world.

Many people deserve to receive a special thank. Without his friendship and support I would not have been able to get as far as I have. I would like to specially thank Giulia Marelli, Silvia Bianchi, Mattia Pelucchi, Ciccio Telesa and Marzia Russo for sharing with me their friendship and endless hours of study. Also I am gratefull to Roberto Sigon, Carlotta Gaggini, Simone Fabbiano, Ilaria Iaconeta and Teresa Terzini. Their support

and friendship has helped me to overcome many obstacles and certainly have made me enjoy my stay in Milan.

I would also like to dedicate this thesis to all my friends from Barcelona. I dedicate an special though to Marc Prades, Joel Calafí, Sergio Sorroche, Claire Vidal, Ulric Celada, Alba Baños, Daniela Tudor, Manu Villaroya, Lluis Planas and Enric Corbella. Despite the distance that separates me from some of them I consider their friendship one of the greatest treasures I have.

Contents

Acknowledgements **7**

List of Figures **15**

List of Tables **27**

1 General introduction **29**
1.1 Floating Breakwaters . . . 31
1.2 Floating Bridges . . . 34
1.3 Submerged floating tunnels . . . 38
1.4 Anchoring structures . . . 39
1.5 Offshore Structures . . . 40
1.6 State of the art . . . 45
1.6.1 Literature review . . . 46
1.6.2 Current status and research needs . . . 49
1.7 Scope and objectives of the thesis . . . 50
1.8 Methodology . . . 51

I Nonlinear analysis of frame and cable structures **55**

2 Basic concepts of nonlinear mechanics **57**
2.1 Kinematic model . . . 58
2.2 Description of strains . . . 59
2.2.1 Green-Lagrange strain tensor . . . 61
2.2.2 Green-Lagrange strain increment tensor . . . 62
2.2.3 Euler Strain tensor . . . 63
2.2.4 Updated Green-Lagrange strain increment tensor . . . 64
2.3 Description of stresses . . . 65
2.3.1 Cauchy's stress tensors . . . 65
2.3.2 Second Piola-Kirchhoff's stress tensor . . . 65
2.3.3 Updated Kirchhoff stress tensor . . . 66
2.3.4 Transformation rules . . . 67
2.4 Principle of Virtual Work . . . 68
2.4.1 Total Lagrangian formulation . . . 70
2.4.2 Updated Lagrangian formulation . . . 71

3 Modeling of frame and cable structures 73
3.1 Cable structures . . . 74
3.1.1 Unextensible catenary . . . 74
3.1.2 Elastic catenary . . . 76
3.1.3 Direct stiffness method . . . 78
3.1.3.1 Total Lagrangian formulation . . . 79
3.1.3.2 Updated Lagrangian formulation . . . 82
3.1.4 Finite element method . . . 85
3.1.4.1 Principle of virtual works . . . 85
3.1.4.2 Stiffness matrix . . . 86
3.1.4.3 Computational aspects . . . 88
3.1.5 Mechanical behaviour of cables . . . 90
3.2 Frame structures . . . 91
3.2.1 Two-dimensional beam finite element modeling . . . 91
3.2.1.1 Theoretical model . . . 91
3.2.1.2 Finite Element formulation . . . 94
3.2.2 Three dimensional beam finite element modeling . . . 95
3.2.2.1 First order formulation . . . 96
3.2.2.2 General formulation . . . 101

4 Numerical methods for non linear analysis 111
4.1 Definition and solution of the non linear problem . . . 112
4.1.1 Stiffness method . . . 112
4.1.2 Incremental load procedure . . . 115
4.1.3 Classic Newton-Raphson scheme . . . 116
4.1.4 Improved Newton-Raphson schemes . . . 119
4.1.4.1 Prediction phase . . . 123
4.1.4.2 Correction phase . . . 125
4.2 Computational aspects . . . 131
4.2.1 Switching . . . 132
4.2.2 Automatic load increment . . . 132
4.2.3 Preconditioning and resolution of the linear system . . . 134

II Nonlinear analysis of floating structures 137

5 Sectional analysis 141
5.1 Modeling of the cross-section . . . 141
5.1.1 Discretization of the cross-section . . . 143
5.1.2 Discretization of the section boundary . . . 143
5.1.3 Modeling holes . . . 143
5.1.4 Discretization of the holes boundary . . . 144
5.2 Geometric properties . . . 145
5.2.1 Area A . . . 146
5.2.2 Static moments S_y and S_z . . . 147
5.2.3 Center of gravity, v_G . . . 147

5.2.4 Inertia moments I_y, I_z . . . 148
5.2.5 Torsional inertia I_x . . . 149
5.3 Fluid-structure interaction . . . 149
5.3.1 Forces due to the fluid . . . 150
5.3.1.1 In-plane forces . . . 150
5.3.1.2 Out-of-plane forces . . . 156
5.3.2 Isolated and non isolated sections . . . 161
5.4 Analysis of prototipal sections . . . 162
5.4.1 2D constitutive equations . . . 163
5.4.1.1 Rectangular section . . . 163
5.4.1.2 Trapezoidal section . . . 167
5.4.1.3 Circular section . . . 172
5.4.1.4 Box section . . . 176
5.4.2 3D constitutive equations . . . 181
5.4.3 Parametric constitutive equations . . . 187

6 First order formulation of 2D cable and frame floating structures 193
6.1 Modified Euler-Bernoulli and Winkler beam model . . . 194
6.2 Finite Element model . . . 196
6.3 Definition of the stiffness coefficient . . . 201
6.4 Cable structure . . . 204
6.5 Computational aspects . . . 206
6.6 Benchmarks . . . 216
6.6.1 Sections and constitutive equations . . . 217
6.6.2 Analysis of beam structures in contact with a fluid . . . 218
6.6.2.1 Benchmark 1 . . . 218
6.6.2.2 Benchmark 2 . . . 219
6.6.2.3 Benchmark 3 . . . 223
6.7 Practical applications . . . 228
6.7.1 Analysis of a floating bridge during the passage of a truck . . . 228
6.7.2 Analysis of a floating bridge under critical loads . . . 237

7 Advanced formulation of 3D cable and frame floating structures 241
7.1 Modified nonlinear Euler-Bernoulli and Saint Venant beam model . . . 242
7.2 Finite element model . . . 244
7.3 Formulation of the contact element for the seabed-cable interaction . . . 246
7.3.1 Contribution of the seabed stiffness . . . 246
7.3.2 Description of the program . . . 247
7.3.3 Modified Arc-Length method . . . 252
7.4 Advanced techniques for nonlinear analysis of floating structures . . . 254
7.4.1 Reference axes of beam elements nodes . . . 255
7.4.2 Reference system of beam elements . . . 256
7.4.3 Stresses of beam elements . . . 258
7.4.4 Reaction forces of the system . . . 260

8 Benchmarks and validation **263**
8.1 Benchmarks . . . 263
8.1.1 Two-member truss under concentrated load . . . 264
8.1.1.1 Analytical solution . . . 264
8.1.1.2 Numerical solution . . . 266
8.1.2 Symmetric elastic cable under self weight . . . 267
8.1.2.1 Analytical solution . . . 268
8.1.2.2 Numerical solution . . . 270
8.1.3 Asymmetric elastic cable under self weight . . . 271
8.1.3.1 Analytical solution . . . 272
8.1.3.2 Numerical solution . . . 274
8.1.4 Euler's Arch . . . 275
8.1.4.1 Analytical solution . . . 276
8.1.4.2 Numerical solution . . . 276
8.1.5 Cantilever beam loaded at the tip . . . 278
8.1.6 Cantilever beam under a moment at the tip . . . 287
8.1.7 Pinned-fixed square diamond frame in tension . . . 293
8.1.8 Circular beam . . . 302
8.1.9 Beam with segmented axis . . . 311
8.1.10 Lee's frame . . . 320
8.1.11 Williams toggle frame . . . 326
8.2 Floating V-shaped beam . . . 331
8.2.1 Analytical solution . . . 332
8.2.2 Numerical solution . . . 332
8.3 Floating beam under twisting moment . . . 334
8.4 Floating bridge under a concentrated load at middle span . . . 339

9 Application to a floating box-girder bridge **343**
9.1 Introduction . . . 343
9.2 Background and historical context . . . 345
9.2.1 Transportation and Mobility in Western Washington . . . 346
9.2.2 Crossing Lake Washington . . . 346
9.2.3 Lacey V. Murrow Bridge . . . 347
9.2.4 Construction of the floating bridge . . . 351
9.3 Analysis of the floating bridge . . . 354
9.3.1 Geometry of the bridge . . . 354
9.3.2 Loading conditions . . . 355
9.3.3 Analysis of the structure under self-weight . . . 356
9.3.4 Analysis of the structure under moving trucks . . . 364
9.3.5 Analysis of the structure under storm conditions . . . 373
9.4 Concluding remarks . . . 383

10 Conclusions **385**
10.1 General Conclusions . . . 385
10.2 Future Developments . . . 386

References **387**

List of Figures

1.1 Typical sections used in the fabrication of floating breakwaters. Image taken from [Tsinker, 1994] . . . 32
1.2 Floating breakwater installed in Holy Loch on the west coast of Scotland. Finnished in 1 Oct 2005. Photo taken from: Holy Loch (Lat: 55.985941, Long: -4.952048) . . . 33
1.3 Typical cable systems used to anchor the floating breakwaters to the seabed 33
1.4 Remaining Bombardon floating breakwater in the coast of Cap Manvieux, where one of the several landing operation of the D-Day was carried out . . 34
1.5 Sketch of the maneuver of the Persian army across the Hellespont during it's war with Greece. . . . 35
1.6 Galata steel floating bridge in Istanbul. Finnished in 1912. Photo taken from: Fatih/Istanbul, Turkey (Lat: 41.018182, Long: 28.973231) . . . 35
1.7 Bergsoysund floating bridge situated in Norway. Photo taken from: Riksvei 70, 6670, Norway (Lat: 62.989537, Long: 7.882260) . . . 36
1.8 Nordhordland floating bridge situated in Norway. Photo taken from: Krossneset 10, 5918, Frekhaug, Norway (Lat: 60.530272, Long: 5.257162) . . . 37
1.9 Yumemai floating bridge situated in Japan, connecting the Maishima and the Yumeshimahigashi islands. Photo taken from: 2 Chome-3-125 Hokukoryokuchi Konohana-ku, Osaka-shi, Osaka-fu, Japan (Lat: 34.661360, Long: 135.396421) . . . 37
1.10 Lacey V. Murrow memorial floating bridge. Photo taken from: Mercer Island, Washington, USA (Lat: 47.587329, Long:-122.253087) . . . 38
1.11 Several supporting system for a submerged floating tunnel . . . 39
1.12 Sketch of a typical Template structure . . . 42
1.13 Sketch of a typical Ice-Resistance monopod platform . . . 43
1.14 Sketch of a typical Gravity platform . . . 44
1.15 Sketch of a Guyer Tower and a Tension-Leg offshore platform . . . 45
1.16 The 6 forces and moments acting on a section element due to the hydrostatic pressure. . . . 52

2.1 Sketch of the procedure to characterize the Eulerian formulation . . . 58
2.2 The movement of the body in the 3 equilibrium configurations . . . 61
2.3 Definition of the Cauchy's stress tensor . . . 65
2.4 Definition of the Second Piola-Kirchhoff Stress Tensor . . . 66
2.5 Definition of the Updated Kirchhoff Stress Tensor . . . 67

3.1 Equilibrium configuration of a catenary 74
3.2 Equilibrium configuration of an elastic catenary 76
3.3 Model used in the direct approach of the cable element (Total Lagrangian Formulation) 79
3.4 Vector that defines the increment of length in the local reference system of the cable element. 80
3.5 Straight element in the updated Lagrangian formulation 82
3.6 Decomposition of the displacements in the parallel and orthogonal part to the current configuration for a straight element 84
3.7 Consitutive law of a cable element. 90
3.8 Generalized displacement for a 2D beam with no shear deformability. . . . 91
3.9 End forces in the 2D Bernoulli's model. 93
3.10 Generalized displacement for a 3D beam with no shear deformability. . . . 96

4.1 Secant iterative procedure to solve the equilibrium equations. 112
4.2 Flow chart of the stiffness method 114
4.3 Possible behaviours of an structure during the deformative path 115
4.4 Tangent iterative procedure to solve the equilibrium equations. 116
4.5 Flow chart of the incremental Newton-Raphson method 118
4.6 Flow chart of the improved Newton-Raphson schemes 120
4.7 Normalization of the force-displacement curve 121
4.8 Definition of the Bergam parameter 122
4.9 Iteration performed in the prediction phase 124
4.10 Flow chart of the prediction phase 125
4.11 Correction phase during the nonlinear procedure 126
4.12 Angle method in the arc-length correction procedure 128
4.13 Sketch of the choice made by the restoring method in the arc-length procedure 129
4.14 Flow chart of the correction phase 130
4.15 Flow chart of the Arc-Length method in the correction phase 131
4.16 Flow chart of Switching procedure 132
4.17 Flow chart of the automatic load increment procedure 134

5.1 General sketch of a section 142
5.2 Representation of the four types of mesh used in the discretization of a section 142
5.3 Sketch of a beam making contact with an hydrostatic fluid 144
5.4 Mapping of a 4-nodes quadrangular element 145
5.5 Beam element seen as a concatenation of infinite sections along its axes . . 150
5.6 Integration of the hydrostatic pressure along the external cotour of the section 151
5.7 Model to compute the forces of a section due to a fluid in a 3D space . . . 152
5.8 Procedure to integrate the hydrostatic pressure in the external boundary of a discretized section 153
5.9 Contribution of each linear element on the total twisting moment 155
5.10 Straight element partially under a fluid 156
5.11 Difference between a section situated at the ends of a beam and a section positioned along the axes 157

5.12 Procedure to integrate the hydrostatic pressure inside a section. 157
5.13 Direction of the hydrostatic pressure on every end section of the beam . . . 158
5.14 Resultants obtained from the integration of the hydrostatic pressure inside the section 159
5.15 Procedure to integrate the hydrostatic pressure inside a discretized section. 160
5.16 Hydrostatic load acting on a covered and uncovered section 162
5.17 Sections that will be analyzed 163
5.18 Sketch of the rectangular section making contact with an unmoved fluid in the 2D model 164
5.19 Sketch of the rectangular section making contact with an unmoved fluid in the 2D model with z bigger than h 165
5.20 Normalized forces and moment acting on the rectangular section partially under a fluid 166
5.21 Normalized forces and moment acting on the rectangular section totally under a fluid 166
5.22 Sketch of the trapezoidal section making contact with an unmoved fluid . . 167
5.23 $f_{x'}$ as a function of α on trapezoidal section partially under a fluid 169
5.24 $f_{z'}$ as a function of α on trapezoidal section partially under a fluid 169
5.25 $m_{y'}$ as a function of α on trapezoidal section partially under a fluid 170
5.26 $f_{x'}$ as a function of β on trapezoidal section partially under a fluid 170
5.27 $f_{z'}$ as a function of β on trapezoidal section partially under a fluid 171
5.28 $m_{y'}$ as a function of β on trapezoidal section partially under a fluid 171
5.29 Sketch of the circular section making contact with an unmoved fluid 172
5.30 Normalized forces and moment acting on the circular section partially under a fluid 175
5.31 Normalized forces and moment acting on the circular section totally under a fluid 175
5.32 Sketch of the box section used in the 3D analysis 176
5.33 $f_{x'}$ force applied in the box section as a function of the vertical displacement 177
5.34 $f_{z'}$ force applied in the box section as a function of the vertical displacement 177
5.35 $m_{y'}$ moment applied in the box section as a function of the vertical displacement 178
5.36 Sketch of the box section with a hole inside 178
5.37 $f_{x'}$ force applied in the box section considering the section covered and uncovered 179
5.38 $f_{z'}$ force applied in the box section considering the section covered and uncovered 180
5.39 $m_{y'}$ moment applied in the box section considering the section covered and uncovered 180
5.40 Initial configuration of the box section in the 3D analysis 181
5.41 Force $f_{x''}$ as a function of the displacement w 182
5.42 Force $f_{z''}$ as a function of the displacement w 183
5.43 Force $m_{y''}$ as a function of the displacement w 183
5.44 Force $f_{x''}$ and moment $m_{x''}$ as a function of the displacement φ_x 184
5.45 Forces $f_{y''}$ and $f_{z''}$ as a function of the displacement φ_x 184
5.46 Moments $m_{x''}$, $m_{y''}$ and $m_{z''}$ as a function of the rotation φ_x 185

5.47 Force $f_{x''}$ as a function of the displacement φ_y . . . 185
5.48 Force $f_{z''}$ as a function of the displacement φ_y . . . 186
5.49 Force $m_{y''}$ as a function of the displacement φ_y . . . 186
5.50 Section in a vertical plane with the variables that govern the problem . . . 187
5.51 Rectangular section . . . 188
5.52 Trapezoidal section . . . 189
5.53 Section number 3 . . . 189
5.54 Vertical reaction produced by the fluid on the rectangular section . . . 190
5.55 Twisting moment produced by the fluid on the rectangular section . . . 190
5.56 Vertical reaction produced by the fluid on the trapezoidal section . . . 191
5.57 Twisting moment produced by the fluid on the trapezoidal section . . . 191
5.58 Vertical reaction produced by the fluid on section number 3 . . . 192
5.59 Twisting moment produced by the fluid on section number 3 . . . 192

6.1 Inclusion of buoyancy springs along the beam . . . 194
6.2 Differences between an element with constant and varying cross section in contact with a fluid . . . 196
6.3 Beam finite element with axial and vertical springs under external and equivalent nodal loads . . . 198
6.4 Beam finite element with axial and bending springs under external and equivalent nodal loads . . . 199
6.5 Beam with a parabolic prestressing cable . . . 199
6.6 Infinitesimal part of a cable in equilibrium . . . 200
6.7 Decomposition of the prestressed beam in two equivalent systems . . . 200
6.8 Model for the fluid-structure static interaction in the beam model. . . . 202
6.9 Computation of the equivalent stiffness in the 2D beam model. . . . 203
6.10 Comparison between the two ways to define the reaction of the fluid against the movement of the section. . . . 204
6.11 The load in the cable is composed by the selfweight and the hydrostatic buoyancy action . . . 205
6.12 Flow chart of the program for the analysis of 2D floating structures . . . 206
6.13 The program positions the floating structure at the depth δz where the weight of the structure is equilibrated with the hydrostatic action . . . 207
6.14 The Archimedes load is a continuous and monotonally increases with the variable δz . . . 208
6.15 Numerical scheme to obtain the equilibrium floating position of the structure considering the selfweight . . . 209
6.16 Situation of the floating structure before anchoring the system to the seabed 210
6.17 Iterative method used to compute the solution of the non linear equation. . 211
6.18 The functions g_1 and g_2 only intersect one time and they both are monotonally decreasing . . . 213
6.19 Flowchart of the procedure to create the elements and nodes of the cable structure . . . 215
6.20 Section 1 - Rectangular section used in the benchmarks . . . 217
6.21 Section 2 - Trapezoidal section used in the benchmarks . . . 218
6.22 Beam benchmark 1 - Flotability analysis of a beam with a rectangular section 218

6.23 Beam benchmark 2 - Flotability analysis of a beam with a trapezoidal section 219
6.24 Benchmark 2 - Iterative procedure in the flotability analysis 220
6.25 Benchmark 2 - Buoyancy stiffness during the flotability analysis 221
6.26 Benchmark 2 - Value of the equilibrium floating position during the iterative procedure 221
6.27 Benchmark 2 - Archimedes force and weight during the procedure analysis 222
6.28 Benchmark 2 - Final equilibrium floating position of the beam 222
6.29 Benchmark 3 - Floating beam under a concentrated load in the middle . . 223
6.30 Benchmark 3 - Finite element model used in the analysis of the third benchmark 224
6.31 Benchmark 3 - Variation of the vertical displacements in the right edge in terms of the number of elements along the beam using the Winkler model . 224
6.32 Benchmark 3 - Error of the vertical displacement increasing the number of elements in the mesh using the Winkler model 225
6.33 Beam benchmark 3 - Vertical displacements in the right edge of the beam using the new finite element model 226
6.34 Beam benchmark 3 - Error of the new finite element model with respect the solution of the Winkler model 226
6.35 Beam benchmark 3 - Vertical displacements in the right edge of the beam using the new finite element model 227
6.36 Beam benchmark 3 - Error of the new finite element model with respect the solution of the Winkler model 227
6.37 Practical applications 1 - Analysis of a floating bridge under the action of a moving vehicle 228
6.38 Practical applications 1 - Shear distribution along the bridge with the truck positioned at $x_c = 0$ meters from the left edge 229
6.39 Practical applications 1 - Bending moment distribution along the bridge with the truck positioned at $x_c = 0$ meters from the left edge 230
6.40 Practical applications 1 - Shear distribution along the bridge with the truck positioned at $x_c = 250$ meters from the left edge 230
6.41 Practical applications 1 - Bending moment distribution along the bridge with the truck positioned at $x_c = 250$ meters from the left edge 231
6.42 Practical applications 1 - Shear distribution along the bridge with the truck positioned at $x_c = 500$ meters from the left edge 231
6.43 Practical applications 1 - Bending moment distribution along the bridge with the truck positioned at $x_c = 500$ meters from the left edge 232
6.44 Practical applications 1 - Shear distribution along the bridge with the truck positioned at $x_c = 750$ meters from the left edge 232
6.45 Practical applications 1 - Bending moment distribution along the bridge with the truck positioned at $x_c = 750$ meters from the left edge 233
6.46 Practical applications 1 - Shear distribution along the bridge with the truck positioned at $x_c = 1000$ meters from the left edge 233
6.47 Practical applications 1 - Bending moment distribution along the bridge with the truck positioned at $x_c = 1000$ meters from the left edge 234
6.48 Practical applications 1 - Bending moment in the left edge of the bridge as a function of the position of the vehicle 235

6.49 Practical applications 1 - Bending moment in the middle of the bridge as a function of the position of the vehicle . . . 236
6.50 Practical applications 1 - Shear in the middle of the bridge as a function of the position of the vehicle . . . 237
6.51 Practical applications 2 - Analysis of a floating bridge under the action of several trucks uniformly distributed along the bridge . . . 238
6.52 Practical applications 2 - Deformed configuration . . . 238
6.53 Practical applications 2 - Bending moment distribution along the bridge . . 239
6.54 Practical applications 2 - Shear distribution along the bridge . . . 239

7.1 Sketch of a deformed beam in contact with a fluid . . . 243
7.2 Cable element making contact with the seabed . . . 247
7.3 Cable element horizontally lying on the seabed . . . 247
7.4 Flow chart of the program for the analysis of 3D floating structures . . . 248
7.5 Flowchart of the iterative procedure in the 3D program . . . 249
7.6 Flowchart of the part where the reference load vector is computed . . . 251
7.7 Variation of the reference system of each beam node during the deformation of the structure . . . 255
7.8 Variation of the reference system of each beam element during the deformation of the structure . . . 256

8.1 Two member truss under concentrated load . . . 264
8.2 Two member truss under concentrated load - Reaction-displacement curve 265
8.3 Two member truss under concentrated load - Reaction-Displacement curve obtained with the numerical model . . . 267
8.4 Symmetric elastic cable under self weight . . . 268
8.5 Symmetric elastic cable under self weight - Deformed configuration considering both the unextensible and elastic catenaries . . . 269
8.6 Symmetric elastic cable under self weight - Axial stress distribution along the deformed elastic catenary . . . 269
8.7 Symmetric elastic cable under self weight - Comparison of displacement between theoretical and finite element models . . . 271
8.8 Asymetric elastic cable under self weight . . . 272
8.9 Assymetric elastic cable under its own self weight - Deformed configuration considering both the unextensible and elastic catenaries . . . 273
8.10 Asymmetric elastic cable under its own self weight - Axial stress distribution along the deformed elastic catenary . . . 273
8.11 Asymmetric elastic cable under self weight - Comparison of displacement between theoretical and finite element models . . . 275
8.12 Euler's arch . . . 276
8.13 Euler's arch - Comparison between analytical and numerical models . . . 278
8.14 Cantilever beam loaded at the tip . . . 278
8.15 Cantilever beam loaded at the tip - Configuration of the beam in several load steps . . . 280
8.16 Cantilever beam loaded at the tip - Equilibrium path corresponding to the horizontal displacement of the point on the left . . . 281

8.17 Cantilever beam loaded at the tip - Equilibrium path corresponding to the vertical displacement of the point on the left . . . 281
8.18 Cantilever beam loaded at the tip - Equilibrium path corresponding to the rotation of the point on the left . . . 282
8.19 Cantilever beam loaded at the tip - Bending moment in the z' axis at the $\lambda = 0.1$ . . . 283
8.20 Cantilever beam loaded at the tip - Shear forces in the y' axis at the $\lambda = 0.1$ 283
8.21 Cantilever beam loaded at the tip - Axial force in the x' axis at the $\lambda = 0.1$ 284
8.22 Cantilever beam loaded at the tip - Bending moment in the z' axis at the $\lambda = 5$ . . . 284
8.23 Cantilever beam loaded at the tip - Shear forces in the y' axis at the $\lambda = 5$ 285
8.24 Cantilever beam loaded at the tip - Axial force in the x' axis at the $\lambda = 5$. 285
8.25 Cantilever beam loaded at the tip - Bending moment in the z' axis at the $\lambda = 10$ . . . 286
8.26 Cantilever beam loaded at the tip - Shear forces in the y' axis at the $\lambda = 10$ 286
8.27 Cantilever beam loaded at the tip - Axial force in the x' axis at the $\lambda = 10$ 287
8.28 Cantilever beam under a moment at the tip . . . 287
8.29 Cantilever beam under a moment at the tip - Configuration of the beam in several load steps . . . 289
8.30 Cantilever beam under a moment at the tip - Equilibrium path corresponding to the horizontal displacement of the point on the left . . . 290
8.31 Cantilever beam under a moment at the tip - Equilibrium path corresponding to the vertical displacement of the point on the left . . . 290
8.32 Cantilever beam loaded at the tip - Equilibrium path corresponding to the rotation of the point on the left . . . 291
8.33 Cantilever beam loaded at the tip - Bending moment in the z' axis at the $\lambda = 0.1$ . . . 292
8.34 Cantilever beam loaded at the tip - Bending moment in the z' axis at the $\lambda = 0.5$ . . . 292
8.35 Cantilever beam loaded at the tip - Bending moment in the z' axis at the $\lambda = 0.75$ . . . 293
8.36 Pinned-fixed square diamond frame in tension . . . 293
8.37 Pinned-fixed square diamond frame in tension - Configuration of the beam in several load steps . . . 295
8.38 Pinned-fixed square diamond frame in tension - Equilibrium path corresponding to the horizontal displacement of the point on the right . . . 296
8.39 Pinned-fixed square diamond frame in tension - Equilibrium path corresponding to the rotation of the point on the right . . . 296
8.40 Pinned-fixed square diamond frame in tension - Equilibrium path corresponding to the vertical displacement of the uppest point . . . 297
8.41 Pinned-fixed square diamond frame in tension - Bending moment in the z' axes at $\lambda = 0.1$ . . . 298
8.42 Pinned-fixed square diamond frame in tension - Shear force in the y' axes at $\lambda = 0.1$ . . . 298
8.43 Pinned-fixed square diamond frame in tension - Axial force in the x' axes at $\lambda = 0.1$ . . . 299

8.44 Pinned-fixed square diamond frame in tension - Bending moment in the z' axes at $\lambda = 5$ . . . 299
8.45 Pinned-fixed square diamond frame in tension - Shear force in the y' axes at $\lambda = 5$ . . . 300
8.46 Pinned-fixed square diamond frame in tension - Axial force in the x' axes at $\lambda = 5$ . . . 300
8.47 Pinned-fixed square diamond frame in tension - Bending moment in the z' axes at $\lambda = 10$ . . . 301
8.48 Pinned-fixed square diamond frame in tension - Shear force in the y' axes at $\lambda = 10$ . . . 301
8.49 Pinned-fixed square diamond frame in tension - Axial force in the x' axes at $\lambda = 10$ . . . 302
8.50 Circular bend . . . 302
8.51 Circular bend - Configuration of the beam in several load steps . . . 304
8.52 Circular bend - Equilibrium path corresponding to the horizontal displacement in the x direction of the free edge . . . 305
8.53 Circular bend - Equilibrium path corresponding to the horizontal displacement in the y direction of the free edge . . . 305
8.54 Circular bend - Equilibrium path corresponding to the vertical displacement of the free edge . . . 306
8.55 Circular bend - Equilibrium path corresponding to the rotation around x axis of the free edge . . . 306
8.56 Circular bend - Equilibrium path corresponding to the rotation around y axis of the free edge . . . 307
8.57 Circular bend - Equilibrium path corresponding to the rotation around z axis of the free edge . . . 307
8.58 Pinned-fixed square diamond frame in tension - Axial force acting in the x' axes at $\lambda = 1.0$ . . . 308
8.59 Pinned-fixed square diamond frame in tension - Shear force acting in the y' axes at $\lambda = 1.0$ . . . 309
8.60 Pinned-fixed square diamond frame in tension - Shear force acting in the z' axes at $\lambda = 1.0$ . . . 309
8.61 Pinned-fixed square diamond frame in tension - Twisting moment acting in the x' axes at $\lambda = 1.0$ . . . 310
8.62 Pinned-fixed square diamond frame in tension - Bending moment acting in the y' axes at $\lambda = 1.0$ . . . 310
8.63 Pinned-fixed square diamond frame in tension - Bending moment acting in the z' axes at $\lambda = 1.0$ . . . 311
8.64 Beam with slope discontinuity . . . 311
8.65 Beam with slope discontinuity - Configuration of the beam in several load steps . . . 313
8.66 Beam with slope discontinuity - Equilibrium path corresponding to the horizontal displacement in the x direction of the free edge . . . 314
8.67 Beam with slope discontinuity - Equilibrium path corresponding to the horizontal displacement in the y direction of the free edge . . . 314

8.68 Beam with slope discontinuity - Equilibrium path corresponding to the vertical displacement of the free edge . . . 315
8.69 Beam with slope discontinuity - Equilibrium path corresponding to the rotation around x axis of the free edge . . . 315
8.70 Beam with slope discontinuity - Equilibrium path corresponding to the rotation around y axis of the free edge . . . 316
8.71 Beam with slope discontinuity - Equilibrium path corresponding to the rotation around z axis of the free edge . . . 316
8.72 Beam with slope discontinuity - Axial force acting in the x' axes at $\lambda = 0.4$ 317
8.73 Beam with slope discontinuity - Shear force acting in the y' axes at $\lambda = 0.4$ 318
8.74 Beam with slope discontinuity - Shear force acting in the z' axes at $\lambda = 0.4$ 318
8.75 Beam with slope discontinuity - Twisting moment acting in the x' axes at $\lambda = 0.4$ . . . 319
8.76 Beam with slope discontinuity - Bending moment acting in the y' axes at $\lambda = 0.4$ . . . 319
8.77 Beam with slope discontinuity - Bending moment acting in the z' axes at $\lambda = 0.4$ . . . 320
8.78 Lee's frame . . . 320
8.79 Lee's frame - Configuration of the beam in several load steps . . . 322
8.80 Lee's frame - Equilibrium path corresponding to the horizontal displacement in the x direction of point A . . . 322
8.81 Lee's frame - Equilibrium path corresponding to the horizontal displacement in the y direction of point A . . . 323
8.82 Lee's frame - Equilibrium path corresponding to the rotation around z axis of point A . . . 323
8.83 Lee's frame - Axial force acting in the x' axes at $\lambda = 0.15$ . . . 324
8.84 Lee's frame - Shear force acting in the y' axes at $\lambda = 0.15$ . . . 325
8.85 Lee's frame - Bending moment acting in the z' axes at $\lambda = 0.15$ . . . 325
8.86 Williams toggle frame . . . 326
8.87 Williams toggle frame - Configuration of the beam in several load steps . . . 327
8.88 Williams toggle frame - Equilibrium path corresponding to the horizontal displacement in the x direction of point A . . . 328
8.89 Williams toggle frame - Axial force acting in the x' axes at $\lambda = 0.045$ . . . 329
8.90 Williams toggle frame - Axial force acting in the x' axes at $\lambda = 1.041$ . . . 329
8.91 Williams toggle frame - Shear force acting in the y' axes at $\lambda = 0.045$ . . . 330
8.92 Williams toggle frame - Shear force acting in the y' axes at $\lambda = 1.041$ . . . 330
8.93 Williams toggle frame - Bending moment acting in the z' axes at $\lambda = 0.045$ 331
8.94 Williams toggle frame - Bending moment acting in the z' axes at $\lambda = 1.041$ 331
8.95 Floating V-Beam subjected to its own self weight . . . 332
8.96 Floating V-Beam subjected to its own self weight - Equilibrium position obtained by the program . . . 334
8.97 Floating beam under twisting moment . . . 335
8.98 Floating beam under twisting moment - Equilibrium path of the vertical displacement of the centroid of the section . . . 336
8.99 Floating beam under twisting moment - Equilibrium path of the rotation of the section . . . 337

8.100Floating beam under twisting moment - Equilibrium position under it's own self weight 338
8.101Floating beam under twisting moment - Equilibrium position when the external twisting moment is equal to $M = 25.5748$ $[kN \cdot m]$ 338
8.102Floating beam under twisting moment - Equilibrium position when the external twisting moment is equal to $M = 0$ $[kN \cdot m]$ 339
8.103Floating bridge submitted to a concentrated load at middle span 340
8.104Floating bridge submitted to a concentrated load at middle span in the middle - Maximum penetration in the fluid as a function of the length of the bridge considering the bridge rigid and flexible 341
8.105Floating bridge submitted to a concentrated load at middle span in the middle - Bending moment at the acting load point as a function of the length of the bridge considering the bridge rigid and flexible 342

9.1 Location of the floating bridge referred to the United States of America . . 344
9.2 Location of the floating bridge referred to the Washington state 344
9.3 Location of the floating bridge in Seattle 345
9.4 Current situation of the Lacey V. Murrow memorial bridge (right) and the new Homer M. Hadley memorial bridge (left). Photo taken from: USA (Lat: 47.586092, Long: -122.290023) 348
9.5 Current situation of the Lacey V. Murrow memorial bridge (right) and the new Homer M. Hadley memorial bridge (left). Photo taken from: USA (Lat: 47.599284, Long: -122.290674) 349
9.6 Only the central parts of both the Lacey V. Murrow and Homer M. Hadley memorial bridges are floating. The parts that connect the bridges with the coast rest on solid columns anchored to the floor. Photo taken from: USA (Lat: 47.600238, Long: -122.285910) 350
9.7 The I-90 railway goes from Seattle (top of the picture) to Bellevue (bottom of the picture) passing through the Mercer island (island in the middle of the picture). Photo taken from: USA (Lat: 47.568654, Long: -122.162035) 351
9.8 In the fist stage of construction, the transition zones were built on each side of the bridge and the first floating pontoon positioned in the middle of the lake 352
9.9 In the second stage, the new pontoon was attached to the previous one and the block of concrete positioned in the lake's bed 353
9.10 The floating bridge of Washington was openned in the 2nd July of 1960 . . 353
9.11 Schematic representation of the floating bridge and the transition zones . . 354
9.12 Cross-section of the bridge 355
9.13 The cables provide an horizontal stiffness to the structure attaching the pontoons with the lake's bed 355
9.14 Structure under self-weight - Axial force acting on the cables N expressed in $[kN]$ 357
9.15 Structure under self-weight - Axial force acting on the bridge N expressed in $[kN]$ 358
9.16 Structure under self-weight - Shear force T_y expressed in $[kN]$ 359
9.17 Structure under self-weight - Shear force T_z expressed in $[kN]$ 360

9.18 Structure under self-weight - Bending moment M_y expressed in $[kN \cdot m]$ . . 361
9.19 Structure under self-weight - Bending moment M_z expressed in $[kN \cdot m]$ . . 362
9.20 The bridge is submitted to a distributed load equal to 30 $\frac{kN}{m}$ with an eccentricity of 6.75 m to simulate 55 trucks, which each one of them weights 30 tones, positioned along 550 m 364
9.21 Structure under self-weight and a set of moving trucks - Axial force acting on the cables N expressed in $[kN]$ 366
9.22 Structure under self-weight and a set of moving trucks - Axial force acting on the bridge N expressed in $[kN]$ 367
9.23 Structure under self-weight and a set of moving trucks - Shear force T_y expressed in $[kN]$ 368
9.24 Structure under self-weight and a set of moving trucks - Shear force T_z expressed in $[kN]$ 369
9.25 Structure under self-weight and a set of moving trucks - Bending moment M_x expressed in $[kN \cdot m]$ 370
9.26 Structure under self-weight and a set of moving trucks - Bending moment M_y expressed in $[kN \cdot m]$ 371
9.27 Structure under self-weight and a set of moving trucks - Bending moment M_z expressed in $[kN \cdot m]$ 372
9.28 The bridge is submitted to a distributed load equal to $p = \gamma_c A_s = 223.46 \frac{kN}{m}$ to simulate the thrust created by the stream of water 374
9.29 Structure under self weight and storm conditions - Axial force acting on the cables N expressed in $[kN]$ 376
9.30 Structure under self weight and storm conditions - Axial force acting on the bridge N expressed in $[kN]$ 377
9.31 Structure under self weight and storm conditions - Shear force T_y expressed in $[kN]$ 378
9.32 Structure under self weight and storm conditions - Shear force T_z expressed in $[kN]$ 379
9.33 Structure under self weight and storm conditions - Bending moment M_x expressed in $[kN \cdot m]$ 380
9.34 Structure under self weight and storm conditions - Bending moment M_y expressed in $[kN \cdot m]$ 381
9.35 Structure under self weight and storm conditions - Bending moment M_z expressed in $[kN \cdot m]$ 382

List of Tables

1.1 Correspondance between the formulation of the constitutive equations for materials and the formulation of these for a section. 52

6.1 Critical vertical load of the bridge 237

8.1 Two member truss under concentrated load - Mechanical and geometrical variables 265
8.2 Two member truss under concentrated load - Parameters for the nonlinear analysis in an incremental iterative scheme 266
8.3 Two member truss under concentrated load - Comparison of the results between the analytical and finite element models 267
8.4 Symmetric elastic cable under self weight - Mechanical and geometrical variables 268
8.5 Symmetric elastic cable under self weight - Parameters for the nonlinear analysis in an incremental iterative scheme 270
8.6 Symmetric elastic cable under self weight - Comparison of the results between the analytical and finite element models 271
8.7 Asymmetric elastic cable under self weight - Mechanical and geometrical variables 272
8.8 Asymmetric elastic cable under self weight - Parameters for the nonlinear analysis in an incremental iterative scheme 274
8.9 Asymmetric elastic cable under self weight - Comparison of the results between the analytical and finite element models 275
8.10 Euler's arch - Parameters for the nonlinear analysis in an incremental iterative scheme 277
8.11 Cantilever beam loaded at the tip - Parameters for the nonlinear analysis in an incremental iterative scheme 279
8.12 Cantilever beam under a moment at the tip - Parameters for the nonlinear analysis in an incremental iterative scheme 288
8.13 Pinned-fixed square diamond frame in tension - Parameters for the nonlinear analysis in an incremental iterative scheme 294
8.14 Circular bend - Parameters for the nonlinear analysis in an incremental iterative scheme 303
8.15 Beam with slope discontinuity - Parameters for the nonlinear analysis in an incremental iterative scheme 312

8.16 Lee's frame - Parameters for the nonlinear analysis in an incremental iterative scheme 321
8.17 Williams toggle frame - Parameters for the nonlinear analysis in an incremental iterative scheme 326
8.18 Floating V-Beam - Parameters for the nonlinear analysis in an incremental iterative scheme 333
8.19 Floating beam under twisting moment - Parameters for the nonlinear analysis in an incremental iterative scheme 335
8.20 Floating bridge submitted to a concentrated load at middle span - Parameters for the nonlinear analysis in an incremental iterative scheme 340

9.1 Structure under self-weight - Parameters for the nonlinear analysis in an incremental iterative scheme 356
9.2 Structure under self weight and a set of moving trucks - Parameters for the nonlinear analysis in an incremental iterative scheme 365
9.3 Structure under self weight and storm conditions - Parameters for the nonlinear analysis in an incremental iterative scheme 374

1 General introduction

Nowadays, where the population and urban development increase and the land-scarce become every year a more alarming problem, city planners and engineers have found to land reclamation a solution to ease the pressure on existing heavily-used land and underground spaces. Using fill materials from seabed, deep underground excavations, and even construction debris, engineers are able to create relatively vast and valuable land from the sea.

Such problems have been cleverly solved in countries like Netherlands, Singapore and Japan, that have expanded their land areas significantly through land reclamation. In spite of the efforts made in this field, the traditional land reclamation is no longer cost effective and new techniques and innovative structures have been developed to deal with these problems, leading to many new and very challenging projects where the floating structures (FS) have been propounded.

As a guideline, land reclamation is appropiate when the water depth is shallow (less than 20 m). When the water depth is large and the seabed is extremely soft, land reclamation is no longer cost effective or sometimes impossible from the engineeristic point of view. From another perspective, land reclamation destroys the marine habitat and may even lead to the movement of toxic sediments due to the construction techniques used. When faced with these natural conditions and environmental consequences, the so called floating structures may offer an attractive alternative solution for reclame land to the sea.

In some European coastal cities, the demanding of recreational facilities has increased according to their attractiveness for the tourism and economical growth. The increased demand due to boating public and industry for more moorage facilities challenges the planners and designers of small-craft harbors to explore all alternatives in developing harbors that have adequate protection from wind waves and boat wakes. Most of the natural harbors developed near population centers, where boating demands are greatest, are overcrowded.

Some of the main applications in which FSs have found their usage is in the storage platforms. One of the greatest engineering challenges today is the development of offshore platforms for water depths larger than 300 m. The traditional way to build floating

storage facilities in the sea is to adapt steel jacket structures or concrete gravity platforms, which are impossible to install (or costly prohibitive) when the depth of the sea is larger than 300 m. As a consequence, a large number of alternatives, lightweight offshore platforms that utilize water buoyancy and cable systems, have been developed, such as: guyed towers; tension leg platforms; moored semi-submersibles; moored tankers, etc.

Usually, FSs are made of steel, concrete or steel-concrete composite. Since watertightness of concrete is important to avoid or limit corrosion of the reinforcement, either watertight concrete or offshore concrete should be used. High-performance concrete containing fly ash and silica fume is most suitable for FSs. From the structural modelling perspective, the effects of creep and shrinkage have a low weight in the stresses and strains produced on those structures, since these two effects develop once the concrete is dry and, as a consequence, their effects can be neglected when FSs are lowered in the sea.

Most of the structures described before has to be somehow anchored to the seabed. The anchorage system will depend on the engineering requirements since it has to ensure that the floating structure is kept in position so that the facilities installed on the floating structure can be reliably operated and to prevent the structure from drifting away under critical sea conditions and storms. A freely drifting floating structure may lead to not only damage to the surrounding facilities but also the loss of human life if a collision with ships occurs.

The design procedure for a mooring system usually follows these steps: first select the mooring method, the shock absorbing material, the quantity and layout of devices to meet the environmental conditions and the operating conditions and requirements. The layout of the mooring dolphins for example is such that the horizontal displacement of the floating structure is adequately controlled and the mooring forces are appropriately distributed. Second, the behaviour of the floating structure under various loading conditions is examined. The layout and quantity of the devices are adjusted so that the displacement of floating structure and the mooring forces do not exceed the allowable values. Finally, devices such as dolphins and guide frames are designed by applying the design load based on the calculated mooring forces.

This thesis will consider several types of FSs. Special attention will be devoted to the characterization and study of the FSs that can be divided in 3 groups:

- FSs related to the water-crossing problem, such as Floating Bridges (FB), Immersed Tunnels (IT) and Submerged Floating Tunnels (SFT).
- Fixed offshore structures (FOS) such as facilities for the extraction of oil and gas and Very Large Floating Structures (VLFS) such as floating airport or storage facilities.
- FSs developed for the wave-protection problems, which are solved by means of Floating BreakWaters (FBW).

1.1 Floating Breakwaters

Floating breakwaters have become an alternative with an active potential in future harbor-marina design. The floating breakwater has been adopted at a number of sites where water depth or other constraints make a fixed structure too costly, and is proposed for countless others. Although there are other uses for floating breakwaters, such as in waterfront construction and operation, beach erosion control and so on, the most prominent applications relate to the small-craft harbor or marina. In order to reduce the wave amplitude impacting the marina infraestructures, breakwaters are constructed nearby. A general rule of thumb is to have a breakwater if the significant wave height is greater than 4 m.

FBWs represent a cost-possibilities alternative to protect small marinas against sea waves and boat wakes under some circumstances, as well as in fields like aquaculture, a growing demand. In fact, the development of a large number of new marinas and recreational harbours all around the world has led to a growing interest in the study of FBWs. Nevertheless, the operational limits of the design currently in use are not precisely known.

Over the past two decades, interest in the study of the behaviour of floating breakwaters, has increased owing to the requirement for the development of large number of small marinas and recreational harbours and because of the environmental considerations in coastal zones have shown a remarkable increase. On one hand, the lower initial investment and the mobility of the structure are attractive to the designer and are evaluated as reliable alternative when the cost of a fixed structure exceeds the economic return to be gained at that location and also perform wave attenuation as well as being useful for boat docks, moorings or walkways. On the other hand, FBWs play an important role in environmental preservation due to their low impact in terms of environmental and visual impact. This is due to the fact that FBWs have a very low impact in the surrounding environtment.

FBWs have generated a great interest in the field of coastal engineering, as they are less expensive compared to conventional breakwaters. In addition, they have several desirable characteristics, such as small capital cost, adaptation to varying harbour shapes and sizes and short construction time and they can be also used to meet location changes, extent of protection required or seasonal demand. They can be used as a temporary protection for offshore activities in hostile environment during construction, drilling works, salvage operation, ... etc. In recent years there has been an increased interest in the use of FBWs as a means of providing protection from wave attack in semiprotected regions. Such structures provide an attractive alternative to more conventional fixed breakwaters in deeper waters, in areas where poor foundation conditions or environmental constraints exist, or where protection is required only temporarly. Floating breakwaters behave either as reflectors or as dissipators of wave energy.

FBWs can be built following many shapes, figure 1.1 shows the typical section.

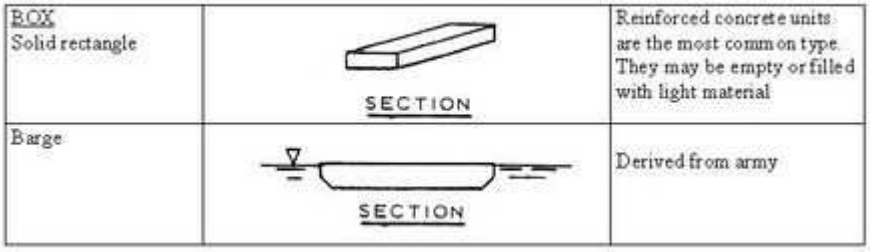

(a) Sections used for Box floating breakwaters

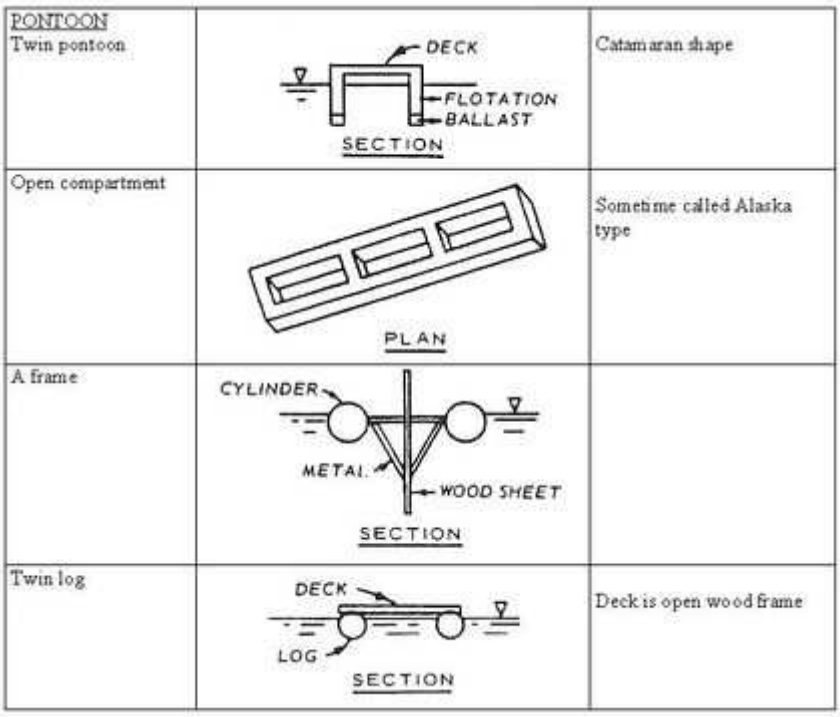

(b) Sections used for Pontoon floating breakwaters

Figure 1.1: Typical sections used in the fabrication of floating breakwaters. Image taken from [Tsinker, 1994]

As an example of real floating breakwater, the FBW situated in Holy Loch on the west coast of Scotland allows to understand better how the FBWs are constructed and how they operate. The breakwater is 240 m long by 3.8 m wide with a total weight of 500 tons. It is made by of 12 large pre-cast concrete pontoons, each 20 m long and 42 tons weighty. The breakwater is held in position on a mooring system 110 m long heavy mooring chains held on thirty 500 kg high holding power anchors. Figure 1.2 shows a shown.

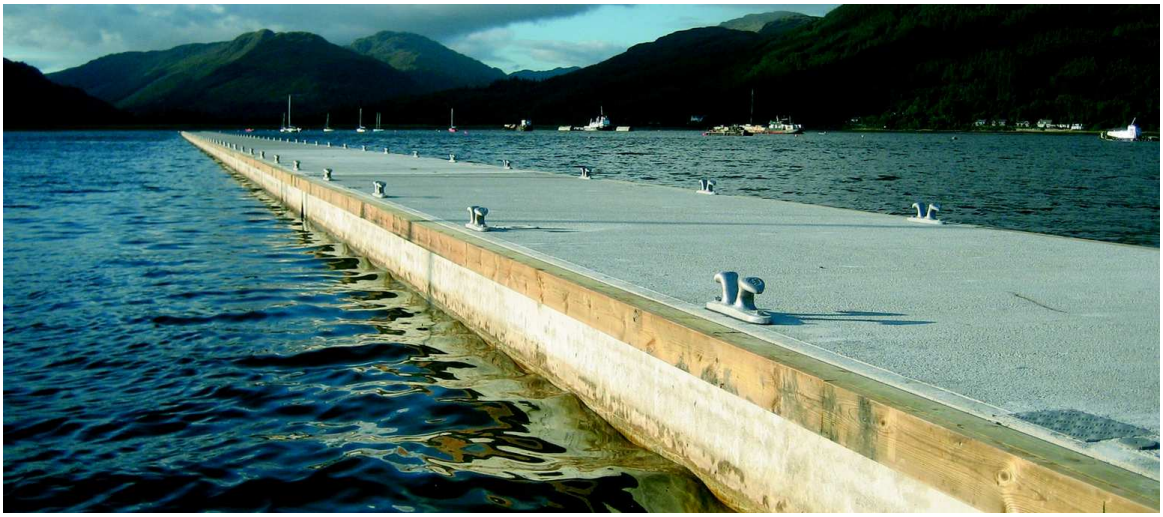

Figure 1.2: Floating breakwater installed in Holy Loch on the west coast of Scotland. Finnished in 1 Oct 2005. Photo taken from: Holy Loch (Lat: 55.985941, Long: -4.952048)

Usually, FBWs are anchored to the seabed using cables systems, as the one installed in Holy Loch on the west coast of Scotlant (Figure 1.2). There are many ways to anchor a FBW to the seafloor and in figure 1.3 two anchorage systems are sketched.

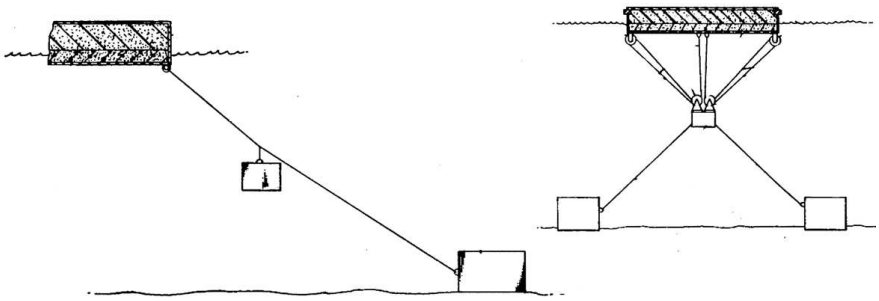

Figure 1.3: Typical cable systems used to anchor the floating breakwaters to the seabed

Military problems have found their solution in the use of FBWs. For example, one of the most famous applications was done during the D-Day in June of 1944. The allies positioned, during the previous days of the operation, the so called "Bombardon" FBWs along the coast of France (Figure 1.4). The FBWs were constructed in 2 separated lines (of about 250 meters of separation) perpendicular to the coast to provide a reduction of the wave length and an increase of the period of the waves. In a remarkable engineering achievement, the decision to use the "Bombardon" FBW was made in early 1943 and theoretical, analytical and experimental analysis were carried out before the D-Day when the "Bombardon" FBW provided shelter for invasion troops for the first 12 days of the operation. Later, the FBW were destroyed by a storm.

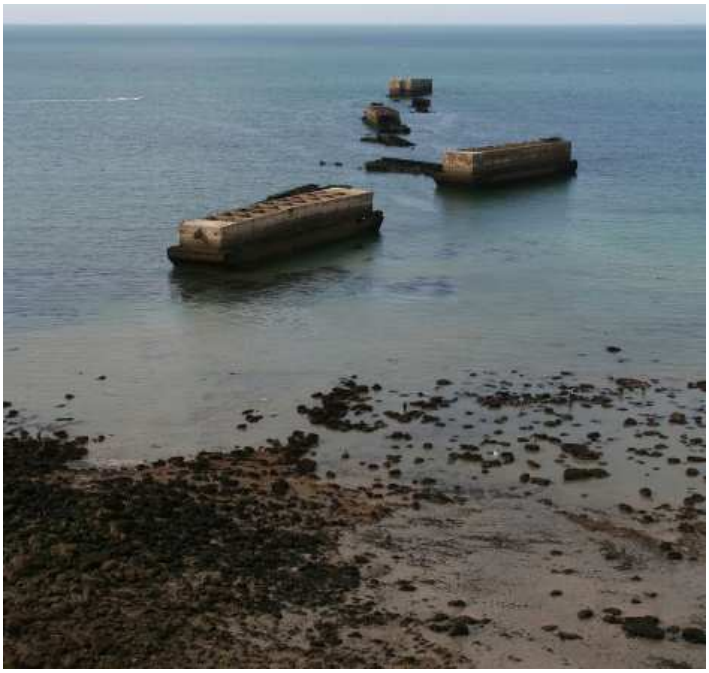

(a) Photo taken from: Cap Manvieux (Lat: 49.345175, Long: -0.639836)

(b) Photo taken from: France (Lat: 49.346009, Long: -0.639740)

Figure 1.4: Remaining Bombardon floating breakwater in the coast of Cap Manvieux, where one of the several landing operation of the D-Day was carried out

1.2 Floating Bridges

Early applications of very large FSs take the form of floating boat bridges over rivers. Around 480 BC, King Xerxes of Persia led his army across the Hellespont, now called the Dardanelles, using two rows of floating bridges, each consisting of about 300 boats laid side by side. Figure 1.5 shows a sketch of the operation.

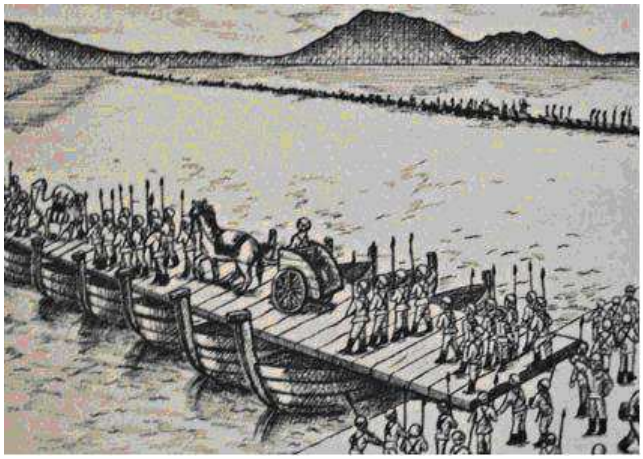

Figure 1.5: Sketch of the maneuver of the Persian army across the Hellespont during it's war with Greece.

In 1874, a 124-m long floating wooden railroad bridge was constructed over the Mississippi River in Wisconsin and it was repeatedly rebuilt and finally abandoned. Brookfield Floating Bridge is still in service and it is the seventh replacement structure of a 98-m long wooden floating bridge. In 1912, the Galata steel floating bridge (figure 1.6) was built across Istanbul's Golden Horn where the water depth is 41 m. The 457-m long bridge consists of 50 steel pontoons connected to each other by hinges. Contrary to engineers' perception that corrosion would pose a serious problem to such floating steel structures, it can be seen that the steel made FBs are a reliable solution for the nowadays water-Cross problems.

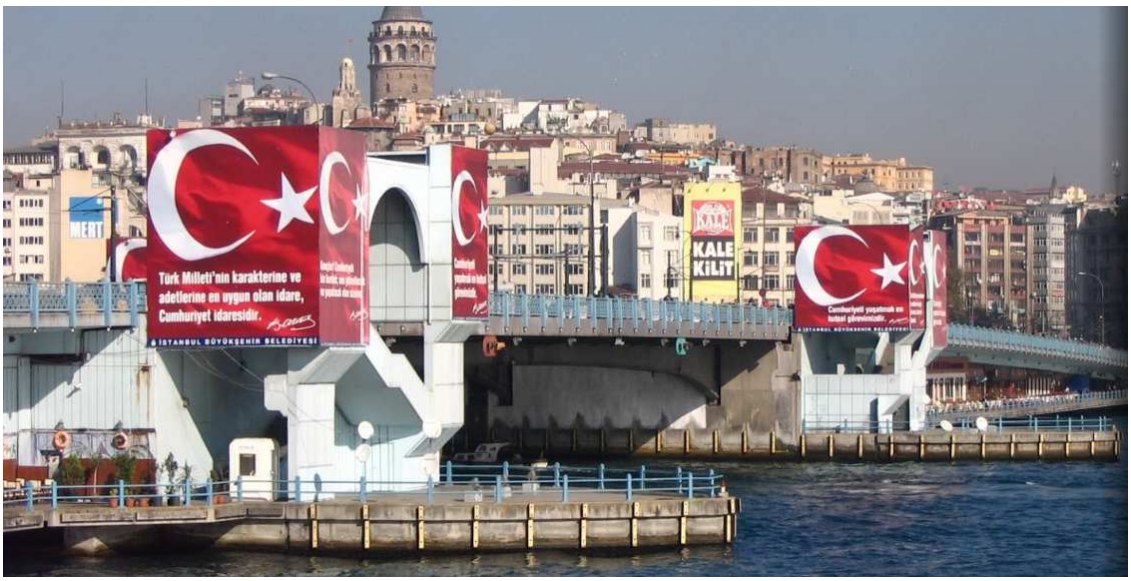

Figure 1.6: Galata steel floating bridge in Istanbul. Finnished in 1912. Photo taken from: Fatih/Istanbul, Turkey (Lat: 41.018182, Long: 28.973231)

Many civil floating bridges have been constructed in countries such as USA, Norway, UK, Japan and Canada. Until now, there are basically two different structural forms for

floating bridges: continuous concrete pontoon-type floating bridges have been utilized in the USA for many years, while steel truss decks supported by discrete pontoons have been constructed in Norway.

More recent floating bridges built from 1990s include the two famous Norwegian floating bridges: 845-m long Bergsoysund Floating Bridge (figure 1.7) built in 1992 near Kristiansund over a fjord depth of 320 m and the 1246-m long Nordhordland Floating Bridge (figure: 1.8) built in 1994 at Salhus over a fjord depth of 500 m. Both bridges are horizontally curved (in the form of funicular curves) to better resist the wave, the water current and wind forces. An interesting pedestrian floating bridge is the 94-m long West India Quay Footbridge which was constructed in 1997. This bridge resembles a giant pond skater.

Figure 1.7: Bergsoysund floating bridge situated in Norway. Photo taken from: Riksvei 70, 6670, Norway (Lat: 62.989537, Long: 7.882260)

Figure 1.8: Nordhordland floating bridge situated in Norway. Photo taken from: Krossneset 10, 5918, Frekhaug, Norway (Lat: 60.530272, Long: 5.257162)

An outstanding floating bridge that was built at the turn of the millennium is the 410-m long Yumemai Bridge (figure 1.9). The bridge is constructed across a water channel, and it floats on two hollow steel pontoons. The bridge can be moved around a pivot axis located at the supports for the crossing of very large ships.

Figure 1.9: Yumemai floating bridge situated in Japan, connecting the Maishima and the Yumeshimahigashi islands. Photo taken from: 2 Chome-3-125 Hokukoryokuchi Konohana-ku, Osaka-shi, Osaka-fu, Japan (Lat: 34.661360, Long: 135.396421)

A special attention will be devoted in further section to the Lacey V. Murrow memorial bridge (see figure 1.10). One of the longest bridges in the world and also one of the oldest (it was finnished in 1940). It is located in the state of Washington in the United States of America.

Figure 1.10: Lacey V. Murrow memorial floating bridge. Photo taken from: Mercer Island, Washington, USA (Lat: 47.587329, Long:-122.253087)

It is worth noting that many armies have in their own floating bridges and floating causeways. Army engineers assemble the floating modules rapidly to form floating bridges for soldiers and vehicles to cross rivers and lakes. Long floating causeways are used by the navy to transport soldiers and equipment from ships to shore.

1.3 Submerged floating tunnels

Even thought the Submerged Floating Tunnel (SFT) concept has been studied by engineers and researchers for some decades, the SFT, also know as "Archimedes Bridge", can be still considered a new and innovative type of infrastructure. In fact, there is no actual SFT being constructed in the world untill now. It represents a challenging structure in terms of it's static and dynamic analysis.

SFT fits as a alternative to cross sea-straits, lakes and other waterways. As we know, the cable suspended bridges are the most common structures to cross this kind of obstacules but the SFT's can take advantage of the water buoyancy and potentially increase it's length.

The SFT serves to all kind of traffic by crossing a body of water between two shores. Engineers can choose from a wide range of sections to build the SFT but usually a section with 2 axis of symmetry is chosen. Subjected to the seabed by anchorage system and subject to the buoyancy force due to the fluid, the SFT can be fixed and mantain an stable position due to the opposite forces system acting on it. This kind of structures are suitable to cross very long distance and deep waters.

The SFT can be divided in 2 elements: the tunnel and the anchorage system. Usually, the tunnel is composed by a circular or polygonal section made of concrete, steel or concrete-steel composite. On the other hand, the anchorage system can be chosen from a wide range of possibilities, such as: pontoons of the surface, columns from the seabed, tensioned anchor bars or cables to the seabed,... etc.

Cables and bars are the most used techniques to anchor the SFT to the seabed since the pontoons system is very sensitive to the water's free surface behaviour and it can be an obstacle to the navigation.

There are several differences between cables and bars: cables have no axial and flexural stiffnesses, bars can reach a straight configuration under the actions of weight and buoyancy while the cables always will have a catenary configuration, the lateral stiffness due to a cable anchorage is lower than a bar system but the bar systems could have some stability problems.

The first time someone mentioned the words "Floating submerged tunnel" was on 1860 by S. Preault. In 1923, the SFT was considered a feasible way to cross the Norway fjords considering that the separation length and the depth were too high for the traiditional tunnels.

As a conclusion, SFT area represents a new method to solve the water-cross problems because has no interaction with the navigation, it is not subjected to the waves action due to its construction depth and can overcome spans of any length.

Figure 1.11 shows several anchorage systems of a SFT.

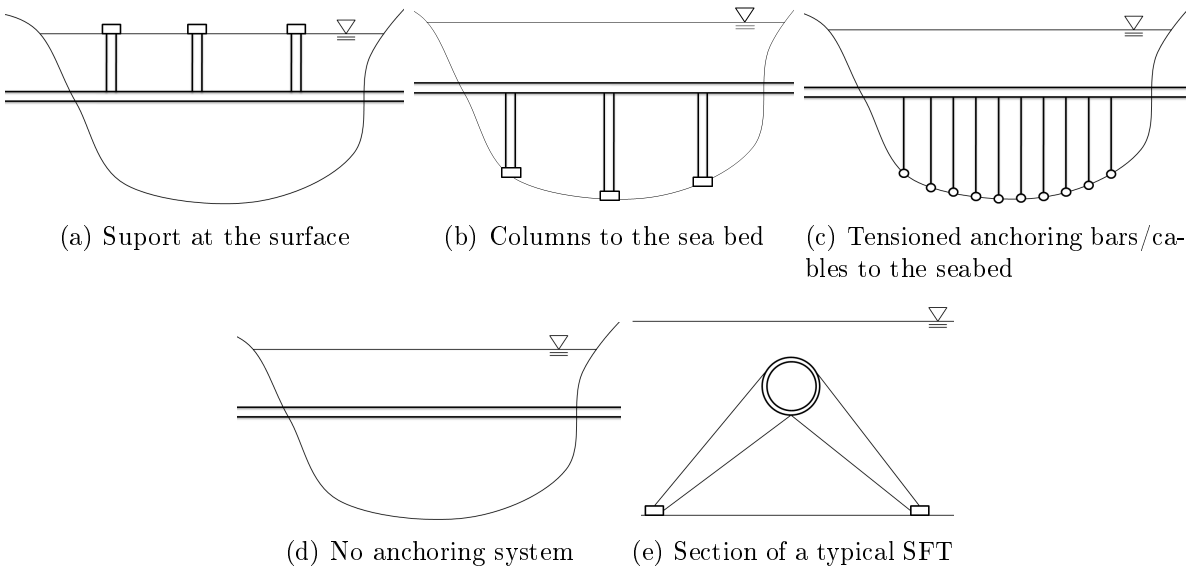

(a) Suport at the surface (b) Columns to the sea bed (c) Tensioned anchoring bars/cables to the seabed

(d) No anchoring system (e) Section of a typical SFT

Figure 1.11: Several supporting system for a submerged floating tunnel

1.4 Anchoring structures

A tensile structure is a construction of elements carrying only tension and no compression or bending. Tensile structures are the most common type of thin-shell structures. Most tensile structures are supported by some form of compression or bending elements,

compression rings or beams.

The tensile structures are considered as one of the most ancient technological expresions of the human being. The ropes of cables were made in ancient times by vegetal fibers twisted to create a thicker and stiffer element.

Cables can be of mild steel, high strength steel, stainless steel, polyester or aramid fibers. Structural cables are made of a series of small strands twisted or bound together to form a much larger cable. Steel cables are either spiral strand, where circular rods are twisted together and unified using a polymer, or locked coil strand, where individual interlocking steel strands form the cable.

The study of the tensile system was one of the first subject that the modern mechanics solved after the invention of the infinitesimal analysis.

From the engineering point of view, one of the main applications for the tensile or cable structures can be found in the construction of suspension bridges or cable-stayed bridges. For example, suspensions bridges are one of the main techniques to cross very large spans between two points.

Despite the great use of cable structures in the traditional structures, they have been used during the past two decades in the construction of the anchorage system for the offshore floating structures and new theoretical techniques for its study have been developed.

Anchor cable systems have traditionally been analysed using closed form solutions of the catenary problem or finite difference representations of the governing differential equations. The finite element method has also been used for solving cable systems, primarily through the use of higher order curved elements. Among the very large range of possible models to study cable elements, the most efficient way of solving such problems is through the use of simple, straight cable elements. As will be shown later, these elements are extremely easy to formulate and cheap to compute. They are well suited for solving problems involving very large displacements, and complex effects like contact problems, prestressing and hydrodynamic forces can easily be accounted for. On the other hand, use of simple elements normally means that more elements and possibly also more degrees of freedom must be used than in the case of higher order elements. However, simple elements are much cheaper to compute and they lead to very narrow band widths in the stiffness matrix and, thus, they are more cost effectively.

1.5 Offshore Structures

The development and positioning of Fixed Offshore Structures (FOS) is a relative new practice in the modern civil engineering. The first time a FOS was used was in 1947, when the first steel structure was installed in open waters in the Gulf of Mexico.

The analysis of this kind of structures differs from conventional structural engineering

mainly in the special problems that have to be considered in the transportation of the structure to the offshore site, its installation and its ability to resist the severe environment.

The main application of the FOSs is in the oil and gas industry, where they are built to provide a fixed platforms to extract the element from the seabed. There are also applications in the military and navigation fields.

The design of this structure is almost the same as the land structures but with the difference that they have to be constructed in one place and transported to another. The need of a FOS is specified by the need of a fixed platform where the operatives work.

There are several examples of FOSs:

- Template structures: They are the most common FOS. The structure is composed by prefabricated steel bars assembled to create a deck where the main structure will be supported. This deck goes from the top of the water's free surface to the seabed, providing for the platform a support that protects it from waves, wind and currents. The depth of applicability for this kind of structure is about 100 m and some examples of it have been installed in Louisiana in the Gulf of Mexico (1940s). The construction and installation of a Template structure plays the main part in its design. The support structure is usually build on land and then is towed to the location where it will be installed. At the installation site, the structure is fixed by means of pipe piles that are inserted into its steel legs and driven to the seafloor.
  A typical Template structure constructed with the procedure previously explained is located off Louisiana in about 100 m of water in the Gulf of Mexico. The deck measures approximately 20x40 m and, including all the operating system, weights about 910 tons. The supporting structure weights about 1820 tons. The pipe piles have 1-1.5 m of external diameter and wall thickness equal to 0.02-0.05 meters. The anchorage and main structures has been designed to resist a lateral load about 14000 kN and a base over-turning moment equal to 970000 KNm. As a comparison, this value is 7 times those caused by extreme wings in a 25-story, 91 m tall land building.
  Apart from oil extraction, the templates structures were also used in the military field, providing a defense infrastructure in the 1950s. The so called "Texas Defense Towers" were installed in the 50s by the government of United States in the northeastern coast. The aim was the radar surveillance for the detection of possible hostile aircraft and ships in an uncovered area. Some of them were located offshore in the Atlantic ocean.
  Other applications of the Template structure is to provide navigational aid to ships. In the 1960s, the templates structures were proposed as a reliable substitute of lightships in many zone of the United States because of economical reasons and also because of their fixed position and reliability in all kinds of weather.
  Figure 1.12 shows an scheme of a typical Template offshore structure.

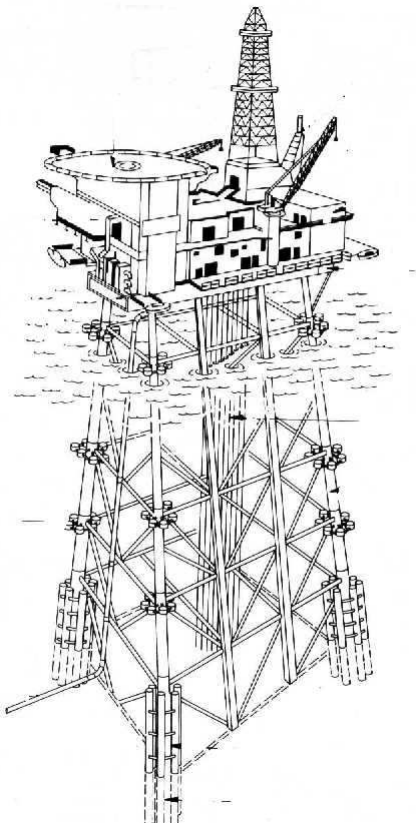

Figure 1.12: Sketch of a typical Template structure

- Ice-Resistant structures: A very important variation in the design and fabrication of offshore structures emerged when the engineers faced the necessity to use this kind of structures in frozen environments. The first time this need appeared was in the 1960s, when an offshore structure were designed and installed in the Cook Inlet, Alaska. The main difference between this new structure and the Template structures is the elimination of the diagonal and horizontal bracings in the tidal range, where they could be struck by the floating ice. To sustain the deck, the engineers decided to built a platform supported on four large-diameter bars. Each column was supported by a circular group of several piles.
  Althought the structure is slightly different to the first one, the fabrication and installation process is almost the same. The structure is built in a waterside facility, towed to the offshore point where it will be installed and anchored to the seabed with piles driven through its legs.
  Another approach can be followed to design the support structure. Instead of using four large-diameter bars, the engineer can use a single-leg platform. To fix the structure and support the deck, main piles are driven through the leg of the structure. Skirt piles are also driven around its base.
  Figure 1.13 shows an scheme of a typical Ice-Resistance offshore structure.

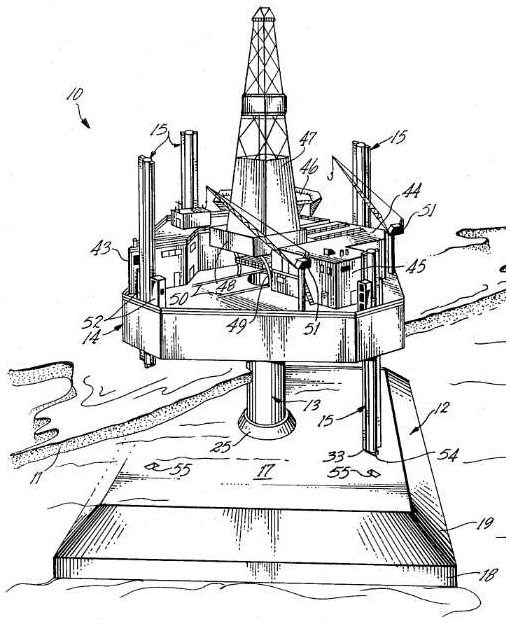

Figure 1.13: Sketch of a typical Ice-Resistance monopod platform

- Gravity structures: Template structures are most suitable to soft-soil zones where deeply driven piles are needed to fix the structures in place and carry the required deck load. Since in regions characterized by hard soil the use of driving piles is costly unefficient, an alternative structure has been developed which uses its own weight to hold itself in place against the lateral loads from waves and wing. These structures have large foundational elements and are usually referred as Gravity structures. This kind of structures were installed in the North sea during the 1970s and the main type is the so called Concrete Depp-Water structure. The construction process of Concrete Deep-Water structures is very different from the Templates and Ice-Resistance strucures. First, the base is constructed in a drydock, and later is floated out and moored to a deep-water harbor. The process is concluded by the slip-forming the large towers in a continuos process untill they are topped off. The structure is then ballasted out and a prefabricated steel deck is floated over the structure and connected to it. Additionally deck modules are then set in place and the entire structure refloated for towing it to the final position where it will be again ballasted to its final operating position.
  The main advantage of gravity structures is their reduced time of on-site installation. This is particularly important in hostile areas such as the north seas, where the unpredictable weather makes the reduction of on-site construction time a very important factor. Another advantage is the weight of the support structure, almost 20 times heavier than the Template structure.
  Not all gravity structures need to be made of concrete. Steel made gravity structures has been constructed off Nigeria, where the presence of rock close to the seafloor make impossible the use of concrete piles to fix the structure in place.
  Figure 1.14 shows an scheme of a typical Gravity offshore structure.

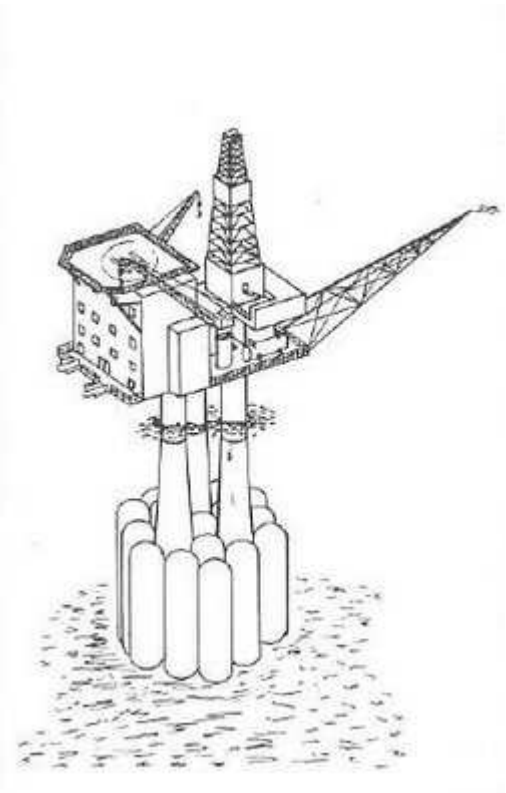

Figure 1.14: Sketch of a typical Gravity platform

- Deep-Water Design structures: For water depth greater than 300 meters, the traditional structures forms such as Templates and Gravity structures lose their applicability and new structural elements have to be designed. Two examples of Deep-Water Design structure are the Guyed towers and the Tension-Leg platforms.
  The Guyed-Tower concept consists of a uniform cross-sectional support structure held upright by several guy lines that run to clump weights on the ocean floor. At the end of the cable structure (the guy lines that support laterally the platform) additional weights are placed to increase the lateral stiffness of the structure. These weights allow the structure to absorb the lateral load produced by waves and wings by swaying back and forth without overloading the guy lines. The Guyer Tower is suitable when the depth is about to 600 meters.
  In the design of the Tension-Leg concept, vertical members are used to anchor the the platform to the seafloor. The upper part of the main structure (the platform) is designed with an excessive buoyancy so as to keep the vertical members in tension. The vertical stiffness is provided entirely by the vertical cable elements that are anchored to the platform on the seabed. On the other hand, the horizontal stiffness, the one that has to counteract lateral load from waves and wing, is provided by the horizontal displacement of the platform, that activates the restoring force produced by the deformation of the cable support system.
  The major advantage of the Tension-Leg elements is its relative low cost growing to increased water depths. The main limitation on the Tension-Leg partforms arises from dynamic inertia forces associated with the lateral oscillations of the platform

in waves. These become significant at water depths of about to 900-1000 meters. Figure 1.15.(a) shows an scheme of a typical Guyed tower offshore structure while Figure 1.15.(b) shows an scheme of a typical Tension-Leg offshore structure.

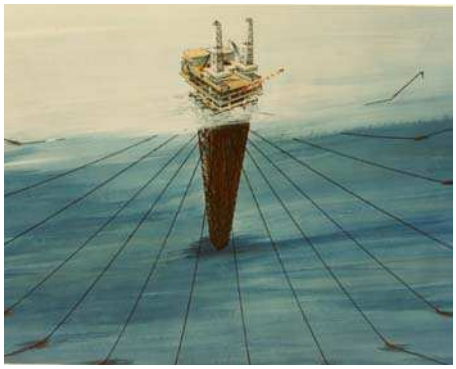

(a) Sketch of a typical Guyed tower offshore platform

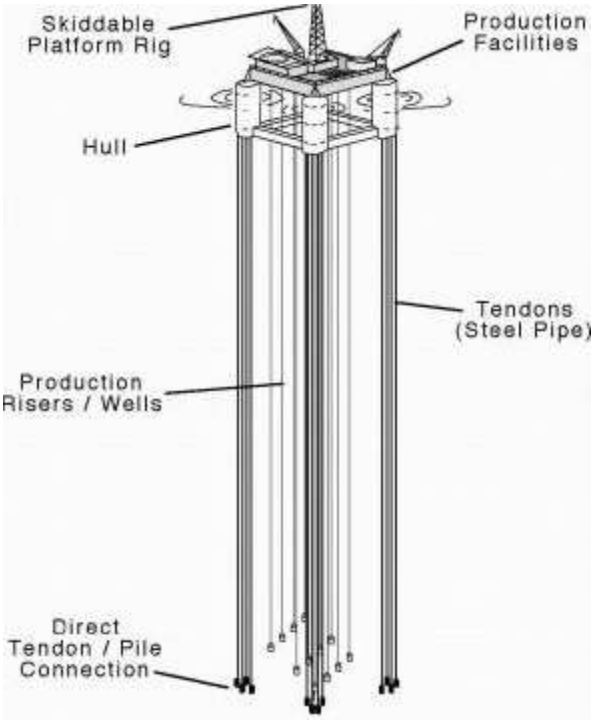

(b) Sketch of a typical Tension-Leg offshore platform

Figure 1.15: Sketch of a Guyer Tower and a Tension-Leg offshore platform

1.6 State of the art

The behaviour of most common offshore structures has been studied since two decades due to its potential application in the nowadays society and civil engineering. Many studies have proposed mathematical models and numerical techniques to properly describe specific characteristics and problems that floating structures are involved with. In the

following, a breaf description of the past work is done. After that, all the studies developed are arranged in three big groups. Finally, the needs that this thesis tries to fullfill are highlighted.

1.6.1 Literature review

The analysis of several floating or submerged pontoons of various cross-sections were studied by Williams [1985], Ratnayake and Christensen [1986] and Williams and Darwiche [1988]. Almost at the same time, the study of floating tire and tethered float arrays was carried out by Harms [1979] and Seymour and Hanes [1979]. These types of breakwaters have been successfully used in a variety of low energy applications. In addition, Jones and Raichlen [1979] have analyzed a sloping float barrier consisting of a row of moored floating pontoons or slabs inclined by ballasting or end-weighting. An experimental study of sloping float barriers has been carried out by Carver and Jensen [2004]. Rigid, flap-like breakwaters that extend the full water depth have been studied by Leach and Sollitt [1985] and Lee and McDougal [1986]. Recently, Kerper and McDougal [1991a] have extended this analysis to include the effects of structural bending and have also experimentally investigated the dynamic behavior of compliant floating breakwaters that extend over the full water depth (Kerper and McDougal [1991b]). Also, Sawaragi and Yasui [1989] have investigated the stresses in silt curtains in currents and waves and reported reasonable agreement between their experimental and theoretical results. In addition, A. N. Williams and McDougal studied the wave transmision and reflection characteristics of a flexible, floating breakwater consisting of a compliant, beam-like structure anchored to the sea bed and kept under tension by a small buoyancy chamber at the tip.

Other authors have focused their attention into the dynamic behaviour of offshore structures subjected to moving loads. As examples, Fry'ba [1971] widely studied the vibration problem of a single-span Euler-Bernoulli beam. Steele [b] and Steele [a] obtained the analytical solution of a Timoshenko beam on an elastic foundation with a moving load by means of Laplace transformation, where the effects of the material and nonlinearities were considered. With a similar approach, Steele solved the problem of a cylindrical shell subjected to traveling pressure waves C.R.. Suzuki investigated the dynamic behavior of a finite beam subjected to moving loads with acceleration by using the energy method and the Fresnel integral.

The foregoing description illustrates a few moving-load-induced vibration problems solved with the (closed-form) analytical method. In recent years, this kind of problem has usually been solved with numerical methods due to the grown of computers computation capacity. For example, Hino and Ananthanarayana [b] studied the dynamic responses of a nonuniform beam due to a moving load with the finite element method. By considering the geometric nonlinearity due to immovable supports, they studied the similar problems by using FEM, Yoshimura and Ananthanarayana, and Galerkin method Hino and Ananthanarayana [a]. For a multi-span nonuniform beam subjected to various moving loads with varying speeds, Wu and Dai solved the problem by using the transfer matrix method incorporated with the mode superposition method. For the similar vibra-

tion problem of a plate, Wu and Lai obtained a solution by means of the FEM.

With reference to cable systems, many studies have been conducted in this field. As an example, Martinelli and Perotti [2001] studied the nonlinear dynamic behaviour of elastic cable systems under wind excitation. Vincenzo Gattulli and Vestroni [2007] proposed some reduction thecniques to study high-dimensional numerical models of cables systems under turbulence loading. In addition, Vincenzo Gattulli and Vestroni [2004] studied the nonlinear behaviour of cables under harmonic loading by means of analytical and finite element models, testing the effectiveness of the analytical model in describing the response and the capability of the finite element models to catch the nonlinear dynamics of cables.

In the field of submerged floating tunnels, few studies have been conducted. As an example, Chunxia [2013] studied the dynamic problems that emerge in this kind of structures.

All the above-mentioned researches discuss the dynamic behavior of on-land structures and the material relating to the dynamic analysis of a floating body on water surface subjected to a moving load is limited. Wu JS [1996] may be considered the first paper concerning this topic, in which Wu and Sheu studied the dynamic response of an un-moored ship hull due to a moving load. Instead of moving loads, Lwin studied the dynamic response of a floating bridge due to wave excitations. Sheu investigated the coupled dynamic response of rigid-body motions and elastic vibrations of a pontoon (500 m length, 20 m width and 10 m depth) subjected to a moving load. Later, Wu and Shih modeled a hinge connected floating bridge and studied his elastic dynamic assuming small displacements, small strains and uncoupling the reaction due to the fluid and the deformation of the bodies. The model used was a Winkler description for the vertical interaction between the fluid and the bridge.

Adee [1975] developed a two-dimensional, linear, theoretical model to predict the performance of catamaran type FBWs in deep water and compared the results with measurements in a model tank and from a prototype installation in the field. Adee and Martin [1974] observed that roll motion does not contribute significantly to the wave transmission performance. An analysis of mooring lines was done starting from static equations of cable equilibrium and included as a restoring force term in the equations of motion for the breakwater Adee [1977]. They concluded that theory significantly under-predicts mooring forces. Sutko and Haden [1974] reported that a square cross-section gives slightly better wave reduction than a triangular, circular or trapezoidal section. Carver [1979] reported that uncrossing the anchor chains has a negligible effect and adding a vertical barrier-plate has little effect on wave-attenuation characteristics and, therefore, appears to be of questionable benefit in reducing transmitted energy. The transmission coefficient was found to be strongly dependent on relative breakwater length (the ratio of the characteristic dimensions of the breakwater to wave length) and weakly dependent on wave steepness.

Yamamoto and Ijima [1980] solved the problems of wave transformation and motions of elastically moored floating objects by direct use of Green's identity formula, and validated their solutions with the experimental investigations. They found that if the moor-

ing system is properly arranged, the wave attenuation by a small draft breakwater can be improved several times compared to the same FBW conventionally moored. Yamamoto [1981] conducted large-scale model tests in a large wave-tank on elastically moored floating breakwaters under the action of regular and random waves. The response of an elastically moored floating breakwater to random waves is reported as essentially the same as the response of the breakwater to periodic waves.

Johansson [1989] showed how the wave protection can be significantly improved by using a rectangular breakwater with a horizontal protruding bottom-plate rather than a rectangular one. This is confirmed both by potential theory(1) and by measurements. The response of a moored vessel to beam waves has been investigated by Isaacson and Wu [1995], based on an idealized representation of the nonlinear stiffness characteristics of the mooring system.

S. A. Sannasiraj and Sundaravadivelu dealed with a comprehensive study on the behaviour of pontoon-type floating breakwaters both theoretically and experimentally. The theoretical model was based on a two-dimensional finite element technique to evaluate the hydrodynamic coefficients and wave exciting forces on the floating structure. The stiffness of the slack mooring lines was modelled as linearized stiffness coefficients derived from basic catenary equations.

Dynamic response analysis of flexible structures induced by moving loads has been also studied by many researchers. L. [1999] has summarized various analytical models used in the vehicle-bridge coupled system. However, with the development of the computer and finite element method (FEM), the numerical method, in which the structures and vehicles can be described more accurately, was adapted by many authors. Wu JJ [2001], Yang YB [2001], Henchi K [1998], Thambiratnam D [1996] and Jones and Raichlen [1979] have developed models and studies using the finite element method that has gradually substituted the traditional analytical method. As a consequence, the methods used for the flexible structures are applied to the analyses of the dynamic responses of floating bridges subjected to moving loads.

Regarding the structural dynamic responses of a floating bridge subjected to moving loads, VJ. [1988] studied the dynamic response problems of a military floating bridge by Runge-Kutta method, where the initial conditions of the wheels, the variety of the speed and the separation between vehicles and bridge were taken into account. Wu JS [1996] investigated the coupled heave and pitch motions of a simplified non uniform ship hull floating on a still water surface and subjected to a moving load, considering the ship hull as a rigid body supported by an elastic foundation with distributed springs and dampers. Wu JS [1998] studied the elastic vibration of a partial-catenary-moored floating bridge (in still water) subjected to a moving load by taking the entire pontoon as a slender beam resting on an elastic foundation, and the influence of hydrodynamic forces as constant added mass, respectively. To simulate the characteristics of the rigid- or hinge-connected

(1) The potential theory is a model that considers the movement of a certain fluid as irrotational, allowing a simplification in the Navier-Stokes governing equations. In this theory, the velocity of a fluid can be expressed as the gradient of an scalar function, this is the reason why is called "potential theory".

floating bridge, the stiffness and mass matrices of two-node beam element with different nodal DOFs are derived. Hydroelastic theories, such as YS [1984] and Price WG [1985], have been applied to the design and research works related to marine structures for several decades (Chen XJ [2003b] and Chen XJ [2003a]) and they are also used to analyze the hydrodynamics of a floating bridge. Ueda S [1996b], Ueda S [1996a], Ueda S [1989], Oka S [2003] and Ikegami K [1989], have reported and obtained the numerical results verified experimentally by a large-scale detailed elastic model test in the wave tank. In these works the structure has been modeled by 3D linear finite elements and the fluid effect has been determined by the solution of 3D water wave problem on the basis of boundary element method taking the free surface, the water depth, the hull vibrations (the motions of the floating units) and the interaction among the floating units within the framework of the linear theory. In addition, Watanabe E [2003] have analyzed its hydroelastic behavior considering the memory effect to the wave damping term into consideration.

In the field of hydroelastic response of floating bridges, many authors have modeled it considering linear theories which can not deal with the nonlinear properties of the structure. Many authors, as Ertekin RC analyzed the hydroelastic responses of the mechanically interconnected military floating bridge under the combined effects of the stationary moving and/or static loads acted on the bridge deck, the current loads and other external loads, and found that the drag forces were comparatively smaller than the model tests due to the neglection of the drag components other than the skin friction and the form drag. Fleischer D [2004] calculated the hydroelastic vibrations of a beam with rectangular cross-section under the effect of a uniformly moving single axle vehicle by using the modal analysis and two-dimensional potential flow theory of the fluid and neglecting the effect of surface waves aside the beam. For most cases, the floating bridge was modeled as a simple beam without taking account of the nonlinearity of connectors and inertia effects of vehicles by assuming the loads as moving concentrated forces. In addition, Fu Shixiaoa and Conga [2005] developed a model considering the nonlinearities of the connectors and inertia effects of loads.

1.6.2 Current status and research needs

Many models and studies have been carried out by many authors around the world. Most of them studied the offshore structures using 3D finite element techniques. Others have emphasized more the analysis and develop models to study offshore structures composed by beam elements. The vast majority of them has focused in one of the following fields:

- **Linear static analysis**: Development of static models using 3D or beam finite element models to study the behaviour of offshore structures considering linear elastic behaviour and fluid-structure interaction within the framework of the linear theory. Most of the most common models for the fluid-structure interaction adopted modified beam on elastic foundation models (model traditionally used in the analysis of beam elements in contact with elastic soils).

- **Linear dynamics analysis**: Development of models using 3D, beam and shell finite elements to study the dynamic behaviour of the offshore structures. The

damping and inertia effects has been taken into account by several hydrodynamic theories (Potential theories, CFD,...).

- **Engineering characterizations**: Developing theoretical and experimental techniques to study the engineeristic characteristic of several offshore structures. For example, many works and papers discuss the design of floating breakwaters to optimize the wave transmission coefficients (variables that measures the ratio between the amplitute of the wave before and after impacting with the breakwater), which is the main property of a floating breakwater in terms of its capability to protect offshore facilities.

In conclusion, it seems that the studies and analysis developed in the past had left a gap that must be fullfilled. As it has been explained before, the need of a new finite element model able to study these structures in all the possible situations that in their service life could happen becomes evident. As a consequence, such new finite element will be an important tool to analyse floating structures modeled as beam elements and will provide the basis for further studies and developments in this field, such as generalization to study the nonlinear dynamics of offshore structures.

1.7 Scope and objectives of the thesis

As it has been shown, there are many different offshore structures that are suitable for its analysis. Besides, most of them are built as a composition of a large number of elements that can be modeled as beam, truss or cable elements. This can be seen in the Template structure for example, where the substructure that supports the main platform can be made of truss or beam elements in a compact frame where the platform can rest. In addition, Floating breakwaters can be modelled as monodimensional frame system and its anchorage system considered as tensile/cable structure (in case it is anchored to the seafloor by cables) or as another frame system (in case it is anchored to the seabed with rigid bars). The same happens with the floating bridges, where all the considerations made with the floating breakwaters in terms of structural modellization can be assumed for this type of structures.

Due to the wide range of floating structures available, it is important to beware in order to develop a rigorous study. From the engineeristic point of view, all the floating structures available are designed to operate in different zones and situations and, as a consequence, the tools that have to be used to analyse them vary from one to other. For this reason, this thesis will be mainly focused in the study of two specific floating structures: the floating breakwaters and the floating bridges.

The reason is because their similarity in terms of structural tipology, areas where they operate, loads which are subjected,...etc. Focusing on these two kind of structures we will be able to offer a better and more accurate description of them and their behaviour and to develop better tools for their analysis.

Therefore, the goals of this thesis are:

- **Static characterization**: The main goal is to completely characterize the static behaviour of offshore structure partially or totally in contact with an unmoved fluid. Many authors have focused their attention in analysis where the structural model and the actions due to the fluid are considered uncoupled and independent. Actually, offshore structures have a great nonlinearity derived from the contact with the fluid. From an intuitive point of view, one can see that the loads produced by the fluid into the structures are strongly dependant on the deformative field. This is an assumption that many studies have considered negligible performing analysis in the field of small displacements and strains in order to be able to uncouple the behaviour of the structure and to consider the effects of the fluid constant during the deformative path.
- **New Finite Element formulation**: The secondary goal is to formulate and present an innovative finite element formulation that unifies the behaviour of beam structures in contact with an static fluid. The nowadays finite element models have been formulated as a modification of the beam on elastic foundation model (essentially used in the study of beam elements in contact with elastic soil). This model, which has provided great results in all the applications considering small displacements, has important limitations when the engineer is required to further analyse the behaviour of offshore structures at ultimate limit state or when large displacements have to be considered. In these cases, better and more sophisticated tools are required to completely analyse and understand the nonlinearities of the structure and to predict the deformative path in all the possible situations the structure will have to face during it's service life.

1.8 Methodology

These aims require the study of the most essential components of each part of the structure.

In the case of beam elements, a deep study about the interaction between the element and the fluid at the sectional level will be developed. A thorough study will be carried out to understand the interaction between 2D bodies (sections in our case) and a generic fluid. This will be studied in terms of the loads produced by the fluid to the section and will be expressed in terms of the resultant forces in the main plane of the section and its perpendicular axis.

To better understand the concept of "Section-Fluid interaction" let us consider a sectional element as the one in figure 1.16. If the section is oriented somehow in the space and is partially or totally under the fluid, it is possible to define the following forces and moments:

$$\boldsymbol{F} = \left\{ \begin{array}{c} F_x \\ F_y \\ F_z \end{array} \right\} = \left\{ \begin{array}{c} \int_\Omega \boldsymbol{P_\Omega}^T \boldsymbol{x'} d\Omega \\ \int_\Gamma \boldsymbol{P_\Gamma}^T \boldsymbol{y'} d\Gamma \\ \int_\Gamma \boldsymbol{P_\Gamma}^T \boldsymbol{z'} d\Gamma \end{array} \right\}; \quad \boldsymbol{M} = \left\{ \begin{array}{c} M_x \\ M_y \\ M_z \end{array} \right\} = \left\{ \begin{array}{c} \int_\Gamma \left(\boldsymbol{v_\Gamma} \times \boldsymbol{P_\Gamma}\right)^T \boldsymbol{x'} d\Gamma \\ \int_\Omega \left(\boldsymbol{v_\Omega} \times \boldsymbol{P_\Omega}\right)^T \boldsymbol{y'} d\Omega \\ \int_\Omega \left(\boldsymbol{v_\Omega} \times \boldsymbol{P_\Omega}\right)^T \boldsymbol{z'} d\Omega \end{array} \right\}$$

$$\boldsymbol{P_\Gamma} = -\gamma_f h \boldsymbol{n} \quad \boldsymbol{P_\Omega} = \gamma_f h \boldsymbol{x'}$$

where the vectors $\boldsymbol{v_\Gamma}$ and $\boldsymbol{v_\Omega}$ are the vectors that define the position of the load point with respect to the center of gravity of the section in the boundary (Γ) and area (Ω). See figure 1.16 for more details.

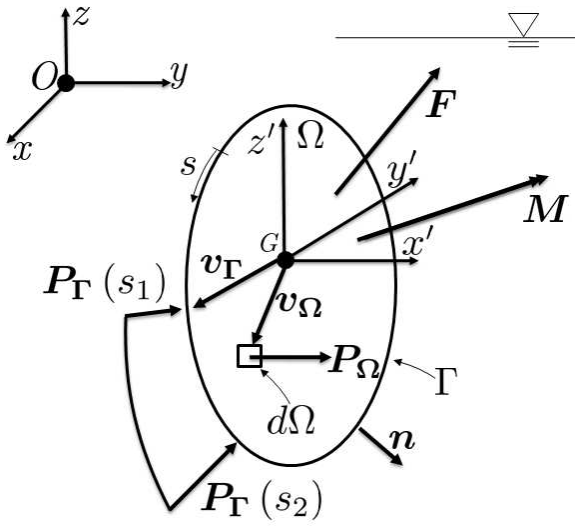

Figure 1.16: The 6 forces and moments acting on a section element due to the hydrostatic pressure.

The characterization of the interaction between the elements of the section and the fluid will be made by the computation and the study of these six components. Indeed, these six forces and moments completely define the stress state of the section inside the fluid and their study as a function of the position and orientation of the section are the main key of this thesis. The "constitutive equations" for a specific section in contact with a fluid will be formulated in further chapters.

The concept of constitutive equations for a specific section is based on the well-known formulation in the mechanic of materials, where stresses are expressed in terms of strains by mathematical equations (constitutive equations of the material). In this case, the study of a section in contact with a fluid, the role of stresses will be played by the resultant forces and moments that the fluid produces to the section while the position (position of the center of gravity of the section $\boldsymbol{v_G}$) and orientation (characterized by a rotation matrix that defines the local axis of the section in a 3D space $\boldsymbol{M_R}$) will play the role of strains. Table 1.1 shows the equivalence between these two concepts.

Stresses	Strains	Resultant efforts	Position and Orientation
$\boldsymbol{\sigma}$	$\boldsymbol{\varepsilon}$	$\boldsymbol{F},\ \boldsymbol{M}$	$\boldsymbol{v_G},\ \boldsymbol{M_R}$
Constitutive equations for materials		Constitutive equations for sections	
$\boldsymbol{\sigma}(\boldsymbol{\varepsilon})$		$\boldsymbol{F}(\boldsymbol{v_G}, \boldsymbol{M_R})\ \ \boldsymbol{M}(\boldsymbol{v_G}, \boldsymbol{M_R})$	

Table 1.1: Correspondance between the formulation of the constitutive equations for materials and the formulation of these for a section.

Once the study and formulation of the constitutive equations for any section is done, the next step will be the use of this equations in a new finite element beam model to study floating structures. As it can be seen, beam elements are the bodies that result from the movement of a cross-section (varying cross-section in general) along an axis defining the beam. The inmediate consequence is that the properties and equations that describe the interaction between the cross-section of the element and the fluid can, somehow, be translated to take into account the interaction between beam elements and the fluid. The procedure and all the equations that govern this complex problem will be explained in the following chapter of the thesis.

The following tools must be developed and the following sub goals must be achieved.

- Study of the interaction between 2D bodies in contact with an unmoved fluid.
- Characterization of a section: in terms of its mechanical and geometric properties and it's fluid-section constituve equations.
- Modify the 2D beam finite element based on the Winkler's approach for the description of elastic foundations. The stiffness of the elastic soil will be substituted by an equivalent stiffness produced by the fluid and will be defined in terms of the constitutive equations of the element's cross-section.
- Formulate a completely new 2D beam finite element model to study beam structures partially or totally surrounded by a fluid considering small displacements and small strains. This model will be tested with the previous one.
- Develop a 2D truss/cable finite element model to study cable structures partially or totally surrounded by a fluid considering big displacements and small strains.
- Formulate a completely new 3D beam finite element to study floating structures surrounded by a fluid considering small displacements and small strains.
- Formulate a completely new 3D beam finite element to study floating structures and the interaction with the surrounding fluid considering big displacements and small strains.
- Develop a 3D beam finite element model to study beam structures partially or totally surrounded by a fluid considering big displacements and big strains.
- Develop a 3D truss finite element model to study cable structures partially or totally surrounded by a fluid considering big displacements and big strains.
- Develop a contact element to study the interaction between cable structures used in the anchorage system of the floating structures and the seabed.

I

NONLINEAR ANALYSIS OF FRAME AND CABLE STRUCTURES

2 Basic concepts of nonlinear mechanics

Structural analysis is the tool to determine the displacements, strains and stresses of a given structure under certain loading conditions.

Among different types of structural analysis, linear elastic analysis is the most common tool for the nowadays works in the civil engineering field. This is due to the fact that most of the projects require structures that should have an elastic behaviour. Most common applications require that the entire structure should not exceed the elastic linear behaviour since, otherwise, a damage of the structure occurs or some underisable phenomena may occur (such as stability problems).

Although the linear elastic analysis is the most used tool, other theories and approaches are required in the analysis of specific phenomena where the linear analysis loses its applicability since it is not able to catch the nonlinear nature of these structures. In particular, a wide range of applications require to take into account properly the nonlinear behavior.

Two classes of nonlinearity can appear in a structure: the *material nonlinearity* and the *geometrical nonlinearity*. The first one is the nonlinearity due to the materials that compose the structure and is produced by changes in the physical response of the material for increasing deformations and it appears in the form of path-dependent and nonunique constitutive laws. The second one represents all the eefects that finite deformations and displacements induce on the global stiffness of the structure under applied loads.

The nonlinear analysis requires that the equation have to be written in the deformed configuration, which a priory is unknown. Only if the displacements and the strains can be considered small the deformed and the undeformed configurations are almost the same and the equilibrium equations can be written in the undeformed configuration.

The analysis performed in this thesis will devoted to *framed structures*. Framed structures are structures composed by elements that are long compared to the dimension of their section.

2.1 Kinematic model

There are two different formulations that can be used in the structural analysis, the *Eulerian formulation* and the *Lagrangian formulation*. The first one considers the *spacial coordinates* (the coordinates associated with the undeformed body) as the reference system to describe the motion of the structure. The second one considers the *material coordinates* as the reference system.

To briefly describe the theory behind the Eulerian approach let's consider a tridimensional body in a certain initial configuration as the one in figure 2.1. The position of a certain point of the continuum in a certain configuration ${}^t\boldsymbol{C}$ is defined as the vector ${}^t\boldsymbol{X} = \left[\begin{array}{ccc} {}^tx_1 & {}^tx_2 & {}^tx_3 \end{array}\right]$ and is called *material coordinate* of the point $\boldsymbol{P}$.

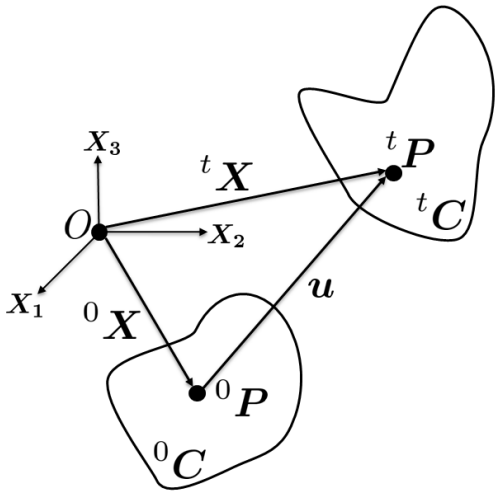

Figure 2.1: Sketch of the procedure to characterize the Eulerian formulation

To completely characterize the position of the point $\boldsymbol{P}$ is convenient to define an ortogonal reference system with the vectors $\{\boldsymbol{X_1}, \boldsymbol{X_2}, \boldsymbol{X_3}\}$ that defines the spacial coordinates. If in the initial configuration the material and spacial coordinates coincide, it can be ensured that the coordinates ${}^t_0\boldsymbol{X}$ represent the coordinates of any point of the domain refered to the initial configuration ${}^0\boldsymbol{C}$ at the time t.

Let us consider the movement of the body from the initial configuration to another configuration called ${}^t\boldsymbol{C}$ in a certain time t. The point $\boldsymbol{P}$ will move from its initial configuration ${}^0\boldsymbol{P}^{(1)}$ to a new one ${}^t_0\boldsymbol{P}^{(2)}$. Considering the instants $\tau : (0 \leq \tau \leq t)$, the movement of the body is characterized by the dependance between $\boldsymbol{X}$ and ${}^t\boldsymbol{X}$ as

(1) The reader is reminded that the left upperindex will be omitted from now on when the variable is defined in the initial configuration

(2) The reader is reminded that the left subscript will be omitted from now on when the variable is refered to the initial configuration

$$\boldsymbol{X} = \boldsymbol{X}\left({}^{\tau}\boldsymbol{X}, \tau\right)$$

and the inverse of this relation must exist and be univocaly determined. Such condition is equivalent to define the Jacobian matrix $\boldsymbol{J}$ as

$$\boldsymbol{J} = \frac{\partial \boldsymbol{X}\left({}^{\tau}\boldsymbol{X}, \tau\right)}{\partial {}^{\tau}\boldsymbol{X}};\ \forall \tau \in (0, t)$$

and that the determinant of the jacobian be greater than zero:

$$|\boldsymbol{J}| > 0$$

Once the vectors ${}^{0}\boldsymbol{P}$ and ${}^{t}\boldsymbol{P}$ (positions of the point $\boldsymbol{P}$ in the configurations ${}^{0}\boldsymbol{C}$ and ${}^{t}\boldsymbol{C}$) have been defined, the *displacement vector* is identified as:

$${}^{t}\boldsymbol{u} = {}^{t}\boldsymbol{X} - \boldsymbol{X} \tag{2.1}$$

The Eulerian approach does not have a very important role in the nonlinear structural analysis. Nevertheless, it has found a great range of applicability in the fluid mechanics field, where unmoved volumes are defined in the domain.

The Lagrangian approach is particularly suitable to be used in the nonlinear step-by-step analysis because one is interested in the deformation of each point during the load procedure. The first step is to divide the loading path of a certain body into several equilibrium configurations: the initial undeformed configuration (${}^{0}\boldsymbol{C}$), the last known configuration (${}^{1}\boldsymbol{C}$), where all the variables such as displacements, strains and stresses are known and the unknown configuration (${}^{2}\boldsymbol{C}$). The problem, is to develop an incremental theory able to define all the variables of the configuration ${}^{2}\boldsymbol{C}$, assuming that in the configuration ${}^{1}\boldsymbol{C}$ the load has been increased by a small amount.

It is very important to understand that, even if the relative displacements from configurations ${}^{2}\boldsymbol{C}$ and ${}^{1}\boldsymbol{C}$ are considered small, the accumulated deformation of the body from ${}^{0}\boldsymbol{C}$ to ${}^{2}\boldsymbol{C}$ can be arbitraly large.

In the Lagrangian approach, depending on the reference configuration that is used, ${}^{0}\boldsymbol{C}$ or ${}^{1}\boldsymbol{C}$ to compute the subsequent configuration ${}^{2}\boldsymbol{C}$, there are two types of formulation: the *Total Lagrangian formulation*, which adopts the configuration ${}^{0}\boldsymbol{C}$ as the reference one and the *Updated Lagrangian formulation*, which considers ${}^{1}\boldsymbol{C}$ as the reference configuration.

2.2 Description of strains

Let us consider three equilibrium positions that help in the description of the movement according to several formulations (Eulerian or Lagrangian formulations). It is known that the strains of a body are intrinsically related with the gradient of the displacements. It can be shown that the strains can be formulated according to different reference systems and, as a consequence, they change depending on the formulation adopted. For simplicity,

only the variables related to the Lagrangian formulation will be defined.

Consider the gradient, as a scalar operator, of a certain function referred to the orthogonal cartesian axis corresponding to the one in the initial configuration. This gradient is called *material gradient* because it expresses the derivative of a certain function with respect to the reference system of the initial configuration.

$$\boldsymbol{\nabla_m} = \left[\begin{array}{ccc} \dfrac{\partial}{\partial \boldsymbol{X}_1} & \dfrac{\partial}{\partial \boldsymbol{X}_2} & \dfrac{\partial}{\partial \boldsymbol{X}_3} \end{array} \right]^T \tag{2.2}$$

Imagine now a certain infinitesimal segment in the initial configuration that has changed during its deformation to the following configuration. The variation of the segment length and orientation can be expressed in terms of the initial configuration, that is:

$${}^t\boldsymbol{dX}_i = \frac{\partial {}^t\boldsymbol{X}_i}{\partial \boldsymbol{X}_j}\boldsymbol{dX}_j = {}^t\boldsymbol{F}_{ij}\boldsymbol{dX}_j \rightarrow {}^t\boldsymbol{dX} = {}^t\boldsymbol{F}\boldsymbol{dX} \tag{2.3}$$

where the Einstein notation has been used to express the sum in the index "j" and the *Lagrangian Deformation Gradient* can be defined as the matrix that has in its components the derivative of the spatial coordinates with respect the material coordinates.

$${}^t\boldsymbol{F}_{ij} = \frac{\partial {}^t\boldsymbol{X}_i}{\partial \boldsymbol{X}_j};\ \boldsymbol{F} = {}^t\boldsymbol{X} \otimes \boldsymbol{\nabla}_{\boldsymbol{m}}^T \tag{2.4}$$

There are many other ways to measure the movement of a continuum. Consider, for example, the variation of the displacements in terms of the position of a certain point (for simplicity the path that the point $\boldsymbol{P}$ performs during the deformative process in figure 2.1). The relation between displacements and position is written in equation 2.1 and its variation can be expressed in terms of the material coordinates as:

$${}^t\boldsymbol{du} = \frac{\partial {}^t\boldsymbol{u}}{\partial \boldsymbol{X}}\boldsymbol{dX} \tag{2.5}$$

Using equation 2.1, the derivative[(3)] of the displacement vector with respect the material coodinates can be written as

$$\frac{\partial {}^t\boldsymbol{u}}{\partial \boldsymbol{X}} = \frac{\partial {}^t\boldsymbol{X}}{\partial \boldsymbol{X}} - \frac{\partial \boldsymbol{X}}{\partial \boldsymbol{X}} = {}^t\boldsymbol{F} - \boldsymbol{I} = {}^t\boldsymbol{J} \tag{2.6}$$

where the variable $\boldsymbol{J}$ is called *Lagrangian Displacement Gradient* and characterizes the variation of the displacements in terms of the material coordinates.

$${}^t\boldsymbol{J}_{ij} = {}^t\boldsymbol{F}_{ij} - \boldsymbol{\delta}_{ij};\ {}^t\boldsymbol{J} = \boldsymbol{u} \otimes \boldsymbol{\nabla}_{\boldsymbol{m}} = {}^t\boldsymbol{F} - \boldsymbol{I} \tag{2.7}$$

[(3)] The derivative of a vector $\boldsymbol{a}$ with respect a vector $\boldsymbol{b}$ is defined as: $\left[\dfrac{\partial \boldsymbol{a}}{\partial \boldsymbol{b}}\right]_{ij} = \dfrac{\partial \boldsymbol{a}_i}{\partial \boldsymbol{b}_j}$

2.2.1 Green-Lagrange strain tensor

Consider the figure 2.2, where a segment PQ is depicted in the three configurations previously defined for the nonlinear analysis.

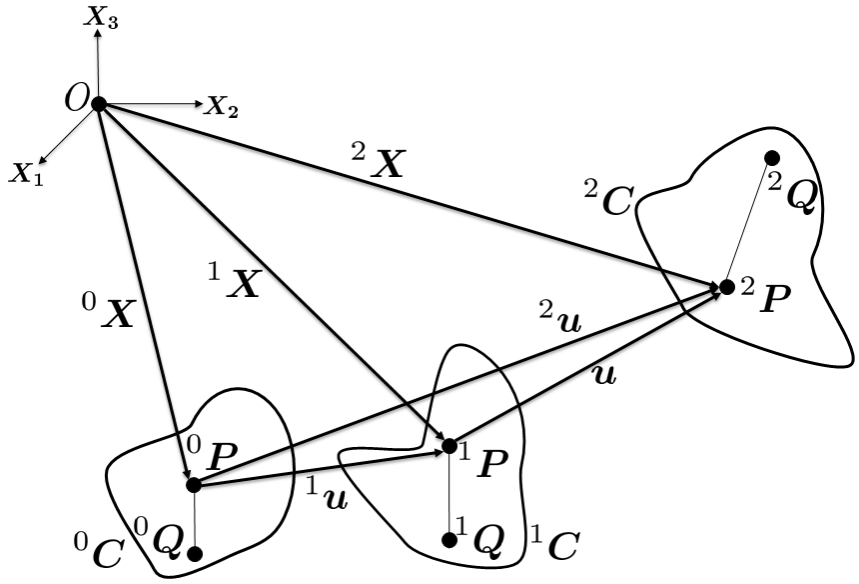

Figure 2.2: The movement of the body in the 3 equilibrium configurations

ds is defined as the distance between these two points in the initial configuration and ${}^t ds$ as the length between these two points in a certain configuration ${}^t\boldsymbol{C}$. Considering equation 2.3, the value of this two lengths can be computed as follows:

$$\begin{gathered} {}^t ds^2 - ds^2 = {}^t\boldsymbol{dX}^{Tt}\boldsymbol{dX} - \boldsymbol{dX}^T\boldsymbol{dX} = \boldsymbol{dX}^{Tt}\boldsymbol{F}^{Tt}\boldsymbol{F}\boldsymbol{dX} - \boldsymbol{dX}^T\boldsymbol{dX} \\ \boldsymbol{dX}^T \underbrace{\left({}^t\boldsymbol{F}^{Tt}\boldsymbol{F} - \boldsymbol{I}\right)}_{2\boldsymbol{E}} \boldsymbol{dX} = 2\boldsymbol{dX}^{Tt}\boldsymbol{E}\boldsymbol{dX} \end{gathered}$$

where the variable ${}^t\boldsymbol{E}$ is called the *Green-Lagrange's Strain Tensor* evaluated in the configuration ${}^t\boldsymbol{C}$ and its expression is

$$ {}^t\boldsymbol{E} = \frac{1}{2}\left({}^t\boldsymbol{F}^{Tt}\boldsymbol{F} - \boldsymbol{I}\right) \tag{2.8}$$

Sometimes, it is convenient to have the Green-Lagrange's strain tensor expressed in terms of the displacements. Considering equation 2.6, it can be written as

$$ {}^t\boldsymbol{E} = \frac{1}{2}\left({}^t\boldsymbol{F}^{Tt}\boldsymbol{F} - \boldsymbol{I}\right) = \frac{1}{2}\left(\left(\boldsymbol{I} + {}^t\boldsymbol{J}\right)^T\left(\boldsymbol{I} + {}^t\boldsymbol{J}\right) - \boldsymbol{I}\right) = \frac{1}{2}\left({}^t\boldsymbol{J} + {}^t\boldsymbol{J}^T + {}^t\boldsymbol{J}^{Tt}\boldsymbol{J}\right) \tag{2.9}$$

Once we have the Green-Lagrange's strain tensor in terms of the Lagrangian displacements gradient, the expression can be modified such as

$$\begin{aligned} {}^t\boldsymbol{E} &= \frac{1}{2}\left(\frac{\partial^t\boldsymbol{u}}{\partial\boldsymbol{X}} + \frac{\partial^t\boldsymbol{u}}{\partial\boldsymbol{X}}^T + \frac{\partial^t\boldsymbol{u}}{\partial\boldsymbol{X}}^T\frac{\partial^t\boldsymbol{u}}{\partial\boldsymbol{X}}\right) \\ {}^t\boldsymbol{E}_{ij} &= \frac{1}{2}\left(\frac{\partial^t\boldsymbol{u}_i}{\partial\boldsymbol{X}_j} + \frac{\partial^t\boldsymbol{u}_j}{\partial\boldsymbol{X}_i} + \frac{\partial^t\boldsymbol{u}_k}{\partial\boldsymbol{X}_i}\frac{\partial^t\boldsymbol{u}_k}{\partial\boldsymbol{X}_j}\right) \end{aligned} \tag{2.10}$$

2.2.2 Green-Lagrange strain increment tensor

In an incremental formulation, the difference between the Green-Lagrange's strain tensor evaluated in two different configurations ($^1\boldsymbol{C}$ and $^2\boldsymbol{C}$) is called the *Green-Lagrange Strain Increment Tensor*. Using equation 2.3:

$$\begin{gathered} {}^2ds^2 - {}^1ds^2 = {}^2\boldsymbol{dX}^{T\,2}\boldsymbol{dX} - {}^1\boldsymbol{dX}^{T\,1}\boldsymbol{dX} = \left({}^2\boldsymbol{F}\boldsymbol{dX}\right)^T\left({}^2\boldsymbol{F}\boldsymbol{dX}\right) - \left({}^1\boldsymbol{F}\boldsymbol{dX}\right)^T\left({}^1\boldsymbol{F}\boldsymbol{dX}\right) \\ = \\ \boldsymbol{dX}^{T\,2}\boldsymbol{F}^{T\,2}\boldsymbol{F}\boldsymbol{dX} - \boldsymbol{dX}^{T\,1}\boldsymbol{F}^{T\,1}\boldsymbol{F}\boldsymbol{dX} = \boldsymbol{dX}^T\underbrace{\left({}^2\boldsymbol{F}^{T\,2}\boldsymbol{F} - {}^1\boldsymbol{F}^{T\,1}\boldsymbol{F}\right)}_{2\boldsymbol{E}}\boldsymbol{dX} \end{gathered} \tag{2.11}$$

The Green-Lagrange strain increment tensor[(4)] can be written as:

$$\boldsymbol{E} = \frac{1}{2}\left({}^2\boldsymbol{F}^{T\,2}\boldsymbol{F} - {}^1\boldsymbol{F}^{T\,1}\boldsymbol{F}\right) \tag{2.12}$$

As done before, the Green-Lagrange strain increment tensor can be written as a functions of the displacement gradient. Using equation 2.6

$$\begin{gathered} 2\boldsymbol{E} = {}^2\left(\boldsymbol{J}+\boldsymbol{I}\right)^{T\,2}\left(\boldsymbol{J}+\boldsymbol{I}\right) - {}^1\left(\boldsymbol{J}+\boldsymbol{I}\right)^{T\,1}\left(\boldsymbol{J}+\boldsymbol{I}\right) \\ = \\ \frac{\partial^2\boldsymbol{u}}{\partial\boldsymbol{X}}^T - \frac{\partial^1\boldsymbol{u}}{\partial\boldsymbol{X}}^T + \frac{\partial^2\boldsymbol{u}}{\partial\boldsymbol{X}} - \frac{\partial^1\boldsymbol{u}}{\partial\boldsymbol{X}} + \frac{\partial^2\boldsymbol{u}}{\partial\boldsymbol{X}}^T\frac{\partial^2\boldsymbol{u}}{\partial\boldsymbol{X}} - \frac{\partial^1\boldsymbol{u}}{\partial\boldsymbol{X}}^T\frac{\partial^1\boldsymbol{u}}{\partial\boldsymbol{X}} \\ = \\ \frac{\partial\boldsymbol{u}}{\partial\boldsymbol{X}}^T + \frac{\partial\boldsymbol{u}}{\partial\boldsymbol{X}} + \frac{\partial\left({}^1\boldsymbol{u}+\boldsymbol{u}\right)}{\partial\boldsymbol{X}}^T\frac{\partial\left({}^1\boldsymbol{u}+\boldsymbol{u}\right)}{\partial\boldsymbol{X}} \\ = \\ \frac{\partial\boldsymbol{u}}{\partial\boldsymbol{X}}^T + \frac{\partial\boldsymbol{u}}{\partial\boldsymbol{X}} + \frac{\partial^1\boldsymbol{u}}{\partial\boldsymbol{X}}^T\frac{\partial^1\boldsymbol{u}}{\partial\boldsymbol{X}} + \frac{\partial^1\boldsymbol{u}}{\partial\boldsymbol{X}}^T\frac{\partial\boldsymbol{u}}{\partial\boldsymbol{X}} + \frac{\partial\boldsymbol{u}}{\partial\boldsymbol{X}}^T\frac{\partial^1\boldsymbol{u}}{\partial\boldsymbol{X}} + \frac{\partial\boldsymbol{u}}{\partial\boldsymbol{X}}^T\frac{\partial\boldsymbol{u}}{\partial\boldsymbol{X}} \end{gathered}$$

where it has been considered that the displacements in the configuration $^2\boldsymbol{C}$ can be written as $^2\boldsymbol{u} = {}^1\boldsymbol{u} + \boldsymbol{u}$.

The expression can be divided in two parts, the linear and the nonlinear component.

$$\begin{gathered} \boldsymbol{E} = \boldsymbol{e} + \boldsymbol{\eta} \\ \boldsymbol{E}_{ij} = \boldsymbol{e}_{ij} + \boldsymbol{\eta}_{ij} \end{gathered} \tag{2.13}$$

$$\begin{gathered} \boldsymbol{e} = \frac{1}{2}\left(\frac{\partial\boldsymbol{u}}{\partial\boldsymbol{X}}^T + \frac{\partial\boldsymbol{u}}{\partial\boldsymbol{X}} + \frac{\partial\boldsymbol{u}}{\partial\boldsymbol{X}}^T\frac{\partial^1\boldsymbol{u}}{\partial\boldsymbol{X}} + \frac{\partial^1\boldsymbol{u}}{\partial\boldsymbol{X}}^T\frac{\partial\boldsymbol{u}}{\partial\boldsymbol{X}}\right) \\ \boldsymbol{e}_{ij} = \frac{1}{2}\left(\frac{\partial\boldsymbol{u}_i}{\partial\boldsymbol{X}_j} + \frac{\partial\boldsymbol{u}_j}{\partial\boldsymbol{X}_i} + \frac{\partial^1\boldsymbol{u}_k}{\partial\boldsymbol{X}_j}\frac{\partial\boldsymbol{u}_k}{\partial\boldsymbol{X}_j} + \frac{\partial\boldsymbol{u}_k}{\partial\boldsymbol{X}_j}\frac{\partial^1\boldsymbol{u}_k}{\partial\boldsymbol{X}_j}\right) \end{gathered} \tag{2.14}$$

(4) It is reminded to the reader that when the upperleft index in a variable $\boldsymbol{a}$ is omitted means that it is refered as the increment of the variable $\boldsymbol{a}$ from configuration $^1\boldsymbol{C}$ to configuration $^2\boldsymbol{C}$: $\boldsymbol{a} \doteq {}^2\boldsymbol{a} - {}^1\boldsymbol{a}$

$$\begin{aligned}\boldsymbol{\eta} &= \frac{1}{2}\left(\frac{\partial \boldsymbol{u}}{\partial \boldsymbol{X}}^T \frac{\partial \boldsymbol{u}}{\partial \boldsymbol{X}}\right)\\ \boldsymbol{\eta}_{ij} &= \frac{1}{2}\left(\frac{\partial \boldsymbol{u}_k}{\partial \boldsymbol{X}_i}\frac{\partial \boldsymbol{u}_k}{\partial \boldsymbol{X}_j}\right)\end{aligned} \tag{2.15}$$

2.2.3 Euler Strain tensor

Sometimes is useful to define the strain tensor accordingly to the reference system in the configuration ${}^2\boldsymbol{C}$, this is called *Euler Strain tensor*.

$$\begin{aligned}{}^2ds^2 - {}^1ds^2 = {}^2\boldsymbol{dX}^T{}^2\boldsymbol{dX} - {}^1\boldsymbol{dX}^T{}^1\boldsymbol{dX}^T = {}^2\boldsymbol{dX}^T{}^2\boldsymbol{dX} - \left(\frac{\partial^1\boldsymbol{X}}{\partial^2\boldsymbol{X}}{}^2\boldsymbol{dX}\right)^T\left(\frac{\partial^1\boldsymbol{X}}{\partial^2\boldsymbol{X}}{}^2\boldsymbol{dX}\right)\\ =\\ {}^2\boldsymbol{dX}^T\underbrace{\left(\boldsymbol{I} + \frac{\partial^2\boldsymbol{X}}{\partial^1\boldsymbol{X}}^T\frac{\partial^2\boldsymbol{X}}{\partial^1\boldsymbol{X}}\right)}_{{}_2\boldsymbol{E}}{}^2\boldsymbol{dX}\end{aligned} \tag{2.16}$$

$$\begin{aligned}{}_2\boldsymbol{E} &= \frac{1}{2}\left(\boldsymbol{I} + \frac{\partial^2\boldsymbol{X}}{\partial^1\boldsymbol{X}}^T\frac{\partial^2\boldsymbol{X}}{\partial^1\boldsymbol{X}}\right)\\ {}_2\boldsymbol{E}_{ij} &= \frac{1}{2}\left(\boldsymbol{\delta}_{ij} + \frac{\partial^1\boldsymbol{X}_k}{\partial^2\boldsymbol{X}_i}\frac{\partial^1\boldsymbol{X}_k}{\partial^2\boldsymbol{X}_j}\right)\end{aligned} \tag{2.17}$$

which, as usual, can be expressed in terms of the displacements considering the equality ${}^1\boldsymbol{X} = {}^2\boldsymbol{X} - \boldsymbol{u}$

$$2_2\boldsymbol{E} = \boldsymbol{I} - \frac{\partial\left({}^2\boldsymbol{X} - \boldsymbol{u}\right)}{\partial^2\boldsymbol{X}}^T\frac{\partial\left({}^2\boldsymbol{X} - \boldsymbol{u}\right)}{\partial^2\boldsymbol{X}} = \frac{\partial \boldsymbol{u}}{\partial^2\boldsymbol{X}} + \frac{\partial \boldsymbol{u}}{\partial^2\boldsymbol{X}}^T - \frac{\partial \boldsymbol{u}}{\partial^2\boldsymbol{X}}^T\frac{\partial \boldsymbol{u}}{\partial^2\boldsymbol{X}} \tag{2.18}$$

Therefore,

$$\begin{aligned}{}_2\boldsymbol{E} &= {}_2\boldsymbol{e} + {}_2\boldsymbol{\eta}\\ {}_2\boldsymbol{E}_{ij} &= {}_2\boldsymbol{e}_{ij} + {}_2\boldsymbol{\eta}_{ij}\end{aligned} \tag{2.19}$$

$$\begin{aligned}{}_2\boldsymbol{e} &= \frac{1}{2}\left(\frac{\partial \boldsymbol{u}}{\partial^2\boldsymbol{X}} + \frac{\partial \boldsymbol{u}}{\partial^2\boldsymbol{X}}^T\right)\\ {}_2\boldsymbol{e}_{ij} &= \frac{1}{2}\left(\frac{\partial \boldsymbol{u}_i}{\partial^2\boldsymbol{X}_j} + \frac{\partial \boldsymbol{u}_j}{\partial^2\boldsymbol{X}_i}\right)\end{aligned} \tag{2.20}$$

$$\begin{aligned}{}_2\boldsymbol{\eta} &= -\frac{1}{2}\left(\frac{\partial \boldsymbol{u}}{\partial^2\boldsymbol{X}}^T\frac{\partial \boldsymbol{u}}{\partial^2\boldsymbol{X}}\right)\\ {}_2\boldsymbol{\eta}_{ij} &= -\frac{1}{2}\left(\frac{\partial \boldsymbol{u}_k}{\partial^2\boldsymbol{X}_i}\frac{\partial \boldsymbol{u}_k}{\partial^2\boldsymbol{X}_j}\right)\end{aligned} \tag{2.21}$$

2.2.4 Updated Green-Lagrange strain increment tensor

The definition of the Green-Lagrange strain increment tensor is very useful in the total Lagrangian formulation but, addopting an incremental approach, a new definition is required. The same approach can be used to define the tensor with respect the configuration ${}^1\boldsymbol{C}$ using equation 2.16 and considering the equality ${}^2\boldsymbol{dX} = \frac{\partial^2 \boldsymbol{X}}{\partial^1 \boldsymbol{X}} {}^1\boldsymbol{dX}$ as follows:

$$ {}^2ds^2 - {}^1ds^2 = {}^1\boldsymbol{dX}^T \underbrace{\left(\frac{\partial^2 \boldsymbol{X}}{\partial^1 \boldsymbol{X}}^T \frac{\partial^2 \boldsymbol{X}}{\partial^1 \boldsymbol{X}} - \boldsymbol{I} \right)}_{{}_2{}_1\boldsymbol{E}} {}^1\boldsymbol{dX} \tag{2.22} $$

The expression of the tensor in terms of the displacements gradient can be deduced considering the equation ${}^2\boldsymbol{X} = {}^1\boldsymbol{X} + \boldsymbol{u}$:

$$ \begin{gathered} {}_2{}_1\boldsymbol{E} = \frac{\partial^2 \boldsymbol{X}}{\partial^1 \boldsymbol{X}}^T \frac{\partial^2 \boldsymbol{X}}{\partial^1 \boldsymbol{X}} - \boldsymbol{I} = \frac{\partial \left({}^1\boldsymbol{X} + \boldsymbol{u} \right)}{\partial^1 \boldsymbol{X}}^T \frac{\partial \left({}^1\boldsymbol{X} + \boldsymbol{u} \right)}{\partial^1 \boldsymbol{X}} - \boldsymbol{I} \\ = \\ \frac{\partial \boldsymbol{u}}{\partial^1 \boldsymbol{X}} + \frac{\partial \boldsymbol{u}}{\partial^1 \boldsymbol{X}}^T + \frac{\partial \boldsymbol{u}}{\partial^1 \boldsymbol{X}}^T \frac{\partial \boldsymbol{u}}{\partial^1 \boldsymbol{X}} \end{gathered} \tag{2.23} $$

Linear and nonlinear components can be written as:

$$ \begin{gathered} {}_1\boldsymbol{E} = {}_1\boldsymbol{e} + {}_1\boldsymbol{\eta} \\ {}_1\boldsymbol{E}_{ij} = {}_1\boldsymbol{e}_{ij} + {}_1\boldsymbol{\eta}_{ij} \end{gathered} \tag{2.24} $$

$$ \begin{gathered} {}_1\boldsymbol{e} = \frac{1}{2} \left(\frac{\partial \boldsymbol{u}}{\partial^1 \boldsymbol{X}} + \frac{\partial \boldsymbol{u}}{\partial^1 \boldsymbol{X}}^T \right) \\ {}_1\boldsymbol{e}_{ij} = \frac{1}{2} \left(\frac{\partial \boldsymbol{u}_i}{\partial^1 \boldsymbol{X}_j} + \frac{\partial \boldsymbol{u}_j}{\partial^1 \boldsymbol{X}_i} \right) \end{gathered} \tag{2.25} $$

$$ \begin{gathered} {}_1\boldsymbol{\eta} = \frac{1}{2} \left(\frac{\partial \boldsymbol{u}}{\partial^1 \boldsymbol{X}}^T \frac{\partial \boldsymbol{u}}{\partial^1 \boldsymbol{X}} \right) \\ {}_1\boldsymbol{\eta}_{ij} = \frac{1}{2} \left(\frac{\partial \boldsymbol{u}_k}{\partial^1 \boldsymbol{X}_i} \frac{\partial \boldsymbol{u}_k}{\partial^1 \boldsymbol{X}_j} \right) \end{gathered} \tag{2.26} $$

Considering equation 2.11 and equation 2.22 the relation between the Green-Lagrange strain tensor (${}_1\boldsymbol{E}$) and the Green-Lagrange strain increment tensor ($\boldsymbol{E}$) can be written as:

$$ \begin{gathered} \boldsymbol{E} = \frac{\partial^1 \boldsymbol{X}}{\partial \boldsymbol{X}}^T {}_1\boldsymbol{E} \frac{\partial^1 \boldsymbol{X}}{\partial \boldsymbol{X}} \\ \boldsymbol{E}_{ij} = \frac{\partial^1 \boldsymbol{X}_k}{\partial \boldsymbol{X}_i} {}_1\boldsymbol{E}_{kl} \frac{\partial^1 \boldsymbol{X}_l}{\partial \boldsymbol{X}_j} \end{gathered} \tag{2.27} $$

and

$$ \begin{gathered} {}_1\boldsymbol{E} = \frac{\partial \boldsymbol{X}}{\partial^1 \boldsymbol{X}}^T \boldsymbol{E} \frac{\partial \boldsymbol{X}}{\partial^1 \boldsymbol{X}} \\ {}_1\boldsymbol{E}_{ij} = \frac{\partial \boldsymbol{X}_k}{\partial^1 \boldsymbol{X}_i} \boldsymbol{E}_{kl} \frac{\partial \boldsymbol{X}_l}{\partial^1 \boldsymbol{X}_j} \end{gathered} \tag{2.28} $$

2.3 Description of stresses

The description of the stress field along a continuum is represented by the stress tensor and there are several ways to define it. In this thesis, only the tensor that are energetically compatible to the strain tensors previously defined will be used.

2.3.1 Cauchy's stress tensors

Adopting the Cauchy's Stress Tensor, also known as Euler's Stress Tensor, the stresses are always defined in the initial configuration. The Cauchy's stress $\boldsymbol{\sigma}_{ij}$ are defined as the internal forces per unit of area acting along the normal and two tangential directions of each face of the parallelepiped depicted in the figure 2.3. This tensor has an important physical meaning but, unfortunately, is less convenient when a nonlinear step-by-step analysis is performed.

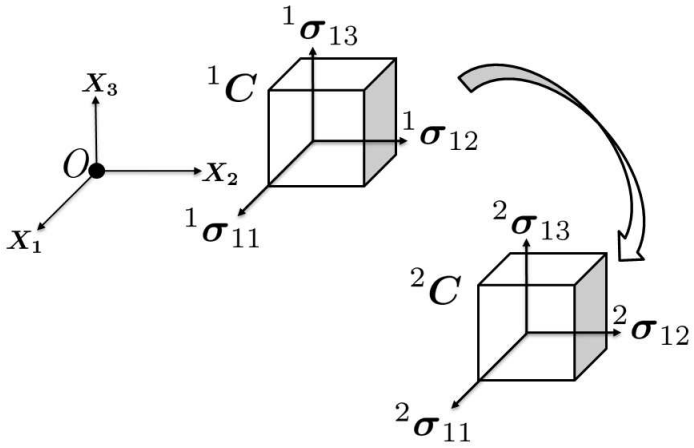

Figure 2.3: Definition of the Cauchy's stress tensor

$$\boldsymbol{\sigma} = \begin{bmatrix} \boldsymbol{\sigma}_{11} & \boldsymbol{\sigma}_{12} & \boldsymbol{\sigma}_{13} \\ \boldsymbol{\sigma}_{21} & \boldsymbol{\sigma}_{22} & \boldsymbol{\sigma}_{23} \\ \boldsymbol{\sigma}_{31} & \boldsymbol{\sigma}_{32} & \boldsymbol{\sigma}_{33} \end{bmatrix} \tag{2.29}$$

2.3.2 Second Piola-Kirchhoff's stress tensor

To define the Second Piola-Kichhoff stress tensor consider a certain infinitesimal parallelepiped that moves from configuration $^0\boldsymbol{C}$ to configurations $^1\boldsymbol{C}$ and $^2\boldsymbol{C}$. Considering the deformation that the parallelepiped undergoes during the path, the stresses of the second Piola-Kirchhoff stress tensor can be defined as the forces per unit area acting along the normal and two tangential directions of the parallelepiped on each configuration, see figure 2.4. In an incremental step-by-step analysis, the stress tensor will be decomposed as

$$^2\boldsymbol{S} = {}^1\boldsymbol{S} + \boldsymbol{S} \tag{2.30}$$

where $\boldsymbol{S}$ is called Kirchhoff Stress Increment Tensor.

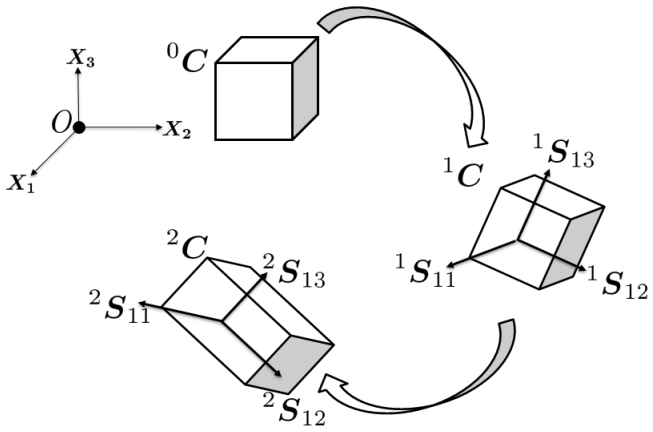

Figure 2.4: Definition of the Second Piola-Kirchhoff Stress Tensor

It can be proved (Yeong-Bin Yang [1994]) that the relation between the Cauchy and the second Piola-Kirchhoff stress tensors is

$$\begin{aligned} {}^2\boldsymbol{S} &= \frac{\rho}{{}^2\rho}\frac{\partial \boldsymbol{X}}{\partial^2 \boldsymbol{X}}^T {}^2\boldsymbol{\sigma}\frac{\partial \boldsymbol{X}}{\partial^2 \boldsymbol{X}} \\ {}^2\boldsymbol{S}_{ij} &= \frac{\rho}{{}^2\rho}\frac{\partial \boldsymbol{X}_i}{\partial^2 \boldsymbol{X}_k}{}^2\boldsymbol{\sigma}_{kl}\frac{\partial \boldsymbol{X}_j}{\partial^2 \boldsymbol{X}_l} \end{aligned} \tag{2.31}$$

and

$$\begin{aligned} {}^2\boldsymbol{\sigma} &= \frac{{}^2\rho}{\rho}\frac{\partial^2 \boldsymbol{X}}{\partial \boldsymbol{X}}^T {}^2\boldsymbol{S}\frac{\partial^2 \boldsymbol{X}}{\partial \boldsymbol{X}} \\ {}^2\boldsymbol{\sigma}_{ij} &= \frac{{}^2\rho}{\rho}\frac{\partial^2 \boldsymbol{X}_i}{\partial \boldsymbol{X}_k}^T {}^2\boldsymbol{S}_{kl}\frac{\partial^2 \boldsymbol{X}_j}{\partial \boldsymbol{X}_l} \end{aligned} \tag{2.32}$$

2.3.3 Updated Kirchhoff stress tensor

Consider now the configuration ${}^1\boldsymbol{C}$ with the Cauchy stress tensor in the orthogonal axis. Imagine an infinitesimal deformation to configuration ${}^2\boldsymbol{C}$ where the parallelepiped is no longer rectangular. It is possible to use the coordinates in configuration ${}^1\boldsymbol{C}$ as the material coordinates to express the variables in the configuration ${}^2\boldsymbol{C}$. The updated Kirchhoff stress tensor is defined as the matrix that contains the forces per unit of area along the normal and tangential directions of each face of the parallelepiped at configuration ${}^2\boldsymbol{C}$.

$${}^2_1\boldsymbol{S} = {}^1\boldsymbol{\sigma} + {}_1\boldsymbol{S} \tag{2.33}$$

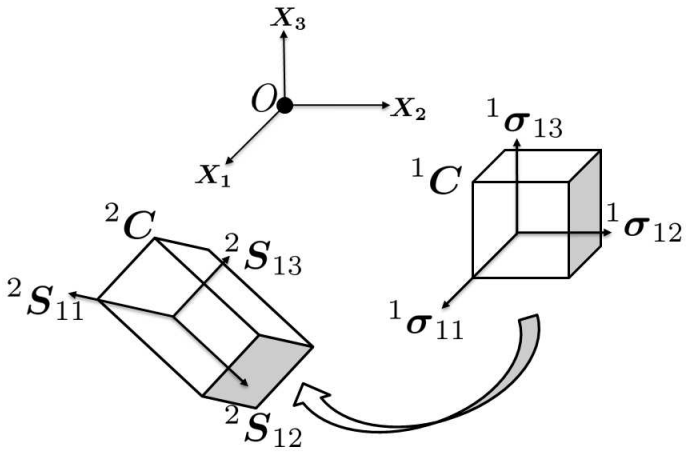

Figure 2.5: Definition of the Updated Kirchhoff Stress Tensor

2.3.4 Transformation rules

The Cauchy stress tensor ${}^2\boldsymbol{\sigma}$ and the updated Kirchhoff stress tensor ${}^2_1\boldsymbol{S}$ can be related by the formulas

$$\begin{aligned} {}^2_1\boldsymbol{S} &= \frac{{}^1\rho}{{}^2\rho}\frac{\partial^1\boldsymbol{X}}{\partial^2\boldsymbol{X}}^T {}^2\boldsymbol{\sigma}\frac{\partial^1\boldsymbol{X}}{\partial^2\boldsymbol{X}} \\ {}^2_1\boldsymbol{S}_{ij} &= \frac{{}^1\rho}{{}^2\rho}\frac{\partial^1\boldsymbol{X}_i}{\partial^2\boldsymbol{X}_k}{}^2\boldsymbol{\sigma}_{kl}\frac{\partial^1\boldsymbol{X}_j}{\partial^2\boldsymbol{X}_l} \end{aligned} \tag{2.34}$$

and

$$\begin{aligned} {}^2\boldsymbol{\sigma} &= \frac{{}^2\rho}{{}^1\rho}\frac{\partial^2\boldsymbol{X}}{\partial^1\boldsymbol{X}}^T {}^2_1\boldsymbol{S}\frac{\partial^2\boldsymbol{X}}{\partial^1\boldsymbol{X}} \\ {}^2\boldsymbol{\sigma}_{ij} &= \frac{{}^2\rho}{{}^1\rho}\frac{\partial^2\boldsymbol{X}_i}{\partial^1\boldsymbol{X}_k}{}^2_1\boldsymbol{S}_{kl}\frac{\partial^2\boldsymbol{X}_j}{\partial^1\boldsymbol{X}_l} \end{aligned} \tag{2.35}$$

The transformation of the second Piola-Kirchhoff stress tensor with respect to different reference systems can be obtained using equation 2.31 and equation 2.35

$$\begin{aligned} {}^2\boldsymbol{S} &= \frac{\rho}{{}^1\rho}\frac{\partial\boldsymbol{X}}{\partial^1\boldsymbol{X}}^T {}^2_1\boldsymbol{S}\frac{\partial\boldsymbol{X}}{\partial^1\boldsymbol{X}} \\ {}^2\boldsymbol{S}_{ij} &= \frac{\rho}{{}^1\rho}\frac{\partial\boldsymbol{X}_i}{\partial^1\boldsymbol{X}_k}{}^2_1\boldsymbol{S}_{kl}\frac{\partial\boldsymbol{X}_j}{\partial^1\boldsymbol{X}_k} \end{aligned} \tag{2.36}$$

The same can be computed in the configuration ${}^1\boldsymbol{C}$

$$\begin{aligned} {}^1\boldsymbol{S} &= \frac{\rho}{{}^1\rho}\frac{\partial\boldsymbol{X}}{\partial^1\boldsymbol{X}}^T {}^1\boldsymbol{\sigma}\frac{\partial\boldsymbol{X}}{\partial^1\boldsymbol{X}} \\ {}^1\boldsymbol{S}_{ij} &= \frac{\rho}{{}^1\rho}\frac{\partial\boldsymbol{X}_i}{\partial^1\boldsymbol{X}_k}{}^1\boldsymbol{\sigma}_{kl}\frac{\partial\boldsymbol{X}_j}{\partial^1\boldsymbol{X}_k} \end{aligned} \tag{2.37}$$

where the stress tensor ${}^1_1\boldsymbol{S}$ has been substituted by ${}^1\boldsymbol{\sigma}$.

Extracting equation 2.37 to equation 2.36 the expression for the relation between the incremental stresses $\boldsymbol{S}$ and ${}_1\boldsymbol{S}$ can be obtained.

$$\begin{aligned} \boldsymbol{S} &= \frac{{}^0\rho}{{}^1\rho}\frac{\partial \boldsymbol{X}}{\partial^1 \boldsymbol{X}}^T {}_1\boldsymbol{S}\frac{\partial \boldsymbol{X}}{\partial^1 \boldsymbol{X}} \\ \boldsymbol{S}_{ij} &= \frac{{}^0\rho}{{}^1\rho}\frac{\partial \boldsymbol{X}_i}{\partial^1 \boldsymbol{X}k}^T {}_1\boldsymbol{S}_{kl}\frac{\partial \boldsymbol{X}_j}{\partial^1 \boldsymbol{X}_l} \end{aligned} \tag{2.38}$$

and inversely

$$\begin{aligned} {}_1\boldsymbol{S} &= \frac{{}^0\rho}{{}^1\rho}\frac{\partial^1 \boldsymbol{X}}{\partial \boldsymbol{X}}^T \boldsymbol{S}\frac{\partial^1 \boldsymbol{X}}{\partial \boldsymbol{X}} \\ {}_1\boldsymbol{S}_{ij} &= \frac{{}^0\rho}{{}^1\rho}\frac{\partial^1 \boldsymbol{X}_i}{\partial \boldsymbol{X}_k}^T \boldsymbol{S}_{kl}\frac{\partial^1 \boldsymbol{X}_j}{\partial \boldsymbol{X}_l} \end{aligned} \tag{2.39}$$

Equations 2.38 and 2.39 are particularly adapted to be used in the Lagrangian formulation as it will be shown in the following sections.

Sometimes, the transformation between the several descriptions of the stress field requires the knowledge of the variation of the density inside the body. Let us consider the principle of conservation of mass. It is obvious that the mass can not vary from one configuration to another during the deformation of the body, so it can be written:

$$\int_{{}^t\Omega} {}^t\rho d^t\Omega = \int_\Omega \rho d\Omega \tag{2.40}$$

Due to the conservation of mass, it is possible to express the density in the configuration ${}^0\boldsymbol{C}$ as a function of the mass in configuration ${}^t\boldsymbol{C}$. Defining the Jacobian as

$$\begin{aligned} {}^t\boldsymbol{J}_{\boldsymbol{A}} &= \frac{\partial^t \boldsymbol{X}}{\partial \boldsymbol{X}} \\ {}^t\boldsymbol{J}_{\boldsymbol{A}ij} &= \frac{\partial^t \boldsymbol{X}_i}{\partial \boldsymbol{X}_j} \end{aligned} \tag{2.41}$$

equation 2.40 can be expressed as

$$\int_{{}^t\Omega} {}^t\rho d^t\Omega = \int_\Omega {}^t\rho \left|{}^t\boldsymbol{J}_{\boldsymbol{A}}\right| d\Omega \tag{2.42}$$

This expresion leads to the following relation

$$\rho = {}^t\rho \left|{}^t\boldsymbol{J}_{\boldsymbol{A}}\right| \tag{2.43}$$

2.4 Principle of Virtual Work

A body in equilibrium should satisfy the equilibrium equations that can be expressed using the Cauchy's stress tensor according to a cartesian axis and satifies also the *Natural boundary conditions*.

$$\begin{aligned} \boldsymbol{\nabla_m} \cdot {}^t\boldsymbol{\sigma} + {}^t\boldsymbol{F} = \boldsymbol{0} \quad & in\ {}^t\Omega \\ {}^t\boldsymbol{\sigma}\,{}^t\boldsymbol{n} = {}^t\boldsymbol{f} \quad & in\ {}^t\Gamma_\sigma \end{aligned} \tag{2.44}$$

which the tensorial product between the Nabla operator and the $\boldsymbol{\sigma}$ tensor can be defined as

$$\left[\boldsymbol{\nabla}_{\boldsymbol{m}} \cdot {}^{t}\boldsymbol{\sigma}\right]_{i} = \frac{\partial^{t}\boldsymbol{\sigma}_{ij}}{\partial^{t}\boldsymbol{X}_{j}} \tag{2.45}$$

and ${}^{t}\Omega$ represents the volume of the body, the vector ${}^{t}\boldsymbol{F}$ denotes the external forces per unit volume acting on the body, ${}^{t}\boldsymbol{f}$ denotes the forces per unit area acting in the ${}^{t}\Gamma_{\sigma}$ boundary and ${}^{t}\boldsymbol{n}$ represents the vector normal to this surface. In the following, the stress field inside a body that satisfies equation 2.44 will be called *Statically admissible stress field*.

In addition, the so called *kinematically admissible displacement field* can be defined as the one that verifies the *Geometric boundary conditions*.

$${}^{t}\boldsymbol{u} = \overline{{}^{t}\boldsymbol{u}} \quad in\ {}^{t}\Gamma_{u} \tag{2.46}$$

in which the boundary ${}^{t}\Gamma_{u}$ represents the part of the boundary of the body where the geometric conditions are imposed (Dirichlet boundary conditions).

Let us consider now a virtual increment of displacements characterized by the symbol $\boldsymbol{\delta u}$. It is obvious that considering this virtual increment kinematically admissible, the following condition is verified

$${}^{t}\boldsymbol{\delta u} = \mathbf{0} \quad in\ {}^{t}\Gamma_{u} \tag{2.47}$$

Considering now a kinematically admissible displacement field and a statically admissible stress field, the *Principle of Virtual Works* can be formulated

$$\int_{{}^{t}\Omega} {}^{t}\boldsymbol{\sigma} : {}^{t}\boldsymbol{\varepsilon} d^{t}\Omega = \int_{{}^{t}\Omega} {}^{t}\boldsymbol{F}^{T\,t}\boldsymbol{\delta u} d^{t}\Omega + \int_{{}^{t}\Gamma_{\sigma}} {}^{t}\boldsymbol{f}^{T\,t}\boldsymbol{\delta u} d^{t}\Gamma_{\sigma} \tag{2.48}$$

where the tensorial product $a : b$ can be defined as

$$\boldsymbol{a} : \boldsymbol{b} = \boldsymbol{a}_{ij}\boldsymbol{b}_{ij}$$

It is well known that the formulation of the Principles of Virtual Works (PVW) is equivalent to impose equilibrium and compatibility to a given system. In other words, the PVW is a necessary and sufficient condition for the equilibrium and compatibility of a system.

As the reader may realize, the PVW has been written with reference to the initial configuration ${}^{0}\boldsymbol{C}$. One can also formulate it considering another configuration as the reference one. In the following, when the PVW is formulated related to the initial configuration the *Total Lagrangian formulation* will be used and when it is formulated related to the last known configuration the *Updated Lagrangian formulation* will be used.

2.4.1 Total Lagrangian formulation

Following the approach developed in the book Yeong-Bin Yang [1994], the following relation needs to be proved

$$\begin{aligned}\int_{{}^2\Omega} {}^2\boldsymbol{\sigma} : {}_2\boldsymbol{\delta e}\ d^2\Omega &= \int_{\Omega} {}^2\boldsymbol{S} : {}^2\boldsymbol{\delta\varepsilon}\ d\Omega \\ \int_{{}^2\Omega} {}^2\boldsymbol{\sigma}_{ij\,2}\boldsymbol{\delta e}_{ij}\ d^2\Omega &= \int_{\Omega} {}^2\boldsymbol{S}_{ij}\,{}^2\boldsymbol{\delta\varepsilon}_{ij}\ d\Omega\end{aligned} \tag{2.49}$$

To do so, let us first consider the relation between the stress tensors ${}^2\boldsymbol{\sigma}$ and ${}^2\boldsymbol{S}$ and between the strain tensors ${}_2\boldsymbol{\delta e}$ and ${}^2\boldsymbol{\delta\varepsilon}$. Equation 2.2.1 allows to write the following equation

$$\delta^2 ds^2 = \delta\left({}^2\boldsymbol{dX}^{T\,2}\boldsymbol{dX}\right) = 2\,{}^2\boldsymbol{dX}^{T\,2}\boldsymbol{\delta dX} = 2\left({}^2\boldsymbol{FdX}\right)^T\left({}^2\boldsymbol{FdX}\right) = 2\boldsymbol{dX}^{T\,2}\boldsymbol{F}^{T\,2}\boldsymbol{\delta F dX} = 2\boldsymbol{dX}^{T\,2}\boldsymbol{\delta E dX}$$

$$\begin{aligned}{}^2\boldsymbol{dX}^{T\,2}\boldsymbol{\delta dX} &= \boldsymbol{dX}^{T\,2}\boldsymbol{\delta E dX} \\ {}^2\boldsymbol{dX}_i\,{}^2\boldsymbol{\delta dX}_i &= \boldsymbol{dX}_i\,{}^2\boldsymbol{\delta E}_{ij}\boldsymbol{dX}_j\end{aligned} \tag{2.50}$$

Also, we can write the following equality

$${}^2\boldsymbol{\delta dX} = \frac{\partial\boldsymbol{\delta u}}{\partial^2\boldsymbol{X}}\,{}^2\boldsymbol{dX} \tag{2.51}$$

and subtitute it in equation 2.50, leading us to

$${}^2\boldsymbol{dX}^T\frac{\partial\boldsymbol{\delta u}}{\partial^2\boldsymbol{X}}\,{}^2\boldsymbol{dX} = \boldsymbol{dX}^{T\,2}\boldsymbol{\delta E dX} \tag{2.52}$$

Further, since ${}_2\boldsymbol{\delta e} = \frac{1}{2}\left(\frac{\partial\boldsymbol{\delta u}}{\partial^2\boldsymbol{X}}^T + \frac{\partial\boldsymbol{\delta u}}{\partial^2\boldsymbol{X}}\right)$, from equation 2.20 we can obtain

$$\boldsymbol{dX}^{T\,2}\boldsymbol{\delta\varepsilon dX} = {}^2\boldsymbol{dX}^T{}_2\boldsymbol{\delta e dX} \tag{2.53}$$

And using the chain rule ${}^2\boldsymbol{dX} = {}^2\boldsymbol{FdX}$, it leads to

$$\begin{aligned}{}^2\boldsymbol{\delta\varepsilon} &= {}^2\boldsymbol{F}^T{}_2\boldsymbol{\delta e}\,{}^2\boldsymbol{F} \\ {}^2\boldsymbol{\delta\varepsilon}_{ij} &= {}^2\boldsymbol{F}_{ki\,2}\boldsymbol{\delta e}_{kl}\,{}^2\boldsymbol{F}_{lj}\end{aligned} \tag{2.54}$$

and

$$\begin{aligned}{}^2\boldsymbol{\delta e} &= {}^2\boldsymbol{F}^{-T}{}_2\boldsymbol{\delta\varepsilon}\,{}^2\boldsymbol{F}^{-1} \\ {}^2\boldsymbol{\delta e}_{ij} &= {}^2\boldsymbol{F}^{-T}_{ki\,2}\boldsymbol{\delta\varepsilon}_{kl}\,{}^2\boldsymbol{F}^{-1}_{lj}\end{aligned} \tag{2.55}$$

The last relations allow to prove the validity of equations 2.49 and, as a consequence, it can be stated that the Piola-Kirchhoff stresses ${}^2\boldsymbol{S}$ and the Green-Lagrange strains ${}^2\boldsymbol{\varepsilon}$ are energetically conjugate.

Further, by defining the surface tensile forces and body forces with respect to the ${}^0\boldsymbol{C}$ configuration as:

$$
\begin{aligned}
{}^2\boldsymbol{f} d\Gamma_\sigma &= {}^2\boldsymbol{f}^2 d\Gamma_\sigma \\
{}^2\boldsymbol{F} d\Omega &= {}^2\boldsymbol{F}^2 d\Omega
\end{aligned}
$$

and using equation 2.49, the principle of virtual work in the ${}^0\boldsymbol{C}$ reference configuration can be formulated.

$$
\int_\Omega {}^2\boldsymbol{S} : {}^2\boldsymbol{\delta\varepsilon}\ d\Omega = \int_\Omega {}^2\boldsymbol{F}^T \boldsymbol{\delta u}\ d\Omega + \int_{\Gamma_\sigma} {}^2\boldsymbol{f}^T \boldsymbol{\delta u}\ d\Gamma_\sigma \tag{2.56}
$$

Considering the separation of the Green-Lagrange strain tensor in its linear and non-linear parts, the principle of virtual work can be rewritten in the following form

$$
\int_\Omega \boldsymbol{S} : \boldsymbol{\delta\varepsilon}\ d\Omega + \int_\Omega {}^1\boldsymbol{S} : \boldsymbol{\delta\eta}\ d\Omega = {}^2\boldsymbol{R} - {}^1\boldsymbol{R} \tag{2.57}
$$

where the ${}^2\boldsymbol{R}$ and ${}^1\boldsymbol{R}$ are defined as

$$
\begin{aligned}
{}^2\boldsymbol{R} &= \int_\Omega {}^2\boldsymbol{F}^T \boldsymbol{\delta u}\ d\Omega + \int_{\Gamma_\sigma} {}^2\boldsymbol{f}^T \boldsymbol{\delta u}\ d\Gamma_\sigma \\
{}^1\boldsymbol{R} &= \int_\Omega {}^1\boldsymbol{S} : \boldsymbol{\delta e}\ d\Omega = \int_\Omega {}^1\boldsymbol{F}^T \boldsymbol{\delta u}\ d\Omega + \int_{\Gamma_\sigma} {}^1\boldsymbol{f}^T \boldsymbol{\delta u}\ d\Gamma_\sigma
\end{aligned} \tag{2.58}
$$

Equation 2.57 states that the difference between the variation of the external work is equal to the increment of energy (deformation plus potential) during the movement from configuration ${}^1\boldsymbol{C}$ to configuration ${}^2\boldsymbol{C}$.

The increment of the Piola-Kirchhoff $\boldsymbol{S}$ can be written in terms of the Green-Lagrange tensor $\boldsymbol{\varepsilon}$ as

$$
\begin{aligned}
\boldsymbol{S} &= \boldsymbol{C} \otimes \boldsymbol{\varepsilon} \\
\boldsymbol{S}_{ij} &= \boldsymbol{C}_{ijkl} \boldsymbol{\varepsilon}_{kl}
\end{aligned} \tag{2.59}
$$

which allows to rewrite the principle of virtual works as

$$
\int_\Omega \boldsymbol{C} \otimes \boldsymbol{\varepsilon\delta\varepsilon}\ d\Omega + \int_\Omega {}^1\boldsymbol{S} : \boldsymbol{\delta\eta}\ d\Omega = {}^2\boldsymbol{R} - {}^1\boldsymbol{R} \tag{2.60}
$$

Equation 2.60 is completely general since no hypothesis has been made on the displacements. Moreover, one can consider the hypothesis of small strains assuming the linearized form of the principle of virtual works.

$$
\boldsymbol{\delta\varepsilon} \simeq \boldsymbol{\delta e} \ \rightarrow \ \int_\Omega \boldsymbol{C} \otimes \boldsymbol{e\delta e}\ d\Omega + \int_\Omega {}^1\boldsymbol{S} : \boldsymbol{\delta\eta}\ d\Omega = {}^2\boldsymbol{R} - {}^1\boldsymbol{R} \tag{2.61}
$$

2.4.2 Updated Lagrangian formulation

In this new approach, is convenient to derive the following expression

$$
\int_{{}^2\Omega} {}^2\boldsymbol{\sigma} : {}_2\boldsymbol{\delta e}\ d^2\Omega = \int_{{}^1\Omega} {}^2_1\boldsymbol{S} : {}^2_1\boldsymbol{\delta\varepsilon}\ d^1\Omega \tag{2.62}
$$

The procedure to derive this new equation is the same as the one followed on subsection 2.4.1, simply changing the reference configuration from ${}^0\boldsymbol{C}$ to ${}^1\boldsymbol{C}$. For more indications, the reader can find the demonstration on Yeong-Bin Yang [1994].

Considering the principle of virtual works referenced to the configuration ${}^1\boldsymbol{C}$, it can be written

$$\int_{{}^1\Omega} {}^2_1\boldsymbol{S} : {}^2_1\boldsymbol{\delta\varepsilon}\; d^1\Omega = \int_{{}^1\Omega} {}^2_1\boldsymbol{F}^T\boldsymbol{\delta u}\; d^1\Omega + \int_{{}^1\Gamma_\sigma} {}^2_1\boldsymbol{f}^T\boldsymbol{\delta u}\; d^1\Gamma_\sigma \tag{2.63}$$

Operating as before, one can divide the strain tensors in its linear and nonlinear parts and write the principle of virtual works as

$$\int_{{}^1\Omega} {}_1\boldsymbol{S} : {}_1\boldsymbol{\delta\varepsilon}\; d^1\Omega + \int_{{}^1\Omega} {}^1\boldsymbol{\sigma} : {}_1\boldsymbol{\delta\eta}\; d^1\Omega = {}^2_1\boldsymbol{R} - {}^1_1\boldsymbol{R} \tag{2.64}$$

$$\begin{aligned} {}^2_1\boldsymbol{R} &= \int_{{}^1\Omega} {}^2_1\boldsymbol{F}^T\boldsymbol{\delta u}\; d^1\Omega + \int_{{}^1\Gamma_\sigma} {}^2_1\boldsymbol{f}^T\boldsymbol{\delta u}\; d^1\Gamma_\sigma \\ {}^1_1\boldsymbol{R} = \int_{{}^1\Omega} {}^1\boldsymbol{\sigma} : {}_1\boldsymbol{\delta e}\; d^1\Omega &= \int_{{}^1\Omega} {}^1_1\boldsymbol{F}^T\boldsymbol{\delta u}\; d^1\Omega + \int_{{}^1\Gamma_\sigma} {}^1_1\boldsymbol{f}^T\boldsymbol{\delta u}\; d^1\Gamma_\sigma \end{aligned} \tag{2.65}$$

There readers should remember that in the configuration ${}^1\boldsymbol{C}$ the Piola-Kirchoff and Cauchy stress tensors coincide. Also, the incremental constitutive equations for the material can be written referenced to thc configuration ${}^1\boldsymbol{C}$ as

$${}_1\boldsymbol{S} = {}_1\boldsymbol{C} \otimes {}_1\boldsymbol{\varepsilon} \tag{2.66}$$

and the principle of virtual works referenced to the configuration ${}^1\boldsymbol{C}$ can be written as

$$\int_{{}^1\Omega} {}_1\boldsymbol{C} \otimes {}_1\boldsymbol{\varepsilon} : {}_1\boldsymbol{\delta\varepsilon}\; d^1\Omega + \int_{{}^1\Omega} {}^1\boldsymbol{\sigma} : {}_1\boldsymbol{\delta\eta}\; d^1\Omega = {}^2_1\boldsymbol{R} - {}^1_1\boldsymbol{R} \tag{2.67}$$

Comparing both formulations (total and updated lagrangian formulations) one can realize that they only differ form the reference configuration.

In addition, considering small strains in the deformative path from configuration ${}^1\boldsymbol{C}$ to configuration ${}^2\boldsymbol{C}$, the *linearized form of PVW* may be obtained.

$$\boldsymbol{\delta\varepsilon} \simeq \boldsymbol{\delta e} \rightarrow \int_{{}^1\Omega} {}_1\boldsymbol{C} \otimes {}_1\boldsymbol{e} : {}_1\boldsymbol{\delta\varepsilon}\; d^1\Omega + \int_{{}^1\Omega} {}^1\boldsymbol{\sigma} : {}_1\boldsymbol{\delta\eta}\; d^1\Omega = {}^2_1\boldsymbol{R} - {}^1_1\boldsymbol{R} \tag{2.68}$$

3 Modeling of frame and cable structures

Many structures in civil engineering can be effectively modelled as a set of beam elements. In a typical structural analysis, the cross-sectional behaviour of each member of a certain frame can be described by the so-called governing differential equations. Different techniques have been developed to approximate the solution and obtain reliable results simplifying the system as much as possible.

One of the main methods developed is the *Structural Matrix method*, which consists in the approximation of the original system by a simplified mathematical model that has a finite number of degrees of freedom. By replacing the original system of differential equations by the matrix equations, engineers are able to study these systems efficiently.

In the Structural Matrix method there are two possible formulations: *Direct Stiffness method* and *Finite Element method*. The first one considers the equilibrium of the element in a strong form, which means that the equilibrium conditions are directly imposed to the element and the matrix equilibrium equations are derived. On the other hand, the finite element method considers a certain displacement field along the element and imposes the equilibrium in a weak or average sense. In the following sections it will be shown how the direct stiffness and finite element methods are used to study cable and beam structures.

Both methods have a very similar approach:

- Divide the entire structure into a certain number of beam elements, reducing the number of degrees of freedom.
- Number both the nodes and the elements of the new idealized structure.
- Derivation of the matrix equilibrium equations (by Stiffness of Finite Element method) for each beam element and transformation into the global reference system.
- Assembly of the equilibrium conditions of each element in the global structural system and impose the boundary conditions.

- Finally, solve the system to obtain the displacements, strains and stresses field, which is the main goal for the engineers who are studying the structure.

The following chapter is devopted to *Cable Structures* and *Frame Structures*. First, the analysis and formulation of cable structures will be presented due to its simplicity compared to frame elements. The study will be carried out by a brief introduction about the theoretical models regarding the direct and finite element methods and discussions about the advantages and disadvantages will be held. Secondly, the study of frame systems will be completely developed in the field of finite element method due to its major applications and also due to the fact that the direct stiffness method is not suitable for analysis of large displacements and strains.

3.1 Cable structures

The analysis of cable structures is a very important topic in the field of civil engineering since 1691 when Huygens, Leibniz and G. Bernoulli found the closed solution of the *unextensible catenary*. The solution of a cable suspended from its ends had been studied by Galileo Galilei in 1691, year in which he proposed the solution of the catenary as a parabola.

On the other hand, new techniques appeared during the last decades due to the increasing computation capacity of computers. These techniques have been developed using direct stiffness and finite element formulation and will be explained later.

3.1.1 Unextensible catenary

Consider a cable that is in equilibrium under the self weight and supported at both ends. Consider, also, a very small piece of this cables as the one in figure 3.1. Considering the equilibrium equations it can be written:

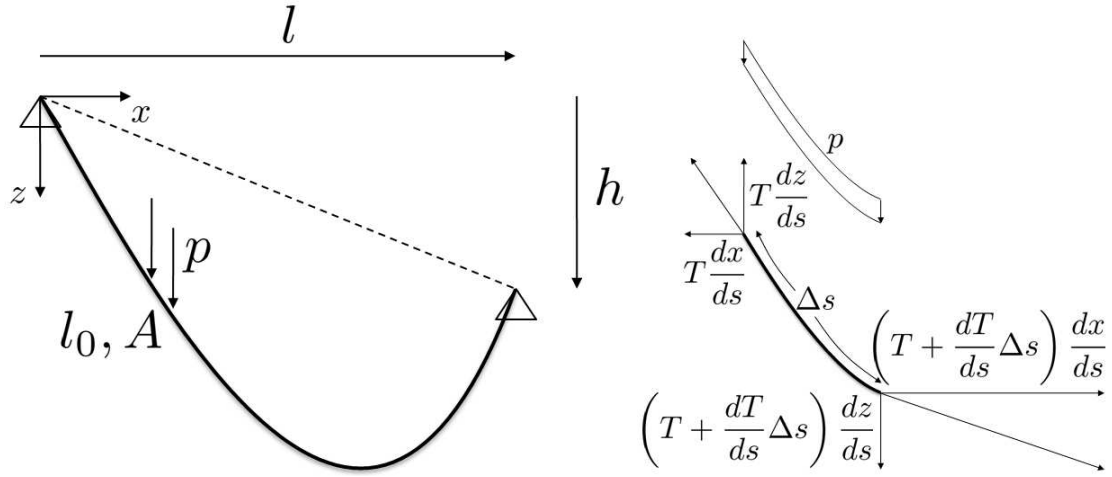

(a) General sketch of a cable supported in both ends (b) Piece of a cable and forces acting on it

Figure 3.1: Equilibrium configuration of a catenary

$$\begin{aligned} x: \quad & T\frac{dx}{ds} + \frac{d}{ds}\left(T\frac{dx}{ds}\right)\Delta s - \frac{dx}{ds} = 0 \\ z: \quad & T\frac{dz}{ds} + \frac{d}{ds}\left(T\frac{dz}{ds}\right)\Delta s - T\frac{dz}{ds} + p\Delta s = 0 \end{aligned} \tag{3.1}$$

And can be derived

$$\begin{aligned} T\frac{dx}{ds} = const = H \rightarrow T = H\frac{dx}{ds} \\ \frac{d}{ds}\left(T\frac{dz}{ds}\right) = -p \end{aligned} \tag{3.2}$$

Combining these two equations and differentiating with respect to x it might be obtained

$$\frac{d}{dx}\left(H\frac{dz}{dx}\right) = -p\frac{ds}{dx} \tag{3.3}$$

and remembering that H is constant along the cable and that

$$ds = \sqrt{dx^2 + dz^2} = \sqrt{dx^2\left(1 + \frac{dz}{dx}^2\right)} = dx\sqrt{1 + z'^2}$$

the equilibrium differential equation is finally obtained

$$H\frac{d^2z}{dx^2} = -p\sqrt{1 + z'^2} \tag{3.4}$$

which solution can be easily obtained (see Quagliaroli [2010]) using proper integration techniques and imposing boundary conditions

$$z\left(x\right) = \frac{H}{p}\left[\cosh\alpha - \cosh\left(\frac{2\beta}{l}x - \alpha\right)\right] \tag{3.5}$$

where α and β are defined as follows:

$$\beta = \frac{pl}{2H}; \quad \sinh\left(\alpha - \beta\right) = \frac{\beta h}{l\sinh\beta} \tag{3.6}$$

From equation 3.5 it is possible to deduce some usefull relations (see Malerba [2010]) as

$$\frac{pl_0}{2H} = \sinh\beta\cosh\left(\alpha - \beta\right) \tag{3.7}$$

that it will be used in future sections of this thesis.

This equation is known as the *catenary equation* and provides a good model to study cable systems in a simplified way. As it can be seen from equation 3.5, in the solution of the differential equation is included the horizontal tension H acting on the cable. This will need some specific developments because the configuration of the cable depends also on the applied load. Therefore, a method to obtain iteratively the configuration of the

cable under an specific load considering the catenary equation will be presented.

Althought the catenary equation represents a great tool to analyse cable systems under uniformly distributed load, it has also limitations in the study of cable systems in a general configuration. Indeed, the catenary equation has several hypothesis behind its formulation:

- The cable is axialy unextensible.
- The load is uniformly applied along the cable.
- The mechanical and geometrical properties of the cable are constant along its length.

These hypothesis make the catenary model not suitable for the study of cable systems under any load and configuration is attempted. To overcome this problem, the elastic behaviour of the cable can be taken into account.

3.1.2 Elastic catenary

The unextensible catenary model has the limitation that it can not deal with elastic systems. As a consequence, a new model is presented for the study of cables. Considering [Irvine, 1992], the equations for the analysis of elastic cable systems can be obtained. Considering a lagrangian approach with the lagrangian variable p (local coordinate of the cable in the deformed configuration), the geometrical conditions can be written as:

$$\left(\frac{dx}{dp}\right)^2 + \left(\frac{dz}{dp}\right)^2 = 1 \tag{3.8}$$

Consider figure 3.2, where an elastic cable is depicted. The equilibrium equations in vertical and horizontal directions are:

$$T\frac{dx}{dp} = H \qquad T\frac{dz}{dp} = V - \frac{Ws}{l_0} \tag{3.9}$$

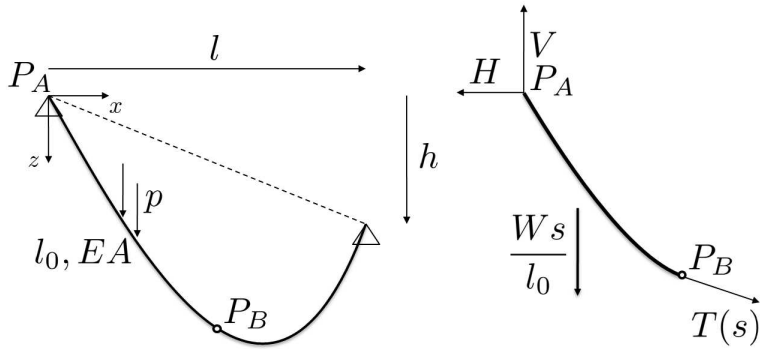

(a) General sketch of an elastic cable supported in both ends

(b) Part of the cable under the tension, between points A and B

Figure 3.2: Equilibrium configuration of an elastic catenary

Considering the Hook's law the following equation can be written.

$$T = EA\varepsilon = EA\frac{dp - ds}{ds} = EA\left(\frac{dp}{ds} - 1\right) \tag{3.10}$$

Squaring both equations on 3.10 and summing them to the tension of the cable as a function of the local coordinate s may be obtained.

$$T(s) = \sqrt{H^2 + \left(V - \frac{Ws}{l_0}\right)^2} \tag{3.11}$$

Considering that $\frac{dx}{ds} = \frac{dx}{dp}\frac{dp}{ds}$ the equilibrium equations might be rewritten as

$$\frac{dx}{dp} = \frac{H}{T} \qquad \frac{dp}{ds} = 1 + \frac{T}{EA} \tag{3.12}$$

Multiplying both equations leads

$$\frac{dx}{ds} = \frac{H}{EA} + \frac{H}{\sqrt{H^2 + \left(V - \frac{Ws}{l_0}\right)^2}} \tag{3.13}$$

which can be integrated to obtain the parametric expression of the $x(s)$ coordinate.

$$x(s) = \frac{H}{EA}s + \frac{Hl_0}{W}\left[\sinh^{-1}\left(\frac{V}{H}\right) - \sinh^{-1}\left(\frac{V - Ws/l_0}{H}\right)\right] \tag{3.14}$$

The same procedure can be adapted for the coordinate $z(s)$.

$$z(s) = \frac{Ws}{EA}\left(\frac{V}{H} - \frac{s}{2l_0}\right) + \frac{Hl_0}{W}\left[\sqrt{1 + \left(\frac{V}{H}\right)^2} - \sqrt{1 + \left(\frac{V - Ws/l_0}{H}\right)^2}\right] \tag{3.15}$$

Equations 3.14, 3.15 and 3.11 completely characterize the solution of the elastic cable problem under the self weight. One may realize that the three equations depend on two variables V and H that are depicted on figure 3.2(b). These two variables have to be obtained from the imposition of two additional conditions. Considering $\bar{l}$ the length of the cable in the deformed configuration and imposing the following boundary conditions

$$s = 0 \rightarrow x = 0, y = 0, p = 0 \tag{3.16}$$

$$s = l_0 \rightarrow x = l, y = h, p = \bar{l} \tag{3.17}$$

the final equations in parametric form may be obtained.

$$x(l_0) = l \rightarrow l = \frac{H}{EA}l_0 + \frac{Hl_0}{W}\left[\sinh^{-1}\left(\frac{V}{H}\right) - \sinh^{-1}\left(\frac{V - W}{H}\right)\right] \tag{3.18}$$

$$z(l_0) = h \rightarrow h = \frac{W l_0}{EA}\left(\frac{V}{H} - \frac{1}{2}\right) + \frac{H l_0}{W}\left[\sqrt{1 + \left(\frac{V}{H}\right)^2} - \sqrt{1 + \left(\frac{V - W}{H}\right)^2}\right] \quad (3.19)$$

Equations 3.18 and 3.19 are a system of two nonlinear equations that must be solved in terms of H and V. Once H and V are computed, the configuration of the cable can be completely characterized using the equations previously described.

The model of the elastic cable under its own self weight is very useful to test the behaviour and performance of the program that will be developed for the analysis of floating structures. Indeed, the anchorage system of floating structures will be composed essentially by cable elements under a fluid and only subjected to their own weight.

Althought the model of the elastic catenary allows to study elastic cable systems, it is quite limited when general cable structures are treated. For example, certain cable systems are not only subjected to the self-weight and require a more advanced and flexible model to be studied with.

To deal with general cable systems, new models in the field of structural matrix formulation have been developed. These models allow a more general approach to deal with cable system and are suitable to be modified in a easy way to take into account new aspects of the behaviour of structures (For example, in this thesis, a new model to deal with contact phenomena between cable elements and the seabed has been developed).

The main characteristic of both finite element and stiffness models is to consider a cable as a concatenation of straight elements that have no flexural or torsional stiffness and can only respond to tension (a cable has a negligible resistance in terms of flexural and compression loads). Considering this, the formulations for both methods will be developed with reference to one straight element and both the stiffness matrix and vector of nodal loads will be derived. These two variables characterize the element and will be used in the assembly of the overall system.

First, the so-called *Direct Stiffness method* is presented, which formulation is based only on equilibrium considerations of the cable element. Secondly, the finite element method will be explained and formulate for cable elements considering large displacements and strains.

3.1.3 Direct stiffness method

The direct stiffness method was developed before the finite element method and has a more intuitive formulation. The total Lagrangian formulation in the 2D space will be first exposed and later the updated Lagrangian formulation in a 3D space will be formulated.

3.1.3.1 Total Lagrangian formulation

Consider a straight element like the one in figure 3.3

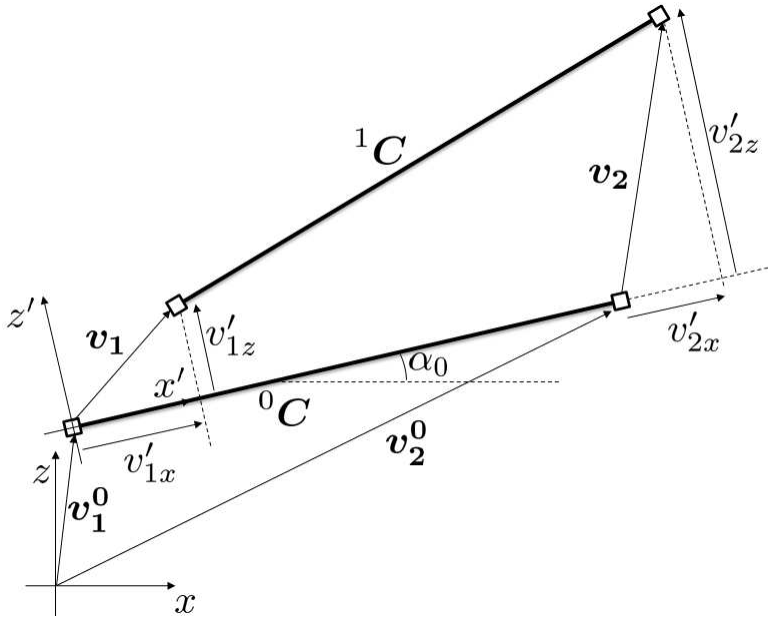

Figure 3.3: Model used in the direct approach of the cable element (Total Lagrangian Formulation)

In the initial configuration $^0\boldsymbol{C}$ the matrix $\boldsymbol{L}$ can be defined as

$$\boldsymbol{L} = \begin{bmatrix} \cos\alpha_0 & \sin\alpha_0 \\ -\sin\alpha_0 & \cos\alpha_0 \end{bmatrix} \tag{3.20}$$

which defines the local reference system in the initial configuration of the cable element. In addition, some other definitions can be made. The position of each node of the element in the configuration $^0\boldsymbol{C}$ is defined as

$$^0\boldsymbol{v}_1 = \begin{bmatrix} ^0\boldsymbol{v}_{1x} & ^0\boldsymbol{v}_{1z} \end{bmatrix}^T;\ ^0\boldsymbol{v}_2 = \begin{bmatrix} ^0\boldsymbol{v}_{2x} & ^0\boldsymbol{v}_{2z} \end{bmatrix}^T \tag{3.21}$$

Once the initial condition of the element is known, the length can be easily compute as

$$l_0 = \left|^0\boldsymbol{v}_2 - ^0\boldsymbol{v}_1\right| \tag{3.22}$$

A displacement from the initial configuration can be referred to the global reference system or the local reference system of the element. The *displacement vector* can be defined in the global reference system as

$$\boldsymbol{v_1} = \begin{bmatrix} v_{1x} & v_{1z} \end{bmatrix}^T;\ \boldsymbol{v_2} = \begin{bmatrix} v_{2x} & v_{2z} \end{bmatrix}^T\ \boldsymbol{v} = \begin{bmatrix} \boldsymbol{v_2}^T & \boldsymbol{v_2}^T \end{bmatrix}^T \tag{3.23}$$

or in the local reference system as:

$$\boldsymbol{v'_1} = \begin{bmatrix} v'_{1x} & v'_{1z} \end{bmatrix}^T;\ \boldsymbol{v'_2} = \begin{bmatrix} v'_{2x} & v'_{2z} \end{bmatrix}^T;\ \boldsymbol{v'} = \begin{bmatrix} \boldsymbol{v'_2}^T & \boldsymbol{v'_2}^T \end{bmatrix}^T \tag{3.24}$$

A relation between these two vectors can be obtained using the transformation matrix defined in equation 3.20

$$\left.\begin{array}{l} \boldsymbol{v_1'} = \boldsymbol{L v_1} \\ \boldsymbol{v_2'} = \boldsymbol{L v_2} \end{array}\right\} \rightarrow \boldsymbol{v'} = \begin{bmatrix} \boldsymbol{L} & \boldsymbol{0} \\ \boldsymbol{0} & \boldsymbol{L} \end{bmatrix} \boldsymbol{v} \tag{3.25}$$

Due to the displacement of each node, the element may suffer an elongation (positive or negative). To compute it, the increment of length during the deformation must be defined. Following the figure 3.4 one can compute the *incremental length vector* as

$$\boldsymbol{\Delta v'} = \boldsymbol{v_2'} - \boldsymbol{v_1'} = \begin{bmatrix} \Delta x' & \Delta z' \end{bmatrix}^T \tag{3.26}$$

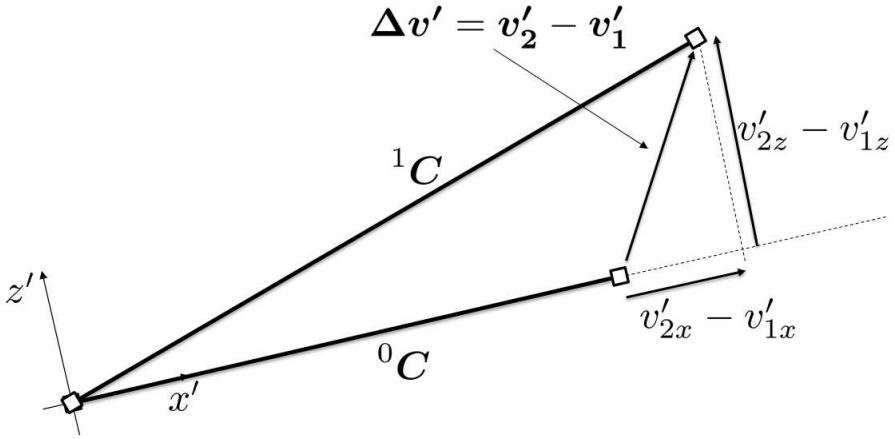

Figure 3.4: Vector that defines the increment of length in the local reference system of the cable element.

This vector can be expressed in terms of the displacement vector as follows

$$\boldsymbol{\Delta v'} = \boldsymbol{v_2'} - \boldsymbol{v_1'} = \boldsymbol{L v_2} - \boldsymbol{L v_1} = \underbrace{\begin{bmatrix} -\boldsymbol{L} & \boldsymbol{L} \end{bmatrix}}_{\boldsymbol{T}} \boldsymbol{v} = \boldsymbol{T v} \tag{3.27}$$

In a displacement-based formulation is important to relate the strain suffered by the element and the displacements at its ends. The new length of the element after the deformation will be

$$l = l_0 + \Delta l_0 = \sqrt{(l_0 + \Delta x')^2 + \Delta z'^2} \tag{3.28}$$

The increment of length Δl_0 can be expressed in terms of the variation of the incremental length vector as

$$\begin{gathered} \delta \Delta l_0 = \frac{\partial \Delta l_0}{\partial \Delta x'} \delta \Delta x' + \frac{\partial \Delta l_0}{\partial \Delta z'} \delta \Delta z' \\ \frac{\partial \Delta l_0}{\partial \Delta x'} = \frac{l_0 + \Delta x'}{l_0 + \Delta l_0}; \; \frac{\partial \Delta l_0}{\partial \Delta z'} = \frac{\Delta z'}{l_0 + \Delta l_0} \\ \delta \Delta l_0 = \underbrace{\begin{bmatrix} \dfrac{\partial \Delta l_0}{\partial \Delta x'} & \dfrac{\partial \Delta l_0}{\partial \Delta z'} \end{bmatrix}}_{\boldsymbol{A}^T} \delta \boldsymbol{\Delta v'} = \boldsymbol{A}^T \delta \boldsymbol{\Delta v'} \end{gathered} \tag{3.29}$$

where the vector $\boldsymbol{A}$ is defined as

$$\boldsymbol{A} = \frac{\partial \Delta l_0}{\partial \boldsymbol{\Delta v'}} = \left[\begin{array}{cc} \frac{\partial \Delta l_0}{\partial \Delta x'} & \frac{\partial \Delta l_0}{\partial \Delta z'} \end{array} \right]^T = \frac{1}{l_0 + \Delta l_0} \left[\begin{array}{cc} l_0 + \Delta x' & \Delta z' \end{array} \right]^T \tag{3.30}$$

Now, let us consider the stress of the element. The constitutive equations of a body which can have only an axial deformation lead to

$$P = P_0 + \frac{EA}{l_0} \Delta l_0 = P_0 + EA\varepsilon \tag{3.31}$$

$$\varepsilon = \frac{\Delta l_0}{l_0}$$

where P is the axial stress inside the element and P_0 is the prestressing at the initial condition.

Formulating the variation of the axial stress in terms of the variation of the incremental length vector the following expression can be obtained:

$$\delta P = \frac{EA}{l_0} \delta \Delta l_0 = \frac{EA}{l_0} \frac{\partial \Delta l_0}{\partial \boldsymbol{\Delta v'}} \delta \boldsymbol{\Delta v'} \tag{3.32}$$

Defining the internal reaction of the element according to the local reference system as follows

$$\boldsymbol{R'} = \frac{\partial \Delta l_0}{\partial \boldsymbol{\Delta v'}} P = \boldsymbol{A} P \tag{3.33}$$

we may compute its variation as done before with the other variables

$$\delta \boldsymbol{R'} = P \delta \boldsymbol{A} + \delta P \boldsymbol{A} = P \frac{\partial \boldsymbol{A}}{\partial \boldsymbol{\Delta v'}} \delta \boldsymbol{\Delta v'} + \boldsymbol{A} \frac{EA}{l_0} \frac{\partial \Delta l_0}{\partial \boldsymbol{\Delta v'}} \delta \boldsymbol{\Delta v'} \tag{3.34}$$

$$\frac{\partial \boldsymbol{A}}{\partial \boldsymbol{\Delta v'}} = \left[\begin{array}{cc} \frac{\partial A_1}{\partial \Delta x'} & \frac{\partial A_1}{\partial \Delta z'} \\ \frac{\partial A_2}{\partial \Delta x'} & \frac{\partial A_2}{\partial \Delta z'} \end{array} \right]$$

$$\frac{\partial A_1}{\partial \Delta x'} = \frac{l^2 - (l_0 + \Delta x')^2}{l^3} \qquad \frac{\partial A_1}{\partial \Delta z'} = -\Delta z' \frac{l_0 + \Delta x'}{l^3}$$

$$\frac{\partial A_2}{\partial \Delta x'} = -\Delta z' \frac{l_0 + \Delta x'}{l^3} \qquad \frac{\partial A_2}{\partial \Delta z'} = \frac{l^2 - \Delta z'^2}{l^3}$$

$$\delta \boldsymbol{R'} = \left(\underbrace{P \frac{\partial \boldsymbol{A}}{\partial \boldsymbol{\Delta v'}}}_{\boldsymbol{D}} + \underbrace{\boldsymbol{A} \frac{EA}{l_0} \boldsymbol{A}^T}_{\boldsymbol{G}} \right) \delta \boldsymbol{\Delta v'} = (\boldsymbol{D} + \boldsymbol{G}) \, \delta \boldsymbol{\Delta v'} = \boldsymbol{K'} \delta \boldsymbol{\Delta v'} \tag{3.35}$$

$$\boldsymbol{D} = P \frac{\partial \boldsymbol{A}}{\partial \boldsymbol{\Delta v'}} = \frac{P}{l^3} \left[\begin{array}{cc} \Delta z'^2 & -\Delta z' \, (l_0 + \Delta x') \\ -\Delta z' \, (l_0 + \Delta x') & (l_0 + \Delta x')^2 \end{array} \right]; \; \boldsymbol{G} = \boldsymbol{A} \frac{EA}{l_0} \boldsymbol{A}^T$$

Once the increment of reaction in the local reference system is known, the translation in the global reference system can be made using the transformation rule previously defined

$$\left.\begin{array}{l} \boldsymbol{R} = \boldsymbol{T}^T \boldsymbol{R}' \\ \boldsymbol{\Delta v}' = \boldsymbol{T v} \end{array}\right\} \rightarrow \delta \boldsymbol{R} = \underbrace{\boldsymbol{T}^T \boldsymbol{K}' \boldsymbol{T}}_{\boldsymbol{K}} \delta \boldsymbol{v} = \boldsymbol{K} \delta \boldsymbol{v} \tag{3.36}$$

Which leads to the definition of the stiffness matrix referenced to the global reference system.

$$\boldsymbol{K} = \boldsymbol{T}^T \boldsymbol{K}' \boldsymbol{T} \tag{3.37}$$

The formulation of the element in 2D space has been obtained and its stiffness matrix computed. The formulation can be generalized to consider also the third component of the displacements, but it will not be developed in the following. This is due to the fact that the total lagrangian formulation is not the best approach to deal with problems that have a strong nonlinear behaviour. In a 3D problem, the nonlinearities increase due to the capacity of the structure to move freely in all direction. In order to develop a program for the analysis of floating structures, the total lagrangian formulation is a method only suitable for 2D analyses considering simple conditions and, for the 3D analyses, the Updated Lagrangian formulation has been used due to its capacity to deal with nonlinearities.

3.1.3.2 Updated Lagrangian formulation

In this part, the updated Lagrangian formulation will be explained in its general 3D approach. Althought there are many other formulations based on higher order degree elements, the formulation adopted is the one that best fits the requierements of our model because certain modifications will be needed to deal with our general purpose nonlinear program. It is also important to remind that the reader could obtain the 2D model of this formulation just considering the third component of the displacement formulation equal to zero.

To start with the formulation, consider the straight element depicted in figure 3.5 where the three configurations that must be studied are plotted.

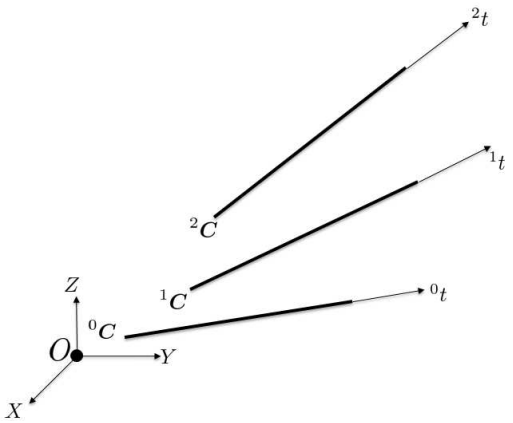

Figure 3.5: Straight element in the updated Lagrangian formulation

First, let us consider some definitions that will be helpful to derive the stiffness matrix of the element. The initial configuration of the element is characterized by the position of the two nodes on each end of the element.

$$ {}^0\boldsymbol{v}_1 = \left[\begin{array}{cc} {}^0\boldsymbol{v}_{1x} & {}^0\boldsymbol{v}_{1y} \end{array} \right]^T ; \; {}^0\boldsymbol{v}_2 = \left[\begin{array}{cc} {}^0\boldsymbol{v}_{2x} & {}^0\boldsymbol{v}_{2y} \end{array} \right]^T \tag{3.38} $$

Also, the element could be subjected to a prestressing defined by the variable P_0 and the tangent vector that defines the direction of the element in the configuration ${}^1\boldsymbol{C}$ can be written as

$$ {}^1\boldsymbol{t} = \frac{1}{l} \left[\begin{array}{ccc} {}^1\boldsymbol{v}_{2x} - {}^1\boldsymbol{v}_{1x} & {}^1\boldsymbol{v}_{2y} - {}^1\boldsymbol{v}_{1y} & {}^1\boldsymbol{v}_{2z} - {}^1\boldsymbol{v}_{1z} \end{array} \right]^T \tag{3.39} $$

Also, let us define the displacement vector as

$$ \boldsymbol{v}_1 = \left[\begin{array}{ccc} \boldsymbol{v}_{1x} & \boldsymbol{v}_{1y} & \boldsymbol{v}_{1z} \end{array} \right]^T ; \; \boldsymbol{v}_2 = \left[\begin{array}{ccc} \boldsymbol{v}_{2x} & \boldsymbol{v}_{2y} & \boldsymbol{v}_{2z} \end{array} \right]^T ; \; \boldsymbol{v} = \left[\begin{array}{cc} \boldsymbol{v}_1 & \boldsymbol{v}_2 \end{array} \right]^T \tag{3.40} $$

Once these displacements are computed, the program will need to update the position of both nodes as follows

$$ \begin{array}{l} {}^2\boldsymbol{x}_1 = {}^0\boldsymbol{x}_1 + \boldsymbol{v}_1 \\ {}^2\boldsymbol{x}_2 = {}^0\boldsymbol{x}_2 + \boldsymbol{v}_2 \end{array} \tag{3.41} $$

Let us consider now the axial force acting inside the element in the configuration ${}^1\boldsymbol{C}$. If the element is subjected to an axial stress equal to P the following vector can be defined

$$ \boldsymbol{P} = \left[\begin{array}{c} \boldsymbol{P}_1 \\ \boldsymbol{P}_2 \end{array} \right] = P \underbrace{\left[\begin{array}{c} -\boldsymbol{t} \\ \boldsymbol{t} \end{array} \right]}_{\boldsymbol{T}} \tag{3.42} $$

On the other hand, due to a displacement from configuration ${}^1\boldsymbol{C}$ to configuration ${}^2\boldsymbol{C}$, there will be an increment in the axial stress inside the element, which can be computed in terms of the displacement vector.

$$ \boldsymbol{\Delta P} = \left(\boldsymbol{T} \frac{EA}{l_0} \boldsymbol{T}^T \right) \boldsymbol{\Delta v} = \frac{EA}{l_0} \left[\begin{array}{cc} \boldsymbol{t}\boldsymbol{t}^T & -\boldsymbol{t}\boldsymbol{t}^T \\ -\boldsymbol{t}\boldsymbol{t}^T & \boldsymbol{t}\boldsymbol{t}^T \end{array} \right] \boldsymbol{\Delta v} \tag{3.43} $$

The elastic stiffness matrix can be defined as follows

$$ \boldsymbol{K_e} = \frac{EA}{l_0} \left[\begin{array}{cc} \boldsymbol{t}\boldsymbol{t}^T & -\boldsymbol{t}\boldsymbol{t}^T \\ -\boldsymbol{t}\boldsymbol{t}^T & \boldsymbol{t}\boldsymbol{t}^T \end{array} \right] \tag{3.44} $$

Let us focus to the geometric contribution. First, the increment of displacement of each node is considered. This vector can be decomposed in two contributions, the one which is parallel to the tangent vector of the element and the orthogonal one. Both can be computed using the following equation

$$ \boldsymbol{\Delta v}_i = \boldsymbol{\Delta v}_{i\parallel} + \boldsymbol{\Delta v}_{i\perp}; \; \forall i = 1, 2 \tag{3.45} $$

The parallel vector can be computed projecting the increment of displacements to the tangent vector of the element.

$$\boldsymbol{\Delta v}_{i\parallel} = \left(\boldsymbol{\Delta v}_i^T \boldsymbol{t}\right) \boldsymbol{t} = \left(\boldsymbol{t}\boldsymbol{t}^T\right) \boldsymbol{\Delta v}_i;\ \forall i = 1,2 \tag{3.46}$$

The orthogonal part can be written as a function of the parallel part

$$\boldsymbol{\Delta v}_{i\perp} = \boldsymbol{\Delta v}_i - \boldsymbol{\Delta v}_{i\parallel} = \boldsymbol{\Delta v}_i - \left(\boldsymbol{t}\boldsymbol{t}^T\right) \boldsymbol{\Delta v}_i = \left(\boldsymbol{I} - \boldsymbol{t}\boldsymbol{t}^T\right) \boldsymbol{\Delta v}_i;\ \forall i = 1,2 \tag{3.47}$$

Considering small displacements between configuration ${}^1\boldsymbol{C}$ and configuration ${}^2\boldsymbol{C}$, the rigid body rotation of the element can be computed as:

$$\tan\theta = \frac{1}{l} \left|\boldsymbol{\Delta v}_{2\perp} - \boldsymbol{\Delta v}_{1\perp}\right| \simeq \theta \tag{3.48}$$

Expressing this equation in a matrix form it might be obtained

$$\boldsymbol{\theta} = \frac{1}{l} \left[\begin{array}{cc} -\left(\boldsymbol{I} - \boldsymbol{t}\boldsymbol{t}^T\right) & \left(\boldsymbol{I} - \boldsymbol{t}\boldsymbol{t}^T\right) \end{array} \right] \left[\begin{array}{c} \boldsymbol{\Delta v}_1 \\ \boldsymbol{\Delta v}_2 \end{array} \right] \tag{3.49}$$

The reader can refer to figure 3.6 for more explanation.

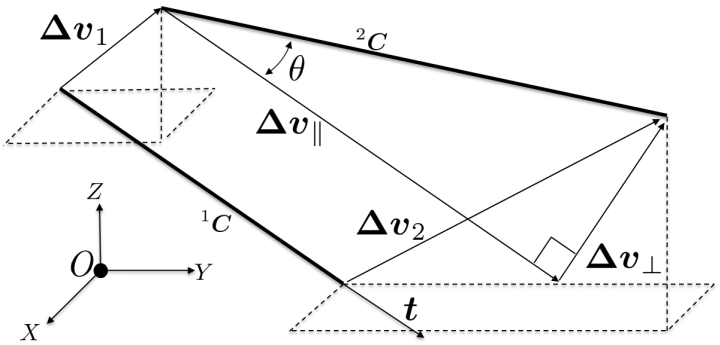

Figure 3.6: Decomposition of the displacements in the parallel and orthogonal part to the current configuration for a straight element

In addition, the variation of the axial stress due to the geometric component can be computed:

$$\boldsymbol{\Delta} P_G = P \left[\begin{array}{c} -\boldsymbol{\theta} \\ \boldsymbol{\theta} \end{array} \right] = \frac{P}{l} \left[\begin{array}{cc} \left(\boldsymbol{I} - \boldsymbol{t}\boldsymbol{t}^T\right) & -\left(\boldsymbol{I} - \boldsymbol{t}\boldsymbol{t}^T\right) \\ -\left(\boldsymbol{I} - \boldsymbol{t}\boldsymbol{t}^T\right) & \left(\boldsymbol{I} - \boldsymbol{t}\boldsymbol{t}^T\right) \end{array} \right] \boldsymbol{\Delta v} \tag{3.50}$$

where, of consequence, the geometric stiffness matrix can be defined as

$$\boldsymbol{K_g} = \frac{P}{l} \left[\begin{array}{cc} \left(\boldsymbol{I} - \boldsymbol{t}\boldsymbol{t}^T\right) & -\left(\boldsymbol{I} - \boldsymbol{t}\boldsymbol{t}^T\right) \\ -\left(\boldsymbol{I} - \boldsymbol{t}\boldsymbol{t}^T\right) & \left(\boldsymbol{I} - \boldsymbol{t}\boldsymbol{t}^T\right) \end{array} \right] \tag{3.51}$$

Once both elastic and geometric stiffness matrices have been computed, the incremental equilibrium equations in matrix form can be written as

$$\boldsymbol{\Delta P} = \left(\boldsymbol{K_e} + \boldsymbol{K_g}\right) \boldsymbol{\Delta v} = \boldsymbol{K_\tau} \boldsymbol{\Delta v} \tag{3.52}$$

The updated lagrangian formulation in a 3D space has been formulated and the incremental equilibrium equations have been written in a matrix form. The direct stiffness

method has found great application before the introduction of more advanced numerical models as the finite element method. The finite element method allows to express the equilibrium conditions formulating a hypothesis on the displacement field inside the element. In the following, the formulation of a finite element model for cable structures under large displacements and large strains will be described using the principle of virtual work.

3.1.4 Finite element method

3.1.4.1 Principle of virtual works

Before starting with the formulation of the element, the expression of the principle of virtual work for straight elements must be derived adopting an incremental formulation.

$$\int_{{}_1\Omega} {}_1\boldsymbol{C} : {}_1\boldsymbol{\varepsilon}\boldsymbol{\delta\varepsilon}\ d^1\Omega + \int_{{}_1\Omega} {}_1\boldsymbol{\sigma} : {}_1\boldsymbol{\delta\eta}\ d^1\Omega = {}^2_1\boldsymbol{R} - {}^1_1\boldsymbol{R} \tag{3.53}$$

$${}^2_1\boldsymbol{R} = \int_{{}_1\Omega} {}^2_1\boldsymbol{F}^T\boldsymbol{\delta u}\ d^1\Omega + \int_{{}_1\Gamma_\sigma} {}^2_1\boldsymbol{f}^T\boldsymbol{\delta u}\ d^1\Gamma_\sigma \tag{3.54}$$

$${}^1_1\boldsymbol{R} = \int_{{}_1\Omega} {}^1\boldsymbol{\sigma} : {}_1\boldsymbol{\delta\varepsilon}\ d^1\Omega = \int_{{}_1\Omega} {}^1_1\boldsymbol{F}^T\boldsymbol{\delta u}\ d^1\Omega + \int_{{}_1\Gamma_\sigma} {}^1_1\boldsymbol{f}^T\boldsymbol{\delta u}\ d^1\Gamma_\sigma \tag{3.55}$$

Considering the decomposition of the Green-Lagrange strain tensor in its linear and nonlinear part and remembering that all the strains except ε_{xx} are zero in a cable element, the expression can be simplified.

$$\int_{{}_1\Omega} Ee_{xx}\delta e_{xx} + E\eta_{xx}\delta e_{xx} + Ee_{xx}\delta\eta_{xx} + E\eta_{xx}\delta\eta_{xx}\ d^1\Omega = {}^2_1R - {}^1_1R \tag{3.56}$$

where a linear elastic material is considered.

The finite element formulation defines a model for the displacements and imposes the principle of virtual works to obtain an equilibrated (in a weak or medium form) solution. Consider that the displacements are distributed as linear functions where the interpolation coefficients are the displacements at the ends (displacements of the nodes).

$$\boldsymbol{U} = \begin{bmatrix} u \\ v \\ w \end{bmatrix} = \begin{bmatrix} u_1N_1(x) + u_2N_2(x) \\ v_1N_1(x) + v_2N_2(x) \\ w_1N_1(x) + w_2N_2(x) \end{bmatrix} \tag{3.57}$$

with

$$N_1(x) = 1 - \frac{x}{l};\ N_2(x) = \frac{x}{l} \tag{3.58}$$

Defining an incremental displacement for each component as

$$\begin{aligned} \Delta u &= u_2 - u_1 \\ \Delta v &= v_2 - v_1 \\ \Delta w &= w_2 - w_1 \end{aligned} \tag{3.59}$$

the strains along the element can be written in terms of these incremental displacements

$$e_{xx} = \frac{\partial u}{\partial x} = \frac{\Delta u}{l} \tag{3.60}$$

$$\eta_{xx} = \frac{1}{2}\left[\left(\frac{\partial u}{\partial x}\right)^2 + \left(\frac{\partial v}{\partial x}\right)^2 + \left(\frac{\partial w}{\partial x}\right)^2\right] = \frac{1}{2}\left[\left(\frac{\Delta u}{l}\right)^2 + \left(\frac{\Delta v}{l}\right)^2 + \left(\frac{\Delta w}{l}\right)^2\right] \tag{3.61}$$

3.1.4.2 Stiffness matrix

The derivation of the principle of virtual work can be obtained for every one of its five parts. Let us start with the first part of the integral reported in equation 3.56 which will provide the elastic stiffness matrix of the element.

$$\int_\Omega E e_{xx}\delta e_{xx} d\Omega = \int_\Omega E\frac{\Delta u}{l}\delta\left(\frac{\Delta u}{l}\right) d\Omega = \boldsymbol{\delta U}^T \boldsymbol{K_e U} \tag{3.62}$$

$$\boldsymbol{K_e} = \frac{EA}{l}\begin{bmatrix} 1 & 0 & 0 & -1 & 0 & 0 \\ 0 & 0 & 0 & 0 & 0 & 0 \\ 0 & 0 & 0 & 0 & 0 & 0 \\ -1 & 0 & 0 & 1 & 0 & 0 \\ 0 & 0 & 0 & 0 & 0 & 0 \\ 0 & 0 & 0 & 0 & 0 & 0 \end{bmatrix} \tag{3.63}$$

The second part can be rewritten as

$$\int_\Omega E\eta_{xx}\delta e_{xx} d\Omega = \int_\Omega E\frac{1}{2}\left[\left(\frac{\Delta u}{l}\right)^2 + \left(\frac{\Delta v}{l}\right)^2 + \left(\frac{\Delta w}{l}\right)^2\right]\delta\left(\frac{\Delta u}{l}\right) d\Omega = \boldsymbol{\delta U}^T \boldsymbol{S_1 U} \tag{3.64}$$

$$\boldsymbol{S_1}(\boldsymbol{U}) = \frac{EA}{2l^2}\begin{bmatrix} \Delta u & \Delta v & \Delta w & -\Delta u & -\Delta v & -\Delta w \\ 0 & 0 & 0 & 0 & 0 & 0 \\ 0 & 0 & 0 & 0 & 0 & 0 \\ -\Delta u & -\Delta v & -\Delta w & \Delta u & \Delta v & \Delta w \\ 0 & 0 & 0 & 0 & 0 & 0 \\ 0 & 0 & 0 & 0 & 0 & 0 \end{bmatrix} \tag{3.65}$$

Following the same procedure for the third part it can be obtained

$$\int_\Omega E e_{xx}\delta\eta_{xx} d\Omega = \int_\Omega E\frac{\Delta u}{l}\frac{1}{2}\delta\left[\left(\frac{\Delta u}{l}\right)^2 + \left(\frac{\Delta v}{l}\right)^2 + \left(\frac{\Delta w}{l}\right)^2\right] d\Omega = \boldsymbol{\delta U}^T \boldsymbol{S_2}\boldsymbol{\delta U} \tag{3.66}$$

where, considering an auxiliary matrix $\boldsymbol{A}$ as

$$\boldsymbol{A} = \begin{bmatrix} 2\Delta u & 0 & 0 \\ \Delta v & \Delta u & 0 \\ \Delta w & 0 & \Delta u \end{bmatrix}$$

the stiffness matrix of the third part can be written as

$$\boldsymbol{S_2}(\boldsymbol{U}) = \frac{EA}{2l^2} \begin{bmatrix} \boldsymbol{A} & -\boldsymbol{A} \\ -\boldsymbol{A} & \boldsymbol{A} \end{bmatrix} \tag{3.67}$$

The fourth part is the most complicated part and the calculus needed to obtain $\boldsymbol{S_3}$ are omitted here for sake of brevity.

$$\begin{gathered} \int_\Omega E\eta_{xx}\delta\eta_{xx}d\Omega \\ = \\ \int_\Omega E\frac{1}{4}\left[\left(\frac{\Delta u}{l}\right)^2 + \left(\frac{\Delta v}{l}\right)^2 + \left(\frac{\Delta w}{l}\right)^2\right]\delta\left[\left(\frac{\Delta u}{l}\right)^2 + \left(\frac{\Delta v}{l}\right)^2 + \left(\frac{\Delta w}{l}\right)^2\right]d\Omega \\ = \\ \boldsymbol{\delta U}^T\boldsymbol{S_3}\boldsymbol{\delta U} \end{gathered} \tag{3.68}$$

$$\boldsymbol{S_3}(\boldsymbol{U}) = \frac{EA}{6l^3} \begin{bmatrix} \boldsymbol{H} & -\boldsymbol{H} \\ -\boldsymbol{H} & \boldsymbol{H} \end{bmatrix} \tag{3.69}$$

where $\boldsymbol{H}$ is defined as

$$\boldsymbol{H} = \begin{bmatrix} 3\Delta u^2 + \Delta v^2 + \Delta w^2 & 2\Delta u\Delta v & 2\Delta u\Delta w \\ 2\Delta u\Delta v & 3\Delta v^2 + \Delta u^2 + \Delta w^2 & 2\Delta v\Delta w \\ 2\Delta u\Delta w & 2\Delta v\Delta w & 3\Delta w^2 + \Delta u^2 + \Delta v^2 \end{bmatrix}$$

The fifth one corresponds to the geometric contribution and can be expressed using the geometric stiffness matrix.

$$\begin{gathered} \int_\Omega \sigma_{xx}\delta\eta_{xx}d\Omega = \int_\Omega \delta\eta_{xx}\underbrace{\int_A \sigma_{xx}dA}_{{}^1_1F_x}dx = \int_\Omega \frac{{}^1_1F_x}{l^2}\left(\Delta u\delta\Delta u + \Delta v\delta\Delta v + \Delta w\delta\Delta w\right)\, d\Omega \\ = \\ \boldsymbol{\delta U}^T\boldsymbol{K_g}\boldsymbol{\delta U} \end{gathered} \tag{3.70}$$

$$\boldsymbol{K_g} = \frac{{}^1_1F_x}{l} \begin{bmatrix} 1 & 0 & 0 & -1 & 0 & 0 \\ 0 & 1 & 0 & 0 & -1 & 0 \\ 0 & 0 & 1 & 0 & 0 & -1 \\ -1 & 0 & 0 & 1 & 0 & 0 \\ 0 & -1 & 0 & 0 & 1 & 0 \\ 0 & 0 & -1 & 0 & 0 & 1 \end{bmatrix} \tag{3.71}$$

The last part is the most easy part and its expression is

$$ {}^{1}_{1}R = \boldsymbol{\delta U}^{T}\,{}^{1}_{1}\boldsymbol{f} \tag{3.72} $$

where the vector ${}^{1}\boldsymbol{f}$ is defined as the external loads applied to the element in the configuration ${}^{1}\boldsymbol{C}$ and the same approach can be adopted for the vector ${}^{2}_{1}\boldsymbol{f}$.

$$ {}^{1}_{1}\boldsymbol{f} = \left[\begin{array}{cccccc} {}^{1}_{1}F_{x1} & {}^{1}_{1}F_{y1} & {}^{1}_{1}F_{z1} & {}^{1}_{1}F_{x2} & {}^{1}_{1}F_{y2} & {}^{1}_{1}F_{z2} \end{array} \right] \tag{3.73} $$

$$ {}^{2}_{1}\boldsymbol{f} = \left[\begin{array}{cccccc} {}^{2}_{1}F_{x1} & {}^{2}_{1}F_{y1} & {}^{2}_{1}F_{z1} & {}^{2}_{1}F_{x2} & {}^{2}_{1}F_{y2} & {}^{2}_{1}F_{z2} \end{array} \right] \tag{3.74} $$

Finally, the incremental equilibrium equations in matrix form can be written as follows

$$ \left(\boldsymbol{K_e} + \boldsymbol{K_g} + \boldsymbol{S_1} + \boldsymbol{S_2} + \boldsymbol{S_3}\right)\boldsymbol{U} + {}^{1}\boldsymbol{f} = {}^{2}\boldsymbol{f} \tag{3.75} $$

3.1.4.3 Computational aspects

From the equations developed in the previous sections, the matrices $\boldsymbol{S_1}$, $\boldsymbol{S_2}$ and $\boldsymbol{S_3}$ are not symmetric. Therefore, during the assembly of the stiffness matrix this leads to a non-symmetric stiffness matrix which increases significantly the computational effort to solve the linear system of equations. As a consequence, a procedure to obtain an equivalent symmetric higher order stiffness matrix is presented. The equivalent matrices will have the same meaning as the previous ones but they will lead to a symmetric stiffness matrix and, consequently, more efficient solving algorithms can be implemented.

The matrices deduced before by means of the principle of virtual works represent five different types of actions that appear when the element moves from configuration ${}^{1}\boldsymbol{C}$ to configuration ${}^{2}\boldsymbol{C}$. Indeed, if the product between the five stiffness matrices and the displacement vector is computed it might be obtained:

$$ \boldsymbol{K_e U} = \left[\begin{array}{cccccc} {}^{1}_{1}f_{xl} & 0 & 0 & -{}^{1}_{1}f_{xl} & 0 & 0 \end{array} \right]^{T} \tag{3.76} $$

$$ \boldsymbol{K_g U} = \frac{E\,{}^{1}_{1}F_{x}}{l} \left[\begin{array}{cccccc} \Delta u & \Delta v & \Delta w & -\Delta u & -\Delta v & -\Delta w \end{array} \right]^{T} \tag{3.77} $$

$$ \boldsymbol{S_1 U} = \left[\begin{array}{cccccc} -{}^{1}_{1}f_{xn} & 0 & 0 & {}^{1}_{1}f_{xn} & 0 & 0 \end{array} \right]^{T} \tag{3.78} $$

$$ \boldsymbol{S_2 U} = \left[\begin{array}{cccccc} -{}^{1}_{1}f_{xl}\dfrac{\Delta u}{l} & -{}^{1}_{1}f_{xl}\dfrac{\Delta v}{l} & -{}^{1}_{1}f_{xl}\dfrac{\Delta w}{l} & {}^{1}_{1}f_{xl}\dfrac{\Delta u}{l} & {}^{1}_{1}f_{xl}\dfrac{\Delta v}{l} & {}^{1}_{1}f_{xl}\dfrac{\Delta w}{l} \end{array} \right]^{T} \tag{3.79} $$

$$ \boldsymbol{S_3 U} = \left[\begin{array}{cccccc} -{}^{1}_{1}f_{xn}\dfrac{\Delta u}{l} & -{}^{1}_{1}f_{xn}\dfrac{\Delta v}{l} & -{}^{1}_{1}f_{xn}\dfrac{\Delta w}{l} & {}^{1}_{1}f_{xn}\dfrac{\Delta u}{l} & {}^{1}_{1}f_{xn}\dfrac{\Delta v}{l} & {}^{1}_{1}f_{xn}\dfrac{\Delta w}{l} \end{array} \right]^{T} \tag{3.80} $$

where the variables ${}^{1}_{1}f_{xl}$ and ${}^{1}_{1}f_{xn}$ are the reaction forces due to the linear and nonlinear part of the Green-Lagrange strain tensor and can be expressed as

$$ {}^{1}_{1}f_{xl} = EAe_{xx} = EA\frac{\Delta u}{l} \tag{3.81} $$

$$ {}^{1}_{1}f_{xn} = EA\eta_{xx} = \frac{1}{2}EA\left(\frac{\Delta u^2}{l^2} + \frac{\Delta v^2}{l^2} + \frac{\Delta w^2}{l^2}\right) \tag{3.82} $$

Each one of these forces have a physical meaning. From the constitutive laws, the force acting on the element in the configuration ${}^{2}\boldsymbol{C}$ can be expressed in terms of the elongation (ι)

$$ {}^{2}_{1}\iota = \frac{{}^{2}l - {}^{1}l}{{}^{1}l} \tag{3.83} $$

where the length in the configuration ${}^{2}\boldsymbol{C}$ can be expressed as

$$ {}^{2}l = \sqrt{\left({}^{1}l + \Delta u\right)^2 + \Delta v^2 + \Delta w^2} \tag{3.84} $$

From geometric considerations, the forces ${}^{1}_{1}f_x$, f_{xl} and f_{xn} can be obtained in configuration ${}^{2}\boldsymbol{C}$

$$ {}_{2}f_{xl} = {}^{1}_{1}f_{xl}\left(1 + {}^{2}_{1}\iota\right) \tag{3.85} $$

$$ {}_{2}f_{xn} = {}^{1}_{1}f_{xn}\left(1 + {}^{2}_{1}\iota\right) = \frac{1}{2}EA\left(\frac{\Delta u^2}{l^2} + \frac{\Delta v^2}{l^2} + \frac{\Delta w^2}{l^2}\right)\left(1 + {}^{2}_{1}\iota\right) \tag{3.86} $$

$$ {}^{1}_{2}f_x = {}^{1}_{1}f_x\left(1 + {}^{2}_{1}\iota\right) \tag{3.87} $$

and these three contributions can be summed up to obtain the force acting on the element in the configuration ${}^{2}\boldsymbol{C}$.

$$ {}^{2}_{2}f_x = {}_{2}f_{xl} + {}_{2}f_{xn} + {}^{1}_{2}f_x = \left[EA\left(\frac{\Delta u}{l} + \frac{1}{2}\left\{\frac{\Delta u^2}{l^2} + \frac{\Delta v^2}{l^2} + \frac{\Delta w^2}{l^2}\right\}\right) + {}^{1}f_x\right]\left(1 + {}^{2}_{1}\iota\right) \tag{3.88} $$

This last equation is very important, since it will be used to compute the actual stress inside a cable element during the restoring phase. In addition, this expression allows to define the equivalent higher order matrices.

The derivation of these new higher order stiffness matrix is performed considering that the forces obtained from their contribution are the same as the ones obtained by the geometric stiffness matrix. So, it is possible to substitute the matrices $\boldsymbol{S_2}$ and $\boldsymbol{S_3}$ by two new symmetric matrices defined as

$$ \boldsymbol{S}^{s}_{\boldsymbol{2}} = \frac{{}^{1}_{1}f_{xl}}{l}\begin{bmatrix} 1 & 0 & 0 & -1 & 0 & 0 \\ 0 & 1 & 0 & 0 & -1 & 0 \\ 0 & 0 & 1 & 0 & 0 & -1 \\ -1 & 0 & 0 & 1 & 0 & 0 \\ 0 & -1 & 0 & 0 & 1 & 0 \\ 0 & 0 & -1 & 0 & 0 & 1 \end{bmatrix} \tag{3.89} $$

$$ \boldsymbol{S}^{s}_{\boldsymbol{3}} = \frac{{}^{1}_{1}f_{xn}}{l}\begin{bmatrix} 1 & 0 & 0 & -1 & 0 & 0 \\ 0 & 1 & 0 & 0 & -1 & 0 \\ 0 & 0 & 1 & 0 & 0 & -1 \\ -1 & 0 & 0 & 1 & 0 & 0 \\ 0 & -1 & 0 & 0 & 1 & 0 \\ 0 & 0 & -1 & 0 & 0 & 1 \end{bmatrix} \tag{3.90} $$

Because of equation 3.75 has to be satisfied, another change has to be made in the matrix $\boldsymbol{S_1}$. Defining the new matrix $\boldsymbol{S_1^s}$ as

$$\boldsymbol{S_1^s} = \boldsymbol{S_1} + \boldsymbol{S_2} - \boldsymbol{S_2^s} = \frac{EA}{2l^2} \begin{bmatrix} \Delta u & \Delta v & \Delta w & -\Delta u & -\Delta v & -\Delta w \\ \Delta v & -\Delta u & 0 & -\Delta v & \Delta u & 0 \\ \Delta w & 0 & -\Delta u & -\Delta w & 0 & \Delta u \\ -\Delta u & -\Delta v & -\Delta w & \Delta u & \Delta v & \Delta w \\ -\Delta v & \Delta u & 0 & \Delta v & -\Delta u & 0 \\ -\Delta w & 0 & \Delta u & \Delta w & 0 & -\Delta u \end{bmatrix} \tag{3.91}$$

the equilibrium equations in matrix form are still satisfied and each contribution is completely symmetric.

3.1.5 Mechanical behaviour of cables

The formulation described before allows to analyse a great variety of structures composed by *cable* elements. The cables are only able to resist tension, therefore a null stiffness in compression and a finite stiffness in tension are considered in the constitutive equations.

$$P = k\varepsilon; \begin{cases} P \geq 0; \ k = EA \\ P < 0; \ k = 0 \end{cases} \tag{3.92}$$

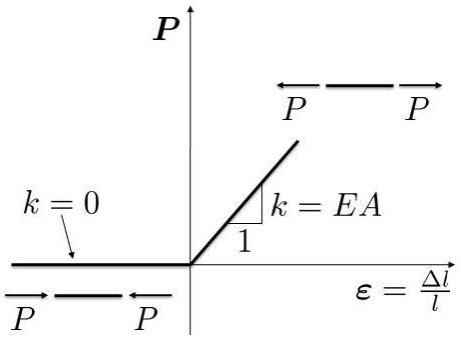

Figure 3.7: Consitutive law of a cable element.

In the code developed, the non linearity of the cable's constitutive equations has been considered. During the iterative procedure, the value of the tension P on each cable element is checked and the stiffness value of the element is evaluated as $k = EA$, if $P > 0$, or $k = 0$, if $P < 0$.

This particular implementation may lead to potential numerical problems because the stiffness matrix of the overall structure may become ill-conditioned since many cable elements would have a null stiffness contribution.

To avoid this problem, advanced numerical techniques have been developed. In next sections, this problem will be explained and some solutions adopted to force the convergence of the program will be discussed.

3.2 Frame structures

In the explanation of the finite element method two approaches will be presented. The explanation will be divided in 2D model (first part) and 3D models (last part of this section).

In the two-dimensional approach, the formulation of an Euler-Bernoulli's beam model with no torsional displacement will be presented. The first order theory will be presented and formulated and the Total Lagrangian formulation will be used to derive the governing equations. The first order theory is the most simple in the study of structures and is the first approach used in this thesis. The formulation of this theory is presented in a 2D space since the study of beam floating structures started, for simplicity, considering only the effects of buoyancy in bodies that freely lie on the water's free surface without capacity to move out of the vertical plane.

Later, a more general approach will be considered, where the contribution of torsional and out of bending displacements are taken into account. The bending and axial model of an Euler-Bernoulli beam and the Saint Venant's torsional model will be used to formulate the displacement field of the beam. This part will be divided in a first formulation that considers small displacements, in which the total lagrangian formulation will be used, and in a second part where large displacements and the second order strains are taken into account. In the second one the updated Lagrangian formulation will be used to formulate the incremental equilibrium equations.

3.2.1 Two-dimensional beam finite element modeling

3.2.1.1 Theoretical model

Let us consider a two dimensional model of a beam. In figure 3.8 a section of an Euler-Bernoulli's beam is depicted and the displacements are considered under the hypothesis of orthogonality between the section and the midline of the beam.

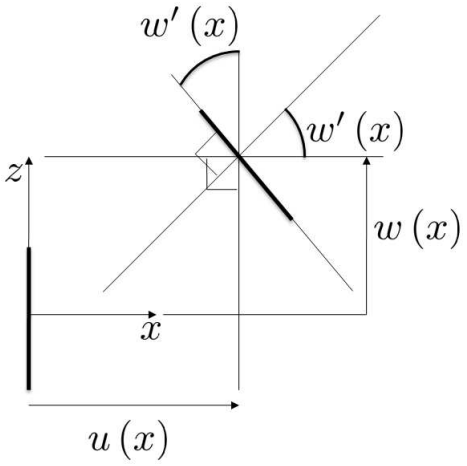

Figure 3.8: Generalized displacement for a 2D beam with no shear deformability.

The displacement field can be derived considering small displacements by simply geometric considerations:

$$\boldsymbol{S} = \left[\begin{array}{c} u\left(x\right) - zw'\left(x\right) \\ w\left(x\right) \end{array} \right] = \boldsymbol{n}\left(z\right)\boldsymbol{u}\left(x\right) \tag{3.93}$$

$$\boldsymbol{u} = \left[u \ w\right]^T\left(x\right) \tag{3.94}$$

$$\boldsymbol{n} = \left[\begin{array}{cc} 1 & -z\dfrac{d}{dx} \\ 0 & 1 \end{array} \right]$$

The variables $u\left(x\right)$ and $w\left(x\right)$ are called *generalized displacements* since all the displacement field is completely characterized by these variables and their derivatives.

The next step is the characterization of the strain field that can be done by means of the linear part of the Green-Lagrange's strain tensor.

$$e_{ij} = \frac{1}{2}\left(\frac{\partial S_i}{\partial X_j} + \frac{\partial S_j}{\partial X_i}\right) \ \rightarrow \ \left\{ \begin{array}{lcccc} \varepsilon_x & = & u'\left(x\right) - zw''\left(x\right) & = & \eta\left(x\right) + z\vartheta\left(x\right) \\ \varepsilon_y & = & 0 & & \\ \varepsilon_z & = & 0 & & \\ \gamma_{xy} & = & 0 & & \\ \gamma_{xz} & = & 0 & & \\ \gamma_{yz} & = & 0 & & \end{array} \right. \tag{3.95}$$

$$\boldsymbol{\varepsilon} = \boldsymbol{b}\left(z\right)\boldsymbol{q}\left(x\right) \tag{3.96}$$

$$\boldsymbol{\varepsilon} = \left[\varepsilon_x\right]$$

$$\boldsymbol{q} = \left[\begin{array}{c} \eta \\ \vartheta \end{array} \right]^T\left(x\right) = \left[\begin{array}{c} u' \\ -w'' \end{array} \right]^T\left(x\right) = \boldsymbol{C} \otimes \boldsymbol{u} \tag{3.97}$$

$$\boldsymbol{b} = \left[\begin{array}{cc} 1 & z \end{array} \right]$$

$$\boldsymbol{C} = \left[\begin{array}{cc} \dfrac{d}{dx} & 0 \\ 0 & -\dfrac{d^2}{dx^2} \end{array} \right] \tag{3.98}$$

The variables which govern the strain field are $\eta\left(x\right)$ and $\theta\left(x\right)$. These variables are called *generalized strains*.

To derive the stress field, the principle of virtual works must be applied. The derivatives of the internal and external works with respect to x are computed first for simplicity.

$$\frac{dL_i}{dx} = \int_A \boldsymbol{\sigma}^T\boldsymbol{\delta\varepsilon}\ dA = \int_A \boldsymbol{\sigma}^T\boldsymbol{b}\ dA\boldsymbol{\delta q} = \boldsymbol{Q}^T\boldsymbol{\delta q} \tag{3.99}$$

$$\boldsymbol{\sigma} = \left[\sigma_x\right]$$

$$\boldsymbol{Q} = \left[\begin{array}{c} N \\ M \end{array} \right] = \int_A \left[\begin{array}{c} \sigma_x \\ z\sigma_x \end{array} \right] dA \tag{3.100}$$

$$\frac{dL_e}{dx} = \boldsymbol{P}^T(x)\,\boldsymbol{u}(x) \tag{3.101}$$
$$\boldsymbol{P} = [n\ p]^T(x)$$

The reader can identify the *generalized stresses* N and M and the *generalized external loads* p and n.

These expressions for the internal and external works can be integrated along the length of the beam to obtain:

$$L_i = \int_0^l \boldsymbol{Q}^T\boldsymbol{\delta q}\ dx = [N\delta u - M\delta w' + M'\delta w]_0^l + \int_0^l -N'\delta u - M''\delta w\ dx \tag{3.102}$$

$$L_e = \int_0^l \boldsymbol{P}^T\boldsymbol{\delta u}\ dx + \boldsymbol{P_c}^T\boldsymbol{\delta u_c} \tag{3.103}$$

where the variables used can be defined as the external forces acting on each end of the beam and the displacements on both ends, see figure 3.9.

$$\begin{array}{lll} \boldsymbol{P_c} = \left[\boldsymbol{P_{c0}}^T\ \boldsymbol{P_{cl}}^T\right]^T & \boldsymbol{P_{c0}} = [N_0\ M_0\ T_0]^T & \boldsymbol{P_{cl}} = [N_l\ M_l\ T_l]^T \\ \boldsymbol{u_c} = [\boldsymbol{u_{c0}}\ \boldsymbol{u_{cl}}]^T & \boldsymbol{u_{c0}} = [u\ w\ w']^T(0) & \boldsymbol{u_{cl}} = [u\ w\ w']^T(l) \end{array} \tag{3.104}$$

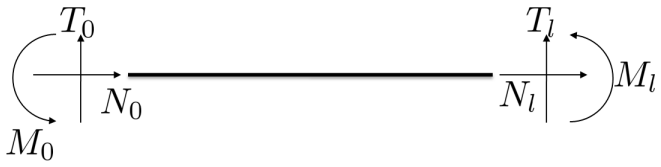

Figure 3.9: End forces in the 2D Bernoulli's model.

The equality between internal and external work leads to the equilibrium equations that govern the Euler-Bernoulli's beam.

$$L_i = L_e \rightarrow \left\{ \begin{array}{rcl} N' + n & = & 0 \\ -M'' + p & = & 0 \end{array} \right. ; \quad \begin{array}{ll} N(0) = N_0 & N(l) + N_l = 0 \\ M(0) = M_0 & M(l) + M_l = 0 \end{array} \tag{3.105}$$

The constitutive laws of the material can be used to obtain the equivalent equilibrium equations in terms of the displacements. Considering an elastic linear material, the generalized stresses can be rewritten as

$$\boldsymbol{Q}^T = \int_A \boldsymbol{b}^T\boldsymbol{\sigma}\ dA = \int_A \boldsymbol{b}^T E\boldsymbol{\varepsilon}\ dA = \int_A \boldsymbol{b}^T E\boldsymbol{b}\ dA\boldsymbol{q} = \boldsymbol{D}\boldsymbol{q} \tag{3.106}$$

$$\boldsymbol{D} = \left[\begin{array}{cc} EA & 0 \\ 0 & EI \end{array} \right] \tag{3.107}$$

The equilibrium equations in terms of displacements can be written as

$$\begin{aligned} EA\frac{du}{dx}(x) + n(x) &= 0 \\ EI\frac{d^4w}{dx^4}(x) + p(x) &= 0 \end{aligned} \tag{3.108}$$

3.2.1.2 Finite Element formulation

Once the theory of the Euler-Bernoulli's beam has been described, the finite element model can be deduced and its stiffness matrix derived. The finite element method starts with the description of the displacement field inside the element adopting an interpolating function (linear, cubic or any other type of function needed) where the interpolation coefficients are the displacements at each node of the element. The interpolation functions must be chosen carefully; in the case of an Euler-Bernoulli's beam they are derived from the solution of the differential equations 3.108 considering no external loads $n(x)$ and $p(x)$.

Solving the homogeneous differential equations, the shape functions can be deduced and the displacement field expressed as:

$$\boldsymbol{u}(x) = \begin{bmatrix} u(x) &= & U_1N_1(x) + U_4N_4(x) \\ w(x) &= & U_2N_2(x) + U_3N_3(x) + U_5N_5(x) + U_6N_6(x) \end{bmatrix} = \boldsymbol{N}(x)\,\boldsymbol{U} \tag{3.109}$$

$$\boldsymbol{N}(x) = \begin{bmatrix} N_1 & 0 & 0 & N_4 & 0 & 0 \\ 0 & N_2 & N_3 & 0 & N_5 & N_6 \end{bmatrix};\ \boldsymbol{U} = [U_1\ \cdots\ U_6]^T$$

$$N_1 = 1 - \frac{x}{l};\ N_4 = \frac{x}{l}$$

$$N_2 = 1 - 3\left(\frac{x}{l}\right)^2 + 2\left(\frac{x}{l}\right)^3 \quad ; \quad N_5 = 3\left(\frac{x}{l}\right)^2 - 2\left(\frac{x}{l}\right)^3$$

$$N_3 = l\left[\frac{x}{l} - 2\left(\frac{x}{l}\right)^2 + \left(\frac{x}{l}\right)^3\right] \quad ; \quad N_6 = l\left[-\left(\frac{x}{l}\right)^2 + \left(\frac{x}{l}\right)^3\right]$$

Using equation 3.97 the strain field can be obtained as

$$\boldsymbol{q} = \boldsymbol{C} \otimes \boldsymbol{u}(x) = \boldsymbol{C} \otimes \boldsymbol{N}(x)\,\boldsymbol{U} = \boldsymbol{B}(x)\,\boldsymbol{U} \tag{3.110}$$

$$\boldsymbol{B}(x) = \begin{bmatrix} N_1' & 0 & 0 & N_4' & 0 & 0 \\ 0 & N_2'' & N_3'' & 0 & N_5'' & N_6'' \end{bmatrix}$$

$$N_1' = -\frac{1}{l};\ N_4' = \frac{1}{l} \tag{3.111}$$

$$\begin{aligned} N_2' = \frac{6x}{l^2}\left(\frac{x}{l} - 1\right) \quad &; \quad N_2'' = \frac{6}{l^2}\left(2\frac{x}{l} - 1\right) \\ N_3' = 1 - 4\frac{x}{l} + 3\left(\frac{x}{l}\right)^2 \quad &; \quad N_3'' = \frac{2}{l}\left(3\frac{x}{l} - 2\right) \\ N_5' = \frac{6x}{l^2}\left(1 - \frac{x}{l}\right) \quad &; \quad N_5'' = \frac{6}{l^2}\left(1 - 2\frac{x}{l}\right) \\ N_6' = \frac{x}{l}\left(3\frac{x}{l} - 2\right) \quad &; \quad N_6'' = \frac{2}{l}\left(3\frac{x}{l} - 1\right) \end{aligned} \tag{3.112}$$

The principle of virtual work can be rewritten to take into consideration the new displacement formulation. The internal virtual work becomes

$$L_i = \int_0^l \boldsymbol{Q}^T \boldsymbol{q}\ dx = \boldsymbol{U}^T \boldsymbol{K_E} \boldsymbol{U} \tag{3.113}$$

$$\boldsymbol{K_E} = \int_0^l \boldsymbol{B}^T \boldsymbol{D} \boldsymbol{B}\ dx = \begin{bmatrix} \frac{EA}{l} & 0 & 0 & -\frac{EA}{l} & 0 & 0 \\ 0 & \frac{12EI}{l^3} & \frac{6EI}{l^2} & 0 & -\frac{12EI}{l^3} & \frac{6EI}{l^2} \\ 0 & \frac{6EI}{l^2} & \frac{4EI}{l} & 0 & -\frac{6EI}{l^2} & \frac{2EI}{l} \\ -\frac{EA}{l} & 0 & 0 & \frac{EA}{l} & 0 & 0 \\ 0 & -\frac{12EI}{l^3} & -\frac{6EI}{l^2} & 0 & \frac{12EI}{l^3} & -\frac{6EI}{l^2} \\ 0 & \frac{6EI}{l^2} & \frac{2EI}{l} & 0 & -\frac{6EI}{l^2} & \frac{4EI}{l} \end{bmatrix} \tag{3.114}$$

Equation 3.114 represents the well known Euler-Bernoulli's elastic stiffness matrix. This stiffness matrix relates the nodal displacement with the nodal reactions on each end of the beam element. Also, the external virtual work can be written in terms of the new displacement field as

$$L_e = \int_0^l \boldsymbol{P}^T \boldsymbol{u} dx = \boldsymbol{f}^T \boldsymbol{U} \tag{3.115}$$

$$\boldsymbol{f} = \int_0^l \boldsymbol{N}^T \boldsymbol{P} dx$$

Finally, the equilibrium equations in a matrix form can be obtained.

$$\boldsymbol{K_E} \boldsymbol{U} = \boldsymbol{f} \tag{3.116}$$

3.2.2 Three dimensional beam finite element modeling

Although the Euler-Bernoulli two dimensional model can be very useful for the analysis of floating structures (as it will be seen in further sections), more advanced finite element techniques are required when the analysis of floating structures is faced in the general form. As it will be exposed in the second part of this thesis, one of the main characteristics of floating structures is their capacity to operate in large displacements. To analize the interaction between the structure and the fluid, a general model is required. In particular, two models will be described.

First, a three dimensional beam model based on the Euler-Bernoulli's and Saint Venant's formulations for the bending and torsional behaviour and considering small displacements is exposed. This model will be developed considering the total lagrangian formulation.

Second, a completely general approach for 3D beam structures considering large displacements will be formulated and discussed. In this case, the updated lagrangian formulation will be used.

3.2.2.1 First order formulation

The first model is based on the Euler-Bernoulli's model for the bending behaviour and on the Saint Venant's hypothesis for the torsional behaviour of the beam. The procedure developed in this model is almost the same as the one used in the subsection 3.2.1. First, the theoretical introduction of the beam model will be exposed and, secondly, the finite element method will be applied to derive the elastic stiffness matrix.

The theoretical model starts with the definition of the displacement field inside the beam. Considering small displacements and the well known torsional formulation of Saint Venant, the displacements can be written as

$$\boldsymbol{S} = \begin{bmatrix} u(x) - yv'(x) - zw'(x) \\ v(x) - z\varphi_x(x) \\ w(x) + y\varphi_x(x) \end{bmatrix} = \boldsymbol{n}(y,z)\,\boldsymbol{u}(x) \tag{3.117}$$

$$\boldsymbol{u} = [u\ v\ w\ \varphi_x]^T(x)$$

$$\boldsymbol{n} = \begin{bmatrix} 1 & -y\dfrac{d}{dx} & -z\dfrac{d}{dx} & 0 \\ 0 & 1 & 0 & -z \\ 0 & 0 & 1 & y \end{bmatrix}$$

where the generalized displacements (axial displacement $u(x)$, bending displacements $v(x)$ and $w(x)$ and torsional displacement $\varphi_x(x)$) are depicted in figure 3.10.

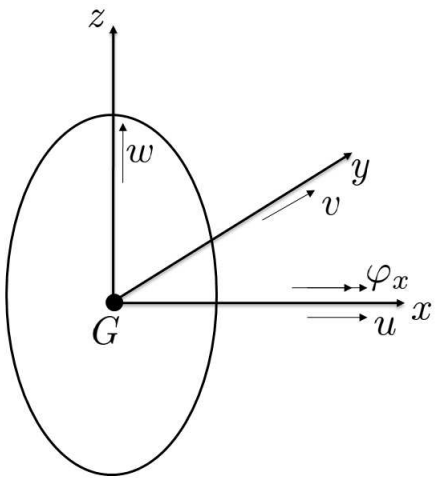

Figure 3.10: Generalized displacement for a 3D beam with no shear deformability.

The computation of the strains is done by means of the Green-Lagrange strain tensor (only its linear part).

$$\begin{array}{rcccc} \varepsilon_x & = & u'(x) - yv''(x) + zw''(x) & = & \eta(x) + y\vartheta_z(x) + z\vartheta_y(x) \\ \varepsilon_y & = & 0 & & \\ \varepsilon_z & = & 0 & & \\ \gamma_{xy} & = & -z\varphi_x'(x) & = & -z\vartheta_x(x) \\ \gamma_{xz} & = & y\varphi_x'(x) & = & y\vartheta_x(x) \\ \gamma_{yz} & = & 0 & & \end{array} \tag{3.118}$$

Arranging properly the expression, it can be written in matrix form assuming the expression

$$\boldsymbol{\varepsilon} = \boldsymbol{b}(y,z)\,\boldsymbol{q}(x) \tag{3.119}$$

where the strain vector and matrix $\boldsymbol{b}$ are defined as

$$\boldsymbol{\varepsilon} = [\varepsilon_x \ \gamma_{xy} \ \gamma_{xz}]^T \tag{3.120}$$

$$\boldsymbol{b} = \begin{bmatrix} 1 & 0 & y & z \\ 0 & -z & 0 & 0 \\ 0 & y & 0 & 0 \end{bmatrix} \tag{3.121}$$

The generalized strains are arranged in a vector defined as

$$\boldsymbol{q} = \begin{bmatrix} \eta \\ \vartheta_y \\ \vartheta_z \\ \vartheta_x \end{bmatrix}^T (x) = \begin{bmatrix} u' \\ -v'' \\ -w'' \\ \varphi_x' \end{bmatrix}^T (x) = \boldsymbol{C} \otimes \boldsymbol{u} \tag{3.122}$$

$$\boldsymbol{C} = \begin{bmatrix} \dfrac{d}{dx} & 0 & 0 & 0 \\ 0 & -\dfrac{d^2}{dx^2} & 0 & 0 \\ 0 & 0 & -\dfrac{d^2}{dx^2} & 0 \\ 0 & 0 & 0 & \dfrac{d}{dx} \end{bmatrix} \tag{3.123}$$

Once the strains are computed, the stress will be deduced as the ones which are energetically conjugate by means of the principle of virtual works. Therefore, the derivative of internal and external works with respect to x are computed.

$$\frac{dL_i}{dx} = \int_A \boldsymbol{\sigma}^T \boldsymbol{\delta\varepsilon}\, dA = \int_A \boldsymbol{\sigma}^T \boldsymbol{b}\, dA \boldsymbol{\delta q} = \boldsymbol{Q}^T \boldsymbol{\delta q} \tag{3.124}$$

The internal work gives the stresses, which are

$$\boldsymbol{\sigma} = [\sigma_x \ \tau_{xy} \ \tau_{xz}]^T \tag{3.125}$$

Integrating properly these stresses along the section, the generalized stresses may be obtained.

$$\boldsymbol{Q} = \begin{bmatrix} N \\ M_y \\ M_z \\ M_t \end{bmatrix} = \int_A \begin{bmatrix} \sigma_x \\ z\sigma_x \\ y\sigma_x \\ -z\tau_{xy} + y\tau_{xz} \end{bmatrix} dA \tag{3.126}$$

On the other hand, the derivative of the external work can be written as

$$\frac{dL_e}{dx} = \boldsymbol{P}^T(x)\,\boldsymbol{u}(x) \tag{3.127}$$

with the generalized external loads defined as

$$\boldsymbol{P} = [n\ p_y\ p_z\ m_t]^T(x) \tag{3.128}$$

Integrating the two expressions along the element, internal and external works may be obtained as:

$$L_i = \int_0^l \boldsymbol{Q}^T \boldsymbol{\delta q}\ dx$$
$$=$$
$$\left[Nu + M_t\varphi_x - M_y w' - M_z v' + M_z' v + M_y' w\right]_0^l + \int_0^l -N'u - M_t'\varphi_x - M_z'' v - M_y'' w\ dx \tag{3.129}$$

$$L_e = \int_0^l \boldsymbol{P}^T \boldsymbol{u}\ dx + \boldsymbol{P_c}^T \boldsymbol{u_c} \tag{3.130}$$

where the variables used are the forces, moments and displacements at each end of the beam.

$$\begin{gathered} \boldsymbol{P_c} = \left[\boldsymbol{P_{c0}}^T\ \boldsymbol{P_{cl}}^T\right]^T \\ \boldsymbol{P_{c0}} = [N_0\ T_{y0}\ T_{z0}\ M_{t0}\ M_{y0}\ M_{z0}]^T;\ \boldsymbol{P_{cl}} = [N_l\ T_{yl}\ T_{zl}\ M_{tl}\ M_{yl}\ M_{zl}]^T \end{gathered} \tag{3.131}$$

$$\boldsymbol{u_c} = [\boldsymbol{u_{c0}}\ \boldsymbol{u_{cl}}]^T;\ \boldsymbol{u_{c0}} = [u\ v\ w\ \varphi_x\ v'\ w']^T(0);\ \boldsymbol{u_{cl}} = [u\ v\ w\ \varphi_x\ v'\ w']^T(l) \tag{3.132}$$

Imposing the equivalence between internal and external work the equilibrium equations are obtained.

$$L_i = L_e \rightarrow \begin{cases} \dfrac{dN}{dx} + n = 0 \\ \dfrac{d^2M_z}{dx^2} + p_y = 0 \\ \dfrac{d^2M_y}{dx^2} + p_z = 0 \\ \dfrac{dM_t}{dx} + m_t = 0 \end{cases} ; \begin{array}{ll} N(0) = N_0 & N(l) + N_l = 0 \\ M_t(l) + M_{tl} = 0 & M_t(0) = M_{t0} \\ M_y(0) = M_{y0} & M_y(l) + M_{yl} = 0 \\ M_z(0) + M_{z0} = 0 & M_z(l) = M_{zl} \end{array} \tag{3.133}$$

Considering now the constitutive laws of a linear elastic material ($\boldsymbol{\sigma} = \boldsymbol{d\varepsilon}$), the equilibrum equations can be derived in terms of the generalized displacements.

$$\boldsymbol{Q}^T = \int_A \boldsymbol{b}^T \boldsymbol{\sigma}\ dA = \int_A \boldsymbol{b}^T \boldsymbol{d\varepsilon}\ dA = \int_A \boldsymbol{b}^T \boldsymbol{db}\ dA \boldsymbol{q} = \boldsymbol{Dq} \tag{3.134}$$

$$\boldsymbol{D} = \begin{bmatrix} EA & 0 & 0 & 0 \\ 0 & EI_y & 0 & 0 \\ 0 & 0 & EI_z & 0 \\ 0 & 0 & 0 & GJ \end{bmatrix}$$

$$\begin{aligned} EA\frac{d^2u}{dx^2}(x) + n &= 0 \qquad & EI_y\frac{d^4w}{dx^4}(x) + p_z &= 0 \\ EI_z\frac{d^4v}{dx^4}(x) + p_y &= 0 \qquad & GJ\frac{d^2\varphi_x}{dx^2}(x) + m_t &= 0 \end{aligned} \tag{3.135}$$

Once the equilibrium equations are computed, the finite element formulation can be defined. The displacement field inside the element as an interpolation between the displacements at the ends is defined as:

$$\boldsymbol{u}(x) = \begin{bmatrix} u(x) &= & U_1 N_{u1}(x) + U_7 N_{u2}(x) \\ v(x) &= & U_2 N_{v1}(x) + U_8 N_{v2}(x) + U_6 N_{v3}(x) + U_{12} N_{v4}(x) \\ w(x) &= & U_3 N_{w1}(x) + U_9 N_{w2}(x) + U_5 N_{w3}(x) + U_{11} N_{w4}(x) \\ \varphi_x(x) &= & U_4 N_{\varphi 1}(x) + U_{10} N_{\varphi 2}(x) \end{bmatrix} = \boldsymbol{N}(x)\boldsymbol{U} \tag{3.136}$$

where the matrix of shape functions and the vector of nodal displacements can now be written as

$$\boldsymbol{N}(x) = \begin{bmatrix} N_{u1} & 0 & 0 & 0 & 0 & 0 & N_{u2} & 0 & 0 & 0 & 0 & 0 \\ 0 & N_{v1} & 0 & 0 & 0 & N_{v3} & 0 & N_{v2} & 0 & 0 & 0 & N_{v4} \\ 0 & 0 & N_{w1} & 0 & N_{w3} & 0 & 0 & 0 & N_{w2} & 0 & N_{w4} & 0 \\ 0 & 0 & 0 & N_{\varphi 1} & 0 & 0 & 0 & 0 & 0 & N_{\varphi 2} & 0 & 0 \end{bmatrix} \tag{3.137}$$

$$\boldsymbol{U} = \begin{bmatrix} U_1 & \cdots & U_{12} \end{bmatrix}^T \tag{3.138}$$

For completeness, the shape functions are reported here.

$$\begin{aligned} N_{u1} = N_{\varphi 1} &= 1 - \frac{x}{l} & N_{u2} = N_{\varphi 2} &= \frac{x}{l} \\ N_{v1} = N_{w1} &= 1 - 3\left(\frac{x}{l}\right)^2 + 2\left(\frac{x}{l}\right)^3 & N_{v2} = N_{w2} &= 3\left(\frac{x}{l}\right)^2 - 2\left(\frac{x}{l}\right)^3 \\ N_{v3} = -N_{w3} &= l\left[\frac{x}{l} - 2\left(\frac{x}{l}\right)^2 + \left(\frac{x}{l}\right)^3\right] & N_{v4} = -N_{w4} &= l\left[-\left(\frac{x}{l}\right)^2 + \left(\frac{x}{l}\right)^3\right] \end{aligned} \tag{3.139}$$

The generalized elastic linear strains can be obtained from equation 3.122 and their expression is

$$\boldsymbol{q} = \boldsymbol{C} \otimes \boldsymbol{u}\,(x) = \boldsymbol{C} \otimes \boldsymbol{N}\,(x)\,\boldsymbol{U} = \boldsymbol{B}\,(x)\,\boldsymbol{U} \tag{3.140}$$

where a new matrix must be defined.

$$\boldsymbol{B}\,(x) = \begin{bmatrix} N'_{u1} & 0 & 0 & 0 & 0 & 0 & N'_{u2} & 0 & 0 & 0 & 0 & 0 \\ 0 & -N''_{v1} & 0 & 0 & 0 & -N''_{v3} & 0 & -N''_{v2} & 0 & 0 & 0 & -N''_{v4} \\ 0 & 0 & -N''_{w1} & 0 & -N''_{w3} & 0 & 0 & 0 & -N''_{w2} & 0 & -N''_{w4} & 0 \\ 0 & 0 & 0 & N'_{\varphi 1} & 0 & 0 & 0 & 0 & 0 & N'_{\varphi 2} & 0 & 0 \end{bmatrix} \tag{3.141}$$

Also in this case, the first and second derivative of the shape functions are included.

$$\begin{aligned} N'_{v1} &= \frac{6x}{l^2}\left(\frac{x}{l} - 1\right) \quad ; \quad N'_{v2} = \frac{6x}{l^2}\left(1 - \frac{x}{l}\right) \\ N'_{v3} &= 1 - 4\frac{x}{l} + 3\left(\frac{x}{l}\right)^2 \quad ; \quad N'_{v4} = \frac{x}{l}\left(3\frac{x}{l} - 2\right) \\ N''_{v1} = N''_{w1} &= \frac{6}{l^2}\left(2\frac{x}{l} - 1\right) \quad ; \quad N''_{v2} = N''_{w2} = \frac{6}{l^2}\left(1 - 2\frac{x}{l}\right) \\ N''_{v3} = -N''_{w3} &= \frac{6x}{l^2} - \frac{4}{l} \quad ; \quad N''_{v4} = -N''_{w4} = \frac{6x}{l^2} - \frac{2}{l} \end{aligned}$$

Expressing the internal virtual work with the new displacement formulation the stiffness matrix associated to the shape functions used may be obtained.

$$L_i = \int_0^l \boldsymbol{Q}^T \boldsymbol{q}\; dx = \boldsymbol{U}^T \boldsymbol{K_E} \tag{3.142}$$

$$\boldsymbol{K_E} = \int_0^l \boldsymbol{B}^T \boldsymbol{D} \boldsymbol{B}\; dx = \begin{bmatrix} \boldsymbol{K_1} & \boldsymbol{K_2} \\ \boldsymbol{K_2}^T & \boldsymbol{K_3} \end{bmatrix} \tag{3.143}$$

with

$$\boldsymbol{K_1} = \begin{bmatrix} \frac{EA}{l} & 0 & 0 & 0 & 0 & 0 \\ 0 & \frac{12EI_z}{l^3} & 0 & 0 & 0 & \frac{6EI_z}{l^2} \\ 0 & 0 & \frac{12EI_y}{l^3} & 0 & -\frac{6EI_y}{l^2} & 0 \\ 0 & 0 & 0 & \frac{GJ}{l} & 0 & 0 \\ 0 & 0 & -\frac{6EI_y}{l^2} & 0 & \frac{4EI_y}{l} & 0 \\ 0 & \frac{6EI_z}{l^2} & 0 & 0 & 0 & \frac{4EI_z}{l} \end{bmatrix} \tag{3.144}$$

$$\boldsymbol{K_2} = \begin{bmatrix} -\frac{EA}{l} & 0 & 0 & 0 & 0 & 0 \\ 0 & -\frac{12EI_z}{l^3} & 0 & 0 & 0 & \frac{6EI_z}{l^2} \\ 0 & 0 & -\frac{12EI_y}{l^3} & 0 & -\frac{6EI_y}{l^2} & 0 \\ 0 & 0 & 0 & -\frac{GJ}{l} & 0 & 0 \\ 0 & 0 & \frac{6EI_y}{l^2} & 0 & \frac{2EI_y}{l} & 0 \\ 0 & -\frac{6EI_z}{l^2} & 0 & 0 & 0 & \frac{2EI_z}{l} \end{bmatrix} \tag{3.145}$$

$$\boldsymbol{K_3} = \begin{bmatrix} \frac{EA}{l} & 0 & 0 & 0 & 0 & 0 \\ 0 & \frac{12EI_z}{l^3} & 0 & 0 & 0 & -\frac{6EI_z}{l^2} \\ 0 & 0 & \frac{12EI_y}{l^3} & 0 & \frac{6EI_y}{l^2} & 0 \\ 0 & 0 & 0 & \frac{GJ}{l} & 0 & 0 \\ 0 & 0 & \frac{6EI_y}{l^2} & 0 & \frac{4EI_y}{l} & 0 \\ 0 & -\frac{6EI_z}{l^2} & 0 & 0 & 0 & \frac{4EI_z}{l} \end{bmatrix} \tag{3.146}$$

Doing the same with the external virtual work it can be obtained

$$L_e = \int_0^l \boldsymbol{P}^T \boldsymbol{u} dx = \boldsymbol{f}^T \boldsymbol{U} \tag{3.147}$$

with the vector $\boldsymbol{f}$ equal to

$$\boldsymbol{f} = \int_0^l \boldsymbol{P}^T \boldsymbol{N} dx \tag{3.148}$$

The equilibrium equations in matrix form can now be written as

$$\boldsymbol{K_E U} = \boldsymbol{f} \tag{3.149}$$

The theories of Euler-Bernoulli and Saint Venant have been presented under the hypothesis of small displacements. This hypothesis will be now removed and a general approach will be presented using the most general equations of the principle of virtual work.

3.2.2.2 General formulation

Although the model presented before (Euler-Bernoulli plus Saint Venant models for the description of bending and torsion behaviour) is an accurate approach to deal with 3D frame structures, more advanced techniques are required when a complete analysis of beam floating structures is attempted. In the following, a completely general three dimensional model considering large displacements is described. In the second part of this thesis, a modification of this model to take into account the fluid structure interaction

will be formulated and discussed.

First of all, the displacement field inside the element must be characterized. In this case, the displacements are

$$\boldsymbol{S} = \begin{bmatrix} u(x) - yv'(x) - zw'(x) \\ v(x) - z\varphi_x(x) \\ w(x) + y\varphi_x(x) \end{bmatrix} \tag{3.150}$$

The strain field can be deduced using the definition of the Green-Lagrange strain tensor.

$$\begin{aligned} e_{xx} = u'(x) - yv''(x) - zw''(x) \quad & \eta_{xx} = \frac{1}{2}\left\{ \begin{array}{l} u'^2 + v'^2 + w'^2 \\ + \\ y^2v''^2 + z^2w''^2 + (z^2+y^2)\varphi_x'^2 \\ + \\ 2\left(-zu'w'' - yu'v'' - zv'\varphi_x' + yw'\varphi_x' + yzv''w''\right) \end{array} \right\} \\ e_{xy} = -\frac{z}{2}\varphi_x' \quad & \eta_{xy} = \frac{1}{2}\left(-u'v' + w'\varphi_x + yv'v'' + zv'w'' + y\varphi_x\varphi_x'\right) \\ e_{xz} = \frac{1}{2}\left(2w' + y\varphi_x\right) \quad & \eta_{xz} = \frac{1}{2}\left(-u'w' + yv''w' + zw'w'' - v'\varphi_x + z\varphi_x\varphi_x'\right) \\ e_{yy} = 0 \quad & \eta_{yy} = \frac{1}{2}\left(v'^2 + \varphi_x^2\right) \\ e_{yz} = 0 \quad & \eta_{yz} = -\frac{v'w'}{2} \\ e_{zz} = 0 \quad & \eta_{zz} = \frac{1}{2}\left(w'^2 + \varphi_x^2\right) \end{aligned} \tag{3.151}$$

The stress field must be characterized with respect the configuration ${}^1\boldsymbol{C}$. Defining the generalized stresses as the ones that are energetically conjugated to the previous strains it may be written:

$$\begin{aligned} {}^1_1F_x &= \int_A {}^1_1\sigma_{xx}dA & {}^1_1F_y &= \int_A {}^1_1\sigma_{yy}dA & {}^1_1F_z &= \int_A {}^1_1\sigma_{zz}dA \\ {}^1_1M_x &= \int_A -z{}^1_1\tau_{xy} + y{}^1_1\tau_{xz}dA & {}^1_1M_y &= \int_A z{}^1_1\sigma_{xx}dA & {}^1_1M_z &= \int_A -y{}^1_1\sigma_{xx}dA \end{aligned} \tag{3.152}$$

The imposition of the principle of virtual works will lead to an equilibrated system. For simplicity, the expression of the principle of virtual work in its updated lagrangian formulation is reported here.

$$\int_{{}^1V} \boldsymbol{S} : {}_1\boldsymbol{\delta\varepsilon} d^1V + \int_{{}^1V} {}^1\boldsymbol{\sigma} : {}_1\boldsymbol{\delta\eta} d^1V = {}^2_1R - {}^1_1R \tag{3.153}$$

$${}^2_1R = \int_{{}^1V} {}^2_1\boldsymbol{f}^T\boldsymbol{\delta u} d^1V + \int_{{}^1S_\sigma} {}^2_1\boldsymbol{t}^T\boldsymbol{\delta u} d^1\Gamma \tag{3.154}$$

$${}^1_1R = \int_{{}^1V} {}^2_1\boldsymbol{\sigma} : \boldsymbol{\delta}_1\boldsymbol{e} d^1V = \int_{{}^1V} {}^1_1\boldsymbol{f}^T\boldsymbol{\delta u} d^1V + \int_{{}^1S_\sigma} {}^1_1\boldsymbol{t}^T\boldsymbol{\delta u} d^1\Gamma \tag{3.155}$$

Considering the displacement field exposed before and neglecting the nonlinear strains with respect to the linear part of the Green-Lagrange strain tensor under the consideration of large displacements but small strains, the principle of virtual works can be rewritten as

$$\begin{gathered}
\overbrace{\int_{{}^1\Omega} E{}^1_1\boldsymbol{e}_{xx} + 4G{}^1_1\boldsymbol{e}_{xy}{}^1_1\boldsymbol{\delta e}_{xy} + 4G{}^1_1\boldsymbol{e}_{xz}{}^1_1\boldsymbol{\delta e}_{xx}\ d^1\Omega}^{Linear\ part} \\
+ \\
\underbrace{\int_{{}^1\Omega} {}^1_1\boldsymbol{\sigma}_{xx}{}^1_1\boldsymbol{\delta\eta}_{xx} + 2{}^1_1\boldsymbol{\sigma}_{xy}{}^1_1\boldsymbol{\delta\eta}_{xy} + 2{}^1_1\boldsymbol{\sigma}_{xz}{}^1_1\boldsymbol{\delta\eta}_{xz} + {}^1_1\boldsymbol{\sigma}_{yy}{}^1_1\boldsymbol{\delta\eta}_{yy} + 2{}^1_1\boldsymbol{\sigma}_{yz}{}^1_1\boldsymbol{\delta\eta}_{yz} + {}^1_1\boldsymbol{\sigma}_{zz}{}^1_1\boldsymbol{\delta\eta}_{zz}\ d^1\Omega}_{Nonlinear\ part} \\
= \\
{}^2_1\boldsymbol{R} - {}^1_1\boldsymbol{R}
\end{gathered} \tag{3.156}$$

where the linear and nonlinear parts of the expression are highlighted.

To obtain the final expression the linear part and the nonlinear part will be treated separately.

$$\begin{gathered}
\int_{{}^1\Omega} E{}^1_1\boldsymbol{e}_{xx} + 4G{}^1_1\boldsymbol{e}_{xy}{}^1_1\boldsymbol{\delta e}_{xy} + 4G{}^1_1\boldsymbol{e}_{xz}{}^1_1\boldsymbol{\delta e}_{xx}\ d^1\Omega \\
= \\
\frac{1}{2}\int_{{}^1\Omega} E\delta\left(u'^2 + y^2v''^2 + z^2w''^2 - 2yu'v'' - 2zu'w'' + 2yzv''w''\right)\ d^1\Omega \\
+ \\
\frac{1}{2}\int_{{}^1\Omega} G\delta\left(y^2 + z^2\right)\varphi_x'^2\ d^1\Omega
\end{gathered} \tag{3.157}$$

Considering that the variables are described in the principal centroidal coordinates, the definitions of the moment of inertia and torsional constant are:

$$I_y = \int_A z^2\ dA;\ I_z = \int_A y^2\ dA;\ J = \int_A y^2 + z^2\ dA = I_y + I_z$$

Equation 3.157 reduces to

$$\int_0^l EAu'\delta u' + EI_yw''\delta w'' + EI_zv''\delta v'' + GJ\varphi_x'\delta\varphi_x'\ dx \tag{3.158}$$

To operate the nonlinear part of the equation 3.156, it might be appropiate to divide it in 5 parts and operate separetely.

The part that has the components of the Cauchy's stress tensor in the x direction is first treated.

$$\begin{gathered}\int_{{}^1\Omega} {}^1_1\boldsymbol{\sigma}_{xx}\,{}^1_1\boldsymbol{\delta\eta}_{xx}\; d^1\Omega \\ = \\ \frac{1}{2}\int_0^l {}^1_1F_x\delta\left(u'^2+v'^2+w'^2\right)+{}^1_1F_x\left(\frac{I_y}{A}\delta w''^2+\frac{I_z}{A}\delta v''^2\right)+\overline{K}\delta\varphi_x'^2\; dx \\ + \\ \int_0^l -{}^1_1M_z\delta\left(w'\varphi_x'\right)-{}^1_1M_y\delta\left(v'\varphi_x'\right)-{}^1_1M_y\delta\left(u'w''\right)+{}^1_1M_z\delta\left(u'v''\right)\; dx\end{gathered} \tag{3.159}$$

where $\overline{K}={}^1_1F_x\dfrac{I_y+I_z}{A}={}^1_1F_x\dfrac{J}{A}$ is the Wagner coefficient.

The second part of the integral is the one with the two xy and xz parts of the Cauchy's stress tensor.

$$\begin{gathered}\int_{{}^1\Omega} 2\,{}^1_1\boldsymbol{\sigma}_{xy}\,{}^1_1\boldsymbol{\delta\eta}_{xy}+2\,{}^1_1\boldsymbol{\sigma}_{xz}\,{}^1_1\boldsymbol{\delta\eta}_{xz}\; d^1\Omega \\ = \\ \int_0^l {}^1_1F_y\delta\left(w'\varphi_x-u'v'\right)-{}^1_1F_z\delta\left(v'\varphi_x+u'w'\right)+(1-\alpha)\,{}^1_1M_x\delta\left(v'w''\right)+\alpha\,{}^1_1M_x\delta\left(w'v''\right)\; dx \\ + \\ \int_0^l\left(\int_A {}^1_1\boldsymbol{\sigma}_{xy}\; dA\right)\delta\left(v'v''+\varphi_x\varphi_x'\right)\; dx+\int_0^l\left(\int_A {}^1_1\boldsymbol{\sigma}_{xz}\; dA\right)\delta\left(w'w''+\varphi_x\varphi_x'\right)\; dx\end{gathered} \tag{3.160}$$

where the torsional parameter α can be defined as

$$\alpha=\frac{\displaystyle\int_A {}^1_1\boldsymbol{\sigma}_{xz}y\; dA}{{}^1_1M_x}=1-\frac{\displaystyle\int_A -{}^1_1\boldsymbol{\sigma}_{xy}z\; dA}{{}^1_1M_x} \tag{3.161}$$

Let us focus on the yy components of the Cauchy's stress tensor.

$$\begin{gathered}\int_{{}^1\Omega} {}^1_1\boldsymbol{\sigma}_{yy}\,{}^1_1\boldsymbol{\delta\eta}_{yy}\; d^1\Omega \\ = \\ \int_0^l\left(\int_A {}^1_1\boldsymbol{\sigma}_{yy}\; dA\right)\frac{1}{2}\delta\left(\varphi_x^2+v'^2\right)\; dx \\ = \\ \int_A {}^1_1\boldsymbol{\sigma}_{xy}y\; dA\left[\varphi_x\delta\varphi_x+v'\delta v'\right]_0^l-\int_0^l\left(\int_A {}^1_1\boldsymbol{\sigma}_{xy}y\; dA\right)\delta\left(\varphi_x\varphi_x'+v'v''\right)\; dx\end{gathered} \tag{3.162}$$

The fourth part of the integral (yz components of the Cauchy's stress tensor) can be written as

$$\begin{gathered}\int_{{}^1\Omega} {}^1_1\boldsymbol{\sigma}_{yz}\, {}^1_1\boldsymbol{\delta\eta}_{yz}\; d^1\Omega \\ = \\ \int_0^l \left(\frac{\partial}{\partial x}\int_A {}^1_1\boldsymbol{\sigma}_{xy} z\; dA\right) \delta\left(v'w'\right)\; dx \\ = \\ -\left(1-\alpha\right){}^1M_x \left[v'\delta w' + w'\delta v'\right]_0^l + \int_0^l \left(1-\alpha\right){}^1M_x \delta\left(v''w' + v'w''\right)\; dx\end{gathered} \tag{3.163}$$

Finally, the zz part of the Cauchy's stress tensor in the nonlinear part of the principle of virtual work is expressed as

$$\begin{gathered}\int_{{}^1\Omega} {}^1_1\boldsymbol{\sigma}_{zz}\, {}^1_1\boldsymbol{\delta\eta}_{zz}\; d^1\Omega \\ = \\ \int_0^l \left(\frac{\partial}{\partial x}\int_A {}^1_1\boldsymbol{\sigma}_{xz} z\; dA\right) \frac{1}{2}\delta\left(\varphi_x^2 + w'^2\right)\; dx \\ = \\ \left(\int_A {}^1_1\boldsymbol{\sigma}_{xz} z\; dA\right) \left[\varphi_x\delta\varphi_x + w'\delta w'\right]_0^l - \int_0^l \left(\int_A {}^1_1\boldsymbol{\sigma}_{xz} z\; dA\right) \delta\left(\varphi_x\varphi_x' + w''w'\right)\; dx\end{gathered} \tag{3.164}$$

The right part of the equality in equation 3.156 has to be formulated in terms of the new displacement field. Let us focus first on the variable ${}^2_1R$ and, as a hypothesis, the beam is considered only loaded at the ends.

For the first node of the beam we can write

$$\begin{gathered}{}^2_1\boldsymbol{R}_1 = \int_{A_1} {}^2_1\boldsymbol{f}^T \boldsymbol{\delta u}\; dA_1 \\ = \\ {}^2_1F_{x1}\delta u_1 + {}^2_1F_{y1}\delta v_1 + {}^2_1F_{z1}\delta w_1 + \left({}^2_1M_{x1} + \left[\int_{A_1} {}^1_2\boldsymbol{\sigma}_{xz} z + {}^1_2\boldsymbol{\sigma}_{xy} y\; dA_1\right] \delta\varphi_{x1}\right) \delta\varphi_{x1} \\ + \\ \left[{}^2_1M_{y1} + {}^1_1M_{z1}\varphi_{x1} + \left(\int_{A_1} {}^1_1\boldsymbol{\sigma}_{xz} z\; dA_1\right) \varphi_{y1} - \left(\int_{A_1} {}^1_1\boldsymbol{\sigma}_{xz} y\; dA_1\right) \varphi_{z1}\right] \delta\varphi_{y1} \\ + \\ \left[{}^2_1M_{z1} - {}^1_1M_{y1}\varphi_{x1} - \left(\int_{A_1} {}^1_1\boldsymbol{\sigma}_{xy} z\; dA_1\right) \varphi_{y1} + \left(\int_{A_1} {}^1_1\boldsymbol{\sigma}_{xy} y\; dA_1\right) \varphi_{z1}\right] \delta\varphi_{z1}\end{gathered} \tag{3.165}$$

Remembering that $\varphi_z = v'$ and $\varphi_y = -w'$ and rearranging

$$
\begin{gathered}
{}^{2}_{1}\boldsymbol{R}_1 = {}^{2}_{1}F_{x1}\delta u_1 + {}^{2}_{1}F_{y1}\delta v_1 + {}^{2}_{1}F_{z1}\delta w_1 + {}^{2}_{1}M_{x1}\delta\varphi_{x1} + {}^{2}_{1}M_{y1}\delta\varphi_{y1} + {}^{2}_{1}M_{z1}\delta\varphi_{z1} \\
+ \\
\left({}^{2}_{1}M_{z1}\right)\delta\varphi_{y1} + \left({}^{2}_{1}M_{y1}\right)\delta\varphi_{x1} + \int_{A_1} {}^{2}_{1}\boldsymbol{\sigma}_{xy} y \; dA_1 \left(\varphi_{x1}\delta\varphi_{x1} + \varphi_{z1}\delta\varphi_{z1}\right) \\
+ \\
\int_{A_1} {}^{2}_{1}\boldsymbol{\sigma}_{xz} z \; dA_1 \left(\varphi_{x1}\delta\varphi_{x1} + \varphi_{y1}\delta\varphi_{y1}\right) + (1-\alpha)\,{}^{2}_{1}M_{x1}\varphi_{y1}\delta\varphi_{z1} - \alpha^{2}_{1}M_{x1}\varphi_{z1}\delta\varphi_{y1}
\end{gathered}
\tag{3.166}
$$

By adopting th same approach for node *2* and summing up the two expressions, it might be obtained:

$$
\begin{gathered}
{}^{2}_{1}\boldsymbol{R} = {}^{2}_{1}\boldsymbol{R}_1 + {}^{2}_{1}\boldsymbol{R}_2 = \boldsymbol{\delta u}^T {}^{2}_{1}\boldsymbol{f} + \left[\left({}^{1}_{1}M_z\varphi_x\right)\delta\varphi_y - \left({}^{1}_{1}M_y\varphi_x\right)\delta\varphi_z\right]_0^l \\
+ \\
\left(\int_A {}^{1}_{1}\boldsymbol{\sigma}_{xy} y \; dA\right)\left[\varphi_x\delta\varphi_x + \varphi_z\delta\varphi_z\right]_0^l + \left(\int_A {}^{1}_{1}\boldsymbol{\sigma}_{xz} z \; dA\right)\left[\varphi_x\delta\varphi_x + \varphi_y\delta\varphi_y\right]_0^l \\
+ \\
\left[(1-\alpha)\,{}^{1}_{1}M_x\varphi_y\delta\varphi_z - \alpha^{1}_{1}M_x\varphi_z\delta\varphi_y\right]_0^l
\end{gathered}
\tag{3.167}
$$

On the other hand, the expression of ${}^{1}_{1}R$ is easier to obtain.

$$
{}^{1}_{1}\boldsymbol{R} = \boldsymbol{\delta u}^T {}^{1}_{1}\boldsymbol{f} \tag{3.168}
$$

where ${}^{2}_{1}\boldsymbol{f}$ and ${}^{1}_{1}\boldsymbol{f}$ have been already defined as:

$$
{}^{2}_{1}\boldsymbol{f} = \left[\begin{array}{cccccccccccc} {}^{2}_{1}F_{x1} & {}^{2}_{1}F_{y1} & {}^{2}_{1}F_{z1} & {}^{2}_{1}M_{x1} & {}^{2}_{1}M_{y1} & {}^{2}_{1}M_{z1} & {}^{2}_{1}F_{x2} & {}^{2}_{1}F_{y2} & {}^{2}_{1}F_{z2} & {}^{2}_{1}M_{x2} & {}^{2}_{1}M_{y2} & {}^{2}_{1}M_{z2} \end{array}\right]^T \tag{3.169}
$$

$$
{}^{1}_{1}\boldsymbol{f} = \left[\begin{array}{cccccccccccc} {}^{1}_{1}F_{x1} & {}^{1}_{1}F_{y1} & {}^{1}_{1}F_{z1} & {}^{1}_{1}M_{x1} & {}^{1}_{1}M_{y1} & {}^{1}_{1}M_{z1} & {}^{1}_{1}F_{x2} & {}^{1}_{1}F_{y2} & {}^{1}_{1}F_{z2} & {}^{1}_{1}M_{x2} & {}^{1}_{1}M_{y2} & {}^{1}_{1}M_{z2} \end{array}\right]^T \tag{3.170}
$$

Substituting all the expressions derived for each part of the integrals:

$$
\begin{gathered}
\int_0^l EAu'\delta u' + EI_y w''\delta w'' + EI_z v''\delta v'' + GJ\varphi'_x\delta\varphi'_x \; dx \\
+ \\
\frac{1}{2}\int_0^l {}^{1}_{1}F_x\delta\left(u'^2 + v'^2 + w'^2\right) + {}^{1}_{1}F_x\left(\frac{I_y}{A}\delta w''^2 + \frac{I_z}{A}\delta v''^2\right) + \overline{K}\delta\varphi_x^2 \; dx \\
+ \\
\int_0^l -{}^{2}_{1}M_z\delta\left(w'\varphi'_x\right) - {}^{2}_{1}M_y\delta\left(v'\varphi'_x\right) - {}^{2}_{1}M_y\delta\left(u'w''\right) + {}^{2}_{1}M_z\delta\left(u'v''\right) \; dx \\
+ \\
\int_0^l {}^{1}_{1}F_y\delta\left(w'\varphi_x - u'v'\right) - {}^{1}_{1}F_z\delta\left(v'\varphi_x + u'w'\right){}^{1}_{1}M_x\delta\left(v''w'\right) \; dx \\
= \\
\boldsymbol{\delta u}^T\left({}^{2}_{1}\boldsymbol{f} - {}^{1}_{1}\boldsymbol{f}\right) + \left[-\left({}^{1}_{1}M_x\varphi_z\right)\delta\varphi_y + \left({}^{1}_{1}M_z\varphi_x\right)\delta\varphi_y - \left({}^{1}_{1}M_y\varphi_x\right)\delta\varphi_z\right]_0^l
\end{gathered}
\tag{3.171}
$$

Finally, to obtain a more compact expression, the following equation can be considered

$$\int_0^l {}^1_1M_x\delta\left(v''w'\right)\ dx = \left[{}^1_1M_x\delta\left(w'v'\right)\right]_0^l - \int_0^l {}^1_1M_x\delta\left(w''v'\right)\ dx$$

rewriting equation 3.171 as

$$\begin{gathered}
\int_0^l EAu'\delta u' + EI_yw''\delta w'' + EI_zv''\delta v'' + GJ\varphi_x'\delta\varphi_x'\ dx \\
+ \\
\frac{1}{2}\int_0^l {}^1_1F_x\delta\left(u'^2+v'^2+w'^2\right) + {}^1_1F_x\left(\frac{I_y}{A}\delta w'^2 + \frac{I_z}{A}\delta v'^2\right) + \overline{K}\delta\varphi_x^2\ dx \\
+ \\
\int_0^l -{}^2_1M_z\delta\left(w'\varphi_x'\right) - {}^2_1M_y\delta\left(v'\varphi_x'\right) - {}^2_1M_y\delta\left(u'w''\right) + {}^2_1M_z\delta\left(u'v''\right)\ dx \\
+ \\
\int_0^l {}^1_1F_y\delta\left(w'\varphi_x - u'v'\right) - {}^1_1F_z\delta\left(v'\varphi_x + u'w'\right){}^1_1M_x\delta\left(v''w'\right)\ dx \\
\int_0^l {}^1_1M_x\delta\left(v''w'\right) - {}^1_1M_x\delta\left(v'w''\right)\ dx \\
= \\
\boldsymbol{\delta u}^T\left({}^2_1\boldsymbol{f} - {}^1_1\boldsymbol{f}\right) \\
+ \\
\left[-\left(\frac{1}{2}{}^1_1M_x\varphi_z\right)\delta\varphi_y + \left({}^1_1M_z\varphi_x\right)\delta\varphi_y - \left({}^1_1M_y\varphi_x\right)\delta\varphi_z + \left(\frac{1}{2}{}^1_1M_x\varphi_y\right)\delta\varphi_z\right]_0^l
\end{gathered} \tag{3.172}$$

which is the most compact form for the principle of virtual work equation for a three dimensional beam considering large displacements and small strains.

Once the expression of the principle of virtual works has been reduced to its most essential form and the displacement field has been characterized, the finite element procedure can be applied to obtain the incremental equilibrium equations in matrix form. First, we consider the first integral of the left-hand side of equation 3.172. The displacement vector is defined as:

$$\boldsymbol{U} = \left[\begin{array}{cccccccccccc} u_1 & v_1 & w_1 & \varphi_{x1} & \varphi_{y1} & \varphi_{z1} & u_2 & v_2 & w_2 & \varphi_{x2} & \varphi_{y2} & \varphi_{z2} \end{array}\right]^T \tag{3.173}$$

Untill now, some hypothesis has been made: the Euler-Bernoulli hyphotesis of plane section applies, the stress resultant in configuration ${}^1\boldsymbol{C}$ has been defined as the ones in equation 3.170 and the axes x, y and z have been adopted as the principal centroidal axes.

For convenience, the first integral of the left-hand part is denoted as I_e and the remaining part as a I_{nl}. The expression of the I_e in equation 3.172 is the same as the one obtained from the small displacements formulation so the corresponding stiffness matrix is the elastic stiffness matrix reported in equation 3.143.

On the other hand, the second part of the integral, corresponding to I_{nl}, has to be treated differently. In order to derive the geometric stiffness matrix, we shall relate all the forces acting on each single section of the element to those acting at the two ends. Based on equilibrium conditions, such relations can be expressed as

$$ {}^{1}_{1}F_{x}(x) = {}^{1}_{1}F_{x2} \tag{3.174} $$

$$ {}^{1}_{1}F_{y}(x) = -\frac{{}^{2}_{1}M_{z1} + {}^{1}_{1}M_{z2}}{l} \tag{3.175} $$

$$ {}^{1}_{1}F_{z}(x) = \frac{{}^{2}_{1}M_{y1} + {}^{1}_{1}M_{y2}}{l} \tag{3.176} $$

$$ {}^{1}_{1}M_{x}(x) = {}^{1}_{1}M_{x2} \tag{3.177} $$

$$ {}^{1}_{1}M_{y}(x) = -{}^{1}_{1}M_{y1}\left(1 - \frac{x}{l}\right) + {}^{1}_{1}M_{y2}\frac{x}{l} \tag{3.178} $$

$$ {}^{1}_{1}M_{z}(x) = -{}^{1}_{1}M_{z1}\left(1 - \frac{x}{l}\right) + {}^{1}_{1}M_{z2}\frac{x}{l} \tag{3.179} $$

Using equation 3.136 for the cross-sectional displacement representation and equations 3.174-3.179 for the initial forces, we can obtain the new expression for I_{nl}. For sake of brevity, only the final geometric stiffness matrix is reported here.

The variation of potential energy of the three dimensional beam can be written as

$$ I_{nl} = \boldsymbol{\delta U}^{T}\boldsymbol{K_g}\boldsymbol{U} \tag{3.180} $$

and the geometric stiffness matrix $\boldsymbol{K_g}$ is

$$ \boldsymbol{K_g} = \begin{bmatrix} a & 0 & 0 & 0 & -d & -e & -a & 0 & 0 & 0 & -n & -o \\ 0 & b & 0 & d & g & k & 0 & -b & 0 & n & -g & k \\ 0 & 0 & c & e & h & g & 0 & 0 & -c & o & -h & -g \\ 0 & d & e & f & i & l & 0 & -d & -e & -f & -i & -l \\ -d & g & h & i & j & 0 & d & -g & h & -i & p & -q \\ -e & k & g & l & 0 & m & e & -k & -g & -l & q & r \\ -a & 0 & 0 & 0 & d & e & a & 0 & 0 & 0 & n & o \\ 0 & -b & 0 & -d & -g & -k & 0 & b & 0 & -n & g & k \\ 0 & 0 & -c & -e & h & -g & 0 & 0 & c & -o & h & g \\ 0 & n & o & -f & -i & -l & 0 & -n & -o & f & i & l \\ -n & -g & -h & -i & p & q & n & g & h & i & j & 0 \\ -o & k & -g & -l & -q & r & o & -k & g & l & 0 & m \end{bmatrix} \tag{3.181} $$

with

$$ a = \frac{{}^{1}_{1}F_{x2}}{l};\ b = \frac{6\,{}^{1}_{1}F_{x2}}{5l} + \frac{12\,{}^{1}_{1}F_{x2}I_z}{Al^3};\ c = \frac{6\,{}^{1}_{1}F_{x2}}{5l} + \frac{12\,{}^{1}_{1}F_{x2}I_y}{Al^3};\ d = \frac{{}^{1}_{1}M_{y1}}{l};\ e = \frac{{}^{1}_{1}M_{z1}}{l} $$

$$ f = \frac{{}^{1}_{1}F_{x2}J}{Al};\ g = \frac{{}^{1}_{1}M_{x2}}{l};\ h = \frac{{}^{1}_{1}F_{x2}}{10} + \frac{6\,{}^{1}_{1}F_{x2}I_y}{Al^2};\ i = \frac{{}^{1}_{1}M_{z1} + {}^{1}_{1}M_{z2}}{6};\ j = \frac{2\,{}^{1}_{1}F_{x2}l}{15} + \frac{4\,{}^{1}_{1}F_{x2}I_y}{Al} $$

$$k = \frac{{}^1_1F_{x2}}{10} + \frac{6{}^1_1F_{x2}I_z}{Al^2};\ l = -\frac{{}^1_1M_{y1} + {}^1_1M_{y2}}{6};\ m = \frac{2{}^1_1F_{x2}l}{15} + \frac{4{}^1_1F_{x2}I_z}{Al};\ n = \frac{{}^1_1M_{y2}}{l};\ o = \frac{{}^1_1M_{z2}}{l}$$

$$p = -\frac{{}^1_1F_{x2}l}{30} + \frac{2{}^1_1F_{x2}I_y}{Al};\ q = -\frac{{}^1_1M_{x2}}{2};\ r = -\frac{{}^1_1F_{x2}l}{30} + \frac{2{}^1_1F_{x2}I_z}{Al}$$

While the left-hand of equation 3.172 has been computed, the right-hand remains unchanged. The bracketed term in the left-hand part represents the virtual work done by the moments induced by the torque ${}^1_1M_x$ and bending moments ${}^1_1M_y$ and ${}^1_1M_z$ undergoing rotations in the three dimensional space. Considering that the moments induced by the initial moments upon rotations relate only to the rotational degrees of freedom of the beam element, the bracketed left-hand expression in equation 3.172 can be written as

$$\boldsymbol{\delta u}^T \left({}^2_1\boldsymbol{f} - {}^1_1\boldsymbol{f}\right) + \left[-\left(\frac{1}{2}{}^1_1M_x\varphi_z\right)\delta\varphi_y + \left({}^1_1M_z\varphi_x\right)\delta\varphi_y - \left({}^1_1M_y\varphi_x\right)\delta\varphi_z + \left(\frac{1}{2}{}^1_1M_x\varphi_y\right)\delta\varphi_z \right]_0^l = \boldsymbol{\delta U}^T \left({}^2_1\boldsymbol{f} - {}^1_1\boldsymbol{f}\right) - \boldsymbol{\delta U}^T \boldsymbol{K_i U} \tag{3.182}$$

where the matrix $\boldsymbol{K_i}$ stands for *induced moments matrix* and its expression is

$$\boldsymbol{K_i} = \begin{bmatrix} \mathbf{0_3} & & & \\ & \boldsymbol{K_{i1}} & & \\ & & \mathbf{0_3} & \\ & & & \boldsymbol{K_{i2}} \end{bmatrix} \tag{3.183}$$

with

$$\boldsymbol{K_{i1}} = \begin{bmatrix} 0 & 0 & 0 \\ {}^1_1M_{z1} & 0 & -\frac{{}^1_1M_{x1}}{2} \\ -{}^1_1M_{y1} & \frac{{}^1_1M_{x1}}{2} & 0 \end{bmatrix};\ \boldsymbol{K_{i2}} = \begin{bmatrix} 0 & 0 & 0 \\ {}^1_1M_{z2} & 0 & -\frac{{}^1_1M_{x2}}{2} \\ -{}^1_1M_{y2} & \frac{{}^1_1M_{x2}}{2} & 0 \end{bmatrix} \tag{3.184}$$

The induced moment matrices have the same order of the geometric stiffness matrix. It is interesting to notice that the matrix $\boldsymbol{K_i}$ is asymmetric. Such a property can be attributed to the lack of conjugateness between the bending moments and displacement derivatives, which have been used as nodal parameters in the finite element formulation. Althought the asymmetry should be always avoided , in this case no further developments are needed to restore the symmetry of the stiffness matrix. During the assembly process, the overall matrix will become symmetric since each element is connected to the others and the conditions of equilibrium for structural joints will be taken into account.

Finally, the incremental equilibrium equations in matrix form can be written as follows:

$$\left(\boldsymbol{K_e} + \boldsymbol{K_g} + \boldsymbol{K_i}\right)\boldsymbol{U} = {}^2_1\boldsymbol{f} - {}^1_1\boldsymbol{f} \tag{3.185}$$

4 Numerical methods for non linear analysis

During the previous chapters, the nonlinear theories and models for the analysis of continuum bodies and cable and frame structures have been exposed and discussed.

Following either the direct stiffness or finite element methods, one can always write the total or incremental equilibrium equations that represents the configuration of the structure in a certain moment t (Here, the parameter t plays the role of a parameter that characterizes the load and deformative path, not necessary related to the actual time). Using the two main formulations explained in this thesis, total or updated lagrangian formulation, the equilibrium equations in total or incremental forms can be obtained and solved to get the displacements, strains and stresses of the structure.

Due to the complexity of the systems treated, analytical techniques can not be applied unless the equations that govern the problem are simple, which only happens when load and boundary conditions are very simple. Advanced numerical techniques have to be developed to solve, or at least approximate, the equilibrium equations. In this chapter, we shall review the most commonly used nonlinear solution schemes. Comments will be provided for each method in terms of *stability* and *efficiency*.

The first method is the *Stiffness method*, which is the most intuitive method to solve the nonlinear equilibrium equations and particularly adapted to be used in the total lagrangian formulation. Then, some numerical procedures will be discussed considering the updated lagrangian formulation. The most simple, commonly used and oldest method is the so-called *Newton-Raphson method*. Others numerical schemes presented in this work are a variation of this method.

Finally, some numerical techniques to deal with high order nonlinear structures are presented. Due to the nonlinearity of certain structures, the Newton-Raphson scheme may not be enough to ensure the convergence of the method and more advanced control procedure are needed. The two procedures presented in this text are *displacement control procedure* and *work control procedure*, both adapted to deal with phenomena of *limit*

points and *snap-back*. These two concepts will be explained in section 4.1.4.

4.1 Definition and solution of the non linear problem

Let us consider the general form of a nonlinear problem.

$$\boldsymbol{G} = \boldsymbol{f}(\boldsymbol{v}) - \boldsymbol{R}(\boldsymbol{v}) = \boldsymbol{0} \tag{4.1}$$

with $\boldsymbol{f}(\boldsymbol{v})$ the external load applied on the structure, $\boldsymbol{R}(\boldsymbol{v})$ the internal reaction of the structure and $\boldsymbol{G}$ the so-called *equilibrium function* which measures how far from the equilibrium the structures is, while $\boldsymbol{v}$ is the displacement vector of the structure.

The system of nonlinear equilibrium equations can be solved in many ways. From the easiest one to the most complex one, the different methods used in this thesis will be exposed and explained. The first one is the stiffness method, where the equilibrium equations are linearized to obtain the so-called *secant stiffness matrix*, which represents the stiffness of a virtual structure in the configuration of the real structure.

4.1.1 Stiffness method

Imagine a certain structure whose displacement-force path can be characterized as the one in figure 4.1. Considering the stiffness method, the principal goal is to describe each configuration of the structure by means of the secant stiffness matrix. Let us consider the general form of the nonlinear problem.

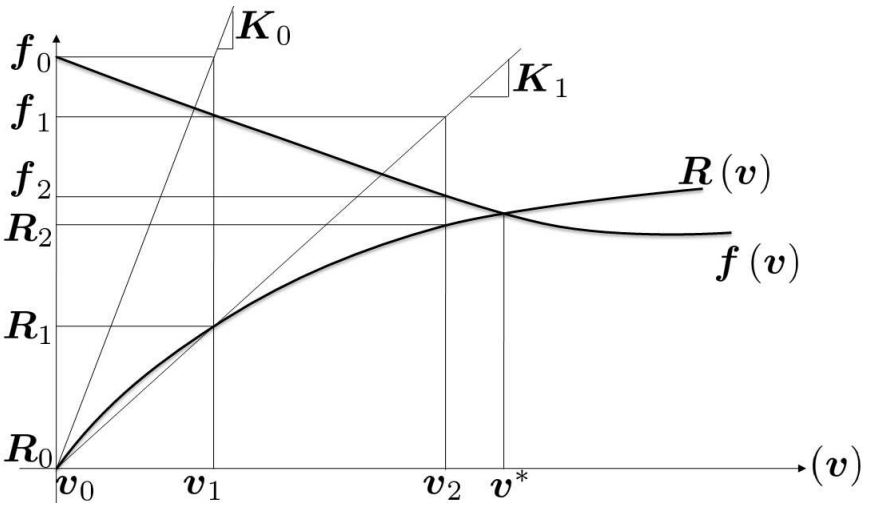

Figure 4.1: Secant iterative procedure to solve the equilibrium equations.

$$\boldsymbol{G} = \boldsymbol{f}(\boldsymbol{v}) - \boldsymbol{R}(\boldsymbol{v}) = \boldsymbol{0} \tag{4.2}$$

From figure 4.1, on each configuration of the structure the equilibrium equations can be rewritten as

$$\boldsymbol{K}(\boldsymbol{v})\,\boldsymbol{v} = \boldsymbol{f}(\boldsymbol{v}) \tag{4.3}$$

with $\boldsymbol{K}(\boldsymbol{v})$ the secant stiffness matrix.

In this chapter, the procedure to obtain the secant stiffness matrix will not be explained due to the fact that it depends completely on the tipology of the structure and it will be considered in chapter 6. For the moment, let us consider that the secant stiffness matrix as a function of the total displacement vector is known.

Under this hypothesis, a flow chart can be stablished (figure 4.2) , which is:

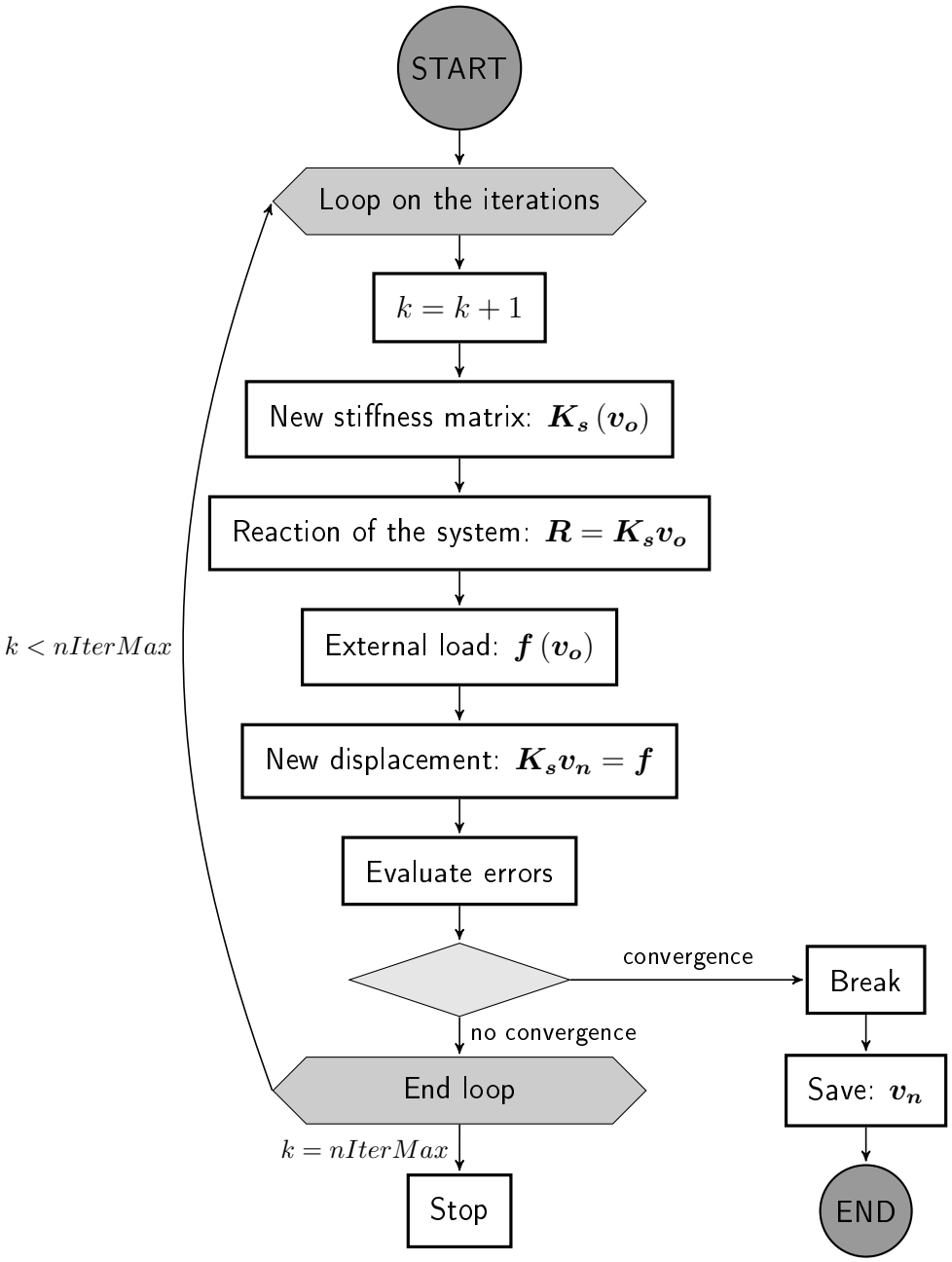

Figure 4.2: Flow chart of the stiffness method

As shown in the flow chart, the main goal of the stiffness method is the computation of the total secant stiffness matrix, which characterizes the response of an equivalent system to an external load. Once the stiffness matrix has been computed, the reaction of the system in the current configuration can be calculated as $\boldsymbol{R} = \boldsymbol{K_s v_o}$ (the current configuration is characterized by the vector $\boldsymbol{v_o}$). The external load, which in general will depend also on the displacements, can be computed considering $\boldsymbol{f}(\boldsymbol{v_o})$. Finally, the new displacement vector $\boldsymbol{v_n}$ can be computed and the convergence checking can be done. In this case, the convergence checking has been considered using the following three errors.

$$\begin{aligned} e_w &= \frac{\left|\boldsymbol{v_o}^T(\boldsymbol{f}-\boldsymbol{R})\right|}{\left|\boldsymbol{v_o}^T\boldsymbol{f}\right|} \leq tol_w \\ e_d &= \frac{|\boldsymbol{v_n}-\boldsymbol{v_o}|}{|\boldsymbol{v_n}|} \leq tol_d \\ e_f &= \frac{|\boldsymbol{f}-\boldsymbol{R}|}{|\boldsymbol{f}|} \leq tol_f \end{aligned} \tag{4.4}$$

which can be defined as *work error*, *displacement error* and *force error* respectively and they are demanded to be smaller than their corresponding tolerances.

4.1.2 Incremental load procedure

Althought the numerical scheme presented before has been adopted in this work in the total lagrangian formulation, it has limitations. In particular, the stiffness method is suitable to be used in structures that presents only a *softening* or *stiffening* (figure 4.3) behaviours. Explained with other words, the structure must behave monotonously.

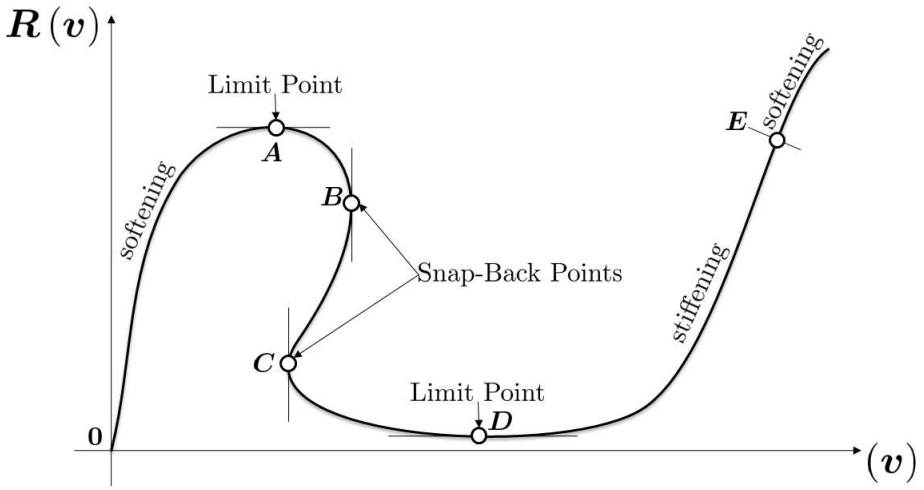

Figure 4.3: Possible behaviours of an structure during the deformative path

If the interest is the *displacement-force curve*, more advanced techniques have to be developed, able to overcome several pathologies that the structure could present during the deformative path (limit and snap-back points, stiffening and softening zones,...).

From now on, the numerical methods known as *Incremental-Iterative algorithms* will be presented. These algorithms consider the general expressions of the nonlinear problem and assume the load vector to be proportional to a certain *reference load vector*.

$$\boldsymbol{f}(\boldsymbol{v}) = \lambda \boldsymbol{f_r} \rightarrow \boldsymbol{G} = \lambda \boldsymbol{f_r} - \boldsymbol{R}(\boldsymbol{v}) = \boldsymbol{0} \tag{4.5}$$

These procedures are known as incremental-iterative because they increase the parameter λ from an initial to a final value and solve the incremental equilibrium equations for each load step. The classic Newton-Raphson scheme presented in the following section uses this technique and allows the study of the path-dependant behaviour of the structure

in terms of displacements and load.

Althought the generality of the Newton-Raphson scheme, structures highly nonlinear require more advanced techniques, which allow the study of the behaviour of the structure around the critic points such as snap-back and limit points and are based on the *Displacement control method* or the *Work control method*, both explained in subsection 4.1.4.

Obviously, an ideal incremental scheme should allow the load increment to vary accordingly to the degree of nonlinearity as exemplified by the stiffness of the structure considered in order to optimize the efficiency of computation. This will be exposed in the last part of this chapter, where automatic algorithms to choose properly the load step will be reported.

4.1.3 Classic Newton-Raphson scheme

Let us consider the nonlinear equilibrium equations with the reference load vector

$$\lambda \boldsymbol{f}_r - \boldsymbol{R}(\boldsymbol{v}) = \boldsymbol{0} \tag{4.6}$$

and consider the situation in which the structure is in equilibrium at a certain configuration ${}^{\lambda}\boldsymbol{C}$ characterized by a value of the parameter λ. In this situation, the incremental equilibrium equation may be established in the new configuration ${}^{\lambda+\Delta\lambda}\boldsymbol{C}$. From now on, the notation will follow this rule: the left superscript index will denote the actual increment load and the left subscript index will indicate the number of iteration performed within the increment load. For example, ${}^{i}_{j}\boldsymbol{\Delta v}$ will be the increment of displacement computed in the iteration number j on the increment load number i.

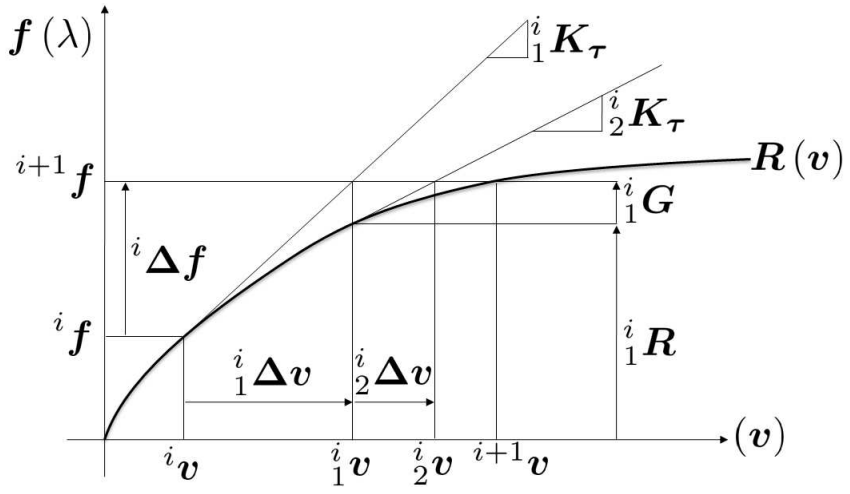

Figure 4.4: Tangent iterative procedure to solve the equilibrium equations.

Figure 4.4 represents the Newton-Raphson scheme in the configuration ${}^{i}\boldsymbol{C}$, where an increment of load has been imposed as ${}^{i+1}\boldsymbol{f} = {}^{i}\boldsymbol{f} + \Delta\lambda \boldsymbol{f}_r$ and the first two iterations in this new incremental load step are depicted and characterized by ${}^{i}_{1}\boldsymbol{K}$ (first tangent stiffness

matrix), ${}^{i}_{1}\boldsymbol{\Delta v}$ (first increment of displacement), ${}^{i}_{1}\boldsymbol{R}$ (reaction of the system at the new incremental configuration) and ${}^{i}_{1}\boldsymbol{G}$ (Equilibrium functions in the incremental configuration).

The flow chart of the Incremental-Iterative Newtion-Raphson method can be written as:

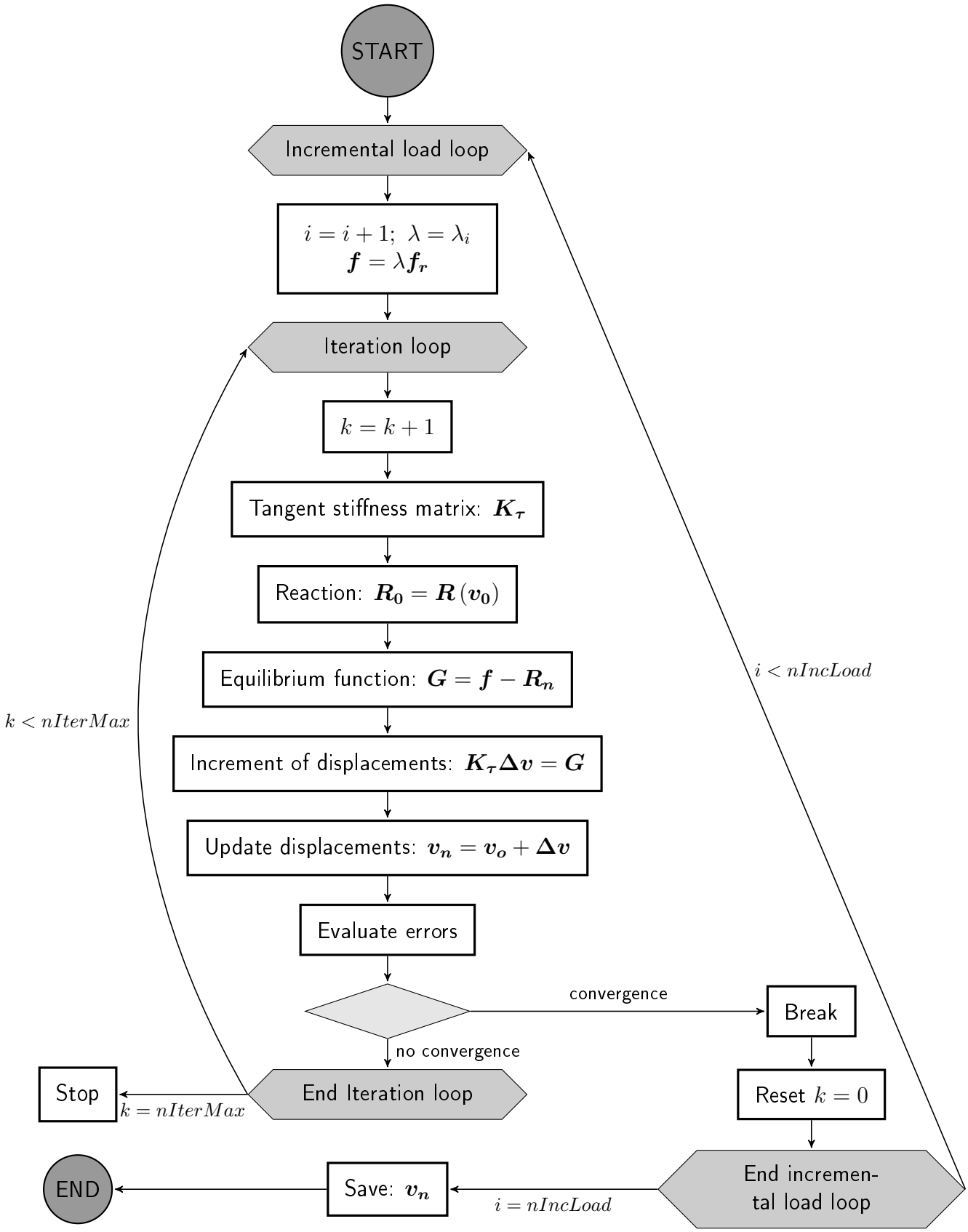

Figure 4.5: Flow chart of the incremental Newton-Raphson method

In the Newton-Raphson procedure, only the maximum number of iterations for each incremental load step has been considered as a control parameter. Indeed, in case the algorithm exceeds the maximum number of iterations without convergence, the program will stop and no outputs will be given. This may happen in situations where the structure does not present a monotonic behaviour (stiffering or softening) or where it presents some limit points or snap-back situations (figure 4.3). To deal with such an inconvenients, new techniques will be explained such as the *Arc Length* and *Work control* methods.

4.1.4 Improved Newton-Raphson schemes

Before describing the new methods, some considerations about new approaches that go beyond the analysis provided by the Newton-Raphson scheme must be said. This section will talk first about the *Prediction phase* and *Correction phase*. Both are vital concepts in the development of the new numerical techniques and will be deeply explained.

As stated previously, the nonlinear deformation process of a structure can be described by three typical configurations: the initial configuration ${}^{0}\boldsymbol{C}$, the last calculated configuration ${}^{1}\boldsymbol{C}$ and the current unknown configuration ${}^{2}\boldsymbol{C}$. To explain better the incremental iterative process in the following sections, a new notation will be used. From now on, the last calculated configuration will be denoted as ${}^{i}\boldsymbol{C}$ and the current unknown configuration as ${}^{i+1}\boldsymbol{C}$.

In the following, all the schemes presented will be divided in two parts. The first part, called prediction phase, will be devoted to compute the direction and amplitude of the load increment, while the second part (correction phase) will be devoted to perform some iterations to obtain the equilibrated system in the new configuration. Figure 4.6 shows the flow chart of the numerical method implemented.

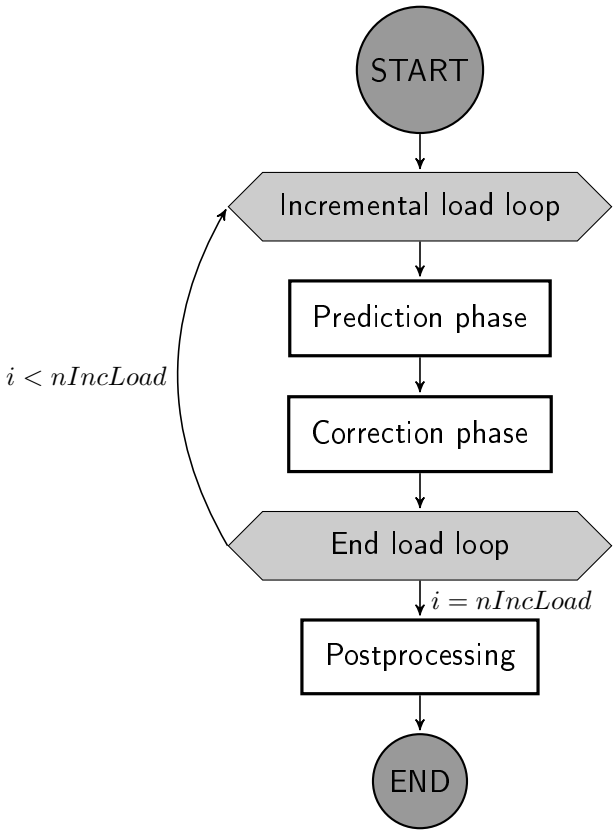

Figure 4.6: Flow chart of the improved Newton-Raphson schemes

Before starting with the explanation of both the arc-length and work control methods, some definitions will be presented. First, the concept of normalization of the *force-displacement path* must be introduced. Then, the indicators that will be used to characterize the quality of the solution and convergence of the iterative method will be presented.

First, consider the force-displacement path depicted in figure 4.7. In a force-displacement path, the force and displacements are measured using different units. This may lead to different values of both variables. To avoid this scale problem, a normalization is required. From now on, the force-displacement path will be normalized and will be plotted in terms of the new variables

$$\begin{aligned} \boldsymbol{V} &= \boldsymbol{v} \\ \boldsymbol{F_r} &= \beta \boldsymbol{f_r} \end{aligned} \tag{4.7}$$

with

$$\beta = \frac{|\boldsymbol{v}|}{|\boldsymbol{f_r}|} \tag{4.8}$$

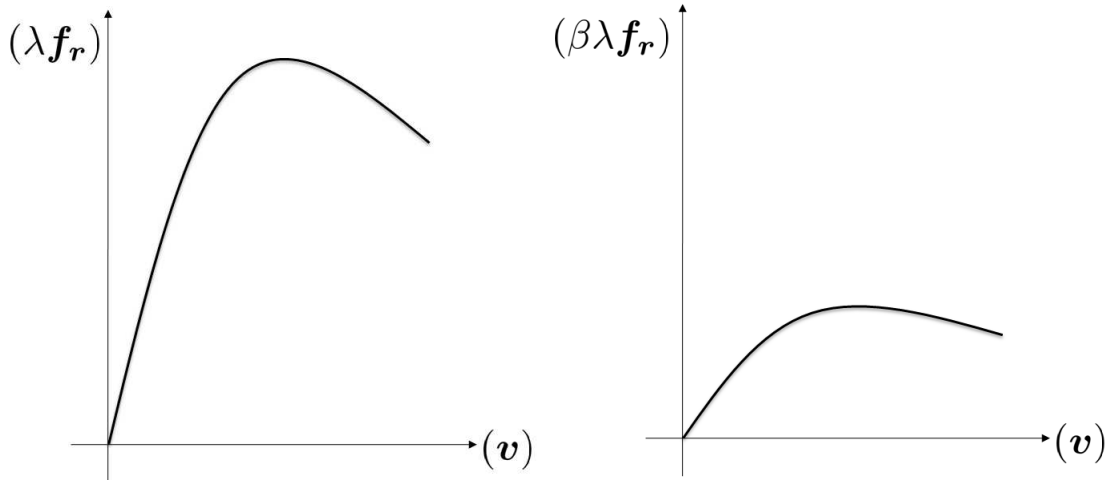

(a) Force-Displacement path without being normalized

(b) Normalized force-Displacement path

Figure 4.7: Normalization of the force-displacement curve

Second, in a general force-displacement path as the one in figure 4.3 on page 115, several zones can be characterized:

- Paths 0-A and D-E: It is an stable zone because an increment in the load has an inmediate increment of displacement and the stiffness matrix is definite positive.
- Paths A-B and C-D: It is an unstable zone because the stiffness matrix is not definite positive. This zone is also called *Pre-critic softening*. Usually the snap-back points are located in this zone.
- Path B-C: Unstable zone. The stiffness matrix is not positive definite. This zone is called *Post-critic softening*.

From the description below, a new parameter to describe the stiffness of the structure in a certain point of the force-displacement path is required. One of the most commonly used parameter is the *Bergam parameter*, also named as *current stiffness parameter* (CSP).

Let us consider the figure 4.8 where three configurations ${}^0\boldsymbol{C}$, ${}^1\boldsymbol{C}$ and ${}^2\boldsymbol{C}$ are depicted in the force-displacement path. Consider, from configuration ${}^0\boldsymbol{C}$ an increment of load equal to $\boldsymbol{\Delta f} = \beta^0\Delta\lambda \boldsymbol{f_r}$ that produces an increment of displacement equal to ${}^0\boldsymbol{\Delta v}$. The same can be establish in configuration ${}^1\boldsymbol{C}$ and ${}^2\boldsymbol{C}$ and in any other configuration defined in the deformative path. Each increment of displacement will produce, associated with the increment of load, a certain increment of work that can be defined as ${}^i\Delta w = \beta^i\Delta\lambda \boldsymbol{f_r}^{Ti}\boldsymbol{\Delta u}$. Consistently, the follow ratio can be defined

$$B = \frac{{}^0\Delta w / \left(\beta^0\Delta\lambda\right)}{{}^i\Delta w / \left(\beta^i\Delta\lambda\right)} = \frac{\boldsymbol{f_r}^{T0}\boldsymbol{\Delta v}}{\boldsymbol{f_r}^{Ti}\boldsymbol{\Delta v}} \tag{4.9}$$

This is the so-called *Bergam parameter* and indicates the ratio between the current stiffness and the stiffness in the initial state. It must be noticed that, for structures that

become soft when the displacements increase, the Bergam parameter decreases (figure 4.3, 0-A path). On the other hand, the Bergam parameter could become negative and even $-\infty$ (figure 4.3 point B). Another definition for the Bergam parameter is the ratio between the increment of elastic energy at the initial configuration and the increment of elastic energy in the current configuration.

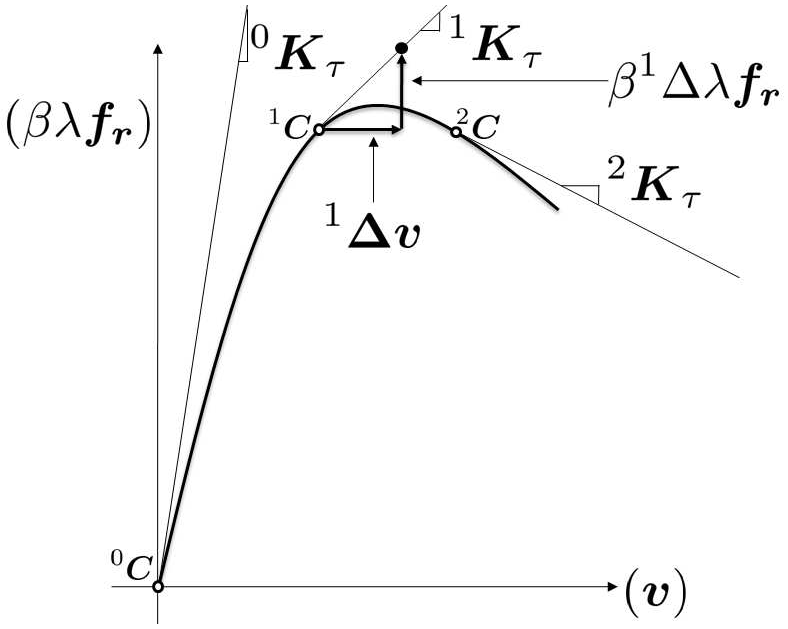

Figure 4.8: Definition of the Bergam parameter

Another important definition is the *Batoz and Dhatt notation*, which will be very useful in the explanation of the two procedures adopted. Imagine an increment of displacements produced in the current configuration ${}^i\boldsymbol{\Delta v}$. This vector has been obtained from the resolution of the linear system

$$ {}^i\boldsymbol{K_\tau}\,{}^i\boldsymbol{\Delta v} = \Delta\lambda\boldsymbol{f_r} + {}^i\boldsymbol{G} \tag{4.10}$$

which can be divided in two contributions defined as

$$ {}^i\boldsymbol{\Delta v} = \Delta\lambda\,{}^i\boldsymbol{\Delta v}_t + {}^i\boldsymbol{\Delta v}_r \tag{4.11}$$

$$ {}^i\boldsymbol{\Delta v}_t = {}^i\boldsymbol{K}_\tau^{-1}\boldsymbol{f_r};\ {}^i\boldsymbol{\Delta v}_r = {}^i\boldsymbol{K}_\tau^{-1\,i}\boldsymbol{G} \tag{4.12}$$

The first displacement vector ${}^i\boldsymbol{\Delta v}_t$ represents the displacement that the structure would have if it was completely linear. On the other hand, the second term is derived from the equilibrium function ${}^i\boldsymbol{G}$.

The two methods will be discussed and their numerical implementation exposed in both the prediction and correction phase. Deep attention will be dedicated to the flowcharts of both methods.

4.1.4.1 Prediction phase

In the prediction phase, the initial iteration (prediction) is performed to obtain an approximation as the linearized solution of the equilibrium equations, of the incremental load step. Later, this solution will be "corrected" in the following phase by means of several methods.

In this phase, the direction and amplitude of the incremental load step will be defined. The need to define the direction of the increment of load is considered because, sometimes, the structure varies its stiffness during the deformative path and, if a force-displacement path analysis is performed, the increment of load has to be defined accordingly to the stiffness at the current configuration. For example, imagine that a certain structure, during its deformative process, is near to the point A in figure 4.3. At this point, the stiffness of the structure presents its first singularity and the structure is not able to counteract any increment[(1)] of load. Obviously, methods to take into account these singularities will be explained.

The prediction phase can be performed using two methods: *Arc-Length* and *Work control* methods. The explanation will start with the arc-length method.

Consider figure 4.9 where an iteration in the prediction phase is depicted. As it can be seen, the arc-length method controls the amplitude of the increment of displacements considering the equality

$$\Delta l^2 = {}^1\boldsymbol{\Delta v}^{T\,1}\boldsymbol{\Delta v} = \left({}^1\Delta\lambda\boldsymbol{\Delta v}_t + \boldsymbol{\Delta v}_r\right)^T \left({}^1\Delta\lambda\boldsymbol{\Delta v}_t + \boldsymbol{\Delta v}_r\right) \tag{4.13}$$

This equation can be solved in terms of the incremental load factor ${}^1\Delta\lambda$ as

$${}^1\Delta\lambda = \frac{\pm\Delta l}{\sqrt{\boldsymbol{\Delta v}_t^T\boldsymbol{\Delta v}_t + \beta^2\boldsymbol{f}_r^T\boldsymbol{f}_r}} \tag{4.14}$$

As it has been proved, the arc-length method imposes a geometric restriction in terms of the amplitude of the displacement vector. The parameter Δl is, indeed, non adimensional. This may lead to some problems in the definition of its value due to the fact that its optimum value might be different for each problem and the units that are used to describe the geometry, mechanical properties and forces. This is one of the disadvantages of the arc-length method.

To overcome this problem, another method will be considered, which is the work control method. In this case, a different restriction can be established in terms of the increment of work produced by the incremental load vector.

$$\overline{\Delta w} = {}^1\Delta\lambda\boldsymbol{f}_r^{T\,1}\Delta\lambda\boldsymbol{\Delta v}_t \tag{4.15}$$

(1) Here, the notation "increment" and "decrement" is considered as an intuitive way to understand what happens on the limit points because the plots are considered in a one-dimensional analysis. In general, the load will be increased or decreased by means of the load factor in a vectorial approach.

This equation can be seen as the restriction in the increment of external work (work produced by the increment of the load). Solving it in terms of $\Delta\lambda$ it can be obtained

$$^1\Delta\lambda = \pm\sqrt{\frac{\overline{\Delta w}}{\boldsymbol{f}_{\boldsymbol{r}}^T \boldsymbol{\Delta v}_t}} \tag{4.16}$$

As it can be seen in equations 4.14 and 4.16, the possible values for the variable $\Delta\lambda$ must be also characterized by its sign. To do so, the Bergam parameter can be used. Indeed, as it has been explained before, the Bergam parameter characterizes the stiffness of the structure in the current configuration referred to the initial configuration. This means that negative values of this parameter indicate the structure is not able to resist positive increments of load and a negative increment must be chosen to follow the deformative path of the structure. On the other hand, positive values of the Bergam parameter indicate the structure can yet resist positive increments of load and the variable $\Delta\lambda$ will be chosen as the positive one.

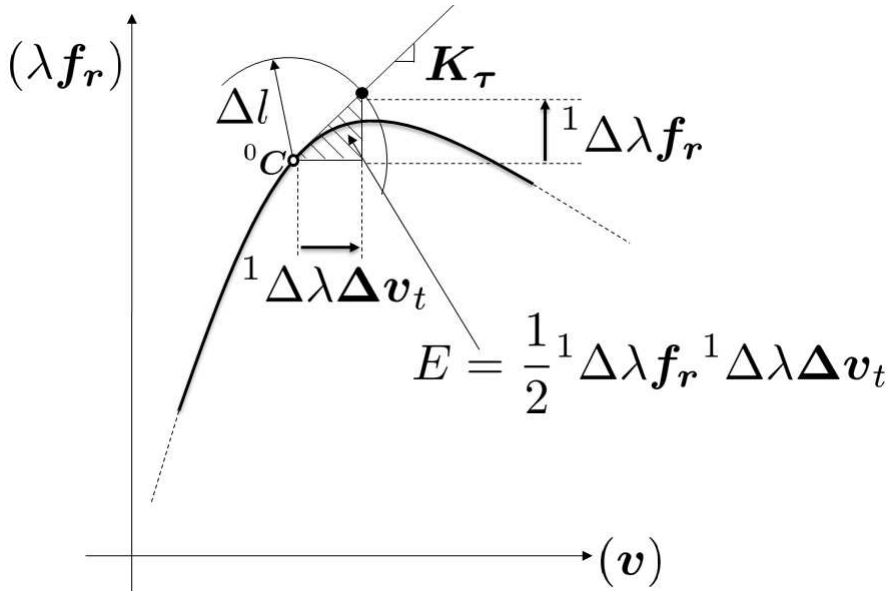

Figure 4.9: Iteration performed in the prediction phase

The flowchart of the prediction phase is therefore presented. It can be noticed the procedures to take into account the current stiffness of the structure by means of the Bergam parameter, the two methods (arc-length and work control) explained before and the choice between increasing or decreasing the load considering the sign of the Bergam parameter.

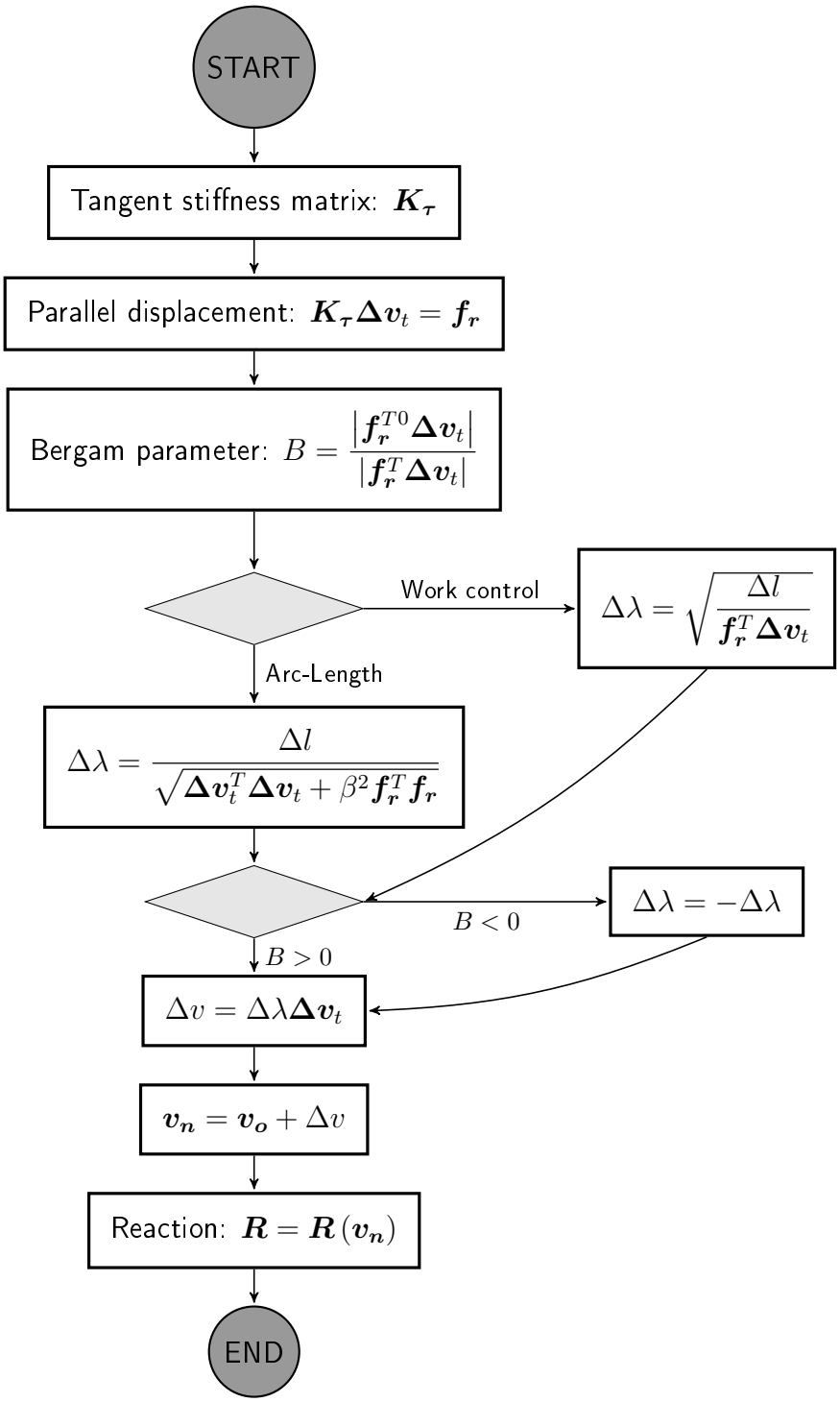

Figure 4.10: Flow chart of the prediction phase

4.1.4.2 Correction phase

In the correction phase, an iterative procedure is performed to satisfy the equilibrium conditions and to give a more accurate solution of the incremental load step. The situation depicted in figure 4.11is considered, where a prediction iteration has been performed and

the actual configuration is not an equilibrated one because it does not lie on the force-displacement equilibrium path. To achieve the equilibrium, a correction scheme must be performed. Iteratively, a new incremental displacement vector $\boldsymbol{\delta v}$ will be computed and added to the already obtained $\boldsymbol{\Delta v}$. Using the notation of Batoz and Dhatt previously explained, it can be written

$$\boldsymbol{\delta v} = \boldsymbol{\delta v}_r + \delta\lambda \boldsymbol{\delta v}_t \tag{4.17}$$

$$\boldsymbol{\delta v}_r = \boldsymbol{K}_{\boldsymbol{\tau}}^{-1}\boldsymbol{G};\ \boldsymbol{\delta v}_t = \boldsymbol{K}_{\boldsymbol{\tau}}^{-1}\boldsymbol{f_r} \tag{4.18}$$

with the variables already defined as: $\boldsymbol{G}$ the equilibrium function, $\boldsymbol{f_r}$ the reference load vector, $\boldsymbol{K_\tau}$ the current tangent stiffness matrix, $\delta\lambda$ the correction increment of the load parameter. This means that, during the correction procedure, the displacements but also the external loads change to ensure the equilibrium in the current configuration.

The two methods proposed for the correction phase will be presented and discussed. The arc-length method is first introducced and after the Work control method will be discussed.

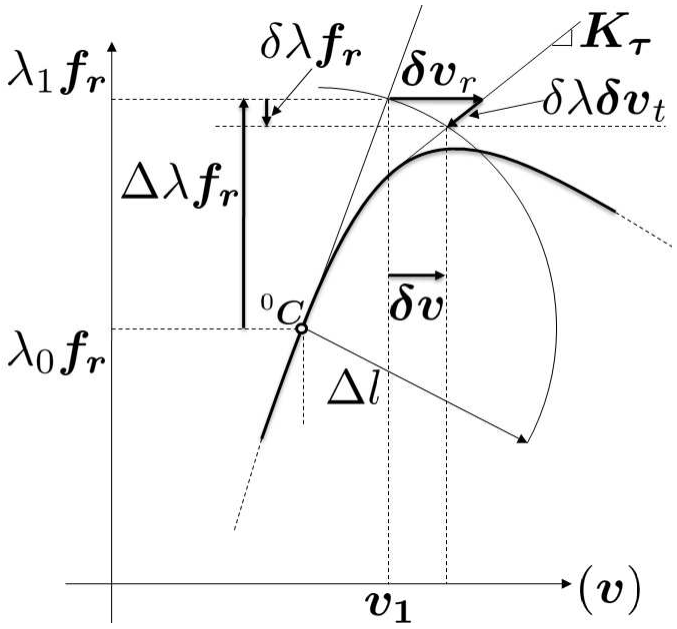

Figure 4.11: Correction phase during the nonlinear procedure

In the arc-length method, a general iteration in the correction procedure is characterized by the increment of load factor ${}^1\delta\lambda$ and the incremental displacement vector ${}^1\boldsymbol{\delta v}$. The arc-length method considers the following restriction on the displacements

$$\Delta l^2 = {}^2\boldsymbol{\Delta v}^{T\,2}\boldsymbol{\Delta v} + {}^2\Delta\lambda \boldsymbol{f_r}^{T\,2}\Delta\lambda \boldsymbol{f_r} \tag{4.19}$$

where the variables in the new configuration ${}^2\boldsymbol{C}$ are defined as

$$\begin{aligned} {}^2\boldsymbol{\Delta v} &= {}^1\boldsymbol{\Delta v} + {}^1\boldsymbol{\delta v} \\ {}^2\Delta\lambda &= {}^1\Delta\lambda + {}^1\delta\lambda \end{aligned} \tag{4.20}$$

Using equations 4.12 and 4.20, it mat be written

$$\left({}^1\boldsymbol{\Delta v}^T + {}^1\boldsymbol{\delta v}^T\right)\left({}^1\boldsymbol{\Delta v} + {}^1\boldsymbol{\delta v}\right) + \left(\beta^1\Delta\lambda + \beta^1\delta\lambda\right)^2 \boldsymbol{f_r}^T\boldsymbol{f_r} = \Delta l^2 \tag{4.21}$$

which can be transformed using equation 4.17 into

$$\left({}^1\boldsymbol{\Delta v}^T + {}^1\boldsymbol{\delta v}_r^T + \beta\delta\lambda\boldsymbol{f_r}^T\right)\left({}^1\boldsymbol{\Delta v} + {}^1\boldsymbol{\delta v}_r + \beta\delta\lambda\boldsymbol{f_r}\right) + \left(\beta^1\Delta\lambda + \beta^1\delta\lambda\right)^2 \boldsymbol{f_r}^T\boldsymbol{f_r} = \Delta l^2 \tag{4.22}$$

This equation can be transformed in a parabolic equation with the following coefficients

$$\begin{gathered} a^1\delta\lambda^2 + b^1\delta\lambda + c = 0 \\ a = \boldsymbol{\delta v}_t^T\boldsymbol{\delta v}_t + \beta^2\boldsymbol{f_r}^T\boldsymbol{f_r} \\ b = 2\boldsymbol{\delta v}_r^T\boldsymbol{\delta v}_r + 2^1\boldsymbol{\Delta v}^T\boldsymbol{\delta v}_t + 2^1\Delta\lambda\beta^2\boldsymbol{f_r}^T\boldsymbol{f_r} \\ c = -\Delta l^2 + {}^1\boldsymbol{\Delta v}^{T1}\boldsymbol{\Delta v} + \boldsymbol{\delta v}_r^T\boldsymbol{\delta v}_r + 2^1\boldsymbol{\Delta v}^T\boldsymbol{\delta v}_r + {}^1\Delta\lambda^2\beta^2\boldsymbol{f_r}^T\boldsymbol{f_r} \end{gathered} \tag{4.23}$$

Solving it, two increments of load factor may be obtained.

$${}^1\delta\lambda_{1,2} = \frac{-b \pm \sqrt{b^2 - 4ac}}{2a} \tag{4.24}$$

For each increment, an incremental displacement vector can be defined as

$$\begin{gathered} {}^1\boldsymbol{\delta v}_1 = \boldsymbol{\delta v}_r + \delta\lambda_1\boldsymbol{\delta v}_t \\ {}^1\boldsymbol{\delta v}_2 = \boldsymbol{\delta v}_r + \delta\lambda_2\boldsymbol{\delta v}_t \end{gathered} \tag{4.25}$$

In this thesis, two methods have been used: *angle method* and *restoring method*.

The angle method consists on choosing the options whose angle with respect the incremental displacement vector defined in the prediction phase ${}^1\boldsymbol{\Delta v}$ is smaller. Consider the two cosines defined as

$$\cos\theta_1 = \frac{{}^1\boldsymbol{\Delta v}^{T1}\boldsymbol{\delta v}_1}{\left|{}^1\boldsymbol{\Delta v}\right|\left|{}^1\boldsymbol{\delta v}_1\right|};\ \cos\theta_2 = \frac{{}^1\boldsymbol{\Delta v}^{T1}\boldsymbol{\delta v}_2}{\left|{}^1\boldsymbol{\Delta v}\right|\left|{}^1\boldsymbol{\delta v}_2\right|} \tag{4.26}$$

This method is easily depicted in figure 4.12, where the two options with their corresponding cosines are considered.

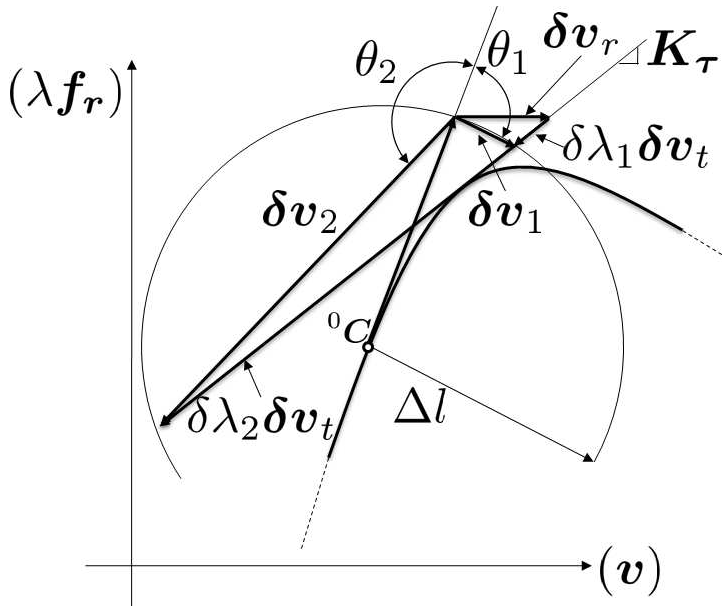

Figure 4.12: Angle method in the arc-length correction procedure

This approach is considered to be bery robust and efficient, but sometimes, when the structure presents strong snap-back conditions, the method is not able to converge and unefficiently small arc parameter Δl must be used.

As a consequence, a second method is presented to deal with situations where the angle method is not able to catch the force-displacement path of the structure. Instead of choosing the incremental displacement vector as done in the angle method, the condition is imposed in the reaction of the two solutions of the system. For example, consider the two solutions of the correction phase $\boldsymbol{\delta v}_1$ and $\boldsymbol{\delta v}_2$ which have been obtained solving equation 4.23.

$$\begin{aligned} {}^2\boldsymbol{v}_1 &= {}^1\boldsymbol{v} + {}^1\boldsymbol{\Delta v} + {}^1\boldsymbol{\delta v}_1 \\ {}^2\boldsymbol{v}_2 &= {}^1\boldsymbol{v} + {}^1\boldsymbol{\Delta v} + {}^1\boldsymbol{\delta v}_2 \end{aligned} \tag{4.27}$$

For each new configuration, the reactions of the system can be computed and compared on each case.

$$\begin{aligned} {}^2\boldsymbol{v}_1 &\rightarrow {}^2\boldsymbol{R}_1 \rightarrow {}^2\boldsymbol{G}_1 \\ {}^2\boldsymbol{v}_2 &\rightarrow {}^2\boldsymbol{R}_2 \rightarrow {}^2\boldsymbol{G}_2 \end{aligned} \tag{4.28}$$

The restoring method considers the solution as the one which equilibrium function has the lowest modulus. In other words, the solution chosen between the two possibles will be the one whose reaction is closer to the external load. See figure 4.13 for more details.

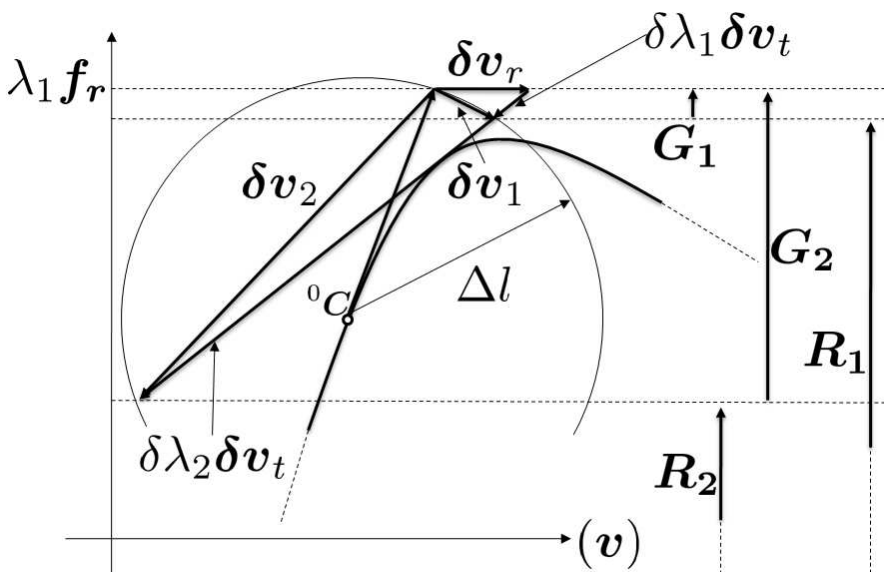

Figure 4.13: Sketch of the choice made by the restoring method in the arc-length procedure

The arc-length method has been described and two possible alternatives have been discussed. Now, the attention is focused on the second method proposed in this thesis, the Work control method.

The restriction that the work control method imposes to the displacements is that the work produced by the increment of force with the new incremental vector in the correction phase must be null. This leads to

$$\delta w = {}^1\delta\lambda \boldsymbol{f_r}^{T\,1}\boldsymbol{\delta v} = 0 \tag{4.29}$$

Using equation 4.17, the equation can be rewritten as

$${}^1\delta\lambda \boldsymbol{f_r}^T \left(\boldsymbol{\delta v}_r + {}^1\delta\lambda \boldsymbol{\delta v}_t\right) = 0 \tag{4.30}$$

This equation has two possible solutions. The first one is the trivial solution, which leads to a null displacement increment (this solution is not interesting for the procedure). On the other hand, the second solution gives an incremental displacement vector that is perpendicular to the reference load vector. Solving equation 4.30 with respect to ${}^1\delta\lambda$, it can be obtained

$${}^1\delta\lambda = -\frac{\boldsymbol{f_r}^T \boldsymbol{\delta v}_r}{\boldsymbol{f_r}^T \boldsymbol{\delta v}_t} \tag{4.31}$$

The correction phase is performed until the reaction of the system in the current configuration equals the external load (or when the equilibrium functions goes under the fixed tolerance) and the increment of displacement is small enough. At each iteration of this process, the two methods exposed may be used to achieve the equilibrium.

In order to clarify the numerical procedure, two flow charts will be presented. The first one corresponds to the flow diagram of the correction procedure with the two methods discussed before (arc-length and work control methods in figure 4.14). The second diagram

focuses on the arc-length methods (figure 4.15) because the number of operations required with this method is larger than the work control method.

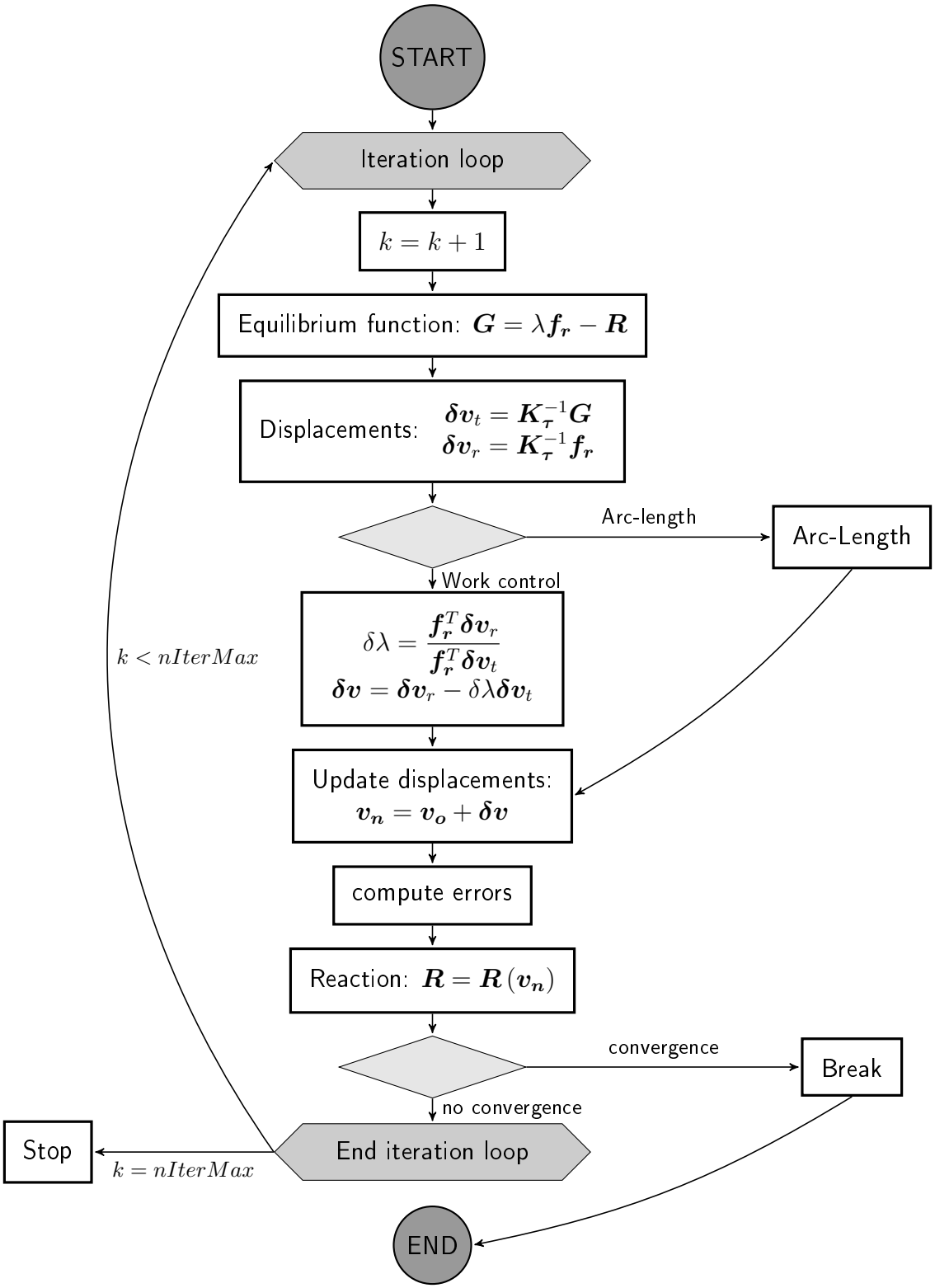

Figure 4.14: Flow chart of the correction phase

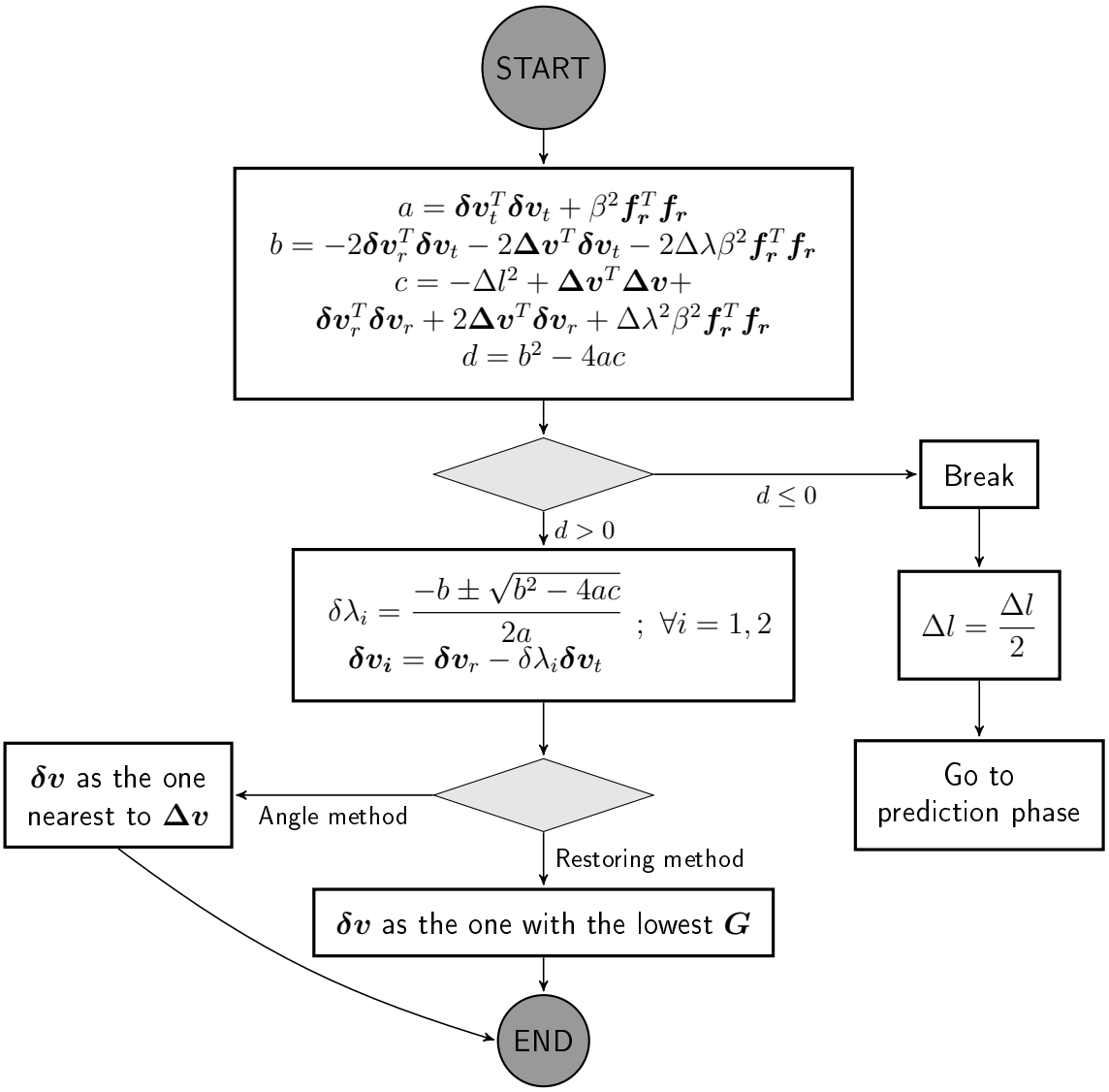

Figure 4.15: Flow chart of the Arc-Length method in the correction phase

4.2 Computational aspects

The different diagrams developed in the prediction and corrections phases might be used together to develop a numerical code to deal with nonlinear structural problems. The diagrams 4.10 and 4.14 are the two most important because define the procedure to follow in the prediction and correction phase, respectively.

Some numerical and computational aspects will be discussed and some procedures to update the performance and efficiency of the code will be provided. The *Switching* procedure will be discussed first. Later, a technique to modify the code to be able to define the load increment automatically will be provided and dicussed in terms of convergence problems.

4.2.1 Switching

Considering figure 4.3, where a general force-displacement path is depicted, the path 0-A has been considered as a stable zone because the stiffness was positive defined (The Bergam parameter has positive values). This part of the path can be faced using a classic Newton-Raphson scheme but, when the zone close to the A point is reached, the scheme may diverge. To solve this problem, a new procedure is presented to deal with. This new procedure, called *Switching procedure*, allows the program to jump from the classic Newton-Raphson to the more advanced Arc-length or work control methods during the iteration process.

To do so, the procedure is based on the Bergam parameter. The user may define a critic Bergam parameter value from which the Switching procedure may be activated. This check in the program must be included in both the prediction and correction phases considering the following flowchart.

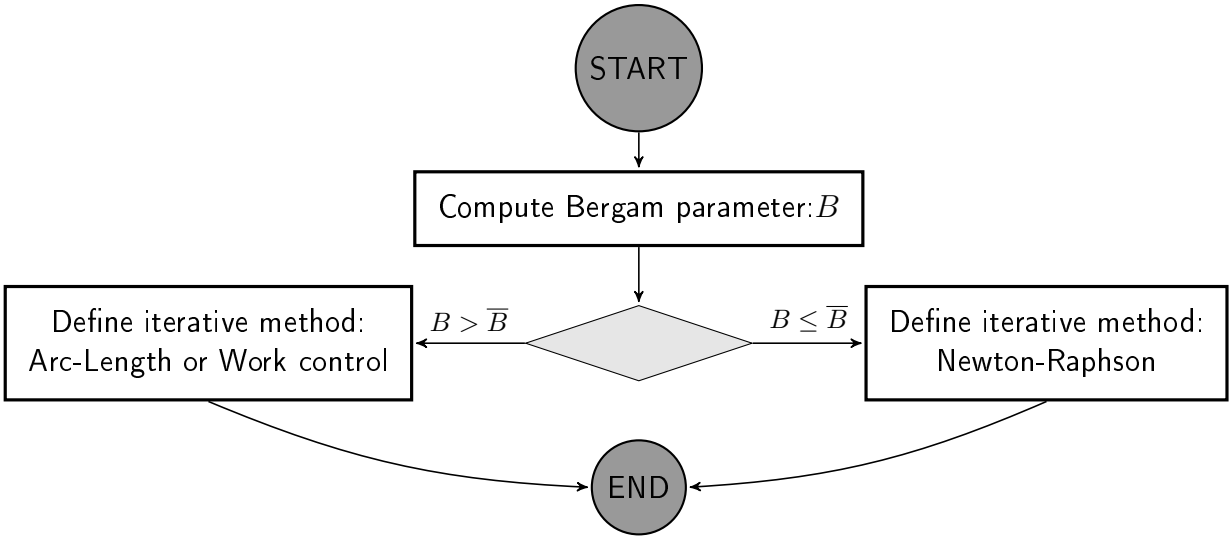

Figure 4.16: Flow chart of Switching procedure

4.2.2 Automatic load increment

Sometimes, the program performs many iterations in the correction phase due to the high nonlinearities of the structure. From the computational point of view, the convergence difficulty may be defined as the number of iterations performed on each correction phase. For example, if the iterations performed are few, the program does not find any difficulty to compute the solution. On the other hand, a large number of iterations may indicate that the increment of load parameter computed in the prediction phase is too big (in case a classic Newton-Raphson scheme is being used) or that the arc length parameter used in the correction phase is not adequate (in case an arc-length procedure is being used).

Let us define I_o as the optimum number of iterations introduced in the code by the user. In addition, I_i is defined as the number of iterations performed in the correction

phase number i. Obviously, if the number of iterations performed in the current correction phase have been bigger the the optimum one, the program could adjust the increment of load factor or the arc-length parameter to take into account the local nonlinearity of the structure responds.

In this thesis, the method proposed to update both the increment of load factor and arc-length parameter is the following

$$^{i+1}\Delta\lambda = {}^{i}\Delta\lambda\sqrt{\frac{I_d}{I_i}};\ {}^{i+1}\Delta l = {}^{i}\Delta l\sqrt{\frac{I_d}{I_i}} \tag{4.32}$$

The following flowchart (figure 4.17) explains where the previous modification must be implemented.

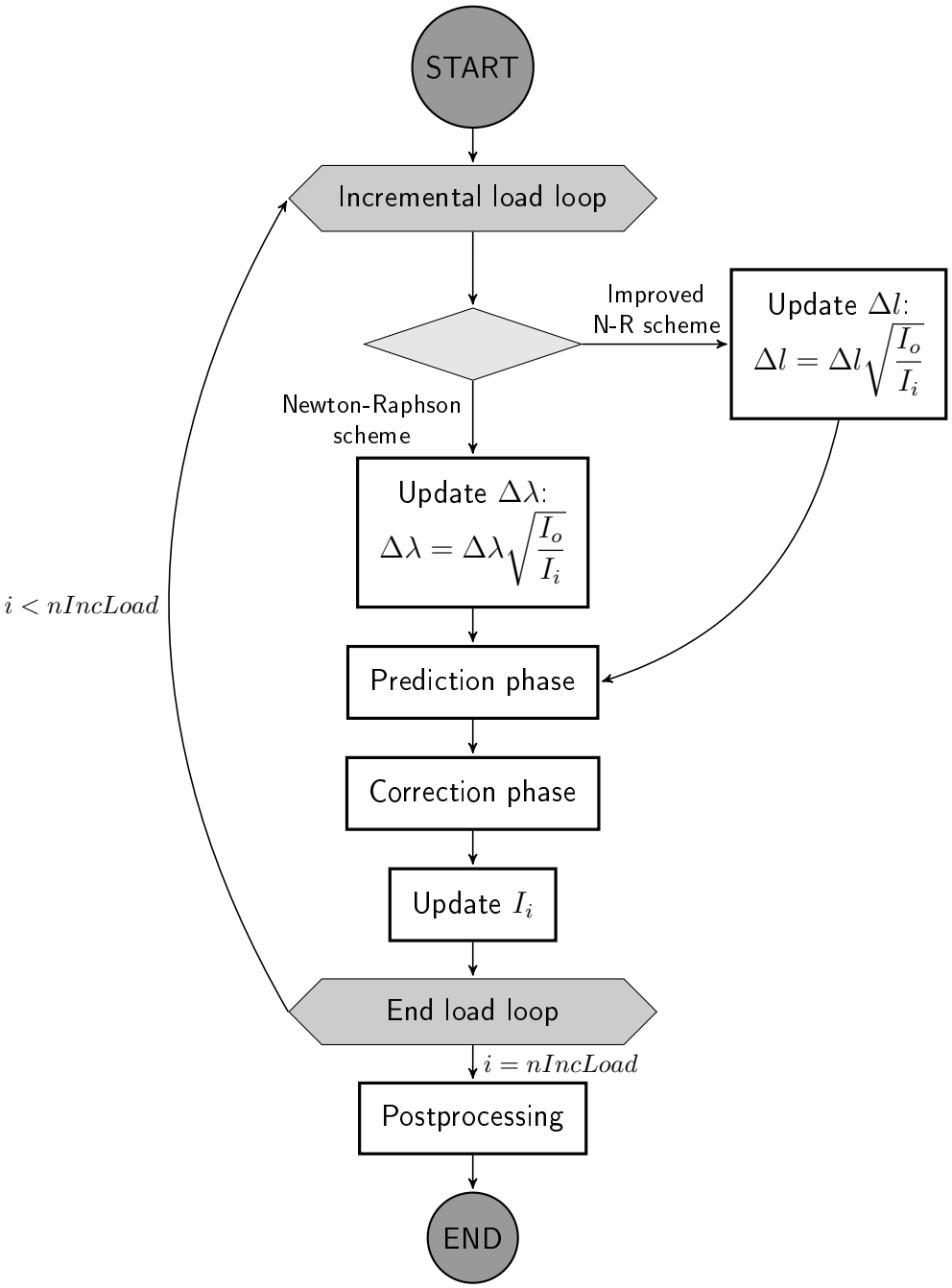

Figure 4.17: Flow chart of the automatic load increment procedure

4.2.3 Preconditioning and resolution of the linear system

Consider the linear system

$$\boldsymbol{K}\boldsymbol{u} = \boldsymbol{f} \tag{4.33}$$

If the entries of $\boldsymbol{K}$ vary greatly in size, it is likely that during the elimination process large entries are summed to small entries, with a consequent onset of rounding errors. To

study this, the condition number of the matrix $\boldsymbol{K}$ must be evaluated.

By definition, the condition number $C(\boldsymbol{K})$ of a matrix $\boldsymbol{K}$ can be defined as

$$C(\boldsymbol{K}) = |\boldsymbol{K}| \left|\boldsymbol{K}^{-1}\right| \tag{4.34}$$

It can be proved (see [Quarteroni, 2000]) that for symmetric definite positive matrices, the expression of the condition number reduces to the ratio between the biggest and the smallest eigenvalue of the matrix, which are expressed as λ_M and λ_m respectively.

$$C(\boldsymbol{K}) = \frac{\lambda_M}{\lambda_m} \tag{4.35}$$

It is well known that the condition number of a matrix affects the stability[(2)] of the linear system. This sentences can be expressed mathematically considering the following formula.

$$\frac{\boldsymbol{\delta u}}{\boldsymbol{u}} \leq \frac{C(\boldsymbol{K})}{1 - C(\boldsymbol{K})} \frac{\boldsymbol{\delta f}}{\boldsymbol{f}} \tag{4.36}$$

In this thesis, a method to precondition the amtrix of the linear system on each iteration of the process has been implemented. Consider a diagonal matrix defined as follows

$$\boldsymbol{D} = \begin{bmatrix} \beta^{r_1} & & \\ & \ddots & \\ & & \beta^{r_n} \end{bmatrix} \tag{4.37}$$

and the preconditioned system

$$\underbrace{\boldsymbol{D}\boldsymbol{K}\boldsymbol{D}}_{\boldsymbol{A}} \underbrace{\boldsymbol{D}^{-1}\boldsymbol{u}}_{\boldsymbol{x}} = \underbrace{\boldsymbol{D}\boldsymbol{f}}_{\boldsymbol{b}} \tag{4.38}$$

This new system can be solved and the vector $\boldsymbol{x}$ obtained. Then, the real vector $\boldsymbol{u}$ can be obtained from $\boldsymbol{x}$ as

$$\boldsymbol{u} = \boldsymbol{D}\boldsymbol{x} \tag{4.39}$$

An important matter is how to choose the matrix $\boldsymbol{D}$. In this work, the method used to obtained the matrix is imposing a restriction in the diagonal terms of the matrix $\boldsymbol{A}$, which is

$$\forall i = 1, \ldots, n \quad 1 \leq |\boldsymbol{A}_{ii}| \leq \beta \tag{4.40}$$

Considering that the diagonal entries of the matrix $\boldsymbol{A}$ can be obtained in terms of the diagonal elements of the matrix $\boldsymbol{K}$ as

$$\boldsymbol{A}_{ii} = \beta^{2r_i} \boldsymbol{K}_{ii} \tag{4.41}$$

[(2)] Here, the term stability is considered as how much the variation of the results $\boldsymbol{\delta u}$ is affectted by a variation in the input of the system $\boldsymbol{\delta f}$

the equation 4.40 leads to the following two conditions on the coefficients r_i.

$$r_m = -\frac{\ln(|\boldsymbol{K}_{ii}|)}{2\ln(\beta)} \leq r_i \leq \frac{\ln(\beta) - \ln(|\boldsymbol{K}_{ii}|)}{2\ln(\beta)} = r_M \tag{4.42}$$

Considering that these two inequalities are always satisfied nomatter the value of $\boldsymbol{K}_{ii}$, a solution that satisfies 4.42 can be found as the medium between r_m and r_M.

$$r_i = \frac{\ln(\beta) - 2\ln(|\boldsymbol{K}_{ii}|)}{4\ln(\beta)} \tag{4.43}$$

The method previously exposed allows to precondition the linear system. During the numerical analysis, this technique has been proved to be very effective.

In addittion, an iterative algorithm has been also implemented to deal with ill-conditioned systems when the method previously explained is not able to completely condition the system. The method implemented is called iterative refinement.

When the matrix of a linear system is ill-conditioned and the technique to condition it fails, the iterative refinement technique can be applied to solve the system. Consider the system 4.33 with an ill-conditioned matrix $\boldsymbol{A}$. The iterative refinement is a technic for improving the accuracy of a solution yielded by a direct method. Suppose that the linear system has been solved, and denote $\boldsymbol{x}^0$ the first solution. Having fixed a tolerance *tol* the iterative refinement performs as follows: for $i = 1, \ldots,$ untill convergence:

1. Compute residual vector: $\boldsymbol{r}^{(i)} = \boldsymbol{f} - \boldsymbol{K}\boldsymbol{x}^{(i)}$
2. Solve the linear system $\boldsymbol{K}\boldsymbol{z} = \boldsymbol{r}^{(i)}$
3. Update solution: $\boldsymbol{x}^{(i+1)} = \boldsymbol{x}^{(i)} + \boldsymbol{z}$
4. If $\dfrac{|\boldsymbol{z}|}{|\boldsymbol{x}^{(i+1)}|} \leq tol$ and $\dfrac{\left|\boldsymbol{r}^{(i)}\right|}{\boldsymbol{f}} \leq tol$ the procedure can stop, otherwise start at step 1.

This procedure allows to solve ill-conditioned systems with relatively well stability. For more details see [Quarteroni, 2000].

II

NONLINEAR ANALYSIS OF FLOATING STRUCTURES

The first part of the thesis has been devoted to the introduction of basic concepts in the field of structural mechanics. In the first section, the definitions of the variables that completely describe the displacement, strain and stress field of a body have been introduced and explained. The last presented the formulation of the principle of virtual work in both the total and updated lagrangian formulations.

Later, the theories adopted to study cable and beam structures have been discussed. A general overview of the two approaches, Total and Updated lagrangian formulation, has been presented and the results of general theory and finite element models formulated. Also, two approaches have been presented to formulate the equilibrium equations in total or incremental form. The stiffness method has been proved to be reliable in the formulation of cable elements in both total and updated lagrangian formulation but has no application in the formulation of beam elements, while the finite element method is considered to be the most accurate approach to formulate the equilibrium equations in terms of the displacement field.

Finally, the numerical methods and algorithms used in this thesis to analyse floating structures have been reported on chapter 4. The most simple method, called stiffness method, has been presented and considered reliable for the analysis of floating structures in a 2D model with the total lagrangian approach. Later, more advanced techniques used in the analysis of general 3D floating structure have been explained and the Newton-Raphson incremental iterative algorithm has been considered. To overcome the limits of such method more advanced techniques have also been considered such as the Arc-Length and Work Control methods.

In this second part, the study of floating structures will be performed. This part, divided in 6 chapters, will be devoted to explain the main concepts behind the new theory developed and also to formulate the new finite element model proposed.

Chapter 5 will be devoted to define and characterize the constitutive equations at a sectional level, one of the new concepts developed in this text. The characterization of a section will be explained and its interaction with the fluid formulated.

In chapter 6, the formulation of the new finite element in a 2D model will be explained and tested with several benchmarcks. The equations developed in the previous chapter will be included in a finite element code to analyse their effects and contributions in terms of equilibrium and displacements of floating structures such as breakwater and floating bridges. The total lagrangian formulation will be considered to perform the analysis of linear elastic structures under small displacements and small strains. Also, the way in which the total stiffness of the structure is computed by means of the new finite element model is explained.

Chapter 7 will be focused on the formulation and analysis of floating structures with a general 3D nonlinear approach. The constitutive equations at a sectional level will be assembled along each finite element to provide a new contribution in the stiffness of the structure considering large displacements and the coupling between axial, bending and

torsional behaviour.

In chapter 8, different benchmarcks will be performed to ensure the accuracy of this new method and real applications will also be studied. Here, all the numerical methods explained in the introductory part will find their application due to the great nonlinearity presented by floating structures in a 3D space.

Chapter 9 is devoted to the analysis of floating bridge situated in the state of Washington in USA. In this final application, the program will be tested with a very challenging application and some concluding remarks about the performance and the results obtained by the program will be discussed.

Finally, in chapter 10 some conclusions will be presented and some indications in the development of future works will be exposed.

5 Sectional analysis

In this chapter, the sectional analysis will be considered. First, the characterization of a section in terms of geometry and its interaction with the fluid will be explained. As it will be shown, the section element (as it has been called in this thesis) is considered as the main factor that will allow to formulate the finite element theory that will be exposed in following chapters. The methodology has been the study of sections in contact with an unmoved fluid and their interaction in terms of forces and moments applied to the section and the current position and orientation of it.

Second, theory and methods used to analyze the section in contact with a fluid will be reported and explained: characterization of the section from the geometrical point of view, material of the section, fluid surrounding the section and its physic properties. Section 5.1 explains the several types of mesh used to define the geometry of the section.

Section 5.2 is devoted to the geometric variables that characterize the section. The geometric properties of a section depend only on the shape of the section and its internal holes. The algorithms used to compute those properties are formulated and explained.

Section 5.3 is the most important part of this chapter. Here, the concept of constitutive equations of a section is defined and the theory explained. The numerical methods to analyse a section in contact with a fluid are developed and deeply explained.

The last part of this chapter is devoted to perform numerical examples on real sections and the procedure to obtain the constitutive equations is better clarified.

5.1 Modeling of the cross-section

Before starting with the characterization of a section, some definitions are needed. Consider the generic section depicted on figure 5.1. First, the boundary of the section (that is the closed curve that surrounds it) will be called *External boundary*. The *holes* of the section will be delimited by the so-called *Internal boundaries*.

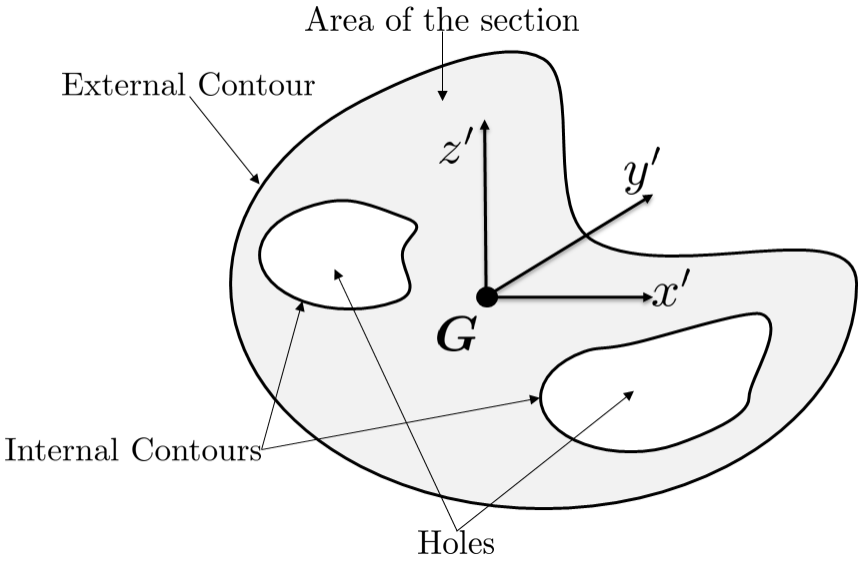

Figure 5.1: General sketch of a section

The section may be divided in 4 parts: the external boundary, the main area of the section, the internal contours (one for each hole) and the holes. A mesh for each part will be created to completely characterize the geometry of the section. First, the *Section mesh*, the one that meshes the area of the section, will be described; later, the *Holes mesh* will be considered and its possible applications will be listed. The other two meshes, the *Internal boundary mesh* and *External boundary mesh* will be explained separately because are the most important in the fluid-section interaction development.

A general introduction on the different meshes is required. Consider figure 5.2, where a meshed ring section[(1)] is depicted. It can be seen how the meshes that describe areas are composed by 4-nodes quadrangular elements and the meshes that describe contours are build with 2-nodes straight elements.

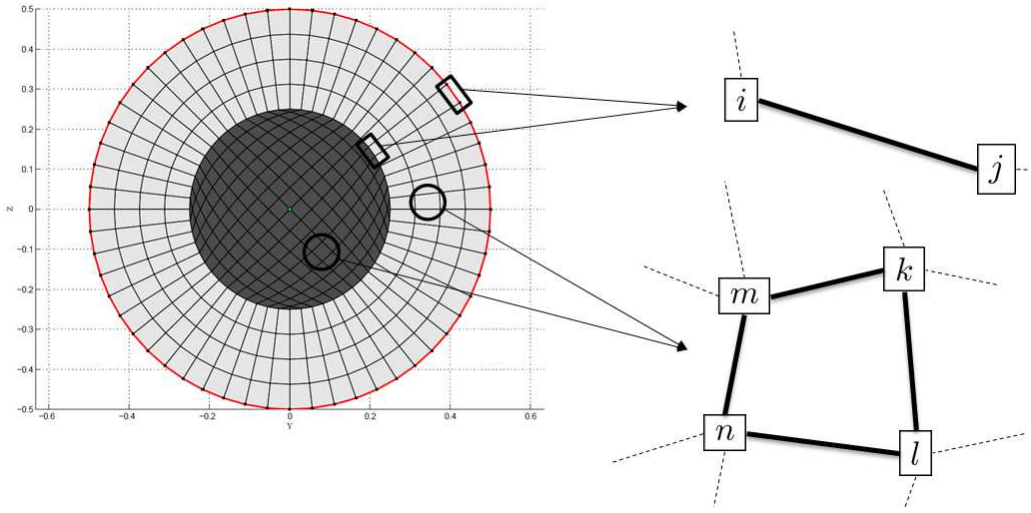

Figure 5.2: Representation of the four types of mesh used in the discretization of a section

[(1)] Ring section means that the section is circular with a concentric hole in its center.

5.1.1 Discretization of the cross-section

The section mesh, composed as a concatenation of 4-nodes quadrangular elements (figure 5.2), has two goals. The first one is to evaluate the area, moments of inertia and torsional stiffness of the section (explained in section 5.2) and the second one is to characterize the fluid-section interaction in terms of the resulting loads that the fluid produces in the area of the section.

The computation of the geometrical properties (position of the center of gravity, $\boldsymbol{v_G}$, area of the section, A and moments of intertia, I_y, I_z and I_x) of the section will be done by means of a numerical integration along the area. The procedures and numerical integration schemes used will be deeply explained in further sections.

On the other hand, the loads produced by the fluid in area of the section will be computed adopting a Gauss numerical integration, as it can be seen in section 5.3.1.2.

5.1.2 Discretization of the section boundary

The boundary of the section is one of the places where the hydrostatic pressure acts and, as a consequence, one of the places where it will be evaluated. The hydrostatic load field will be integrated along the curve that defines the boundary to obtain the resulting forces. It must be noted that these forces will be contained in the plane of the section and could be expressed in the local reference system of the section (F'_y and F'_z). Another effect that may appear in a section with a generic shape is a twisting moment M_t (usually in sections that are not symmetric).

The elements used are 2-node straight elements. The concatenation of those elements will define a closed curve (boundary of the section) and, opportunely oriented (counterclockwise), will define a surface inside.

5.1.3 Modeling holes

The mesh built in the holes of the section is very useful and some definitions are required. Consider a beam in contact with an unmoved fluid as the one in figure 5.3. For constructive porposes, one may consider to cover both sections A and B (depicted in the figure) with a waterproof material to prevent the passage of fluid inside the beam. It is known that the capability to float of this kind of structures is, in part, due to the ability to block the entrance of fluid inside them. Let us consider, as example, a concrete beam. By the Archimedes principle, the beam will sink because the specific self-weight of the concrete is two and a half times larger than the sea water.

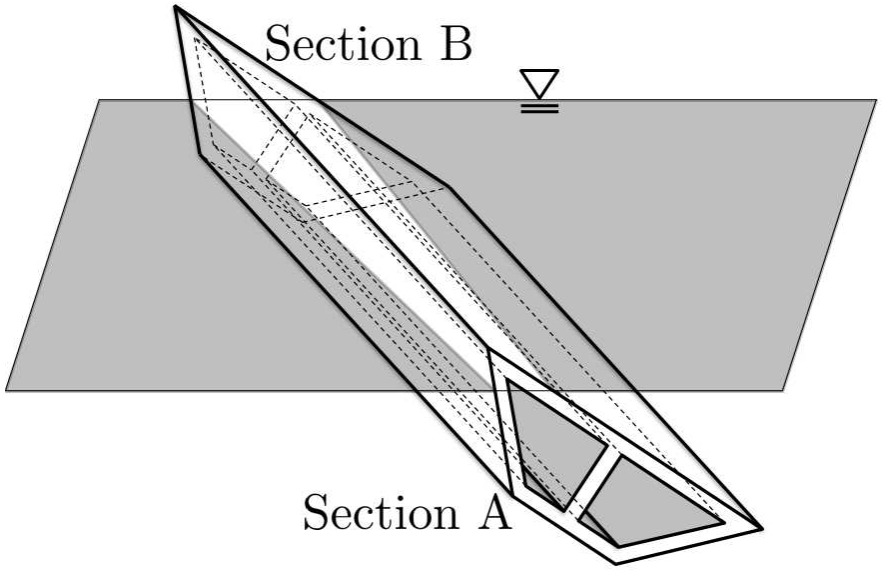

Figure 5.3: Sketch of a beam making contact with an hydrostatic fluid

Therefore, it is possible to define two new types of section. The sections that are covered (*Isolated Section*) to block the pass of the fluid and the ones which are not (*Non Isolated Section*). This will lead to some differences in the static behaviour of the section and, of consequence, the static behaviour of the beam composed by this sections will change. This study will be performed in detail on subsection 5.3.2, where the integration in the area of the section and inside the holes (in case the section is covered) will be formulated and derived for both types of sections.

It is important to notice that, in this thesis, the hypothesis of a non-structural waterproof material is considered. This means that the material used to protect the interior of the beam has no structural properties, since the only effect is the blockage of the fluid. Only the sections at each end of the beam are considered for the installation of this material.

5.1.4 Discretization of the holes boundary

The holes of the section must be also meshed since in some cases the beam will not be protected at the ends and the hydrostatic pressure will be integrated also inside. One may consider this case as an extreme case. Indeed, from a construction point of view, engineers would like to avoid the condition in which the beam are not protected against the fluid penetration. Nevertheless, the analysis of this situation will also be carried out to analyse the critical behaviour of floating structure under extreme conditions.

In this mesh, the elements are considered as 2-nodes straight elements. In the program the holes will also be oriented opportunely to integrate the hydrostatic pressure along the boundary defined by a closed curved.

5.2 Geometric properties

The geometric variables are the area A of the section, the two bending inertia I_y and I_z and the torsional inertia I_x.

These variables are the well known variables needed in a typical finite element code to properly model the behaviour of a beam using the Euler-Bernoulli and Saint Venant displacement models. Later on, the parts concerning to the fluid-section interaction model will be exposed in a more detailed way.

Consider a 4-nodes quadrangular element as the one depicted in figure 5.4. All the elements inside the section and inside the holes are elements as the one depicted and have been built considering a *mapping*.

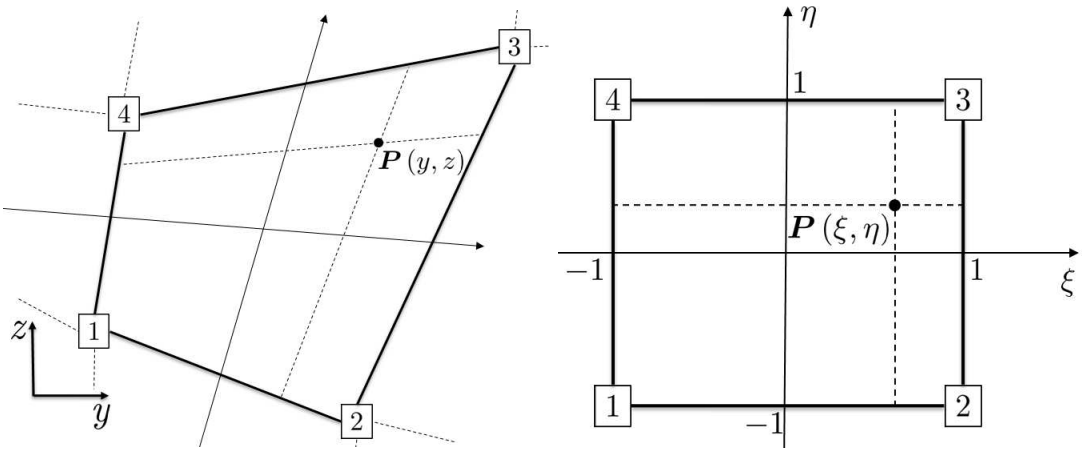

(a) Sketch of one element of the section mesh (b) Element in the natural coordinates

Figure 5.4: Mapping of a 4-nodes quadrangular element

The mapping is shown in figure 5.4, where a 4-nodes squared element is depicted in a normalized space. The following formula describes the mapping of each element.

$$\boldsymbol{p} = \begin{bmatrix} y \\ z \end{bmatrix} = \boldsymbol{N}(\xi, \eta)\, \boldsymbol{r} \tag{5.1}$$

$$\boldsymbol{N}(\xi, \eta) = \begin{bmatrix} \boldsymbol{N}_1 & \boldsymbol{N}_2 & \boldsymbol{N}_3 & \boldsymbol{N}_4 \end{bmatrix} \tag{5.2}$$

$$\boldsymbol{N}_i = N_i \boldsymbol{I_2} \quad N_i = \frac{1}{4}(1 + \xi_i \xi)(1 + \eta_i \eta) \quad \xi_i, \eta_i = \pm 1$$

$$\boldsymbol{r} = \begin{bmatrix} x_1 & z_1 & x_2 & z_2 & x_3 & z_3 & x_4 & z_4 \end{bmatrix}^T \tag{5.3}$$

The mapping allows to compute the derivative of the global coordinates with respect the natural coordinates, once is defined the *Jacobian* of the transformation as the matrix that contains the derivative early mentioned.

$$\boldsymbol{J} = \begin{bmatrix} \dfrac{\partial y}{\partial \xi} & \dfrac{\partial z}{\partial \xi} \\ \dfrac{\partial y}{\partial \eta} & \dfrac{\partial z}{\partial \eta} \end{bmatrix} \tag{5.4}$$

To derive the derivatives that are included in the Jacobian matrix, the relation between the global and natural coordinates are needed,

$$y = y(\xi, \eta) = \sum_{i=1}^{4} N_i(\xi, \eta)\, y_i \qquad z = z(\xi, \eta) = \sum_{i=1}^{4} N_i(\xi, \eta)\, z_i$$

which leads to

$$\frac{\partial y}{\partial \xi} = \sum_{i=1}^{4} \frac{\partial N_i(\xi, \eta)}{\partial \xi} y_i \qquad \frac{\partial y}{\partial \eta} = \sum_{i=1}^{4} \frac{\partial N_i(\xi, \eta)}{\partial \eta} y_i$$

$$\frac{\partial z}{\partial \xi} = \sum_{i=1}^{4} \frac{\partial N_i(\xi, \eta)}{\partial \xi} z_i \qquad \frac{\partial z}{\partial \eta} = \sum_{i=1}^{4} \frac{\partial N_i(\xi, \eta)}{\partial \eta} z_i$$

with

$$\frac{\partial N_i(\xi, \eta)}{\partial \xi} = \frac{1}{4}\xi_i(1 + \eta_i \eta) \quad \frac{\partial N_i(\xi, \eta)}{\partial \eta} = \frac{1}{4}\eta_i(1 + \xi_i \xi) \tag{5.5}$$

The analytical expression of the Jacobian may be written as

$$\boldsymbol{J}(\xi, \eta) = \begin{bmatrix} -(1-\eta) & (1-\eta) & (1+\eta) & -(1+\eta) \\ -(1-\xi) & -(1+\xi) & (1+\xi) & (1-\xi) \end{bmatrix} \begin{bmatrix} y_1 & z_1 \\ y_2 & z_2 \\ y_3 & z_3 \\ y_4 & z_4 \end{bmatrix} \tag{5.6}$$

and its determinant can be obtained performing the previous product.

$$|\boldsymbol{J}| = \frac{1}{8}\left[(y_{13}z_{24} - y_{24}z_{13}) + (y_{34}z_{12} - y_{12}z_{34})\,\xi + (y_{23}z_{14} - y_{14}z_{23})\,\eta\right] \tag{5.7}$$

With

$$y_{ij} = y_i - y_j \qquad z_{ij} = z_i - z_j$$

5.2.1 Area A

The area of the section will be computed using the *section mesh*. A Gauss integration is performed to compute the structural area of the section as the sum of the area of each element located in the section mesh.

First, the area of the section may be written as

$$A = \int_{\Omega} d\Omega \tag{5.8}$$

which has to be equal to the sum of the areas of each element.

$$A = \sum_{i=1}^{N_e} \int_{\Omega_i} d\Omega_i \tag{5.9}$$

The integral inside the summatory can be computed considering the mapping earlier described. Considering the change variable defined in equation 5.1, the integral becomes

$$A = \sum_{i=1}^{N_e} \int_{-1}^{1} \int_{-1}^{1} |\boldsymbol{J}| \; d\eta \; d\xi \tag{5.10}$$

where the notation $|\boldsymbol{J}|$ represents the determinant of the Jacobian.

The following integral can be easily solved on each quadrangular element and the final expression for the area can be written. In adittion, considering that the determinant of the Jacobian is a linear function in terms of the natural coordinates, the integral can be reduced to the evaluation of its value in the center of the element (equation 5.7).

$$A = 4 \sum_{i=1}^{N_e} |\boldsymbol{J}_i \left(\xi = 0, \eta = 0\right)| \tag{5.11}$$

5.2.2 Static moments S_y and S_z

The static moments might be computed considering the contribution of each element of the section. Consider the definition of the static moments as

$$S_y = \int_{\Omega} y \; d\Omega \quad S_z = \int_{\Omega} z \; d\Omega \tag{5.12}$$

and considering, as done before, the division of the section in a certain number of elements and performing the integrals on each one of them it may lead to:

$$S_y = \sum_{i=1}^{N_e} \int_{\Omega_i} y \; d\Omega_i \qquad S_z = \sum_{i=1}^{N_e} \int_{\Omega_i} z \; d\Omega_i \tag{5.13}$$

Considering now that the function inside the integral is a linear function, the value of the integration on each element can be computed as the product between the area of the element and the coordinate of its center of gravity.

$$S_y = \sum_{i=1}^{N_e} y_{Gi} A_i \qquad S_z = \sum_{i=1}^{N_e} z_{Gi} A_i \tag{5.14}$$

5.2.3 Center of gravity, v_G

In an structural beam finite element model, the external loads must be transformed to obtain equivalent loads. Usually, general loads are transformed in equivalent loads positioned on the midline of the beam to express them as a sum of axial, bending and torsional

loads (concentrated or distributed).

The midline of a beam is considered a straight line that goes from the center of gravity of the section situated at the first edge of the beam to the centroid of the section positioned in the second edge. Therefore, the computation of the center of gravity of any section is required.

Let us consider the definition of centroid.

$$\boldsymbol{r_G} = \begin{bmatrix} y_G \\ z_G \end{bmatrix} = \frac{1}{A}\int_\Omega \boldsymbol{r}\ d\Omega \tag{5.15}$$

where $\boldsymbol{r} = \begin{bmatrix} y \\ z \end{bmatrix}$ is the position vector and A the total area of the section (computed in subsection 5.2.1). Considering equation 5.12, the position of the center of gravity can be written as a function of the static moments.

$$\boldsymbol{r_G} = \frac{1}{A}\int_\Omega \begin{bmatrix} y \\ z \end{bmatrix}\ d\Omega = \frac{1}{A}\begin{bmatrix} \int_\Omega y\ d\Omega \\ \int_\Omega z\ d\Omega \end{bmatrix} = \frac{1}{A}\begin{bmatrix} S_y \\ S_z \end{bmatrix} \tag{5.16}$$

5.2.4 Inertia moments $I_y,\ I_z$

The bending stiffness of a beam can be obtained by means of two contributions. The first contribution is due to the mechanical properties of the beam. The Young modulus of the material, E, is the factor that controls the mechanical contribution to the bending stiffness with respect an axes and in this thesis is considered constant.

On the other hand, the geometrical contribution in the bending stiffness is the moment of intertia of a section, I. Obviously, the moment of inertia can be computed for each one of the two axes of the section. Considering the principal axes of the section, the definition of the intertia moments is

$$I_y = \int_\Omega (z - z_G)^2\ d\Omega \qquad I_z = \int_\Omega (y - y_G)^2\ d\Omega \tag{5.17}$$

The value of this integrals along the section can be decomposed in the contribution on each element as follows

$$I_y = \sum_{i=1}^{N_e}\int_{\Omega_i} (z - z_G)^2\ d\Omega_i \qquad I_z = \sum_{i=1}^{N_e}\int_{\Omega_i} (y - y_G)^2\ d\Omega_i \tag{5.18}$$

Considering a Gauss integration scheme, inside each element, the same integral may be written considering the change variable defined in equation 5.1 (here indicate only I_y for sake of brevity)

$$I_y = \sum_{i=1}^{N_e}\int_{\Omega_i} (z - z_G)^2\ d\Omega_i = \sum_{i=1}^{N_e}\int_{-1}^{1}\int_{-1}^{1} |\boldsymbol{J}(\xi,\eta)|\,(z(\xi,\eta) - z_G)^2\ d\eta\ d\xi \tag{5.19}$$

which can be approximated as follows

$$I_y = \sum_{i=1}^{N_e} \left[\sum_{k=1}^{N_G} \sum_{l=1}^{N_G} w_k w_l \left| \boldsymbol{J}_{kl} \right| \left(z_{kl} - z_G \right)^2 \right] \tag{5.20}$$

with

$$\boldsymbol{J}_{kl} = \boldsymbol{J}\left(\xi_k, \eta_l\right) \qquad z_{kl} = z\left(\xi_k, \eta_l\right)$$

The same can be done for the other moment of inertia.

$$I_z = \sum_{i=1}^{N_e} \left[\sum_{k=1}^{N_G} \sum_{l=1}^{N_G} w_k w_l \left| \boldsymbol{J}_{kl} \right| \left(y_{kl} - y_G \right)^2 \right] \tag{5.21}$$

5.2.5 Torsional inertia I_x

Many definitions, based on several displacement models, can be assumed to the torsional inertia of a section. The model used in this thesis is the one developed by Saint Venant and considers the contribution of the torsional displacement as a rigid body rotation with respect the normal axis of the section that passes throught the center of gravity. Only in this hypothesis, the torsional inertia moment can be computed as the sum of each moment of inertia previously computed.

$$I_x = \int_\Omega \left(y - y_G\right)^2 + \left(z - z_G\right)^2 \, d\Omega = \int_\Omega \left(y - y_G\right)^2 \, d\Omega + \int_\Omega \left(z - z_G\right)^2 \, d\Omega = I_y + I_z \tag{5.22}$$

5.3 Fluid-structure interaction

The innovative aspect of this thesis is the study of the behaviour of a beam element surrounded by a fluid as a result of the interaction between each section along the axes and the fluid. Consider figure 5.5, where a beam element is depicted. Consider also that this element is somehow in contact with an unmoved fluid. From a mathematical point of view, it is possible to define a new stiffness of the beam that takes into account the resistance produced by the fluid to the movement of the body. Considering the physics of the problem, the interaction (resistance of the fluid to the movement of the beam) between fluid and beam could be analyzed taken into account the contribution of each section along the axes. To take into account this contribution, the analysis of single sections in contact to a fluid will be carried out in the following.

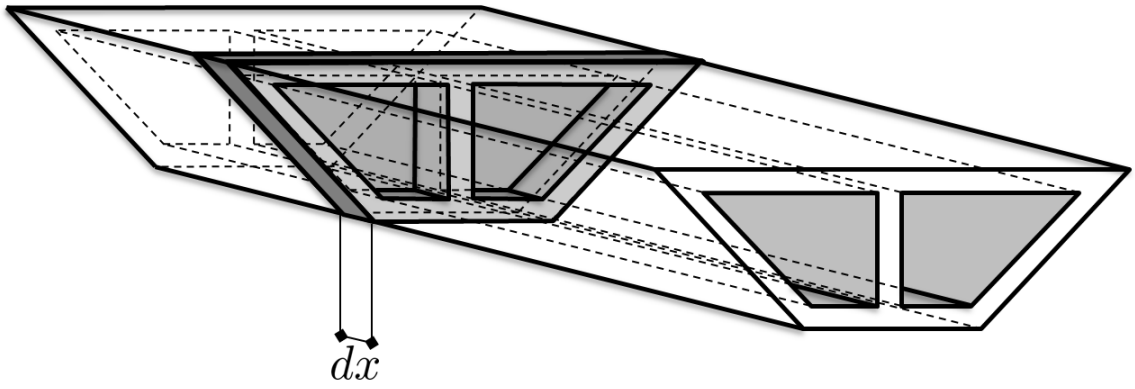

Figure 5.5: Beam element seen as a concatenation of infinite sections along its axes

The model presented considers the section as a 3D solid with an infinitessimal thickness. The hydrostatic load is integrated along its boundaries and area (in case the section is located in one of the two ends of the beam) to obtain the resulting forces and moments applied on the center of gravity of the section. It might be noticed that the section is considered as a rigid body which can only translate and rotate. This hypothesis allows the model to work with the resulting of the forces and moments produced by the fluid.

The resulting forces and moments will be then properly introduced in a finite element code to study floating structures with this new stiffness contribution produced by the fluid. For the moment, the equations that govern the static behaviour of the section in terms of the forces and moments produced by a fluid are presented and deeply discussed.

5.3.1 Forces due to the fluid

The resulting forces and moments produced by a fluid surrounding a section are presented and the methodologies to compute them are explained. For simplicity, the forces and moments and their explanations are divided in two groups. The first group are the forces contained in the plane of the section, which are $F_{z'}$ and $F_{y'}$ along the z' and y' axes and the twisting moment M_t along the x' axes. The second group is composed by the forces and moments that result from the integration of the hydrostatic pressure inside the area of the section, which are the moments $M_{y'}$ and $M_{z'}$ along the y' and z' axes and the force $F_{x'}$ along the x' axes.

For the first group, the value of the forces and moments are computed by means of an integration along the boundary of the section and, on the other hand, the forces and moments of the second group are obtained as a result of an integration inside the area of the section. Different techniques are adopted to perform the integration along the boundary and the area of the section and will be deeply discussed in this subsection.

5.3.1.1 In-plane forces

The forces that are the result of the integration along the boundary of the section are here defined. First, the integration method used in sections that are within a beam isolated by the entrance of the fluid on each edge is presented. Later, the inclusion of non isolated

beams will be considered and the generalization of the method will be presented.

Consider figure 5.6, where a generic section partially submerged in a fluid and the hydrostatic pressure along the external boundary are depicted.

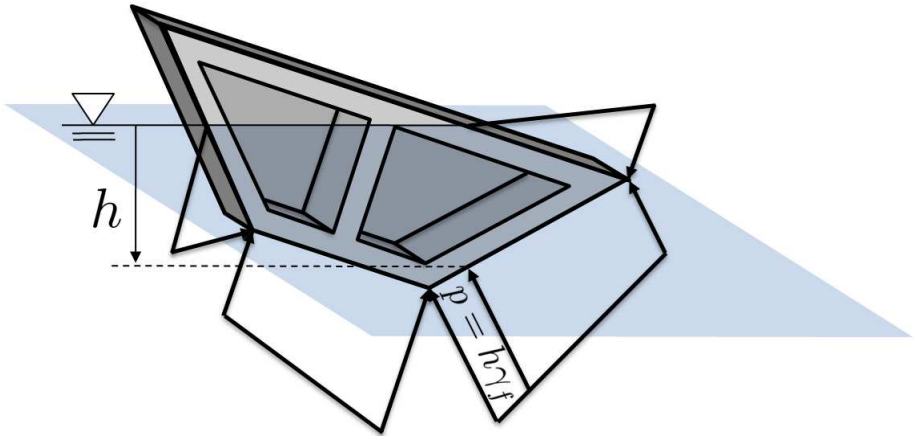

Figure 5.6: Integration of the hydrostatic pressure along the external cotour of the section

As it can be seen, the hydrostatic pressure is proportional to the depth from the fluid surface and is governed by the equation

$$P = h\gamma_f \tag{5.23}$$

with h is the depth measured from the surface and γ_f is the self-weight of the fluid.

It is well known that the pressure of the fluid follows the direction normal to the surface. This allows to define the pressure vector as

$$\boldsymbol{P} = -P\boldsymbol{n} \tag{5.24}$$

with $\boldsymbol{n}$ defined as the vector normal to the surface.

Now, the basic concepts to formulate the equations that governs the resulting forces and moments due to a fluid surrounding a section have been explained. Considering a generic boundary of a section depicted in figure 5.7, the equations to compute the forces and moments can be written.

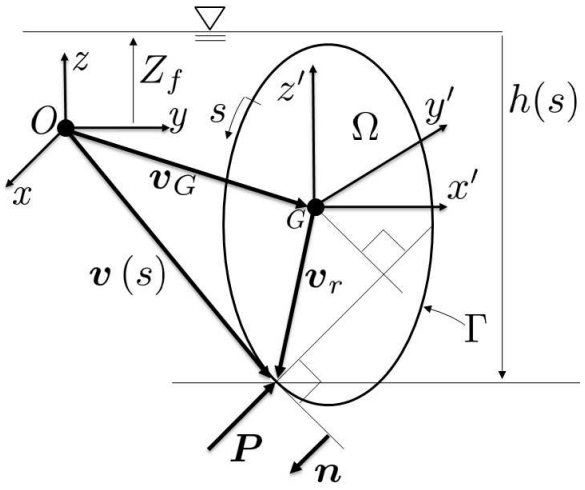

Figure 5.7: Model to compute the forces of a section due to a fluid in a 3D space

Let us define $\boldsymbol{F}$, the vector whose components are the forces contained in the plane of the section and M_t the resulting twisting moment acting on the section.

$$\boldsymbol{F} = \begin{bmatrix} F_{y'} \\ F_{z'} \end{bmatrix} \tag{5.25}$$

$\boldsymbol{F}$ can be computed integrating the hydrostatic pressure along the length of the boundary.

$$\boldsymbol{F} = \int_{\Gamma} \begin{bmatrix} \boldsymbol{P}^T \boldsymbol{y'} \\ \boldsymbol{P}^T \boldsymbol{z'} \end{bmatrix} H\left(h\right) \, d\Gamma \tag{5.26}$$

where H is the *Heaviside* function. Its definition is written here..

$$H(h) = \begin{cases} 1 & ; \quad h \geq 0 \\ 0 & ; \quad h < 0 \end{cases} ; \qquad h = Z_f - \boldsymbol{v}\left(s\right)_z \tag{5.27}$$

The variables Z_f and $\boldsymbol{v}\left(s\right)$ are depicted in figure 5.7.

Following the same procedure, the twisting moment can be derived.

$$M_t = \int_{\Gamma} \left(\boldsymbol{v_r} \times \boldsymbol{P}\right)^T \boldsymbol{x'} H\left(h\right) d\Gamma \tag{5.28}$$

In the last equation, the relative position vector $\boldsymbol{v_r}$ has been used and its expression is (figure 5.7)

$$\boldsymbol{v_r} = \boldsymbol{v}\left(s\right) - \boldsymbol{v_G} \tag{5.29}$$

Now, the expressions of the two forces contained in the plane of the section and the twisting moment have been formulated. Althought the expressions developed are valid for a generic boundary, the equations must be adapted to consider a discretized boundary. The mesh used to define the boundary of the sections is composed by 2-nodes straight elements. The integrals previously developed can be reformulated to take into account

the discrete boundary.

Consider equation 5.26. The integral can be seen as the contribution of the hydrostatic pressure on each straight element.

$$\boldsymbol{F} = \int_{\Gamma} \begin{bmatrix} \boldsymbol{P}^T \boldsymbol{y'} \\ \boldsymbol{P}^T \boldsymbol{z'} \end{bmatrix} H(h)\ d\Gamma \simeq \sum_{i=1}^{N_{ec}} \int_{\Gamma_i} \begin{bmatrix} \boldsymbol{P}^T \boldsymbol{y'} \\ \boldsymbol{P}^T \boldsymbol{z'} \end{bmatrix} H(h)\ d\Gamma_i \tag{5.30}$$

$$M_t = \int_{\Gamma} (\boldsymbol{v_r} \times \boldsymbol{P})^T \boldsymbol{x'} H(h)\, d\Gamma \simeq \sum_{i=1}^{N_{ec}} \int_{\Gamma_i} (\boldsymbol{v_r} \times \boldsymbol{P})^T \boldsymbol{x'} H(h)\, d\Gamma_i \tag{5.31}$$

The Heaviside function can be removed from the integral, performing the evaluation only in the elements that are in contact with the fluid. Considering the element in contact with the fluid in the summatory and removing the others, the previous expression can be written as

$$\sum_{i=1}^{N_{ec}} \int_{\Gamma_i} \begin{bmatrix} \boldsymbol{P}^T \boldsymbol{y'} \\ \boldsymbol{P}^T \boldsymbol{z'} \end{bmatrix} H(h)\ d\Gamma_i = \sum_{j=1}^{n_{ec}} \overbrace{\int_{\Gamma_j} \begin{bmatrix} \boldsymbol{P}^T \boldsymbol{y'} \\ \boldsymbol{P}^T \boldsymbol{z'} \end{bmatrix} d\Gamma_j}^{\boldsymbol{F_j}} \tag{5.32}$$

$$\sum_{i=1}^{N_{ec}} \int_{\Gamma} (\boldsymbol{v_r} \times \boldsymbol{P})^T \boldsymbol{x'} H(h)\, d\Gamma = \sum_{j=1}^{n_{ec}} \underbrace{\int_{\Gamma_j} (\boldsymbol{v_r} \times \boldsymbol{P})^T \boldsymbol{x'} d\Gamma_j}_{M_{tj}} \tag{5.33}$$

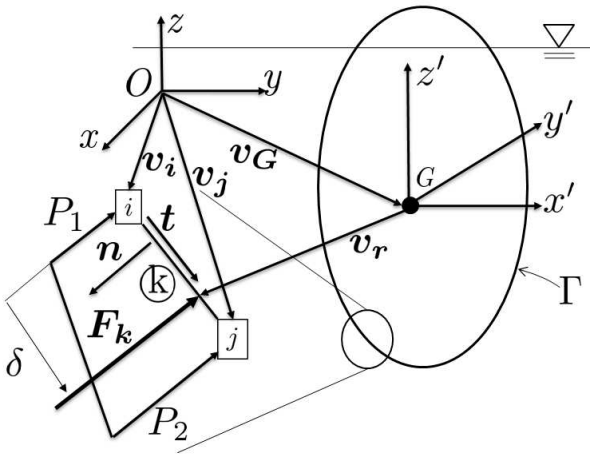

Figure 5.8: Procedure to integrate the hydrostatic pressure in the external boundary of a discretized section

Two possible paths can be considered. The first possibility is that all the element is under water. On the other hand, only part of the element is submerged. The expression previously derived can be rewritten to take into account the two possibilities as follows.

$$\sum_{j=1}^{n_{ec}} \boldsymbol{F_j} = \underbrace{\sum_{k=1}^{n_{ec1}} \boldsymbol{F_k}}_{\text{Elements totally under water}} + \underbrace{\sum_{l=1}^{n_{ec2}} \boldsymbol{F_l}}_{\text{Elements partially under water}} \tag{5.34}$$

$$\sum_{j=1}^{n_{ec}} M_t = \underbrace{\sum_{k=1}^{n_{ec1}} M_{tk}}_{\text{Elements totally under water}} + \underbrace{\sum_{l=1}^{n_{ec2}} M_{tl}}_{\text{Elements partially under water}} \tag{5.35}$$

The first part corresponds to the elements that are completely under water (both nodes of the element are under water) and their formulation is now explained.

Consider figure 5.8. A 2-nodes straight element and the hydrostatic pressure considered as a linear function along the element are depicted. $P_1 = h_i\gamma_f$ and $P_2 = h_j\gamma_f$ are defined as the values of the pressure on each node of the element, the vectors $\boldsymbol{v_i}$ and $\boldsymbol{v_j}$ as the position of each node of the element, $l = |\boldsymbol{v_i} - \boldsymbol{v_j}|$ as the length of the element, $\boldsymbol{t} = \dfrac{\boldsymbol{v_j} - \boldsymbol{v_i}}{l}$ as the tangent vector and $\boldsymbol{n} = \boldsymbol{x'} \times \boldsymbol{t}$ as the normal vector to the section of the element. If the integration of the linear hydrostatic pressure along the element is performed, the resultant force can be written as

$$\boldsymbol{F_k} = -\frac{\boldsymbol{P_i} + \boldsymbol{P_j}}{2} l \begin{bmatrix} \boldsymbol{n}^T\boldsymbol{y'} \\ \boldsymbol{n}^T\boldsymbol{z'} \end{bmatrix} \tag{5.36}$$

The twisting moment produced by the hydrostatic pressure on the element can be computed considering the equivalent position of the resulting pressure force on the element. The idea is create an equivalent system composed by only one vector that will provide the same resulting force and twisting moment (with respect the first node of the element) of the distributed linear load applied along the element. Considering figure 5.8, to determine the distance δ the resulting force $\boldsymbol{F_k}$ may be placed in a point along the element where the moment with respect the node i is equal to the moment produced by the distributed load.

$$F_k\delta = \int_0^l \left(P_1 + \frac{P_2 - P_1}{l}\eta\right)\eta d\eta \rightarrow \delta = \frac{l^2}{6}\frac{2P_2 + P_1}{F_k} \tag{5.37}$$

Once the distance from the first node is computed, the position with respect the center of gravity can be computed as

$$\boldsymbol{v_r} = \boldsymbol{v_i} + \delta\boldsymbol{t} - \boldsymbol{v_G} \tag{5.38}$$

and the contribution of this element to the twisting moment can be calculated following the sketch in figure 5.9.

$$M_{tk} = \begin{vmatrix} \widehat{i} & \widehat{j} & \widehat{k} \\ 0 & \boldsymbol{v_{ry'}} & \boldsymbol{v_{rz'}} \\ 0 & \boldsymbol{F_{ky'}} & \boldsymbol{F_{kz'}} \end{vmatrix} = \boldsymbol{v_{ry'}}\boldsymbol{F_{kz'}} - \boldsymbol{v_{rz'}}\boldsymbol{F_{ky'}} \tag{5.39}$$

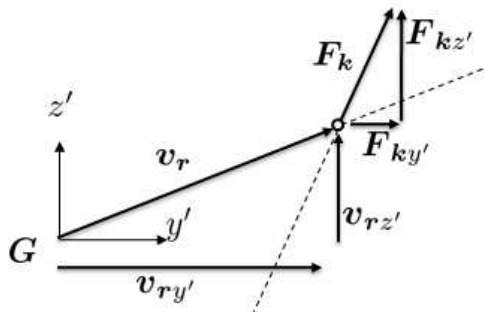

Figure 5.9: Contribution of each linear element on the total twisting moment

Once the contribution in the forces and twisting moment of a totally submerged element have been formulated, the attention shall be focused on the elements that are partially under the fluid.

It is important to notice that all the equations developed previously can be also used to determine the contribution, in terms of forces and twisting moment, of an element that is partially under the fluid. As it can be seen in figure 5.10, the part of the element under the fluid can be considered as an independent new element. Indeed, defining an intermediate node in the contact between the element and the free surface of the fluid, it is possible to repeat the procedure earlier developed to compute the contribution corresponding to the part of the element that is under the fluid.

If the second node of the element is under the fluid, the first node of the new element may be defined as the point where the element and the fluid intersect. On the other hand, if the first point of the element is under the fluid, the second node of the new element may be defined as the point where the element and the fluid intersect. Once the 2 nodes of the new element have been characterized, the procedure explained for elements completely under the fluid can be applied to determine the contribution of this new element.

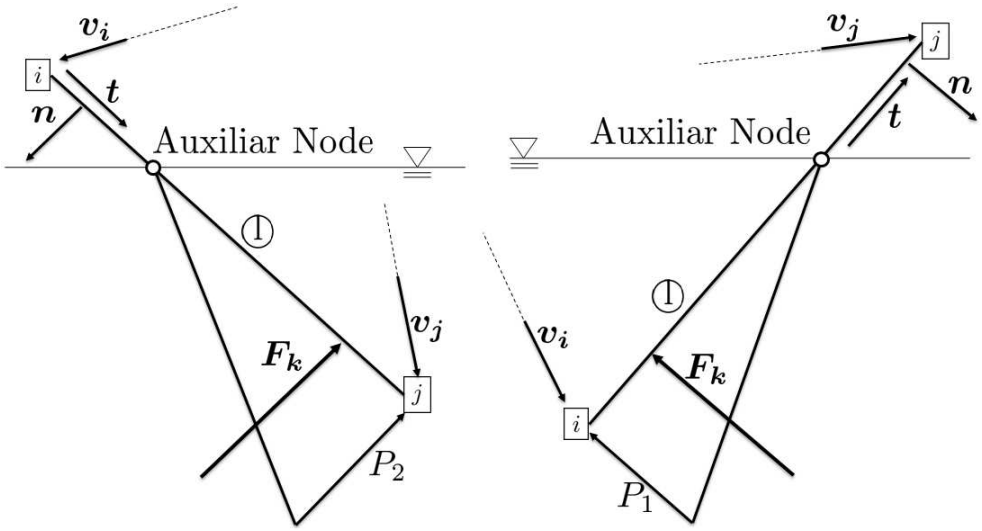

(a) The second node is inside the fluid (b) The first node is inside the fluid

Figure 5.10: Straight element partially under a fluid

The forces and moment derived from the integration of the hydrostatic pressure in the external boundary of the section have been derived. These forces and moment are the most important ones due to the fact that will provide to the beam its floating capacity.

The formulation of the forces and moments resulted from the integration inside the area of the section will be presented and the numerical techniques explained.

5.3.1.2 Out-of-plane forces

In this subsection, the forces coming from the integration inside the area of the section are defined and computed. One can notice that the integration inside the area is only required when the section is placed in one of the two edges of a beam. Indeed, the sections situated along the axes of the beam will not be under normal pressure[(2)] because their area is not directely in contact with the fluid. On the other hand, the sections situated at each end of the beam will be under the hydrostatic pressure.

For a better understanding, consider figure 5.11. A beam partially under a fluid is depicted and the two types of sections are highlighted. The section that is called *Inside Section* will not be loaded on its area by the hydrostatic pressure, since it is applied only on the external boundary. On the other hand, the sections placed at the ends of the beam will be subjected to the pressure either on the external boundary either on internal area.

[(2)] The term *normal* is referred with respect to the plane of the section

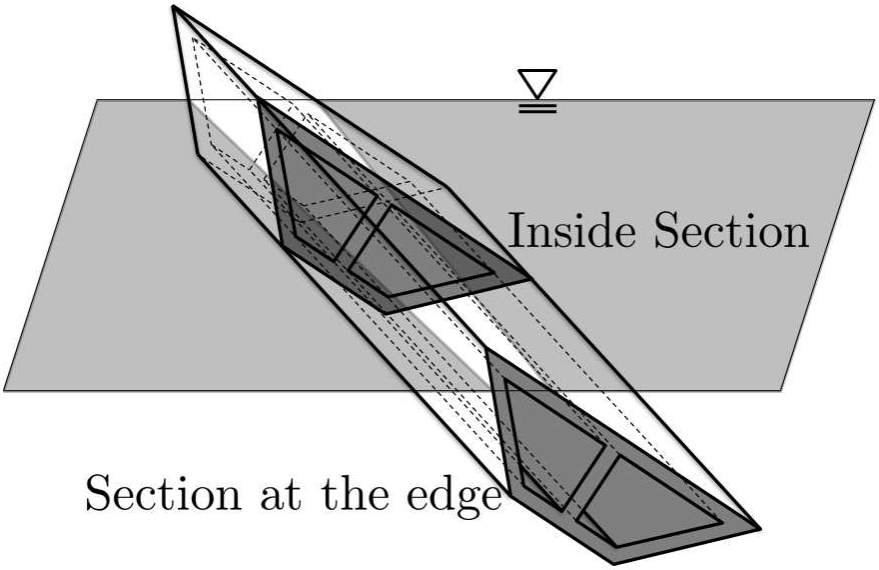

Figure 5.11: Difference between a section situated at the ends of a beam and a section positioned along the axes

The behaviour of these two types of section is different and, consequently, their contribution to the stiffness of the beam will be radically distinct. Now, the theory to compute the forces and moments due to the fluid in the area of a section is presented. A particular explanation will be dedicated to the definition of the forces and moments acting on the section and the way they can be computed.

First, consider figure 5.12, where a generic section under a fluid is depicted. The vector $\boldsymbol{v_G}$ is defined as the position of the centroid in the global reference system, the vector $\boldsymbol{v}$ as a generic position inside the area of the section, the vector $\boldsymbol{v_r}$ as the relative position of this point with respect the center of gravity, the pressure vector $\boldsymbol{P}$ as the pressure in a certain depth h and the height of the fluid with respect the global reference system Z_f.

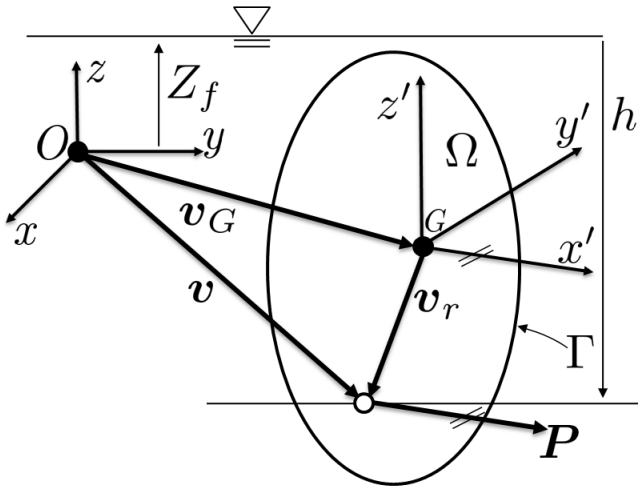

Figure 5.12: Procedure to integrate the hydrostatic pressure inside a section.

The pressure is always orthogonal to the surface where it is applied, so the vector $\boldsymbol{P}$ can be written as

$$\boldsymbol{P} = \gamma_f h \boldsymbol{x'} \tag{5.40}$$

The sign of the vector $\boldsymbol{P}$ is considered only taking into account the configuration and situation of the section inside an element. Consider for example the two sections located on each end of the beam in figure 5.13. As it can be seen, both sections have the same orientation but the hydrostatic pressure acts in opposite directions depending on which section is analysed.

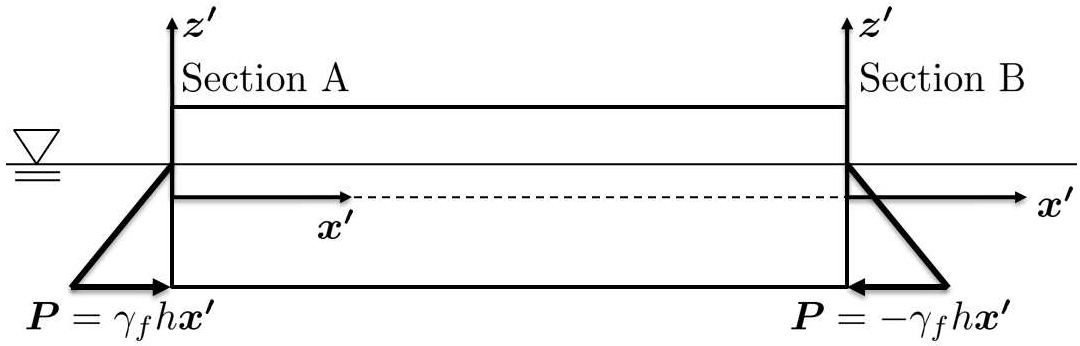

Figure 5.13: Direction of the hydrostatic pressure on every end section of the beam

If section A is analyzed (section positioned at the beginning of the beam) the resulting pressure will have the same sense as the vector $\boldsymbol{x'}$, while on section B the resulting will have the opposite sense. This is a phenomena that depends entirely on the configuration of the beam and not by the section itself. In the nonlinear finite element code developed, this consideration is taken into account by means of the local axes of the beam element and integrating (considering the sign[3] of the pressure vector) the pressure inside the area of the section. For simplicity, only the formulation for the section A will be reported.

Since the pressure is always normal to the section area, the resulting forces and moments will be defined by three elements. First, the resulting force, in the $\boldsymbol{x'}$ axes ($F_{x'}$), is obtained by performing the integration and, second, two moments along the axes $M_{y'}$ and $M_{z'}$ are computed. In figure 5.14, the resulting forces and moment are depicted.

[3] Here, the *sign* should be understood as the sense of the pressure vector. If the *dot* product between the vector $\boldsymbol{P}$ and $\boldsymbol{x'}$ is positive we'll say $\boldsymbol{P}$ has positive sign, otherwise $\boldsymbol{P}$ will be considered negative.

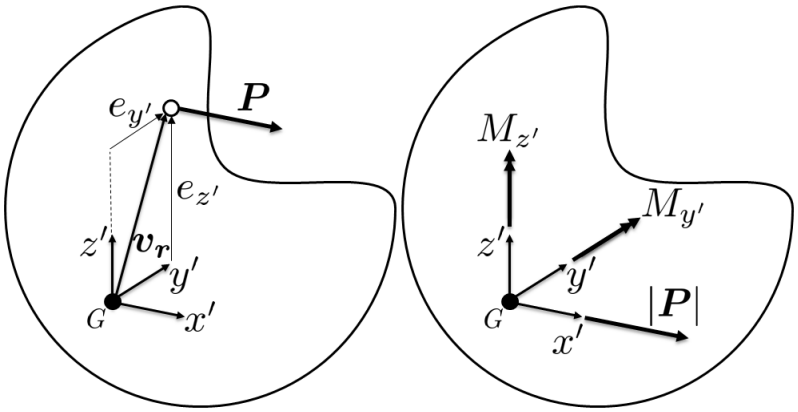

Figure 5.14: Resultants obtained from the integration of the hydrostatic pressure inside the section

Consider $F_{x'}$ as the resulting force in the $\boldsymbol{x'}$ direction and the moments $M_{y'}$ and $M_{z'}$ as the moments coming from the integration on both the $\boldsymbol{y'}$ and $\boldsymbol{z'}$ axes. It is possible to define the moment vector as

$$\boldsymbol{M} = \begin{bmatrix} M_{y'} \\ M_{z'} \end{bmatrix} \tag{5.41}$$

and compute the three resulting forces and moments as

$$F_{x'} = \int_{\Omega} \boldsymbol{P}^T \boldsymbol{x'} H\left(h\right) \, d\Omega \tag{5.42}$$

$$\boldsymbol{M} = \int_{\Omega} \begin{bmatrix} \left(\boldsymbol{v_r} \times \boldsymbol{P}\right)^T \boldsymbol{y'} \\ \left(\boldsymbol{v_r} \times \boldsymbol{P}\right)^T \boldsymbol{z'} \end{bmatrix} H\left(h\right) \, d\Omega \tag{5.43}$$

with

$$\boldsymbol{v_r} = \boldsymbol{v} - \boldsymbol{v_G} = \begin{bmatrix} e_{y'} & e_{z'} \end{bmatrix}^T \tag{5.44}$$

where the *Heaviside* function has been used again and its definition is reported in equation 5.27.

Once the definition of the force and moments resulted from the integration within the area of the section have been presented, the expressions can be modified to deal with section composed by 4-nodes quadrangular elements. Consider figure 5.15, where a discretized section has been depicted. The domain of the section is divided in N_{ea} elements, each one with an individual contribution

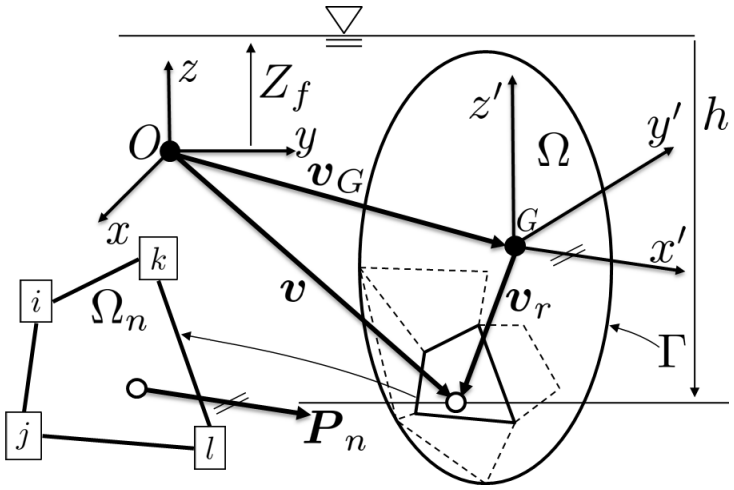

Figure 5.15: Procedure to integrate the hydrostatic pressure inside a discretized section.

$$F_{x'} = \int_{\Omega} \boldsymbol{P}^T \boldsymbol{x'} H\left(h\right)\ d\Omega \simeq \sum_{i=1}^{N_{ea}} \int_{\Omega_i} \boldsymbol{P}^T \boldsymbol{x'} H\left(h\right)\ d\Omega_i \tag{5.45}$$

$$\boldsymbol{M} = \int_{\Omega} \left[\begin{array}{c} \left(\boldsymbol{v_r} \times \boldsymbol{P}\right)^T \boldsymbol{y'} \\ \left(\boldsymbol{v_r} \times \boldsymbol{P}\right)^T \boldsymbol{z'} \end{array} \right] H\left(h\right)\ d\Omega \simeq \sum_{i=1}^{N_{ea}} \int_{\Omega_i} \left[\begin{array}{c} \left(\boldsymbol{v_r} \times \boldsymbol{P}\right)^T \boldsymbol{y'} \\ \left(\boldsymbol{v_r} \times \boldsymbol{P}\right)^T \boldsymbol{z'} \end{array} \right] H\left(h\right)\ d\Omega_i \tag{5.46}$$

The Heaviside function can be removed from both expressions just performing the integral in the elements that are partially or totally under the fluid.

$$F_{x'} = \sum_{i=1}^{N_{ea}} \int_{\Omega_i} \boldsymbol{P}^T \boldsymbol{x'} H\left(h\right)\ d\Omega_i = \sum_{i=1}^{n_{ea}} \int_{\Omega_i} \boldsymbol{P}^T \boldsymbol{x'}\ d\Omega_i \tag{5.47}$$

$$\boldsymbol{M} = \sum_{i=1}^{N_{ea}} \int_{\Omega_i} \left[\begin{array}{c} \left(\boldsymbol{v_r} \times \boldsymbol{P}\right)^T \boldsymbol{y'} \\ \left(\boldsymbol{v_r} \times \boldsymbol{P}\right)^T \boldsymbol{z'} \end{array} \right] H\left(h\right)\ d\Omega_i = \sum_{i=1}^{n_{ea}} \int_{\Omega_i} \left[\begin{array}{c} \left(\boldsymbol{v_r} \times \boldsymbol{P}\right)^T \boldsymbol{y'} \\ \left(\boldsymbol{v_r} \times \boldsymbol{P}\right)^T \boldsymbol{z'} \end{array} \right]\ d\Omega_i \tag{5.48}$$

Considering the elements used to define the area of the section and the linearity of the load with respect the depth, a numerical Gauss integration scheme can be used to compute the value of the previous integrals. Making the change variable it may be obtained

$$F_{x'} = \sum_{i=1}^{n_{ea}} \int_{\Omega_i} \overbrace{\boldsymbol{P}^T \boldsymbol{x'}}^{F_F}\ d\Omega_i = \sum_{i=1}^{n_{ea}} \int_{-1}^{1} \int_{-1}^{1} F_F \left|\boldsymbol{J}\right|\ d\xi\ d\eta \tag{5.49}$$

$$\boldsymbol{M} = \sum_{i=1}^{n_{ea}} \int_{\Omega_i} \underbrace{\left[\begin{array}{c} \left(\boldsymbol{v_r} \times \boldsymbol{P}\right)^T \boldsymbol{y'} \\ \left(\boldsymbol{v_r} \times \boldsymbol{P}\right)^T \boldsymbol{z'} \end{array} \right]}_{\boldsymbol{F_M}}\ d\Omega_i = \sum_{i=1}^{n_{ea}} \int_{-1}^{1} \int_{-1}^{1} \boldsymbol{F_M} \left|\boldsymbol{J}\right|\ d\eta\ d\xi \tag{5.50}$$

Applying the numerical Gauss scheme, the previous integrals can be transformed in an equivalent form using summatories.

$$F_{x'} = \sum_{i=1}^{n_{ea}} \int_{-1}^{1} \int_{-1}^{1} F_F \left|\boldsymbol{J}\right| \; d\xi \; d\eta = \sum_{i=1}^{n_{ea}} \left(\sum_{j=1}^{N_G} \sum_{k=1}^{N_G} F_F \left(\eta_j, \xi_k\right) \left|\boldsymbol{J}\left(\eta_j, \xi_k\right)\right| w_j w_k \right) \tag{5.51}$$

$$\boldsymbol{M} = \sum_{i=1}^{n_{ea}} \int_{-1}^{1} \int_{-1}^{1} \boldsymbol{F_M} \left|\boldsymbol{J}\right| \; d\eta \; d\xi = \sum_{i=1}^{n_{ea}} \left(\sum_{j=1}^{N_G} \sum_{k=1}^{N_G} \boldsymbol{F_M} \left(\eta_j, \xi_k\right) \left|\boldsymbol{J}\left(\eta_j, \xi_k\right)\right| w_j w_k \right) \tag{5.52}$$

Once the forces and moments given by the hydrostatic pressure in a section have been derived, they can be arranged in a more compact way. Consider the vector of forces and moments defined as

$$\boldsymbol{F} = \begin{bmatrix} F_{x'} \\ F_{y'} \\ F_{z'} \end{bmatrix}; \qquad \boldsymbol{M} = \begin{bmatrix} M_{x'} \\ M_{y'} \\ M_{z'} \end{bmatrix} \tag{5.53}$$

The forces $F_{y'}$ and $F_{z'}$ have been obtained from the integration along the boundary, and, on the other hand, the force $F_{x'}$ is the result of the hydrostatic pressure applied in the area of the section. In addition, only the moment $M_{x'}$ is produced by the pressure acting on the boundary and the moments $M_{y'}$ and $M_{z'}$ have been considered as a result from the pressure in the area.

The equations to compute all the six forces and moments listed before have been explained and the numerical techniques used for the integration have been formulated. The next section is devoted to the characterization of the so-called *isolated* and *non isolated* sections, previously mentioned in the introduction of this chapter. The special treatment of the isolated section is due to the fact that they behave in a completely different way from the non isolated sections.

5.3.2 Isolated and non isolated sections

As previously explained, an isolated section is a section that is protected with a waterproof material to block the entrance of the fluid inside the beam. They are always located at the ends of the beam.

The behaviour of these sections is different from the non isolated ones. Consider figure 5.16, where an isolated and non isolated section is depicted.

- Isolated section: The hydrostatic pressure acts on the structural area of the section, the area of the holes and the external boundary of the section.
- Non isolated section: The hydrostatic pressure acts on the structural area of the section, the boundary of the holes and the external boundary of the section.

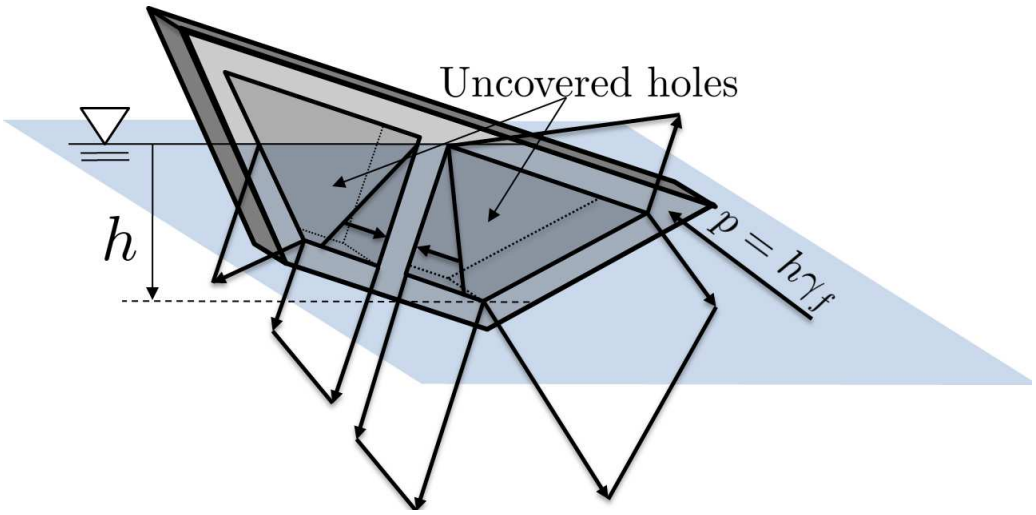

(a) Pressure acting on the boundary of the holes in an uncovered section

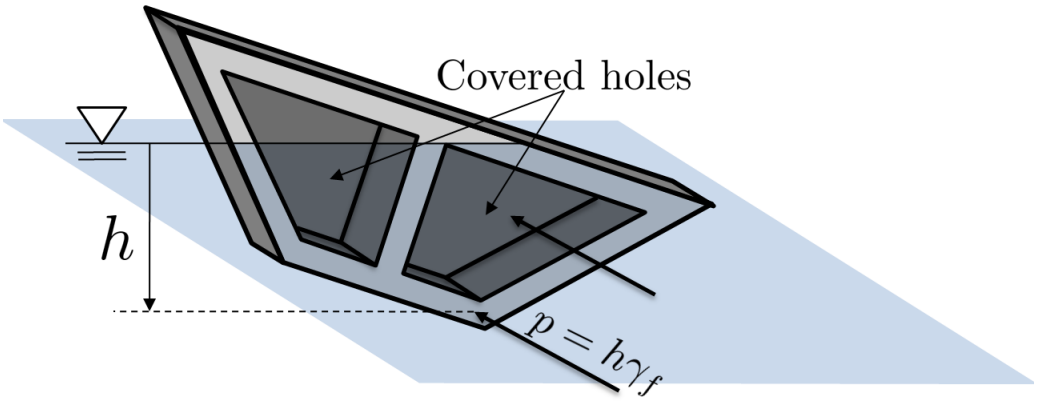

(b) Pressure acting on the area of the holes in a covered section

Figure 5.16: Hydrostatic load acting on a covered and uncovered section

Consider first an isolated section. The pressure will act also on the boundary of each hole and is computed by using equations 5.30 and 5.31.

On the other hand, the integration of the hydrostatic pressure within the area of the holes for the isolated section can be easily taken into account including the contribution of the 4-nodes elements following equations 5.45 and 5.46.

5.4 Analysis of prototipal sections

In this paragraph, some sections are analyzed both considering both the 2D and 3D models.

Figure 5.17 shows the sections analyzed.

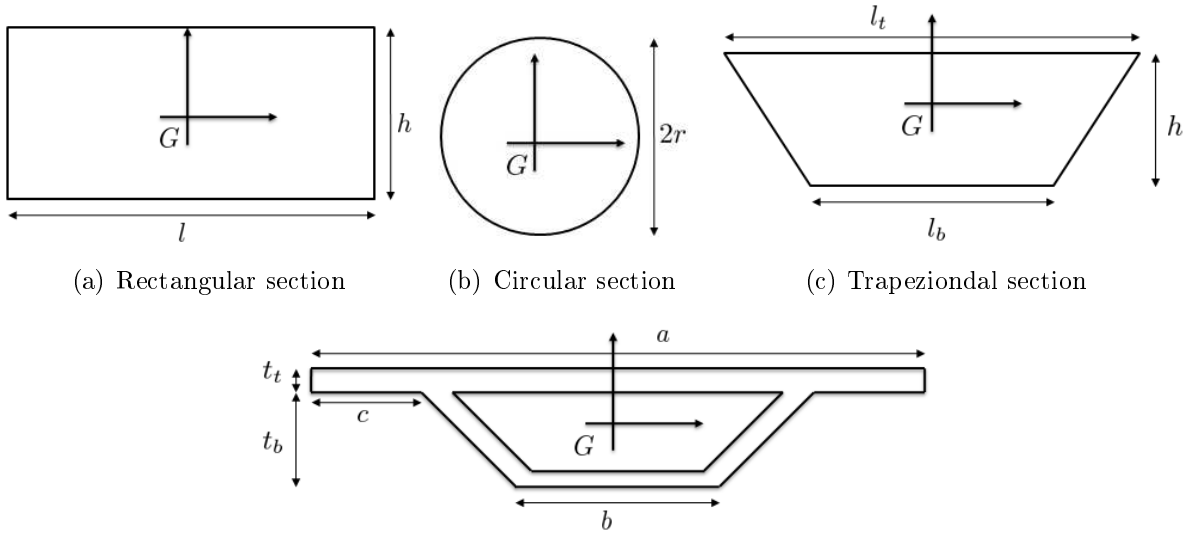

(a) Rectangular section (b) Circular section (c) Trapeziondal section

(d) Box section

Figure 5.17: Sections that will be analyzed

Althought the equations previously described can be used assuming any position and orientation of the section, the constitutive equations will be first derived considering that the sections are contained in a vertical plane and the only degree of freedom is the vertical displacement. This condition will be used to formulate the beam model developed in chapter 6, where a new finite element model will be defined and tested under the hypothesis of small displacements in the 2D space. In this part, four sections will be analyzed: rectangular, trapezoidal, circular and box sections.

Later, the constitutive equations for sections free to move in their six degrees of freedom will be derived and described deeply to understand the physics behind the fluid-section interaction.

Then, the box section will be again analyzed considering it not isolated against the entrance of the fluid and the integration of the hydrostatic pressure will be also performed along the boundary of the holes contained in the section.

5.4.1 2D constitutive equations

5.4.1.1 Rectangular section

The rectangular section is one of the most used sections in the field of floating structures. Usually, the floating breackwaters are built adopting this type of section due to its capacity to float and because its simplicity in the fluid-section interaction.

The constitutive equations of the section are presented and deeply discussed. The explanation will start with the simplified model based on the constitutive equations in

the 2D model.

Consider figure 5.18, where the rectangular section partially under a fluid is depicted. Since the problem develops only in the vertical plane, the main variable is the depth of the section inside the fluid z.

$$F_{x'} = \begin{cases} \dfrac{l\gamma_f}{2} z^2 & z \leq h \\ \dfrac{h\gamma_f l}{2} (2z - h) & z > h \end{cases} \tag{5.54}$$

$$F_{z'} = \begin{cases} l\gamma_f z & z \leq h \\ l\gamma_f h & z > h \end{cases} \tag{5.55}$$

$$M_{y'} = \begin{cases} \dfrac{l\gamma_f}{12} z^2 (3h - 2z) & z \leq h \\ \dfrac{l\gamma_f}{12} h^3 & z > h \end{cases} \tag{5.56}$$

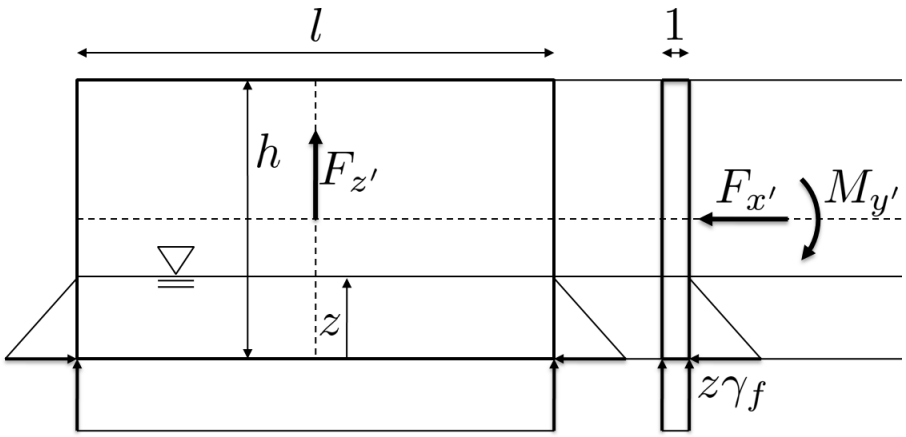

Figure 5.18: Sketch of the rectangular section making contact with an unmoved fluid in the 2D model

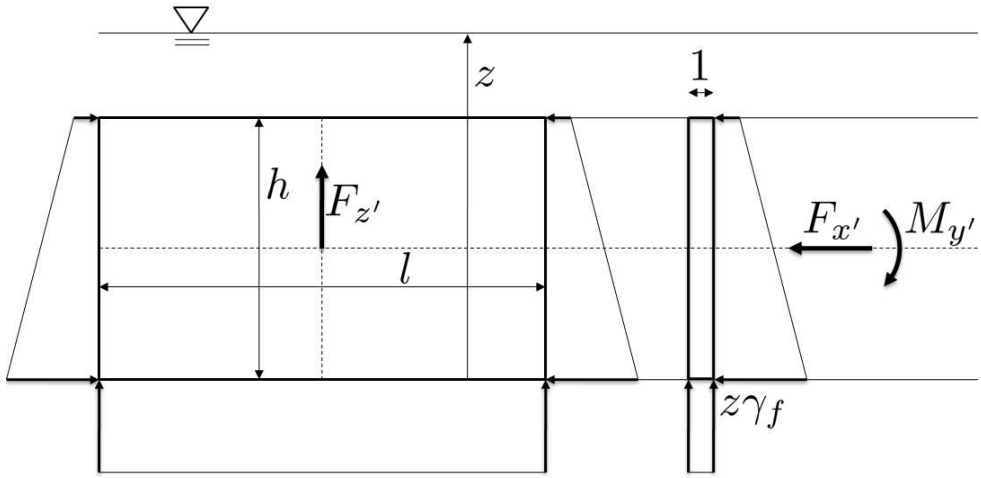

Figure 5.19: Sketch of the rectangular section making contact with an unmoved fluid in the 2D model with z bigger than h

To better analyse the behaviour of this section in contact with the fluid, three variables are defined in order to normalize the previous equations. $\overline{F}$, a force per unit length, $\overline{p}$, a force per unit area and $\overline{M}$ a moment per unit length.

$$\overline{F} = \frac{l\gamma_f h^2}{2} \qquad \overline{p} = lh\gamma_f \qquad \overline{M} = \frac{l\gamma_f h^3}{12} \tag{5.57}$$

Considering these three variables, the loads may be written in an adimensional form.

$$f_{x'} = \frac{F_{x'}}{\overline{F}} = \begin{cases} \eta^2 & \eta \leq 1 \\ (2\eta - 1) & \eta > 1 \end{cases} \tag{5.58}$$

$$f_{z'} = \frac{F_{z'}}{\overline{p}} = \begin{cases} \eta & \eta \leq 1 \\ 1 & \eta > 1 \end{cases} \tag{5.59}$$

$$m_{y'} = \frac{M_{y'}}{\overline{M}} = \begin{cases} \eta^2 (3 - 2\eta) & \eta \leq 1 \\ 1 & \eta > 1 \end{cases} \tag{5.60}$$

with

$$\eta = \frac{z}{h} \tag{5.61}$$

Numerical analyses have been performed and the following figures show the three adimensional variables ($f_{x'}$, $f_{z'}$ and $m_{y'}$) as functions of the adimensional coordinate η.

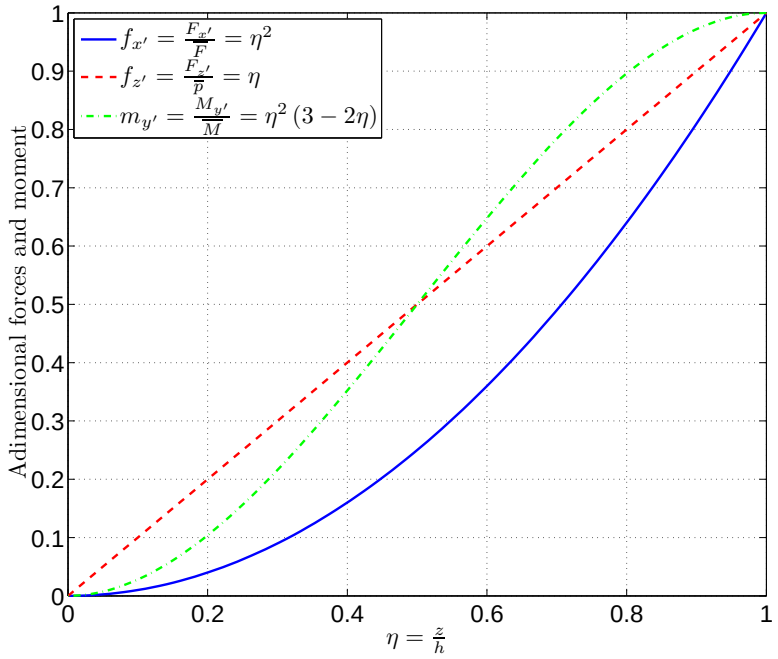

Figure 5.20: Normalized forces and moment acting on the rectangular section partially under a fluid

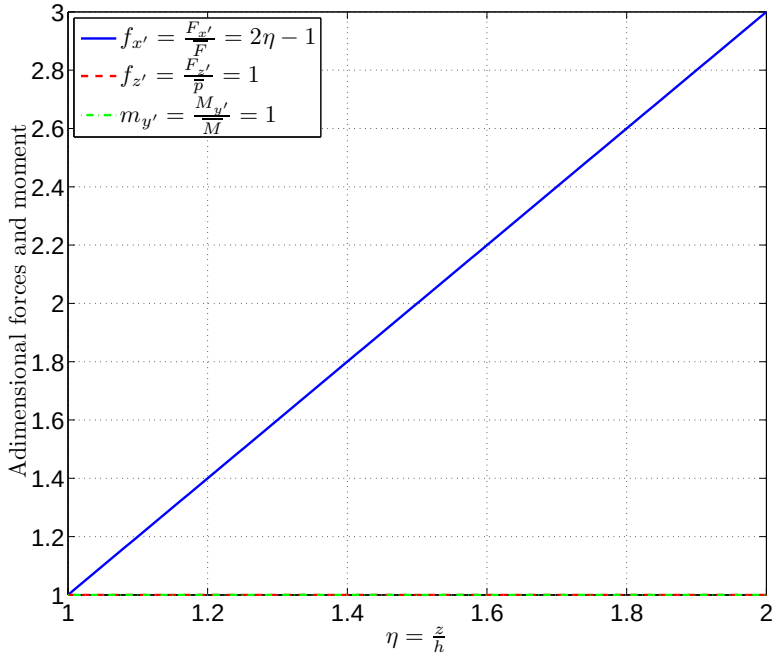

Figure 5.21: Normalized forces and moment acting on the rectangular section totally under a fluid

5.4.1.2 Trapezoidal section

This kind of section has a very good floating capability and may carry out large weight without increasing the twisting moment acting on it's centroid.

The trapezoidal section has been traditionally used in the construction of bridges.

Figure 5.22 shows the sketch of the trapezoidal section. The constitutive equations in the 2D model will be derived.

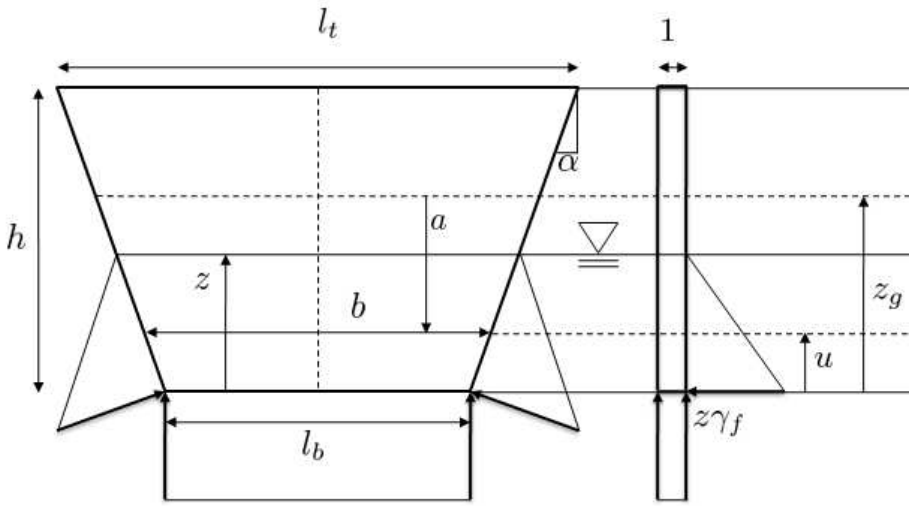

Figure 5.22: Sketch of the trapezoidal section making contact with an unmoved fluid

The expression of the forces $F_{x'}$ and $F_{z'}$ and the moment $M_{y'}$ are first derived. To do so, the integration of the hydrostatic pressure can be performed inside the area under the fluid. First, the load acting on the x axes is computed using the following integral:

$$F_{x'} = \int_0^z \gamma_f \left(z - u\right) b\left(u\right) \; du \tag{5.62}$$

From the sketch depicted in figure 5.22, one can deduce the expression of the thickness b as

$$b\left(u\right) = l_b + \underbrace{\frac{l_t - l_b}{h}}_{\alpha > 0} u \tag{5.63}$$

where it has been considered (as an hypothesis) that $\alpha > 0$.

The previous equation can be substituted in equation 5.62. The integral becomes:

$$F_{x'} = \int_0^z \gamma_f \left(z - u\right) \left(l_b + \alpha u\right) \; du \tag{5.64}$$

Performing the integral, the analytical expression of the force $F_{x'}$ may be obtained:

$$F_{x'} = \frac{\gamma_f z}{6} z^2 \left(3 l_b + \alpha z\right) \tag{5.65}$$

Considering the Archimede's principle, the vertical load produced by the fluid can be computed considering the submerged area multiplied by the self weight of the fluid.

$$F_{z'} = \gamma_f \frac{l_b + b(z)}{2} z = \frac{\gamma_f z}{2} (2l_b + \alpha z) \tag{5.66}$$

Finally, the moment produced by the fluid on the section can be computed with the following integral.

$$M_{y'} = \int_0^z \gamma_f (z - u)\, b(u)\, a(u)\ du \tag{5.67}$$

where the two variables b and a are depicted in figure 5.22. Solving the integral one might obtain the following result.

$$M_{y'} = \frac{\gamma_f z^2}{12} \left(6 l_b z_g + 2z (\alpha z_g - l_b) + 3\alpha z^2\right) \tag{5.68}$$

with z_g the position of the centroid.

$$z_g = h \frac{4l_t - l_b}{6l_t} \tag{5.69}$$

Once the constitutive equations have been derived, it is possible to normalize them considering the three following variables:

$$\overline{F} = \frac{\gamma_f h^2}{6} (3l_b + \alpha h)\,;\ \overline{p} = \frac{\gamma_f h}{2} (2l_b + \alpha h)\,;\ \overline{M} = \frac{\gamma_f h^2}{12} \left(6 l_b z_g + 2h (\alpha z_g - l_b) + 3\alpha h^2\right) \tag{5.70}$$

$$\beta = \frac{l_b}{h} \qquad \eta = \frac{z}{h} \tag{5.71}$$

Substituting the five variables previously defined in the constitutive equations, the normalized constitutive equations of a trapezoidal section can be obtained.

$$f_{x'} = \frac{F_{x'}}{\overline{F}} = \eta^2 \frac{3\beta + \alpha\eta}{3\beta + \alpha} \tag{5.72}$$

$$f_{z'} = \frac{F_{z'}}{\overline{p}} = \eta \frac{2\beta + \alpha\eta}{2\beta + \alpha} \tag{5.73}$$

$$z_g = \frac{3\beta + 4\alpha}{6(\beta + \alpha)} h \tag{5.74}$$

$$m_{y'} = \frac{M_{y'}}{\overline{M}} = \eta^2 \frac{A + B\eta + C\eta^2}{A + B + C} \tag{5.75}$$

with

$$A = \beta (3\beta + 4\alpha) \qquad B = -\alpha\beta + \frac{4}{3}\alpha^2 - 2\beta^2 \qquad C = 3\alpha (\alpha + \beta)$$

Numerical simulations have been carried out and the results are presented in the following. Special attention has been given to the parameters α and β. First, three plots

show the influence of the variable α on the forces $f_{x'}$, $f_{z'}$ and moment $m_{y'}$. Later, the same will be done with other three plots considering the variable α fixed and varying β.

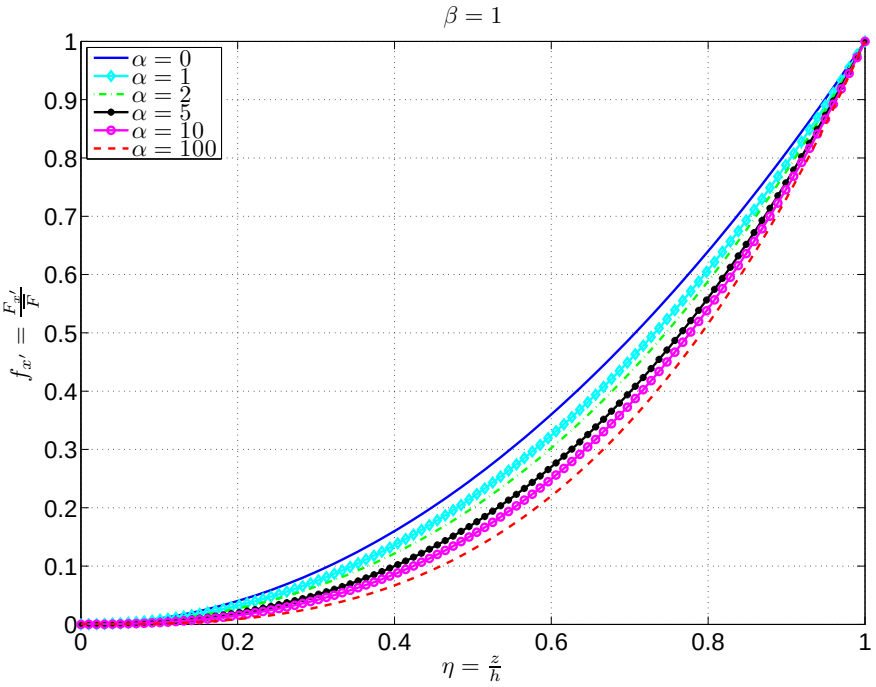

Figure 5.23: $f_{x'}$ as a function of α on trapezoidal section partially under a fluid

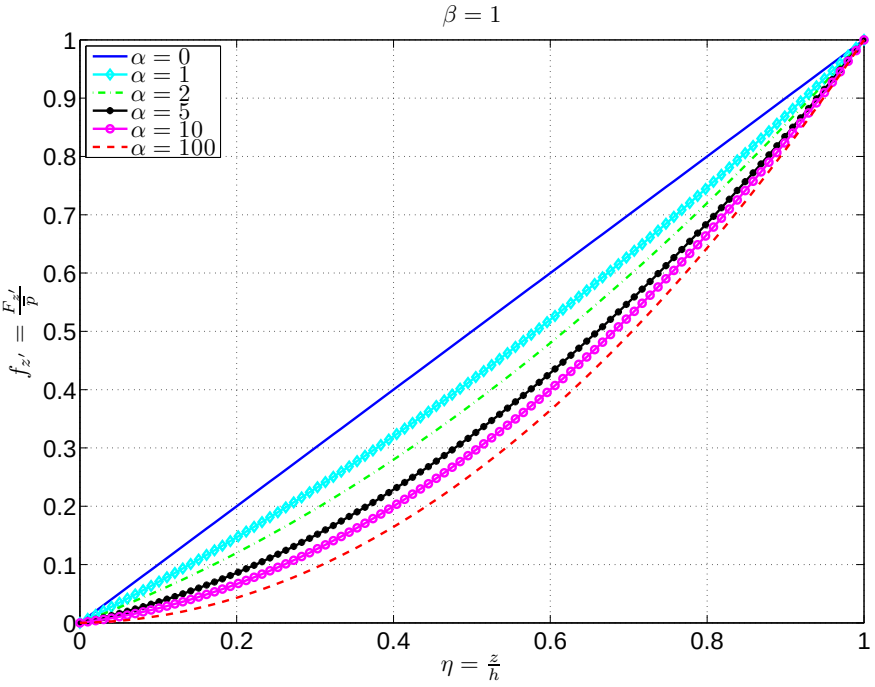

Figure 5.24: $f_{z'}$ as a function of α on trapezoidal section partially under a fluid

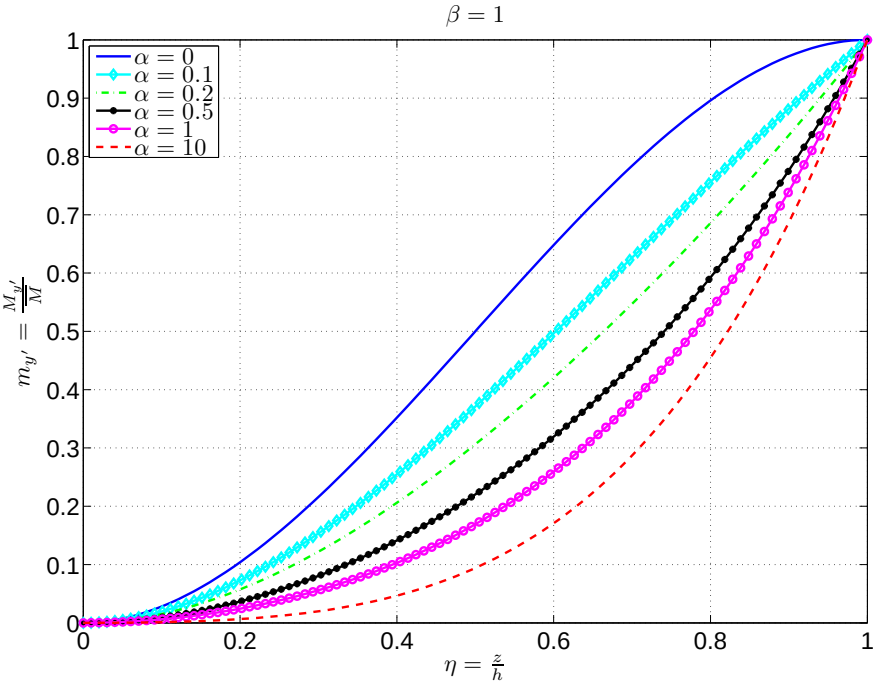

Figure 5.25: $m_{y'}$ as a function of α on trapezoidal section partially under a fluid

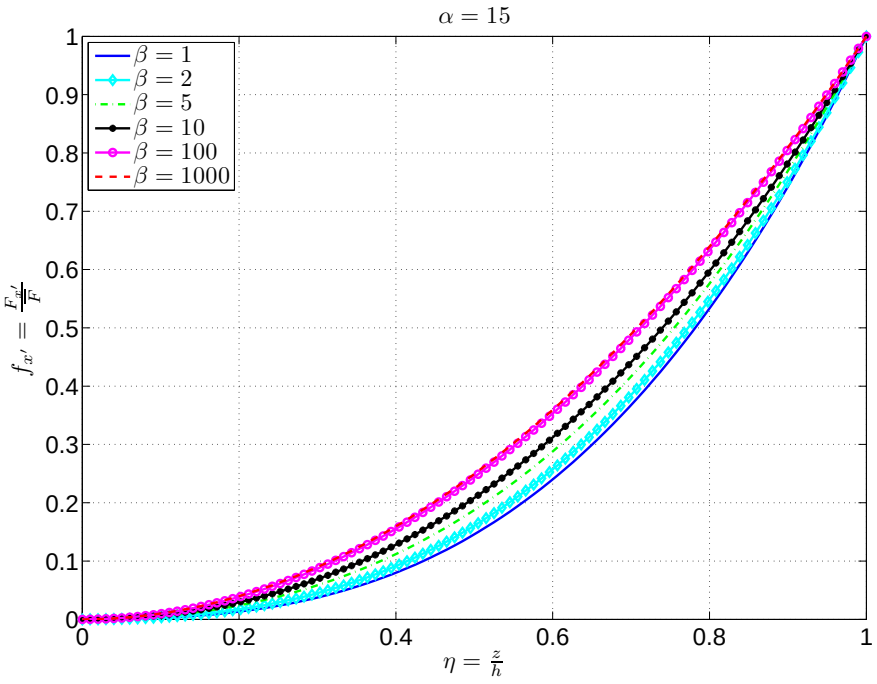

Figure 5.26: $f_{x'}$ as a function of β on trapezoidal section partially under a fluid

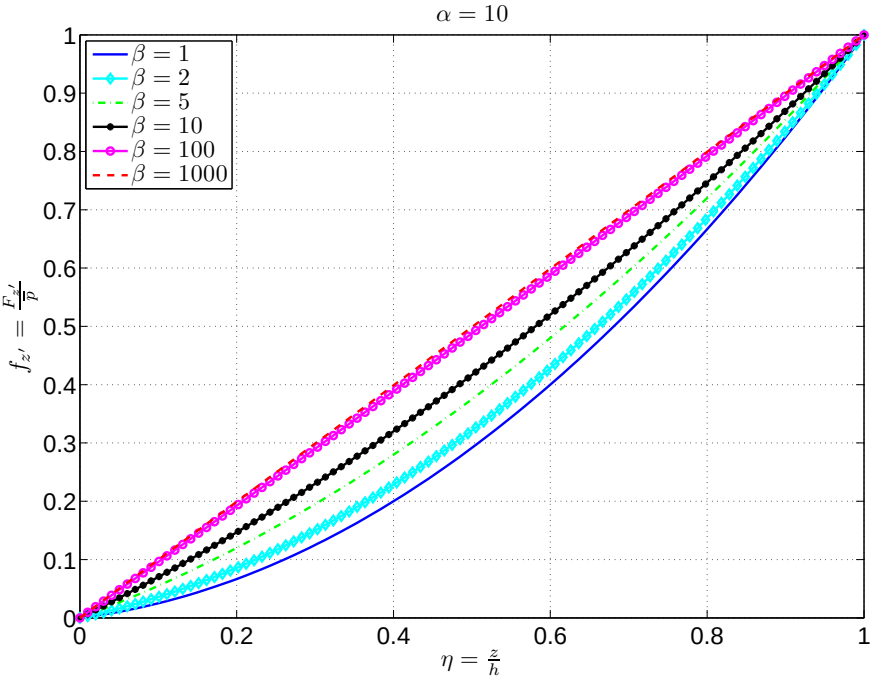

Figure 5.27: $f_{z'}$ as a function of β on trapezoidal section partially under a fluid

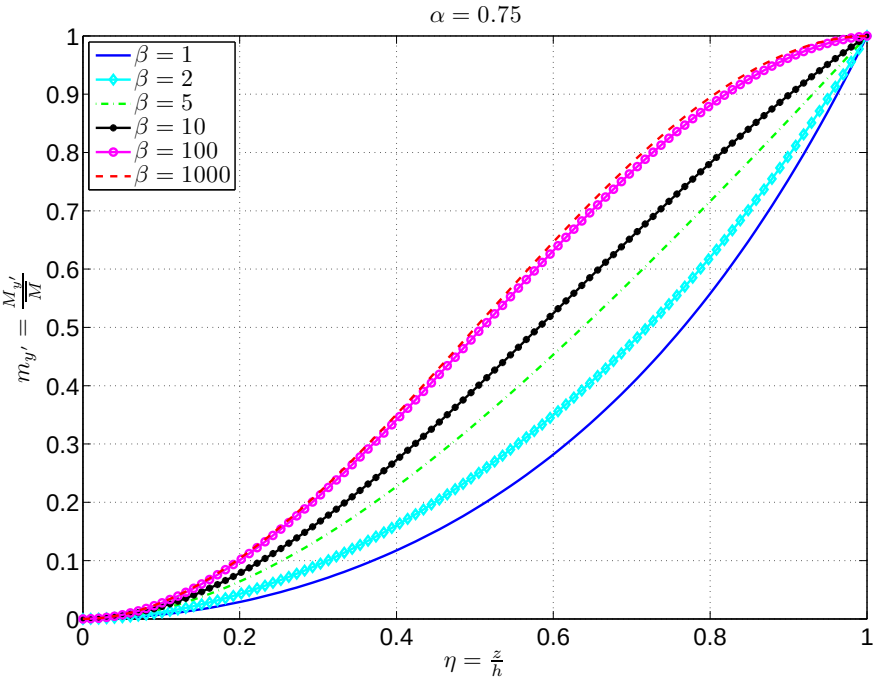

Figure 5.28: $m_{y'}$ as a function of β on trapezoidal section partially under a fluid

It must be noticed that the equations previously derived are only valid when the section is partially under the fluid. It can be also noticed that the vertical load and the moment will not increase after the fluid completely covers the section. The only force

which increases is $F_{x'}$. To analyse the behaviour of the section completely under water the following equation has been considered.

$$F_{x'} = F_{x'}\left(z = h\right) + \gamma_f \left(z - h\right) h \frac{l_t + l_b}{2} \tag{5.76}$$

The previous equation can be normalized and it's final expresion is

$$f_{x'}\left(\eta > 1\right) = f_{x'}\left(\eta = 1\right) + 3\left(\eta - 1\right) \frac{2\beta + \alpha}{3\beta + \alpha} \tag{5.77}$$

5.4.1.3 Circular section

A circular section is analyzed. Usually, anchorage systems are built constructing heavy weighted concrete supports on the seabed and connecting cables to them. This cables usually are made by steel elements with circular sections.

The constitutive equations of this section are particularly important since circular cables are used in this work to anchore the floating structures with the seabed.

Consider the figure 5.29, where a circular section partially under a fluid is depicted. The problem can be modeled considering just the vertical displacement as the main variable.

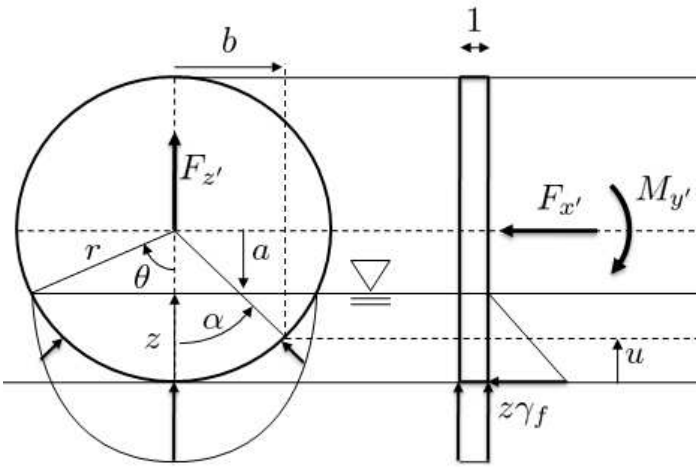

Figure 5.29: Sketch of the circular section making contact with an unmoved fluid

To analytically derive the constitutive equations, the auxiliary variable θ may be used. Considering the definition of $F_{x'}$, the following equation can be written.

$$F_{x'} = 2 \int_0^z \gamma_f \left(z - u\right) b \; du \tag{5.78}$$

Considering the equalities

$$z = r\left(1 - \cos\theta\right) \qquad u = r\left(1 - \cos\alpha\right) \qquad b = r \sin\alpha \tag{5.79}$$

the previous integral might be written as follows.

$$F_{x'}(\theta) = 2\int_0^{\theta} \sin^2\alpha\,(\cos\alpha - \cos\theta)\;\, d\alpha \tag{5.80}$$

The final expression of the normal pressure can be obtained solving the previous integral.

$$F_{x'} = \frac{\gamma_f r^3}{6}\left(4\sin^3\theta - 3\cos\theta\,[2\theta - \sin 2\theta]\right) \tag{5.81}$$

For the vertical load a similar expression can be derived considering the area of the circle under the fluid. By Archimede's principle, this area is realated to the vertical load applied on the section.

$$F_{z'} = 2\int_0^{z} \gamma_f b(u)\;\, du \tag{5.82}$$

Considering equations 5.79, the integral can be solved in terms of the variable θ.

$$F_{z'} = \frac{\gamma_f r^2}{2}(2\theta - \sin 2\theta) \tag{5.83}$$

Finally, the moment in the y axes can be computed considering the integral in equation 5.84.

$$M_{y'} = \int_0^{z} \gamma_f\,(z-u)\,b(u)\,a(u)\;\, du \tag{5.84}$$

The integral can be solved using equations 5.79 and its expression is

$$M_{y'} = \frac{\gamma_f r^4}{48}\left(3\,[4\theta - \sin 4\theta] - 32\cos\theta\sin^3\theta\right) \tag{5.85}$$

Adopting the same procedure used for the rectangular section, the equations can be normalized considering the three variables listed in equation 5.86.

$$\overline{F} = \pi\gamma_f r^3 \qquad \overline{p} = \pi\gamma_f r^2 \qquad \overline{M} = \frac{\gamma_f r^4}{4}\pi \tag{5.86}$$

Normalizing equations 5.81, 5.83 and 5.85 it might be obtained

$$f_{x'} = \frac{F_{x'}}{\overline{F}} = \frac{1}{6\pi}\left(4\sin^3\theta - 3\cos\theta\,[2\theta - \sin 2\theta]\right) \tag{5.87}$$

$$f_{z'} = \frac{F_{z'}}{\overline{p}} = \frac{1}{2\pi}(2\theta - \sin 2\theta) \tag{5.88}$$

$$m_{y'} = \frac{M_{y'}}{\overline{M}} = \frac{1}{12\pi}\left(3\,[4\theta - \sin 4\theta] - 32\cos\theta\sin^3\theta\right) \tag{5.89}$$

These three equations are the constitutive equations of the circular section in contact with a fluid but they can also be expressed using the variable z. It can be seen from figure 5.29 that the variable z will give a more intuitive description of the constitutive equations althoguht the expressions are much more complex.

Considering the adimensional variable $\eta = \dfrac{z}{2r}$ and the following trigonometric identities

$$\cos\theta(z) = 1 - \frac{z}{r} = 1 - 2\eta \tag{5.90}$$

$$\sin\theta(z) = \sqrt{\frac{z}{r}\left(2 - \frac{z}{r}\right)} = 2\sqrt{\eta(1-\eta)} \tag{5.91}$$

$$\sin 2\theta = 2\sin\theta\cos\theta \qquad \cos 2\theta = \cos^2\theta - \sin^2\theta \tag{5.92}$$

The constitutive equations in terms of the adimensional variable η may be written as follows.

$$f_{x'} = \frac{1}{6\pi}\left(\begin{array}{c} 32\left[\eta(1-\eta)\right]^{3/2} - \\ 3(1-2\eta)\left[2\arccos(1-2\eta) - 4\sqrt{\eta(1-\eta)}(1-2\eta)\right] \end{array}\right) \tag{5.93}$$

$$f_{z'} = \frac{1}{\pi}\left(\arccos(1-2\eta) - 2\sqrt{\eta(1-\eta)}(1-2\eta)\right) \tag{5.94}$$

$$m_{y'} = \frac{1}{12\pi}\left(\begin{array}{c} 3\left[4\arccos(1-2\eta) - 8\sqrt{\eta(1-\eta)}(1-2\eta)\left([1-2\eta]^2 - 4\eta[1-\eta]\right)\right] \\ -256(1-2\eta)\left[\eta(1-\eta)\right]^{3/2} \end{array}\right) \tag{5.95}$$

From a mathematical point of view, the constitutive equations can be written in a more compact way considering the angular variable θ but, on the other hand, are not suitable to be used in the program because the constitutive equations must be written in terms of the generalized displacements of the section (the three displacemnts of the centroid plus the three Euler rotations). The equations 5.93, 5.94 and 5.95 provide the analytical expressions to completely describe the behaviour of the section in contact with a fluid.

Some numerical tests have been performed and the plots of the three forces and moment are reported in figure 5.30 and 5.31

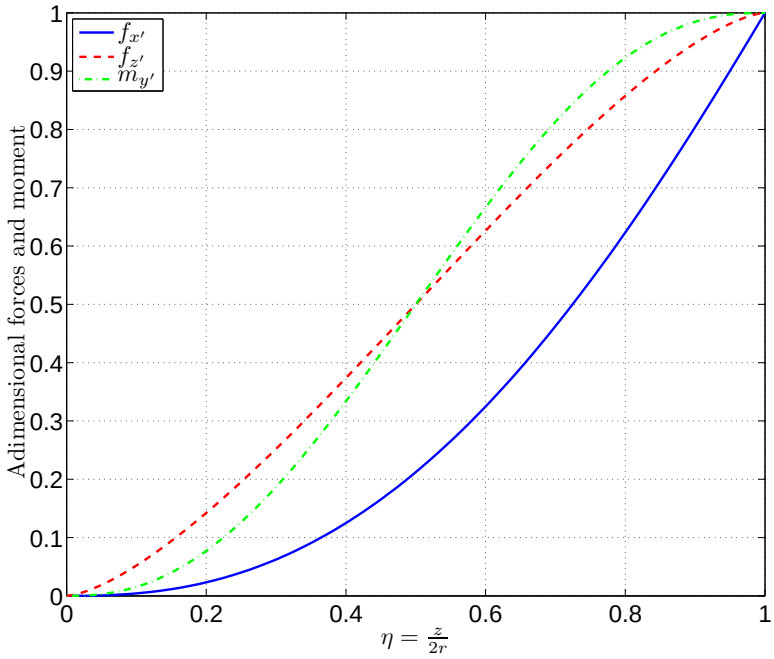

Figure 5.30: Normalized forces and moment acting on the circular section partially under a fluid

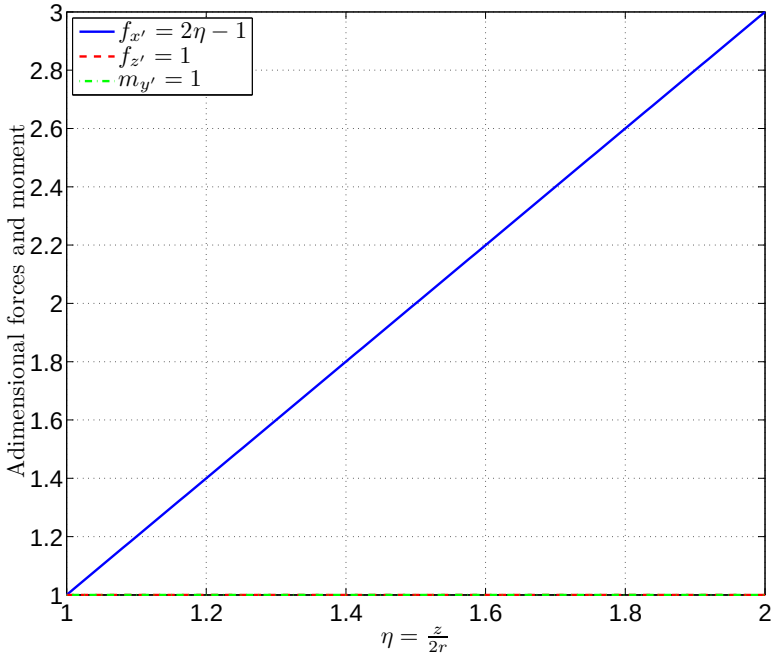

Figure 5.31: Normalized forces and moment acting on the circular section totally under a fluid

5.4.1.4 Box section

The analysis of a box section is performed. Following the same approach presented up to now, the 2D model is first introduced and the 3D constitutive equations will be presented later.

From the analysis performed earlier, one may consider that the constitutive equations in the 2D space can always be expressed in terms of some variables that govern the problem. This is not completely true. Sometimes, due to the shape of the section, the problem could not be characterized with the integrals used to describe the forces and moments. In those cases, numerical techniques are required and the meshes described in section 5.1 can be very useful. In addition, the generality of the program developed can not depend on the viability of describing analytically the constitutive equations, so the numerical expressions (Gauss integration for each element on the mesh) described in section 5.3 will be implemented to deal with a generic shape section with or witout holes.

The 2D constitutive equations for a box section will be numerically derived. As considered before, the only variable in the problem is the vertical displacement. Consider figure 5.32, where the box section used is depicted. The measures chosen to characterize the geometry of the section are (all units in meters)

$$b = 10 \qquad c = 5 \qquad a = 30 \qquad t_t = 2 \qquad t_b = 5 \tag{5.96}$$

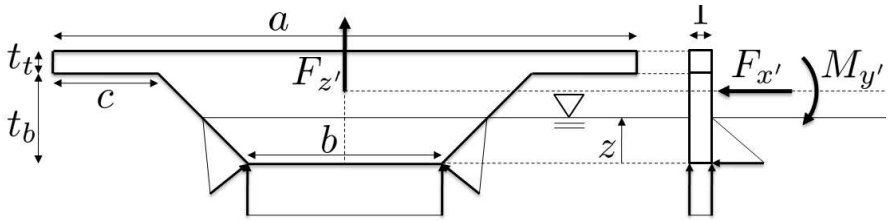

Figure 5.32: Sketch of the box section used in the 3D analysis

Performing the numerical analysis, the following figures have been obtained. It might be noticed that the figures have been normalized to better understand the interaction between the fluid and the section. The forces and moment used to normalize are the maximum force per unit length ($\overline{F}$), force per unit area ($\overline{p}$) and moment per unit length ($\overline{M}$) that $F_{x'}$, $F_{z'}$ and $M_{y'}$ respectively reached.

$$\overline{F} = 3.7782e+03 \left[\frac{kN}{m}\right] \qquad \overline{p} = 1.3500e+03 \left[\frac{kN}{m^2}\right] \qquad \overline{M} = -5.2212e+03 \left[\frac{kNm}{m}\right]$$

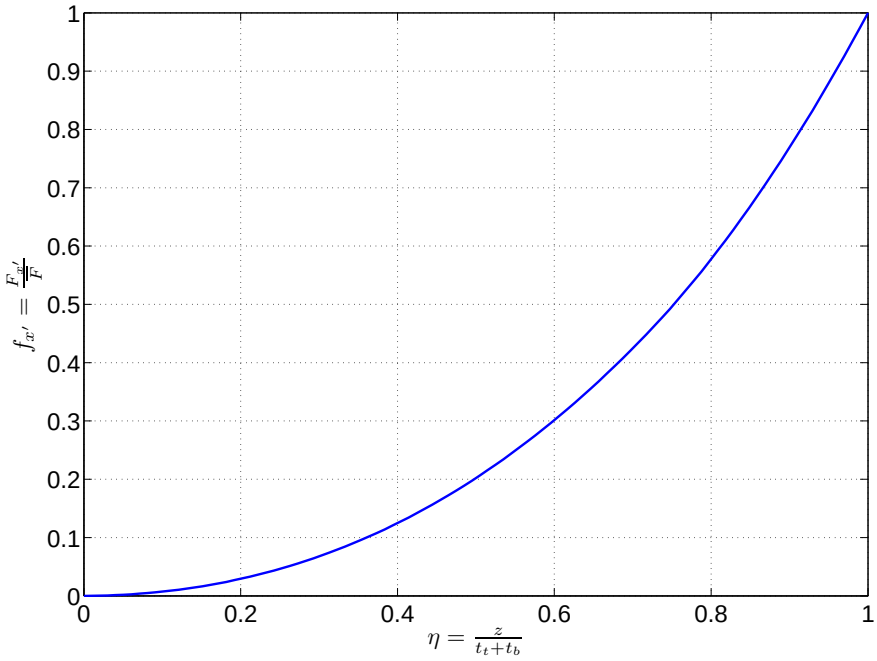

Figure 5.33: $f_{x'}$ force applied in the box section as a function of the vertical displacement

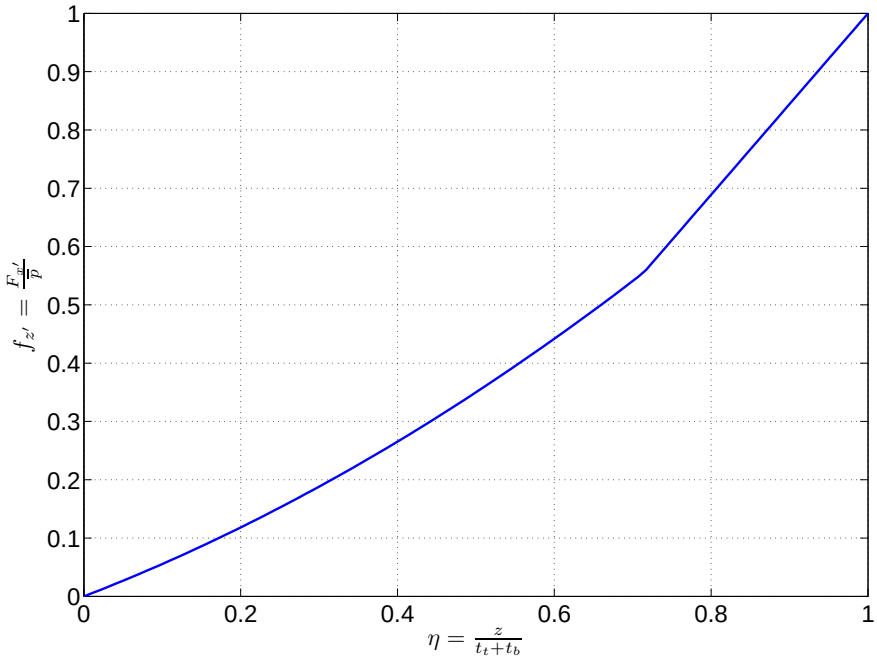

Figure 5.34: $f_{z'}$ force applied in the box section as a function of the vertical displacement

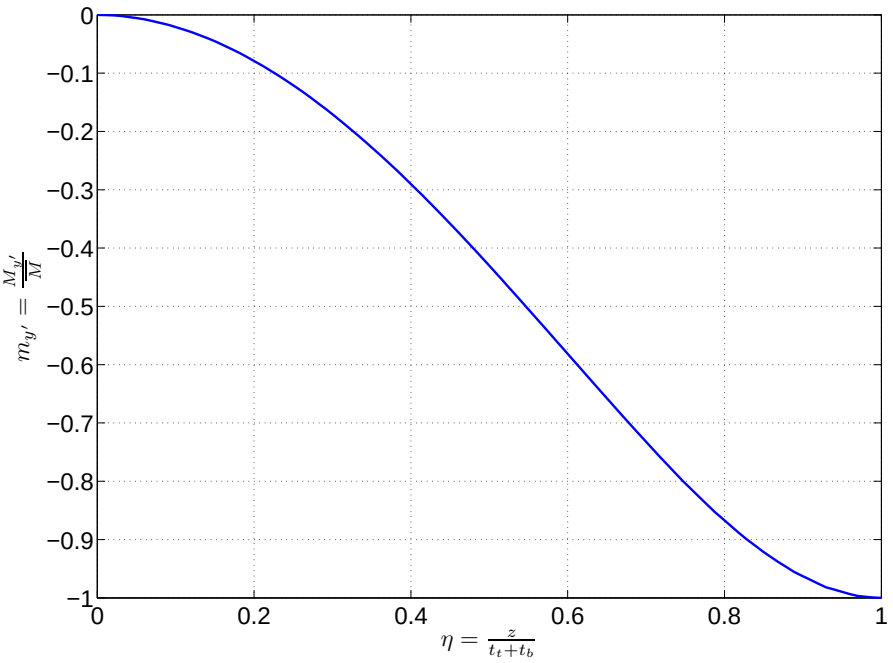

Figure 5.35: $m_{y'}$ moment applied in the box section as a function of the vertical displacement

Consider now the same section but with a hole in the middle as depicted in figure 5.36. The constitutive equations will change their expression to take into account the contribution of the hydrostatic pressure in the boundary of the hole and $F_{x'}$ will decrease due to the fact that the area of the hole will not contribute to the normal pressure.

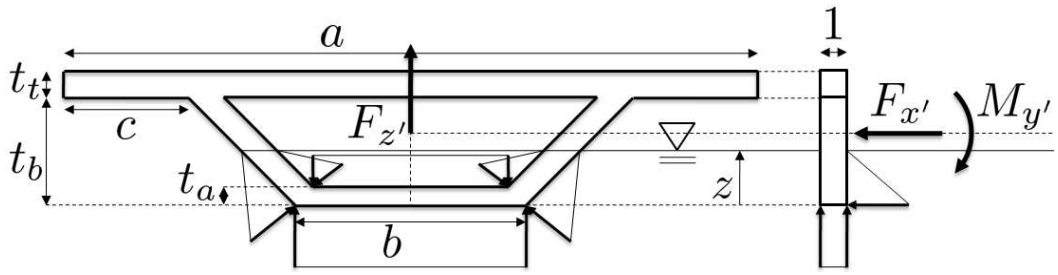

Figure 5.36: Sketch of the box section with a hole inside

In this case, the constitutive equations can also be obtained using the program developed. Considering the geometry previously described, a reduction in the normal pressure and the vertical force is expected. The following figures show the relation between the forces and moment and the vertical displacement (non isolated section) and are compared to the previous ones (isolated section). One can observe the reduction in the three forces and moments due to the fact that now the hydrostatic pressure is also integrated in the boundary of the hole and the area of the section has been reduced.

Figure 5.37 shows the normal pressure acting on the section reduces its value since the section has less area. In addition, figure 5.38 shows the reduction of the $f_{z'}$ because the

pressure in the boundary of the hole has a negative effect in the total Archimede's force. Finally, figure 5.39 shows also the reduction of the moment due to the same reason. Here, the reduction of the area in a zone under the centroid produces a reduction[(4)].

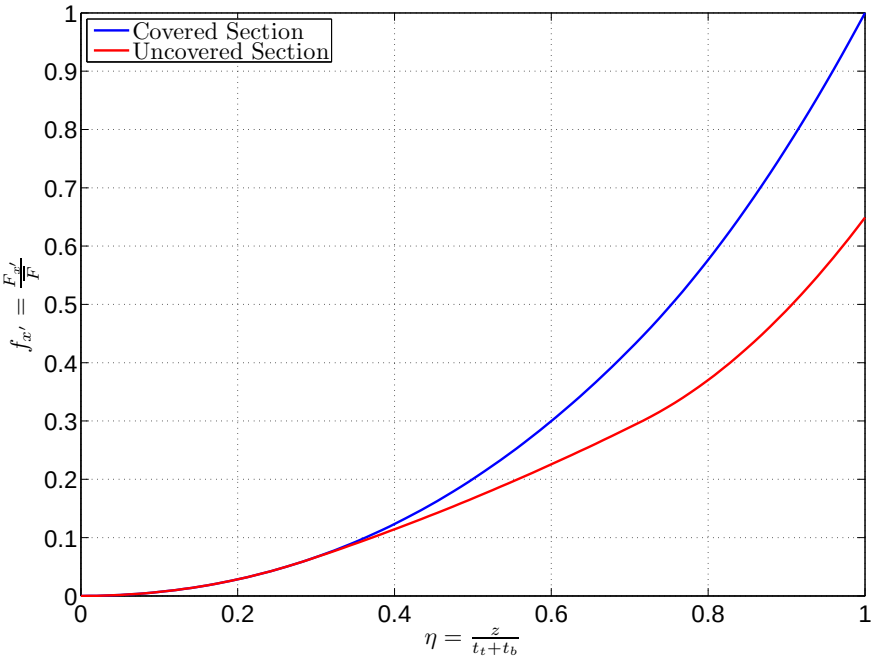

Figure 5.37: $f_{x'}$ force applied in the box section considering the section covered and uncovered

[(4)] Althought the moment is negative, a reduction is understood in an absolute value sense. We measure the reduction of the maximum moment in the section (negative or positive).

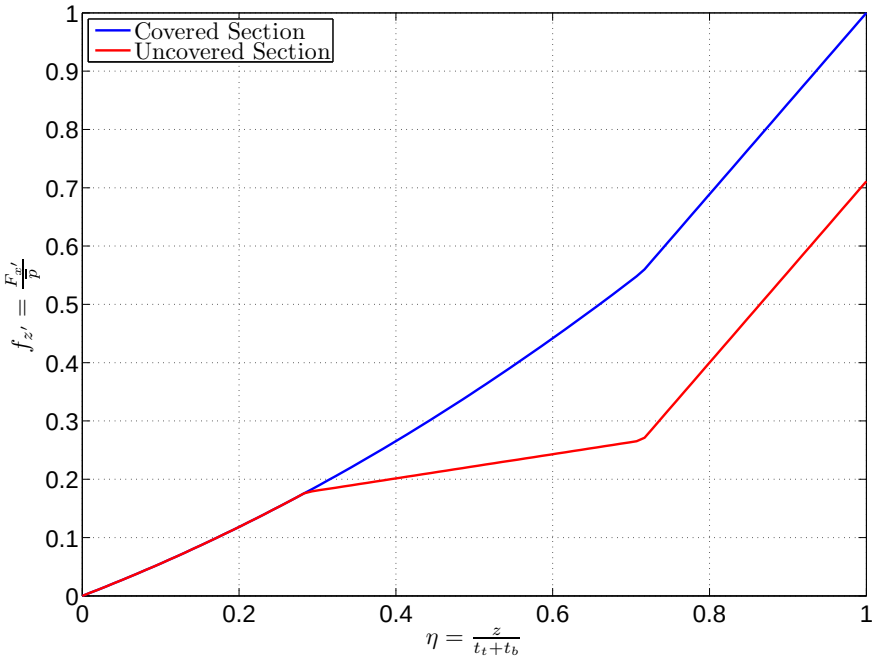

Figure 5.38: $f_{z'}$ force applied in the box section considering the section covered and uncovered

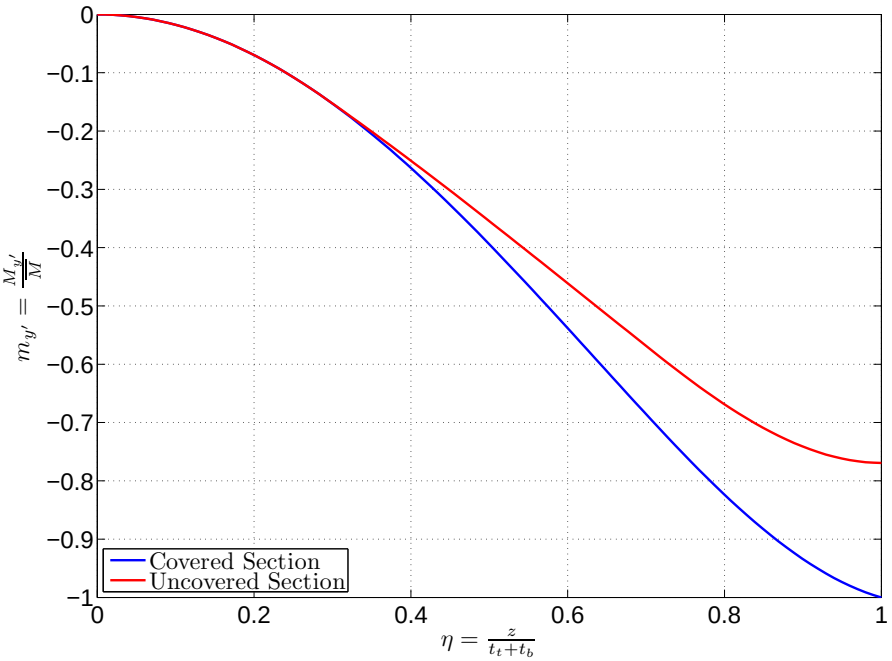

Figure 5.39: $m_{y'}$ moment applied in the box section considering the section covered and uncovered

The results obtained emphasize the influence that isolating a section has in the con-

stitutive equations. In addition, it must be said that this influence can also affect the 3D behaviour of the section in contact with a fluid. In the following, the analysis will be performed considering an isolated section.

5.4.2 3D CONSTITUTIVE EQUATIONS

To obtain the constitutive equations in the 3D model, one must be able to compute the six forces and moments acting on the section considering just the position of the centroid and the orientation of the section itself (defined by the local reference system of the section).

The program developed allows to analyse the behaviour of the section in contact with a fluid in any position and orientation. Due to the great variability that the shape of the section could have, the generic position and orientation of the section and the holes inside it, the analytical expressions of the constitutive equations in the 3D model can not be obtained. Therefore, the numerical algorithm already developed is required to perform the analysis.

Althought the numerical analysis is able to completely define the six forces and moments acting on the section under any configuration, only the main results will be shown. The purpose of this last part is to study the relative importance of each one of the six degrees of freedom.

Consider the figure 5.40, where the initial configuration of the section is depicted. The section is contained in a vertical plane defined by the axes y' and z' and the gravity vector goes in the opposite sense with respect to the z' axes. The analysis will be performed considering the following displacements:

- Δw: Increment of displacement in the z'.
- $\Delta\varphi_x$: Increment of rotation in the x'.
- $\Delta\varphi_y$: Increment of rotation in the y'.

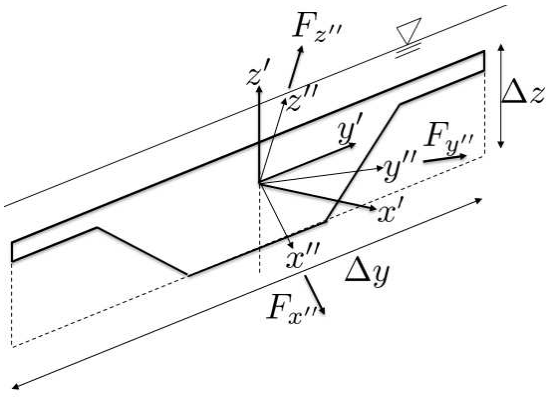

Figure 5.40: Initial configuration of the box section in the 3D analysis

From figure 5.40, one may realize that the increment of displacements in the x' and y' axes does not modify any of the six forces and moments that act on the section. Indeed, the fact that for any displacement in both x' and y' axes the section remains at the same height and does not change its orientation implies that the forces and moments will remain constant during the movement.

It is important to notice that the results will be expressed considering the reference system that moves or rotates with the section for each one of the four degrees of freedom that are being analyzed. So, if figure 5.40 is considered, the forces and moments will be expressed in the reference system depicted as $\{x'', y'', z''\}$.

To present the results of this analysis, the following variables have been chosen as the ones that will normalize the equations.

$$\overline{F} = \gamma_f A_s l_c \qquad \overline{p} = \gamma_f A_s \qquad \overline{M} = \gamma_f A_s l_c^2 \tag{5.97}$$

with l_c and A_s the characteristic length and structural area of the section.

$$l_c = \sqrt{\Delta y^2 + \Delta z^2} \tag{5.98}$$

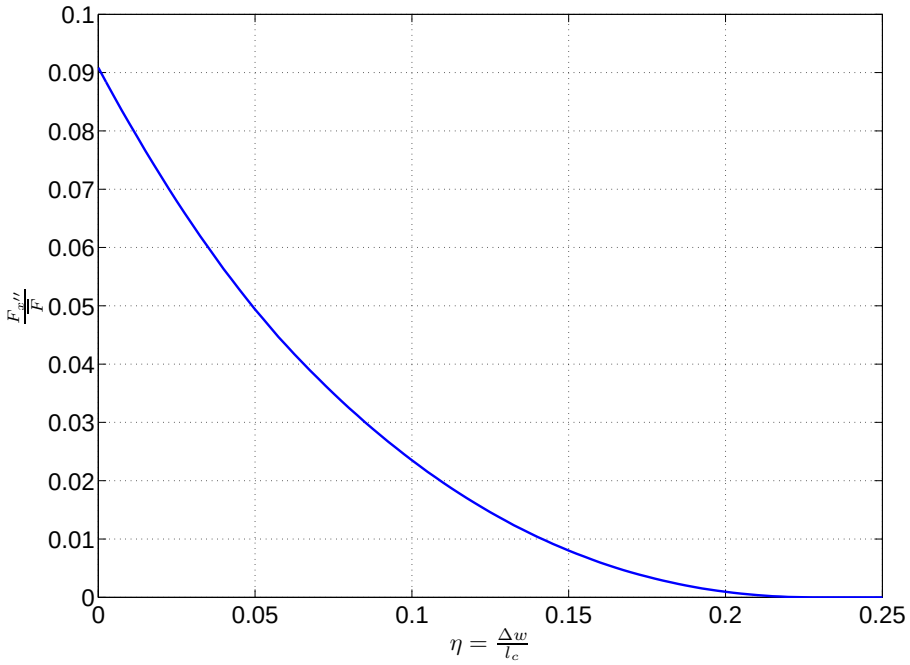

Figure 5.41: Force $f_{x''}$ as a function of the displacement w

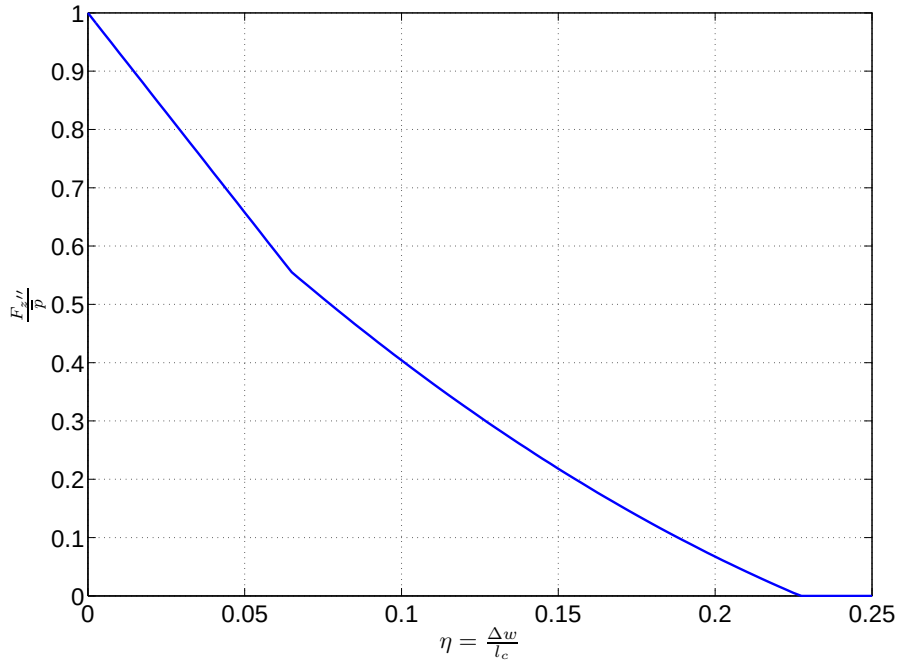

Figure 5.42: Force $f_{z''}$ as a function of the displacement w

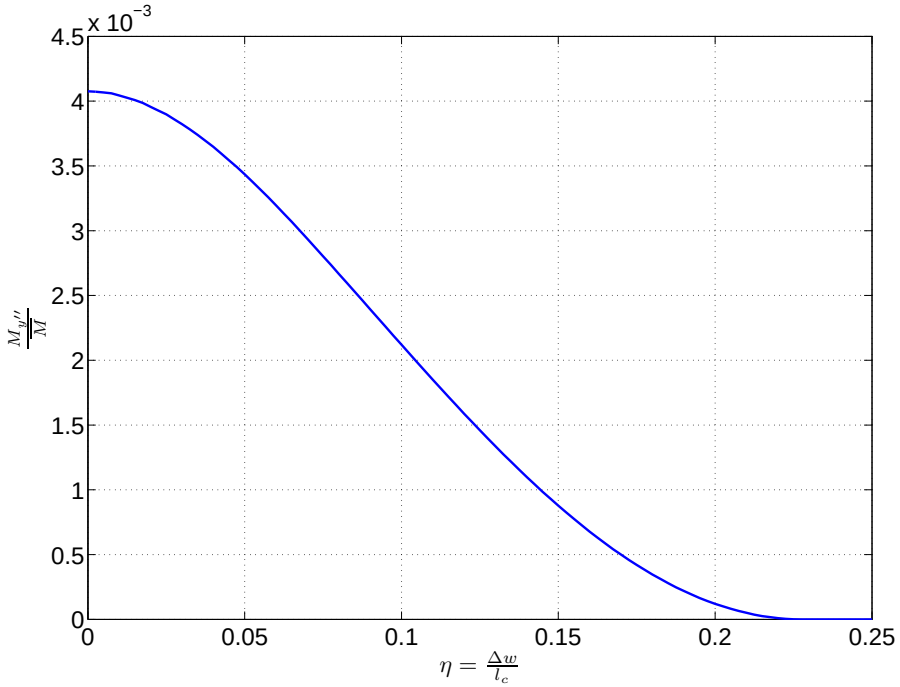

Figure 5.43: Force $m_{y''}$ as a function of the displacement w

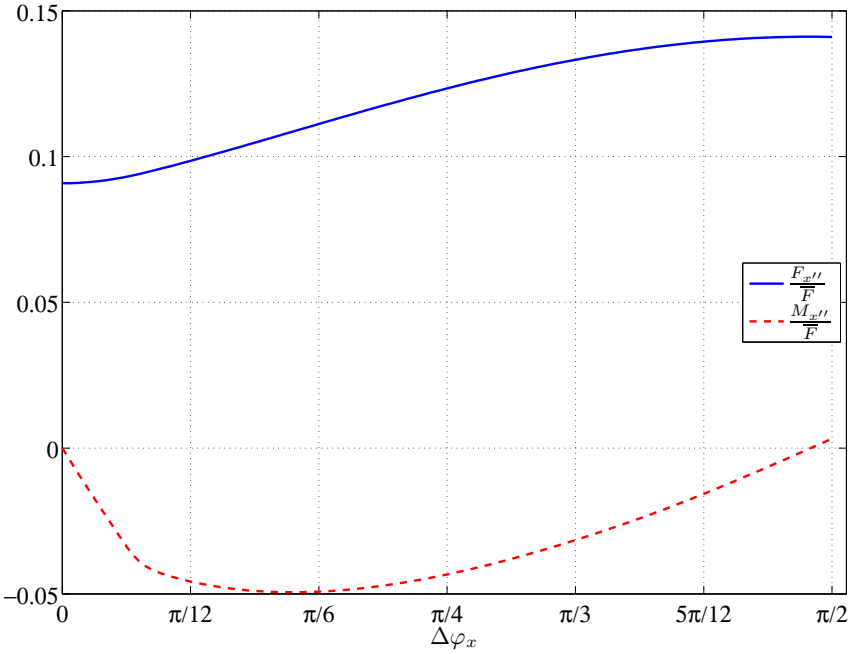

Figure 5.44: Force $f_{x''}$ and moment $m_{x''}$ as a function of the displacement φ_x

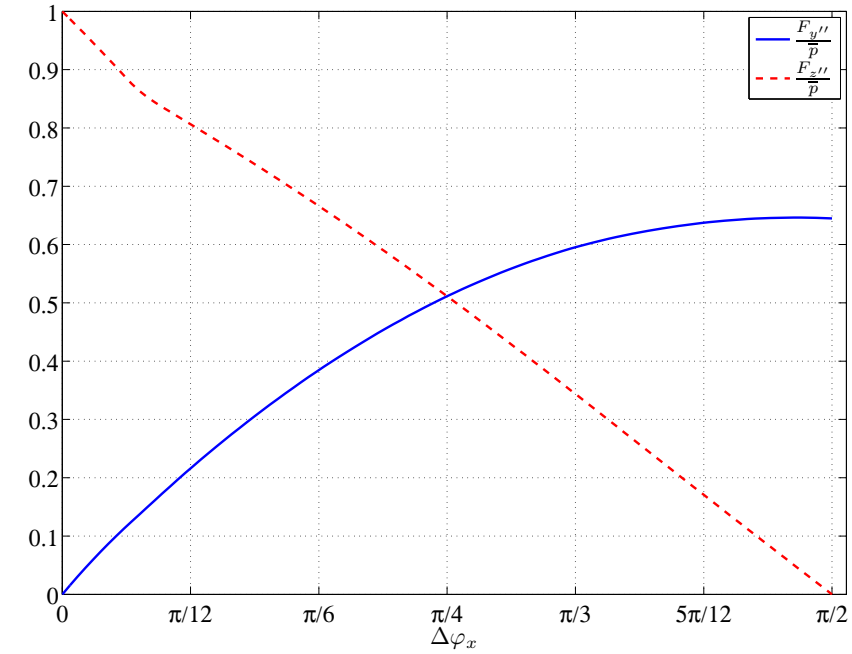

Figure 5.45: Forces $f_{y''}$ and $f_{z''}$ as a function of the displacement φ_x

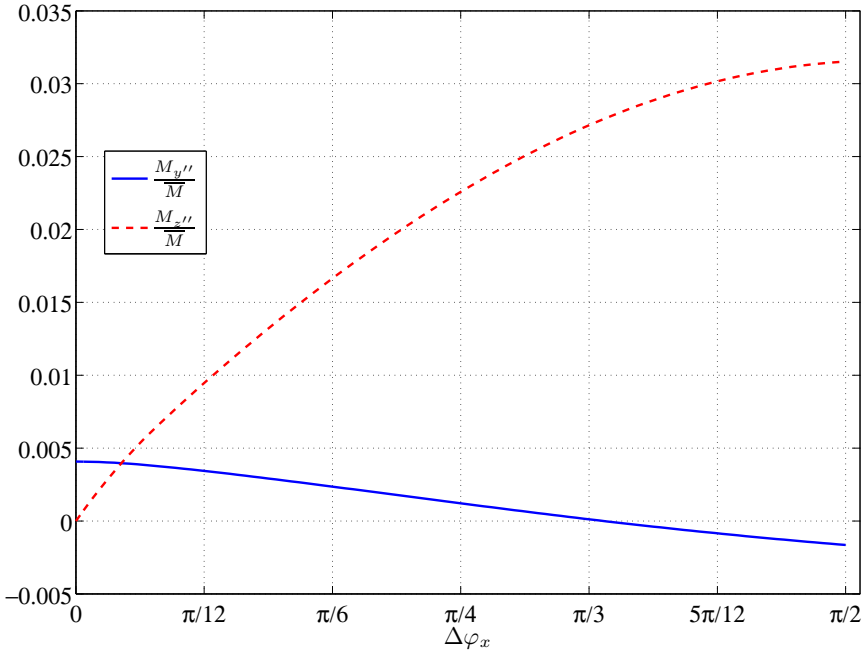

Figure 5.46: Moments $m_{x''}$, $m_{y''}$ and $m_{z''}$ as a function of the rotation φ_x

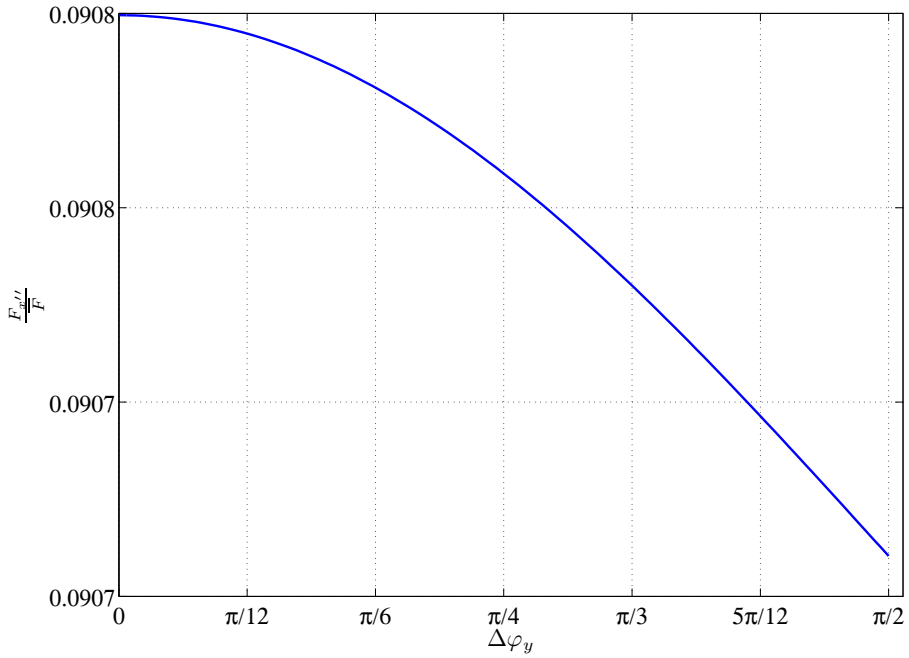

Figure 5.47: Force $f_{x''}$ as a function of the displacement φ_y

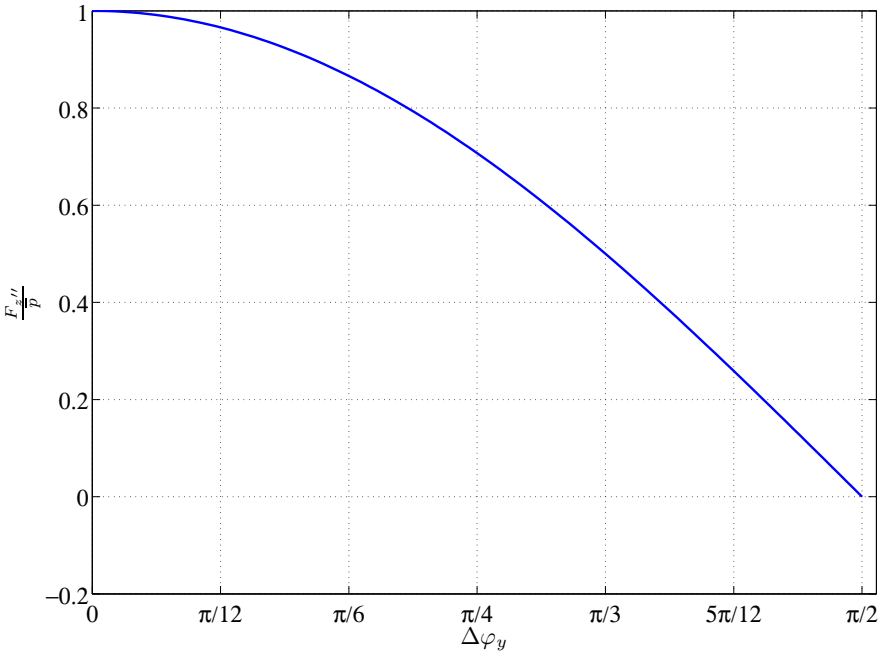

Figure 5.48: Force $f_{z''}$ as a function of the displacement φ_y

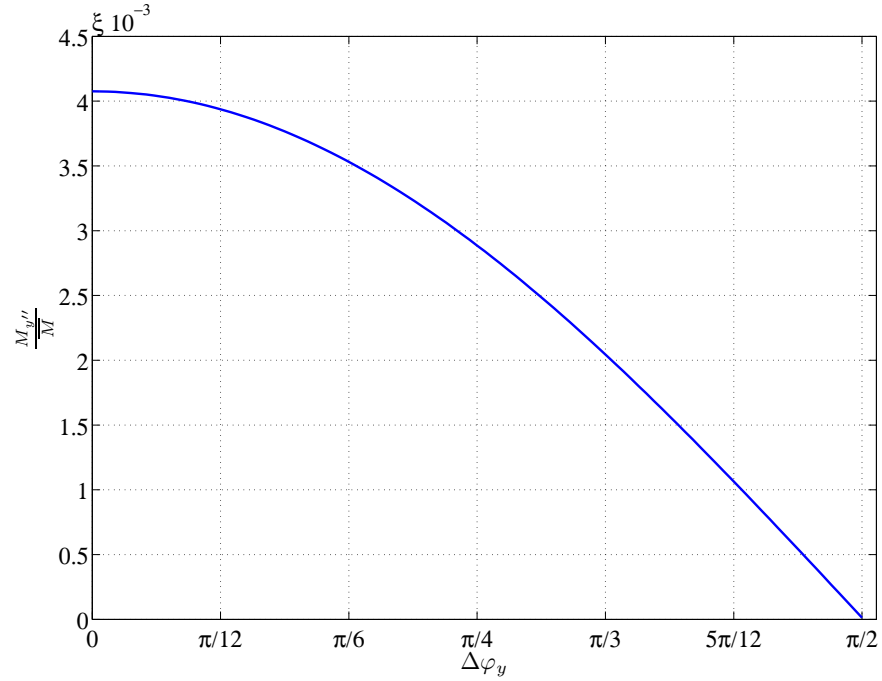

Figure 5.49: Force $m_{y''}$ as a function of the displacement φ_y

As the figures have shown, the great variability in the constitutive equations strongly depends on the shape of the section but also on the position and orientation. As it has

been explained before, the constitutive equations of a section relates the forces and moments acting on it (the three forces and moments acting on each axes of the section) as a function of the position of the centroid ($\boldsymbol{v_G}$) and the orientation of the section (characterized by the rotation matrix $\boldsymbol{M_R}$).

As a conclusion, it can be said that there is a univocal relation between the forces and moments and the configuration (shape, position and orientation) of the section and many variables affect the forces and moments in many ways.

The program developed has been considered a great tool to analyse the fluid-section interaction in all the conditions previously mentioned. In the following, the constitutive equations will be obtained numerically and will be treated and adapted to model the interaction of beam elements in contact with a fluid. In chapter 6 the 2D model will be presented and in chapter 7 the model will be extended to deal with floating structure in a general 3D approach.

5.4.3 Parametric constitutive equations

Now, a brief study on some sections will be carried out. The study will be focused on the constitutive equations in the 3D space, more precisely in the interaction between the twisting rotation and the vertical penetration of the section inside the fluid. The model developed in chapter 7 will be able to take into account the interaction between flexural and twisting rotations that the structures may suffer. To emphasize the influence that the torsional behaviour (in terms of fluid-structure interaction) has in the constitutive equations of the section, three sections will be analysed. The main goal here is to develop the constitutive equations of the sections contained in a vertical plane as a function of the vertical displacement and torsional rotation. As a result, the vertical force and twisting moment produced by the fluid to the section will be plotted and some discussions will be exposed. Figure 5.50 shows a generic section contained in a vertical plane in contact with a fluid and the two main variables that governs the problem $\left(\xi = \dfrac{h}{H(\alpha)},\ \alpha\right)$ are depicted.

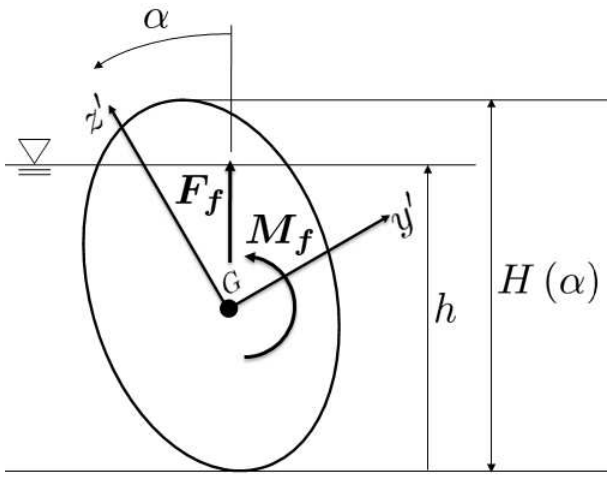

Figure 5.50: Section in a vertical plane with the variables that govern the problem

The analysis will be performed computing the vertical force and twisting moment acting on the section for each pair of coordinates $(h,\ \alpha)$. The force per unit length F_f will be normalized with respect the maximum vertical load that the fluid can produces $P = \gamma_f A_s$. In addition, the twisting moment per unit length will be normalized with respect a generic twisting moment $M = \gamma_f A_s H(\alpha)$. In the x-axis of all the plots, the actual height with respect the lowest point of the section will be normalized with respect the height of the section for each angle α, which means that a normalized length defined as $\xi = \dfrac{h}{H(\alpha)}$ will be used to characterize the vertical penetration in the fluid.

The sections used in this analysis are the rectangular section (Figure 5.51), the trapezoidal section (Figure 5.52) and the section number 3 (Figure 5.53).

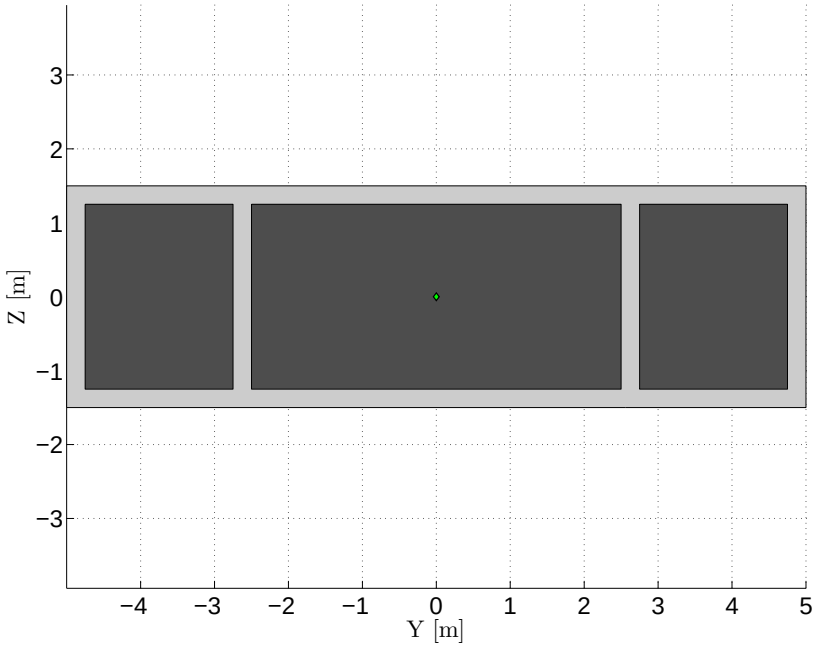

Figure 5.51: Rectangular section

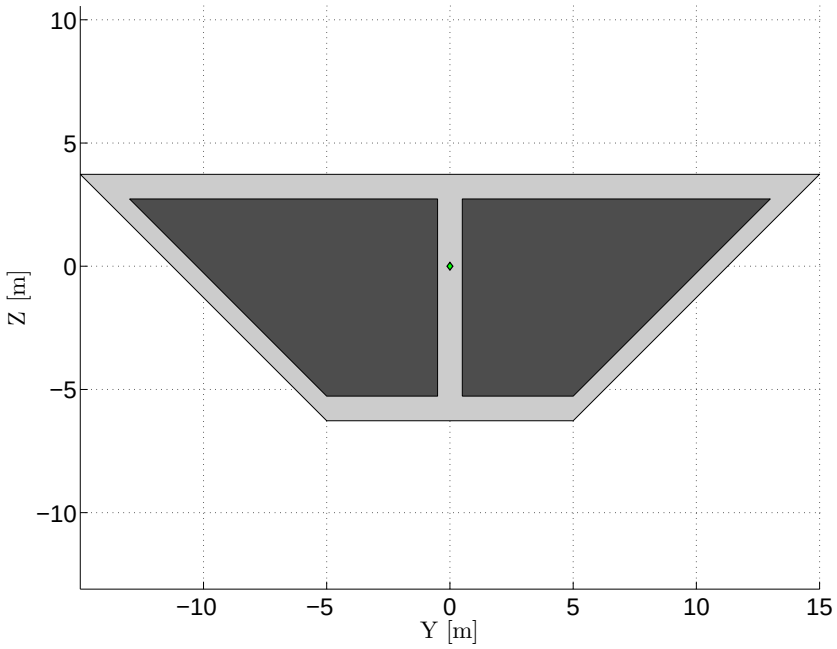

Figure 5.52: Trapezoidal section

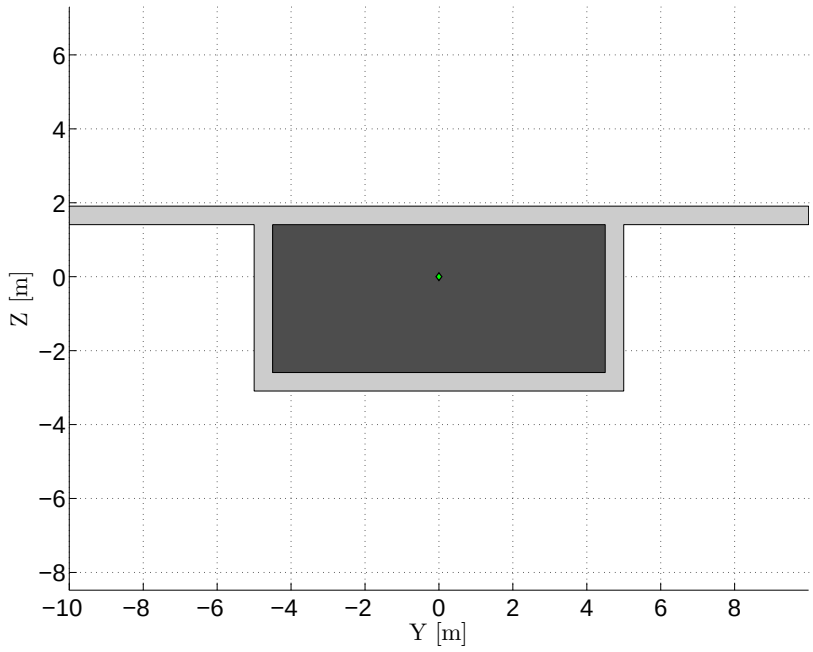

Figure 5.53: Section number 3

The constitutive equations in terms of the two normalized variables (ξ, α) are now presented. In this case, only the vertical force and twisting moment acting on the section will be shown. Figures 5.54 and 5.55 show the vertical force and twisting moment acting

on the trapezoidal section. Figures 5.56 and 5.57 show the vertical force and twisting moment for the trapezoidal section and figures 5.58 and 5.59 show the vertical force and twisting moment acting on section number 3.

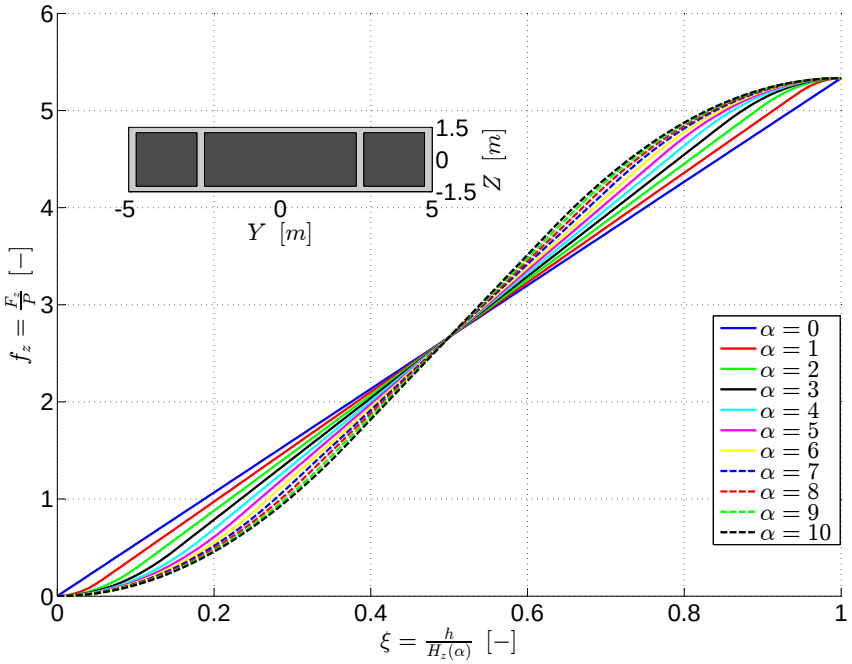

Figure 5.54: Vertical reaction produced by the fluid on the rectangular section

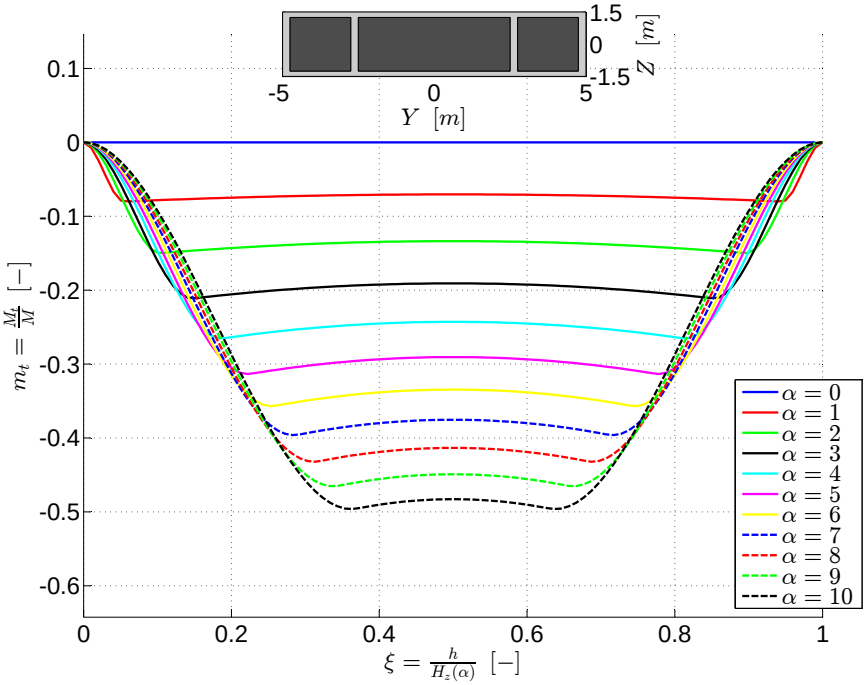

Figure 5.55: Twisting moment produced by the fluid on the rectangular section

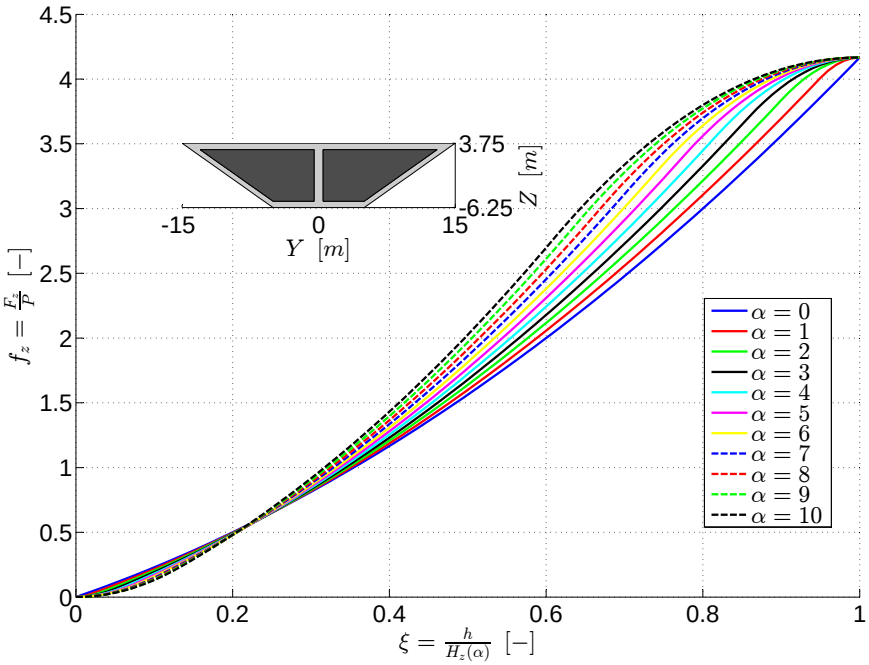

Figure 5.56: Vertical reaction produced by the fluid on the trapezoidal section

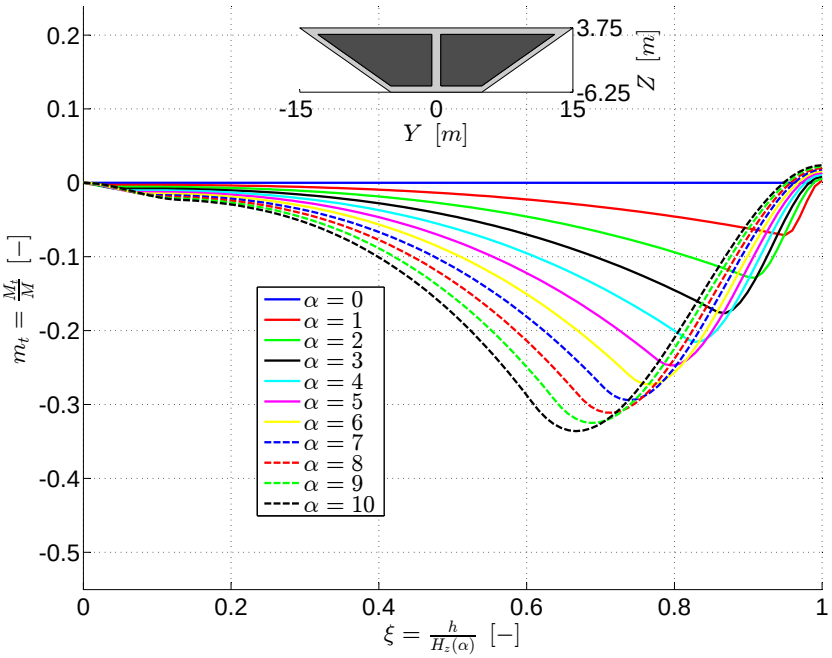

Figure 5.57: Twisting moment produced by the fluid on the trapezoidal section

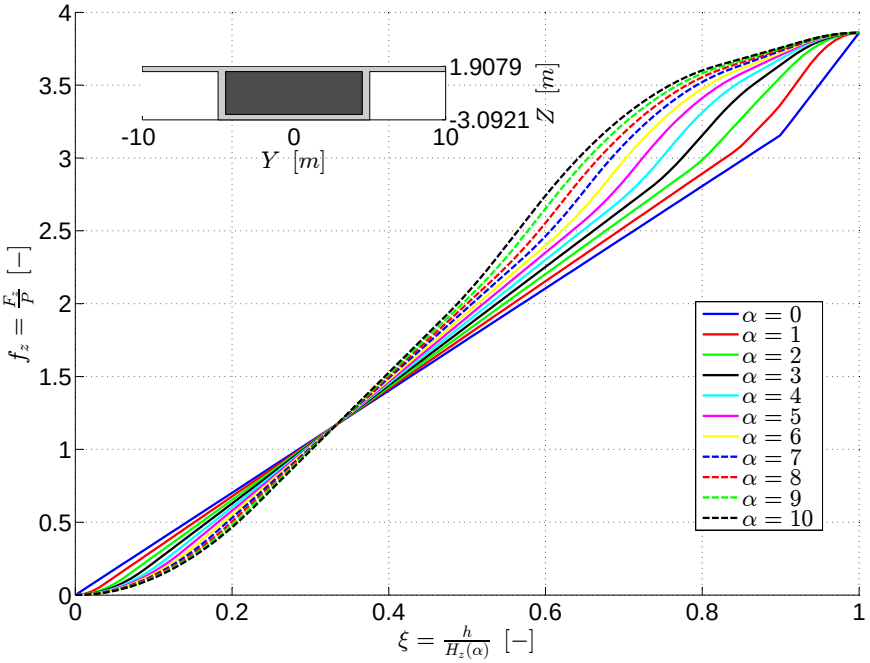

Figure 5.58: Vertical reaction produced by the fluid on section number 3

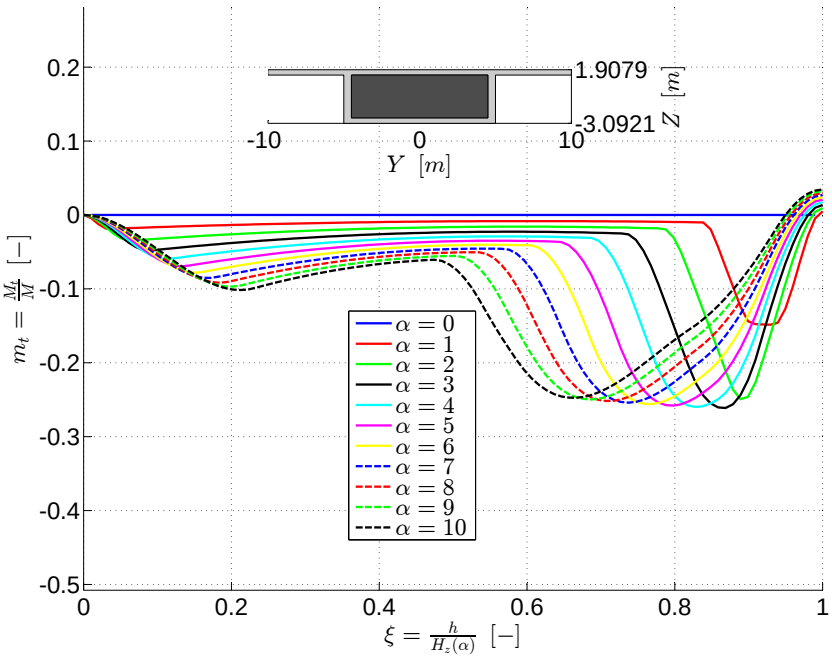

Figure 5.59: Twisting moment produced by the fluid on section number 3

6 First order formulation of 2D cable and frame floating structures

In this chapter, the new finite element developed is presented considering a 2D model. First, the modified Euler-Bernoulli's beam model is presented following the same procedure previously developed in chapter 3, starting from the displacement field at the sectional level and deriving consequently the strain field. In addition, the stress field energetically compatible with the generalized strains will be calculated and a new contribution will be included in the formulation of the principle of virtual works for the beam element. In particular, this new contribution, that will lead to a new generalized strain and stress will be the contribution of the buoyancy phenomena. Finally, the new equilibrium equations will be derived and the formulation of the finite element model will be introduced considering a simplified displacement field inside the element with shape functions properly defined.

The model developed, as it will be explained, is based on the well known Winkler model, which, for the analysis of soil-structure interaction, considers a reaction in the soil proportional to the depth of the beam. In our approach, such property is adapted to simulate the buoyancy effects produced by the fluid surrounding the beam. Subsequently, the theory of the new finite element is presented explaining how to compute the vertical buoyancy stiffness. As it will be seen, althought the model is very similar to the Winkler model, some improvements have been introduced to properly characterize the nonlinearity inherent in the buoyancy problems. Indeed, at each depth of the beam corresponds a different buoyancy load that must be integrated along the boundary of the section to obtain the buoyancy stiffness, since the hydrostatic pressure strongly depends on the shape of the section (see chapter 5).

Later, the cable structures will be treated.

The last part of this chapter is devoted to computational aspects. Floating structures composed by beams and anchorage systems made with cables have some peculiarities. In particular, the vertical stiffness of the structure is entirely produced by the floating capacity of the beam structure and, on the other hand, the stiffness in the horizontal plane

(plane defined by the free surface of the fluid) is produced by the anchorage system. It can be noticed that the vertical stiffness completely depends on the way the beam makes contact with the fluid and the horizontal stiffness depends on the tension in the cables, numerical problems can arise. Therefore, possible solutions have been proposed.

Finally, the last part will present some benchmarks and practical applications that the program developed allow to analyse.

6.1 Modified Euler-Bernoulli and Winkler beam model

The theory behind the new formulation is presented. The model is formulated under the hypothesis of planar behaviour, small rotations and displacements and elastic linear behaviour of the materials, following the design approach for this kind of structures (floating bridges and breakwaters essentially), for example the requirement of small vertical displacements[(1)].

To introduce the formulation developed, consider equation 3.99 on section 3.2.1, where the classic Euler-Bernoulli model was introduced. In addition to the previously defined generalized strains, a spring that is attached to the beam in the bottom part can be introduced as it can be seen in figure 6.1

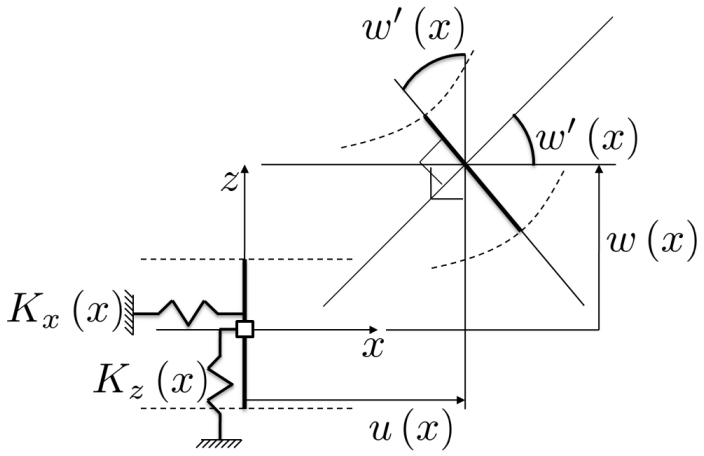

Figure 6.1: Inclusion of buoyancy springs along the beam

The displacement field of the classic Euler-Bernoulli beam does not change, while the expression of the internal work per unit length changes. Considering equation 3.99, the expression of the new internal work per unit length can be formulated as

$$\frac{dL_i}{dx} = \boldsymbol{Q}^T \boldsymbol{\delta q} + \boldsymbol{\delta u}^T \boldsymbol{K_s}(x)\, \boldsymbol{u} \tag{6.1}$$

with the variables $\boldsymbol{Q}$ and $\boldsymbol{q}$ and $\boldsymbol{u}$ defined in equations 3.100, 3.97 and 3.94 respectively and the new variables $\boldsymbol{K_s}$ defined as

[(1)] Consider for example a car that moves along the floating bridge. It will not be situable that the deformation and vertical displacement of the bridge exceed a certain quantity because it will be dangerous for the people that uses it.

$$\boldsymbol{K_s}(x) = \begin{bmatrix} K_x(x) & 0 \\ 0 & K_z(x) \end{bmatrix} \tag{6.2}$$

On the other hand, the external work per unit length does not change and can be expressed as

$$\frac{dL_e}{dx} = \boldsymbol{P}^T(x)\,\boldsymbol{u}(x) \tag{6.3}$$

with

$$\boldsymbol{P} = [n\ p]^T(x)$$

The equilibrium equations of this new beam can be obtained integrating the internal and external works per unit length along the element. The expressions of the internal and external works are

$$\begin{gathered} L_i = \int_0^l \boldsymbol{Q}^T\boldsymbol{\delta q} + \boldsymbol{\delta u}^T\boldsymbol{K_s}(x)\,\boldsymbol{u}\,dx \\ = \\ [N\delta u - M\delta w' + M'\delta w]_0^l + \int_0^l -N'\delta u - M''\delta w + \boldsymbol{\delta u}^T\boldsymbol{K_s u}\,dx \end{gathered} \tag{6.4}$$

$$L_e = \int_0^l \boldsymbol{P}^T\boldsymbol{\delta u}\,dx + \boldsymbol{P_c}^T\boldsymbol{\delta u_c} \tag{6.5}$$

where the variables $\boldsymbol{P_c}$, $\boldsymbol{u_c}$ are defined in equation 3.104. Through the equivalence of both internal and external virtual work, the equilibrium conditions of this new element may be obtained.

$$L_i = L_e \rightarrow \left\{ \begin{array}{rcl} N' + n & = & K_x u \\ -M'' + p & = & K_z w \end{array} \right. ; \begin{array}{ll} N(0) = N_0 & N(l) + N_l = 0 \\ M(0) = M_0 & M(l) + M_l = 0 \end{array} \tag{6.6}$$

It can be shown that the inclusion of a distributed axial and vertical springs along the element does not modify the boundary conditions of the beam, already reported in equation 3.105. Now, the equilibrium equations in terms of the generalized stresses can be modified to take into account the constitutive equations of the beam and to express them in terms of the generalized displacements.

Considering the constitutive equations of the Euler-Bernoulli's beam reported in 3.106:

$$\begin{array}{rcl} EA\dfrac{d^2u}{dx^2}(x) + n(x) & = & K_x(x)\,u(x) \\ EI\dfrac{d^4w}{dx^4}(x) + p(x) & = & K_z(x)\,w(x) \end{array} \tag{6.7}$$

It must be noticed that the equilibrium equations previously derived are valid under the hypothesis of constant cross section along the element, since the hydrostatic pressure is integrated along the boundary of the section under the hypothesis that this pressure is contained in the plane of the section. Considering figure 6.2, one may realize that

the fluid-section interaction in an element with constant or varying cross section are completely different. In this thesis, only the elements with constant cross section have been considered.

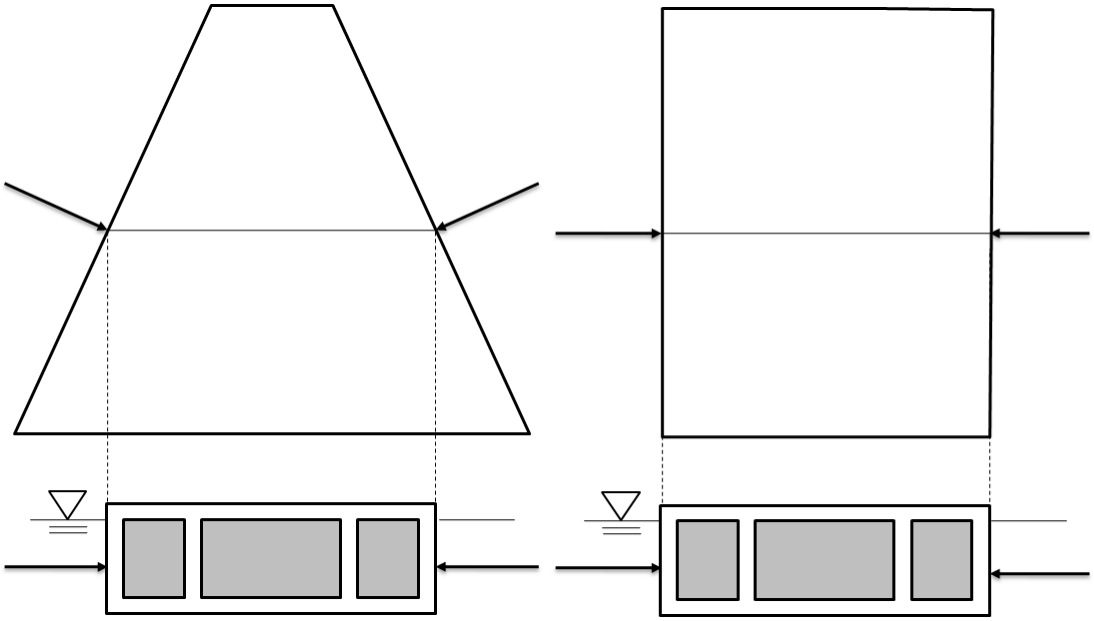

(a) The hydrostatic pressure is not contained in the plane of the section if the beam has a varying cross section

(b) The hydrostatic pressure is contained in the plane of the section if the beam has a constant cross section

Figure 6.2: Differences between an element with constant and varying cross section in contact with a fluid

6.2 Finite Element model

Once the theoretical introduction of the new structural model has been presented, let us consider the associated finite element model. Consider that the displacement field inside the beam is interpolated using the nodal displacements. Cubic shape functions have been used since there is no exact solution to equations 6.7 (The functions $K_x(x)$ and $K_z(x)$ are completely arbitrary).

$$\boldsymbol{u}(x) = \begin{bmatrix} u(x) & = & U_1 N_1(x) + U_4 N_4(x) \\ w(x) & = & U_2 N_2(x) + U_3 N_3(x) + U_5 N_5(x) + U_6 N_6(x) \end{bmatrix} = \boldsymbol{N}(x)\,\boldsymbol{U} \tag{6.8}$$

$$\boldsymbol{N}(x) = \begin{bmatrix} N_1 & 0 & 0 & N_4 & 0 & 0 \\ 0 & N_2 & N_3 & 0 & N_5 & N_6 \end{bmatrix}$$

$$N_1 = 1 - \frac{x}{l};\ N_4 = \frac{x}{l}$$

$$\begin{aligned} N_2 &= 1 - 3\left(\frac{x}{l}\right)^2 + 2\left(\frac{x}{l}\right)^3 \quad ; \quad N_5 = 3\left(\frac{x}{l}\right)^2 - 2\left(\frac{x}{l}\right)^3 \\ N_3 &= l\left[\frac{x}{l} - 2\left(\frac{x}{l}\right)^2 + \left(\frac{x}{l}\right)^3\right] \quad ; \quad N_6 = l\left[-\left(\frac{x}{l}\right)^2 + \left(\frac{x}{l}\right)^3\right] \end{aligned} \tag{6.9}$$

$$\boldsymbol{U} = [U_1 \ \cdots \ U_6]^T \tag{6.10}$$

Following the same procedure of chapter 4, the strains inside the element may be derived considering the differential operator $\boldsymbol{C}$ defined in equation 3.98.

$$\boldsymbol{q} = \boldsymbol{C} \otimes \boldsymbol{u}\,(x) = \boldsymbol{C} \otimes \boldsymbol{N}\,(x)\,\boldsymbol{U} = \boldsymbol{B}\,(x)\,\boldsymbol{U} \tag{6.11}$$

with $\boldsymbol{B}$ defined as

$$\boldsymbol{B}\,(x) = \begin{bmatrix} N_1' & 0 & 0 & N_4' & 0 & 0 \\ 0 & N_2'' & N_3'' & 0 & N_5'' & N_6'' \end{bmatrix} \tag{6.12}$$

The first and second derivative of the cubic and linear functions have been already reported in equations 3.111 and 3.112.

The internal virtual work can be rewritten considering the displacement field previously defined.

$$L_i = \int_0^l \boldsymbol{Q}^T\boldsymbol{q} + \boldsymbol{u}^T\boldsymbol{K_s}\boldsymbol{u}\ dx = \boldsymbol{\delta U}^T\left(\boldsymbol{K_E} + \boldsymbol{K_N}\right)\boldsymbol{U} \tag{6.13}$$

where the first matrix $\boldsymbol{K_E}$ is the already defined Euler-Bernoulli stiffness matrix and its expression can be found in equation 3.114.

The second stiffness matrix $\boldsymbol{K_N}$ comes from the buoyancy action produced by the fluid. It might be noticed that both contribution are independant due to the displacement formulation used.

$$\boldsymbol{K_E} = \int_0^l \boldsymbol{B}^T\boldsymbol{D}\boldsymbol{B}\ dx \tag{6.14}$$

$$\boldsymbol{K_N} = \int_0^l \boldsymbol{N}^T\boldsymbol{K_s}\boldsymbol{N}dx \tag{6.15}$$

In addition, the external virtual work can be computed as done before (equation 3.115).

$$L_e = \int_0^l \boldsymbol{P}^T\boldsymbol{u}dx = \boldsymbol{f}^T\boldsymbol{U} \tag{6.16}$$

$$\boldsymbol{f} = \int_0^l \boldsymbol{N}^T\boldsymbol{P}dx \tag{6.17}$$

Finally, the equilibrium equations of the beam element in matrix form can be written as follows.

$$\boldsymbol{K}\boldsymbol{U} = \left(\boldsymbol{K_E} + \boldsymbol{K_N}\right)\boldsymbol{U} = \boldsymbol{f} \tag{6.18}$$

Once the total[(2)] equilibrium equations in matrix form have been written, the equivalent nodal loads of the new beam finite element may be computed. Let us consider figure 6.3, where the finite element has been depicted.

[(2)] Here, the word total is used to emphasize the fact that the equilibrium equations have been written in the undeformed configuration under the hypothesis of small displacements. Therefore, the matrix derived is the total stiffness matrix refered to the initial configuration.

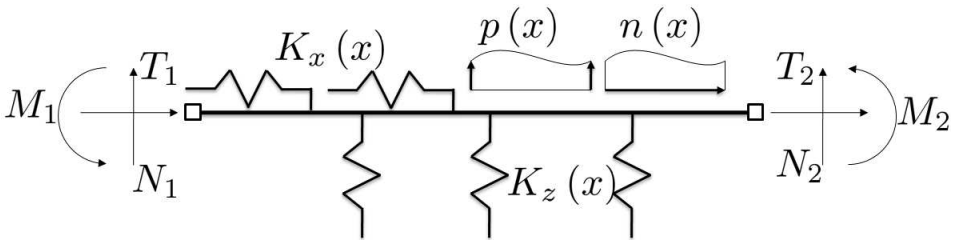

Figure 6.3: Beam finite element with axial and vertical springs under external and equivalent nodal loads

The equivalent nodal loads in the element may be defined as the vector with the following components.

$$\boldsymbol{f} = \left[\begin{array}{cccccc} N_1 & T_1 & M_1 & N_2 & T_2 & M_2 \end{array} \right]^T \tag{6.19}$$

The equivalent nodal loads can be divided in two groups. The first one is the contribution of the external loads $p(x)$ and $n(x)$ ($\boldsymbol{f_e}$) and the second one is the contribution of the prestressing action ($\boldsymbol{f_p}$).

$$\boldsymbol{f} = \boldsymbol{f_e} + \boldsymbol{f_p} \tag{6.20}$$

From the theory developed in chapter 4, one may obtain the equivalent nodal forces due to external loads $p(x)$ and $n(x)$ considering the equivalence between the work done by the external loads and the one done by the equivalent nodal forces under the displacement field defined in equation 6.8.

$$\boldsymbol{f_e} = \int_0^l \boldsymbol{P}^T(x)\, \boldsymbol{N}(x)\, dx \tag{6.21}$$

In the program, $p(x)$ is considered as a linear load and $n(x)$ as a constant load (see figure 6.4). Taken into account this hypothesis, the external loads may be written as

$$\boldsymbol{P} = \left[\begin{array}{c} n(x) \\ p(x) \end{array} \right] = \left[\begin{array}{c} n_l(x) + n_{sw}(x) \\ p_l(x) + p_{sw}(x) \end{array} \right] \tag{6.22}$$

$$n_l(x) = p_x;\ n_{sw}(x) = -\gamma A \sin(\alpha) \tag{6.23}$$

$$p_l(x) = p_{z1} + \frac{p_{z2} - p_{z1}}{l} x;\ p_{sw}(x) = -\gamma A \cos(\alpha) \tag{6.24}$$

with $n_l(x)$, $n_{sw}(x)$ and $p_l(x)$ are the axial and bending loads produced by the external loads, while $p_{sw}(x)$ is the selfweight of the beam.

Considering that the vector $\boldsymbol{P}$ has both linear components, a Gauss integration can be used to obtain the equivalent nodal forces.

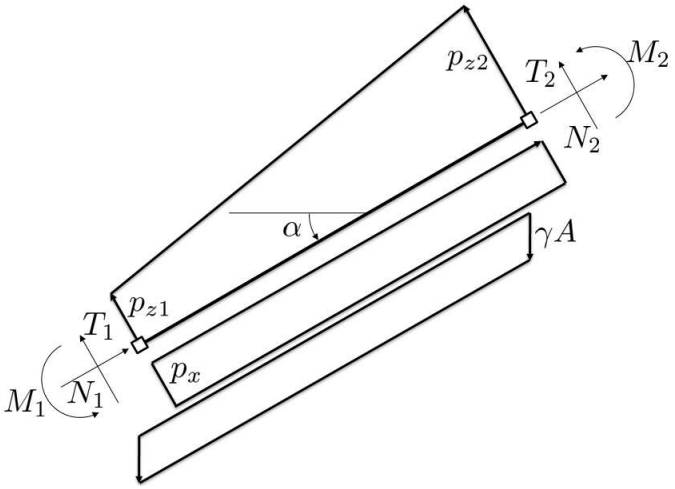

Figure 6.4: Beam finite element with axial and bending springs under external and equivalent nodal loads

$$\boldsymbol{f_e} = \int_0^l \boldsymbol{P}^T(x)\,\boldsymbol{N}(x)\,dx = \int_{-1}^{1} \underbrace{\boldsymbol{P}^T(\eta)\,\boldsymbol{N}(\eta)}_{\boldsymbol{F_f}}\,d\eta = \frac{l}{2}\sum_{i=1}^{N_G} w_i \boldsymbol{F_f}(\eta_i) \tag{6.25}$$

Considering that the vector $\boldsymbol{P}$ has linear functions and the matrix $\boldsymbol{N}$ has cubic functions, the product will produce functions of degree four. These functions can be exactly integrated using a 3-points Gauss scheme.

The contribution of the prestressing can be modelled considering parabolic cables inside each beam element as the one depicted in figure 6.5.

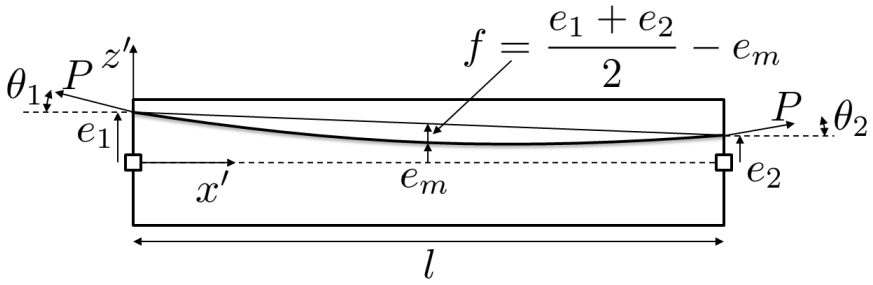

Figure 6.5: Beam with a parabolic prestressing cable

$$\left.\begin{aligned} e(x') &= a + bx + cx^2 \\ e(0) &= e_1 \\ e(l/2) &= e_m \\ e(l) &= e_2 \end{aligned}\right\} \rightarrow e(x) = e_1 + \frac{4e_m - e_2 - 3e_1}{l}x + 2\frac{e_1 + e_2 - 2e_m}{l^2}x^2 \tag{6.26}$$

It can be proved that in parabolic cables the curvature is constant with a value equal to

$$\chi = 4\frac{e_1 + e_2 - 2e_m}{l^2} = \frac{8f}{l^2} \tag{6.27}$$

Considering an infinitesimal part of the cable depicted in figure 6.6 and imposing the equilibrium the load produced by the beam to the cable may be found.

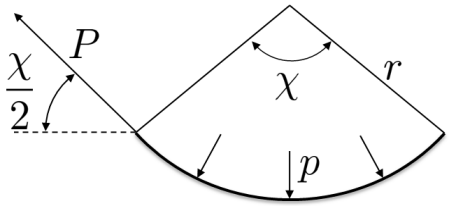

Figure 6.6: Infinitesimal part of a cable in equilibrium

Due to the pretension, the cable will produce a constant load that can be computed as

$$pr\chi = 2\left(P\sin\frac{\chi}{2}\right) \rightarrow p = \chi P \tag{6.28}$$

Considering equation 6.27, the final expression for the constant load distributed alond the element may be written.

$$p = \frac{8f}{l^2}P \tag{6.29}$$

Once the equivalent constant load along the element is computed, the system depicted in figure 6.5 can be decomposed in the sum of two systems represented in the following figure.

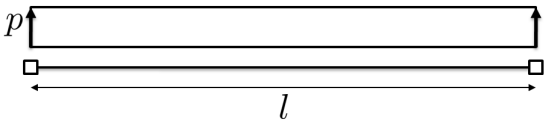

(a) Contribution of the constant load

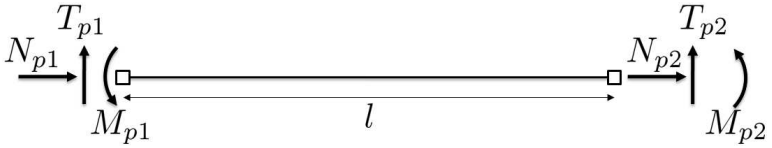

(b) Contribution of the prestressing at the edges

Figure 6.7: Decomposition of the prestressed beam in two equivalent systems

with

$$\begin{array}{lll} N_{p1} = P\cos\theta_1 & T_{p1} = P\sin\theta_1 & M_{p1} = -P\cos\theta_1 e_1 \\ N_{p2} = -P\cos\theta_2 & T_{p2} = -P\sin\theta_2 & M_{p2} = P\cos\theta_2 e_2 \end{array} \tag{6.30}$$

The two contributions in the equivalent nodal forces vector due to prestressing are

$$\boldsymbol{f_p} = \boldsymbol{f_{p1}} + \boldsymbol{f_{p2}} \tag{6.31}$$

$$\boldsymbol{f_{p1}} = \begin{bmatrix} 0 & \frac{pl}{2} & \frac{pl^2}{12} & 0 & \frac{pl}{2} & -\frac{pl^2}{12} \end{bmatrix}^T \tag{6.32}$$

$$\boldsymbol{f_{p2}} = \begin{bmatrix} P & P\theta_1 & -Pe_1 & -P & -P\theta_2 & Pe_2 \end{bmatrix}^T \tag{6.33}$$

where the hypothesis of small angles has been considered. The angles θ_1 and θ_2 must be computed evaluating the first derivative of the parabola on every edge of the beam with the following formulas.

$$\theta_1 = e'(0) = 4e_m - e_2 - 3e_1 \qquad \theta_2 = e'(l) = \theta_1 + \frac{8f}{l} \tag{6.34}$$

The equilibrium equations of the beam element have been derived and the stiffness matrix and the vector of equivalent nodal loads have been computed for external loads and prestressing cables.

The new model requires the definition of two functions that compose the matrix defined in equation 6.2. This matrix represents the buoyancy effect produced by the fluid surrounding the beam and must be computed according to the relative configuration of the beam with respect the fluid's free surface.

6.3 Definition of the stiffness coefficient

Consider figure 6.8, where a beam element under a fluid is depicted. The buoyancy action on the beam is the result of the sum of the actions that the fluid produces on each section along the beam axis. Considering a generic section situated at the coordinate x' of the local axis of the beam, the variables that govern the position and the orientation of the section are $\boldsymbol{v}(x')$ and $\theta(x')$. These variables are both functions of the local coordinate of the element x' and are directly related to the nodal positions of the element and their displacements.

From this figure, the global configuration of each section along the local axis of the element can be characterized. The position of each section will be defined by the position of the first node of the element in the global reference system plus its displacement (computed as an interpolation of the displacements of the beam using the shape functions). On the other hand, the rotation with respect a vertical plane will be computed in the same way but considering the derivative of the shape functions.

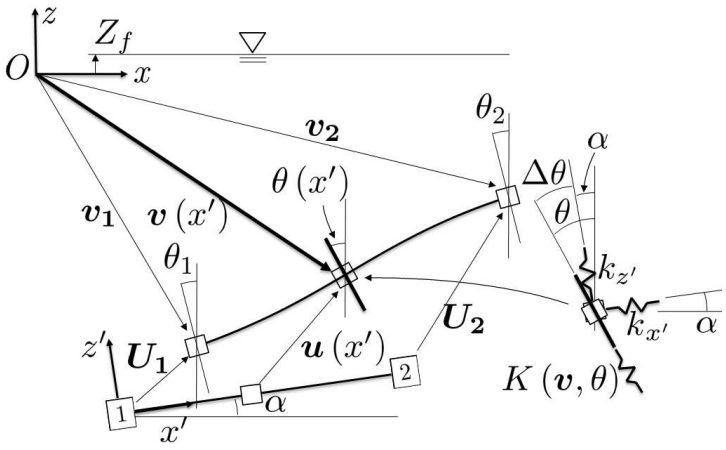

Figure 6.8: Model for the fluid-structure static interaction in the beam model.

The position of the generic section can be written as:

$$\boldsymbol{v}(x') = \boldsymbol{v_1} + \boldsymbol{t}x' + \boldsymbol{u}(x') \tag{6.35}$$

where $\boldsymbol{v_1}$ is the position of the first node of the element in the undeformed configuration, $\boldsymbol{t}$ is the tangent vector of the element in the undeformed configuration and $\boldsymbol{u}(x')$ is the displacement of the section due to the deformation of the beam. From equation 6.8, the displacements of the section can be expressed in terms of the nodal displacements and the shape functions evaluated in the x' local coordinate.

$$\boldsymbol{u}(x') = \boldsymbol{N}(x')\boldsymbol{U} \tag{6.36}$$

where $\boldsymbol{U}$ is defined in equation 6.10.

The angle θ in the deformed configuration can be expressed as the sum of two contributions.

$$\theta = \alpha + \Delta\theta \tag{6.37}$$

The first contribution, α, is the angle with respect to the horizontal axis that the beam element has in the undeformed configuration and $\Delta\theta$ is the rotation that the section has soffered due to the deformation of the beam. Considering that the rotation is the derivative of the displacements $w(x')$ in the local reference system, the rotation may be expressed as

$$\Delta\theta(x') = U_2\frac{dN_2}{dx'}(x') + U_3\frac{dN_3}{dx'}(x') + U_5\frac{dN_5}{dx'}(x') + U_6\frac{dN_6}{dx'}(x') \tag{6.38}$$

where the shape functions used are defined in equation 6.9.

The model of the spring takes into account the depth of the element and the rotation of the section with respect the undeformed configuration. Consider figure 6.9 where the section at coordinate x' has been identified. In this sketch, the important variables $\boldsymbol{v}$ and θ are highlighted and the integration along the boundary of the section can be performed to obtain the buoyancy force F. Once the force has been computed, the stiffness in the

plane of the section may be evaluated dividing this force by the depth of the lowest point of the section as depicted in figure 6.9.

$$K = \frac{F}{h} \tag{6.39}$$

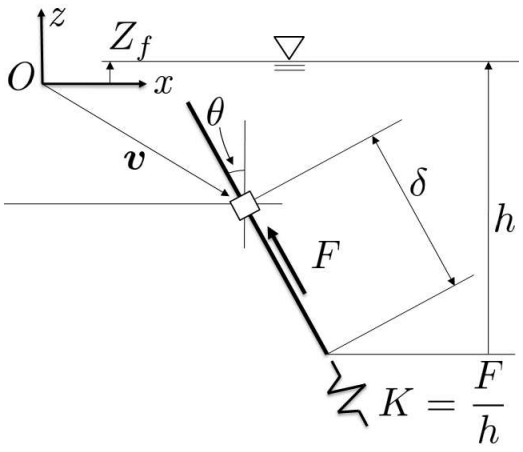

Figure 6.9: Computation of the equivalent stiffness in the 2D beam model.

The last step is to transform the stiffness from the plane of the section into the local reference system of the beam in the undeformed configuration, as follow:

$$\begin{aligned} K_{z'} &= K \cos \Delta\theta \\ K_{x'} &= K \sin \Delta\theta \end{aligned} \tag{6.40}$$

The depth of the lowest point might be computed considering the variable δ (that is an intrinsic geometric characteristic of the section), the angle of rotation and the vertical position of the centroid.

$$h\left(\boldsymbol{v}, \theta\right) = Z_f - \boldsymbol{v}_z + \delta \cos \theta \tag{6.41}$$

One may consider that the choice of the bottom part of the section as the point from which to compute the buoyancy stiffness is not appropiate. Indeed, the first choice was to express the stiffness in terms of the vertical displacement of the centroid of the section (which corresponts to the nodal displacement in the beam finite element model).

This choice seems, a priori, a better approach but it involves some numerical problems. Consider figure 6.10, where the vertical hydrostatic load (R) is plotted in terms of the displacements of the centroid (v_G) and the displacement of the lowest point of the section (h).

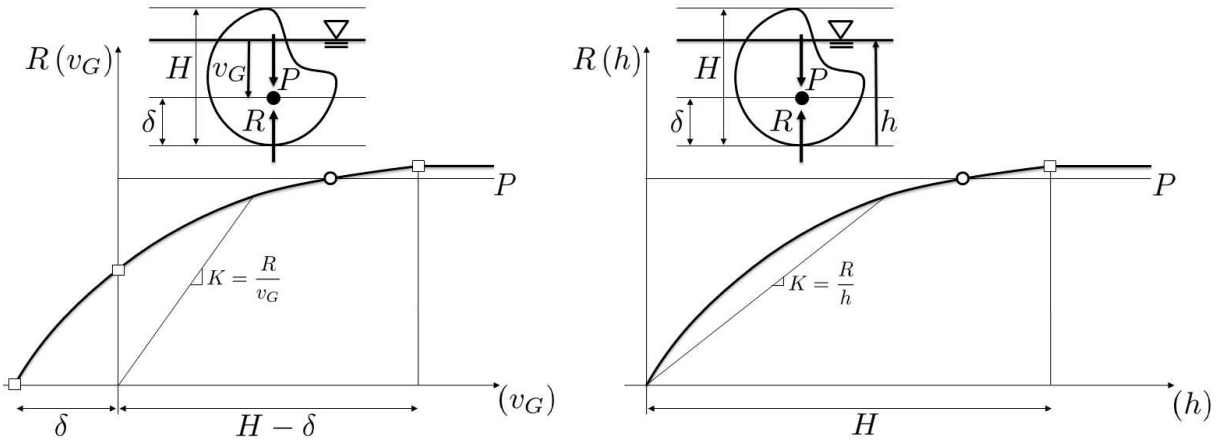

(a) Reaction of the fluid against the displacement of the centroid.

(b) Reaction of the fluid against the displacement of the water with respect the bottom point of the section.

Figure 6.10: Comparison between the two ways to define the reaction of the fluid against the movement of the section.

It is possible to see that the definition of the buoyancy stiffness in terms of v_G presents a singularity when the centroid coincides with the fluid's free surface (when $v_G = 0$). Indeed, at this point, the reaction due to the fluid is larger than zero and the vertical displacement is null. This situation has been proved to be critical in the numerical algorithm where the sections with their centroid near to the free surface of the fluid had large stiffnesses. As a consequence, the stiffness matrix is ill-conditioning.

This problem is, in part, related to the numerical scheme used to solve the nonlinear equilibrium equations. Indeed, the method adopts a stiffness scheme where the global stiffness matrix, refered to the undeformed configuration, is computed at each iteration and the buoyancy stiffness is integrated along the element. This problems could be avoid if a tangent approach were used.

To avoid this situation, the constitutive equations of the sections in the 2D model have been expresed in terms of the vertical displacement of the bottom point of the section. This allows to have the situation shown in figure 6.10.b. In this case, there are no singularities and for each point the buoyancy stiffness can be computed without problems.

The theory of the new finite element model for the analysis of floating beam structures has been reported. Usually, this kind of structures are anchored to the seabed using cable systems. Therefore, a brief explanation of the models and algorithms used to study cable structures in the 2D model for the analysis of frame and cable floating structures will be performed.

6.4 Cable structure

In the 2D model, two aproaches have been introduced in the program for the analysis of cable structures: the direct stiffness method and the finite element method.

From section 3.1.3, the direct stiffness method imposes the equilibrium in the deformed configuration and the stiffness matrix can be obtained as a function of the displacements.

On the other hand, the finite element method defines a displacement field inside the cable element and obtains the equilibrium equations in the matrix form considering the principle of virtual works.

The only important aspect to highlight is the way in which the vector of equivalent nodal loads in the element under the fluid is computed. Indeed, the vector of nodals loads is essentially composed by the selfweight of the cable and the external loads acting on the cable. Due to the hydrostatic buoyancy load, the cable will suffer an upside force since it is in contact with the fluid. To compute this force the definition of an equivalent selfweight of the cable that takes into account the Archimede's force should be considered.

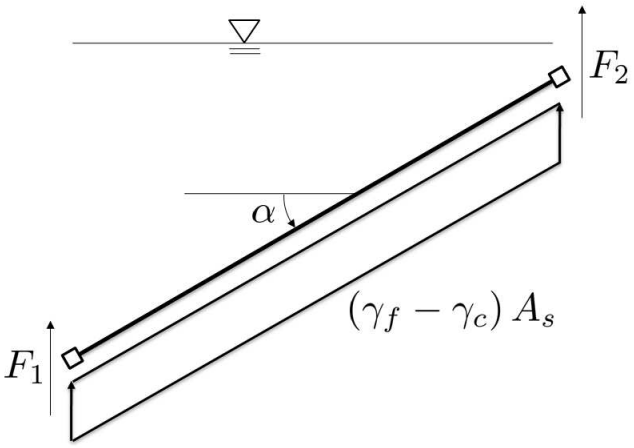

Figure 6.11: The load in the cable is composed by the selfweight and the hydrostatic buoyancy action

Consider the load produced by the selfweight of the cable and the hydrostatic buoyancy. The total load acting on the cable can be written as

$$\boldsymbol{F_T} = \boldsymbol{F_{sw}} + \boldsymbol{F_a} \tag{6.42}$$

where $\boldsymbol{F_{sw}}$ and $\boldsymbol{F_a}$ denote the load produced by the selfweight and the Archimedes buoyancy.

$$\boldsymbol{F_{sw}} = -\int_0^l \gamma_c A_s \; dx\boldsymbol{z} \qquad \boldsymbol{F_a} = \int_0^l \gamma_f A_s \; dx\boldsymbol{z} \tag{6.43}$$

$$\boldsymbol{F_T} = \int_0^l (\gamma_f - \gamma_c)\, A_s \; dx\boldsymbol{z} \tag{6.44}$$

Once the total load has been integrated along the cable element, the equivalent nodal loads in the global reference system can be obtained by dividing it by two and applied on each node of the element for the subsequent assembly.

$$F_1 = F_2 = \frac{|\boldsymbol{F_T}|}{2} sign\,(\gamma_f - \gamma_c) \tag{6.45}$$

The definition of the function *sign* is included for completeness.

$$sign\,(x) = \begin{cases} 1 & x > 0 \\ 0 & x = 0 \\ -1 & x < 0 \end{cases} \tag{6.46}$$

6.5 Computational aspects

A flowchart of the developed program to analyse 2D floating structures is presented. The program is divided into seven parts, each one of them includes several subroutines.

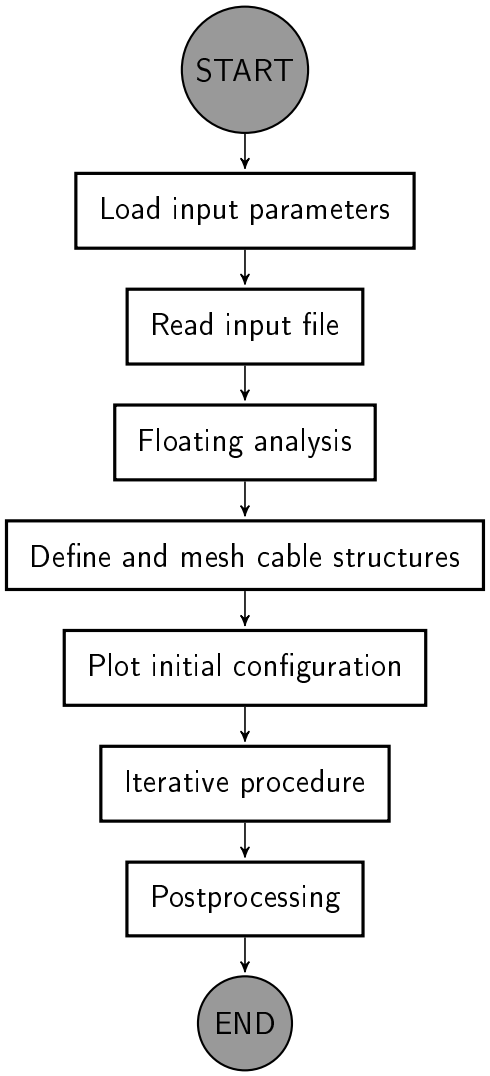

Figure 6.12: Flow chart of the program for the analysis of 2D floating structures

The first step (*Load input parameters*) is devoted to the definition of the variables that characterize the performance of the program. In this part, the user defines the

tolerance in terms of displacements, forces and work to control the convergence of the iterative procedure and defines also some options to characterize the format of the output. The second part is the so-called *Read input file*, where the input file is opened to completely characterize the structure, the cables, the fluid, and the mechanical properties.

Then, the program starts the so-called *Floating analysis*, which is a very important part of the program and requires a deeper explanation. In the input file, only the geometry of the floating structure is defined but the initial configuration must be computed by the program. Consider for example figure 6.13, where the beam floating structure is depicted before and after the positioning made by the program.

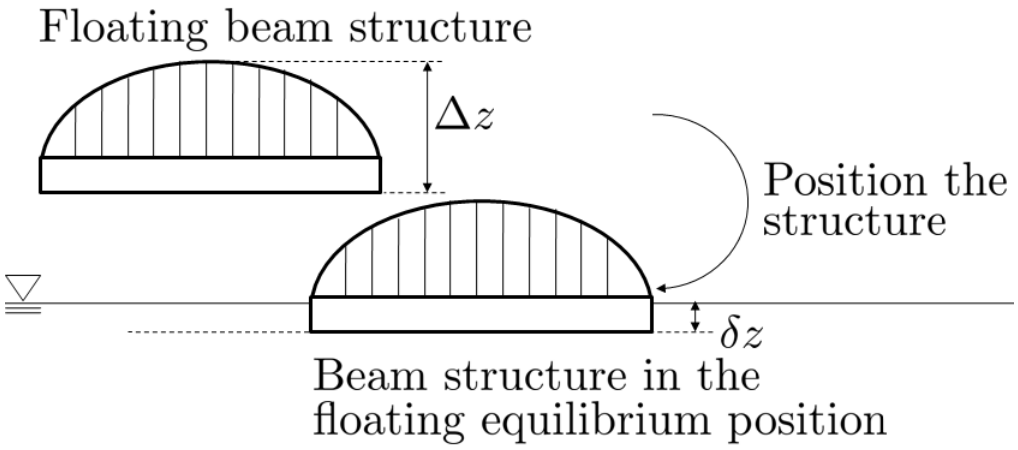

Figure 6.13: The program positions the floating structure at the depth δz where the weight of the structure is equilibrated with the hydrostatic action

The main goal of this part of the program is to compute the variable δz which characterizes the floating equilibrium position of the overall structure. To calculate it, the program must solve a nonlinear problems that can be defined with the following equation.

$$W = A\left(\delta z\right) \tag{6.47}$$

With W and A the weight of the structure and the hydrostatic load.

The problem that must be solved is the determination of the variable δz that satisfies the equality represented in equation 6.47. Before starting the explanation, some considerations can be made.

It can be proved that the functions $A\left(\delta z\right)$ monotonically increases as a function of δz. Indeed, the Archimede's load may be written in terms of the volume of the structure (V) under the fluid as

$$A\left(\delta z\right) = \gamma_f V\left(\delta z\right) \tag{6.48}$$

with γ_f the selfweight of the fluid.

Considering an increment of the variable δz, the new hydrostatic buyancy force can be written as

$$A\left(\delta z+\varepsilon\right)=A\left(\delta z\right)+\underbrace{\Delta A\left(\varepsilon\right)}_{>0} \tag{6.49}$$

From the previous equation, one may realize that the volume under the fluid is a continuous function and monotonally increases when $\varepsilon > 0$ (see figure 6.14) but it is not necessary differentiable with respect to δz.

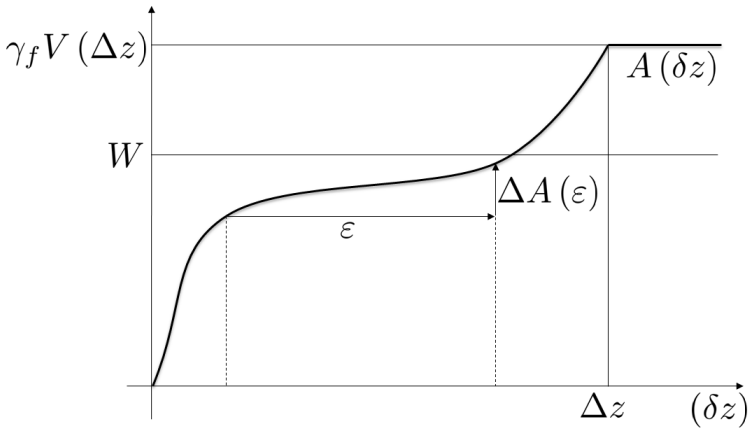

Figure 6.14: The Archimedes load is a continuous and monotonally increases with the variable δz

To solve this nonlinear problem, an incremental iterative scheme has been chosen considering a linearization the function $A\left(\delta z\right)$ as

$$A\left(\delta z+\varepsilon\right)\simeq A\left(\delta z\right)+\varepsilon\frac{dA}{d\left(\delta z\right)} \tag{6.50}$$

As it has been said before, the function A may not be differentiable, therefore an approximation is considered.

$$A\left(\delta z\right)\simeq A\left(\delta z\right)+\varepsilon\frac{\Delta A}{\Delta\left(\delta z\right)} \tag{6.51}$$

The numerical scheme is explained in the following flowchart.

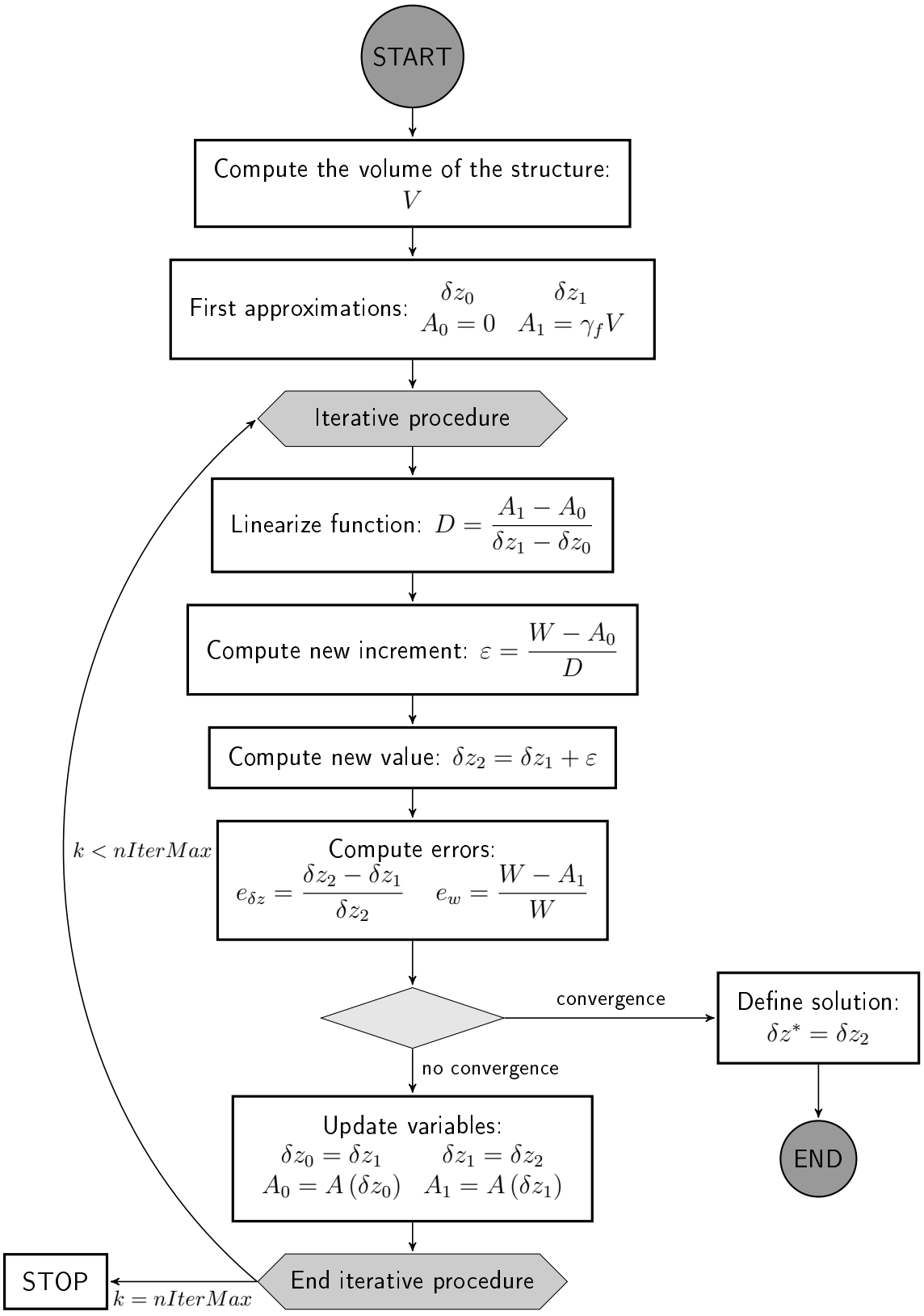

Figure 6.15: Numerical scheme to obtain the equilibrium floating position of the structure considering the selfweight

Once the floating equilibrium position has been computed, the program proceeds to the next step, that is to connect the floating structure with the seabed by means of the cable anchorage system.

Usually, the offshore floating structures are first constructed and positioned in the sea. Then, once the structure has reached its floating equilibrium position, the floating beam is anchored to the seabed using cable systems. The program has been developed emulating this construction procedure. First, the structure is positioned on the fluid surface and a numerical iterative procedure is launched to find the floating equilibrium position considering the structure as a rigid body. Then, the cables (previously defined in the input file by the user) are attached to the beam and anchored to the seafloor in specific points defined by the user.

To position the cables (step number 4, *Define and mesh cable structures*) that will be used as anchorage system of the floating beam, a nonlinear problem has to be solved. Consider first the figure 6.16, where a floating beam structure has been positioned adopting the floating analysis.

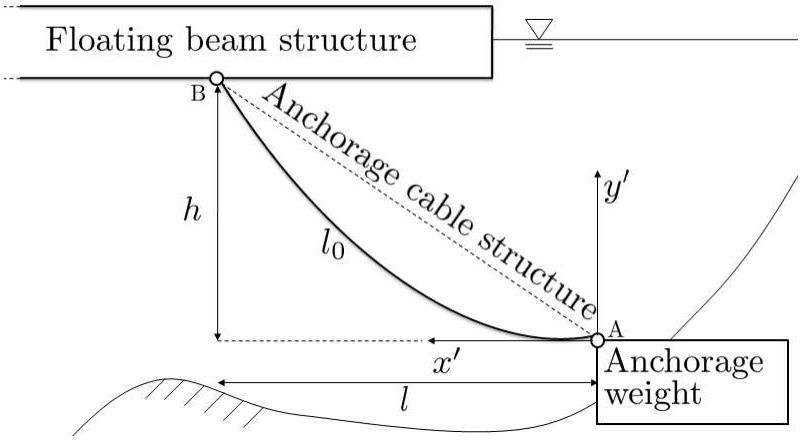

Figure 6.16: Situation of the floating structure before anchoring the system to the seabed

Once the equilibrium floating position of the beam structure has been computed, the program is able to determine the coordinates of the points in the beam structure where the cables will be attached. On the other hand, through the input file, the program already knows the coordinates of all the anchorage points situated in the seabed. Now, for each cable defined in the input file, the program must characterize the configuration of a cable with the beginning and end points defined.

This problem can be solved in different ways, but the simplest procedure has been considered. It must be noticed that the goal is to define the initial configuration of the cables and then mesh them to obtain the nodes and elements that will define the cable structure. As a consequence, the catenary model explained in section 3.1.1 can be used.

Imagine that the coordinates of the anchorage point (point A) and the point where the cable is connected to the beam structure (point B) are defined respectively as follows.

$$\boldsymbol{r_a} = \begin{bmatrix} x_a \\ z_a \end{bmatrix}; \boldsymbol{r_b} = \begin{bmatrix} x_b \\ z_b \end{bmatrix} \tag{6.52}$$

Considering a reference system, as the one depicted in figure 6.16, positioned in the anchorage point where the x' axis is horizontal and in the direction where the point B is positioned and the z' goes upside, the program must determine the configuration of the underformable cable considering the initial point at coordinates $(0, 0)$ and the second point at coordinates

$$l_0 = x_b - x_a \qquad h = z_b - z_a \tag{6.53}$$

Considering the nomenclature used in section 3.1.1, the program determines all the unknown coefficients in equation 3.5. Considering the following variables

$$f_1 = \frac{pl_0}{2H} \qquad f_2 = \sinh\beta\cosh\left(\alpha - \beta\right) \tag{6.54}$$

$$y = \ln\left(H\right) \quad g_1 = \ln\left(f_1\right) = \ln\frac{pl_0}{2} - y \quad g_2 = \ln\left(f_2\right) = \ln\left(\sinh\beta\cosh\left(\alpha - \beta\right)\right) \tag{6.55}$$

the mathematical problem that the program internally solves can be defined as follows.

$$g_1\left(H\right) = g_2\left(H\right) \tag{6.56}$$

The solution adopts a variation of the classic Newton-Raphson scheme. In this case, the equation to be solved is strongly nonlinear and a particular scheme is required. Considering an initial approximation y_0, the program is able to iterate following the recursive form represented here.

$$g_2\left(y_i\right) + \frac{dg_2}{dy}\left(y_i\right)\Delta y = g_1\left(y_i\right) - \Delta y \rightarrow \Delta y = \frac{g_1\left(y_i\right) - g_2\left(y_i\right)}{\frac{dg_2}{dy}\left(y_i\right) + 1} \tag{6.57}$$

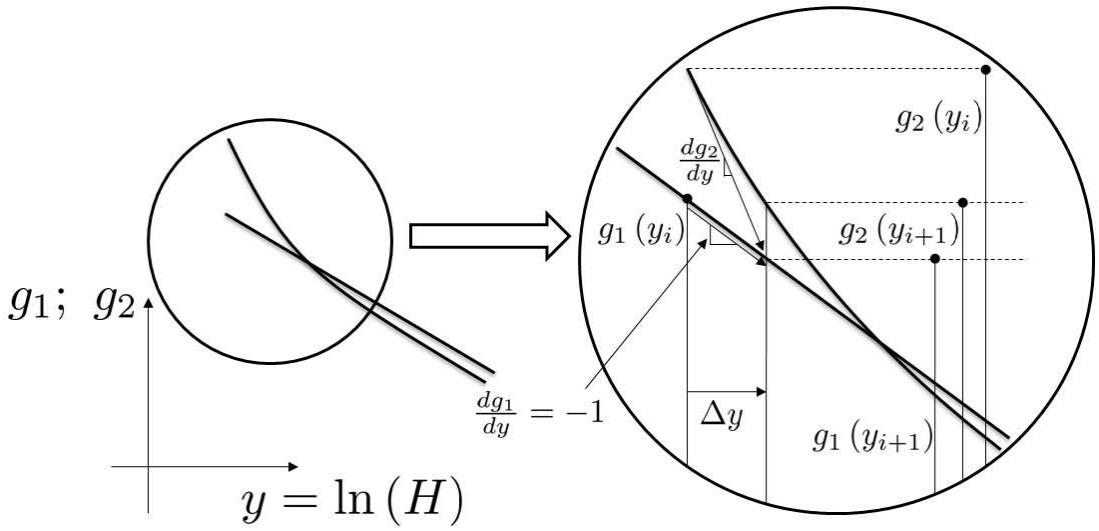

Figure 6.17: Iterative method used to compute the solution of the non linear equation.

The derivatives of the functions g_1 and g_2 with respect of y and H can be obtained as:

$$\frac{dg_2}{dy} = \frac{dg_2}{dH}\frac{dH}{dy} \qquad \frac{dg_1}{dy} = -1 \tag{6.58}$$

$$\frac{dg_2}{dH} = \frac{\cosh\beta}{\sinh\beta}\frac{d\beta}{dH} + \frac{\sinh(\alpha-\beta)}{\cosh(\alpha-\beta)}\left(\frac{d\alpha}{dH} - \frac{d\beta}{dH}\right) \qquad \frac{dH}{dy} = e^y \tag{6.59}$$

$$\frac{d\beta}{dH} = -\frac{pl}{2H^2} \qquad \frac{d\alpha}{dH} = \frac{d\beta}{dH}\left(\frac{h}{l}\frac{\sinh\beta - \beta\cosh\beta}{\cosh(\alpha-\beta)\sinh^2\beta} + 1\right) \tag{6.60}$$

The reader may realize that the method requires an initial (and accurate) approximation for the variable H. If the procedure must be completely automatic, the initial approximation must be defined either in the input file by the user either by the program internally. The first approximation is certainly very difficult to define because it depends on the geometrical conditions of each cable. However, the transformation in the logaritmical space made in equation 6.55 produces in the functions g_1 and g_2 a very particular form. If both functions are plotted, as it can be seen in figure 6.18, there is only one point where both functions intersect and, in addition, they are monotonically decreasing. This allows the program to perform an automatic procedure to determine a value in the left part of the curve (where $g_2 > g_1$) and iterate from that point.

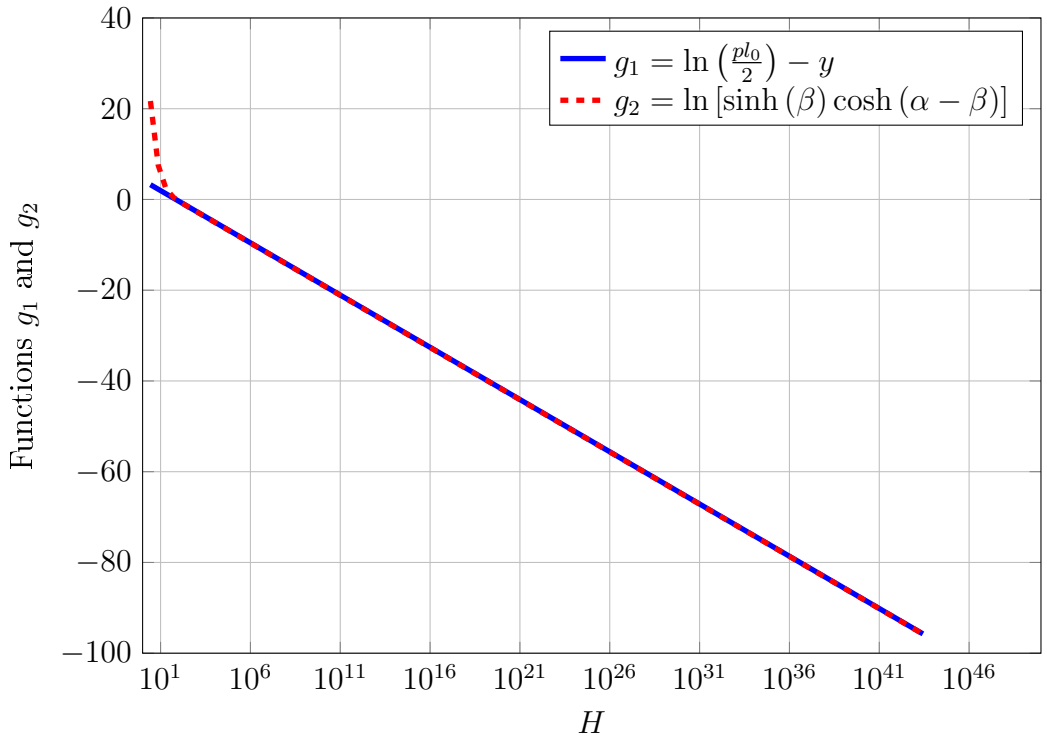

(a) Representation of the functions g_1 and g_2 in the logaritmic space

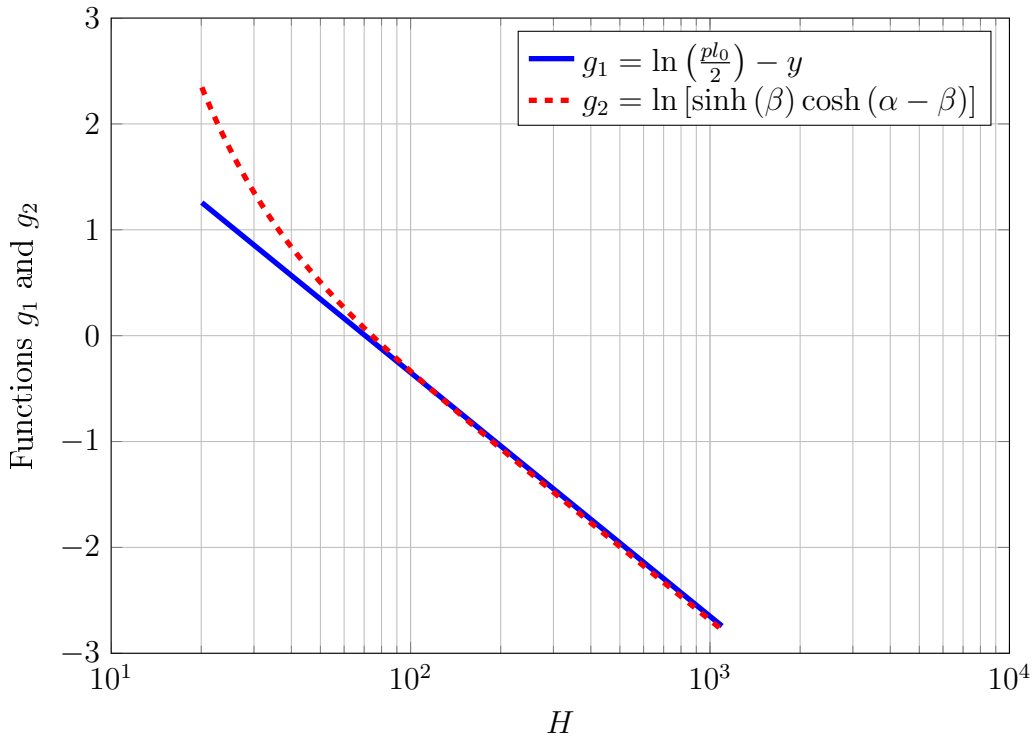

(b) Zoom in the zone of interest

Figure 6.18: The functions g_1 and g_2 only intersect one time and they both are monotonally decreasing

Due to the quadratic convergence of the algorithm implemented, the solution can be found quickly. Once the position and configuration of the unextensible catenary is found, the program reads the number of elements in which the cable is divided and computes the coordinates of the nodes. The procedure is repeated for each cable in the structure and the program automatically updates the necessary variables to take into account the nodes and elements that progressively appear for each cable descretization.

The program gets from the input the number of nodes and computes the coordinates of all of them considering they are uniformly spaced in the x' axis.

$$\boldsymbol{x} = \left[\begin{array}{cccc} x_1 & ... & x_n \end{array} \right] \rightarrow z_i = \frac{H}{p} \left[\cosh \alpha - \cosh \left(\frac{2\beta}{l} x_i - \alpha \right) \right] \quad \forall i = 1, \cdots, n \tag{6.61}$$

Although this procedure seems a rude approximation, it has been proved to be very effective and very accurate. Indeed, once the initial position of all cable has been determined, the iterative elastic problem can start considering the true geometrical properties of the cable elements. The catenary equation has been considered as the first approximation for solving the problem and allows the program to avoid ill-conditioning problems related with possible unstressed cable elements.

The explanation of step 4 (Define and mesh cable structure) can be summarized in the following flowchart.

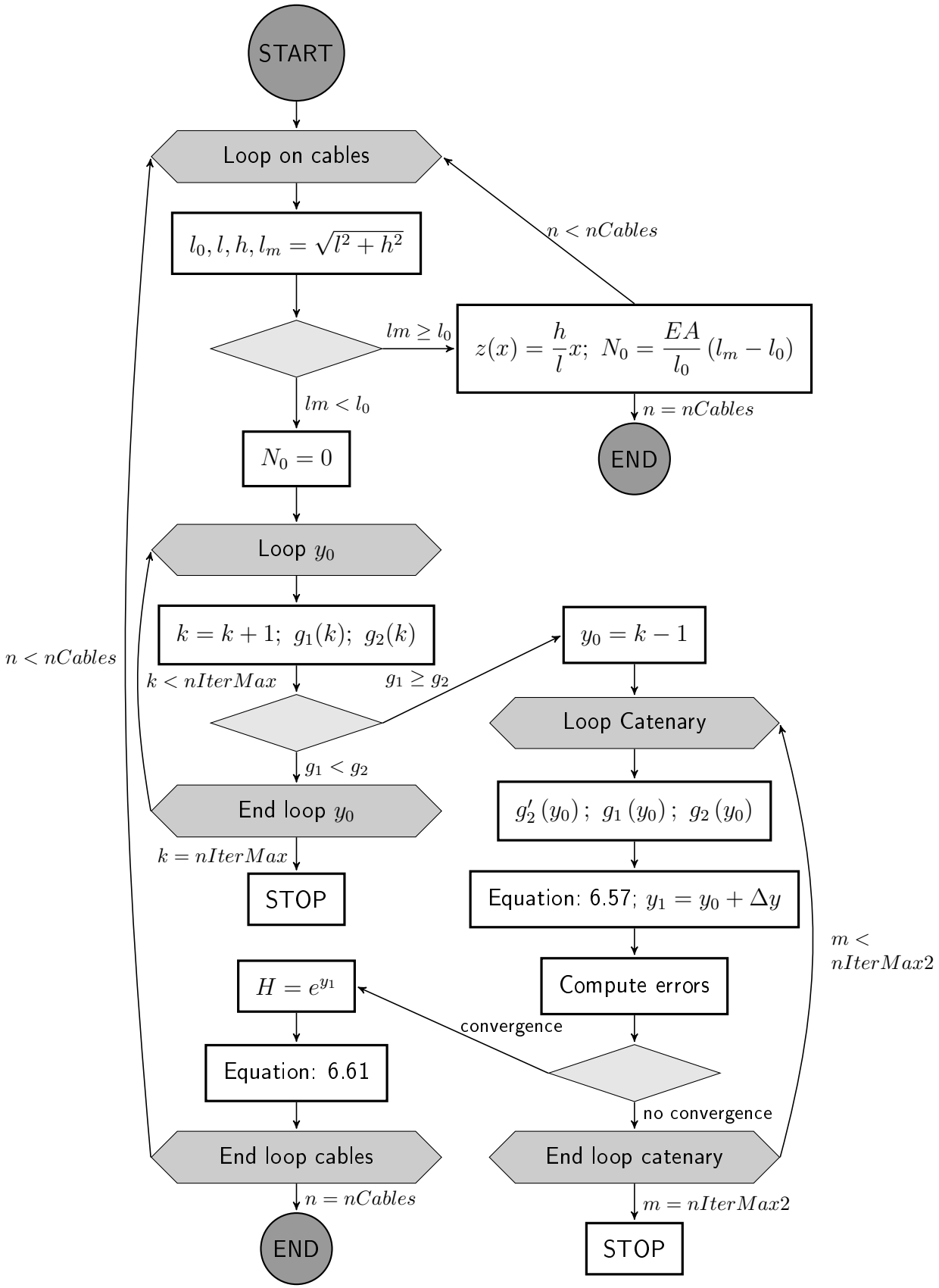

Figure 6.19: Flowchart of the procedure to create the elements and nodes of the cable structure

The program plots the initial configuration before starting the iterative procedure. Since the user does not choose directly the initial configuration of the overall system, the program plots it to allow the user to analyse possible problems. The flowchart of this part is omitted because it does not represent an important aspect in the resolutive procedure.

Once the initial configuration of the overall structure has been plotted, the program starts the so-called *Iterative procedure*. A stiffness procedure to solve the nonlinear equilibrium equations is launched.

The iterative procedure is the most computationally expensive part of the code and the program automatically saves the variables either there is either there is not convergence.

The last part of the program, the *Postprocessing*, is devoted to compute the stresses of each cable and beam element and print the output file. The procedure to compute the stresses is very simple. For each beam element, first the displacements of its nodes are identified from the displacement vector. After, the displacements are transformed considering the offsets that the elements may have and converted in the local reference system of the element. Considering $\boldsymbol{K_e}$, the local stiffness matrix previously stored during the iterative procedure, $\boldsymbol{v_e}$ the displacements of each node and $\boldsymbol{f_e}$ the equivalent nodal loads vector in the local reference system of the element, the stresses may be computed in the final configuration of the element as

$$\boldsymbol{\sigma} = \boldsymbol{K_e v_e} - \boldsymbol{f_e} \tag{6.62}$$

The value of the axial stress on each cable element can be easily computed. Indeed, one only needs to know the initial and final position of both nodes of the element, compute the increment (or decrement) of length and compute the axial strain and the axial stress with the constitutive equations of the material.

$$N = N_0 + \frac{EA}{l_0}\Delta l \tag{6.63}$$

To check the reliability and the performance of the program, some benchmarks are considered.

The benchmarks will be divided in two parts. First, beam strucures in contact with a fluid and with no cables anchorage system will be analysed. Second, frame floating structures will be analysed under vertical and horizontal loads.

6.6 Benchmarks

First, the sections used in the benchmarks will be presented and a brief discussion about their consitutive equations is presented. Later, floatability analysis of constant cross section beam elements is presented.

In the last part, a comparison between the analysis of a floating beam with the new finite element model and the analysis of the same beam with the Winkler model is carried out.

6.6.1 Sections and constitutive equations

Section 1: Rectangular section

The rectangular section is shown in figure 6.20.

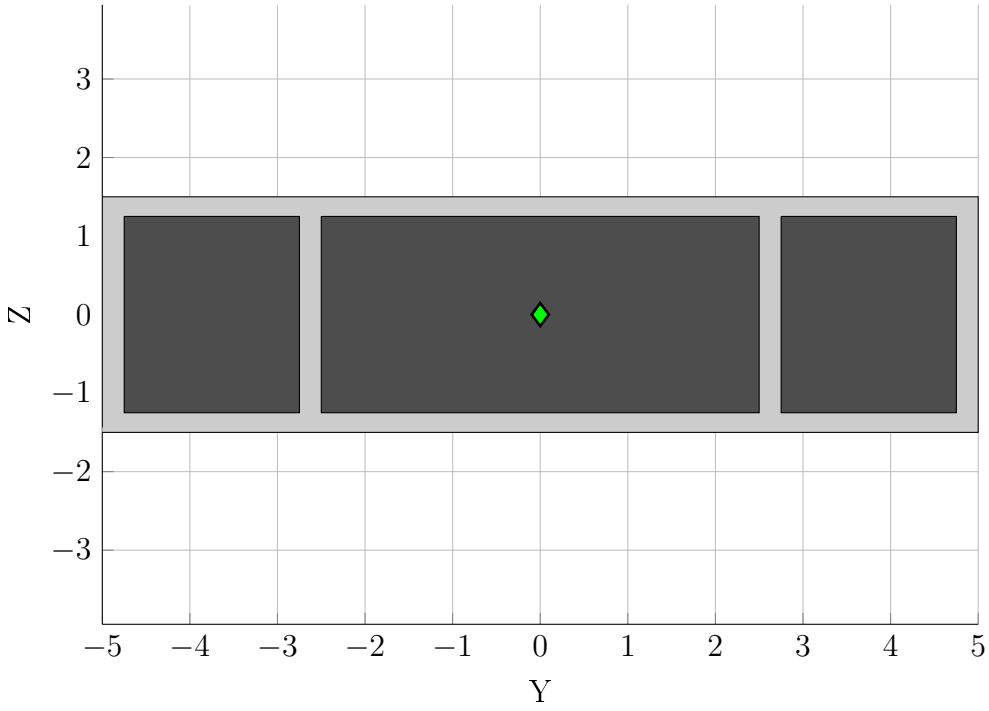

Figure 6.20: Section 1 - Rectangular section used in the benchmarks

The rectangular section has a very simple consitutive equation. Indeed, considering the equation 5.57 and 5.59, the constitutive equation of the rectangular section may be written as:

$$F_z = \overline{p}\eta = lh\gamma_f \frac{z}{h} = l\gamma_f z \tag{6.64}$$

with z the coordinate that starts at the bottom point of the section and and goes upside.

Section 2: Trapezoidal section

The trapezoidal section is shown in figure 6.21.

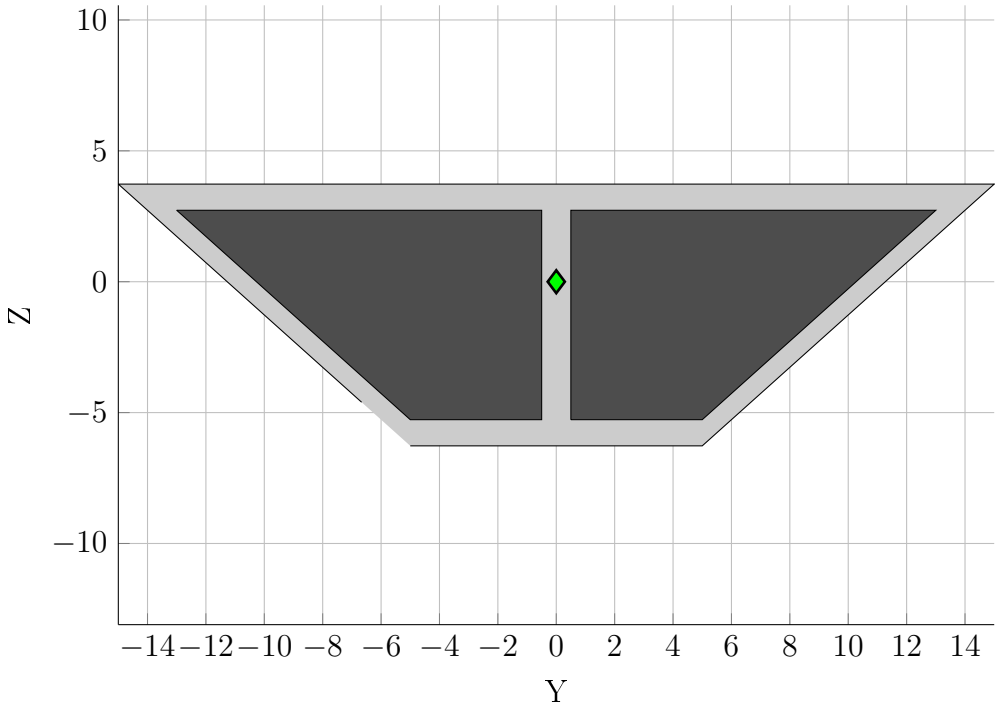

Figure 6.21: Section 2 - Trapezoidal section used in the benchmarks

The trapezoidal section has a more complex consitutive equation. Indeed, considering the equation 5.70 and 5.73, we may written the constitutive equation of our trapezoidal section as

$$F_z = \overline{p} f_z = \frac{\gamma_f z}{2}\left(2l_b + \frac{l_t - l_b}{2} z\right) \tag{6.65}$$

6.6.2 Analysis of beam structures in contact with a fluid

6.6.2.1 Benchmark 1

The first benchmark is the study of the flotability capacity of a 100 meters long beam with a rectangular section as the one depicted in figure 6.22.

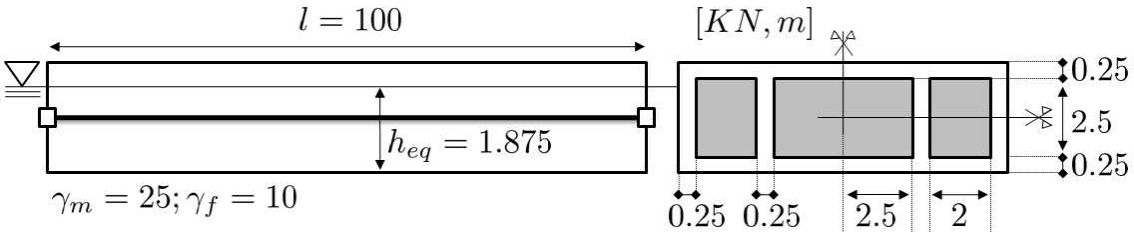

Figure 6.22: Beam benchmark 1 - Flotability analysis of a beam with a rectangular section

The main goal is to compute the floating equilibrium position of this beam. This will be done integrating the hydrostatic pressure along the boundary (not inside the holes, since the section of this beam is isolated). A simple calculation allows to predict

the equilibrium floating position h_{eq}. Considering the vertical equilibrium equation, the hydrostatic load will have to counteract the weight of the beam, so it can be written

$$h_{eq} b \gamma_f l = \gamma_m A_s \gamma_m l \rightarrow h_{eq} = \frac{A_s}{b} \frac{\gamma_m}{\gamma_f} \tag{6.66}$$

Considering the properties of the section, the equilibrium position can be computed.

$$A_s = 7.5; \quad b = 10 \rightarrow h_{eq} = 1.875 \tag{6.67}$$

The program will use the constitutive equation of the rectangular section previously reported and, addopting a secant scheme, the same value is obtained. Indeed, from equation 6.64 the stiffness with respect the initial configuration may be computed as

$$F_z = K(z)\, z \rightarrow K(z') = \gamma_f l \tag{6.68}$$

A very interesting conclusion is that the floating structures with rectangular section have a constant buoyancy stiffness which directly depends on the thickness of the section and the selfweight of the fluid. This leads to a linear problem that can be easily solved.

6.6.2.2 Benchmark 2

A flotability analysis of a beam with a trapezoidal section is performed. Due to the non-linear constitutive equations of the trapezoidal section, the program needs some iterations to obtain the solution of the analysis. The beam is depicted in figure 6.23.

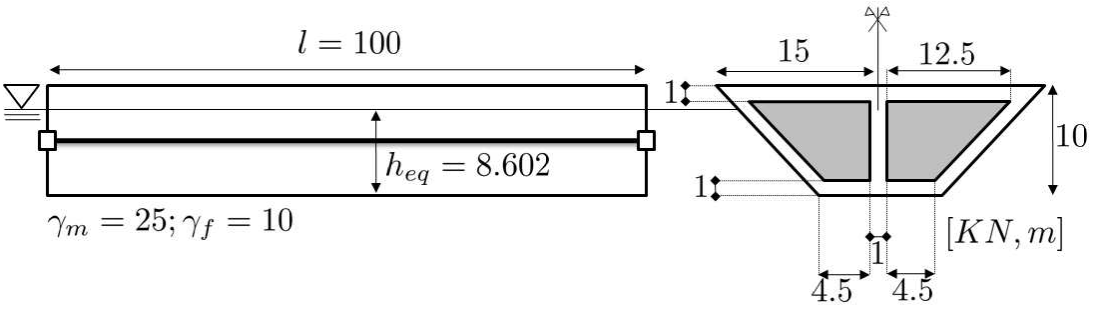

Figure 6.23: Beam benchmark 2 - Flotability analysis of a beam with a trapezoidal section

Considering the same procedure adopted in the previous benchmark, the final equilibrium floating position can be computed making the equivalence between the resulting of the hydrostatic load and the weight of the beam.

$$F_z = \gamma_m A_s \rightarrow \alpha h_{eq} + h_{eq}^2 = \beta \tag{6.69}$$

with

$$\alpha = \frac{2 l_b h}{l_t l_b} \qquad \beta = \frac{2 \gamma_m A_s h}{\gamma_f (l_t - l_b)}$$

The solution of this equation is

$$h_{eq} = \frac{\alpha \pm \sqrt{\alpha^2 + 4\beta}}{2} \tag{6.70}$$

and substituting the numerical values of the benchmark and considering the positive solution we obtain

$$h_{eq} = 8.602 \tag{6.71}$$

Figure 6.24 shows the iterative procedure performed with the stiffness method, figure 6.25 shows the buoyancy stiffness during the procedure, figure 6.26 shows the equilibrium floating position during the iterative process, figure 6.27 shows the external force (weight of the beam per unit length) and the reaction (hydrostatic load per unit length) of the system as a function of the iterations and the last figure (figure 6.28) shows the final configuration of the beam floating in the fluid.

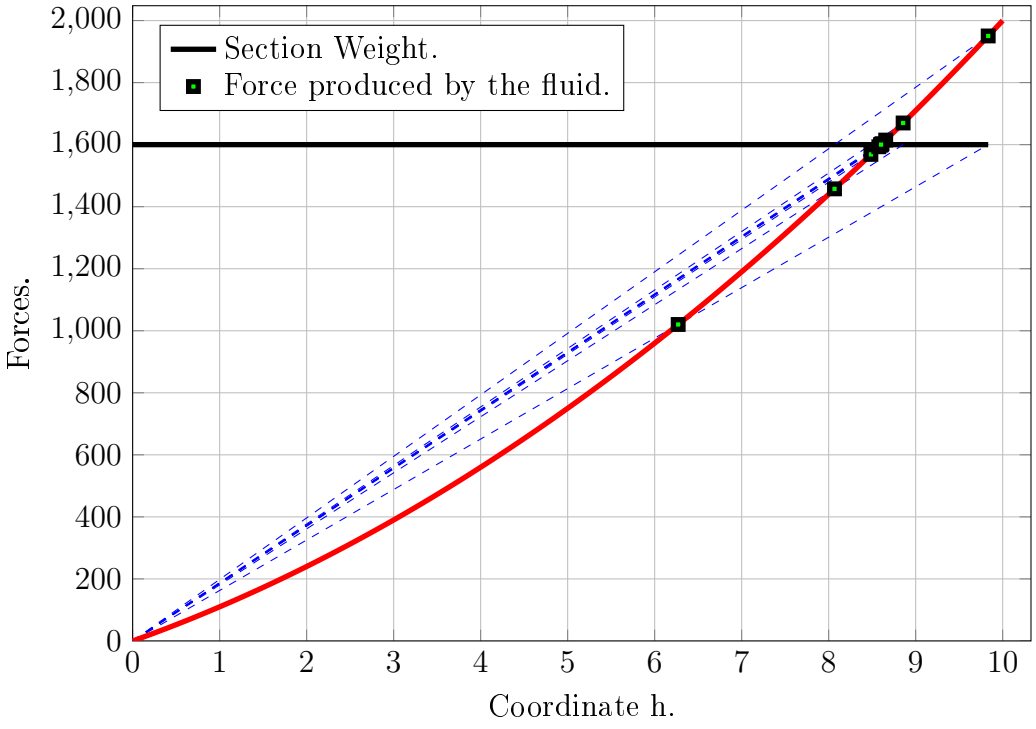

Figure 6.24: Benchmark 2 - Iterative procedure in the flotability analysis

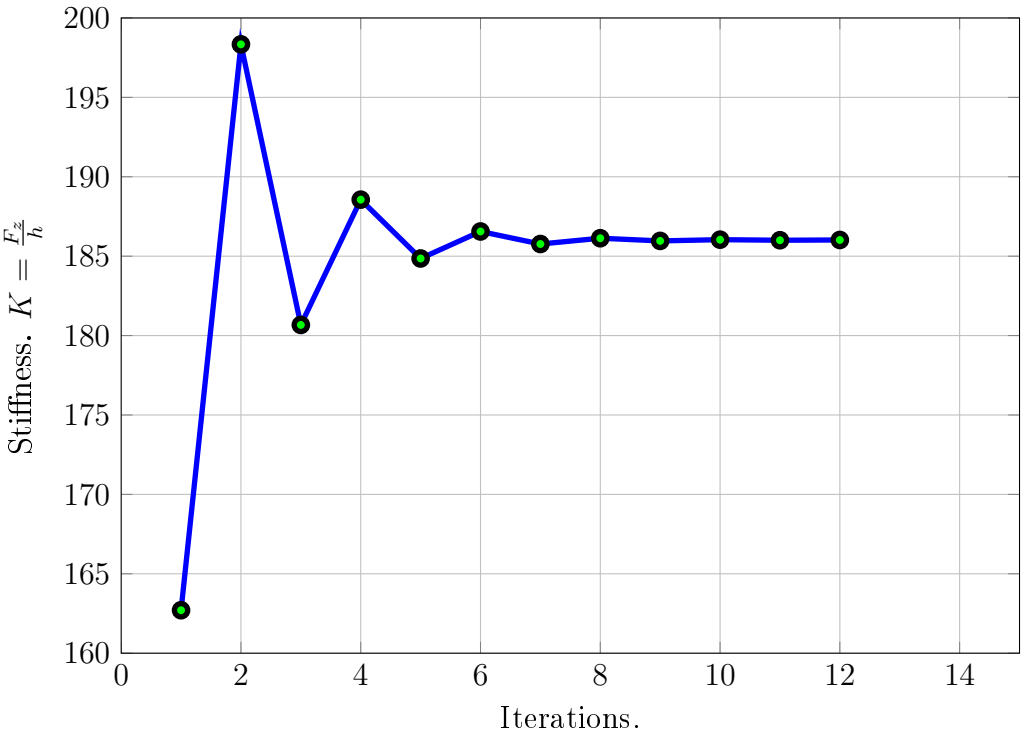

Figure 6.25: Benchmark 2 - Buoyancy stiffness during the flotability analysis

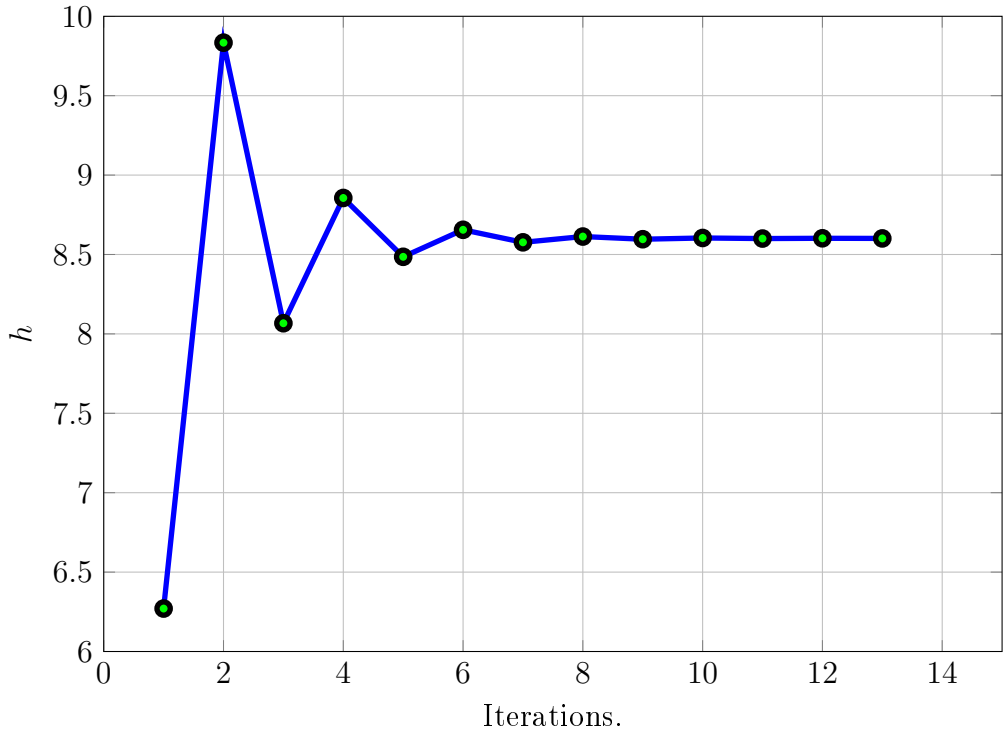

Figure 6.26: Benchmark 2 - Value of the equilibrium floating position during the iterative procedure

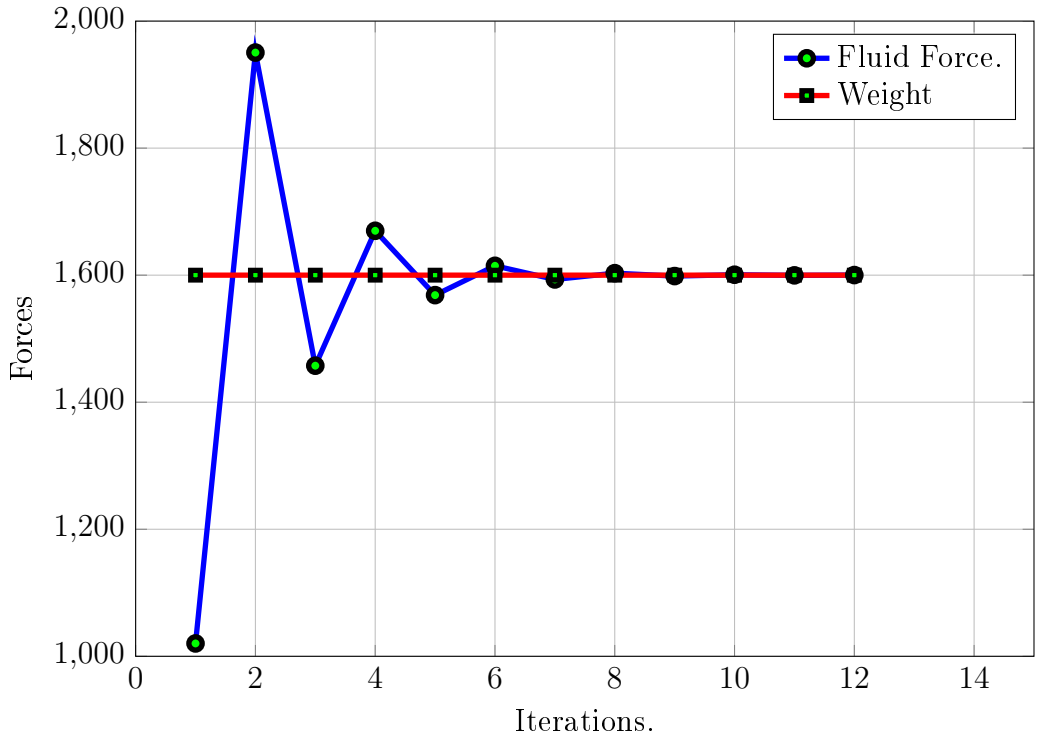

Figure 6.27: Benchmark 2 - Archimedes force and weight during the procedure analysis

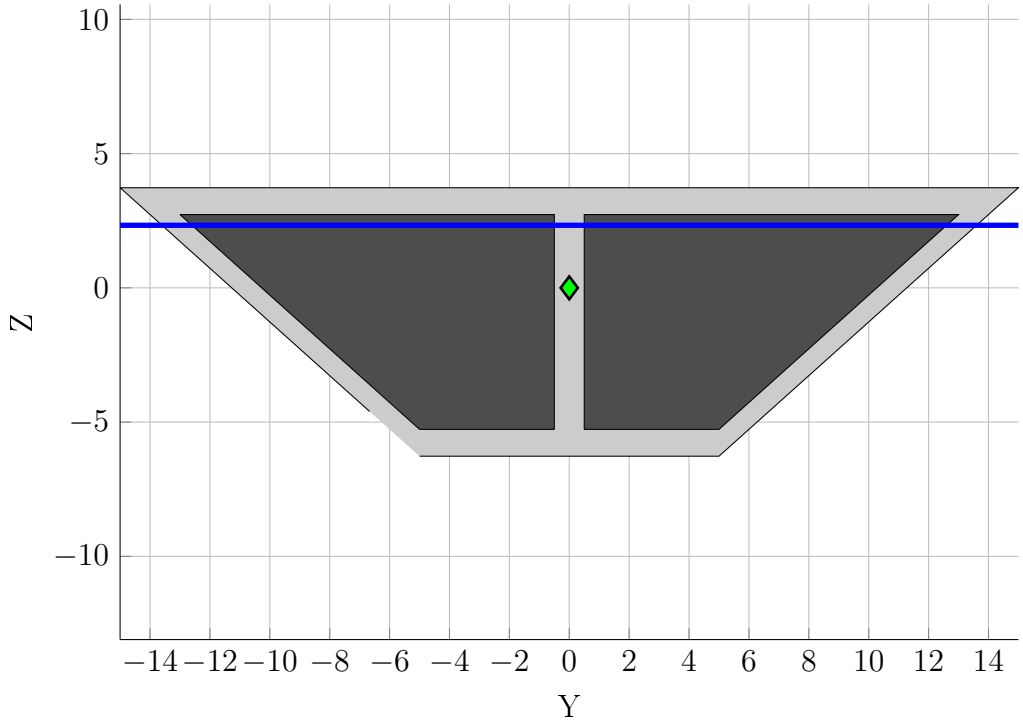

Figure 6.28: Benchmark 2 - Final equilibrium floating position of the beam

6.6.2.3 Benchmark 3

The last benchmark concerning the interaction between floating structures and a fluid surrounding them is a long beam simply supported in a fluid's free surface under a concentrated vertical load in the middle. The section of the beam will be the one in figure 6.20.

The Winkler model will be also used to analyse the same beam on elastic foundation with the same vertical stiffness as the one computed in this benchmark[(3)].

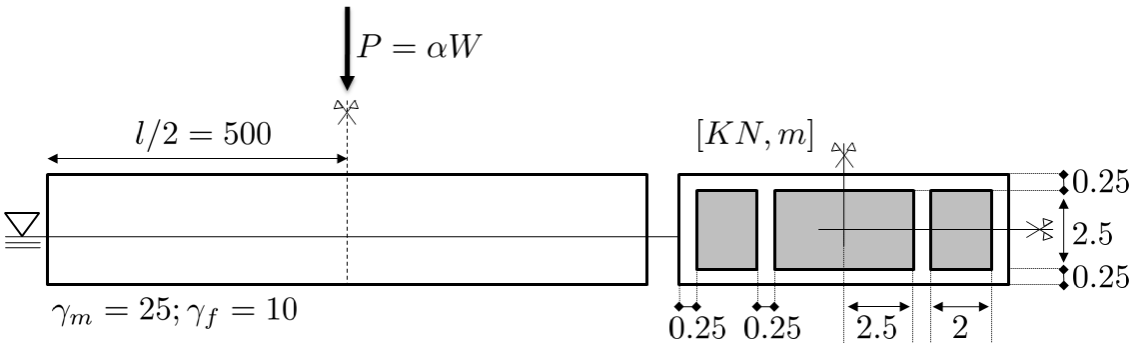

Figure 6.29: Benchmark 3 - Floating beam under a concentrated load in the middle

To ensure the floatability capacity of the beam, a concentrated load P proportional to the total weight of the beam W will be applied considering the restriction

$$W + \alpha P < \gamma_f A_s l \tag{6.72}$$

This equation means that the total vertical load can not exceed the maximum hydrostatic reation produced by the fluid. Otherwise, the beam will not be able to float and the solution will diverge.

To perform the analysis with the Winkler model, it is needed to ensure the accuracy of the solution. Therefore, a sensitivity analysis changing the number of elements will be performed, until the displacement in the middle reaches a constant value. Once the solution of the Winkler model is obtained, the analysis will be performed with the new finite element model and a comparison in terms of displacements and stresses at specific points will be performed.

The model can be simplified exploiting the symmetry. Indeed, the geometry of the problem can be reduced and only half beam needs to be analyzed. The following figure shows the finite element model used in the finite element analysis.

(3) Remember that the buoyancy stiffness in the vertical direction of a rectangular section is constant, so this kind of problem can be modelled with a Winkler model and the results will coincide.

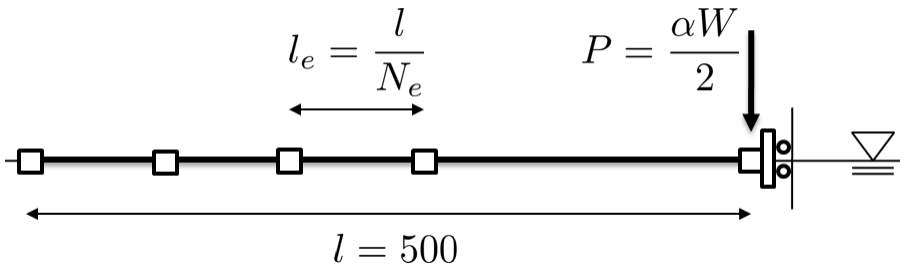

Figure 6.30: Benchmark 3 - Finite element model used in the analysis of the third benchmark

The sensitivity analysis of the Winkler problem is presented. In figure 6.31 the variation of vertical displacement computed at the right end of the beam is plotted as a function of the number elements along the beam.

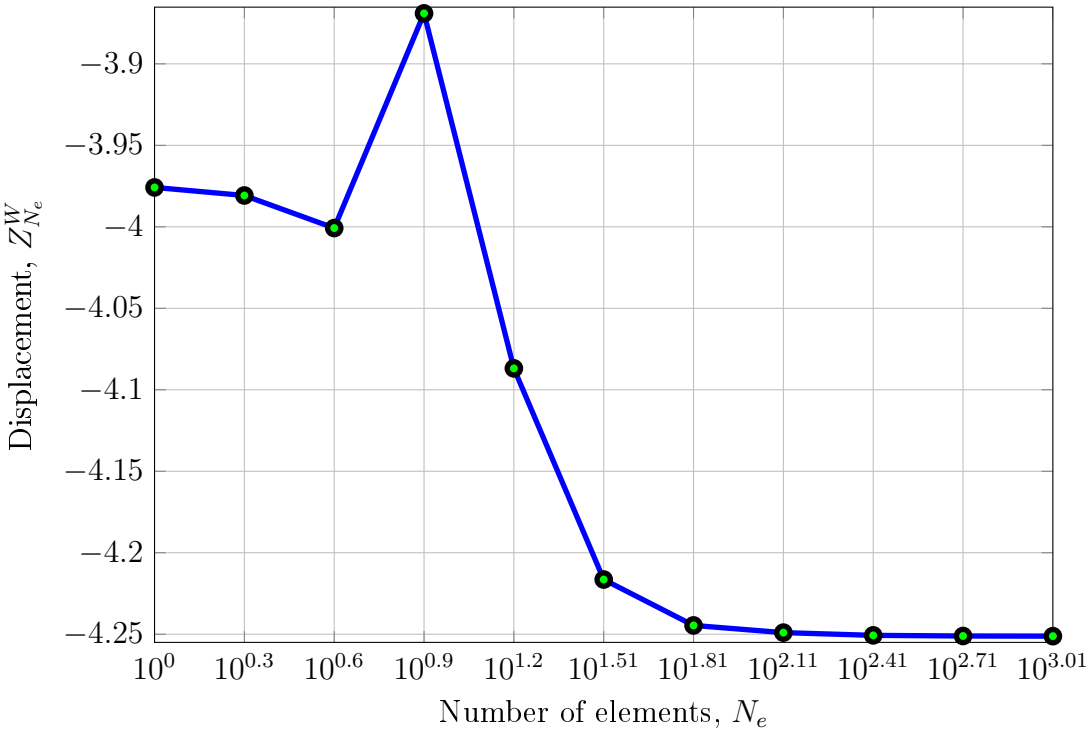

Figure 6.31: Benchmark 3 - Variation of the vertical displacements in the right edge in terms of the number of elements along the beam using the Winkler model

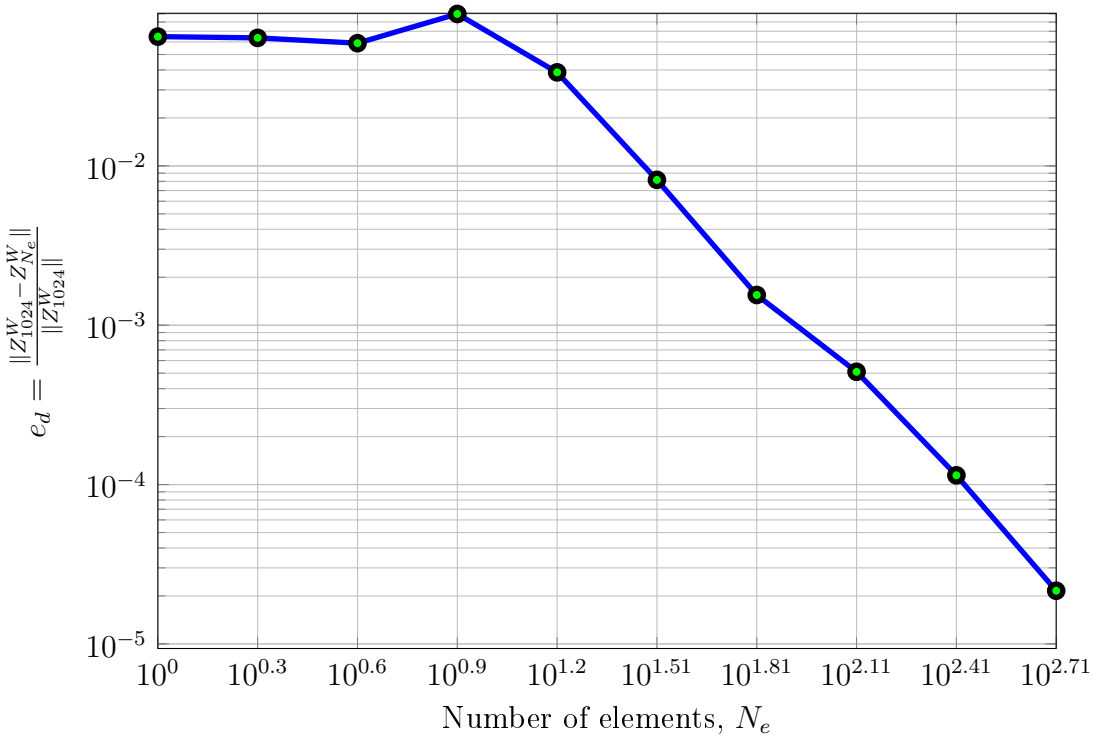

Figure 6.32: Benchmark 3 - Error of the vertical displacement increasing the number of elements in the mesh using the Winkler model

Considering that after 128 elements the displacement remains almost constant, the error can be computed with respect to the mesh of 1024 elements as it has been made in figure 6.32.

As a conclusion of the sensitivity analysis, it can be said that the solution is enoughly accurated after $n_e = 512$ elements. The analysis will be performed using the new finite element formulation and the results will be compared in terms of displacement and bending moment at the right end of the beam.

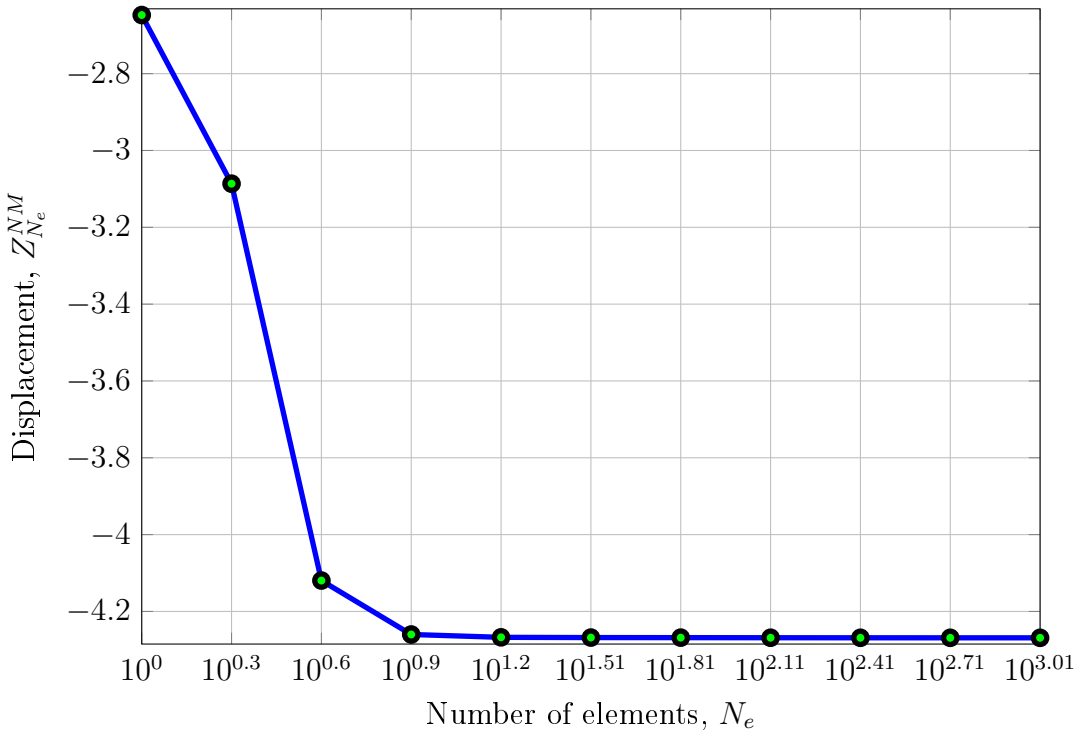

Figure 6.33: Beam benchmark 3 - Vertical displacements in the right edge of the beam using the new finite element model

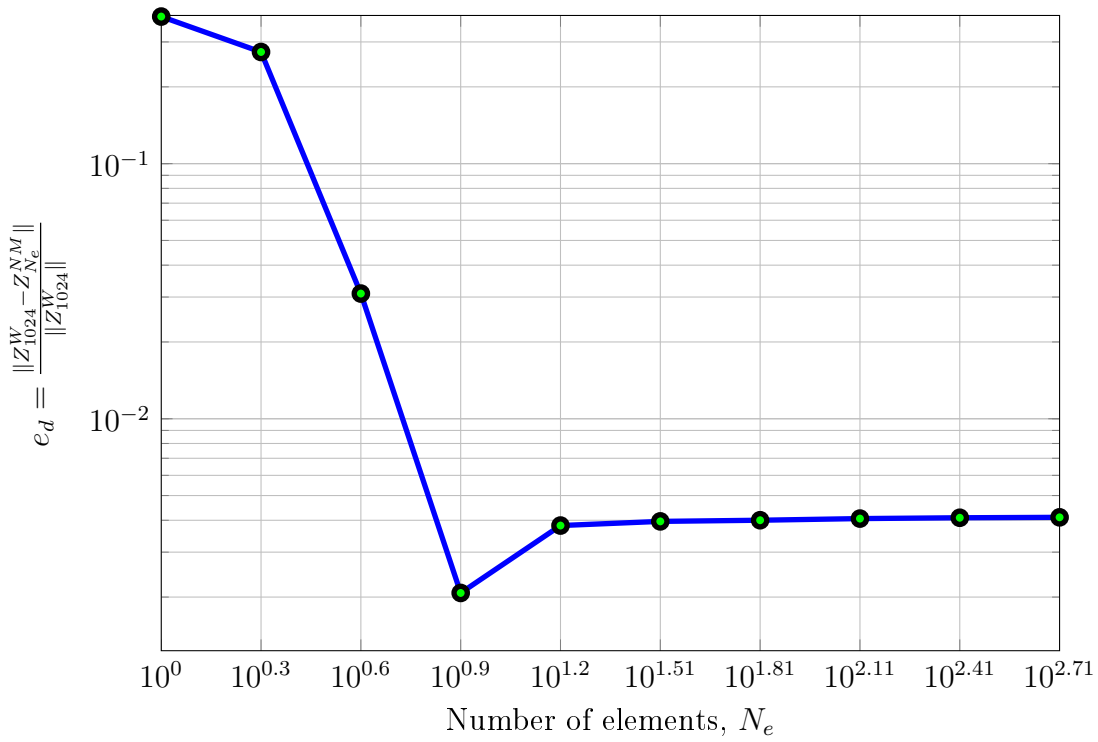

Figure 6.34: Beam benchmark 3 - Error of the new finite element model with respect the solution of the Winkler model

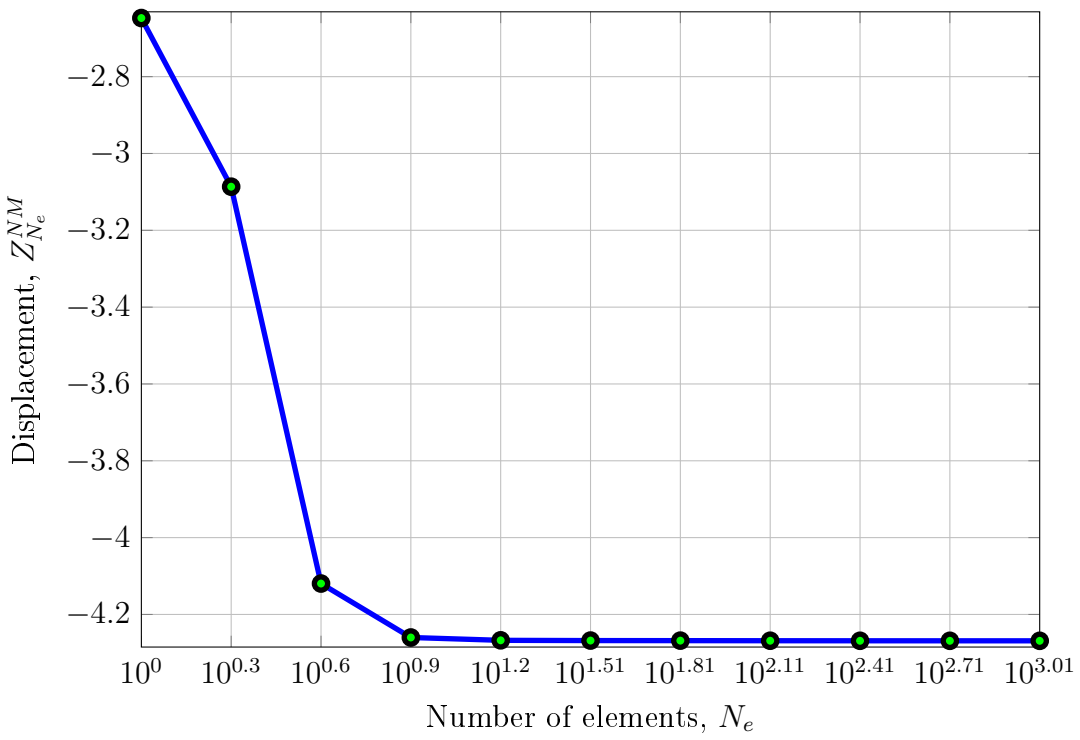

Figure 6.35: Beam benchmark 3 - Vertical displacements in the right edge of the beam using the new finite element model

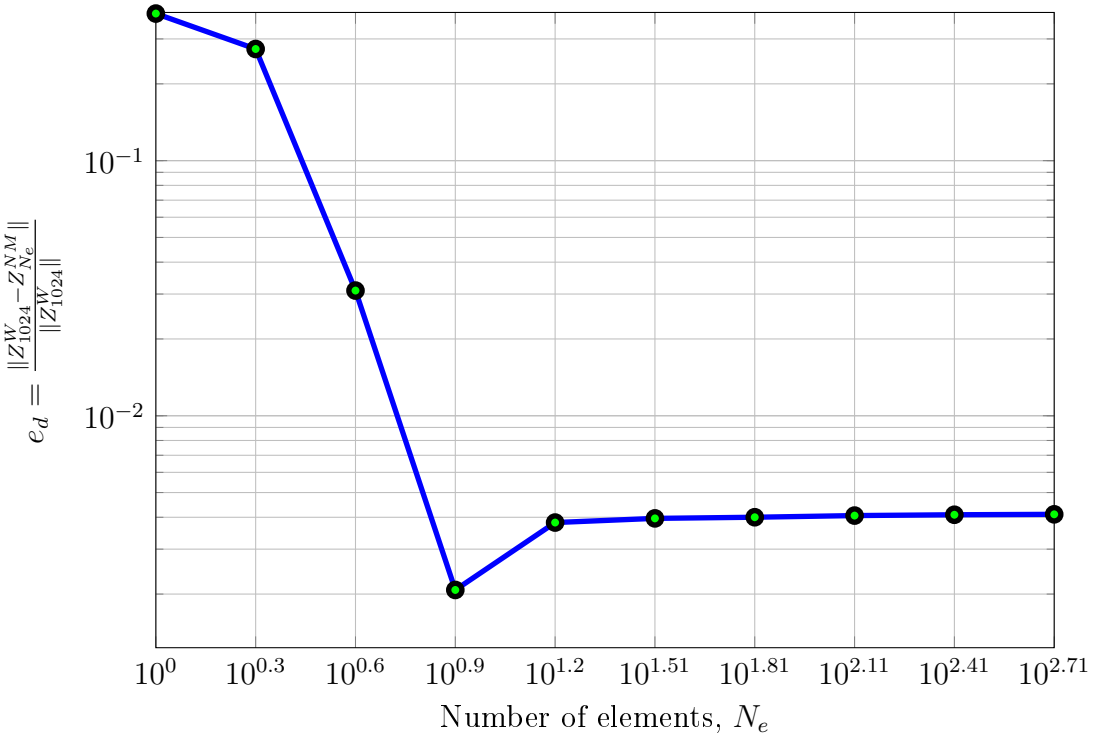

Figure 6.36: Beam benchmark 3 - Error of the new finite element model with respect the solution of the Winkler model

We can deduce that the new finite element model developed is more accurate and computationally less expensive than the Winkler's one because the results are accurate enough with a lower number of elements.

6.7 Practical applications

The benchmarks have proved the reliability of the new finite element model.

Therefore, real applications of the new finite element model will be performed considering typical situations of floating structures.

6.7.1 Analysis of a floating bridge during the passage of a truck

A floating bridge with no anchoring system is analysed under the action of a moving vehicle. The analysis will be performed considering the velocity of the vehicle small in order to consider a static problem.

The bridge is restrained on the left part. Usually, this kind of structures are not completely restrained because they must be able to somehow follow the possible variation in the level of the fluid (an example is the variation of the sea level when strong tides are presented). To properly model this, floating structure are usually connected to the coast allowing the relative vertical displacement in the conection.

On the opposite side of the bridge, a completely free edge is imposed because usually the construction must be built allowing possible horizontal displacements that the bridge may suffer (for example, due to thermic expansion or horizontal loads). Otherwise, the floating structure could suffer some spurious stresses. The scheme of the bridge is presented in figure 6.37.

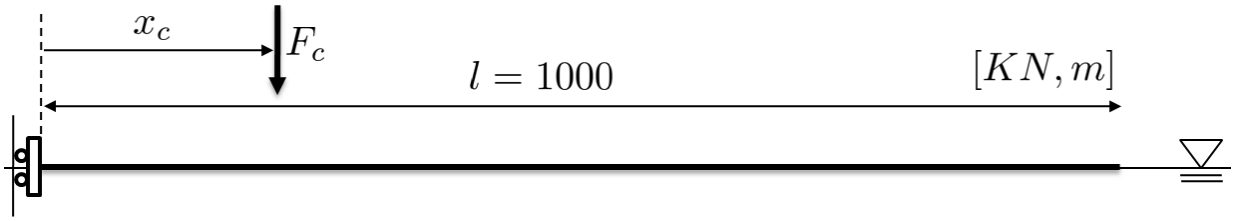

Figure 6.37: Practical applications 1 - Analysis of a floating bridge under the action of a moving vehicle

The section of the bridge is depicted in figure 6.21 The concentrated vertical load F_c represents a vehicle that moves from the right side to the left side. Its value has been considered equal to $F_c = 300\ KN$ (which is the weight of a truck with 30 tones mass). The results will be presented in terms of displacements and stresses and the coupling between the axial and bending behaviour will be highlighted.

The following figures represent the distribution of the bending moment and shear stress along the span of the bridge when the truck is situated at $x_c = 0$ (figures 6.39 and 6.38)

$x_c = 250$ (figures 6.41 and 6.40), $x_c = 500$ (figures 6.43 and 6.42), $x_c = 750$ (figures 6.45 and 6.44) and $x_c = 1000$ (figures 6.47 and 6.46) meters from the left edge respectively.

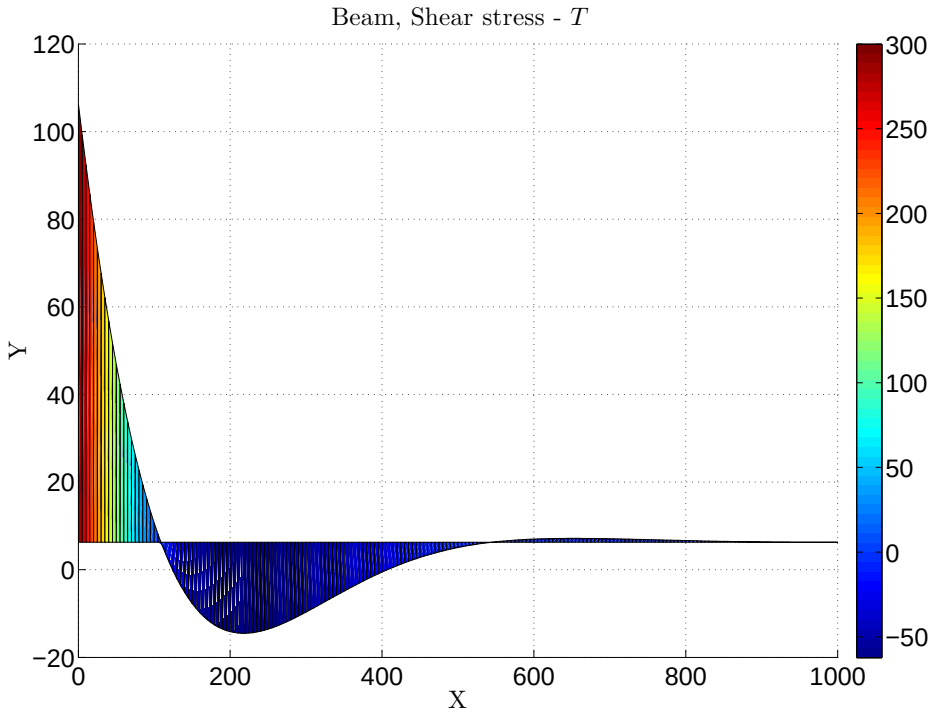

Figure 6.38: Practical applications 1 - Shear distribution along the bridge with the truck positioned at $x_c = 0$ meters from the left edge

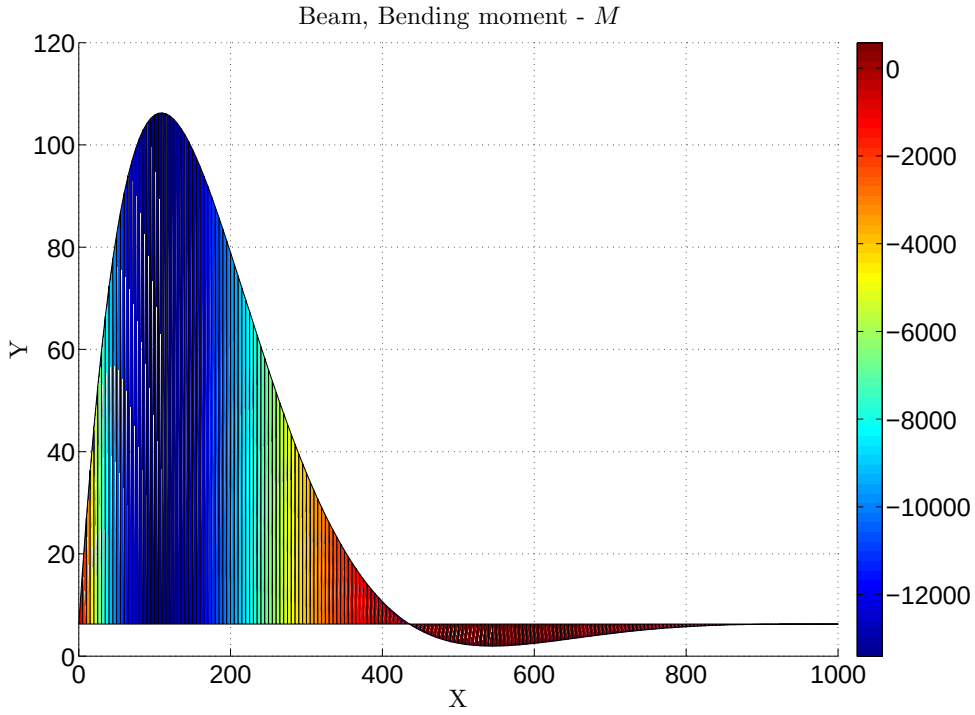

Figure 6.39: Practical applications 1 - Bending moment distribution along the bridge with the truck positioned at $x_c = 0$ meters from the left edge

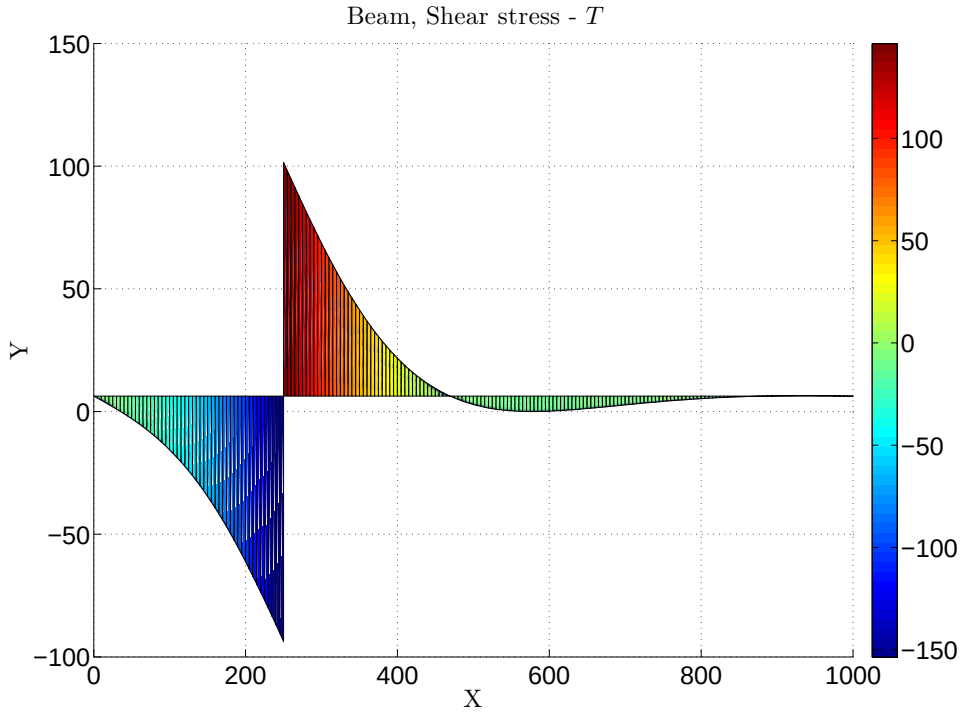

Figure 6.40: Practical applications 1 - Shear distribution along the bridge with the truck positioned at $x_c = 250$ meters from the left edge

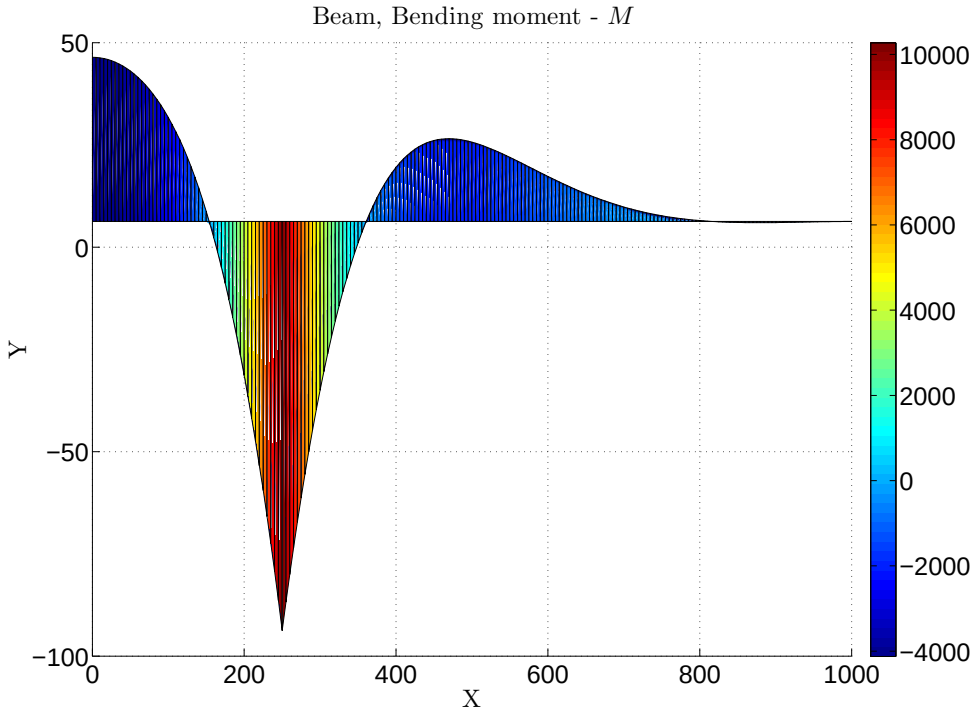

Figure 6.41: Practical applications 1 - Bending moment distribution along the bridge with the truck positioned at $x_c = 250$ meters from the left edge

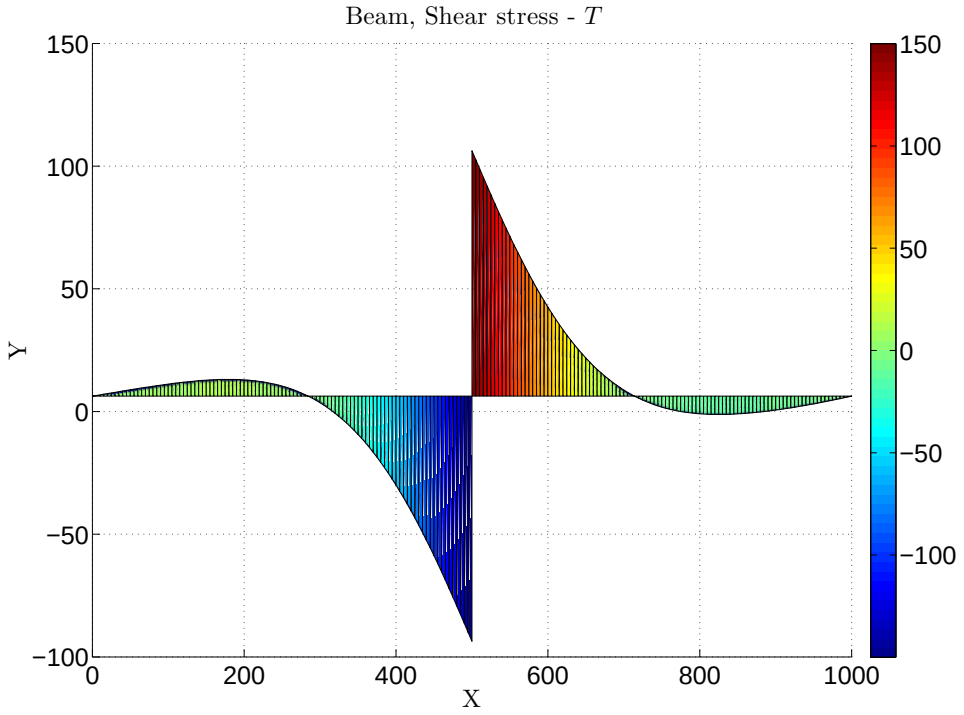

Figure 6.42: Practical applications 1 - Shear distribution along the bridge with the truck positioned at $x_c = 500$ meters from the left edge

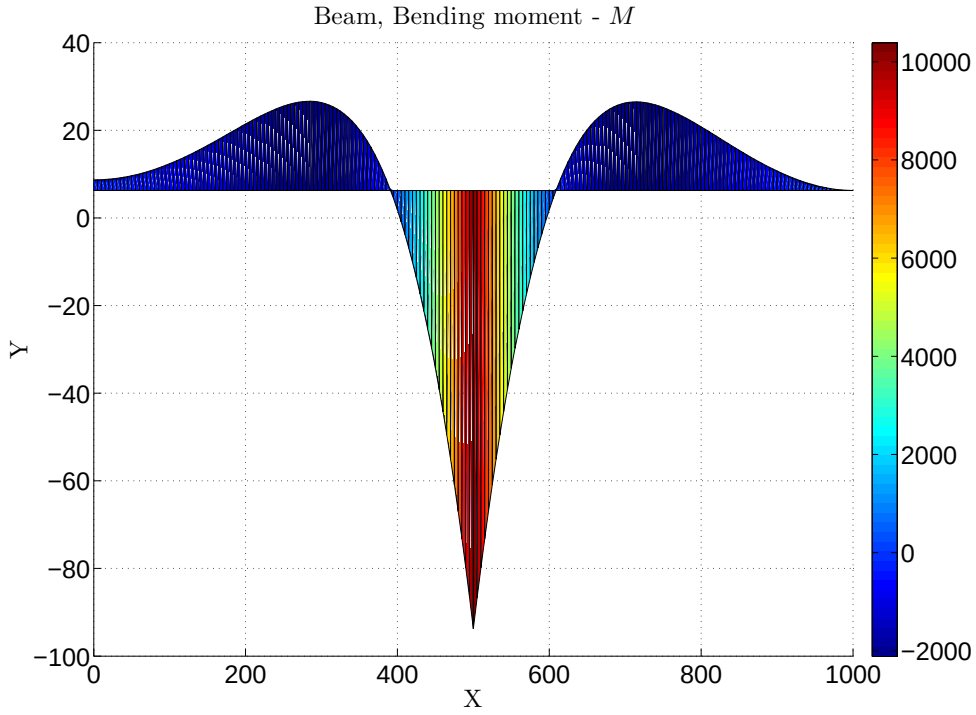

Figure 6.43: Practical applications 1 - Bending moment distribution along the bridge with the truck positioned at $x_c = 500$ meters from the left edge

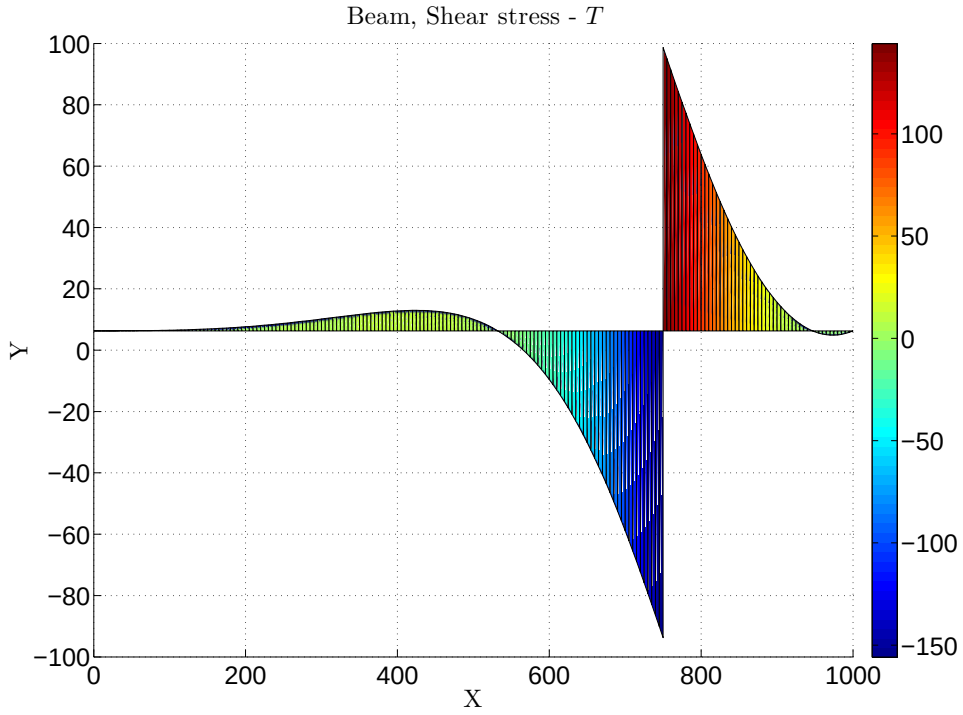

Figure 6.44: Practical applications 1 - Shear distribution along the bridge with the truck positioned at $x_c = 750$ meters from the left edge

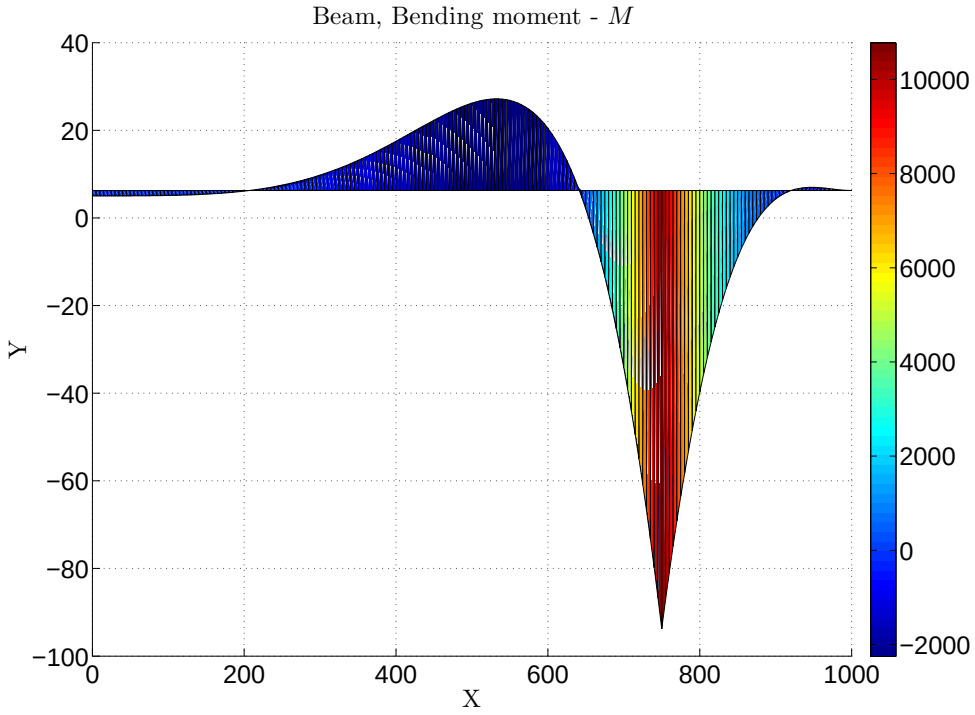

Figure 6.45: Practical applications 1 - Bending moment distribution along the bridge with the truck positioned at $x_c = 750$ meters from the left edge

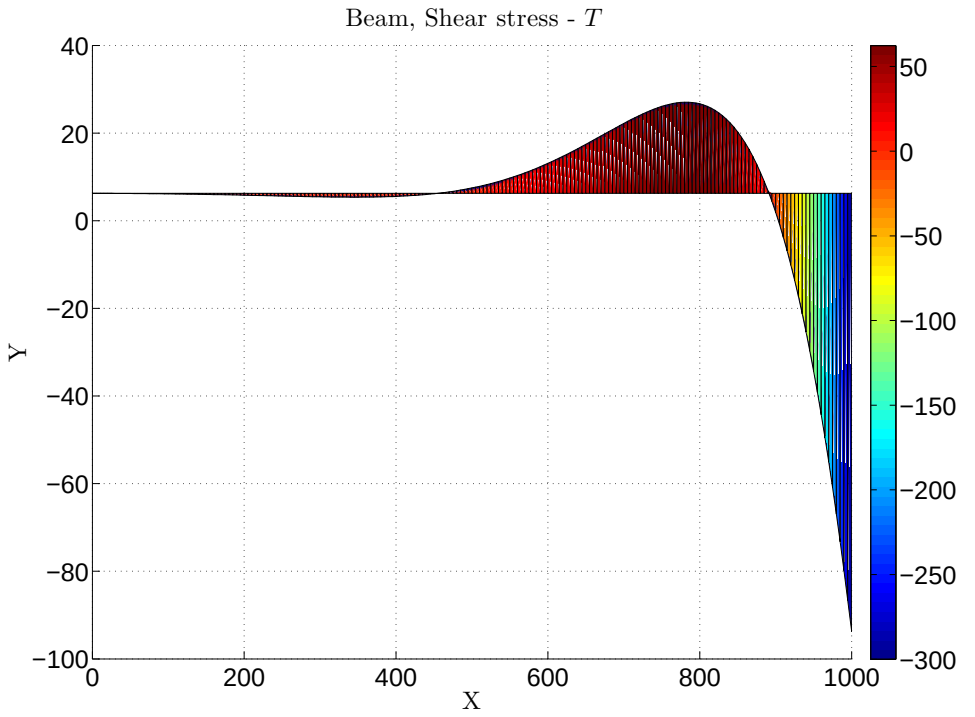

Figure 6.46: Practical applications 1 - Shear distribution along the bridge with the truck positioned at $x_c = 1000$ meters from the left edge

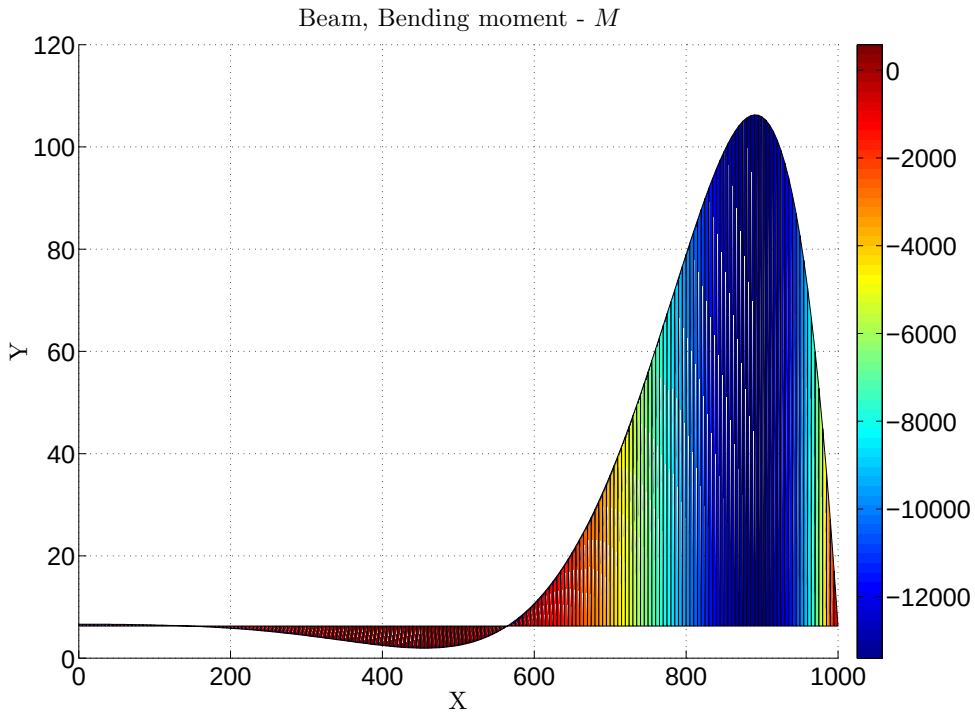

Figure 6.47: Practical applications 1 - Bending moment distribution along the bridge with the truck positioned at $x_c = 1000$ meters from the left edge

The analysis of a truck moving from the left edge to the right edge of the bridge has been carried out and the bending moment and shear stress in important points of the bridge are depicted in the following figures. Figure 6.48 shows the bending moment acting on the left edge of the bridge and figures 6.50 and 6.49 shows the shear stress and bending moment acting on the middle of the bridge respectively.

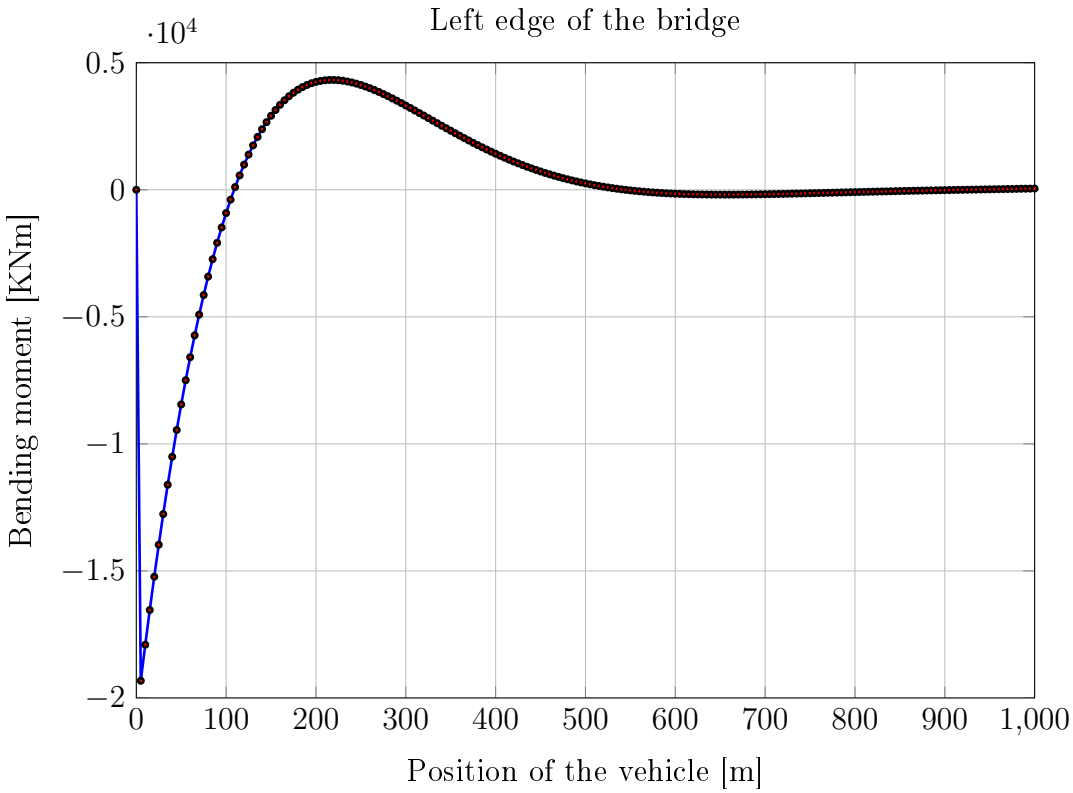

Figure 6.48: Practical applications 1 - Bending moment in the left edge of the bridge as a function of the position of the vehicle

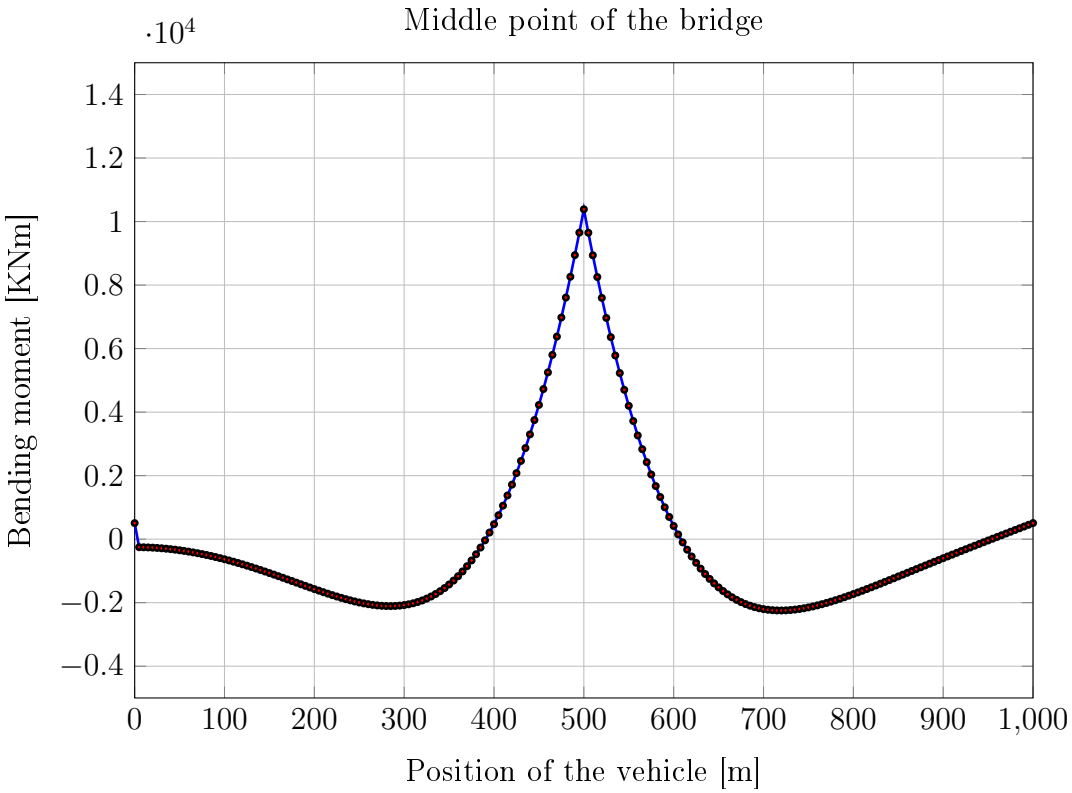

Figure 6.49: Practical applications 1 - Bending moment in the middle of the bridge as a function of the position of the vehicle

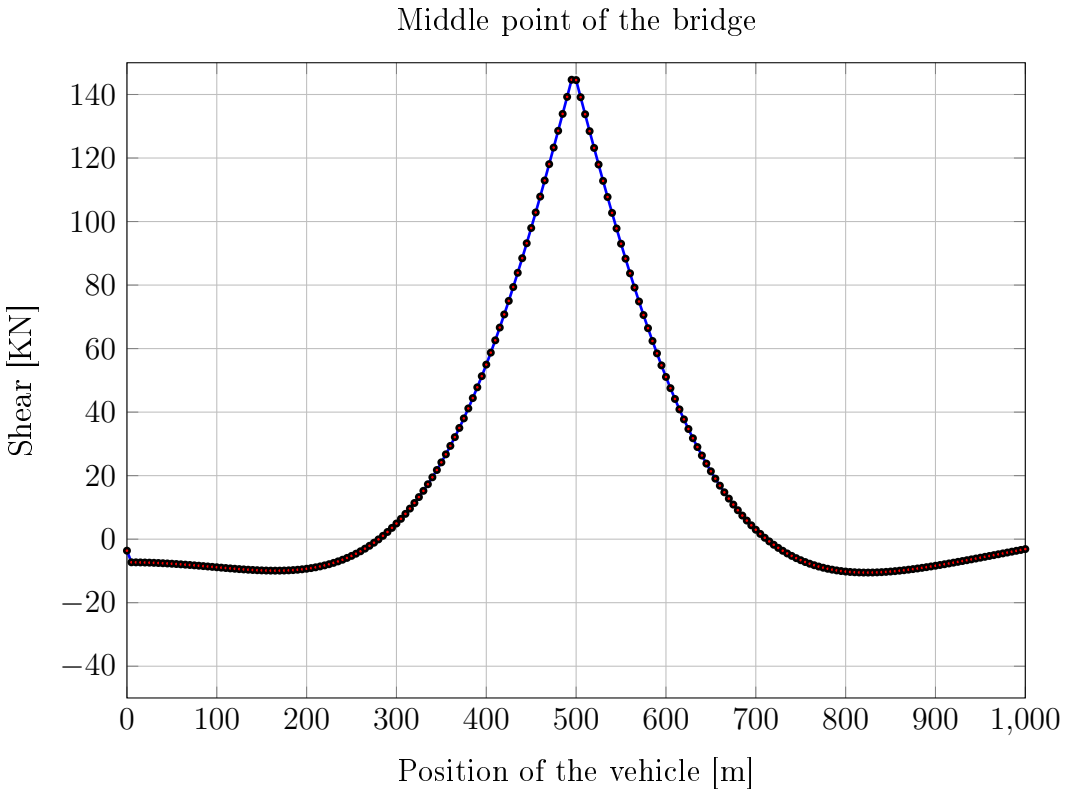

Figure 6.50: Practical applications 1 - Shear in the middle of the bridge as a function of the position of the vehicle

6.7.2 Analysis of a floating bridge under critical loads

The same bridge will be now analysed considering a completely restrained edge in the left part. The geometrical and mechanical properties remains constant with respect the previous applications.

In this application, the flotability capacity of the bridge will be tested. A certain number of trucks will be positioned along the bridge to produce a vertical load near to the maximum load capacity of the bridge[(4)]. Considering the weight and that the bridge is opportunely protected against the fluid penetration, we are able to compute the critical load of the bridge, listed in the following table.

γ_m $[KN/m^3]$	A_s $[m^2]$	l $[m]$	γ_f $[KN/m^3]$	A_t $[m^2]$
25	64	1000	10	200
Weight of the bridge $[KN]$			1.6e6	
Maximum Archimedes reaction $[KN]$			5e6	
Critical load of the bridge $[KN]$			**3.4e6**	

Table 6.1: Critical vertical load of the bridge

[(4)] Remember that every floating structure has a critical load considered as the load that the buoyancy hydrostatic reaction is not able to counteract.

In figure 6.51 the scheme of the bridge is depicted.

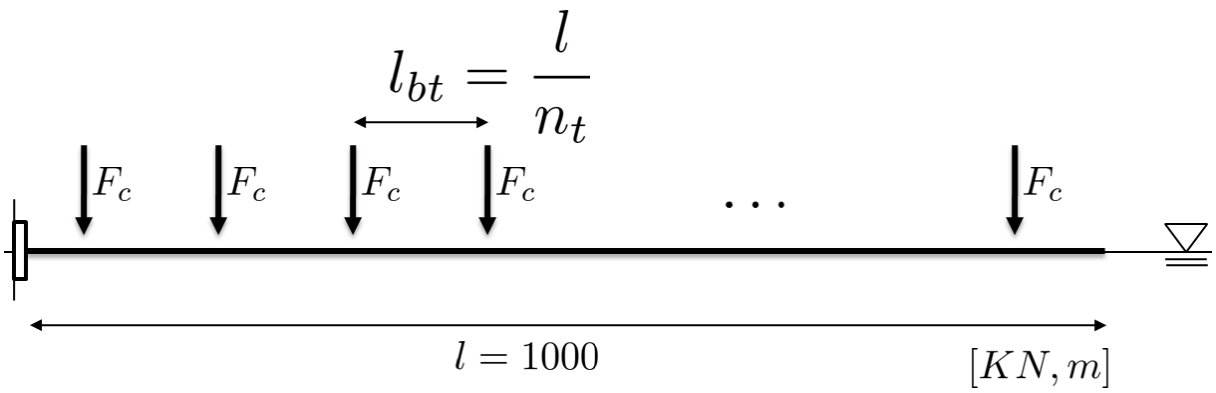

Figure 6.51: Practical applications 2 - Analysis of a floating bridge under the action of several trucks uniformly distributed along the bridge

The following analysis has been performed considering a distributed load along the bridge equal to $p_c = 100\,[KN/m]$, which is equivalent to place 200 trucks of 50 tones each one separated by a distance of 5 meters. Figure 6.52 shows the deformed configuration and figures 6.53 and 6.54 show the distribution of bending moment and shear force along the bridge.

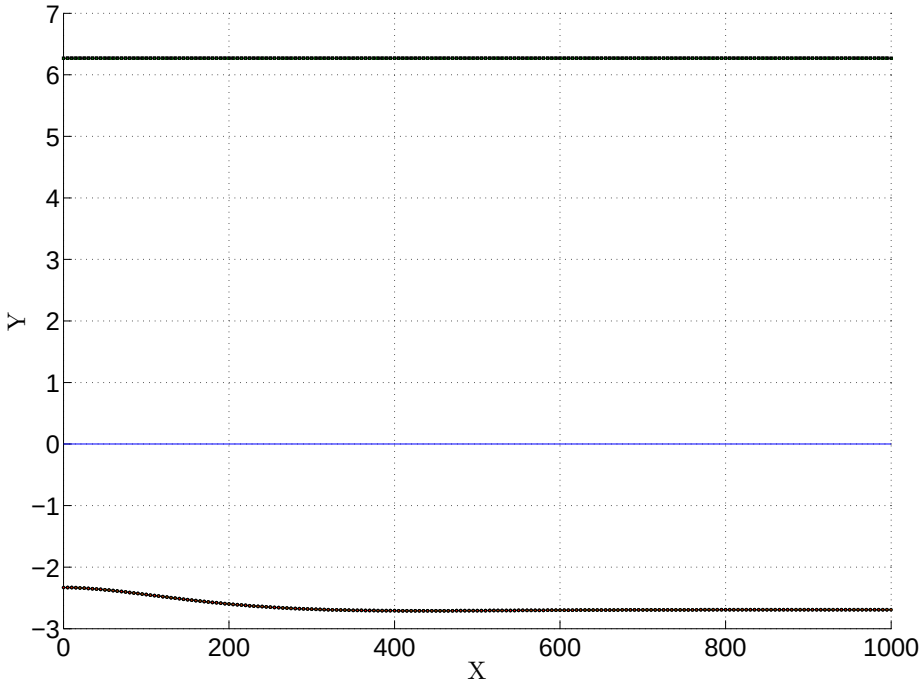

Figure 6.52: Practical applications 2 - Deformed configuration

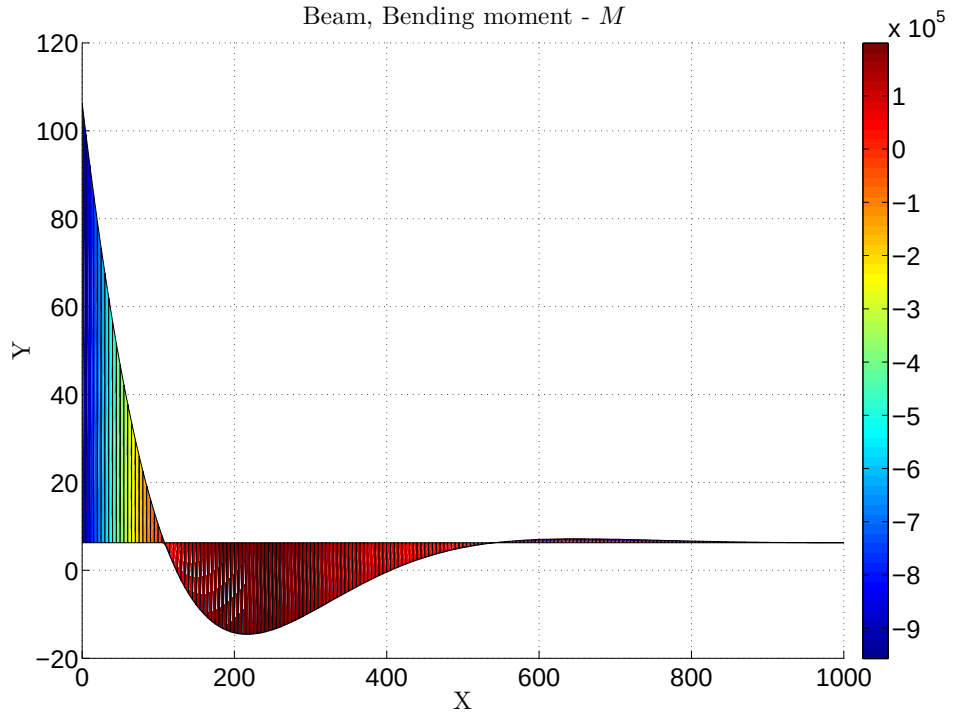

Figure 6.53: Practical applications 2 - Bending moment distribution along the bridge

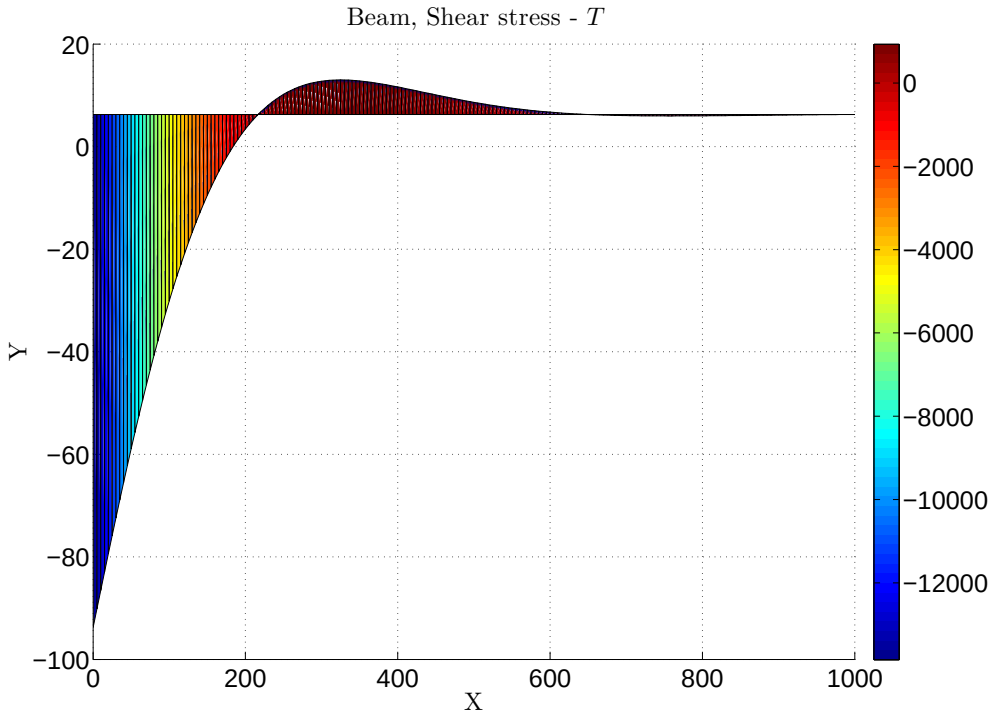

Figure 6.54: Practical applications 2 - Shear distribution along the bridge

The benchmarks developed provided good results in terms of displacements and stresses.

The floatability analysis have been proved to be very reliable and turned out to be a great tool to analyse floating beam structures in contact with fluid. In addition, the comparison between the Winkler model and the proposed new finite element model presents remarcable results in terms of displacements and stresses.

It must be said that the analysis of combined cable and frame structures did not provide good results using the thecnique previously described. Indeed, the great nonlinearity that cable structures requires more advanced numerical techniques. As the reader may remember, the stiffness method was used to solve the nonlinear system of equations because of the fact that the formulation of the beam element was developed considering the total lagrangian formulation. This numerical scheme (the stiffness method) is suitable for analysis where the overall structure has a stiffening or softening behaviour during the deformative path. The method is not able to follow the equilibrium path during the load procedure if the structure presents snap-through or snap-back behaviours.

In the following, the generalization of the finite element model introduced in this chapter will be formulated and implemented in a general 3D nonlinear finite element code to analyse combined cable and frame floating structures.

7 Advanced formulation of 3D cable and frame floating structures

In this chapter, a general 3D model for combined cable and frame floating structures will be presented. As seen in the previous chapter, the model developed to analyse floating structures in a vertical plane (where only axial and bending behaviour were taken into consideration) has been proved to be very suitable in the analysis of floating structures but not reliable for the analysis of combined frame and cable structures.

Indeed, the behaviour of cables structures is more complex than the analysis of floating structures under vertical loads. Moreover, a stiffening behaviour appears as the penetration in the fluid increases. On the other hand, the stiffness of cables depends on the stress field inside them and in general it does not have a stiffening or softening behaviour and the stiffness method is not considered suitable for their analysis.

To overcome this problem, a generalized 3D model considering the fluid-section interaction developed in chapters 5 and 6 will be formulated. The basic concepts developed in previous sections will be unified to develop a model for the analysis of frame and cable floating structures under arbitrary loads and taking into account large displacements.

First, the Euler-Bernoulli and Saint Venant beam model under large displacements explained in section 3.2.2.2 will be modified to consider the effects produced by the interaction between the section and the fluid in the 3D space.

Later, the associated finite element model will be developed and special attention will be given to the part where the fluid-section interaction stiffness is included in the tangent stiffness matrix of the beam element.

Finally, a special section will be devoted to the explanation of how the fluid-section interaction stiffness is computed in the model and how it is formulated in the reference system of the beam element during the deformative path of the structure.

The model is also able to analyse cable elements that anchore the floating structure to

the seabed. A section will be dedicated to the explanation of the model used to formulate the cable finite element and particular attention is devoted to the formulation of new a contact element able to study the interaction of the cable in contact with the seafloor.

The most important computational aspects will be considered to highlight the numerical problems found during the analysis and the techniques used to solve them. It will be shown that the preconditioning of the system will have an important influence.

In conclusions, some benchmarks and real applications to test the new model will be carried out to prove the capability of the model proposed.

7.1 Modified nonlinear Euler-Bernoulli and Saint Venant beam model

To formulate the new beam element using the updated lagrangian approach, consider equation 3.172. As it has been explained in chapter 3, this equation represents the most compact expression of the principle of virtual works for a beam element under no restrictions of any type (material behaviour or displacements magnitude) formulated with the updated incremental lagrangian approach. The purpose is to include a contribution that takes into account the increment of work computed by the fluid surrounding the beam.

The model is formulated under the following hypothesis: 3D displacement field, no restriction on the displacements magnitude and linear elastic behaviour of the materials.

The contribution of the fluid surrounding the beam in the displacement field will be opportunely linearized and expressed in terms of equivalent springs. Following the procedure developed for the analysis of floating structures in the 2D space, the contribution of the fluid will be considered adopting a spring matrix.

The constitutive equations of a section allow to write the forces acting on the section as a function of the configuration of the section itself. Considering the integration of those forces along the boundary of the section and that the section does not deform itself[(1)] the three forces and moment acting on the centroid of the section can be computed. These forces and moments are: F_{ys}, force acting on the first principal axes of the section (y_s); F_{zs}, force acting on the second principal axes of the section (z_s) and M_{xs}, twisting moment acting on the axes orthogonal to the plane of the section (x_s).

These three forces and moment completely characterize the actions of the fluid to the section and depend on the configuration of the section itself. Consider now figure 7.1, where a deformed beam element in a certain configuration is depicted. The increment of virtual work that must be added in equation 3.172 can be express in terms of the virtual variation of the displacements in the three axes of the section.

[(1)] This is one of the main hypothesis in the Euler-Bernoulli model, where the section is considered undeformable and orthogonal to the deformed main line of the beam.

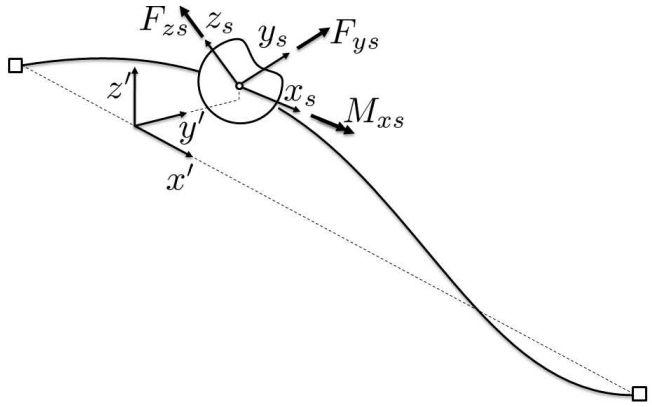

Figure 7.1: Sketch of a deformed beam in contact with a fluid

$$\delta\Delta W_f = \int_0^l \Delta F_{ys}\delta\left(\Delta u_{ys}\right) + \Delta F_{zs}\delta\left(\Delta u_{zs}\right) + \Delta M_{xs}\delta\left(\Delta\varphi_{xs}\right)\ dx \tag{7.1}$$

In the general formulation of the beam element (section 3.2.2.2) the equilibrium equations (and the formulation of principle of virtual work) are considered in the actual configuration of the beam and expressed in terms of incremental displacements. This means that the unknowns are the increment of displacements that the beam suffers during its motion from the actual configuration to the next one. In the previous equation, the symbol Δ has been used to emphasize the fact that increment of displacements are being considered.

Using the constitutive equations of the section, the increment of forces and moments in terms of the increment of displacements of the section can be written as follows:

$$\Delta F_{ys} = \frac{\partial F_{ys}}{\partial u_{xs}}\Delta u_{xs} + \frac{\partial F_{ys}}{\partial u_{ys}}\Delta u_{ys} + \frac{\partial F_{ys}}{\partial u_{zs}}\Delta u_{zs} + \frac{\partial F_{ys}}{\partial \varphi_{xs}}\Delta\varphi_{xs} + \frac{\partial F_{ys}}{\partial \varphi_{ys}}\Delta\varphi_{ys} + \frac{\partial F_{ys}}{\partial \varphi_{zs}}\Delta\varphi_{zs} \tag{7.2}$$

$$\Delta F_{zs} = \frac{\partial F_{zs}}{\partial u_{xs}}\Delta u_{xs} + \frac{\partial F_{zs}}{\partial u_{ys}}\Delta u_{ys} + \frac{\partial F_{zs}}{\partial u_{zs}}\Delta u_{zs} + \frac{\partial F_{zs}}{\partial \varphi_{xs}}\Delta\varphi_{xs} + \frac{\partial F_{zs}}{\partial \varphi_{ys}}\Delta\varphi_{ys} + \frac{\partial F_{zs}}{\partial \varphi_{zs}}\Delta\varphi_{zs} \tag{7.3}$$

$$\Delta M_{xs} = \frac{\partial M_{xs}}{\partial u_{xs}}\Delta u_{xs} + \frac{\partial M_{xs}}{\partial u_{ys}}\Delta u_{ys} + \frac{\partial M_{xs}}{\partial u_{zs}}\Delta u_{zs} + \frac{\partial M_{xs}}{\partial \varphi_{xs}}\Delta\varphi_{xs} + \frac{\partial M_{xs}}{\partial \varphi_{ys}}\Delta\varphi_{ys} + \frac{\partial M_{xs}}{\partial \varphi_{zs}}\Delta\varphi_{zs} \tag{7.4}$$

Adopting a matrix notation, the derivative of the six forces and moments that the fluid applies to the section are:

$$\boldsymbol{K_{fs}} = \begin{bmatrix} \frac{\partial F_{xs}}{\partial u_{xs}} & \frac{\partial F_{xs}}{\partial u_{ys}} & \frac{\partial F_{xs}}{\partial u_{zs}} & \frac{\partial F_{xs}}{\partial \varphi_{xs}} & \frac{\partial F_{xs}}{\partial \varphi_{ys}} & \frac{\partial F_{xs}}{\partial \varphi_{zs}} \\ \frac{\partial F_{ys}}{\partial u_{xs}} & \frac{\partial F_{ys}}{\partial u_{ys}} & \frac{\partial F_{ys}}{\partial u_{zs}} & \frac{\partial F_{ys}}{\partial \varphi_{xs}} & \frac{\partial F_{ys}}{\partial \varphi_{ys}} & \frac{\partial F_{ys}}{\partial \varphi_{zs}} \\ \frac{\partial F_{zs}}{\partial u_{xs}} & \frac{\partial F_{zs}}{\partial u_{ys}} & \frac{\partial F_{zs}}{\partial u_{zs}} & \frac{\partial F_{zs}}{\partial \varphi_{xs}} & \frac{\partial F_{zs}}{\partial \varphi_{ys}} & \frac{\partial F_{zs}}{\partial \varphi_{zs}} \\ \frac{\partial M_{xs}}{\partial u_{xs}} & \frac{\partial M_{xs}}{\partial u_{ys}} & \frac{\partial M_{xs}}{\partial u_{zs}} & \frac{\partial M_{xs}}{\partial \varphi_{xs}} & \frac{\partial M_{xs}}{\partial \varphi_{ys}} & \frac{\partial M_{xs}}{\partial \varphi_{zs}} \\ \frac{\partial M_{ys}}{\partial u_{xs}} & \frac{\partial M_{ys}}{\partial u_{ys}} & \frac{\partial M_{ys}}{\partial u_{zs}} & \frac{\partial M_{ys}}{\partial \varphi_{xs}} & \frac{\partial M_{ys}}{\partial \varphi_{ys}} & \frac{\partial M_{ys}}{\partial \varphi_{zs}} \\ \frac{\partial M_{zs}}{\partial u_{xs}} & \frac{\partial M_{zs}}{\partial u_{ys}} & \frac{\partial M_{zs}}{\partial u_{zs}} & \frac{\partial M_{zs}}{\partial \varphi_{xs}} & \frac{\partial M_{zs}}{\partial \varphi_{ys}} & \frac{\partial M_{zs}}{\partial \varphi_{zs}} \end{bmatrix} \tag{7.5}$$

The increment of the forces and moments acting on the section can be written in terms of the increment of the displacements of the section itself as:

$$\boldsymbol{\Delta F_s} = \boldsymbol{K_{fs}} \boldsymbol{\Delta U_s} \tag{7.6}$$

with $\boldsymbol{\Delta F_s}$ and $\boldsymbol{\Delta U_s}$ defined as

$$\boldsymbol{\Delta F_s} = \begin{bmatrix} F_{xs} & F_{ys} & F_{zs} & M_{xs} & M_{ys} & M_{zs} \end{bmatrix}^T \tag{7.7}$$

$$\boldsymbol{\Delta U_s} = \begin{bmatrix} \Delta u_{xs} & \Delta u_{ys} & \Delta u_{zs} & \Delta \varphi_{xs} & \Delta \varphi_{ys} & \Delta \varphi_{zs} \end{bmatrix}^T \tag{7.8}$$

The increment of virtual work due to the action of the fluid on each section along the beam axis can be rewritten as

$$\delta \Delta W_f = \int_0^l \delta \boldsymbol{\Delta U_s}^T \boldsymbol{\Delta F_s} \, dx = \int_0^l \delta \boldsymbol{\Delta U_s}^T \boldsymbol{K_{fs}} \boldsymbol{\Delta U_s} \, dx \tag{7.9}$$

The increment of virtual work has been derived considering the action of the fluid on each section of the beam. As it might be realized, this contribution has not been expressed in terms of the generalized displacements of the beam (axial displacement u, the displacements v and w and torsional rotation φ_x). However, this is not required in the theoretical development because the increment of displacements at each section of the beam axis can be directly expressed as a function of the nodal displacements of the element.

7.2 Finite element model

The attention is now focused on the formulation of the finite element model associated to this new beam element.

Considering the shape functions matrix previously defined in equation 3.137, the displacement of each point along the beam during the deformative procedure can be computed. In addition, the increment of displacements of each section can be expressed in terms of the increment of displacements along the beam[(2)].

$$\boldsymbol{\Delta U_s} = \boldsymbol{T_{bs}} \boldsymbol{\Delta U'} \tag{7.10}$$

where the matrix $\boldsymbol{T_{bs}}$ is a transformation matrix that relates the reference system of the finite element beam and the principal axes of the section in the actual configuration. Substituting equation 7.10 in equation 7.9, the following expression for the increment of work can be obtained.

$$\delta \Delta W_f = \int_0^l \delta \left(\boldsymbol{T_{bs}} \boldsymbol{\Delta U'} \right)^T \boldsymbol{K_{fs}} \left(\boldsymbol{T_{bs}} \boldsymbol{\Delta U'} \right) \, dx \tag{7.11}$$

Rearranging the previous expression it can be written:

$$\delta \Delta W_f = \int_0^l \delta \boldsymbol{\Delta U'}^T \underbrace{\boldsymbol{T_{bs}^T} \boldsymbol{K_{fs}} \boldsymbol{T_{bs}}}_{\boldsymbol{K_{fb}}} \boldsymbol{\Delta U'} \, dx = \int_0^l \boldsymbol{\Delta U'}^T \boldsymbol{K_{fb}} \boldsymbol{\Delta U'} \, dx \tag{7.12}$$

Consider now the matrix $\boldsymbol{N_b}$ defined as

$$\boldsymbol{N_b}(x) = \begin{bmatrix} N_{u1} & 0 & 0 & 0 & 0 & 0 & N_{u2} & 0 & 0 & 0 & 0 & 0 \\ 0 & N_{v1} & 0 & 0 & 0 & N_{v3} & 0 & N_{v2} & 0 & 0 & 0 & N_{v4} \\ 0 & 0 & N_{w1} & 0 & N_{w3} & 0 & 0 & 0 & N_{w2} & 0 & N_{w4} & 0 \\ 0 & 0 & 0 & N_{\varphi 1} & 0 & 0 & 0 & 0 & 0 & N_{\varphi 2} & 0 & 0 \\ 0 & 0 & -N'_{w1} & 0 & -N'_{w3} & 0 & 0 & 0 & -N'_{w2} & 0 & -N'_{w4} & 0 \\ 0 & N'_{v1} & 0 & 0 & 0 & N'_{v3} & 0 & N'_{v2} & 0 & 0 & 0 & N'_{v4} \end{bmatrix} \tag{7.13}$$

where the shape functions have been defined in equation 3.139.

This matrix allows to express the six variables, three displacements and three rotations, of any point of the beam as a function of the nodal displacements ($\boldsymbol{\Delta U}$) in the local reference system of the beam.

$$\boldsymbol{\Delta U'} = \boldsymbol{N_b}(x) \, \boldsymbol{\Delta U} \tag{7.14}$$

It should be remember that the vector $\boldsymbol{\Delta U}$ is the increment of the vector previously defined in equation 3.138.

Substituting the last expression in the previous equation of the increment of virtual work the following expression may be obtained.

$$\delta \Delta W_f = \int_0^l \delta \left(\boldsymbol{N_b}(x) \, \boldsymbol{\Delta U} \right)^T \boldsymbol{K_{fb}} \left(\boldsymbol{N_b}(x) \, \boldsymbol{\Delta U} \right) \, dx \tag{7.15}$$

[(2)] It must be realize that the formulation used considers small deformations, which means that the increment of displacements of the section and the correponding point of the beam axis only differ in the local reference system in which they are expressed

The expression can be opportunely rearranged and the increment of virtual work due to the fluid action along the finite element can be finally written as follows.

$$\delta\Delta W_f = \delta\boldsymbol{\Delta U}^T \underbrace{\int_0^l \boldsymbol{N_b}^T(x)\,\boldsymbol{K_{fb}}\boldsymbol{N_b}(x)\;dx}_{\boldsymbol{K_f}}\boldsymbol{\Delta U} = \delta\boldsymbol{\Delta U}^T\boldsymbol{K_f}\boldsymbol{\Delta U} \tag{7.16}$$

The matrix $\boldsymbol{K_f}$ represents the stiffness contribution due to the interaction between the beam and the fluid. This matrix can be directly included in equation 3.185 to define a new incremental equilibrium equation in a matrix form for the new finite element.

$$(\boldsymbol{K_e} + \boldsymbol{K_g} + \boldsymbol{K_i} + \boldsymbol{K_f})\,\boldsymbol{\Delta U} = {}^{2}_{1}\boldsymbol{f} - {}^{1}_{1}\boldsymbol{f} \tag{7.17}$$

The interaction between the beam and the fluid only affects the stiffness of the structure and does not include any contribution in the external forces. Indeed, one may consider to integrate the hydrostatic pressure along the boundary of the beam to obtain the equivalent nodal loads and study the beam-fluid interaction considering the contribution of the second in the external loads. This is a mistake because the structure needs, in part, the fluid to resist[3] the external loads. Although the contribution of the hydrostatic load in the external loads is physically consistent, the linearization of the incremental equilibrium equations leads to ill-conditioned matrices and the system does not have enough stiffness to counteract any kind of load.

7.3 Formulation of the contact element for the seabed-cable interaction

As it has been done for the 2D model, cables are used to anchore the floating structures to the seabed. To analyse them, the formulation developed in section 3.1.4 will be used and the incremental equilibrium equations will be formulated in an updated lagrangian approach.

In addition, to take into account the interaction between the seabed and the cable elements in contact one with each other, a new contact element will be developed to take into account the contribution of the topography of the seafloor.

7.3.1 Contribution of the seabed stiffness

Consider figure 7.2, where a cable element in contact with the seafloor is depicted. The model used to study the interaction between the seabed and the cable is a variation of the model traditionally used for the study of soil-structure interaction. The soil is considered as elastic and characterized by a stiffness constant.

[3] As you may remember, the vertical stiffness of floating structures is due to the archimede's load produced by the fluid.

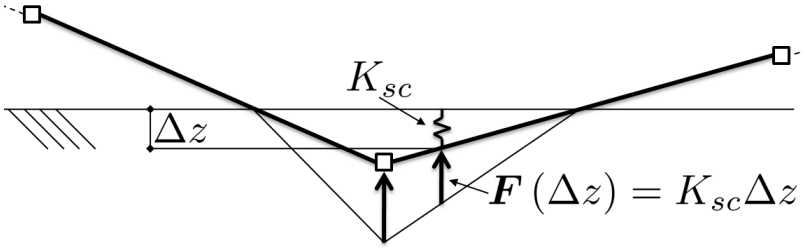

Figure 7.2: Cable element making contact with the seabed

The stiffness constant can be chosen to define a realistic penetration length (see [Pal G. Bergan and Sandsmark, 1985]). In this case, the elastic constant that characterizes the soil has been considered as follows. Consider a cable element that horizontally lies in the seafloor as the one depicted in figure 7.3. Considering the mechanical and geometrical properties of the cable and the prescribed penetration, the stiffness per unit length that the soil may be obtained.

$$K_{sc} = \frac{\gamma A}{\Delta z^*} \tag{7.18}$$

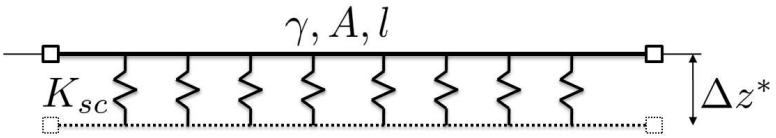

Figure 7.3: Cable element horizontally lying on the seabed

The stiffness previously defined acts in the vertical direction and is directly summed to the vertical stiffness of each cable node in contact with the seafloor.

7.3.2 Description of the program

In this section, a description of the developed program to analyse 3D floating structures is presented. The program is divided in seven independent parts. The following flowchart shows each one of them.

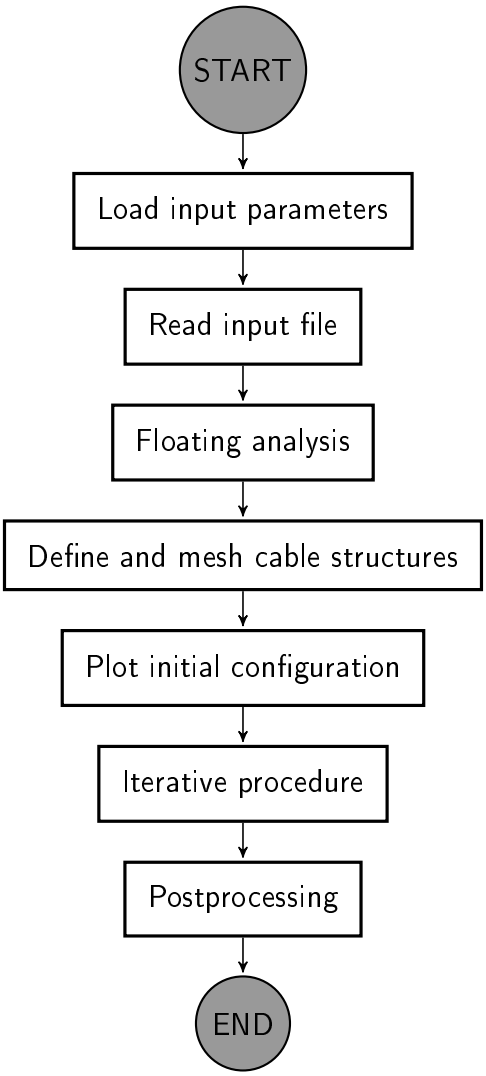

Figure 7.4: Flow chart of the program for the analysis of 3D floating structures

Although the main structure is exactly the same as the 2D program, several differences have been implemented.

The first five parts are essentially the same as the ones previously described. Despite it, some modifications are required in each of them to deal with 3D floating structures. Indeed, the number of parameters required in the first part of the program (*Load input parameters*) increases. Different models can be prescribed by the user to study both beam and cable elements (de Saint Venant and Wagner Vlasov for the torsional behaviour, Euler-Bernoulli and Timoshenko for the bending and shear behaviour, direct and finite element approach for the study of cable elements, ...). A deep explanation of this part is omitted because the reader is not supposed to use the program and the explanation does not contribute in the general understanding of what this chapter talks about.

In the second part, *Read input file*, the program reads the input file. The main differences for 2D and 3D problems are referred to the number of degrees of freedom that

each node now has, the inclusion of the equivalent stiffness that characterizes the soil behaviour and the inclusion of a list of auxiliary vectors and points that allow the program to internally compute the local reference system of each beam element.

The third part, *Floating analysis*, works exactly as the one explained in sectione 6.5. However, there is a difference between the two procedures in the way the nonlinear equation that defines the floating equilibrium position is solved.

The fourth part, *Define and mesh cable structures*, works exactly in the same way of equivalent part of the 2D program. The cables are first positioned in the space by means of the catenary equation and then are meshed considering the number of nodes that the user requires.

Finally, the program plots the initial configuration of the overall structure and save it in the desired folder the user has previously defined.

Once the five first parts have been accomplished, the program starts the *Iterative procedure*. Here, the program is completely different to perform an incremental iterative scheme to solve the nonlinear equilibrium equations of the structure under large displacements[(4)]. In this part, the programs computes first the reference load vector that will progressively incremented (by means of the load factor λ) during the iterative procedure. The following flowchart shows how this part works.

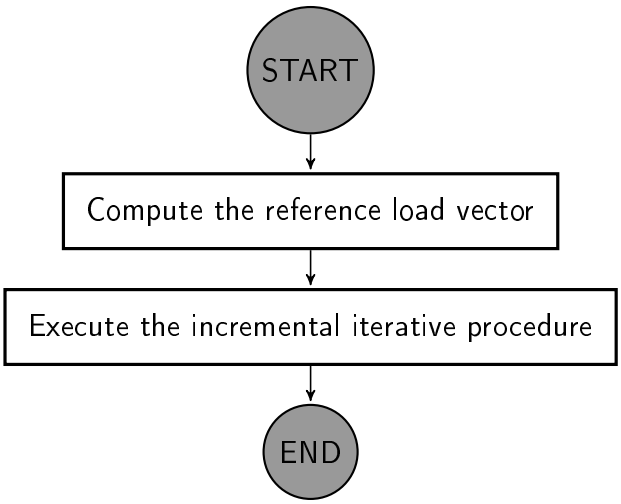

Figure 7.5: Flowchart of the iterative procedure in the 3D program

In the first part the reference load vector is computed. A loop along the beam elements, cable elements and nodes is performed and each contribution (selfweight, concentrated load in the nodes, prestressing cables, imposed deformations,.. etc) is summed to the

[(4)] Remember that the 3D program uses and incremental iterative procedure where the equilibrium equations in an incremental form can be written as: $\boldsymbol{R} + \boldsymbol{K_T}\boldsymbol{\Delta U} = (\lambda + \Delta\lambda)\,\boldsymbol{f_r}$. Where $\boldsymbol{f_r}$ is a reference load vector previously defined.

reference nodal load that is already expressed in the global reference system. The following flowchart shows how the procedure works.

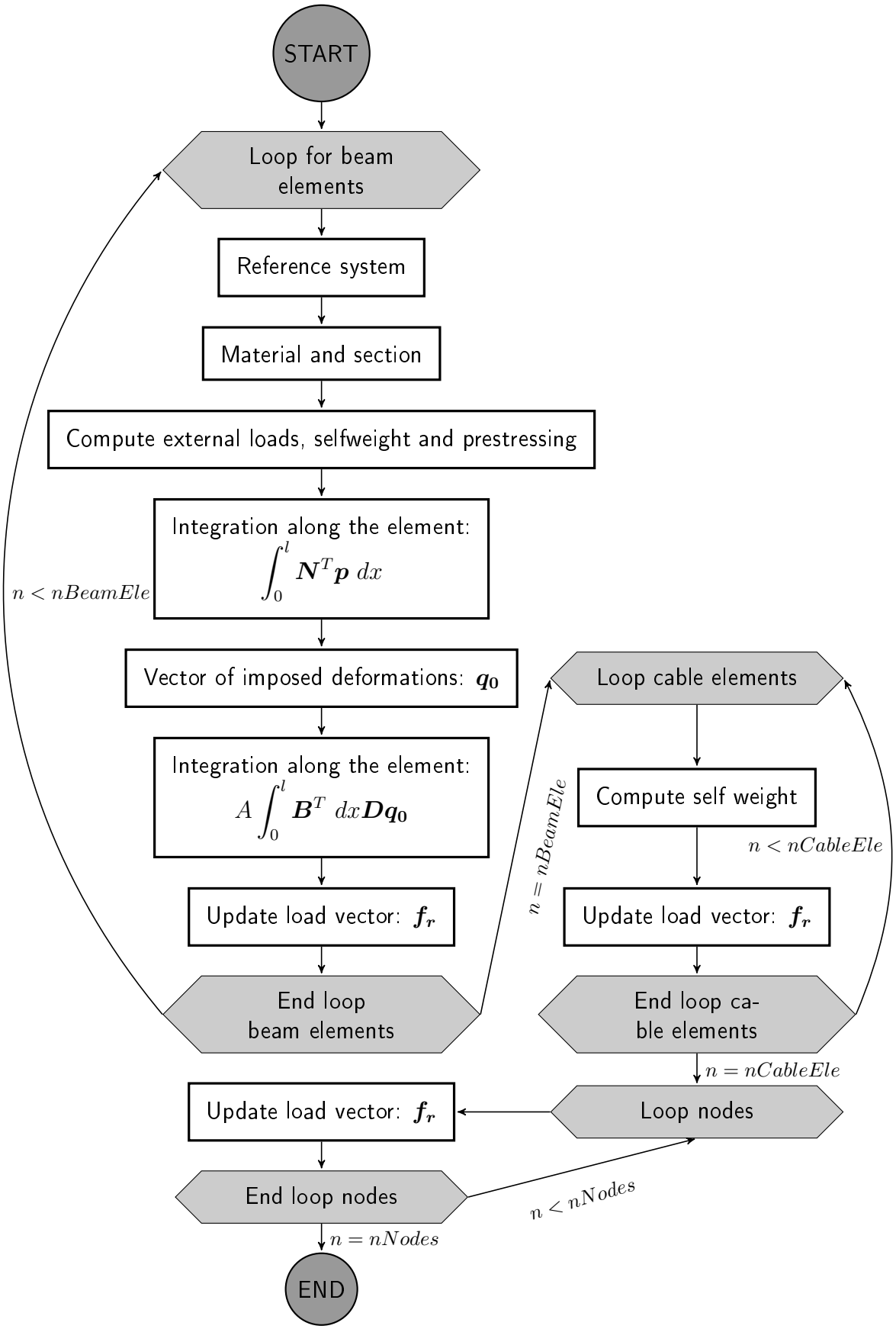

Figure 7.6: Flowchart of the part where the reference load vector is computed

As it can be seen from the previous flowchart, the program performs three loops. One loop on the beam elements, one on the cable elements and one on the nodes. The beam elements contribute in the reference load vector with their self weight, possible external loads applied to them, imposed deformations (thermal variations for example) and pre-stressing. The cable elements only contribute to the reference load with their self weight while the nodes only contribute if concentrated external loads are applied.

The way in which the equivalent nodal loads are computed can be found in section 6.2. The computation of the equivalent nodal loads was developed for the 2D case, but it can be easily generalized to the 3D.

The case of the equivalent nodal loads due to the self weight of the cable element can be easily computed considering the total weight of it distributed to each node of the element. The equivalent nodal loads of the self weight on a cable element will be computed as follows.

$$\boldsymbol{f_c} = \frac{\gamma_m A_c l}{2} \left[\begin{array}{cccccc} 0 & 0 & -1 & 0 & 0 & -1 \end{array} \right]; \; \gamma_m = \gamma_c - \gamma_f \tag{7.19}$$

In this equation γ_m is the equivalent self weight per unit volume (difference between the self weight of the cable, γ_c and the self weight of the fluid γ_f), A_c is the area of the cross section of the cable and l is the length of the cable element.

Once the reference load vector $\boldsymbol{f_r}$ has been computed, the program starts an incremental iterative procedure to compute the equilibrium position on each configuration defined by the load factor λ during the deformative path. The procedure stops if a maximum or minimum load factor is achieved or until the program is not able to converge anymore. The incremental iterative scheme follows the procedure explained in section 4.1.4.

7.3.3 Modified Arc-Length method

As the reader may remember from section 4.1.4, the arc-length method has been used to control the displacement of the structure during the control procedure. The advantages and disadvantadges of this method have been discussed and special attention were given to the fact that the arc-length method consists on a mathematical limitation on the displacements. Indeed, the module of the displacements is restricted on each iteration. This leads to an inconsistent compatibility equation where the limitation on the displacement is directly imposed considering both the displacements and rotation of the beam and/or cable structure (see equation 4.13 and 4.19).

It might be noticed that the limitation of the norm of the displacement vector means the restriction condition is being imposed to a vector that has both displacements and rotation as components expressed in different units (length for the displacements and radians for the rotations). This makes the arc length method very unappropiate for certain problems.

To avoid this problem, a modification on the arc-length method has been formulated

to make the method more robust.

From a physical point of view, on every problem of the structural analysis it is possible to define a characteristic length L_c, force F_c and moment M_c. These three variables can be introduced in the formulation of the arc-length equations. The normalized displacement and force vector can be defined as:

$$\boldsymbol{v_a} = \boldsymbol{H_d v} \tag{7.20}$$

$$\boldsymbol{f_{ra}} = \boldsymbol{H_f f_r} \tag{7.21}$$

with the matrices $\boldsymbol{H_d}$ and $\boldsymbol{H_f}$ defined as follows.

$$\boldsymbol{H_{dij}} = \frac{1}{L_c}\delta_{ij}F(i) \tag{7.22}$$

$$\boldsymbol{H_{fij}} = \frac{1}{M_c}\delta_{ij}F(i) \tag{7.23}$$

In these definitions, δ_{ij} is the well known Kronecker's function, defined as:

$$\delta_{ij} = \begin{cases} 1 & i = j \\ 0 & i \neq j \end{cases} \tag{7.24}$$

In addition, the function $F(i)$ is a function that depends on the degree of freedom (rotation or displacement) of the vector $\boldsymbol{v}_i$.

$$F(i) = \begin{cases} 1 & \boldsymbol{v_i}\ displacement \\ L_c & \boldsymbol{v_i}\ rotation \end{cases} \tag{7.25}$$

Imposing equations 4.13 and 4.19 on the normalized displacement and force vector, the new expression for the arc-length in the prediction and correction phases may be obtained.

$$^1\Delta\lambda = \frac{\pm\Delta l}{\sqrt{\boldsymbol{\Delta v}_t^T \boldsymbol{D_d} \boldsymbol{\Delta v}_t + \beta^2 \boldsymbol{f_r}^T \boldsymbol{D_f} \boldsymbol{f_r}}}; \quad \begin{matrix} \boldsymbol{D_d} = \boldsymbol{H_d}^T \boldsymbol{H_d} \\ \boldsymbol{D_f} = \boldsymbol{H_f}^T \boldsymbol{H_f} \end{matrix} \tag{7.26}$$

$$\begin{gathered} a\,^1\delta\lambda^2 + b\,^1\delta\lambda + c = 0 \\ a = \boldsymbol{\delta v}_t^T \boldsymbol{D_d} \boldsymbol{\delta v}_t + \beta^2 \boldsymbol{f_r}^T \boldsymbol{D_f} \boldsymbol{f_r} \\ b = -2\boldsymbol{\delta v}_r^T \boldsymbol{D_d} \boldsymbol{\delta v}_r - 2\,^1\boldsymbol{\Delta v}^T \boldsymbol{D_d} \boldsymbol{\delta v}_t - 2\,^1\Delta\lambda\beta^2 \boldsymbol{f_r} \boldsymbol{D_f} \boldsymbol{f_r} \\ c = -\Delta l^2 + {}^1\boldsymbol{\Delta v}^T \boldsymbol{D_d}\,^1\boldsymbol{\Delta v} + \boldsymbol{\delta v}_r^T \boldsymbol{D_d} \boldsymbol{\delta v}_r + 2\,^1\boldsymbol{\Delta v}^T \boldsymbol{D_d} \boldsymbol{\delta v}_r + {}^1\Delta\lambda^2\beta^2 \boldsymbol{f_r}^T \boldsymbol{D_f} \boldsymbol{f_r} \end{gathered} \tag{7.27}$$

The imposition of the arc-length in both the prediction and corrections phases has been proved to be very efficient and much more general than the previous formulation. Indeed, the new formulation of the arc-length method imposes a restriction in a normalized displacement vector which allows a better control since it does not depend on the units of measure used.

7.4 Advanced techniques for nonlinear analysis of floating structures

Due to the strong nonlinearity that floating structures anchored to the seabed present, a general porpose 3D finite element program has been developed under the hypothesis of large displacements. In addition, the updated lagrangian formulation expresses the incremental equilibrium equations with respect the last known configuration of the structure.

These considerations require that, during the deformation of the structure, both the reference systems of cable and beam elements are updated. Also, the reaction of the system must always be related to the global reference system (where the reference load vector is expressed). In addition, during the incremental procedure previously explained, the reaction of the system has to be computed as the sum of the nodal reaction of each element of the structure. These nodal reactions directly depend on the deformative state that the element is suffering and have to be computed considering the natural deformations of each element on each configuration.

In summary, to completely characterize the equilibrium of the structure on each configuration the reference system, the natural deformations and the equivalent nodal forces acting on each element must be computed.

First, the explanation of how to update the reference system, compute the displacement of each element considering its rigid body and deformative motion and compute the stresses on each configuration is explained. Later, the assembly of each nodal loads from each elements to obtain the reaction of the system will be exposed. To better understand the procedure, the initial configuration of the structure will be separated from the others because it is the only one for which the reaction depends completely on the configuration and not on the deformation of the structure.

In this part, techniques and methods to completely characterize the actual configuration of the structure are exposed. First, the way in which the reference system of cable and beam elements is updated is presented. Second, the natural deformations and stresses on each element in the actual configuration will be deduced and the equivalent nodal loads derived from them. Finally, the reaction of the system will be presented as the assembly of each nodal reaction of each element in the structure.

Let us assume a generic incremental step, where the increment of displacements of the structure $\boldsymbol{\Delta U}$ has already been computed from the incremental equilibrium equation, which means that the increment of displacements for each element $\boldsymbol{\Delta u}$ can be easily computed. The problem now is to calculate the nodal forces ${}^{2}\boldsymbol{f}$ for each element in the new configuration, given the nodal displacements $\boldsymbol{\Delta u}$. In the following, an approach based on the difference between rigid body displacement and natural deformations is presented. In this approach, the orientation of the ends of each element are updated taking into account the natural deformations $\boldsymbol{\Delta u_n}$.

7.4.1 Reference axes of beam elements nodes

For a space frame element, six degrees of freedom are needed on each end of the element. To this porpose, an orthogonal reference axis is attached on each node belonging to the frame structure. The position of node i and the axes attached on the node i at configuration ${}^k\boldsymbol{C}$ are denoted as ${}^k\boldsymbol{r}_i = \left[{}^kx_i, {}^ky_i, {}^kz_i\right]^T$ and ${}^k\boldsymbol{Q}_i = \left[{}^k\boldsymbol{\xi}_i, {}^k\boldsymbol{\eta}_i, {}^k\boldsymbol{\varsigma}_i\right]$ respectively.

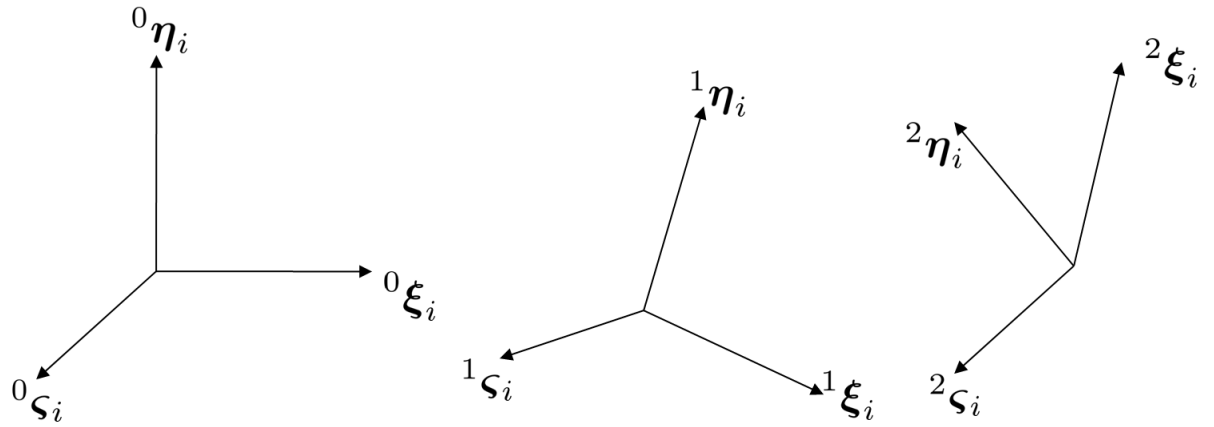

(a) Reference system attached to the node, configuration 0

(b) Reference system attached to the node, configuration 1

(c) Reference system attached to the node, configuration 2

Figure 7.7: Variation of the reference system of each beam node during the deformation of the structure

Due to the displacement and rotation on each degree of freedom of the node from configuration ${}^1\boldsymbol{C}$ to configuration ${}^2\boldsymbol{C}$, the position and the reference system will suffer a variation that can be easily computed. In the first case, the position of the node can be update using the following formula.

$$ {}^2\boldsymbol{r}_i = {}^1\boldsymbol{r}_i + \boldsymbol{\Delta U}_i \tag{7.28} $$

$$ \boldsymbol{\Delta U}_i = \left[\begin{array}{ccc} \Delta u_x & \Delta u_y & \Delta u_z \end{array} \right]_i^T $$

On the other hand, the new orientation of the node must be computed using the Euler's finite rotation formula. Considering the vector of rotations

$$ \boldsymbol{\Delta\theta}_i = \left[\begin{array}{ccc} \Delta\theta_x & \Delta\theta_y & \Delta\theta_z \end{array} \right]^T \tag{7.29} $$

the total rotation can be computed as the norm of this vector and the rotation vector can also be computed considering the direction of the previous vector.

$$ \Delta\theta = |\boldsymbol{\Delta\theta}| \tag{7.30} $$

$$ \boldsymbol{n} = \frac{\boldsymbol{\Delta\theta}}{\Delta\theta} \tag{7.31} $$

Now, the transformation of axes can be performed as follows.

$$ {}^{2}\boldsymbol{Q}_i = \left[\cos\alpha \boldsymbol{I_3} + \sin\alpha \boldsymbol{A} + (1-\cos\alpha)\,\boldsymbol{B}\right] {}^{1}\boldsymbol{Q}_i \tag{7.32} $$

$$ \boldsymbol{A} = \begin{bmatrix} 0 & -n_z & n_y \\ n_z & 0 & -n_x \\ -n_y & n_x & 0 \end{bmatrix} \qquad \boldsymbol{B} = \boldsymbol{n}\boldsymbol{n}^T $$

7.4.2 Reference system of beam elements

The variation of the element axes and nodal section axes in the deformation process of member will be discussed. The section axes for node $i = a, b$ of the beam element at configuration ${}^{k}\boldsymbol{C}$ are denoted by ${}^{k}\boldsymbol{P}_i = \left[{}^{k}\boldsymbol{\alpha}_i, {}^{k}\boldsymbol{\beta}_i, {}^{k}\boldsymbol{\gamma}_i\right]$ and the reference system of the beam element as ${}^{k}\boldsymbol{R} = \left[{}^{k}\boldsymbol{x}', {}^{k}\boldsymbol{y}', {}^{k}\boldsymbol{z}'\right]$.

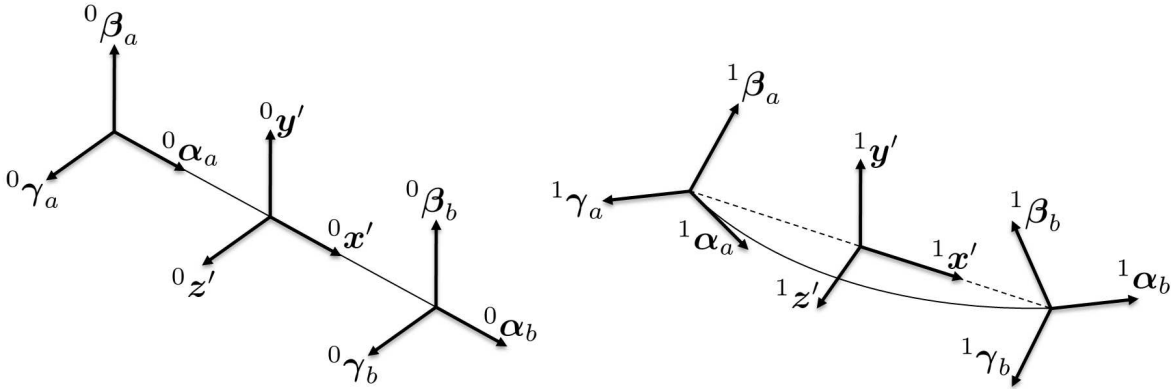

(a) Reference system of end sections and element, configuration 0

(b) Reference system of end sections and element, configuration 1

Figure 7.8: Variation of the reference system of each beam element during the deformation of the structure

During its deformative path, the centroidal axes of the element will become curved and the two end sections in general will not remain parallel to each other. On each configuration of the element, the element axis ${}^{k}\boldsymbol{x}'$ can be defined as the axis passing throught the centroid of both end sections. Moreover, by assuming a certain plane ${}^{k}\boldsymbol{S}$ perpendicular to the ${}^{k}\boldsymbol{x}'$ axis, the two other axis of the element in the current configuration (${}^{k}\boldsymbol{y}'$ and ${}^{k}\boldsymbol{z}'$) can be defined as the average of the projections of the major and minor principal directions, repectively, of the two end sections on the plane ${}^{k}\boldsymbol{S}$. The procedure to obtain the new reference axes of the element is presented.

The section axes of both end nodes at configuration ${}^{0}\boldsymbol{C}$ can be related to the reference axes as follows.

$$ {}^{0}\boldsymbol{P}_{a,b} = {}^{0}\boldsymbol{R}\,{}^{0}\boldsymbol{Q}_{a,b} \tag{7.33} $$

Based on the assumption of rigid joints, the transformation between the reference axes and section axes of the element nodes will remain unchanged. Under this assumption,

the relation between the reference axes of each node and the reference axes of each end section on every configuration can be written.

$$ {}^{k}\boldsymbol{P}_{a,b} = {}^{0}\boldsymbol{R}\,{}^{k}\boldsymbol{Q}_{a,b} \tag{7.34} $$

The ${}^{k}\boldsymbol{x}'$ axis in the configuration ${}^{k}\boldsymbol{C}$ can be computed considering the actual position of both end nodes of the element.

$$ {}^{k}\boldsymbol{x}' = \frac{{}^{k}\boldsymbol{r}_b - {}^{k}\boldsymbol{r}_a}{{}^{k}l} \qquad {}^{k}l = \left| {}^{k}\boldsymbol{r}_b - {}^{k}\boldsymbol{r}_a \right| \tag{7.35} $$

By defining ${}^{k}\boldsymbol{S}$ as a plane normal to the axes ${}^{k}\boldsymbol{x}'$, the projections of the sections axes ${}^{k}\boldsymbol{\beta}$ and ${}^{k}\boldsymbol{\gamma}$ for nodes a and b on ${}^{k}\boldsymbol{S}$ plane can be written as follows.

$$ {}^{k}\boldsymbol{\beta}^{*}_{a,b} = {}^{k}\boldsymbol{\beta}_{a,b} - \left({}^{k}\boldsymbol{\beta}^{T}_{a,b}\,{}^{k}\boldsymbol{x}' \right) {}^{k}\boldsymbol{x}' \qquad {}^{k}\boldsymbol{\gamma}^{*}_{a,b} = {}^{k}\boldsymbol{\gamma}_{a,b} - \left({}^{k}\boldsymbol{\gamma}^{T}_{a,b}\,{}^{k}\boldsymbol{x}' \right) {}^{k}\boldsymbol{x}' \tag{7.36} $$

Normalizing those vectors

$$ {}^{k}\overline{\boldsymbol{\beta}}_{a,b} = \frac{{}^{k}\boldsymbol{\beta}^{*}_{a,b}}{\left| {}^{k}\boldsymbol{\beta}^{*}_{a,b} \right|} \qquad {}^{k}\overline{\boldsymbol{\gamma}}_{a,b} = \frac{{}^{k}\boldsymbol{\gamma}^{*}_{a,b}}{\left| {}^{k}\boldsymbol{\gamma}^{*}_{a,b} \right|} \tag{7.37} $$

In general, the section axes will not be parallel so their projection will not be the same. Taken their average, the two other axes of the element can be obtained.

$$ {}^{k}\boldsymbol{e}_y = {}^{k}\overline{\boldsymbol{\beta}}_a + {}^{k}\overline{\boldsymbol{\beta}}_b \qquad {}^{k}\boldsymbol{e}_z = {}^{k}\overline{\boldsymbol{\gamma}}_a + {}^{k}\overline{\boldsymbol{\gamma}}_b \tag{7.38} $$

Normalizing them.

$$ {}^{k}\overline{\boldsymbol{e}}_y = \frac{{}^{k}\boldsymbol{e}_y}{\left| {}^{k}\boldsymbol{e}_y \right|} \qquad {}^{k}\overline{\boldsymbol{e}}_z = \frac{{}^{k}\boldsymbol{e}_z}{\left| {}^{k}\boldsymbol{e}_z \right|} \tag{7.39} $$

Based on the property that the diagonals of the rhombus are perpendicular to each other and that they divide the interior angles of the rhombus into two equal parts, the diagonals of the rhombus formed by the vectors ${}^{k}\overline{\boldsymbol{e}}_y$ and ${}^{k}\overline{\boldsymbol{e}}_z$ can be expressed as

$$ {}^{k}\boldsymbol{e}_1 = {}^{k}\overline{\boldsymbol{e}}_y + {}^{k}\overline{\boldsymbol{e}}_z \qquad {}^{k}\boldsymbol{e}_2 = {}^{k}\overline{\boldsymbol{e}}_y - {}^{k}\overline{\boldsymbol{e}}_z \tag{7.40} $$

which can be normalized as follows.

$$ {}^{k}\overline{\boldsymbol{e}}_1 = \frac{{}^{k}\boldsymbol{e}_1}{\left| {}^{k}\boldsymbol{e}_1 \right|} \qquad {}^{k}\overline{\boldsymbol{e}}_2 = \frac{{}^{k}\boldsymbol{e}_2}{\left| {}^{k}\boldsymbol{e}_2 \right|} \tag{7.41} $$

Rotating the unit vectors ${}^{k}\overline{\boldsymbol{e}}_1$ and ${}^{k}\overline{\boldsymbol{e}}_2$ counterclockwise by $\dfrac{\pi}{4}$ radians the section axes for the frame element becomes as follows.

$$ {}^{k}\boldsymbol{y} = \frac{1}{\sqrt{2}} \left({}^{k}\overline{\boldsymbol{e}}_1 + {}^{k}\overline{\boldsymbol{e}}_2 \right) \qquad {}^{k}\boldsymbol{z} = \frac{1}{\sqrt{2}} \left({}^{k}\overline{\boldsymbol{e}}_1 - {}^{k}\overline{\boldsymbol{e}}_2 \right) \tag{7.42} $$

The computation of the three vectors that define the reference system of the element in the current configuration allows to update the rotation matrix that defines this reference system.

$$ {}^{k}\boldsymbol{R} = \left[\begin{array}{ccc} {}^{k}\boldsymbol{x}' & {}^{k}\boldsymbol{y}' & {}^{k}\boldsymbol{z}' \end{array} \right] \tag{7.43} $$

7.4.3 Stresses of beam elements

This section regards the natural deformations and the subsequently nodal forces on each element of the structure. For this purpose, the displacement increments $\boldsymbol{\Delta u}$ obtained from the incremental equations of equilibrium can be decomposed into two parts: the rigid body displacements $\boldsymbol{\Delta u_r}$ and the natural member deformations $\boldsymbol{\Delta u_n}$.

For a frame element with six degrees of freedom for each node, the natural deformation vector $\boldsymbol{\Delta u_n}$ can be expressed as follows.

$$\boldsymbol{\Delta u_n} = \begin{bmatrix} 0 & 0 & 0 & \theta_{xa} & \theta_{ya} & \theta_{za} & u_b & 0 & 0 & \theta_{xb} & \theta_{yb} & \theta_{zb} \end{bmatrix}^T \tag{7.44}$$

The simplest one to calculated is the axial deformation, that can be computed by its definition.

$$u_b = {}^k l - {}^{k-1} l \tag{7.45}$$

The other components of the natural deformation vector can be determined from the nodal section axes and element axes at ${}^{k-1}\boldsymbol{C}$ and ${}^{k}\boldsymbol{C}$. First, the vectors that define the reference axes of the end section can be expressed in terms of the element axes in configuration ${}^{k}\boldsymbol{C}$ with respect the initial configuration as

$${}^{k}_{k}\boldsymbol{P} = {}^{k}_{0}\boldsymbol{R}^T \, {}^{k}_{0}\boldsymbol{P} \tag{7.46}$$

where the subscript "0" indicates that the reference configuration is ${}^{0}\boldsymbol{C}$, and ${}^{k}\boldsymbol{R}$ is the transformation matrix for the element at the configuration ${}^{k}\boldsymbol{C}$ with respect the global reference system.

Consequently, the strain increments of the element at both nodes during the incremental step can be expressed with reference to the ${}^{k-1}\boldsymbol{C}$ section axes as follows:

$${}^{k-1,k}_{k-1}\boldsymbol{P}_{a,b} = {}^{k}_{k}\boldsymbol{P}_{a,b} \, {}^{k-1}_{k-1}\boldsymbol{P}^T_{a,b} \tag{7.47}$$

It has been shown that as the element moves from ${}^{k-1}\boldsymbol{C}$ to ${}^{k}\boldsymbol{C}$, the three axes ${}^{k}_{0}\boldsymbol{P}_{a,b}$ embedded at node a and b rotate and become ${}^{k}_{k-1}\boldsymbol{P}_{a,b}$. In this new configuration, the amount of rotation $\theta_{a,b}$ at nodes a and b can be obtained. Let us consider the vector

$${}^{k}_{k-1}\boldsymbol{n}_{a,b} = \begin{bmatrix} n_1 & n_2 & n_3 \end{bmatrix}^T \tag{7.48}$$

subjected to the condition $\left|{}^{k}_{k-1}\boldsymbol{n}_{a,b}\right| = 1$.

Further, by letting the reference systems of both end sections be

$${}^{k-1}_{0}\boldsymbol{\alpha}_{a,b} = \begin{bmatrix} 1 & 0 & 0 \end{bmatrix}^T \qquad {}^{k}_{k-1}\boldsymbol{\alpha}_{a,b} = \begin{bmatrix} \alpha_1 & \alpha_2 & \alpha_3 \end{bmatrix}^T \tag{7.49}$$

$${}^{k-1}_{0}\boldsymbol{\beta}_{a,b} = \begin{bmatrix} 0 & 1 & 0 \end{bmatrix}^T \qquad {}^{k}_{k-1}\boldsymbol{\beta}_{a,b} = \begin{bmatrix} \beta_1 & \beta_2 & \beta_3 \end{bmatrix}^T \tag{7.50}$$

$${}^{k-1}_{0}\boldsymbol{\gamma}_{a,b} = \begin{bmatrix} 0 & 0 & 1 \end{bmatrix}^T \qquad {}^{k}_{k-1}\boldsymbol{\gamma}_{a,b} = \begin{bmatrix} \gamma_1 & \gamma_2 & \gamma_3 \end{bmatrix}^T \tag{7.51}$$

and imposing the Euler's formula to the three equations, it can be proved that the vector ${}^{k}_{k-1}\boldsymbol{n}$ and rotation $\theta_{a,b}$ satisfy the following equations.

$$ {}^{k}_{k-1}\boldsymbol{n}_{a,b} = -\frac{1}{\lambda}\left[\begin{array}{ccc} \gamma_2-\beta_3 & \alpha_3-\gamma_1 & \beta_1-\alpha_2 \end{array}\right]^T \tag{7.52} $$

$$ \lambda^2 = (\gamma_2-\beta_3)^2 + (\alpha_3-\gamma_1)^2 + (\beta_1-\alpha_2)^2 \tag{7.53} $$

$$ \sin\theta_{a,b} = \frac{\lambda}{2} \tag{7.54} $$

The vector ${}_{k-1}\boldsymbol{n}_{a,b}$ has been referred to the section axes ${}^{k-1}_{0}\boldsymbol{P}$. It can also be transformed into the element axes as follows:

$$ {}^{k}_{0}\boldsymbol{n}_{a,b} = {}^{k-1}_{0}\boldsymbol{P}\,{}^{k}_{k-1}\boldsymbol{n} \tag{7.55} $$

With the previous expression, the natural rotations of the element can be expressed as

$$ \left[\begin{array}{ccc} \theta_{xa} & \theta_{ya} & \theta_{za} \end{array}\right]^T = \theta_a\,{}^{k}_{0}\boldsymbol{n}_a \tag{7.56} $$

$$ \left[\begin{array}{ccc} \theta_{xb} & \theta_{yb} & \theta_{zb} \end{array}\right]^T = \theta_b\,{}^{k}_{0}\boldsymbol{n}_b \tag{7.57} $$

Once the natural deformations of the element have been computed, the forces acting on the nodes due to the deformation of the element ($\boldsymbol{f_{nd}}$) can be calculated as

$$ {}^{k}_{k}\boldsymbol{f_{nd}} = {}^{k-1}_{k-1}\boldsymbol{f_{nd}} + {}^{k-1}_{k-1}\boldsymbol{K_\tau}\boldsymbol{\Delta u_n} \tag{7.58} $$

where ${}^{k-1}_{k-1}\boldsymbol{K_\tau}$ is the first contribution of the tangent stiffness matrix defined as:

$$ {}^{k-1}_{k-1}\boldsymbol{K_\tau} = {}^{k-1}_{k-1}\boldsymbol{K_e} + {}^{k-1}_{k-1}\boldsymbol{K_g} + {}^{k-1}_{k-1}\boldsymbol{K_i} \tag{7.59} $$

This formula means that the nodal forces due to the deformation acting on the element at the final configuration ${}^{k}\boldsymbol{C}$ can be seen as the sum of the nodal forces in the previous configuration plus the contribution of the natural deformation in the current configuration.

To compute the stresses acting on each end of the element, it is required to include the nodal forces due to the external loads ($\boldsymbol{f_{el}}$), the self weight ($\boldsymbol{f_{sw}}$) and the interaction between the beam and the fluid ($\boldsymbol{f_{hl}}$).

The easiest one to be computed is the nodal force due to the self weight of the beam. During the load procedure, the structure deforms itself and the local reference system of the beam element changes. The contribution of the self weight in the nodal forces must be refered to the local reference system of the element. Considering a generic configuration of a beam element characterized by the load parameter λ, the following equation can be written:

$$ \boldsymbol{f_{sw}} = \left[\begin{array}{cccccccccccc} \frac{p_{x'}l}{2} & \frac{p_{y'}l}{2} & \frac{p_{z'}l}{2} & 0 & -\frac{p_{z'}l^2}{12} & \frac{p_{y'}l^2}{12} & \frac{p_{x'}l}{2} & \frac{p_{y'}l}{2} & \frac{p_{z'}l}{2} & 0 & \frac{p_{z'}l^2}{12} & -\frac{p_{y'}l^2}{12} \end{array}\right]^T \tag{7.60} $$

where the variables $p_{x'}$, $p_{y'}$ and $p_{z'}$ can be computed as follows

$$p_{x'} = -\lambda\gamma_m A\frac{l_0}{l}\left(\boldsymbol{z}^T\boldsymbol{x'}\right) \tag{7.61}$$

$$p_{y'} = -\lambda\gamma_m A\frac{l_0}{l}\left(\boldsymbol{z}^T\boldsymbol{y'}\right) \tag{7.62}$$

$$p_{z'} = -\lambda\gamma_m A\frac{l_0}{l}\left(\boldsymbol{z}^T\boldsymbol{z'}\right) \tag{7.63}$$

where the vectors $\boldsymbol{x'}$, $\boldsymbol{y'}$ and $\boldsymbol{z'}$ define the local reference system of the element in the current configuration, γ_m stands for the self weight of the material, A is the area of the section of the element, l is the actual length of the element and l_0 is the length of the element in the initial configuration.

In addition, the nodal forces produced by the external loads and hydrostatic loads can be easily computed with an integration along the element as follows:

$$\boldsymbol{f_{el}} = \int_0^l \boldsymbol{N}^T\boldsymbol{f}\ dx' \tag{7.64}$$

$$\boldsymbol{f_{hl}} = \int_0^l \boldsymbol{N}^T\boldsymbol{f_h}\ dx' \tag{7.65}$$

where the matrix $\boldsymbol{N}$ has been defined in equation 3.137 and the vectors $\boldsymbol{f_{el}}$ and $\boldsymbol{f_{hl}}$ are the external and hydrostatic loads in the local reference system of the element.

$$\boldsymbol{f} = \begin{bmatrix} n & p'_y & p'_z & m_t \end{bmatrix}^T (x') \tag{7.66}$$

$$\boldsymbol{f_h} = \begin{bmatrix} 0 & p_{hy'} & p_{hz'} & m_{ht} \end{bmatrix}^T (x') \tag{7.67}$$

Once the several nodal forces have been computed, the forces and moments at the ends of the element can be computed by simple equilibrium considerations as follows:

$$\boldsymbol{\sigma} = \boldsymbol{f_{nd}} - (\boldsymbol{f_{sw}} + \boldsymbol{f_{el}} + \boldsymbol{f_{hl}}) \tag{7.68}$$

7.4.4 Reaction forces of the system

The attention is now focused on the computation of the reaction of the system $\boldsymbol{R}$.

Therefore, the contribution of each element has to be taken into account. Considering the reference system $\boldsymbol{T}_e$ of each element, the forces and moments at the ends due to the deformation of the element $\boldsymbol{f_{nd}}$ and the forces and moments at ends produced by the fluid $\boldsymbol{f_{hl}}$ in the local reference system of each element in the current configuration, the reaction of the system can be computed as follows:

$$\boldsymbol{R} = \boldsymbol{R_0} + \sum_{e=1}^{N_e} \boldsymbol{L}_e^T\boldsymbol{T}_e^T\left(\boldsymbol{f_{nd}} - \boldsymbol{f_{hl}}\right) \tag{7.69}$$

where the matrix $\boldsymbol{L}_e$ is called the connectivity matrix and relates the global degrees of freedom of the structure with the degrees of freedom of each element as

$$\boldsymbol{u}_e = \boldsymbol{L}_e \boldsymbol{U} \tag{7.70}$$

8 Benchmarks and validation

In this chapter, a deep analysis on several benchmarks will be carried out to ensure the accuracy and reliability of the program developed. As the reader may remember, the program has been developed considering several hypothesis: large displacements and finite rotations, small deformations with respect the reference system of the beam element and linear elastic material.

The chapter is divided in two parts. The first part is devoted to the analysis of several benchmarks obtained from literature. Cable structures under self weight will be analysed and also ordinary structures composed by beam elements will be studied. In addition, simple analysis of floating beam structures will be considered and the solutions will be compared with the analytical results.

The second part of this chapter is devoted to the study of floating structures composed by cable and beam elements. Here, the proposed element will be validated. It should be emphasized that, as most studies in the past have not developed similar models for the study of floating structures, the results in this second part have not been compared with other results from literature.

8.1 Benchmarks

Some benchmarks are analyzed to test the performance of the program developed. The analysis will be carried out and results compared with analytical solutions.

First, some cases concerning cable structures will be carried out and compared with the solutions provided by the unextensible and elastic catenary models.

Second, the classic example of nonlinear behaviour provided by the Euler's arch is analyzed and the reaction-displacement respons curve is depicted using both the analytical and numerical models.

Finally, some benchmarks concerning the behaviour of floating beam structures are performed. Here, the analytical solution will be developed when possible and the com-

parison will be made in terms of displacements and stresses in particular points of the structure.

8.1.1 Two-member truss under concentrated load

The problem of two truss elements restrained to each end and loaded in the middle as the one depicted in figure 8.1 is analyzed. The reaction-displacement respons curve is first obtained analytically and then compared with the numerical results.

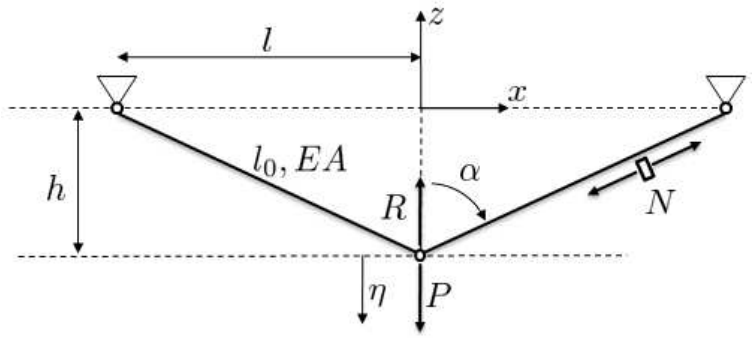

Figure 8.1: Two member truss under concentrated load

8.1.1.1 Analytical solution

The solution of the problem can be obtained analytically. First, the reaction of the system corresponding to the degree of freedom of the structure can be expressed as:

$$R = 2N\cos\alpha \tag{8.1}$$

where N is the axial force of the bars and α is the angle between the vertical and each one of the bars.

Considering the constitutive equation of the bars, the axial stress can be written in terms of the elongation Δl.

$$N = \frac{EA}{l_0}\Delta l \tag{8.2}$$

where Δl can be computed as:

$$\Delta l = l - l_0 \tag{8.3}$$

$$l = \sqrt{l^2 + (h+\eta)^2} \qquad l_0 = \sqrt{l^2 + h^2}$$

By geometrical considerations, the cosine of α can be written in terms of the vertical displacement η.

$$\cos\alpha = \frac{h+\eta}{l} \tag{8.4}$$

Substituting equations 8.2, 8.3 and 8.4 in equation 8.1, the following nonlinear equilibrium equation in terms of the vertical displacement η can be obtained.

$$R = 2\frac{EA}{l_0}\left(\sqrt{l^2 + (h+\eta)^2} - l_0\right)\frac{h+\eta}{\sqrt{l^2 + (h+\eta)^2}} \tag{8.5}$$

The derivative of the reaction with respect to the variable η can be obtained.

$$\frac{dR}{d\eta} = 2\frac{EA}{l_0 l}\left[(h+\eta)\frac{dl}{d\eta} + (l - l_0)\left(l - [h+\eta]\frac{dl}{d\eta}\right)\right] \tag{8.6}$$

$$\frac{dl}{d\eta} = \frac{h+\eta}{\sqrt{l^1 + (h+\eta)^2}} = \cos\alpha$$

Considering the numerical values reported in the following table the reaction-displacement curve can be depicted in figure 8.2

$E\ [kN/m^2]$	$A\ [m^2]$	$l_0\ [m^2]$	$l\ [m]$	$h\ [m]$	$P\ [kN]$
2e8	0.164588	25.0075	25	0.612361	318.98445

Table 8.1: Two member truss under concentrated load - Mechanical and geometrical variables

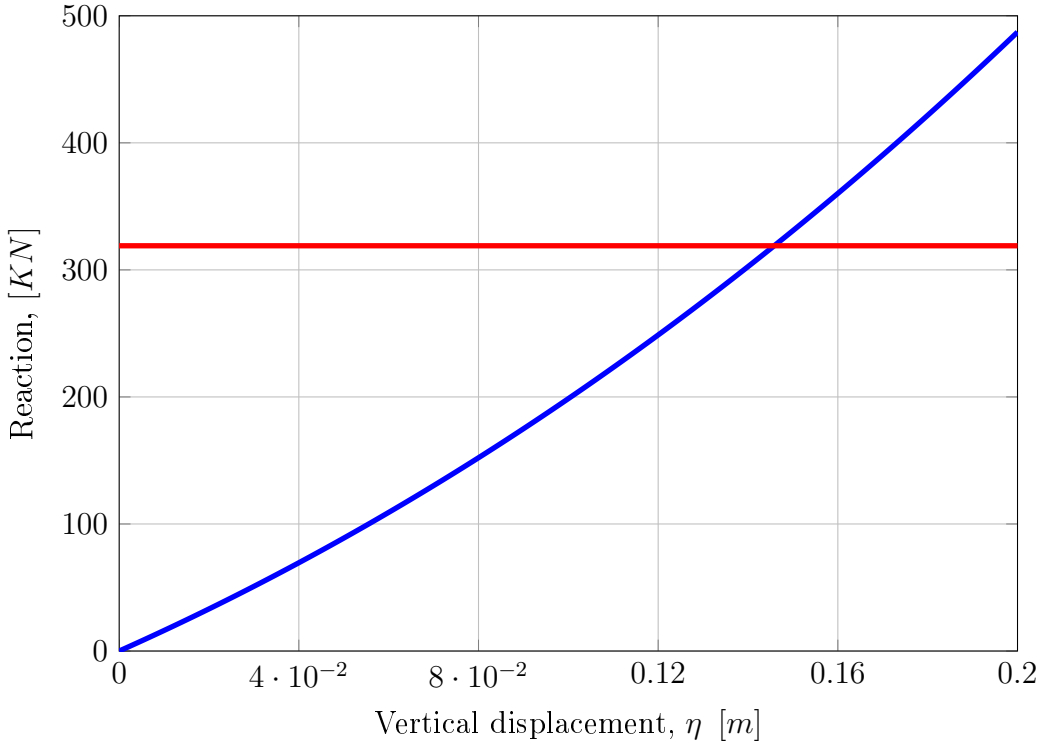

Figure 8.2: Two member truss under concentrated load - Reaction-displacement curve

Solving the nonlinear equilibrium equation with a Newton-Raphson scheme, the displacement η that defines the equilibrium position is reported in table 8.3. With the

displacement computed, the other variables can be calculated and are reported in the same table.

8.1.1.2 Numerical solution

The analysis of the structure depicted in figure 8.1 has been also carried out with the finite element code. The variables used are reported in table 8.2.

Concept	Symbol	Value
Structural model		
Model for cable structure	M_{cs}	FEM
Model for beam structure	M_{bs}	-
Model for flexural behaviour	M_{fb}	-
Model for torsional behaviour	M_{tb}	-
Parameters for the analysis		
Tolerance in the equilibrium	Tol_G	1e-4
Tolerance in the displacements	Tol_D	1e-4
Tolerance in the energy	Tol_W	1e-4
Maximum number of iterations correction phase	I_M	10
Method used in the correction phase	-	Arc-length/Angle
Initial Arc-length value	Δl_I	0.5
Critical Bergan value for the switching	$\overline{B}$	0.25
Initial increment of load	$\Delta\lambda_I$	0.05
Final load parameter	λ_F	1
Maximum number of increments	Inc_M	50
Optimum number of iterations correction phase	I_O	5
Update parameters during the incremental procedure	-	No

Table 8.2: Two member truss under concentrated load - Parameters for the nonlinear analysis in an incremental iterative scheme

Performing the incremental iterative analysis, the reaction-displacement curve is obtained and reported in figure 8.3. It must be noted that the reference system used in the finite element analysis has the positive displacements and forces upside. As it can be seen in the figure, the program is able to completely characterize the reaction-displacement path and the equilibrium configuration is computed for each displacement (curved depicted in figure 8.3).

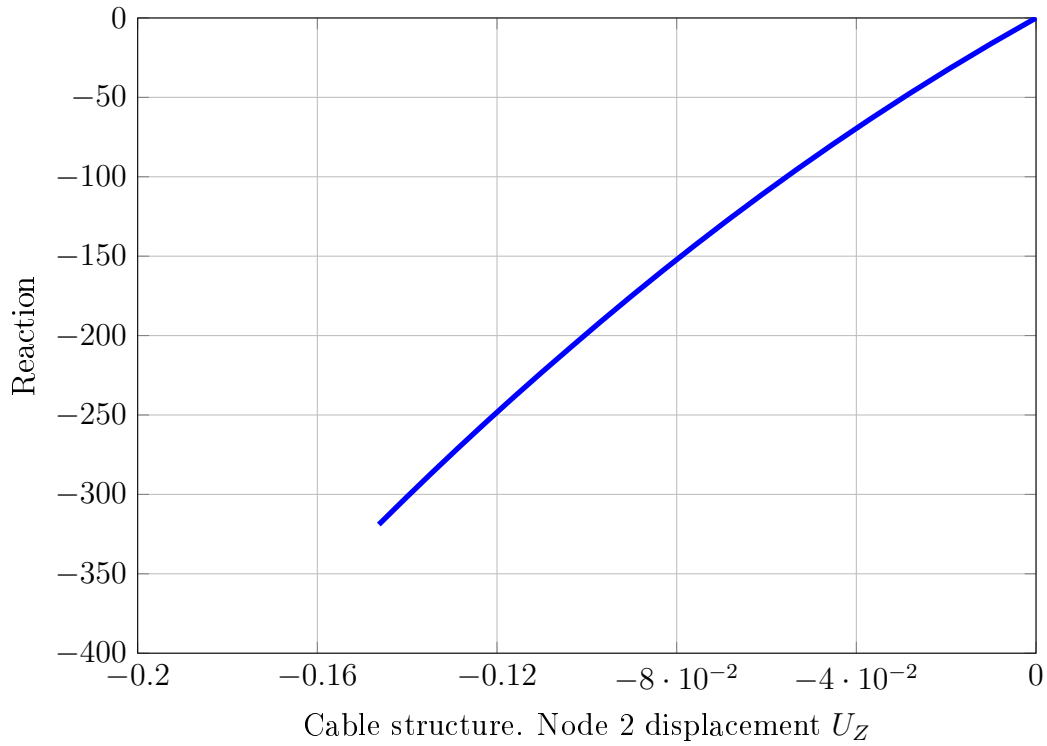

Figure 8.3: Two member truss under concentrated load - Reaction-Displacement curve obtained with the numerical model

Finally, the comparison in terms of displacement and stress of each element are summed up in table 8.3.

Concept	**Symbol/Units**	**Analytical solution**	**FEM solution**	**Error**[%]
Vertical Displacement	η $[m]$	0.1459	0.145835	4e-2
Axial stress	N $[kN]$	5261.1436	5260.68	8e-3
Reaction of the system	R $[kN]$	318.9842	318.984	6.27e-5

Table 8.3: Two member truss under concentrated load - Comparison of the results between the analytical and finite element models

8.1.2 Symmetric elastic cable under self weight

A cable symmetrically restrained from both ends and subjected to its own selfweight is analyzed.

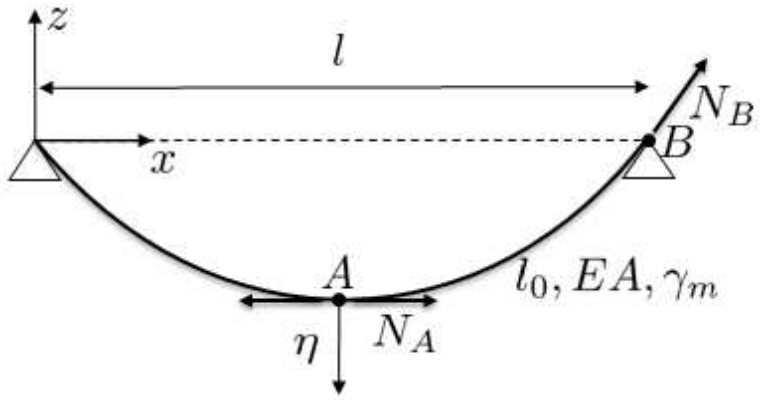

Figure 8.4: Symmetric elastic cable under self weight

First, the analytical solution of the problem will be obtained using the unextensible and the elastic catenary models. Then the displacements and stresses will be compared with the results of the program at points A and B (figure 8.4).

8.1.2.1 Analytical solution

The analytical solution of this problem can be obtained considering the model provided in section 3.1.2, where the governing equations of the elastic cable were introduced. The geometrical and mechanical characteristics used in this benchmarks are reported in table 8.4.

E $[kN/m^2]$	A $[m^2]$	l_0 $[m]$	l $[m]$	γ_m $[kN/m^3]$
2e8	0.164588	50.02	50	77.5

Table 8.4: Symmetric elastic cable under self weight - Mechanical and geometrical variables

Using the elastic catenary model, the deformed configuration of the cable can be depicted in figure 8.5. In this figure, the unextensible catenary solution has also been included for completeness. In addition, the distribution of the axial stress along the deformed elastic cable is depicted in figure 8.6.

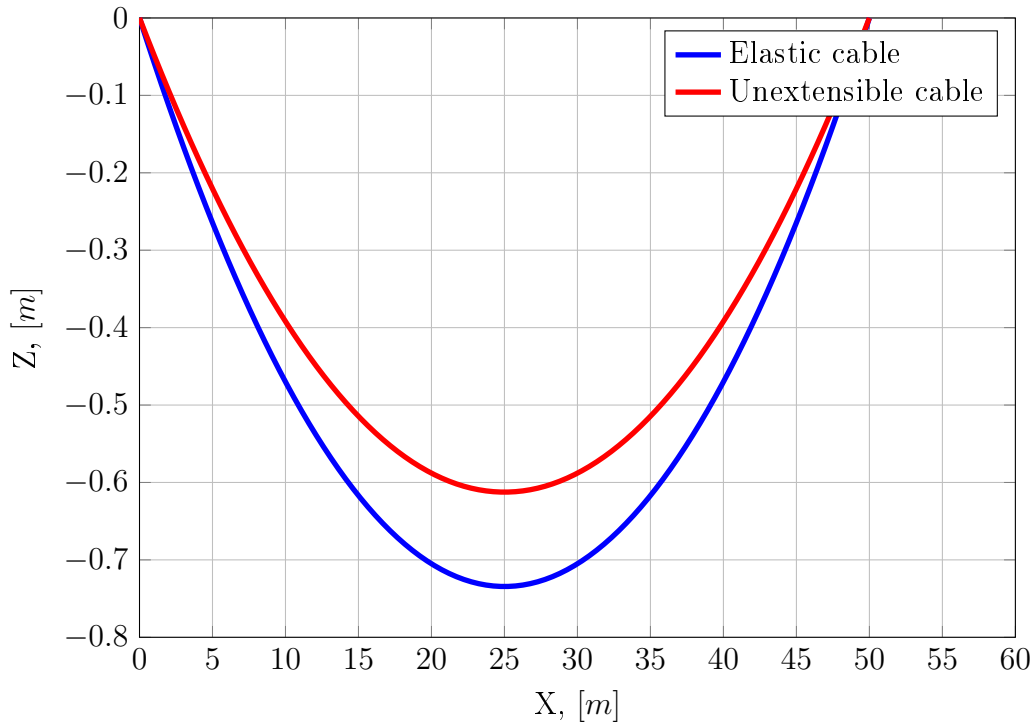

Figure 8.5: Symmetric elastic cable under self weight - Deformed configuration considering both the unextensible and elastic catenaries

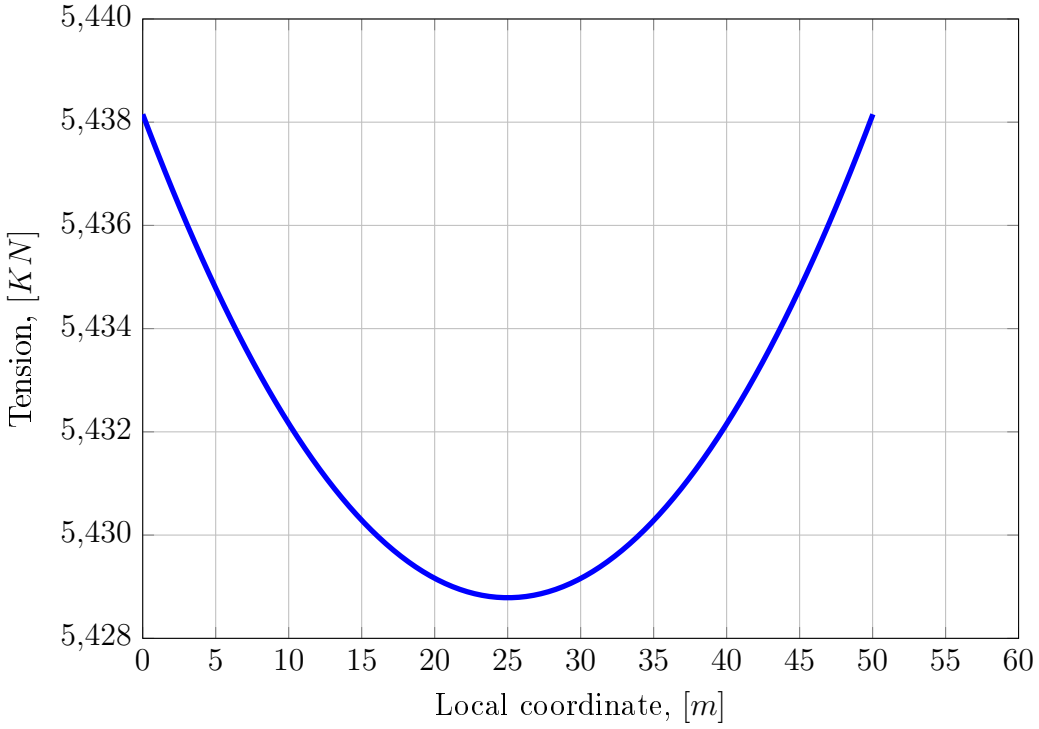

Figure 8.6: Symmetric elastic cable under self weight - Axial stress distribution along the deformed elastic catenary

As control variables, the displacement and the tension in the middle of the cable and the tension at each end of the cable have been computed with the theoretical model and reported in table 8.6.

8.1.2.2 Numerical solution

Now, the cable will be analyzed considering the finite element model developed in this work. The number of straight finite elements used is equal to 149. In table 8.5 the parameters and models used in the program are listed.

Concept	Symbol	Value
Structural model		
Model for cable structure	M_{cs}	FEM
Model for beam structure	M_{bs}	-
Model for flexural behaviour	M_{fb}	-
Model for torsional behaviour	M_{tb}	-
Parameters for the analysis		
Tolerance in the equilibrium	Tol_G	1e-4
Tolerance in the displacements	Tol_D	1e-4
Tolerance in the energy	Tol_W	1e-4
Maximum number of iterations correction phase	I_M	25
Method used in the correction phase	-	Arc-length/Angle
Initial Arc-length value	Δl_I	0.5
Critical Bergan value for the switching	$\overline{B}$	0.25
Initial increment of load	$\Delta\lambda_I$	0.05
Final load parameter	λ_F	1
Maximum number of increments	Inc_M	50
Optimum number of iterations correction phase	I_O	5
Update parameters during the incremental procedure	-	No

Table 8.5: Symmetric elastic cable under self weight - Parameters for the nonlinear analysis in an incremental iterative scheme

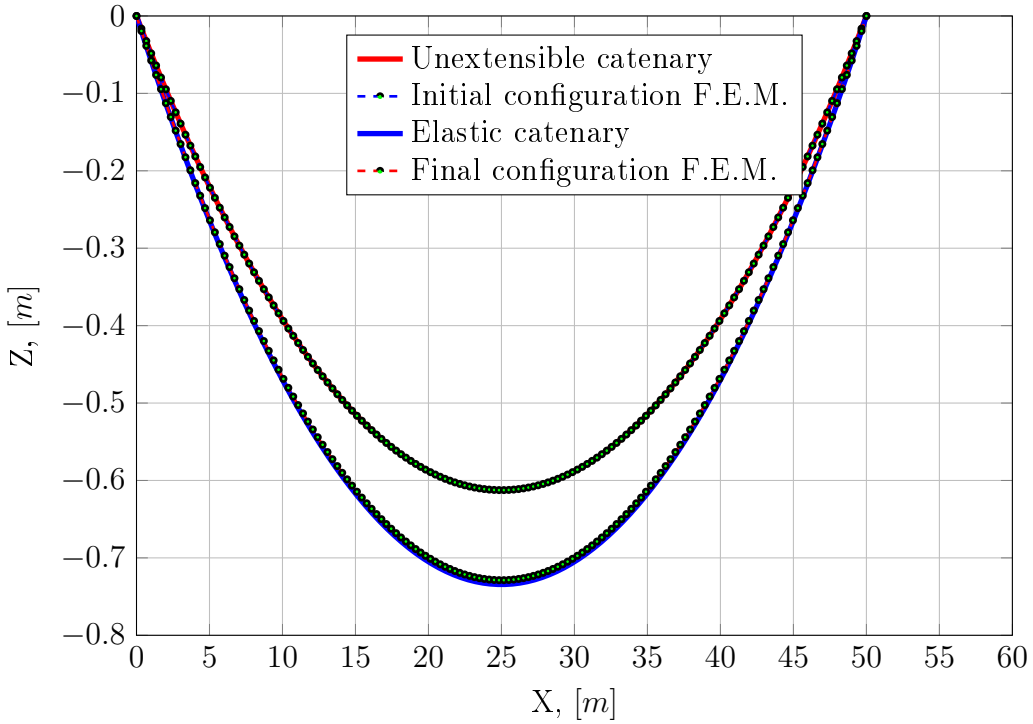

Figure 8.7: Symmetric elastic cable under self weight - Comparison of displacement between theoretical and finite element models

Finally, the comparison in terms of displacement and stresses at the specified points are summed up in table 8.6.

Concept	**Symbol/Units**	**Analytical solution**	**FEM solution**	**Error**[%]
Vertical Displacement	η $[m]$	0.1164	0.116341	5e-2
Axial stress point A	N_A $[kN]$	5428.8	5470.02	7.5e-1
Axial stress point B	N_B $[kN]$	5438.2	5479.19	7.5e-1

Table 8.6: Symmetric elastic cable under self weight - Comparison of the results between the analytical and finite element models

8.1.3 Asymmetric elastic cable under self weight

Now, a cable assymmetrically restrained from both ends and subjected to its own self-weight is analyzed.

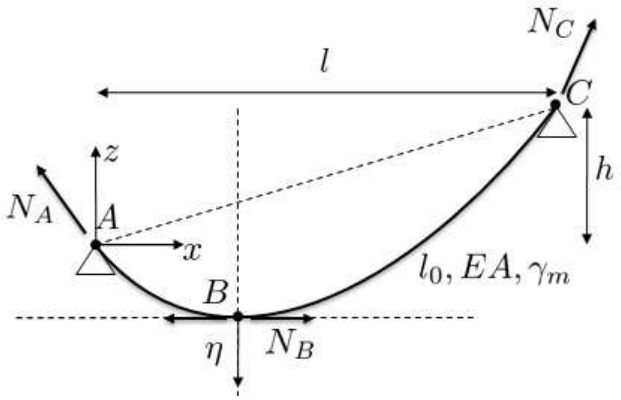

Figure 8.8: Asymetric elastic cable under self weight

First, the analytical solution of the problem will be obtained using the catenary and the elastic catenary models. Then the displacements and stresses will be compared with the results of the program at points A, B and C (figure 8.8).

8.1.3.1 Analytical solution

The analytical solution of this problem can be obtained considering the model provided in section 3.1.2, where the governing equations of the elastic cable were introduced. The geometrical and mechanical characteristics used in this benchmarks are reported in table 8.7.

$E\ [kN/m^2]$	$A\ [m^2]$	$l_0\ [m]$	$l\ [m]$	$h\ [m]$	$\gamma_m\ [kN/m^3]$
2e8	0.164588	51.1	50	10	77.5

Table 8.7: Asymmetric elastic cable under self weight - Mechanical and geometrical variables

Using the elastic catenary model, the deformed configuration of the cable can be depicted in figure 8.9. In this figure, the unextensible catenary solution has also been included for completeness. In addition, the distribution of the axial stress along the deformed elastic cable is depicted in figure 8.10.

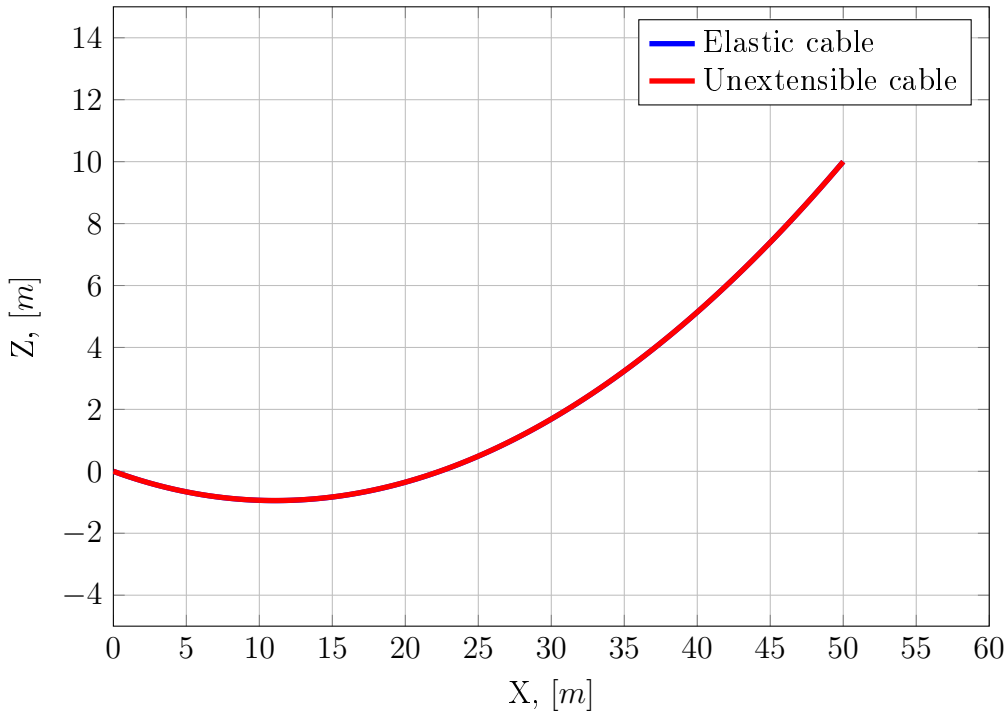

Figure 8.9: Assymetric elastic cable under its own self weight - Deformed configuration considering both the unextensible and elastic catenaries

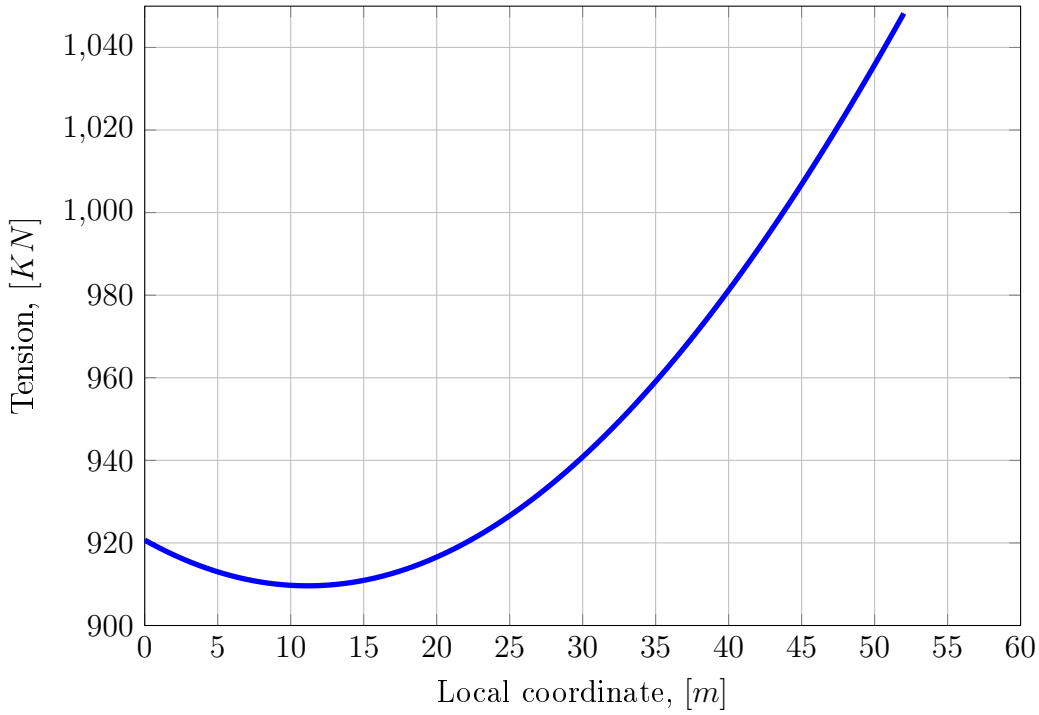

Figure 8.10: Asymmetric elastic cable under its own self weight - Axial stress distribution along the deformed elastic catenary

As control variables, the displacements and stresses at points A, B and C have been

computed with the theoretical model and reported in table 8.9.

8.1.3.2 Numerical solution

Now, the cable will be analyzed considering the finite element model developed in this work. The number of straight finite elements used is equal to 149. In table 8.8 the parameters and models used in the program are listed.

Concept	Symbol	Value
Structural model		
Model for cable structure	M_{cs}	FEM
Model for beam structure	M_{bs}	-
Model for flexural behaviour	M_{fb}	-
Model for torsional behaviour	M_{tb}	-
Parameters for the analysis		
Tolerance in the equilibrium	Tol_G	1e-4
Tolerance in the displacements	Tol_D	1e-4
Tolerance in the energy	Tol_W	1e-4
Maximum number of iterations correction phase	I_M	25
Method used in the correction phase	-	Arc-length/Angle
Initial Arc-length value	Δl_I	0.5
Critical Bergan value for the switching	$\overline{B}$	0.25
Initial increment of load	$\Delta\lambda_I$	0.05
Final load parameter	λ_F	1
Maximum number of increments	Inc_M	50
Optimum number of iterations correction phase	I_O	5
Update parameters during the incremental procedure	-	No

Table 8.8: Asymmetric elastic cable under self weight - Parameters for the nonlinear analysis in an incremental iterative scheme

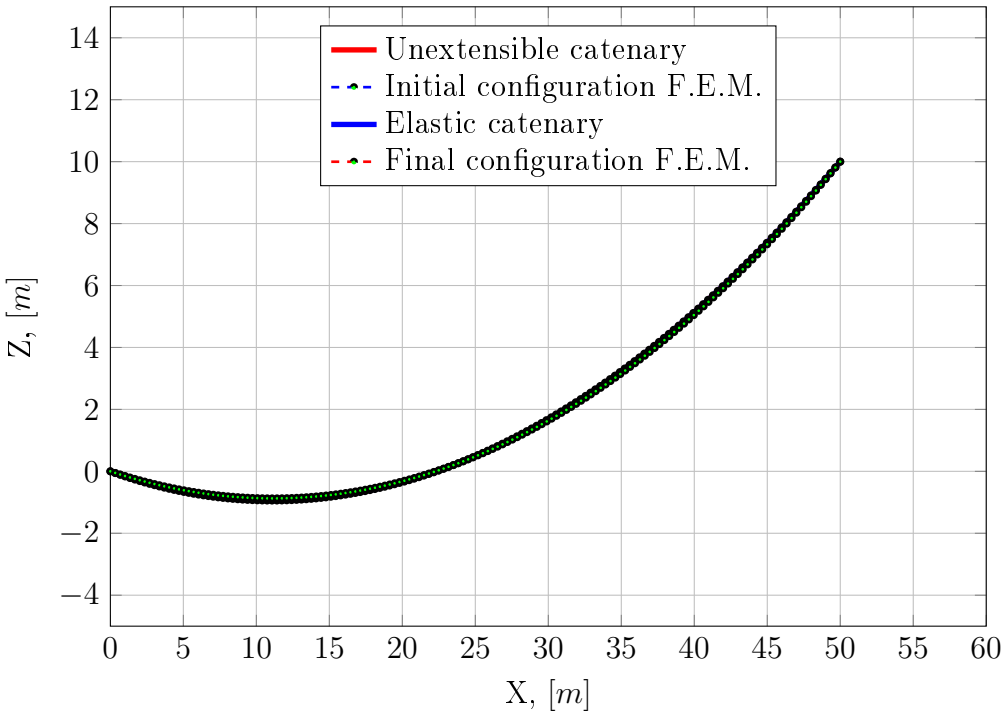

Figure 8.11: Asymmetric elastic cable under self weight - Comparison of displacement between theoretical and finite element models

Finally, the comparison in terms of displacement and stresses at the specified points are summed up in table 8.9.

Concept	**Symbol/Units**	**Analytical solution**	**FEM solution**	**Error**[%]
Vertical Displacement	η $[m]$	0.07491	0.074895	2e-2
Axial stress point A	N_A $[kN]$	920.6824	918.683	2e-1
Axial stress point B	N_B $[kN]$	909.7976	907.891	2e-1
Axial stress point C	N_C $[kN]$	1048.2	1045.35	2e-1

Table 8.9: Asymmetric elastic cable under self weight - Comparison of the results between the analytical and finite element models

8.1.4 Euler's Arch

The classic Euler's arch problem will now be analyzed. The reaction-displacement curve will be analytically and numerically computed and compared. In figure 8.12, a sketch of the problem is depicted. The beam will be analyzed as a beam element (and not with a cable element) and the capability of the program to update the reference system of beam elements in terms of their natural deformations will also be tested[(1)].

[(1)] As it can be seen, the problem analyzed with cable elements and beam elements leads to the same solution if the program is able to catch the natural deformations of the beam element.

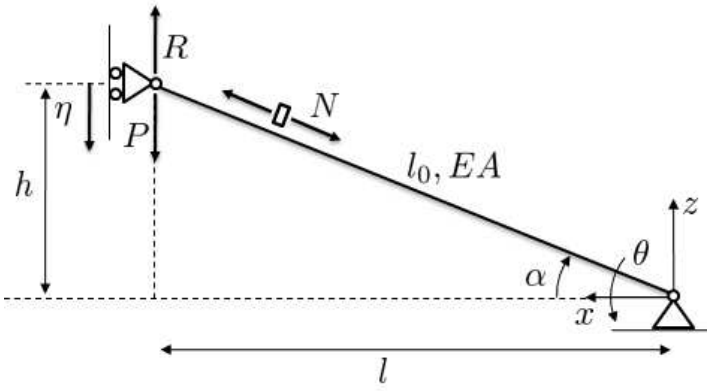

Figure 8.12: Euler's arch

8.1.4.1 Analytical solution

Considering equilibrium in the left node, the following equation can be written.

$$R = N \sin \alpha \tag{8.7}$$

The constitutive equation of the beam is

$$N = \frac{EA}{l_0} \Delta l \tag{8.8}$$

where the increment of length can be written as:

$$\Delta l = l - l_0 \tag{8.9}$$

The length of the beam in the current configuration can be written in terms of the displacement η as follows:

$$l = \sqrt{l^2 + (h - \eta)^2} \qquad l_0 = \sqrt{l^2 + h^2} \tag{8.10}$$

By geometrical considerations the sine of the angle α can be written also as a function of η.

$$\sin \alpha = \frac{h - \eta}{l} \tag{8.11}$$

Substituting equations 8.8, 8.9, 8.10 and 8.11 in equation 8.7 the equilibrium equation in terms of the displacement η may be obtained.

$$R = \frac{EA}{l_0} \left(\sqrt{l^2 + (h - \eta)^2} - l_0 \right) \frac{h - \eta}{\sqrt{l^2 + (h - \eta)^2}} \tag{8.12}$$

8.1.4.2 Numerical solution

Now, the Euler's arch will be analyzed considering the finite element model developed in this work. In table 8.10 the parameters and models used in the program are listed.

Concept	Symbol	Value
Structural model		
Model for cable structure	M_{cs}	-
Model for beam structure	M_{bs}	FEM
Model for flexural behaviour	M_{fb}	Euler-Bernoulli
Model for torsional behaviour	M_{tb}	Saint Venant
Parameters for the analysis		
Tolerance in the equilibrium	Tol_G	1e-4
Tolerance in the displacements	Tol_D	1e-4
Tolerance in the energy	Tol_W	1e-4
Maximum number of iterations correction phase	I_M	25
Method used in the correction phase	-	Arc-length/Angle
Initial Arc-length value	Δl_I	0.5
Critical Bergan value for the switching	$\overline{B}$	0.25
Initial increment of load	$\Delta\lambda_I$	0.05
Final load parameter	λ_F	1
Maximum number of increments	Inc_M	50
Optimum number of iterations correction phase	I_O	5
Update parameters during the incremental procedure	-	No

Table 8.10: Euler's arch - Parameters for the nonlinear analysis in an incremental iterative scheme

The reaction-displacement curve analytically and numerically obtained are confronted in figure 8.13

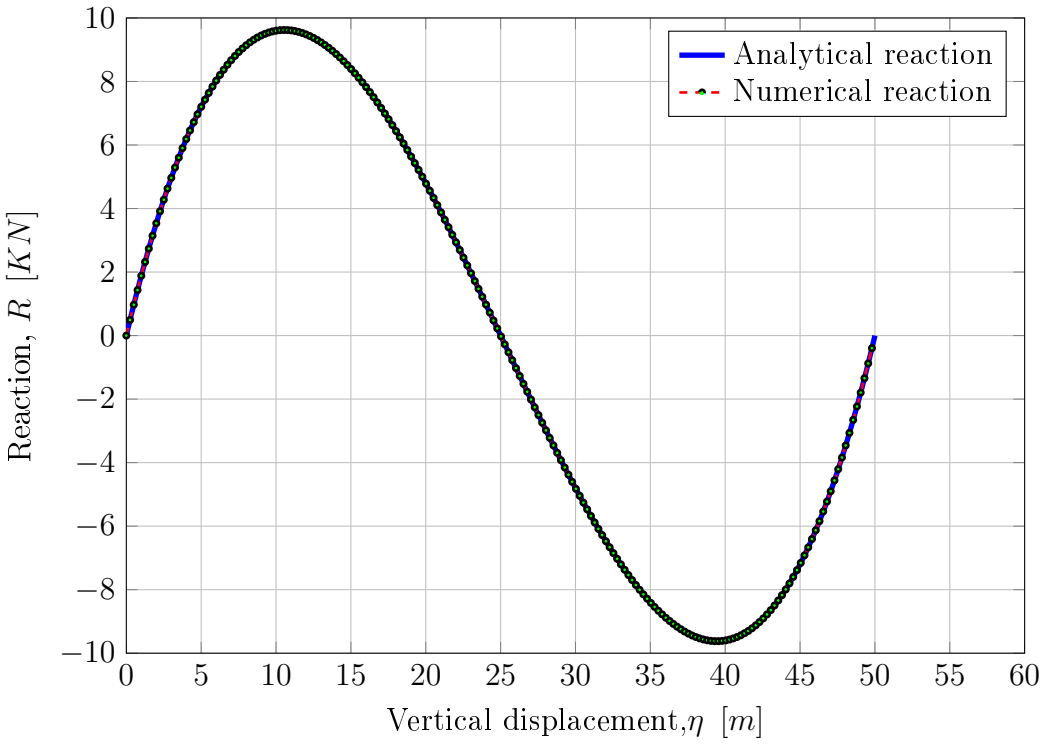

Figure 8.13: Euler's arch - Comparison between analytical and numerical models

8.1.5 Cantilever beam loaded at the tip

One important aspect of this benchmark is that it involves considerable large displacements relative to the cantilever length (the elastic beam is loaded up to a point corresponding to a vertical displacement of around 80% of the original length). Figure 8.14 shows a general view of the problem.

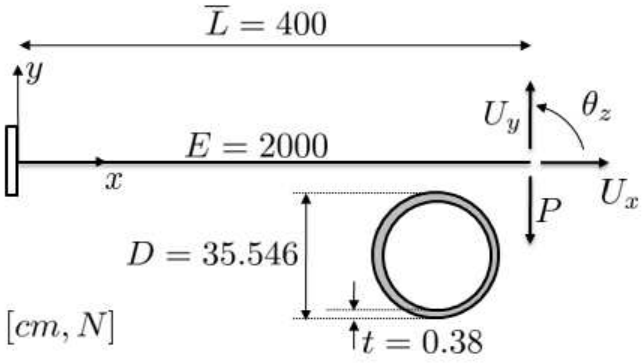

Figure 8.14: Cantilever beam loaded at the tip

Now, the cantilever beam loaded at the tip will be analyzed considering the finite element model developed in this work. In table 8.11 the parameters and models used in the program are listed.

Concept	Symbol	Value
Structural model		
Model for cable structure	M_{cs}	-
Model for beam structure	M_{bs}	FEM
Model for flexural behaviour	M_{fb}	Euler-Bernoulli
Model for torsional behaviour	M_{tb}	Saint Venant
Parameters for the analysis		
Tolerance in the equilibrium	Tol_G	1e-3
Tolerance in the displacements	Tol_D	1e-3
Tolerance in the energy	Tol_W	1e-3
Maximum number of iterations correction phase	I_M	100
Method used in the correction phase	-	Arc-length/Restoring
Initial Arc-length value	Δl_I	0.1
Minimum Bergan value for the switching	B_m	0.5
Maximum Bergan value for the switching	B_M	100
Initial increment of load	$\Delta\lambda_I$	0.05
Final load parameter	λ_F	10
Maximum number of increments	Inc_M	200
Optimum number of iterations correction phase	I_O	50
Update parameters during the incremental procedure	-	No

Table 8.11: Cantilever beam loaded at the tip - Parameters for the nonlinear analysis in an incremental iterative scheme

The solution obtained with the model developed are compared with the ones obtained by [de Souza, 2000]. As it can be seen, the results match very well considering elastic linear material. It should be emphasized that, as most papers only provide the results in graphical form, only a reasonable accurate comparison can be done, due to the inaccuracy in obtaining numerical values from the presented plots.

Some final results provided by the program are listed here considering the normalized vertical load defined as follows:

$$\lambda = \frac{P\overline{L}^2}{EI} \tag{8.13}$$

First, figure 8.15 shows several configurations of the beam during the load procedure.

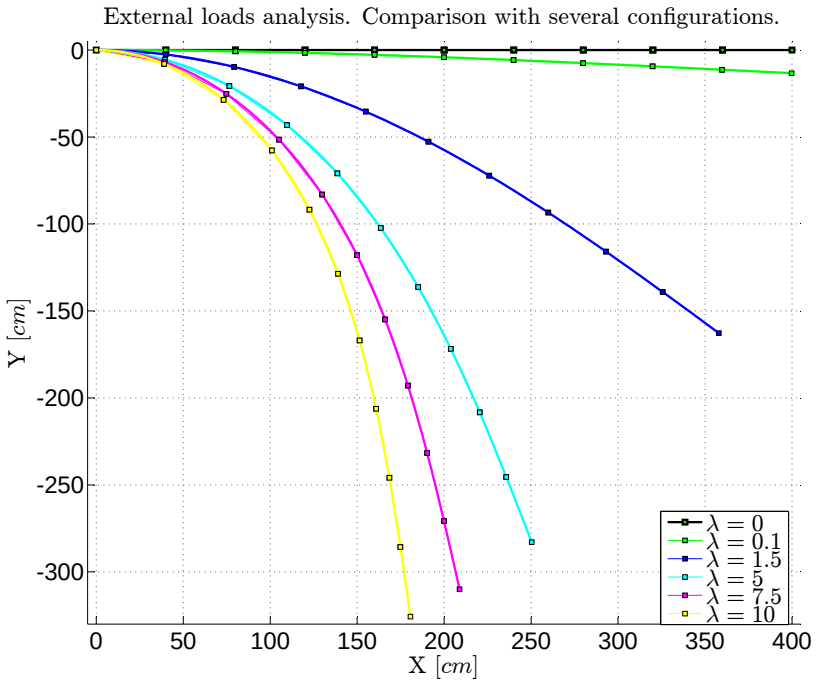

Figure 8.15: Cantilever beam loaded at the tip - Configuration of the beam in several load steps

The equilibrium paths corresponding to the right point of the beam are plotted. Figure 8.16 shows the equilibrium path of the horizontal displacement, figure 8.17 shows the equilibrium path of the vertical displacement and figure 8.18 shows the equilibrium path of the rotation.

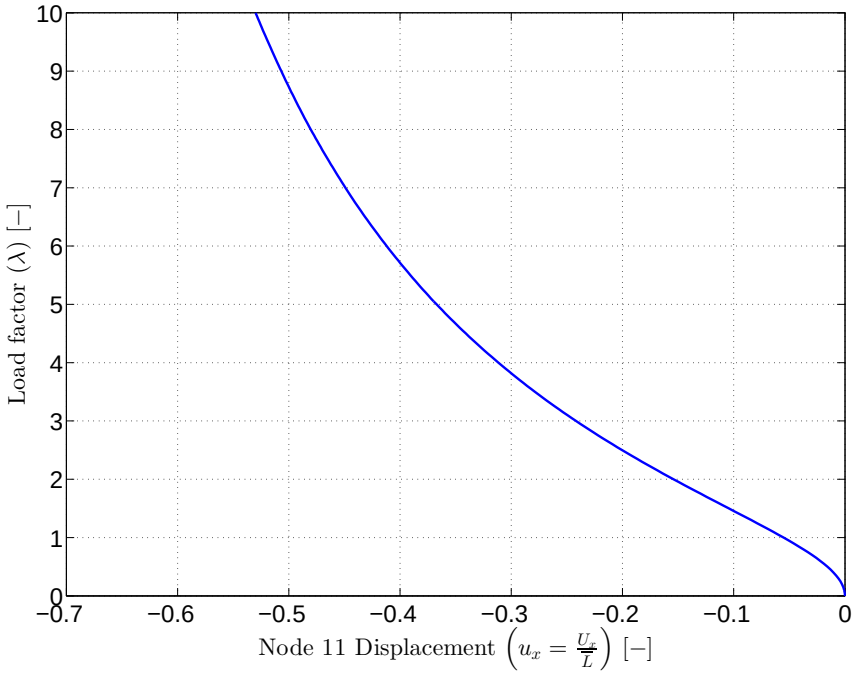

Figure 8.16: Cantilever beam loaded at the tip - Equilibrium path corresponding to the horizontal displacement of the point on the left

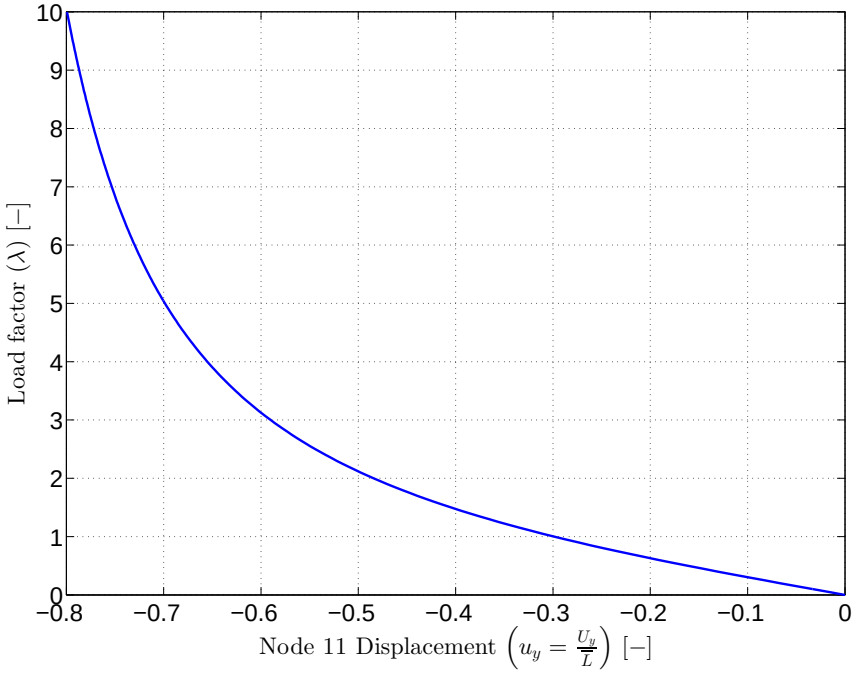

Figure 8.17: Cantilever beam loaded at the tip - Equilibrium path corresponding to the vertical displacement of the point on the left

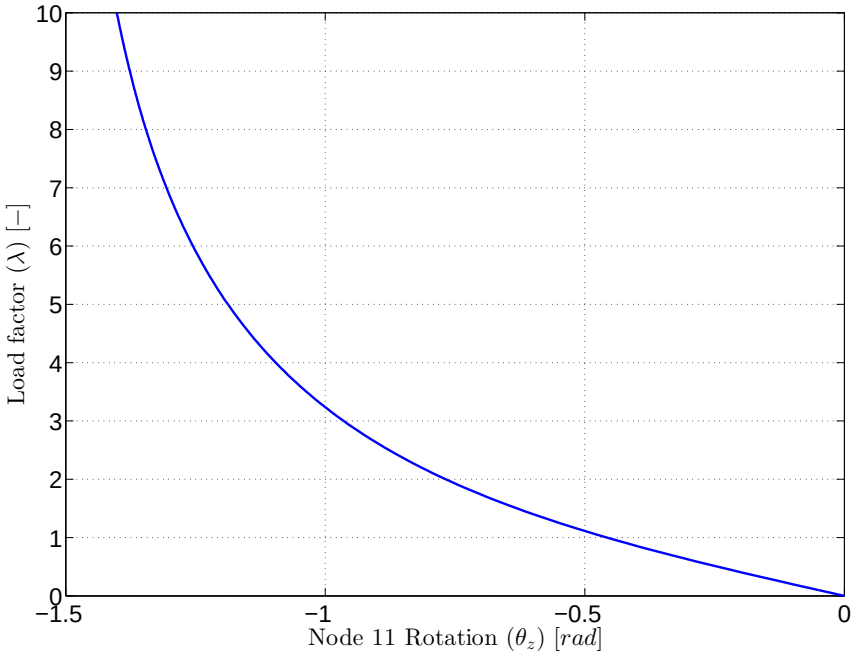

Figure 8.18: Cantilever beam loaded at the tip - Equilibrium path corresponding to the rotation of the point on the left

After the equilibrium paths have been plotted for the most important node of the structure, our attention is focused on the displacement and stress field of the structure assuming predefined load factors. In the following, the configuration, the bending moment in the z axis, the shear force in the local axis y' of the elements and the axial will be plotted. Figures 8.19, 8.20 and 8.21 show the bending moment, shear force and axial force when the load corresponds to $\lambda = 0.1$. The same forces and moments are represented when the load corresponds to $\lambda = 5$ in figures 8.22, 8.23 and 8.24 and figures 8.25, 8.26 and 8.27 show the final configuration of the beam when $\lambda = 10$.

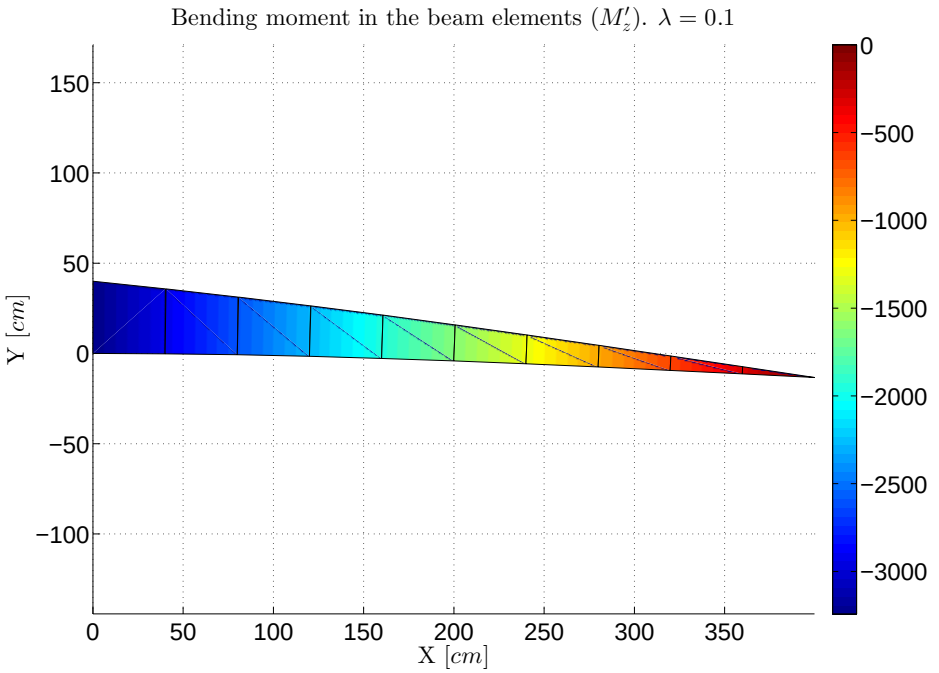

Figure 8.19: Cantilever beam loaded at the tip - Bending moment in the z' axis at the $\lambda = 0.1$

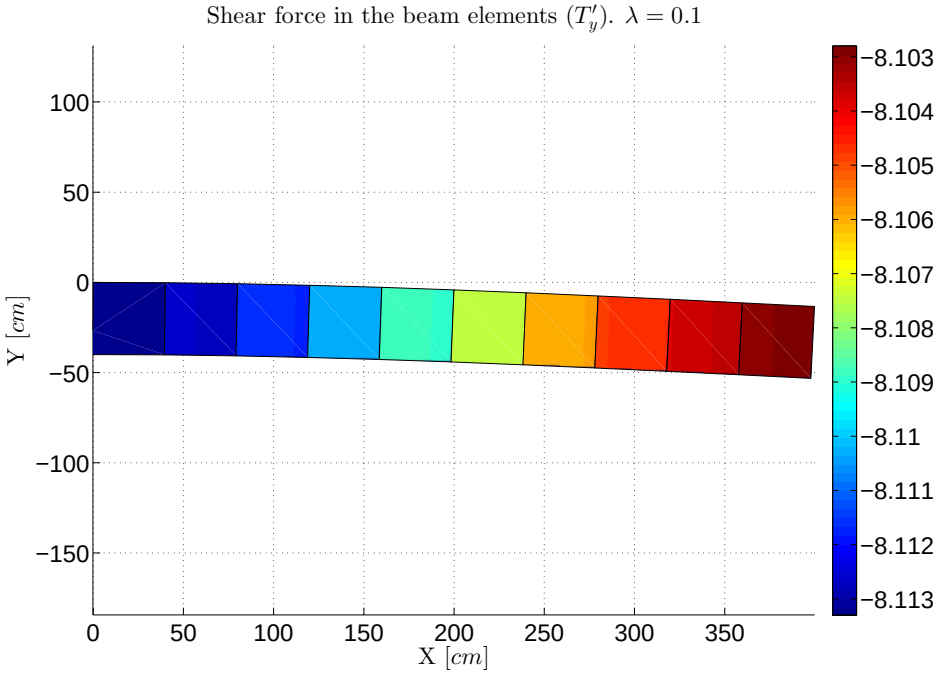

Figure 8.20: Cantilever beam loaded at the tip - Shear forces in the y' axis at the $\lambda = 0.1$

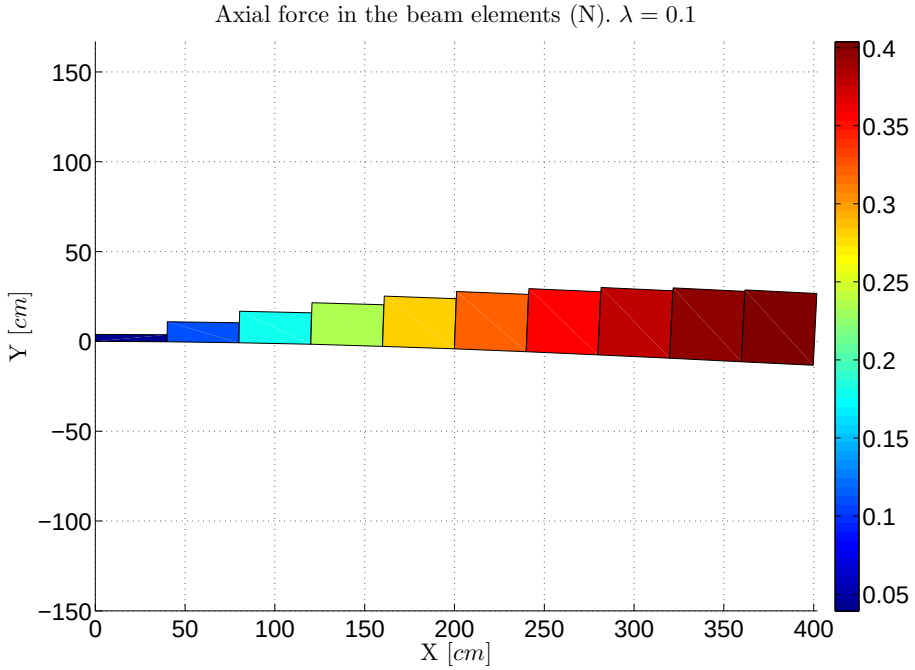

Figure 8.21: Cantilever beam loaded at the tip - Axial force in the x' axis at the $\lambda = 0.1$

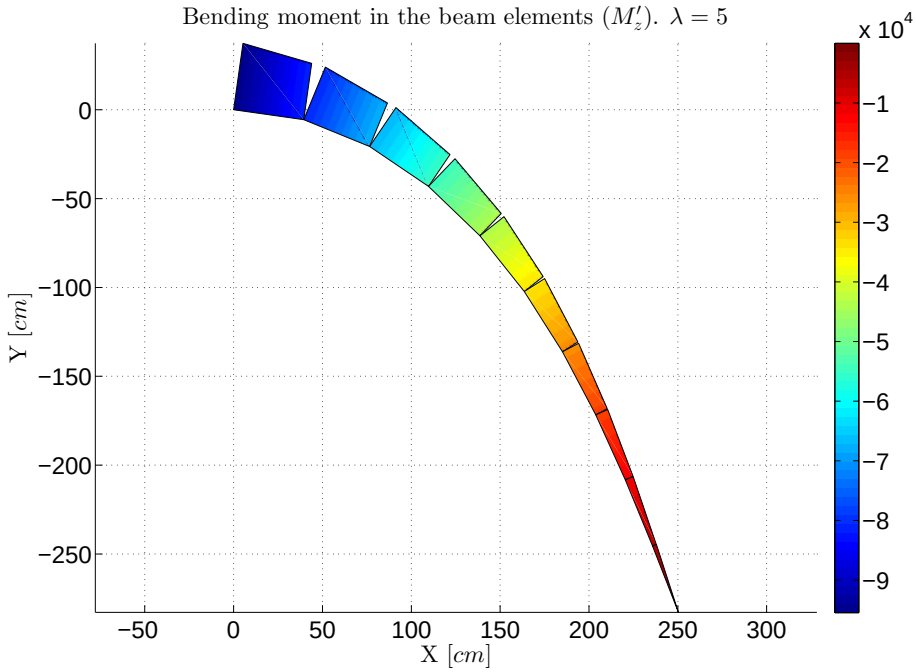

Figure 8.22: Cantilever beam loaded at the tip - Bending moment in the z' axis at the $\lambda = 5$

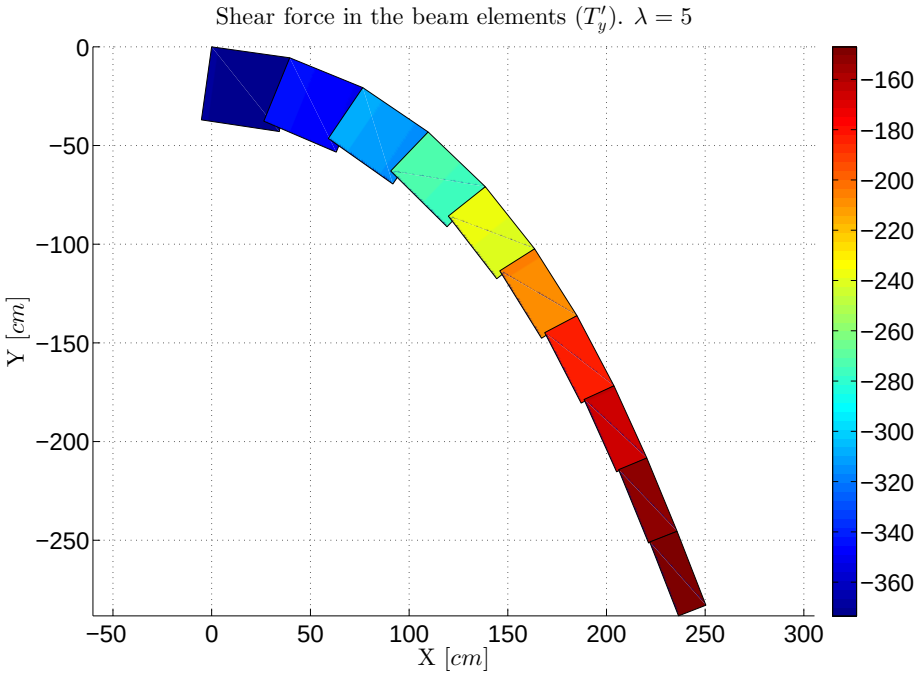

Figure 8.23: Cantilever beam loaded at the tip - Shear forces in the y' axis at the $\lambda = 5$

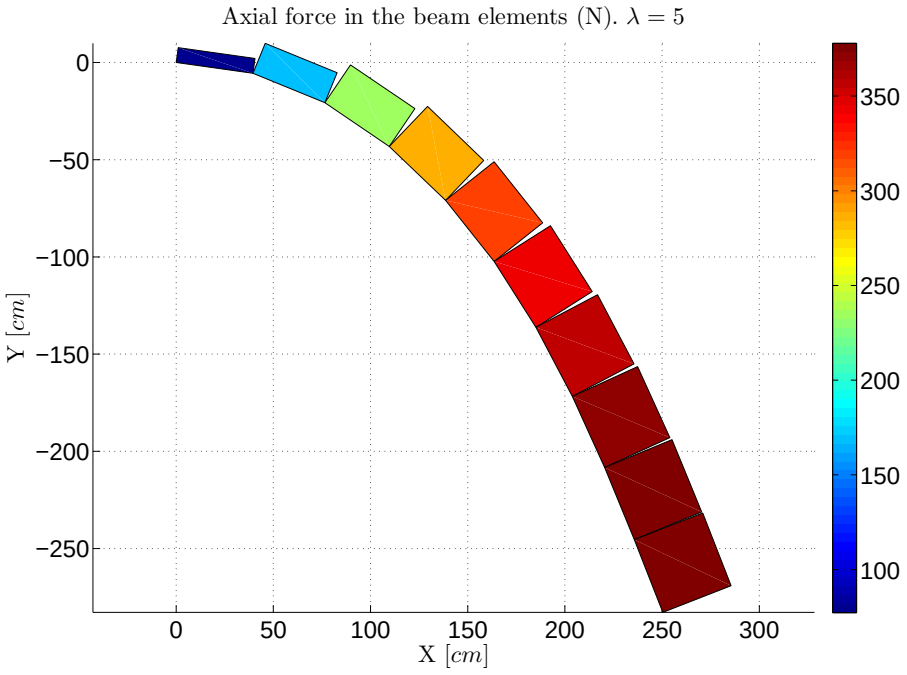

Figure 8.24: Cantilever beam loaded at the tip - Axial force in the x' axis at the $\lambda = 5$

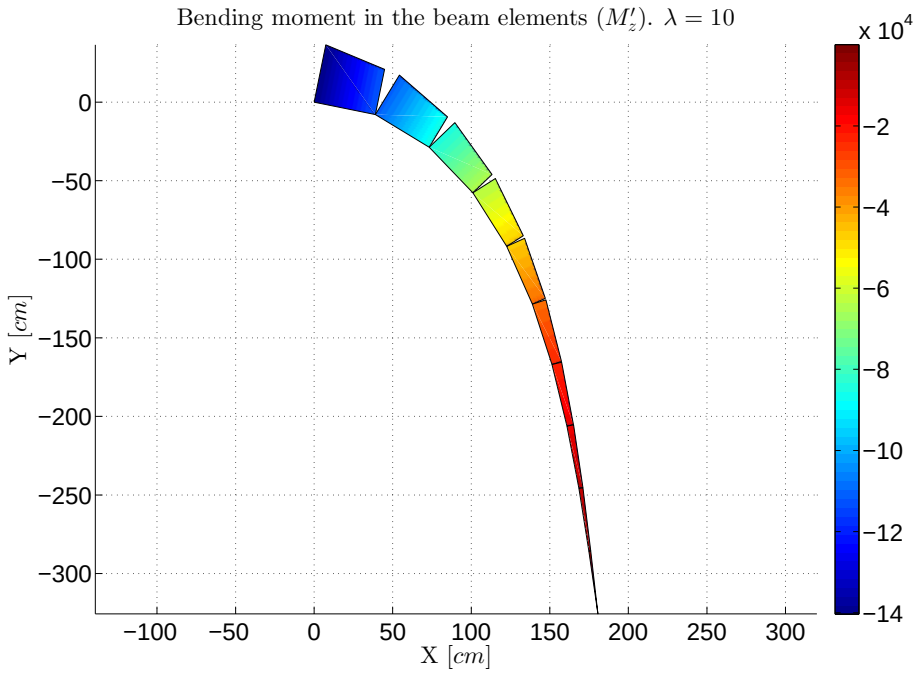

Figure 8.25: Cantilever beam loaded at the tip - Bending moment in the z' axis at the $\lambda = 10$

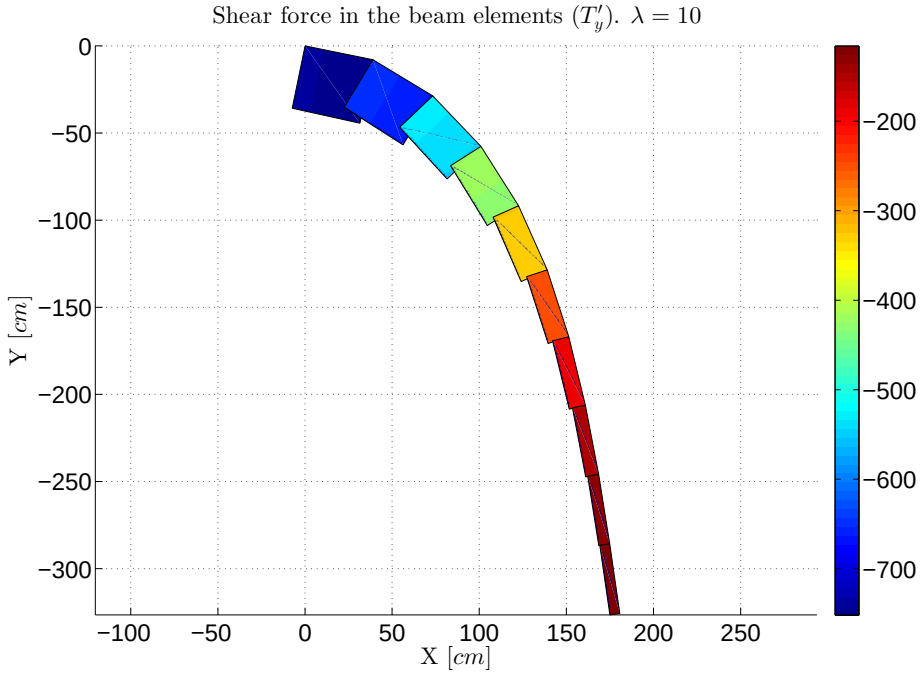

Figure 8.26: Cantilever beam loaded at the tip - Shear forces in the y' axis at the $\lambda = 10$

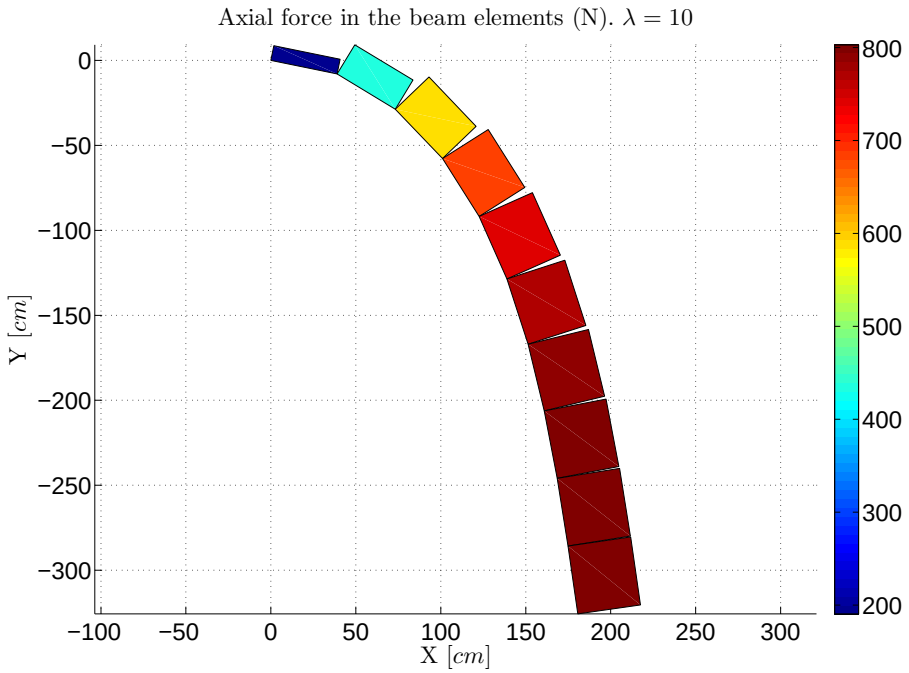

Figure 8.27: Cantilever beam loaded at the tip - Axial force in the x' axis at the $\lambda = 10$

8.1.6 Cantilever beam under a moment at the tip

The classical problem of a cantilever beam subjected to a moment at the free end is illustrated in figure 8.28. Clearly, for a prismatic elastic beam, the exact solution for the deformed shape of this problem is a perfect circle, since the bending moment, and hence the curvature, is constant along the beam. However, the expression for the curvature of the beam was approximated, in this formulation, as the second derivative of the transverse displacements with respect to the axis coordinate x. The objective of this analysis is to validate the corotational formulation implemented to solve finite strain problems, as long as the structural members are subdivided into small elements. With these considerations, this problem is a good test for the described corotational formulation in three dimensions, since it involves very large rotations (up to 720 degrees).

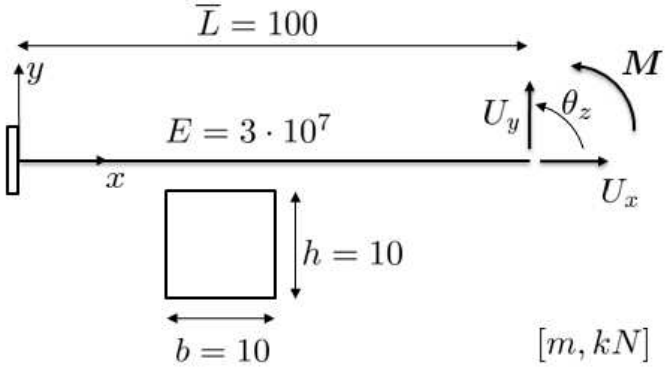

Figure 8.28: Cantilever beam under a moment at the tip

Now, the cantilever beam under a moment at the tip will be analyzed considering the finite element model developed in this work. In table 8.12 the parameters and models used in the program are listed.

Concept	Symbol	Value
Structural model		
Model for cable structure	M_{cs}	-
Model for beam structure	M_{bs}	FEM
Model for flexural behaviour	M_{fb}	Euler-Bernoulli
Model for torsional behaviour	M_{tb}	Saint Venant
Parameters for the analysis		
Tolerance in the equilibrium	Tol_G	1e-3
Tolerance in the displacements	Tol_D	1e-3
Tolerance in the energy	Tol_W	1e-3
Maximum number of iterations correction phase	I_M	100
Method used in the correction phase	-	Arc-length/Restoring
Initial Arc-length value	Δl_I	0.1
Minimum Bergan value for the switching	B_m	0.5
Maximum Bergan value for the switching	B_M	100
Initial increment of load	$\Delta\lambda_I$	0.05
Final load parameter	λ_F	10
Maximum number of increments	Inc_M	200
Optimum number of iterations correction phase	I_O	50
Update parameters during the incremental procedure	-	No

Table 8.12: Cantilever beam under a moment at the tip - Parameters for the nonlinear analysis in an incremental iterative scheme

The solution obtained with the model developed are compared with the ones obtained by [de Souza, 2000]. As it can be seen, the results match very well considering elastic linear material.

Some final results provided by the program are listed here considering the normalized moment defined as follows:

$$\lambda = \frac{M\overline{L}}{\pi EI} \tag{8.14}$$

First, figure 8.29 shows several configurations of the beam during the load procedure.

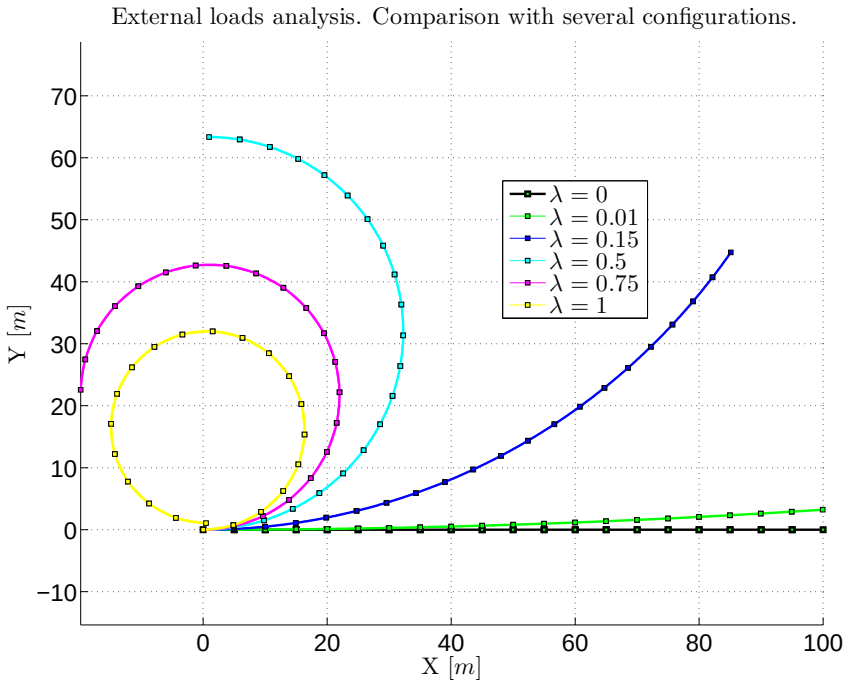

Figure 8.29: Cantilever beam under a moment at the tip - Configuration of the beam in several load steps

The equilibrium paths corresponding to the right point of the beam are plotted. Figure 8.30 shows the equilibrium path of the horizontal displacement, figure 8.31 shows the equilibrium path of the vertical displacement and figure 8.32 shows the equilibrium path of the rotation.

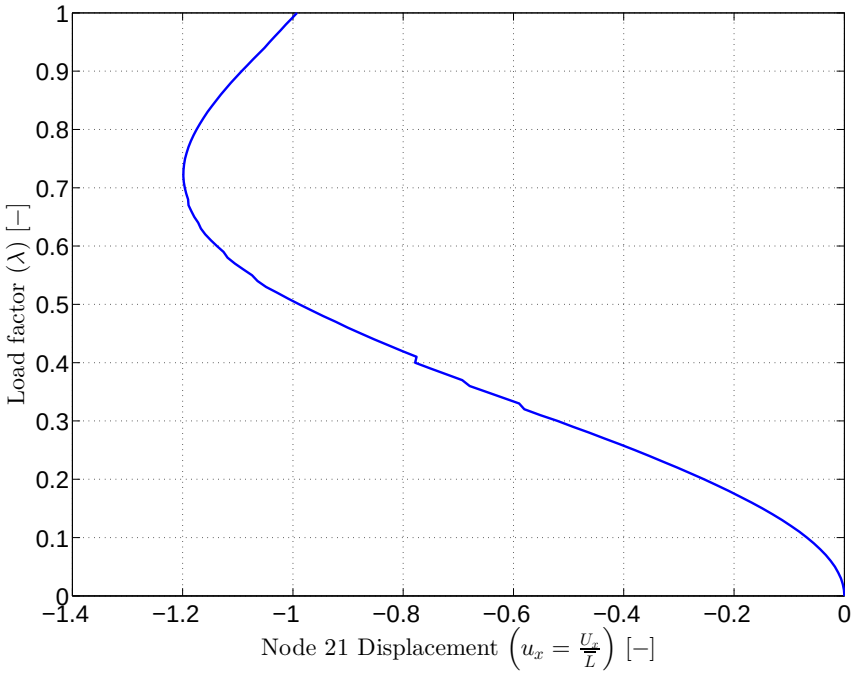

Figure 8.30: Cantilever beam under a moment at the tip - Equilibrium path corresponding to the horizontal displacement of the point on the left

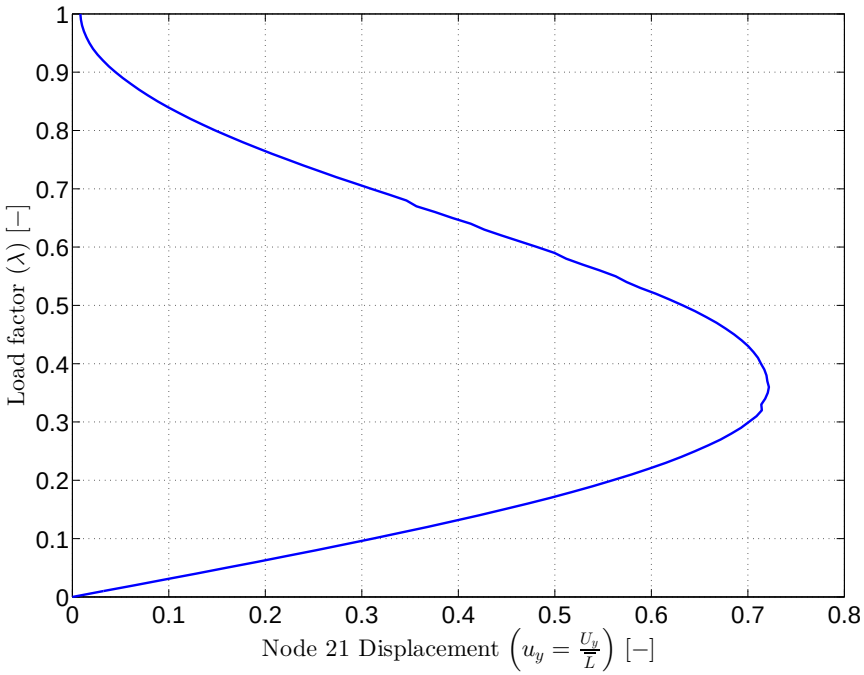

Figure 8.31: Cantilever beam under a moment at the tip - Equilibrium path corresponding to the vertical displacement of the point on the left

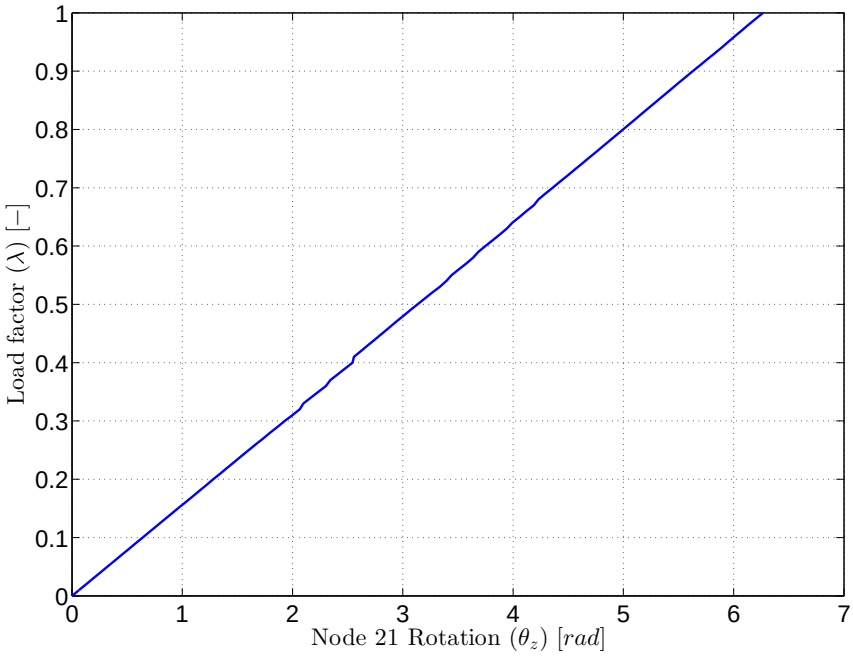

Figure 8.32: Cantilever beam loaded at the tip - Equilibrium path corresponding to the rotation of the point on the left

After the equilibrium paths have been plotted for the most important node of the structure, our attention is focused on the displacement and stress field of the structure in some particular load factors. In the following, the configuration, the bending moment in the z axis, the shear force in the local axis y' of the elements and the axial will be plotted. Figures 8.33, 8.34 and 8.35 show the bending moment when the load is up to $\lambda = 0.1$, $\lambda = 0.5$ and $\lambda = 0.75$ respectively.

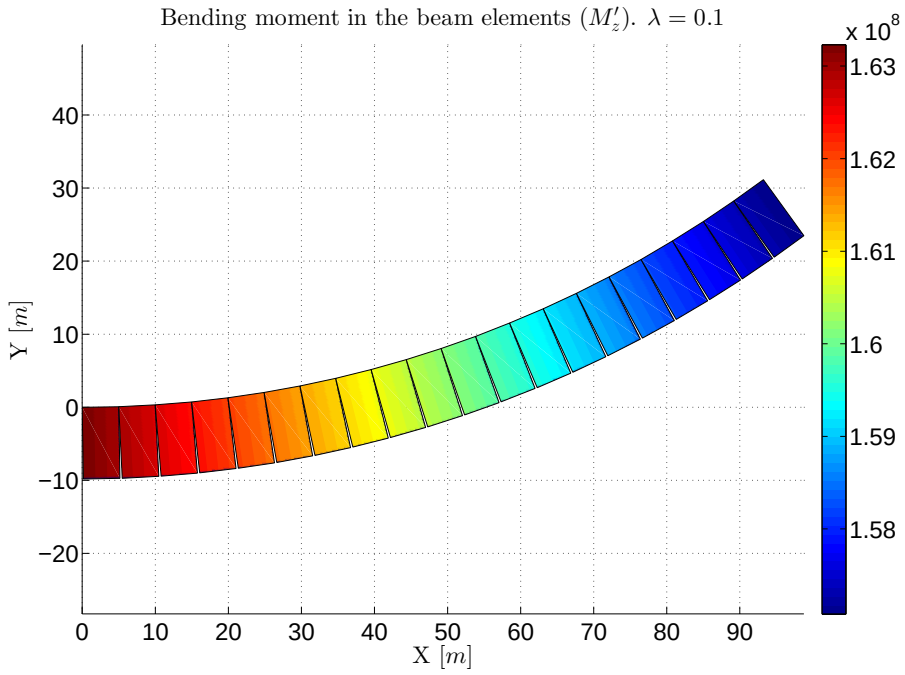

Figure 8.33: Cantilever beam loaded at the tip - Bending moment in the z' axis at the $\lambda = 0.1$

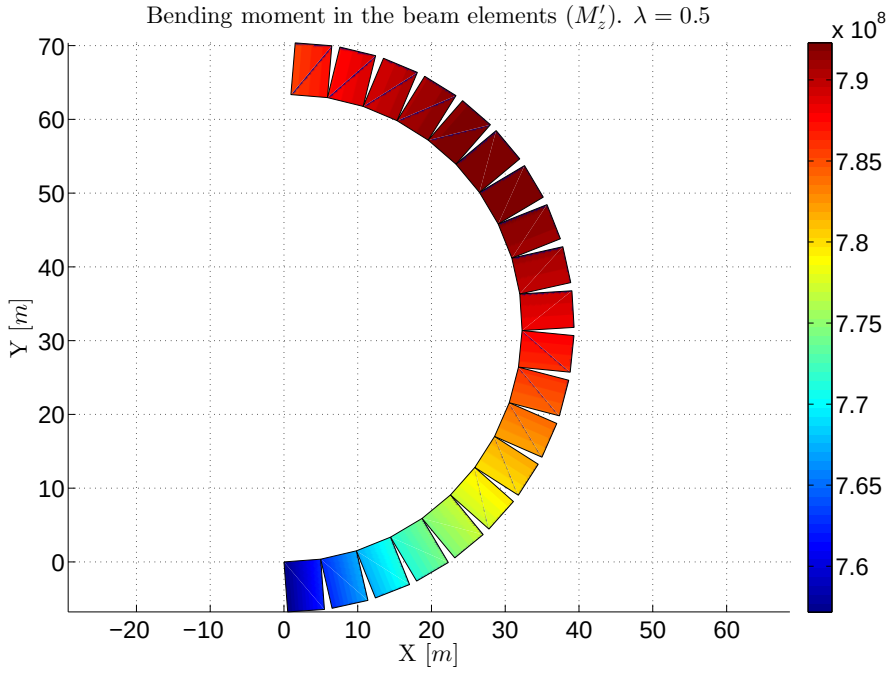

Figure 8.34: Cantilever beam loaded at the tip - Bending moment in the z' axis at the $\lambda = 0.5$

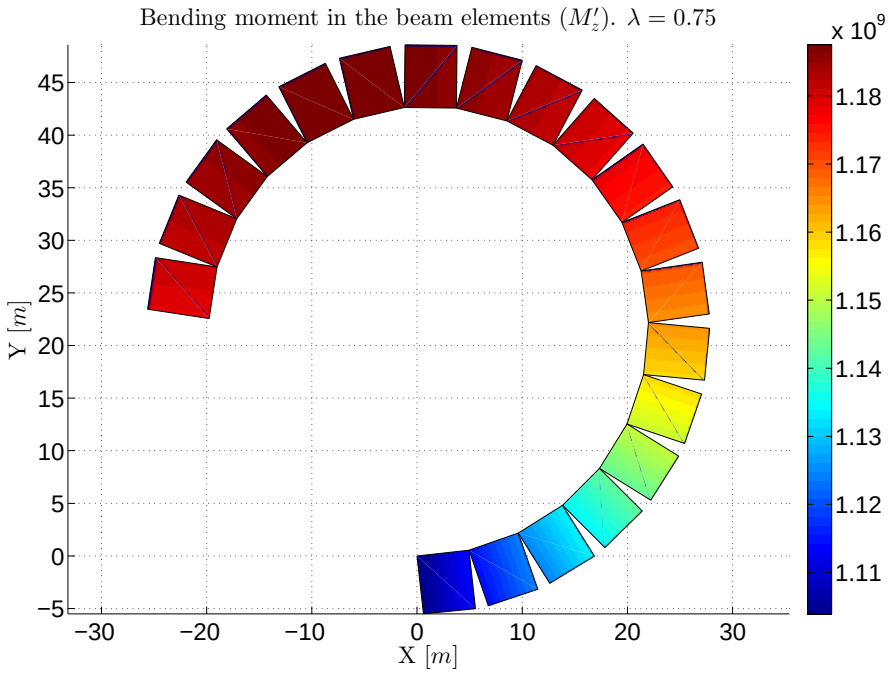

Figure 8.35: Cantilever beam loaded at the tip - Bending moment in the z' axis at the $\lambda = 0.75$

8.1.7 Pinned-fixed square diamond frame in tension

A pinned-fixed square diamond frame is loaded in tension as shown in figure 8.36. Since the problem is symmetric, only half of the diamond is analyzed. The problem is analyzed by using five elements per member.

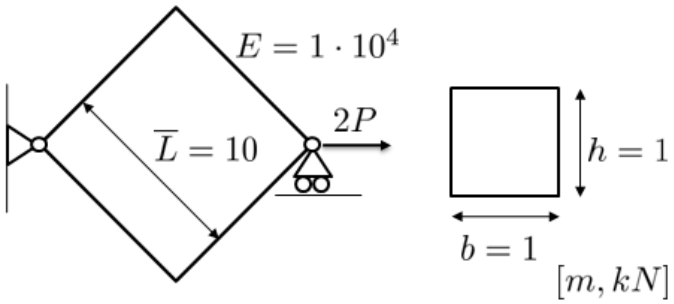

Figure 8.36: Pinned-fixed square diamond frame in tension

Now, the pinned-fixed square diamond frame in tension will be analyzed considering the finite element model developed in this work. In table 8.13 the parameters and models used in the program are listed.

Concept	Symbol	Value
Structural model		
Model for cable structure	M_{cs}	-
Model for beam structure	M_{bs}	FEM
Model for flexural behaviour	M_{fb}	Euler-Bernoulli
Model for torsional behaviour	M_{tb}	Saint Venant
Parameters for the analysis		
Tolerance in the equilibrium	Tol_G	1e-3
Tolerance in the displacements	Tol_D	1e-3
Tolerance in the energy	Tol_W	1e-3
Maximum number of iterations correction phase	I_M	100
Method used in the correction phase	-	Arc-length/Restoring
Initial Arc-length value	Δl_I	0.1
Minimum Bergan value for the switching	B_m	0.5
Maximum Bergan value for the switching	B_M	100
Initial increment of load	$\Delta\lambda_I$	0.05
Final load parameter	λ_F	10
Maximum number of increments	Inc_M	200
Optimum number of iterations correction phase	I_O	50
Update parameters during the incremental procedure	-	No

Table 8.13: Pinned-fixed square diamond frame in tension - Parameters for the nonlinear analysis in an incremental iterative scheme

The solution obtained with the model developed are compared with the ones obtained by [P. Nanakorn, 2006]. Good agreement between both results can be observed from the comparison considering linear elastic material.

Some final results provided by the program are listed here considering the normalized force defined as follows:

$$\lambda = \frac{P\overline{L}^2}{EI} \tag{8.15}$$

First, figure 8.37 shows several configurations of the beam during the load procedure.

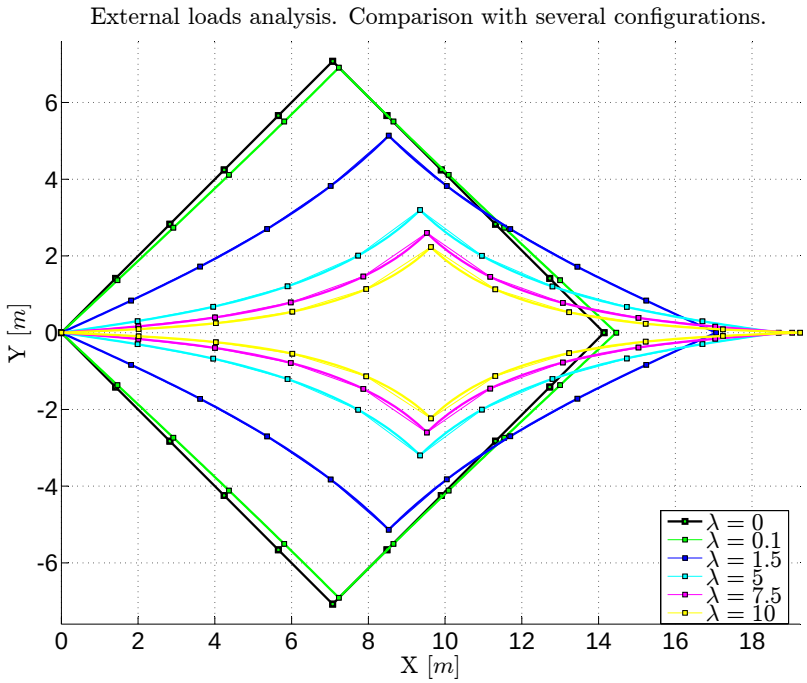

Figure 8.37: Pinned-fixed square diamond frame in tension - Configuration of the beam in several load steps

The equilibrium paths corresponding to the right point of the beam and the point at the uppest position are plotted. Figure 8.38 and figure 8.39 show the equilibrium paths of the horizontal displacement and the rotation of the point positioned on the right of the square frame respectively. In addition, figure 8.40 shows the equilibrium path of the vertical displacement of the uppest point of the structure.

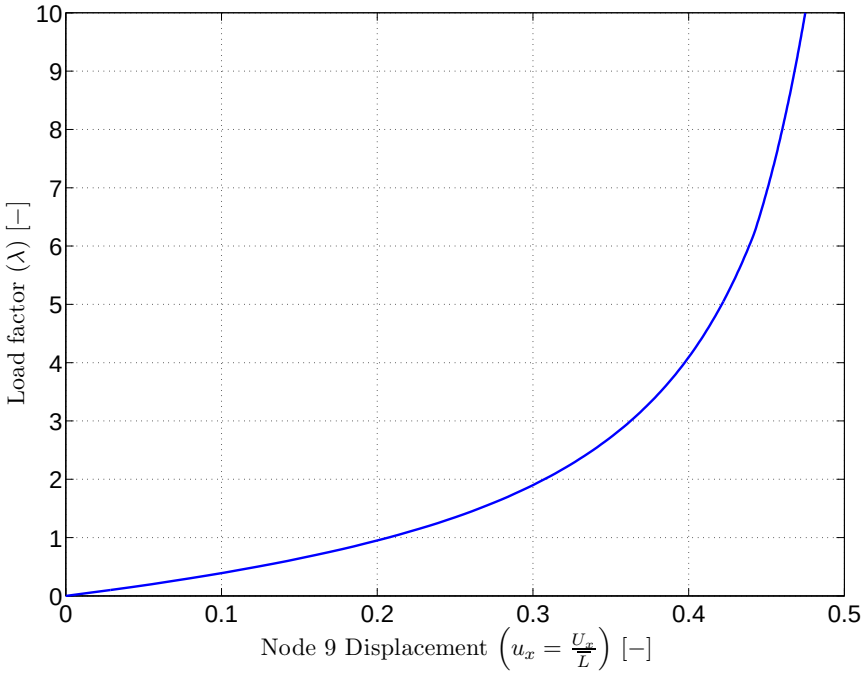

Figure 8.38: Pinned-fixed square diamond frame in tension - Equilibrium path corresponding to the horizontal displacement of the point on the right

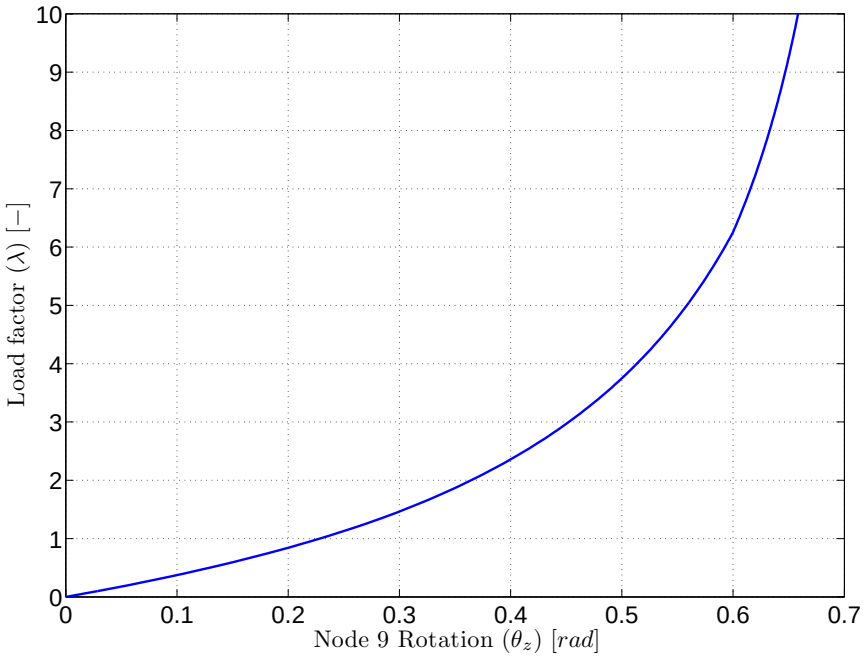

Figure 8.39: Pinned-fixed square diamond frame in tension - Equilibrium path corresponding to the rotation of the point on the right

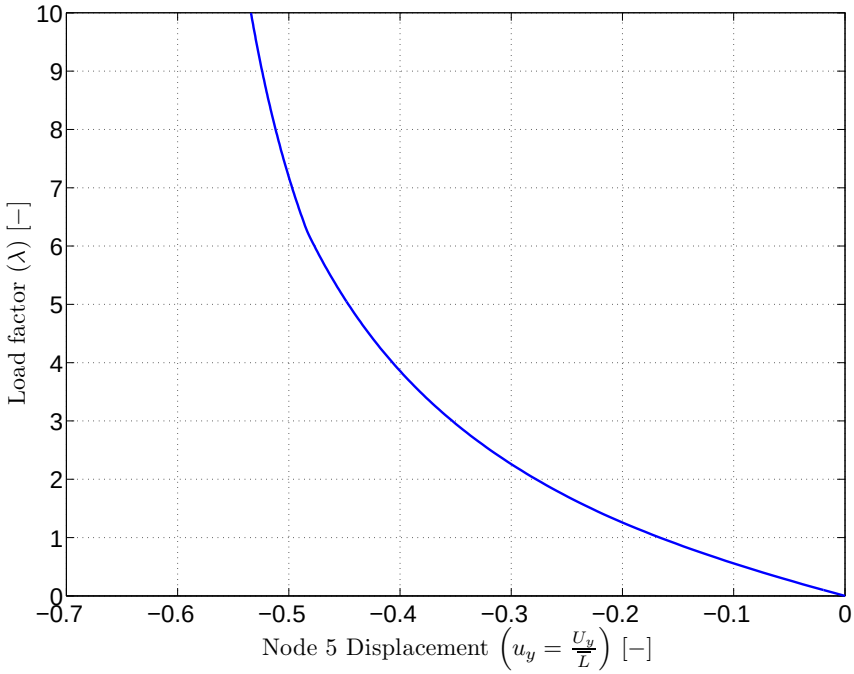

Figure 8.40: Pinned-fixed square diamond frame in tension - Equilibrium path corresponding to the vertical displacement of the uppest point

After the equilibrium paths have been plotted for the most important nodes of the structure, our attention is focused on the displacement and stress field of the structure in some particular load factors. In the following the bending moment in the z axis, the shear force in the local axis y' and the axial force of the elements will be plotted. Figures 8.41, 8.42 and 8.43 show the bending moment, shear force and axial force when the load is at $\lambda = 0.1$. The same forces and moments are represented when the load is at $\lambda = 5$ in figures 8.44, 8.44 and 8.44 and figures 8.47, 8.48 and 8.49 show the final configuration of the beam when $\lambda = 10$.

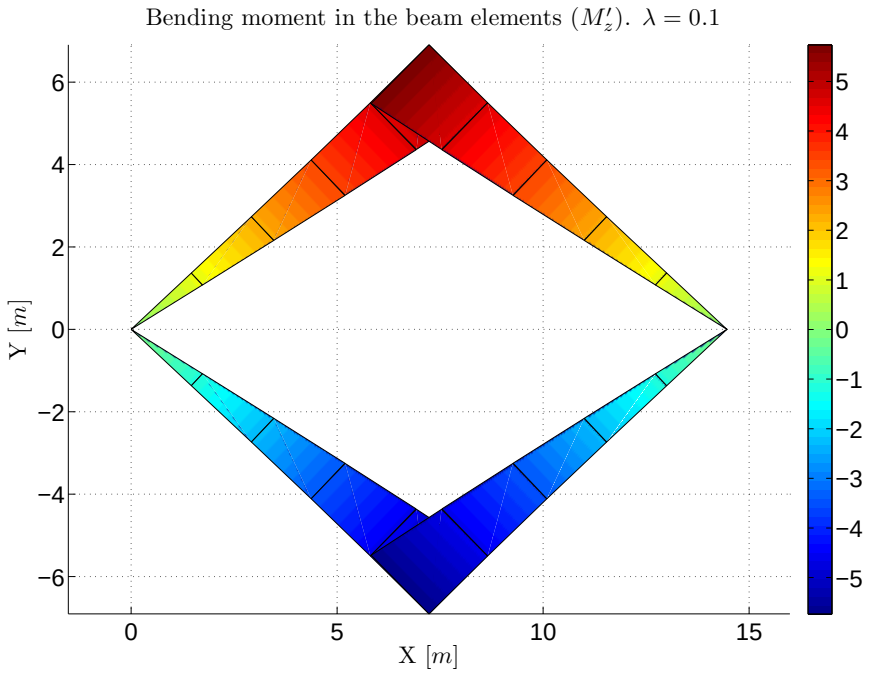

Figure 8.41: Pinned-fixed square diamond frame in tension - Bending moment in the z' axes at $\lambda = 0.1$

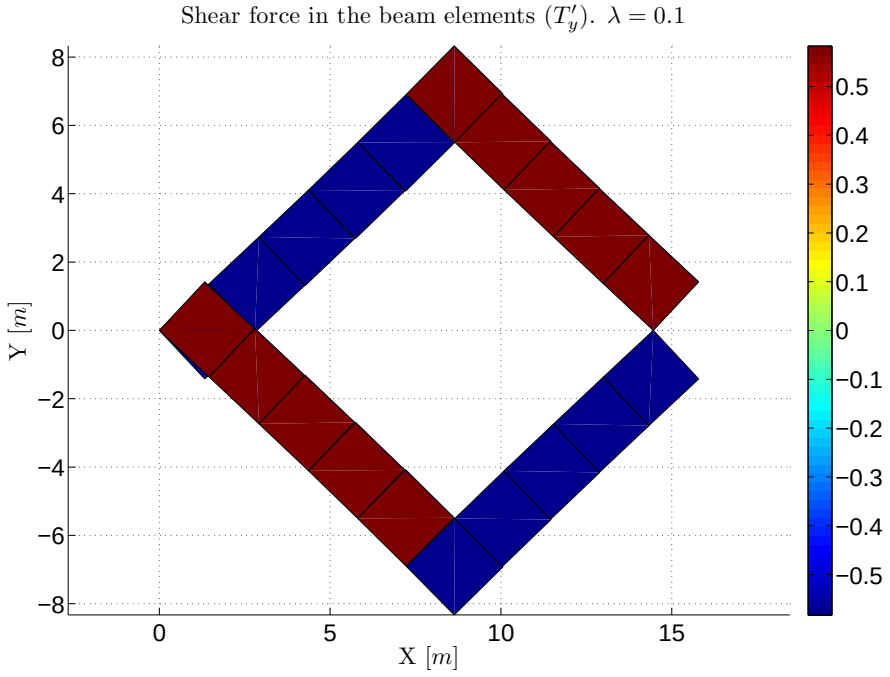

Figure 8.42: Pinned-fixed square diamond frame in tension - Shear force in the y' axes at $\lambda = 0.1$

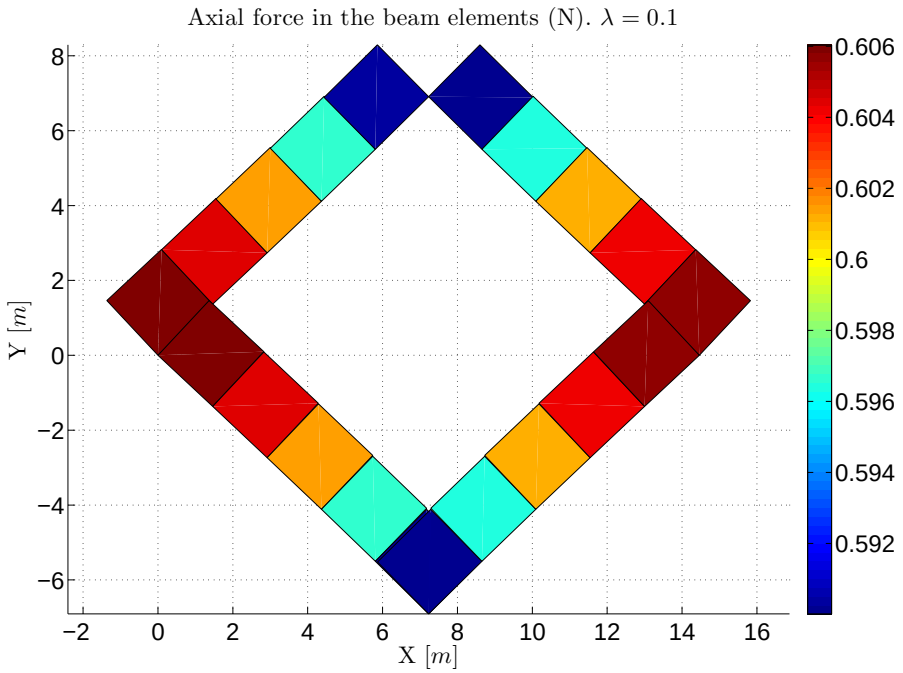

Figure 8.43: Pinned-fixed square diamond frame in tension - Axial force in the x' axes at $\lambda = 0.1$

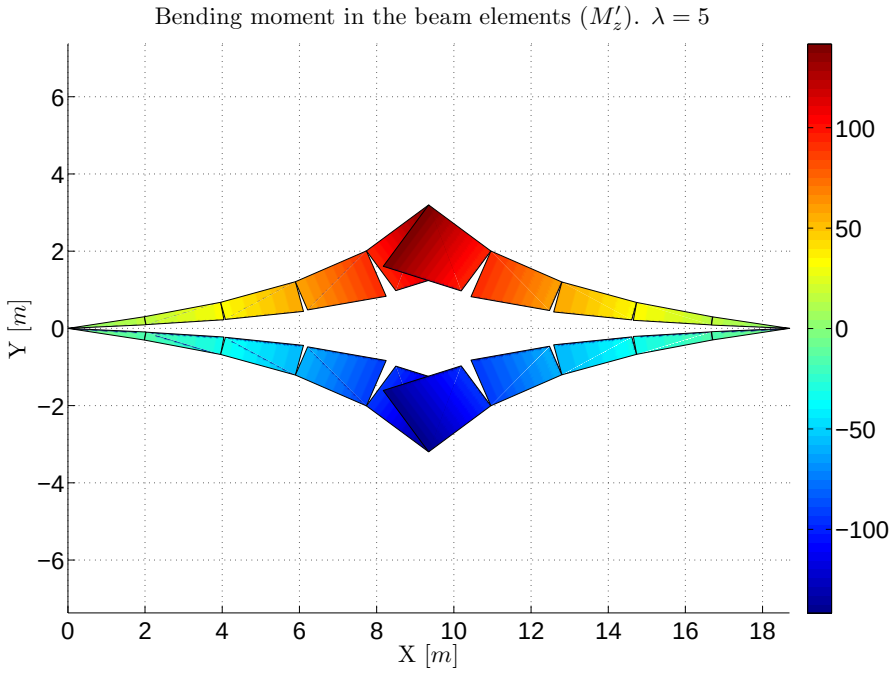

Figure 8.44: Pinned-fixed square diamond frame in tension - Bending moment in the z' axes at $\lambda = 5$

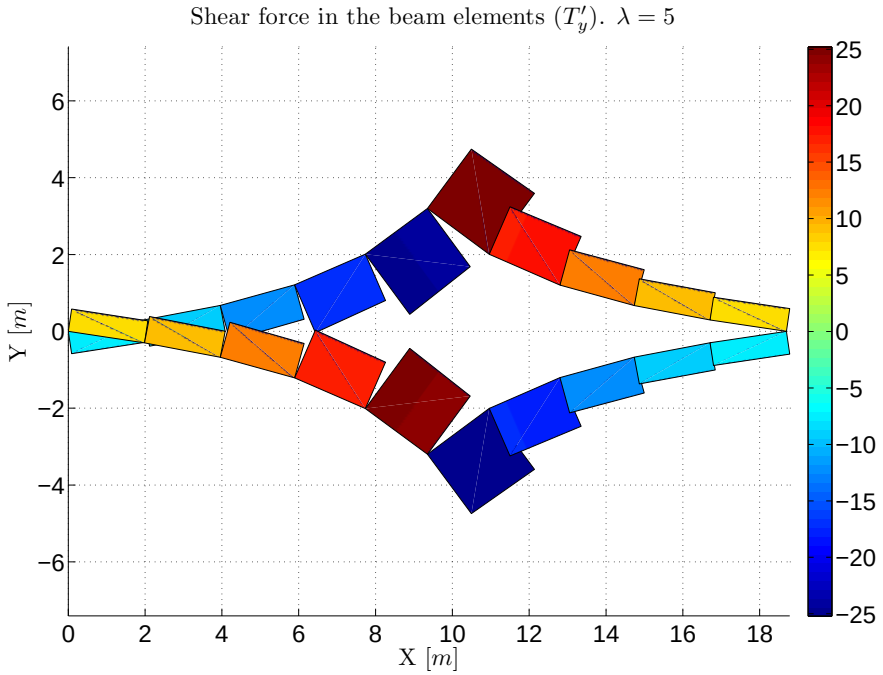

Figure 8.45: Pinned-fixed square diamond frame in tension - Shear force in the y' axes at $\lambda = 5$

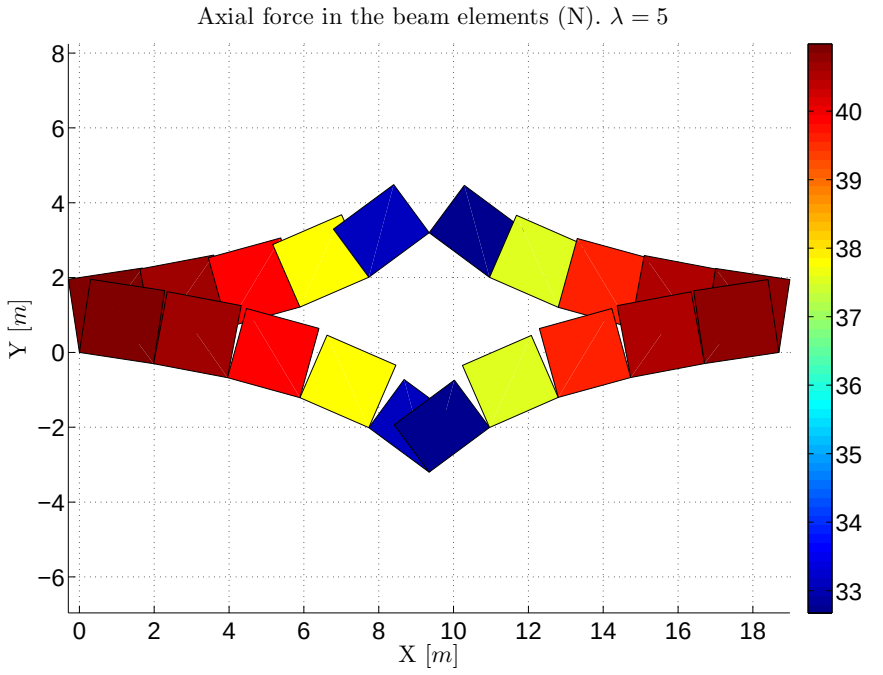

Figure 8.46: Pinned-fixed square diamond frame in tension - Axial force in the x' axes at $\lambda = 5$

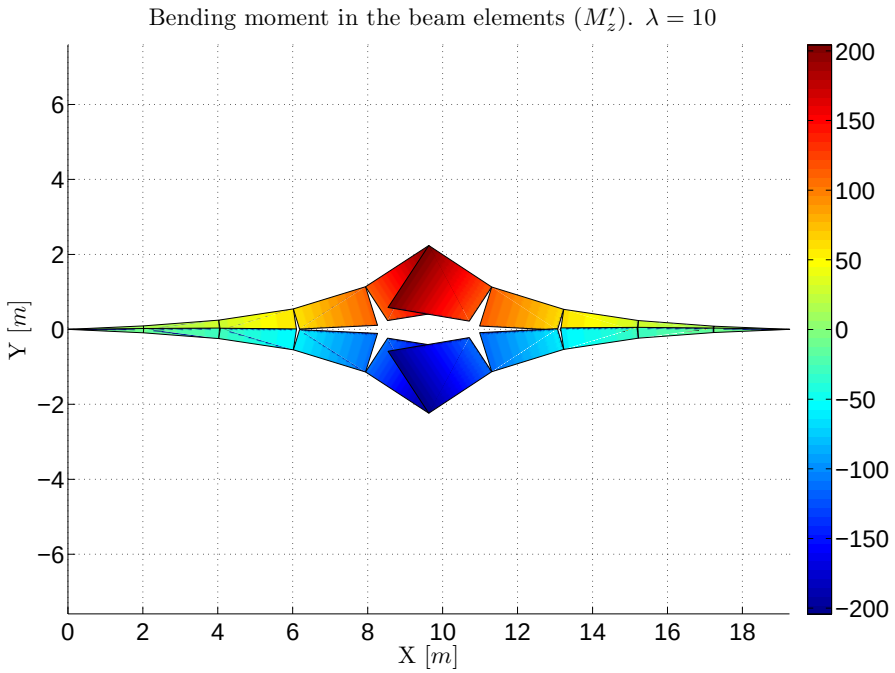

Figure 8.47: Pinned-fixed square diamond frame in tension - Bending moment in the z' axes at $\lambda = 10$

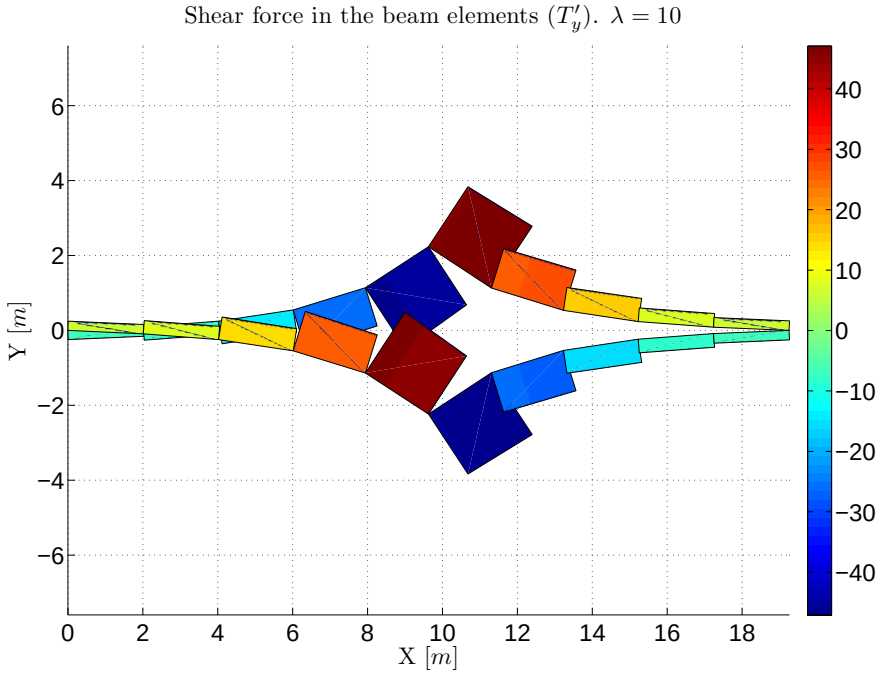

Figure 8.48: Pinned-fixed square diamond frame in tension - Shear force in the y' axes at $\lambda = 10$

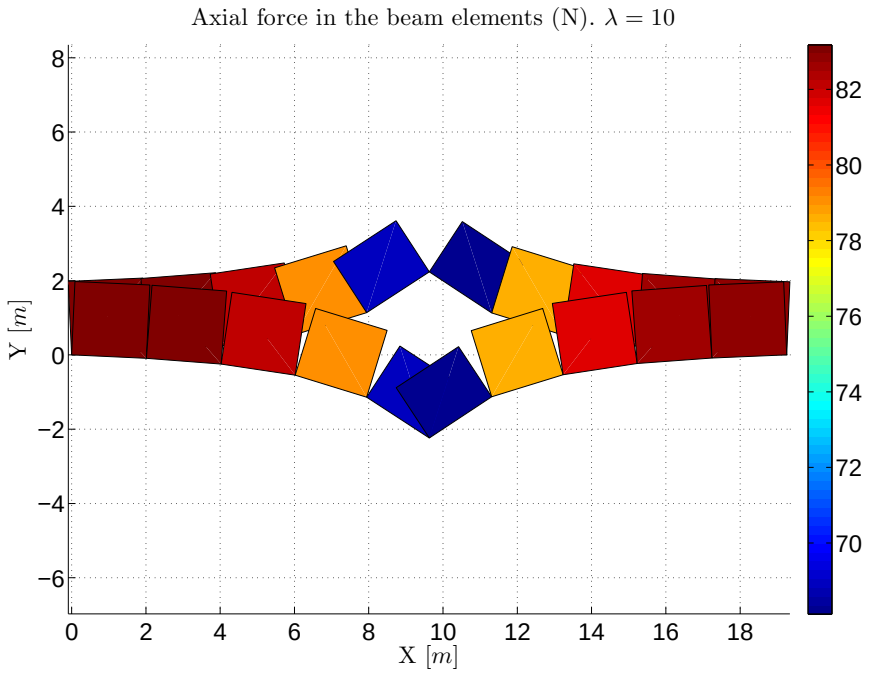

Figure 8.49: Pinned-fixed square diamond frame in tension - Axial force in the x' axes at $\lambda = 10$

8.1.8 Circular beam

A circular beam contained in the X-Y plane is loaded with a concentrated load at its free edge as shown in figure 8.50. The problem is analyzed by using ten elements.

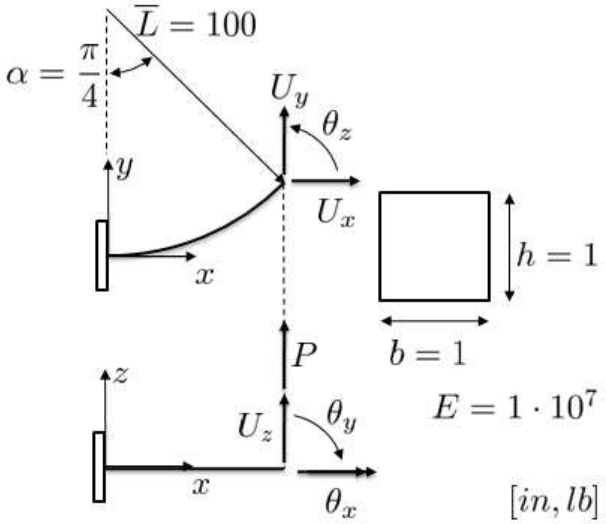

Figure 8.50: Circular bend

Now, the circular beam will be analyzed considering the finite element model developed in this work. In table 8.14 the parameters and models used in the program are listed.

Concept	Symbol	Value
Structural model		
Model for cable structure	M_{cs}	-
Model for beam structure	M_{bs}	FEM
Model for flexural behaviour	M_{fb}	Euler-Bernoulli
Model for torsional behaviour	M_{tb}	Saint Venant
Parameters for the analysis		
Tolerance in the equilibrium	Tol_G	1e-3
Tolerance in the displacements	Tol_D	1e-3
Tolerance in the energy	Tol_W	1e-3
Maximum number of iterations correction phase	I_M	100
Method used in the correction phase	-	Arc-length/Restoring
Initial Arc-length value	Δl_I	0.1
Minimum Bergan value for the switching	B_m	0.4
Maximum Bergan value for the switching	B_M	100
Initial increment of load	$\Delta\lambda_I$	0.01
Final load parameter	λ_F	1.5
Maximum number of increments	Inc_M	150
Optimum number of iterations correction phase	I_O	50
Update parameters during the incremental procedure	-	No

Table 8.14: Circular bend - Parameters for the nonlinear analysis in an incremental iterative scheme

The solution obtained with the model developed are compared with the ones obtained by [B.A. Izzuddin]. Good agreement between both results can be observed from the comparison considering linear elastic material.

Some final results provided by the program are listed here considering the normalized force defined as follows:

$$\lambda = \frac{P\overline{L}^2}{EI} \tag{8.16}$$

First, figure 8.51 shows several configurations of the beam during the load procedure.

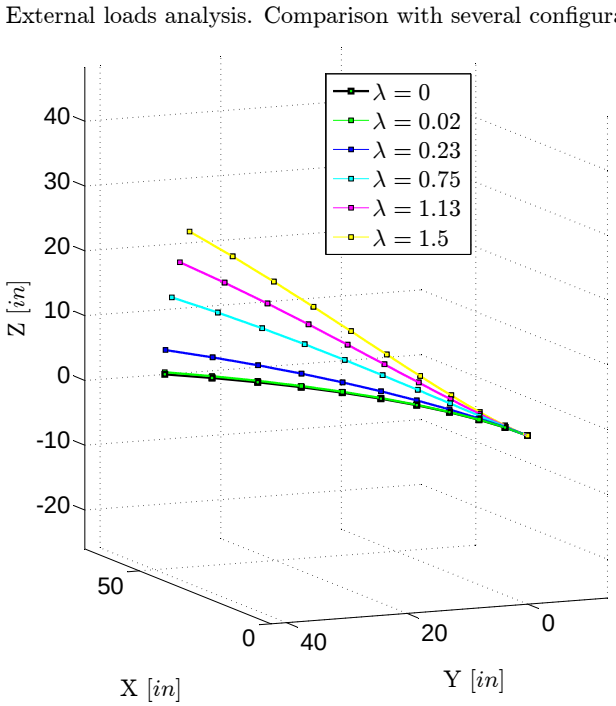

Figure 8.51: Circular bend - Configuration of the beam in several load steps

The equilibrium paths corresponding to the free edge of the beam are plotted. Figures 8.52, 8.53 and 8.54 show the equilibrium paths of the displacements in the x, y and z directions, respectively. In addition, figures 8.55, 8.56 and 8.57 show the equilibrium paths of the rotations around the x, y and z axes of the free edge of the beam.

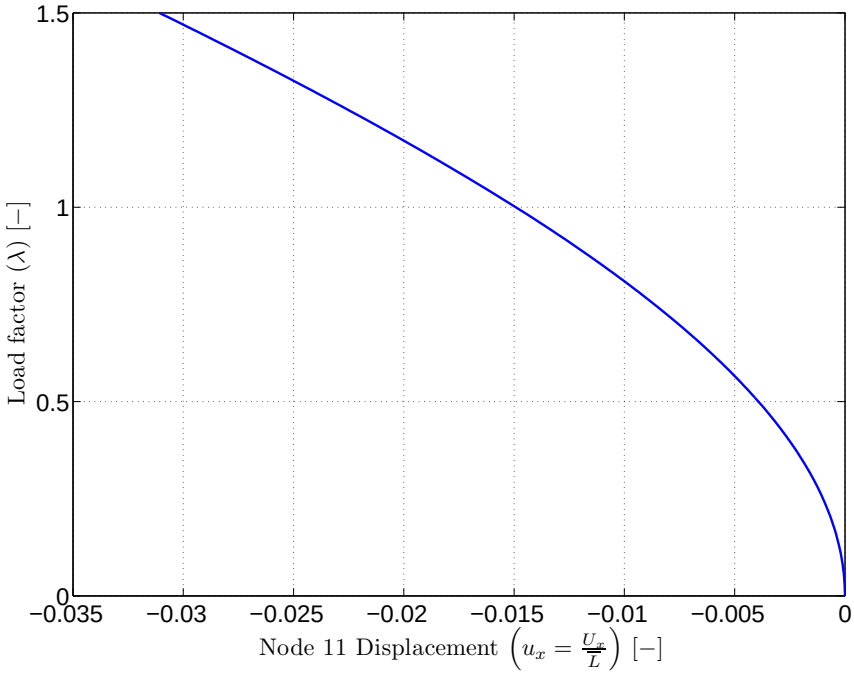

Figure 8.52: Circular bend - Equilibrium path corresponding to the horizontal displacement in the x direction of the free edge

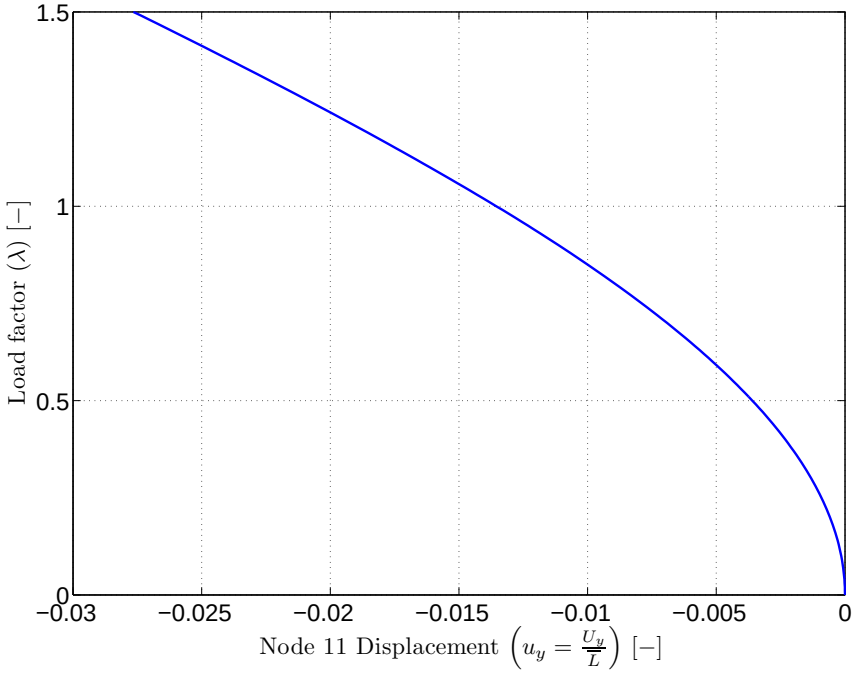

Figure 8.53: Circular bend - Equilibrium path corresponding to the horizontal displacement in the y direction of the free edge

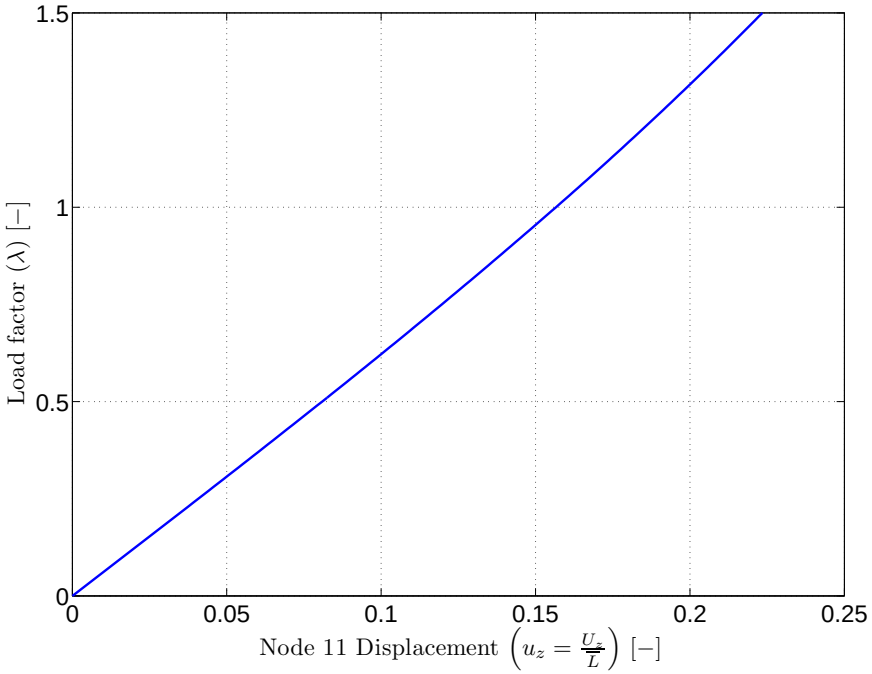

Figure 8.54: Circular bend - Equilibrium path corresponding to the vertical displacement of the free edge

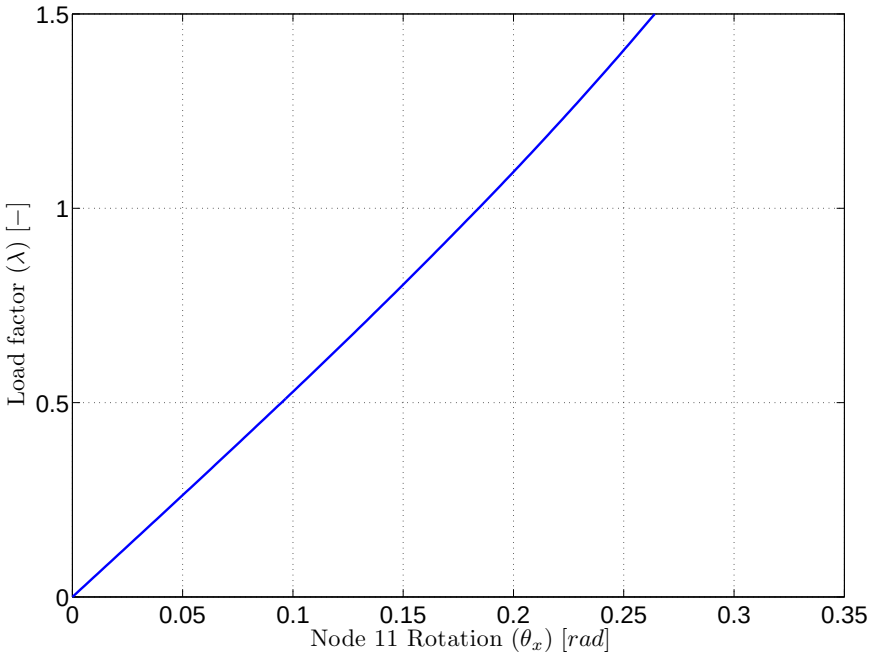

Figure 8.55: Circular bend - Equilibrium path corresponding to the rotation around x axis of the free edge

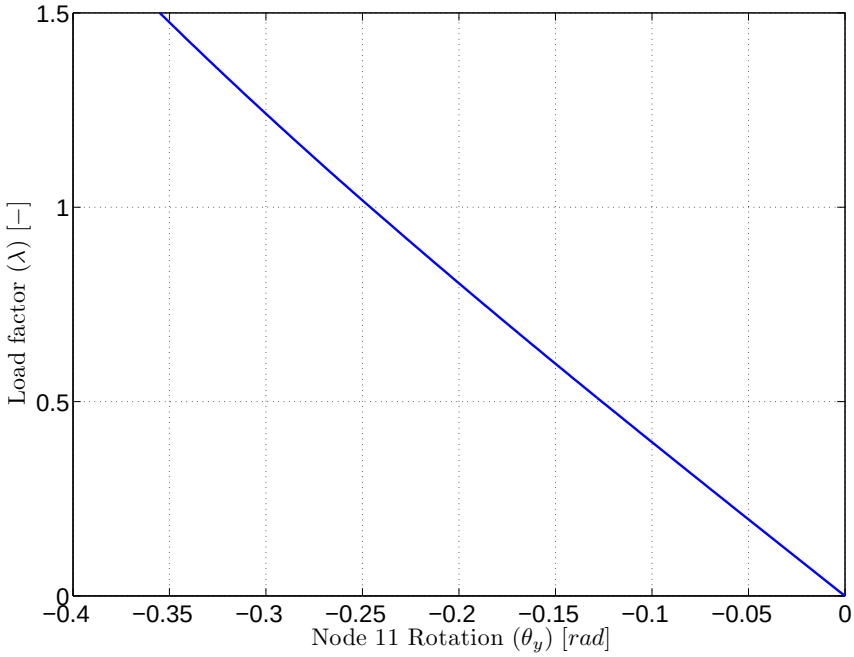

Figure 8.56: Circular bend - Equilibrium path corresponding to the rotation around y axis of the free edge

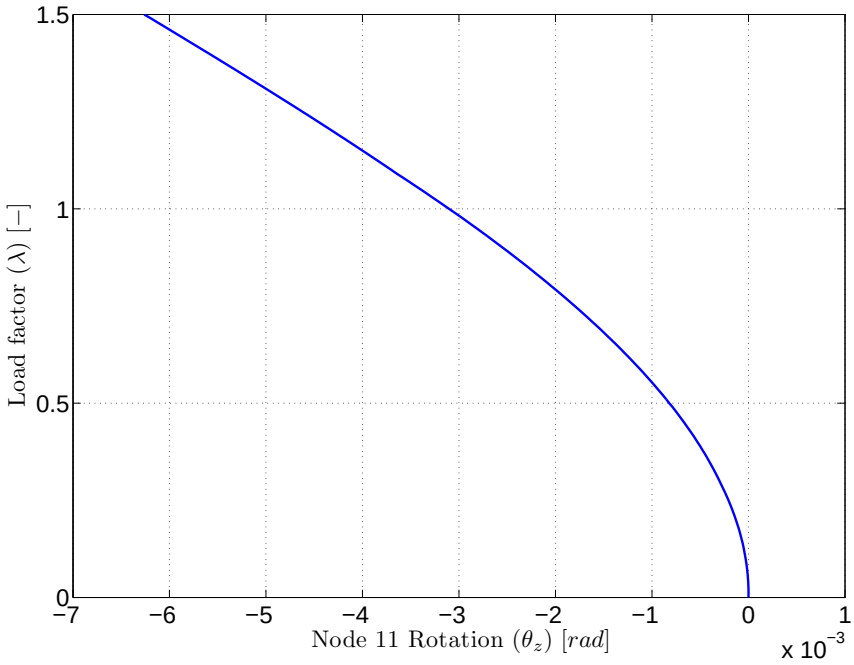

Figure 8.57: Circular bend - Equilibrium path corresponding to the rotation around z axis of the free edge

After the equilibrium paths have been plotted for the free edge of the circular can-

tilever, our attention is focused on the displacement and stress field of the structure in some particular load factors. In the following, the three internal forces and the three internal moments acting on each element of the structure when $\lambda = 1.0$ are plotted in figures 8.58 (axial force), 8.59 (shear force in the y' axis), 8.60 (shear force in the z' axis), 8.61 (twisting moment), 8.62 (Bending moment in the y' axis) and 8.63 (Bending moment in the z' axis).

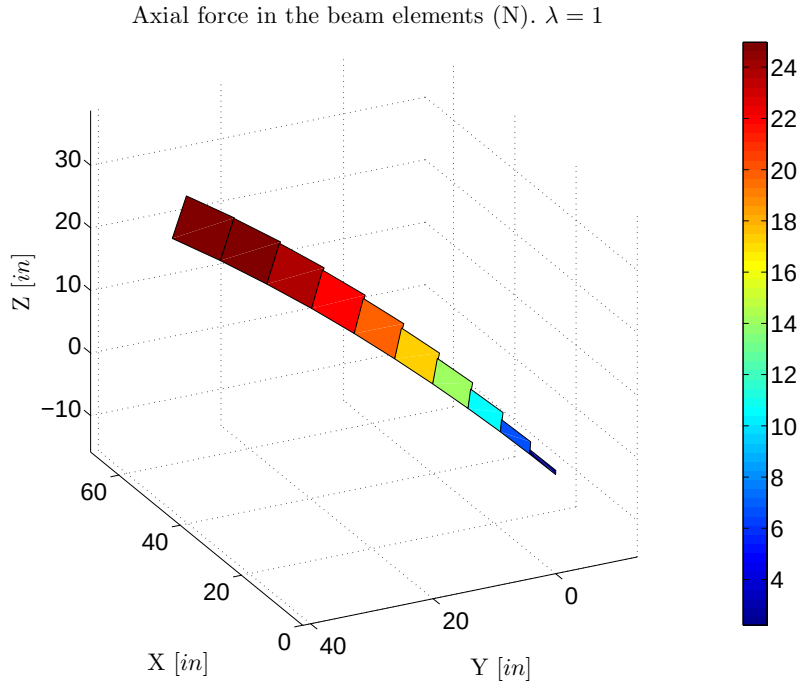

Figure 8.58: Pinned-fixed square diamond frame in tension - Axial force acting in the x' axes at $\lambda = 1.0$

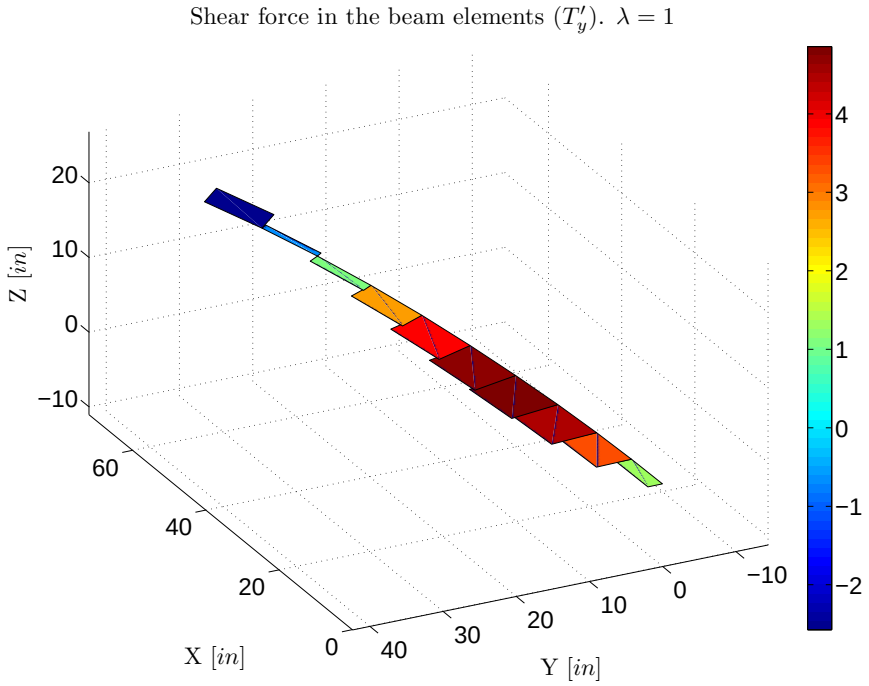

Figure 8.59: Pinned-fixed square diamond frame in tension - Shear force acting in the y' axes at $\lambda = 1.0$

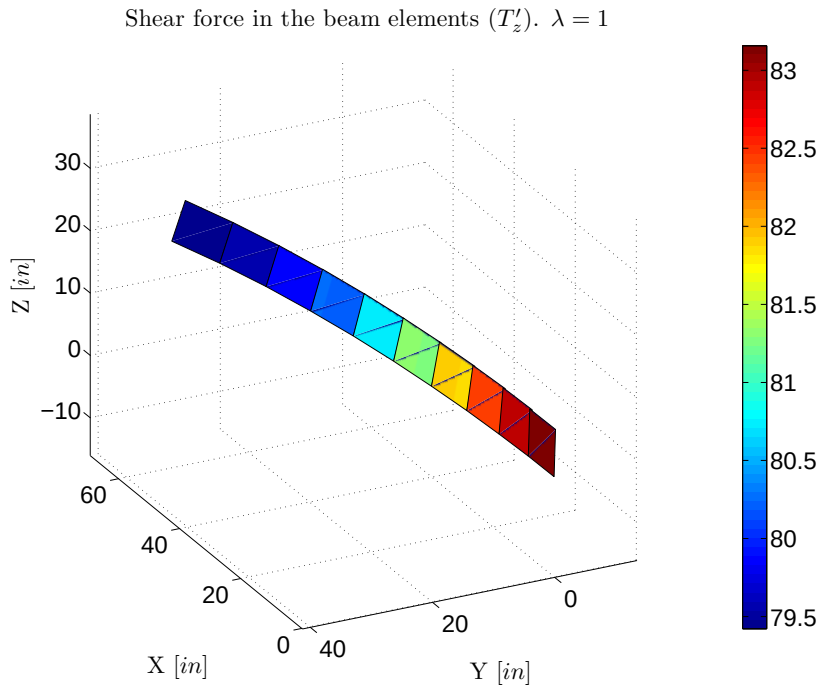

Figure 8.60: Pinned-fixed square diamond frame in tension - Shear force acting in the z' axes at $\lambda = 1.0$

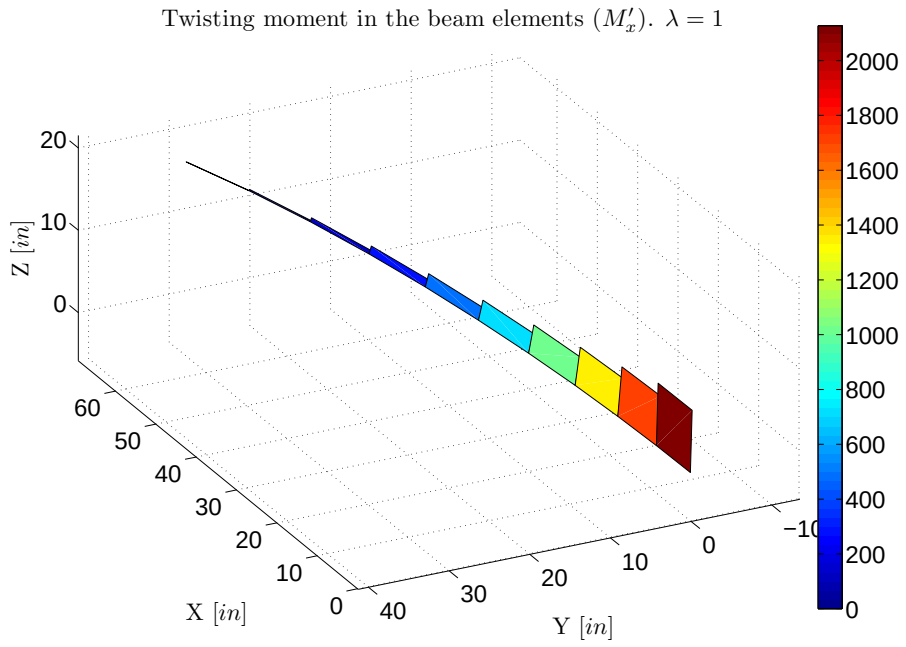

Figure 8.61: Pinned-fixed square diamond frame in tension - Twisting moment acting in the x' axes at $\lambda = 1.0$

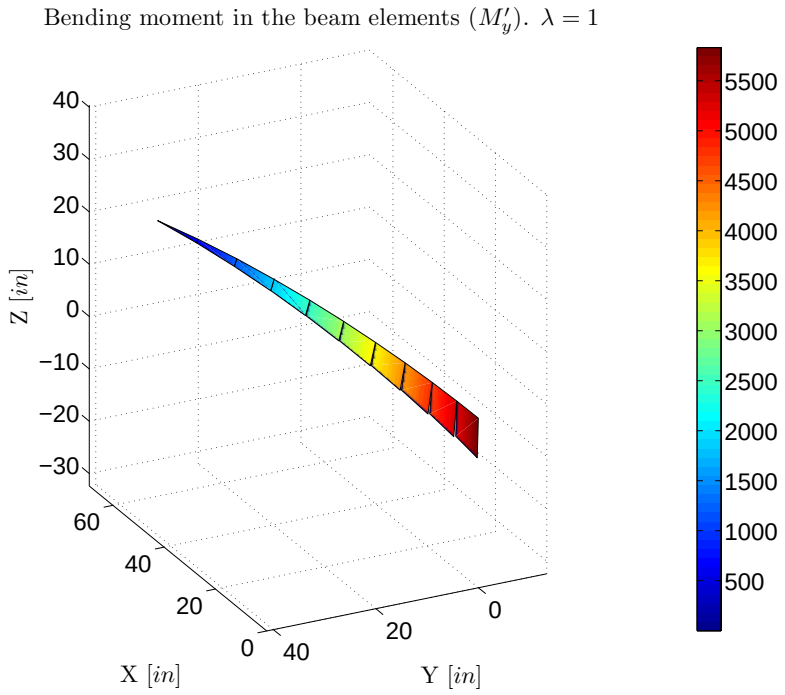

Figure 8.62: Pinned-fixed square diamond frame in tension - Bending moment acting in the y' axes at $\lambda = 1.0$

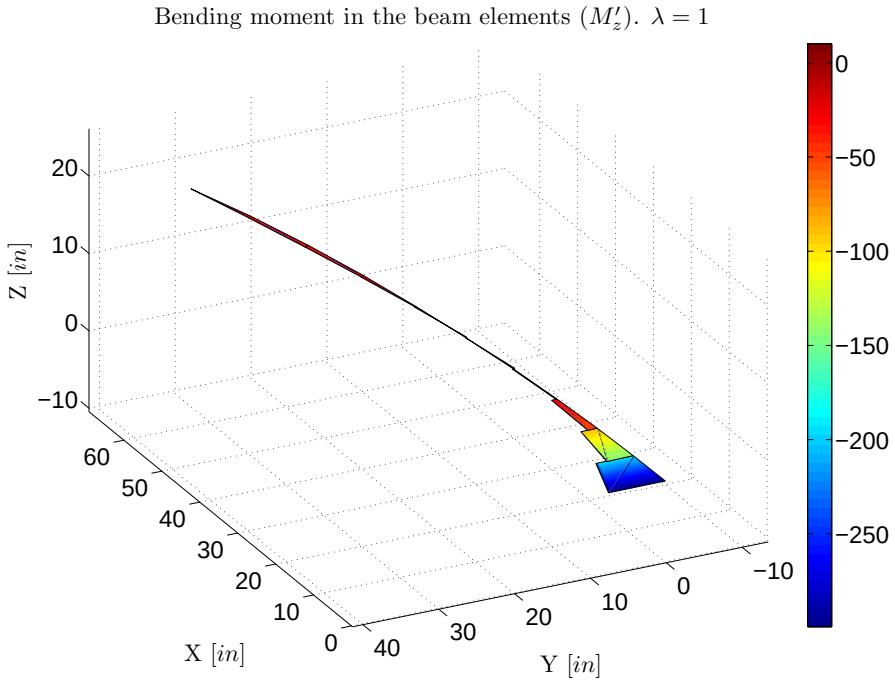

Figure 8.63: Pinned-fixed square diamond frame in tension - Bending moment acting in the z' axes at $\lambda = 1.0$

8.1.9 Beam with segmented axis

A cantilever beam as the one in figure 8.50 is analysed under two concentrated loads on its free edge. The problem is analyzed by using five elements for each member.

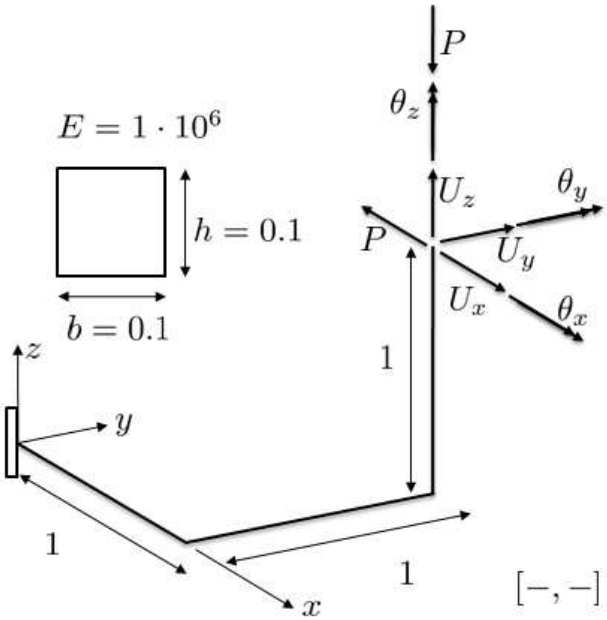

Figure 8.64: Beam with slope discontinuity

Now, the beam with slope discontinuity will be analyzed considering the finite element model developed in this work. In table 8.15 the parameters and models used in the program are listed.

Concept	Symbol	Value
Structural model		
Model for cable structure	M_{cs}	-
Model for beam structure	M_{bs}	FEM
Model for flexural behaviour	M_{fb}	Euler-Bernoulli
Model for torsional behaviour	M_{tb}	Saint Venant
Parameters for the analysis		
Tolerance in the equilibrium	Tol_G	1e-3
Tolerance in the displacements	Tol_D	1e-3
Tolerance in the energy	Tol_W	1e-3
Maximum number of iterations correction phase	I_M	100
Method used in the correction phase	-	Arc-length/Restoring
Initial Arc-length value	Δl_I	0.1
Minimum Bergan value for the switching	B_m	0.4
Maximum Bergan value for the switching	B_M	100
Initial increment of load	$\Delta\lambda_I$	0.01
Final load parameter	λ_F	0.4
Maximum number of increments	Inc_M	40
Optimum number of iterations correction phase	I_O	50
Update parameters during the incremental procedure	-	No

Table 8.15: Beam with slope discontinuity - Parameters for the nonlinear analysis in an incremental iterative scheme

The solution obtained with the model developed are compared with the ones obtained by [S. R. Eugster and Glocker, 2013]. Good agreement between both results can be observed from the comparison considering linear elastic material.

Some final results provided by the program are listed here. Due to the fact that the paper that has been used to check the results does not specify the units used in the analysis, the results will be shown in terms of a normalized load equal to the actual load.

$$\lambda = F \tag{8.17}$$

First, figure 8.65 shows several configurations of the beam during the load procedure.

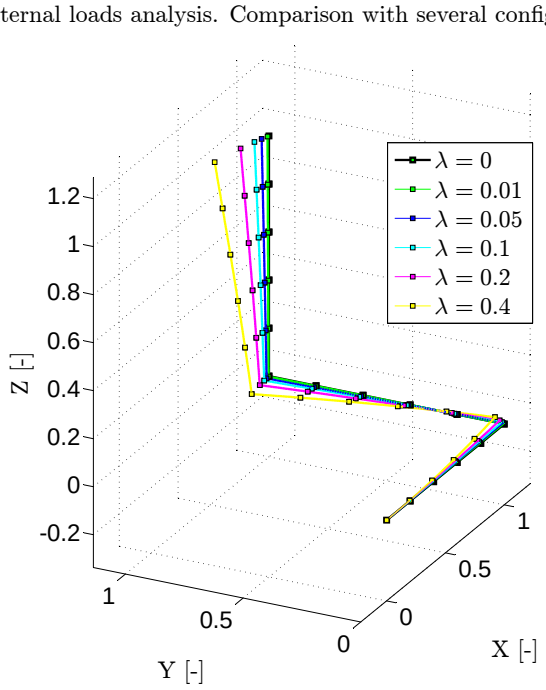

Figure 8.65: Beam with slope discontinuity - Configuration of the beam in several load steps

The equilibrium paths corresponding to the free edge of the beam are plotted. Figures 8.66, 8.67 and 8.68 show the equilibrium paths of the displacements in the x, y and z directions, respectively. In addition, figures 8.69, 8.70 and 8.71 show the equilibrium paths of the rotations around the x, y and z axes of the free edge of the beam.

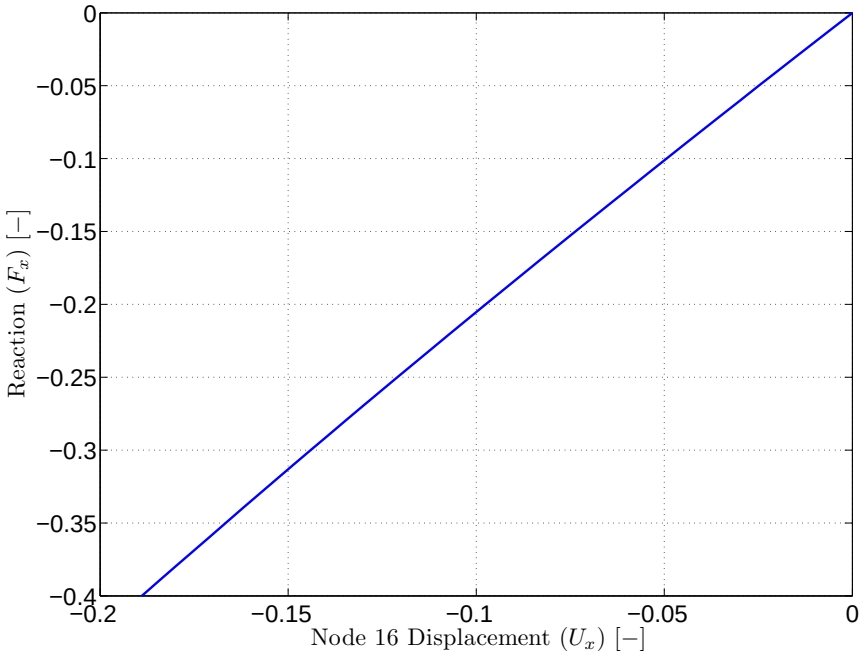

Figure 8.66: Beam with slope discontinuity - Equilibrium path corresponding to the horizontal displacement in the x direction of the free edge

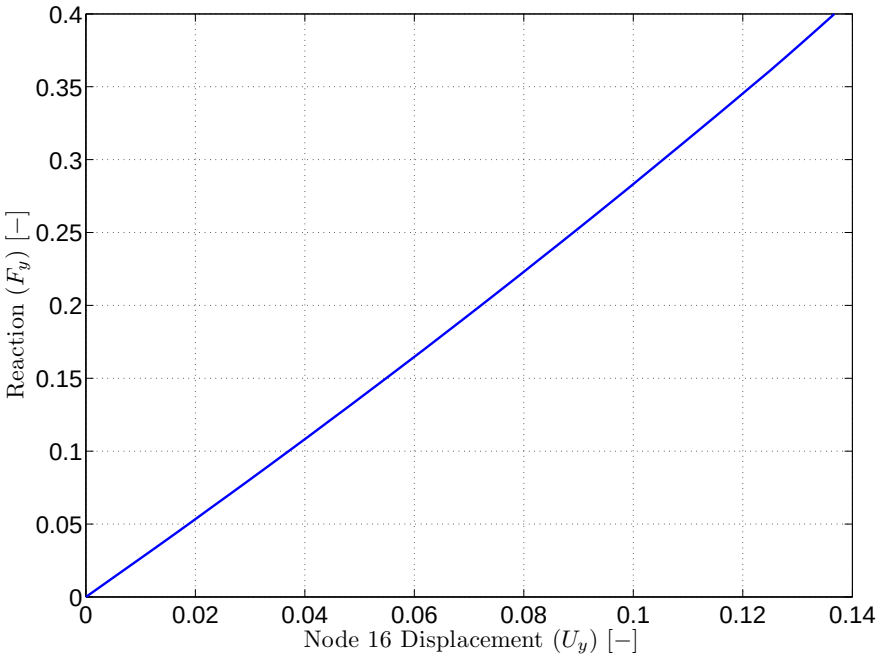

Figure 8.67: Beam with slope discontinuity - Equilibrium path corresponding to the horizontal displacement in the y direction of the free edge

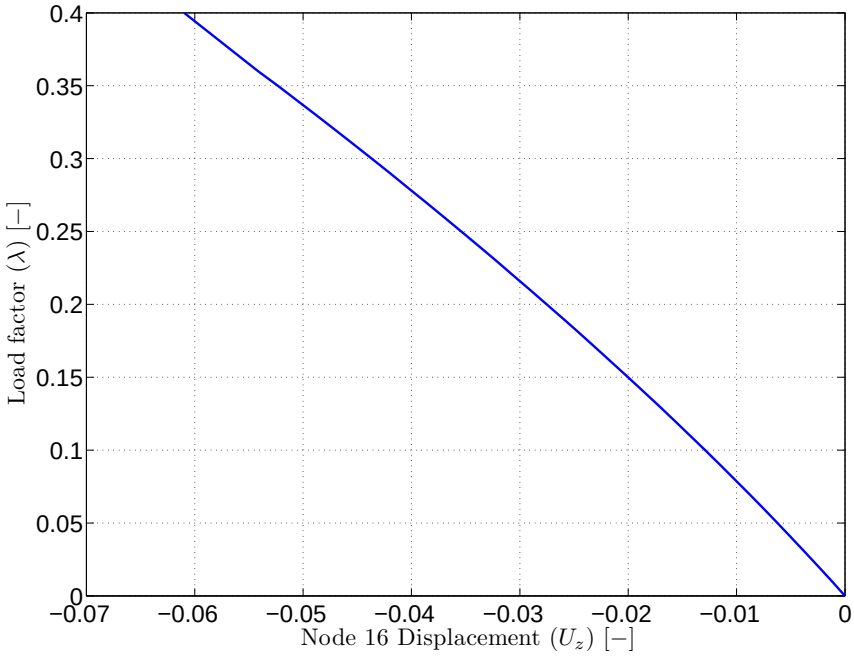

Figure 8.68: Beam with slope discontinuity - Equilibrium path corresponding to the vertical displacement of the free edge

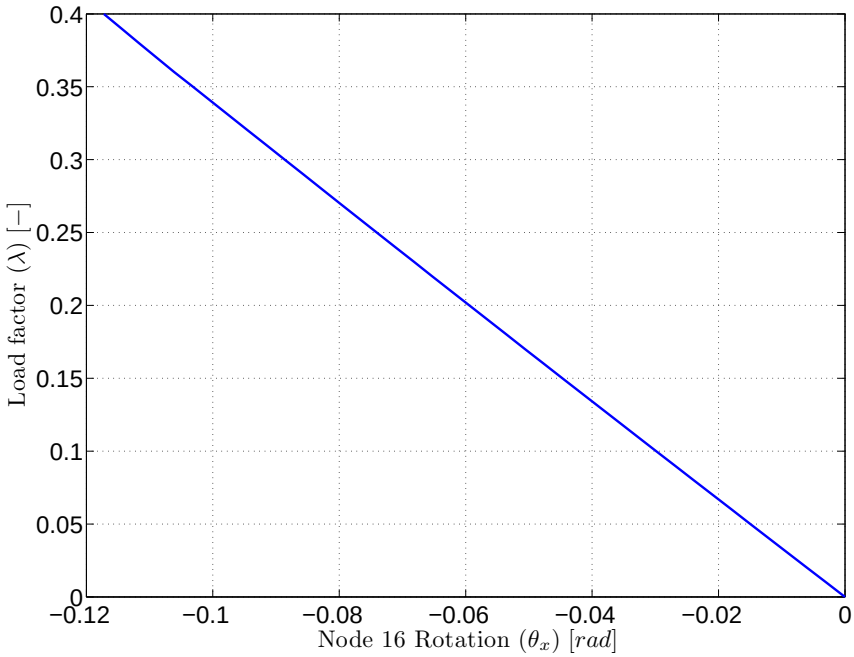

Figure 8.69: Beam with slope discontinuity - Equilibrium path corresponding to the rotation around x axis of the free edge

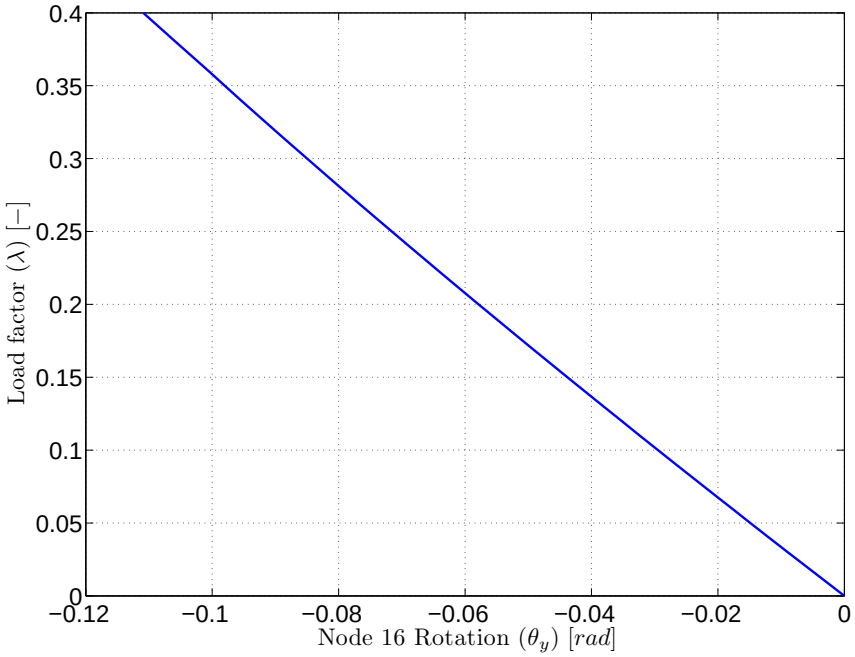

Figure 8.70: Beam with slope discontinuity - Equilibrium path corresponding to the rotation around y axis of the free edge

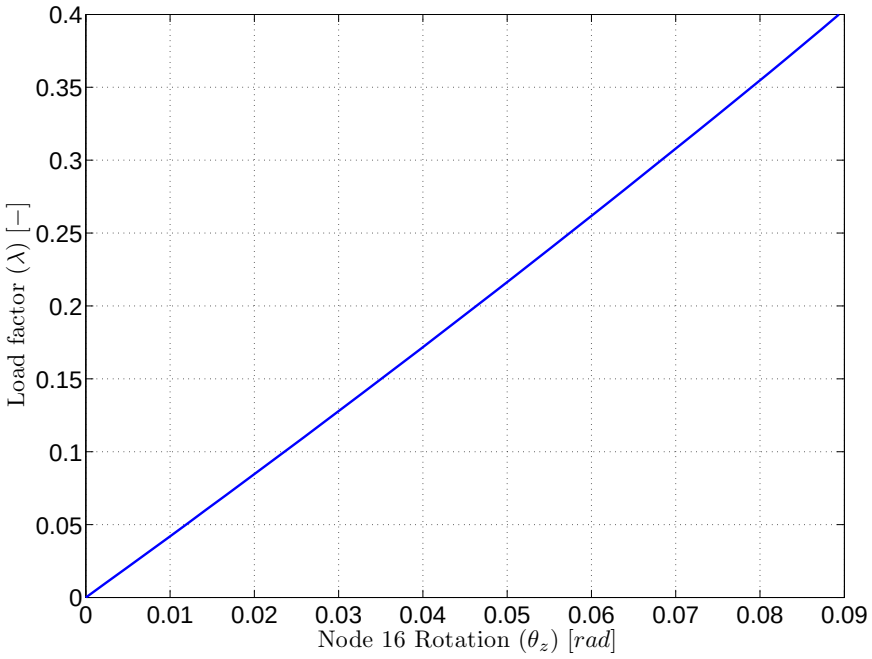

Figure 8.71: Beam with slope discontinuity - Equilibrium path corresponding to the rotation around z axis of the free edge

After the equilibrium paths have been plotted for the free edge of the cantilever, our

attention is focused on the displacement and stress field of the structure in some particular load factors. In the following, the three internal forces and the three internal moments acting on each element of the structure when $\lambda = 0.4$ are plotted in figures 8.72 (axial force), 8.73 (shear force in the y' axis), 8.74 (shear force in the z' axis), 8.75 (twisting moment), 8.76 (Bending moment in the y' axis) and 8.77 (Bending moment in the z' axis).

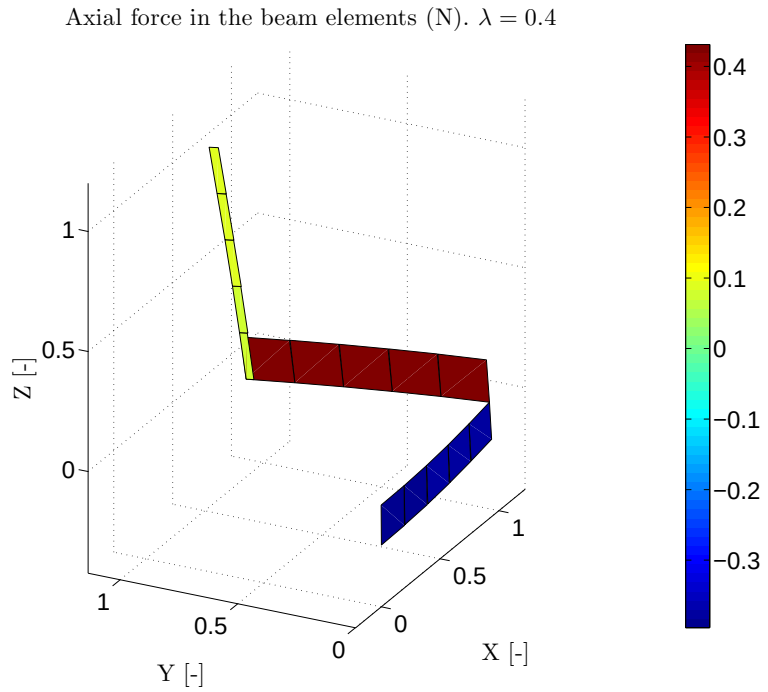

Figure 8.72: Beam with slope discontinuity - Axial force acting in the x' axes at $\lambda = 0.4$

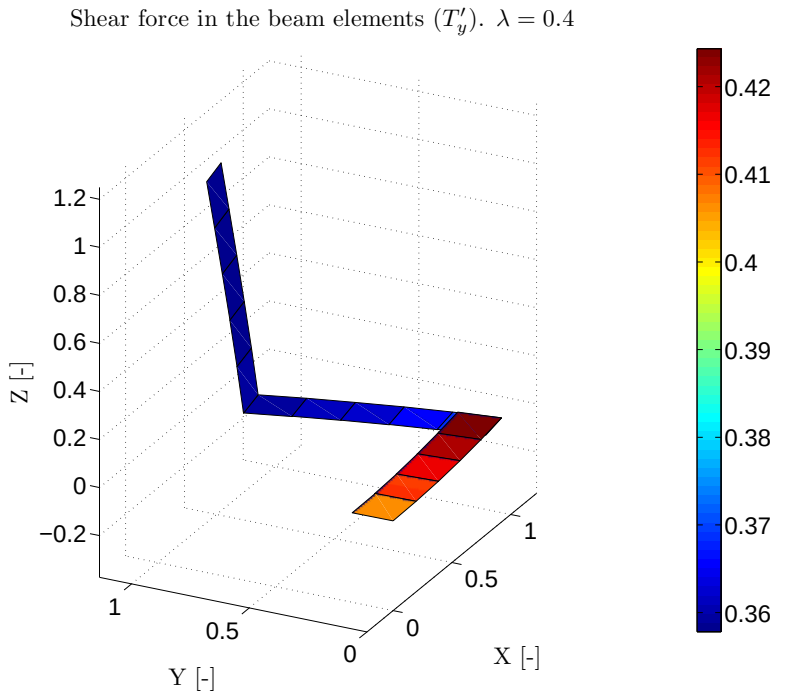

Figure 8.73: Beam with slope discontinuity - Shear force acting in the y' axes at $\lambda = 0.4$

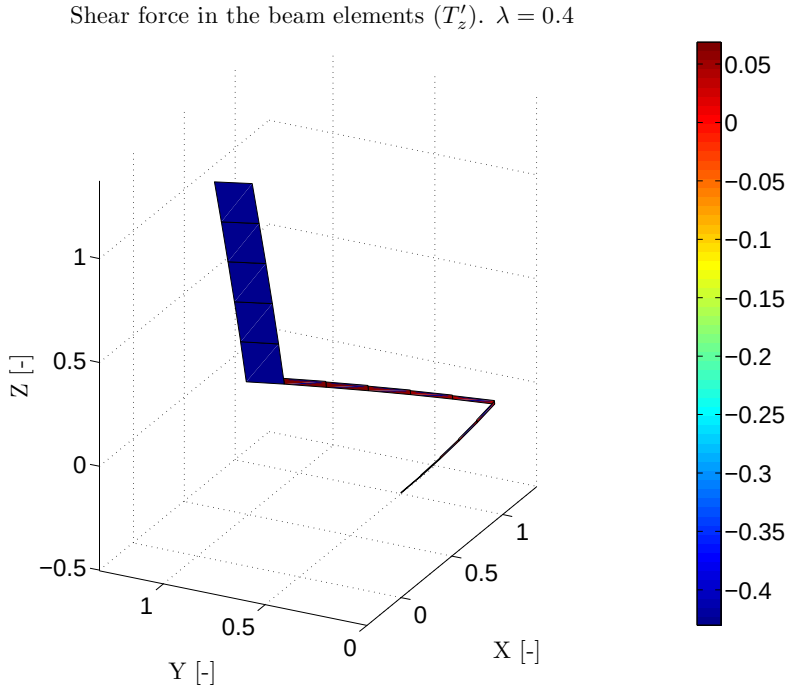

Figure 8.74: Beam with slope discontinuity - Shear force acting in the z' axes at $\lambda = 0.4$

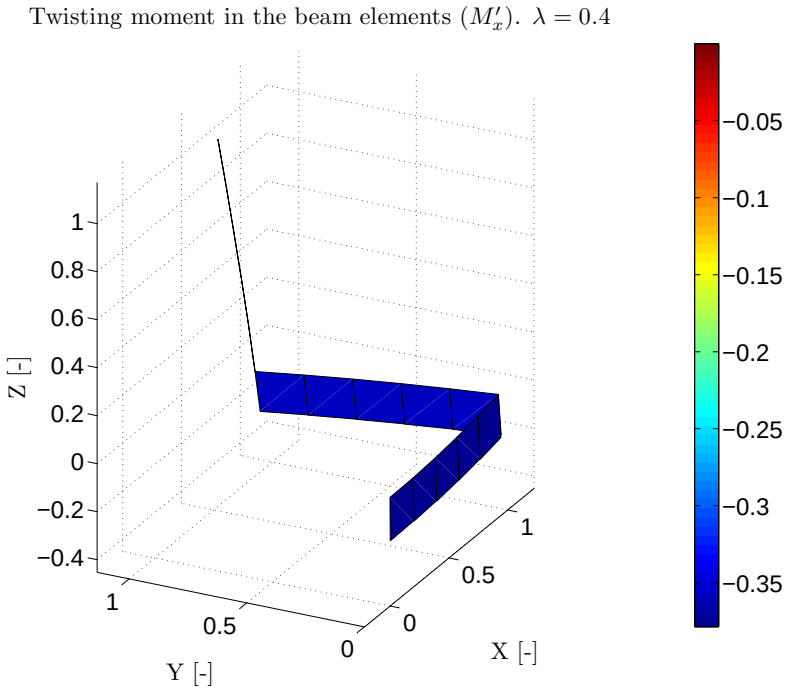

Figure 8.75: Beam with slope discontinuity - Twisting moment acting in the x' axes at $\lambda = 0.4$

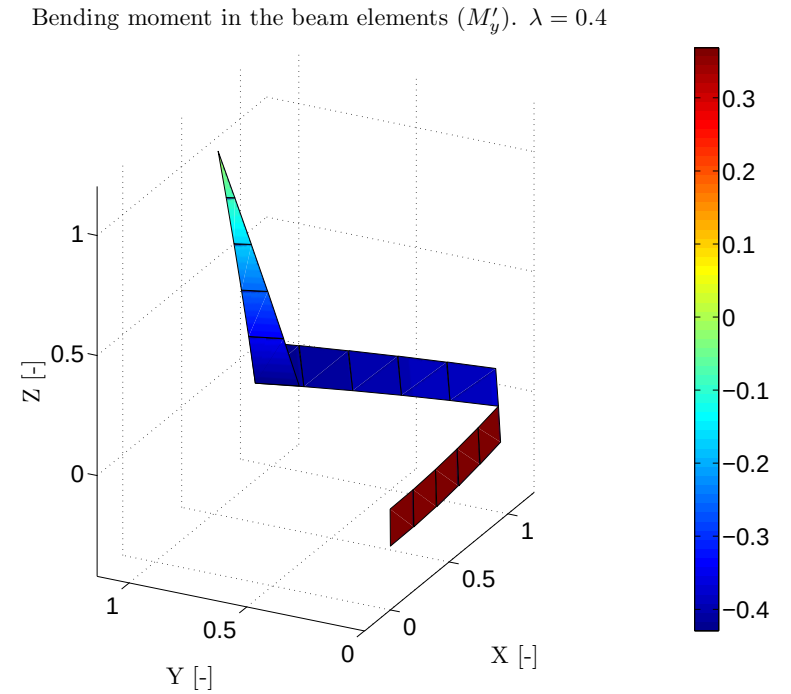

Figure 8.76: Beam with slope discontinuity - Bending moment acting in the y' axes at $\lambda = 0.4$

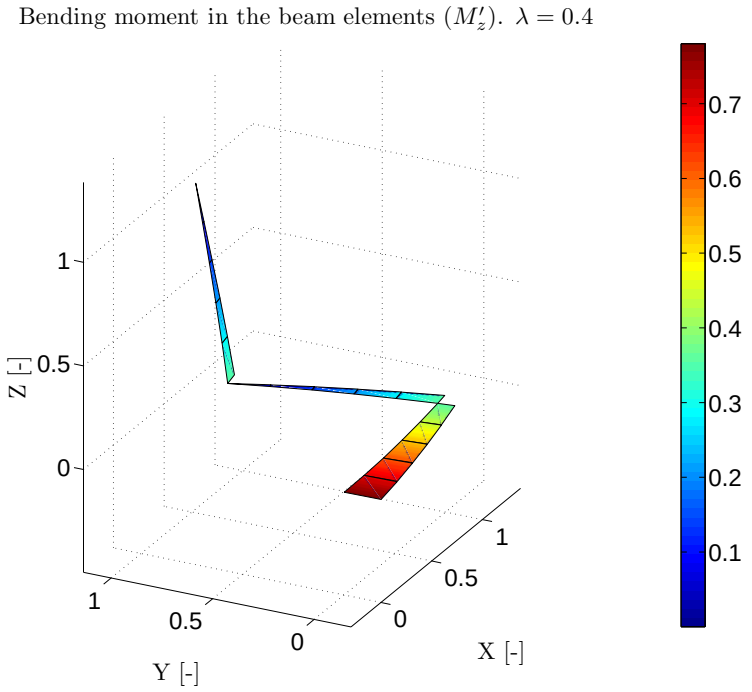

Figure 8.77: Beam with slope discontinuity - Bending moment acting in the z' axes at $\lambda = 0.4$

8.1.10 Lee's frame

A frame contained in the X-Y plane is analyzed under a concentrated load as it is shown in figure 8.78. The problem is analyzed using ten elements for each member.

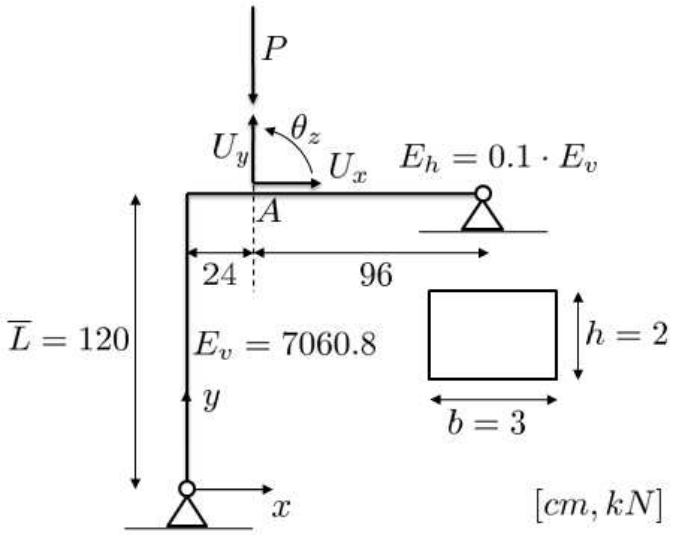

Figure 8.78: Lee's frame

Now, the Lee's frame will be analyzed considering the finite element model developed in this work. In table 8.16 the parameters and models used in the program are listed.

Concept	Symbol	Value
Structural model		
Model for cable structure	M_{cs}	-
Model for beam structure	M_{bs}	FEM
Model for flexural behaviour	M_{fb}	Euler-Bernoulli
Model for torsional behaviour	M_{tb}	Saint Venant
Parameters for the analysis		
Tolerance in the equilibrium	Tol_G	1e-3
Tolerance in the displacements	Tol_D	1e-3
Tolerance in the energy	Tol_W	1e-3
Maximum number of iterations correction phase	I_M	100
Method used in the correction phase	-	Arc-length/Restoring
Initial Arc-length value	Δl_I	0.1
Minimum Bergan value for the switching	B_m	0.4
Maximum Bergan value for the switching	B_M	100
Initial increment of load	$\Delta\lambda_I$	0.005
Final load parameter	λ_F	0.15
Maximum number of increments	Inc_M	40
Optimum number of iterations correction phase	I_O	50
Update parameters during the incremental procedure	-	No

Table 8.16: Lee's frame - Parameters for the nonlinear analysis in an incremental iterative scheme

The solution obtained with the model developed are compared with the ones obtained by [de Souza, 2000]. Good agreement between both results can be observed from the comparison considering linear elastic material.

Some final results provided by the program are listed here. The results will be exposed in terms of the load factor λ.

$$\lambda = \frac{P}{P^*} \qquad P^* = 20\ kN \tag{8.18}$$

First, figure 8.79 shows several configurations of the beam during the load procedure.

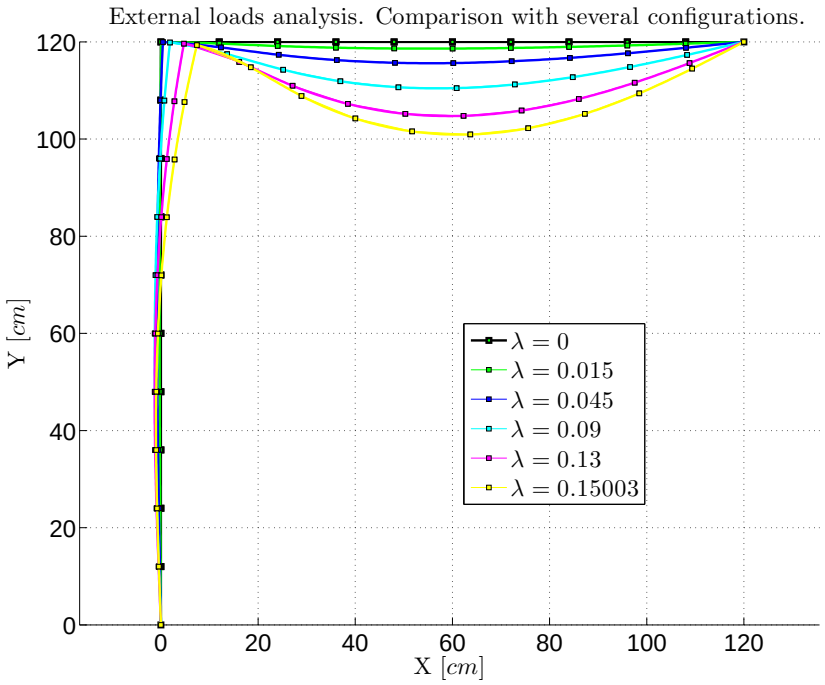

Figure 8.79: Lee's frame - Configuration of the beam in several load steps

The equilibrium paths corresponding to the point A are plotted. Figures 8.80 and 8.81 show the equilibrium paths of the displacements in the x and y directions, respectively. In addition, figure 8.82 shows the equilibrium path of the rotation around z axis.

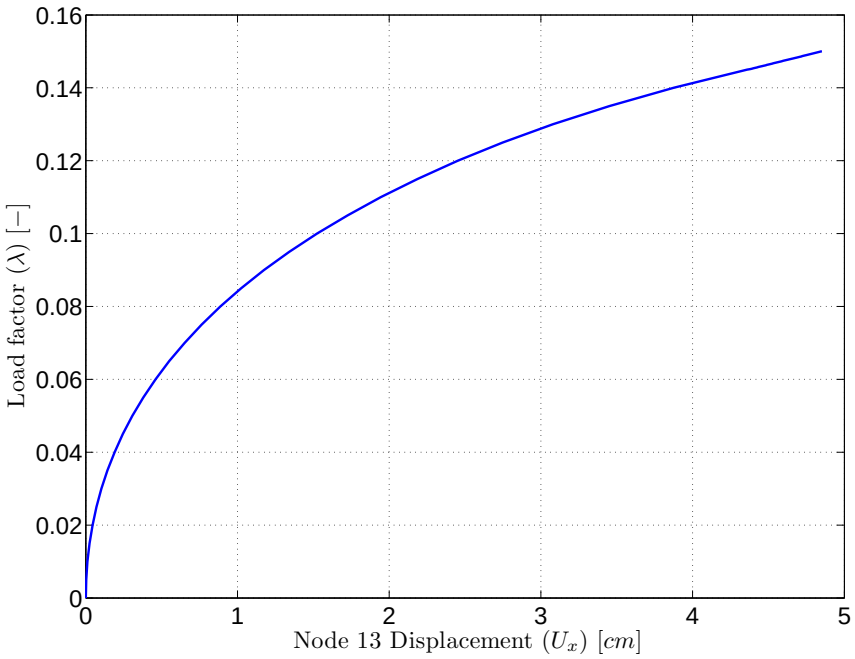

Figure 8.80: Lee's frame - Equilibrium path corresponding to the horizontal displacement in the x direction of point A

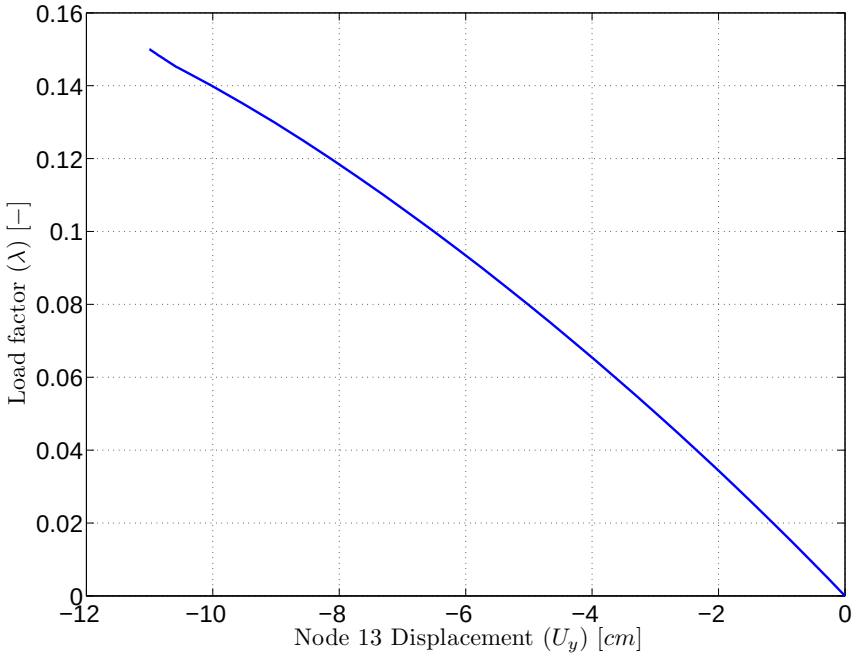

Figure 8.81: Lee's frame - Equilibrium path corresponding to the horizontal displacement in the y direction of point A

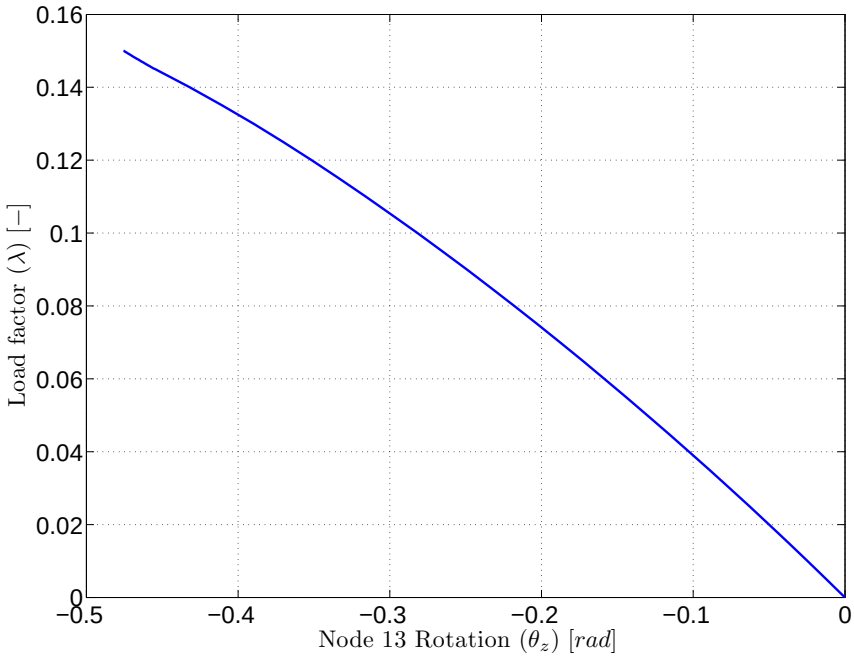

Figure 8.82: Lee's frame - Equilibrium path corresponding to the rotation around z axis of point A

After the equilibrium paths have been plotted, our attention is focused on the displace-

ment and stress field of the structure in some particular load factors. In the following, the internal forces and moment acting on each element of the structure when $\lambda = 1.5$ are plotted in figures 8.83 (axial force), 8.84 (shear force in the y' axis) and 8.85 (Bending moment in the z' axis).

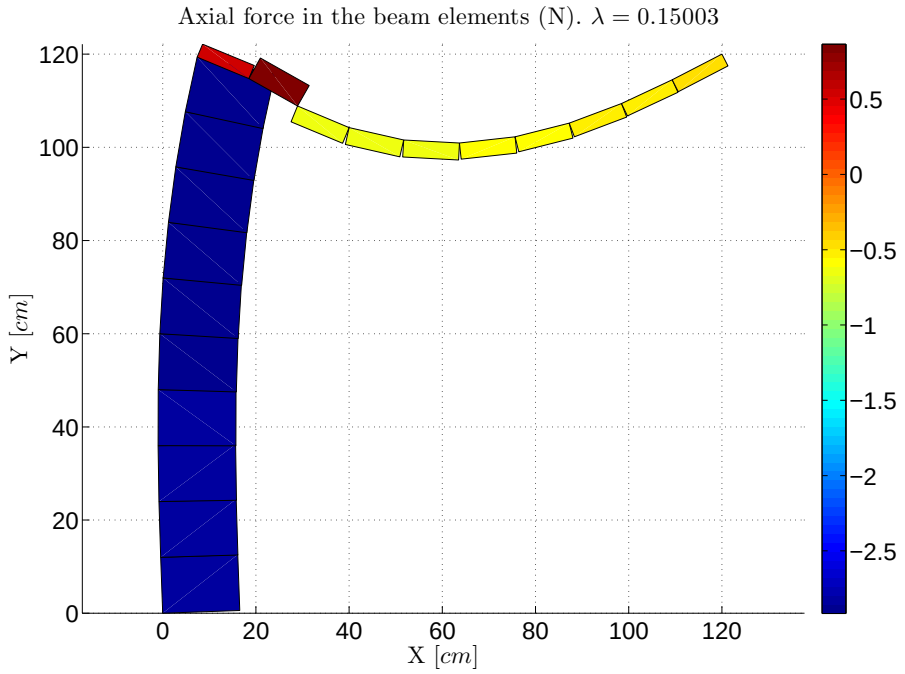

Figure 8.83: Lee's frame - Axial force acting in the x' axes at $\lambda = 0.15$

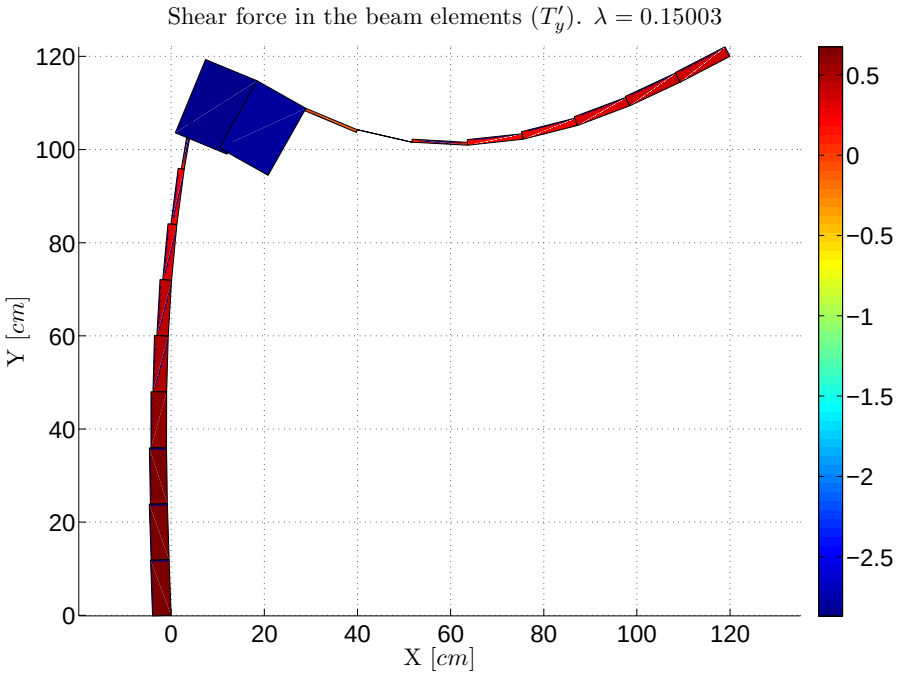

Figure 8.84: Lee's frame - Shear force acting in the y' axes at $\lambda = 0.15$

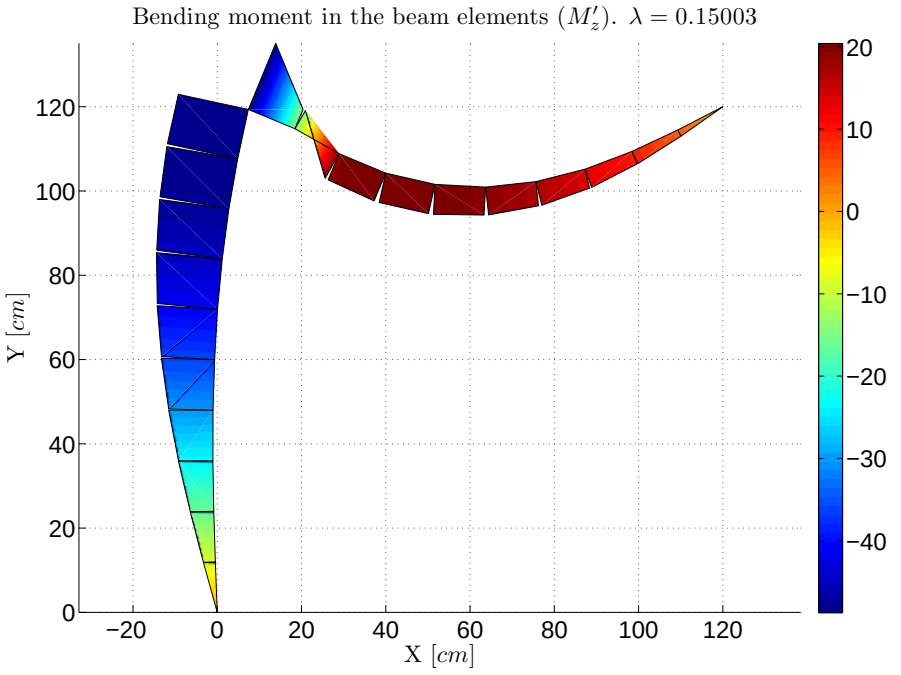

Figure 8.85: Lee's frame - Bending moment acting in the z' axes at $\lambda = 0.15$

8.1.11 Williams toggle frame

A frame contained in the X-Y plane is analyzed under a concentrated load as it is shown in figure 8.86. The problem is analyzed using 12 elements for each member.

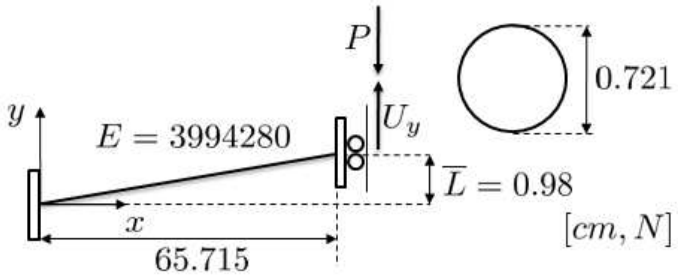

Figure 8.86: Williams toggle frame

Now, the Williams toggle frame will be analyzed considering the finite element model developed in this work. In table 8.17 the parameters and models used in the program are listed.

Concept	Symbol	Value
Structural model		
Model for cable structure	M_{cs}	-
Model for beam structure	M_{bs}	FEM
Model for flexural behaviour	M_{fb}	Euler-Bernoulli
Model for torsional behaviour	M_{tb}	Saint Venant
Parameters for the analysis		
Tolerance in the equilibrium	Tol_G	1e-3
Tolerance in the displacements	Tol_D	1e-3
Tolerance in the energy	Tol_W	1e-3
Maximum number of iterations correction phase	I_M	100
Method used in the correction phase	-	Arc-length/Restoring
Initial Arc-length value	Δl_I	0.1
Minimum Bergan value for the switching	B_m	0.4
Maximum Bergan value for the switching	B_M	100
Initial increment of load	$\Delta\lambda_I$	0.001
Final load parameter	λ_F	1
Maximum number of increments	Inc_M	1000
Optimum number of iterations correction phase	I_O	50
Update parameters during the incremental procedure	-	No

Table 8.17: Williams toggle frame - Parameters for the nonlinear analysis in an incremental iterative scheme

The solution obtained with the model developed are compared with the ones obtained by [de Souza, 2000]. Good agreement between both results can be observed from the comparison considering linear elastic material.

Some final results provided by the program are listed here. The results will be shown in terms of the load factor λ.

$$\lambda = \frac{P}{P^*} \qquad P^* = 350\ N \tag{8.19}$$

First, figure 8.87 shows several configurations of the beam during the load procedure.

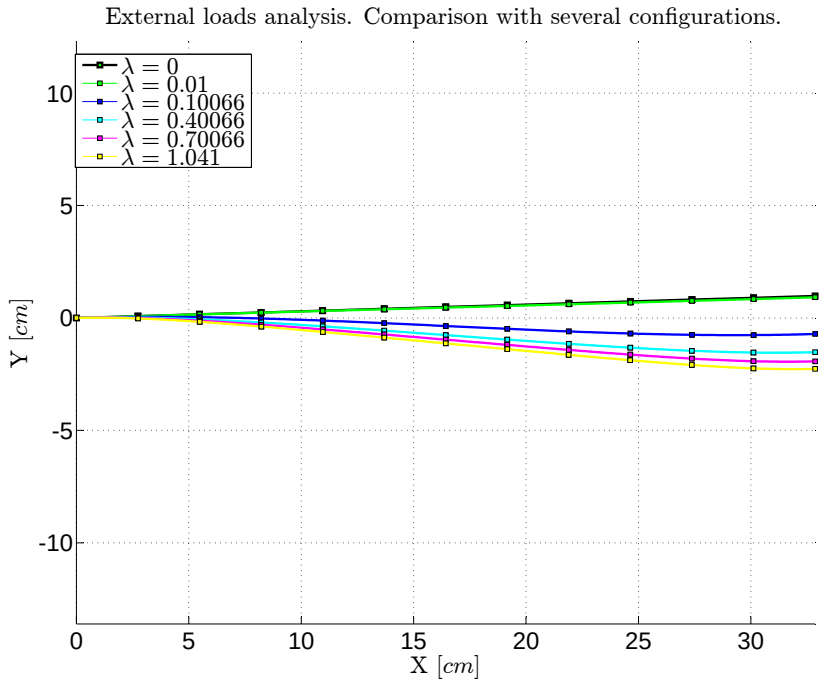

Figure 8.87: Williams toggle frame - Configuration of the beam in several load steps

The equilibrium path corresponding to the right point of the frame is plotted. Figure 8.88 shows the equilibrium path of the displacements in the y direction.

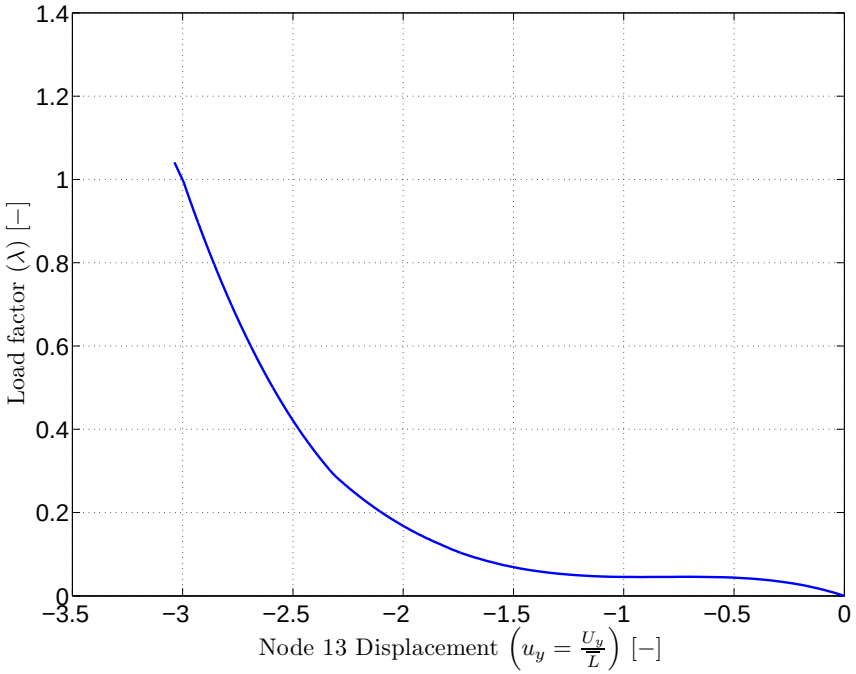

Figure 8.88: Williams toggle frame - Equilibrium path corresponding to the horizontal displacement in the x direction of point A

After the equilibrium path have been plotted, our attention is focused on the displacement and stress field of the structure in some particular load factors. In the following, the internal forces and moment acting on each element of the structure when $\lambda = 0.045$ and $\lambda = 1.041$ are plotted in figures 8.89 and 8.90 (axial force), 8.91 and 8.92 (shear force in the y' axis) and 8.93 8.94 (Bending moment in the z' axis).

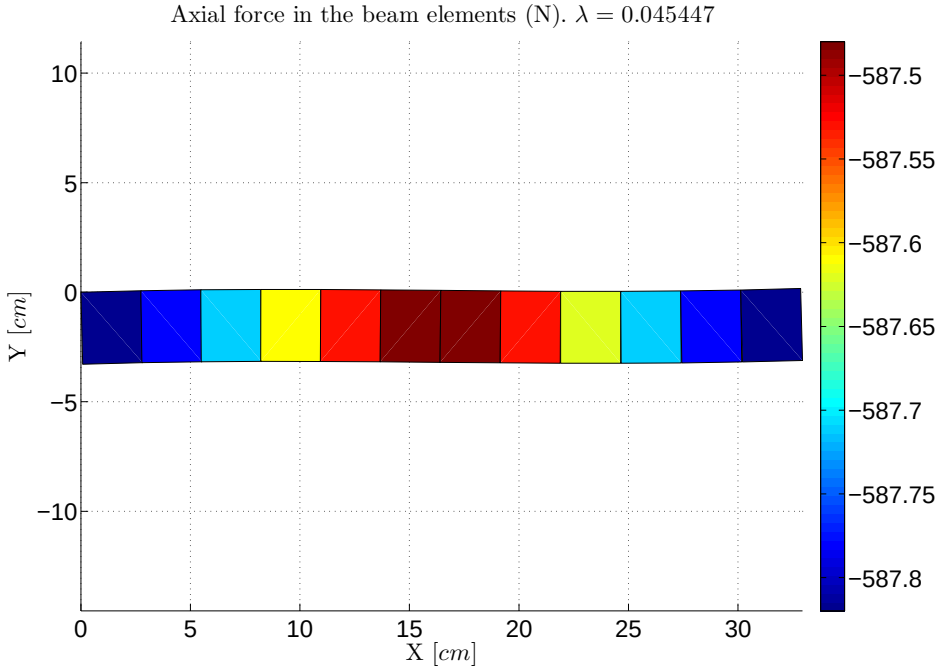

Figure 8.89: Williams toggle frame - Axial force acting in the x' axes at $\lambda = 0.045$

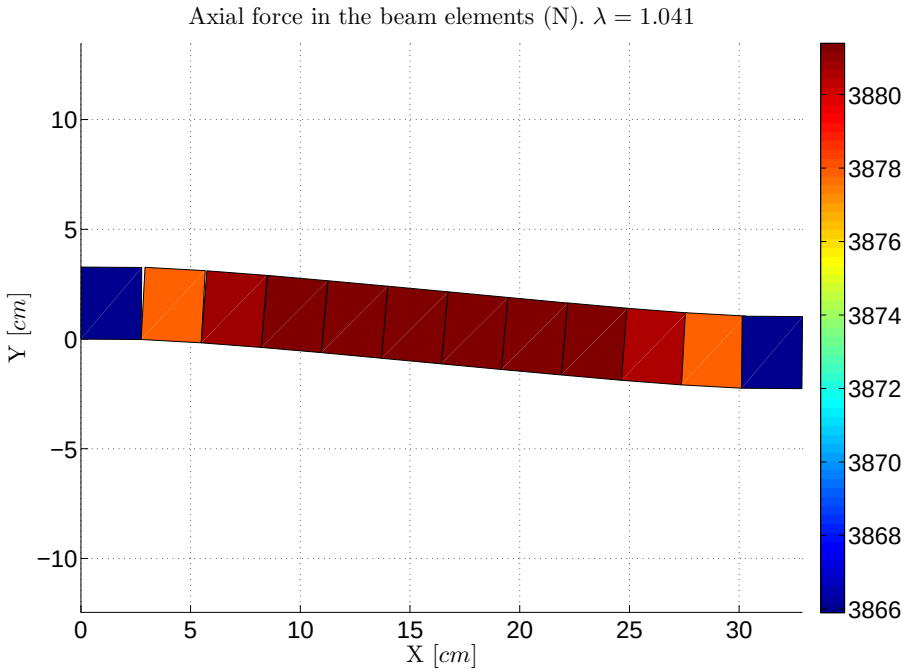

Figure 8.90: Williams toggle frame - Axial force acting in the x' axes at $\lambda = 1.041$

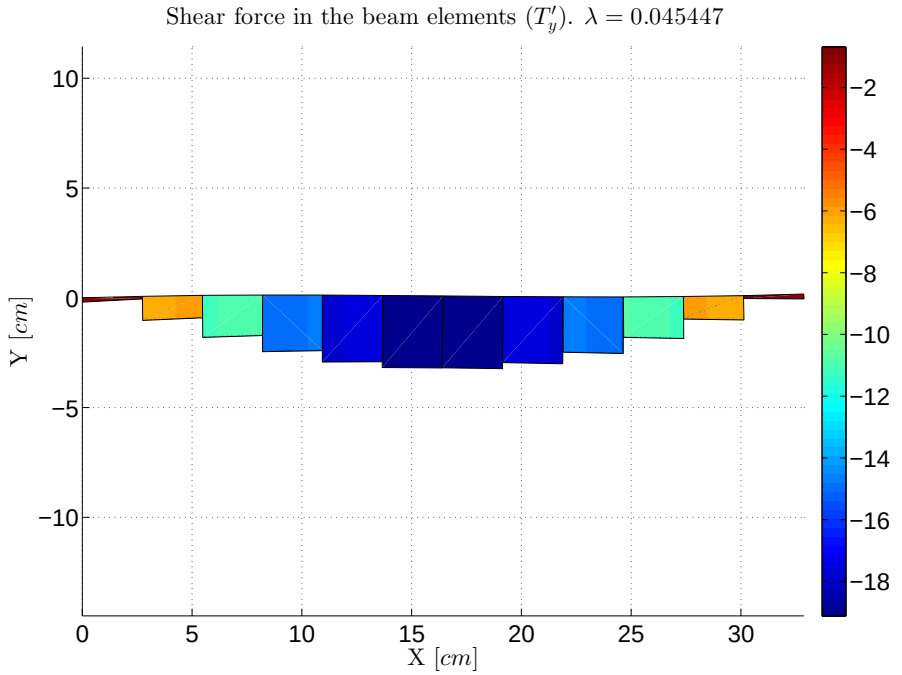

Figure 8.91: Williams toggle frame - Shear force acting in the y' axes at $\lambda = 0.045$

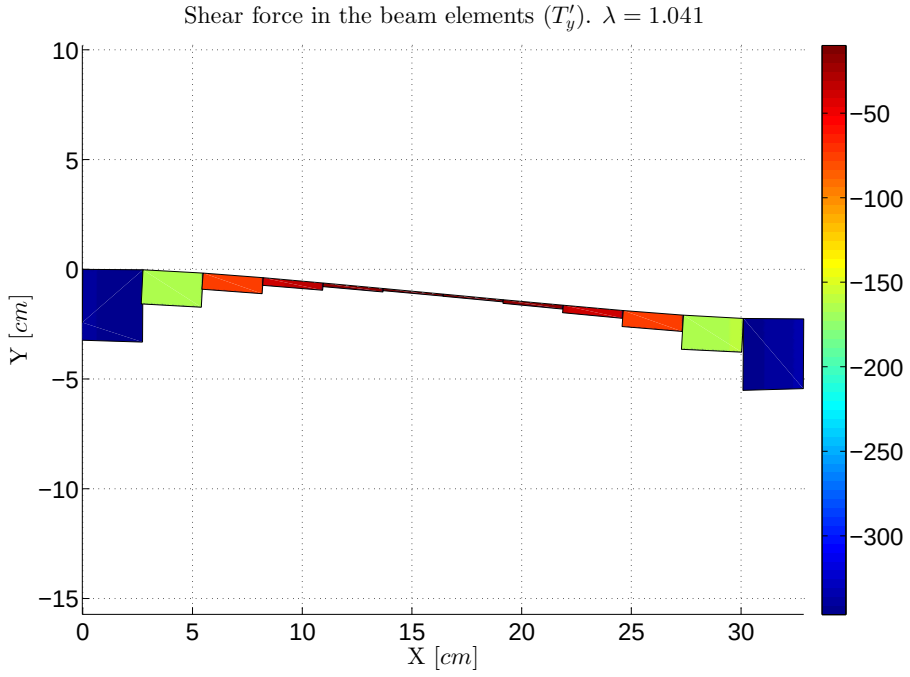

Figure 8.92: Williams toggle frame - Shear force acting in the y' axes at $\lambda = 1.041$

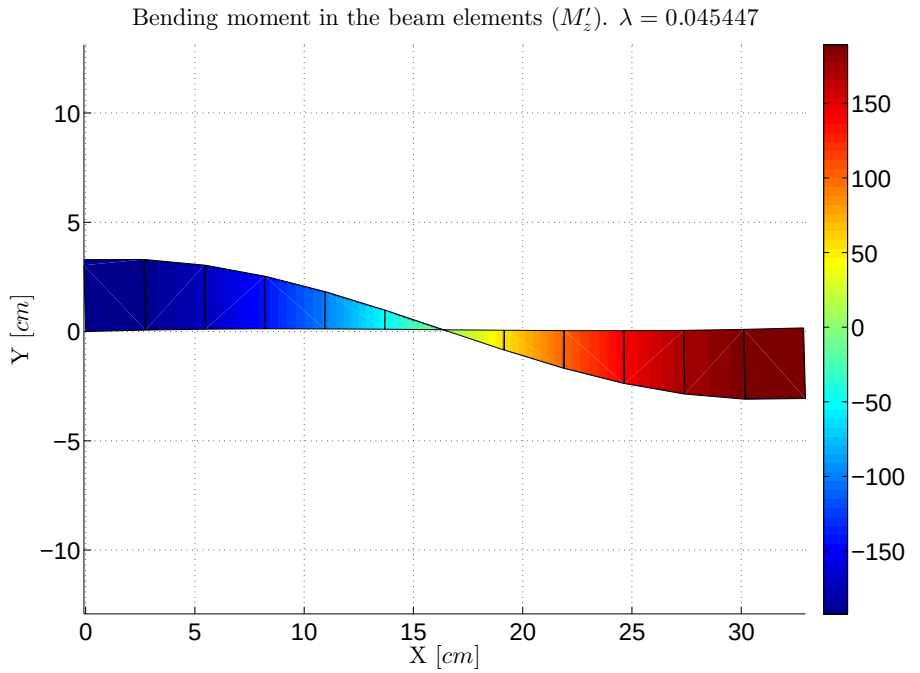

Figure 8.93: Williams toggle frame - Bending moment acting in the z' axes at $\lambda = 0.045$

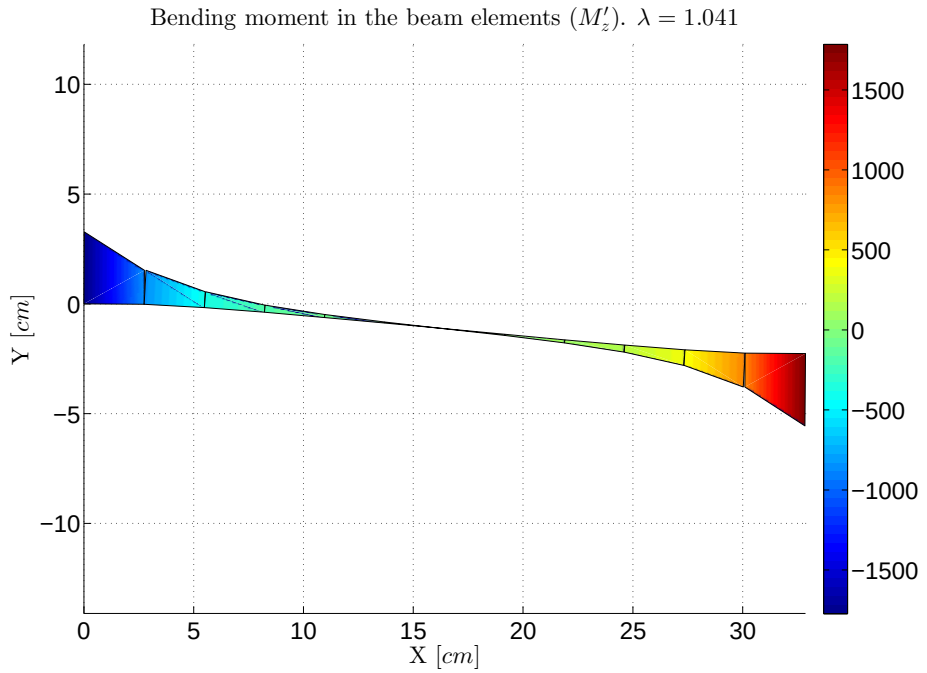

Figure 8.94: Williams toggle frame - Bending moment acting in the z' axes at $\lambda = 1.041$

8.2 Floating V-shaped beam

A simply floating beam with a V form as the one depicted in figure 8.95 is analyzed.

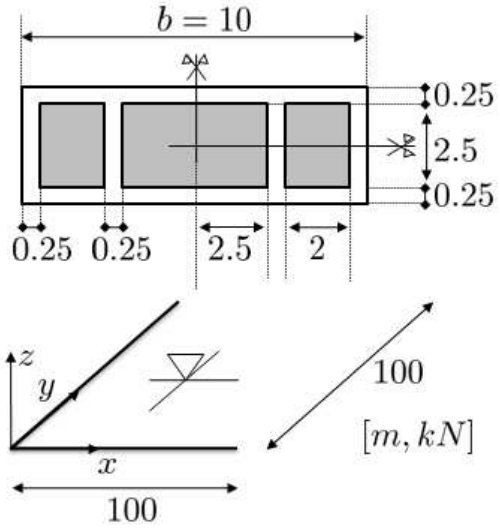

Figure 8.95: Floating V-Beam subjected to its own self weight

8.2.1 Analytical solution

In this case, the analytical solution is very simple to obtain. Indeed, the simmetry of the problem ensures that the stresses inside both beam will be null. The rotational degrees of freedom at each end of the beam will not be activated and only the vertical displacement of the beams will completely define the solution of the problem. In addition, due to the nature of the problem, in the equilibrium position the hydrostatic load will completely counteract the self weight of the beam and the beam will not require any deformation to equilibrate itself. In conclusion, the only variable that defines the solution of the problem is the vertical displacement of the three nodes (edges of each beam) that define the floating structure.

Due to the fact that the section is rectangular, the buoyancy stiffness is constant during the load procedure (see 5.4.1.1) and is equal to:

$$K_f = \gamma_f b = 100 \ \left[\frac{kN}{m}\right] \tag{8.20}$$

Considering the equilibrium equation

$$2\gamma_f b h_{eq} l = 2\gamma_m A_s l \rightarrow h_{eq} = \frac{\gamma_m A_s}{\gamma_f b} = 1.875 \ [m] \tag{8.21}$$

8.2.2 Numerical solution

Now, the floating V-beam will be analyzed considering the finite element model developed in this work. In table 8.18 the parameters and models used in the program are listed.

Concept	Symbol	Value
Structural model		
Model for cable structure	M_{cs}	-
Model for beam structure	M_{bs}	FEM
Model for flexural behaviour	M_{fb}	Euler-Bernoulli
Model for torsional behaviour	M_{tb}	Saint Venant
Parameters for the analysis		
Tolerance in the equilibrium	Tol_G	1e-3
Tolerance in the displacements	Tol_D	1e-3
Tolerance in the energy	Tol_W	1e-3
Maximum number of iterations correction phase	I_M	100
Method used in the correction phase	-	Arc-length/Restoring
Initial Arc-length value	Δl_I	0.1
Minimum Bergan value for the switching	B_m	0.4
Maximum Bergan value for the switching	B_M	10
Initial increment of load	$\Delta\lambda_I$	1
Final load parameter	λ_F	1
Maximum number of increments	Inc_M	5
Optimum number of iterations correction phase	I_O	50
Update parameters during the incremental procedure	-	No

Table 8.18: Floating V-Beam - Parameters for the nonlinear analysis in an incremental iterative scheme

The solution of the finite element program completely matches with the analytical results and the following figure (figure 8.96) shows the equilibrium position obtained by the program.

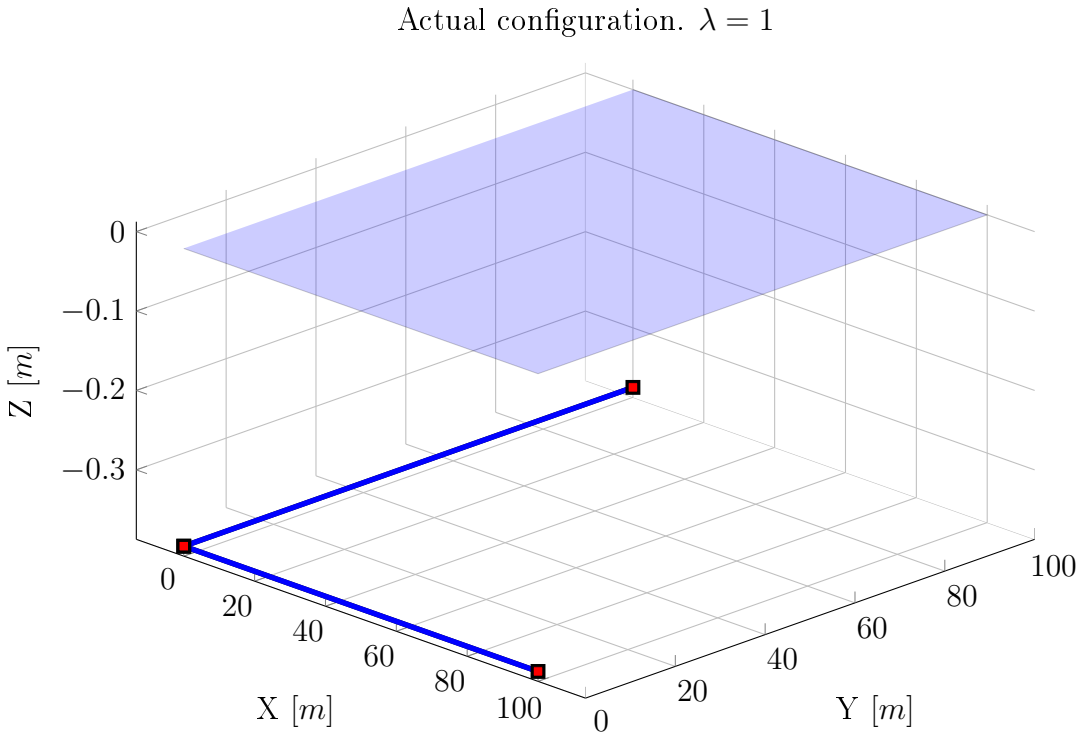

Figure 8.96: Floating V-Beam subjected to its own self weight - Equilibrium position obtained by the program

The nodal position relative to the free surface of the fluid obtained by the program is -0.375. This agrees with the analytical solution. Indeed, the centroid of the section of the beam (position of the node in the finite element program) is located 1.5 meters above the bottom part of the beam.

8.3 Floating beam under twisting moment

A simply straight floating beam as the one depicted in figure 8.97 is analyzed.

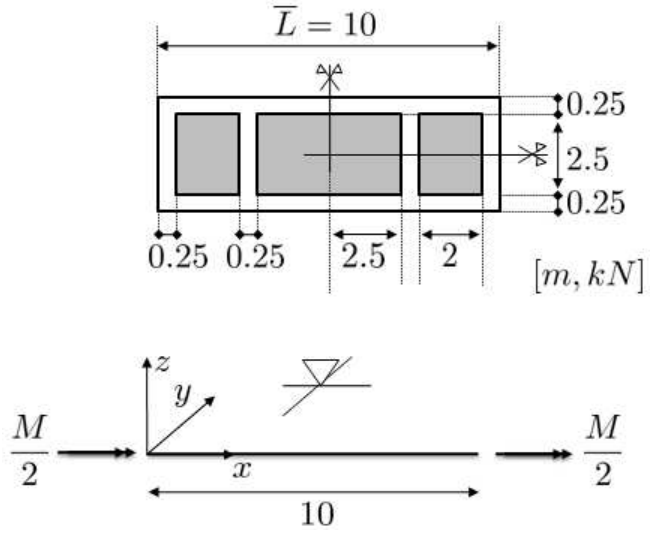

Figure 8.97: Floating beam under twisting moment

Now, the floating beam under twisting moment will be analyzed considering the finite element model developed in this work. In table 8.19 the parameters and models used in the program are listed.

Concept	Symbol	Value
Structural model		
Model for cable structure	M_{cs}	-
Model for beam structure	M_{bs}	FEM
Model for flexural behaviour	M_{fb}	Euler-Bernoulli
Model for torsional behaviour	M_{tb}	Saint Venant
Parameters for the analysis		
Tolerance in the equilibrium	Tol_G	1e-3
Tolerance in the displacements	Tol_D	1e-3
Tolerance in the energy	Tol_W	1e-3
Maximum number of iterations correction phase	I_M	100
Method used in the correction phase	-	Arc-length/Restoring
Initial Arc-length value	Δl_I	0.01
Minimum Bergan value for the switching	B_m	0.4
Maximum Bergan value for the switching	B_M	1.2
Initial increment of load	$\Delta\lambda_I$	0.01
Final load parameter	λ_F	1
Maximum number of increments	Inc_M	100
Optimum number of iterations correction phase	I_O	50
Update parameters during the incremental procedure	-	No

Table 8.19: Floating beam under twisting moment - Parameters for the nonlinear analysis in an incremental iterative scheme

The solution provided by the finite element model developed in this work provides, for every value of M, the equilibrium position in terms of the vertical displacement and

rotation of the beam. In the following, the equilibrium path of both degrees of freedom (vertical displacement and twisting rotation) are depicted in figures 8.98 (vertical displacement of the centroid of the beam) and 8.99 (rotation with respect the normal axis of the section).

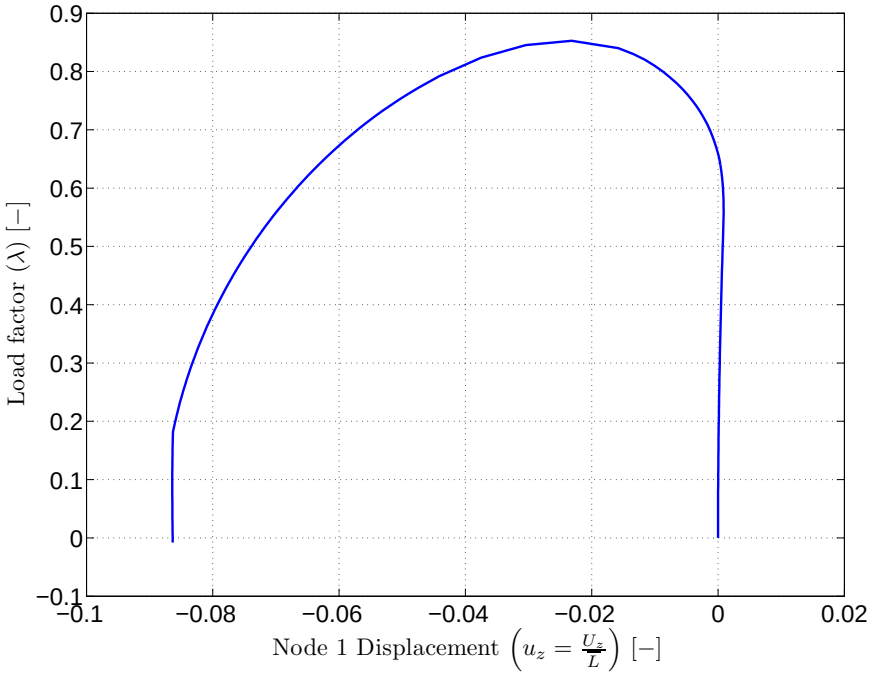

Figure 8.98: Floating beam under twisting moment - Equilibrium path of the vertical displacement of the centroid of the section

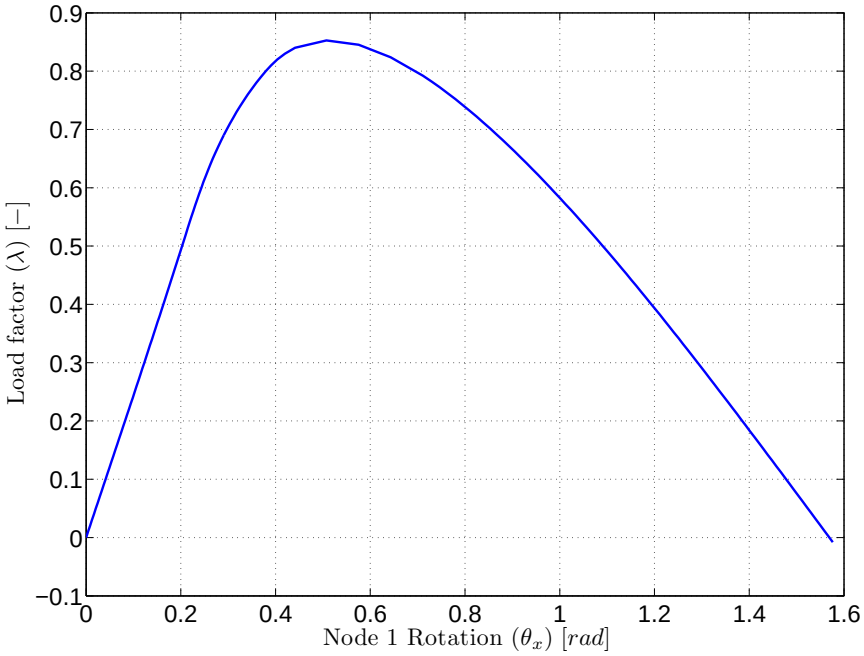

Figure 8.99: Floating beam under twisting moment - Equilibrium path of the rotation of the section

In addition, the equilibrium positions of the beam under its own self weight, when the beam has rotated $\alpha = \frac{\pi}{6}$ (which corresponds to an external twisting moment equal to $M = 25.5748\ [kN \cdot m]$) and $\alpha = \frac{\pi}{2}$ radians (which corresponds to a self-equilibrated configuration of the beam, $M = 0$) are depicted in figures 8.100, 8.101 and 8.102 respectively.

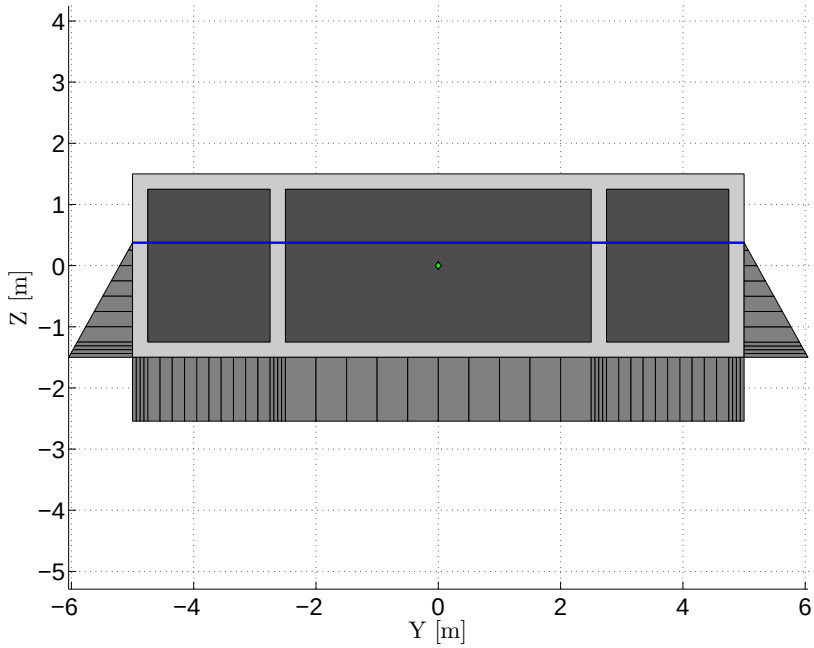

Figure 8.100: Floating beam under twisting moment - Equilibrium position under it's own self weight

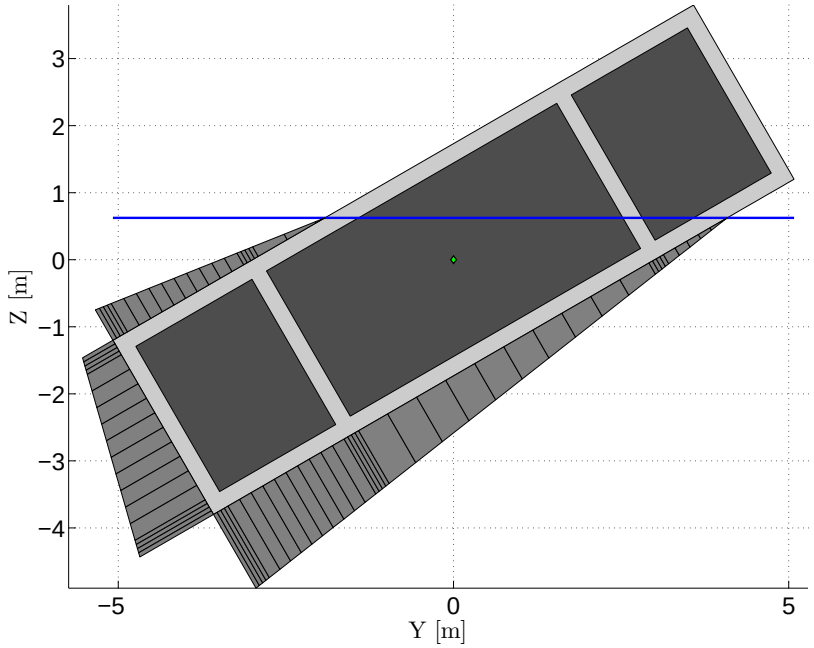

Figure 8.101: Floating beam under twisting moment - Equilibrium position when the external twisting moment is equal to $M = 25.5748\ [kN \cdot m]$

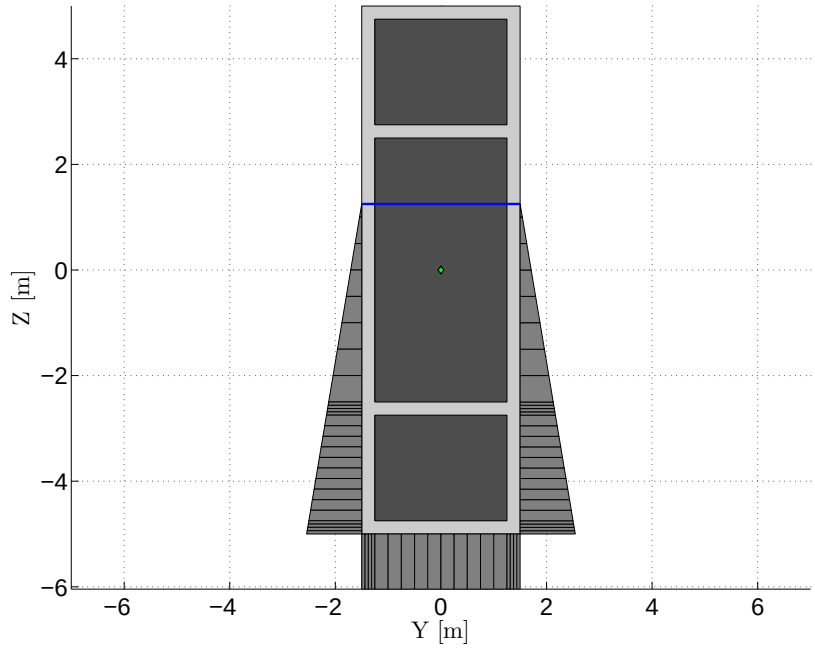

Figure 8.102: Floating beam under twisting moment - Equilibrium position when the external twisting moment is equal to $M = 0\ [kN \cdot m]$

8.4 Floating bridge under a concentrated load at middle span

Now, a floating bridge with a concentrated load in the middle will be analysed. The main goal is to study the influence of the deformability in the internal forces and moments acting on the bridge. Such influence will be measured comparing the results of the analysis with the analytical results obtained considering the bridge completely rigid. The bridge is made of concrete and the concentrated load applied in the bridge will simulate a 30 tones truck so will be equal to 300 kN. The bridge is depicted in figure 8.103.

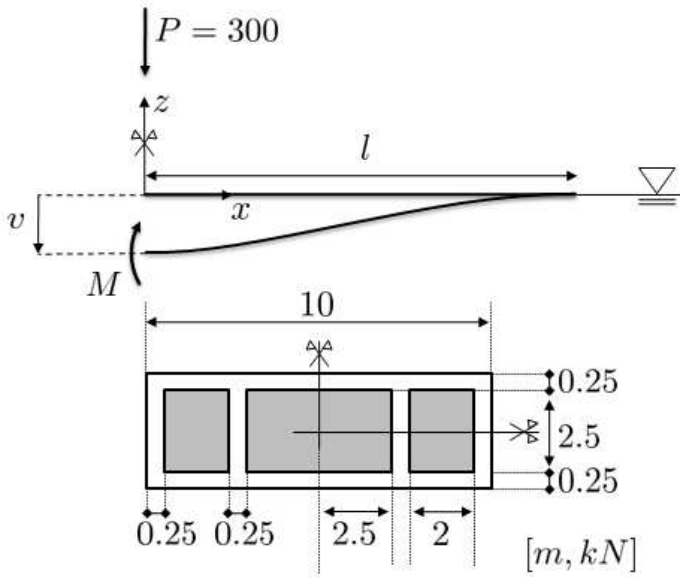

Figure 8.103: Floating bridge submitted to a concentrated load at middle span

Now, the floating bridge submitted to a concentrated load at middle span in the middle will be analyzed considering the finite element model developed in this work. In table 8.20 the parameters and models used in the program are listed.

Concept	**Symbol**	**Value**
Structural model		
Model for cable structure	M_{cs}	-
Model for beam structure	M_{bs}	FEM
Model for flexural behaviour	M_{fb}	Euler-Bernoulli
Model for torsional behaviour	M_{tb}	Saint Venant
Parameters for the analysis		
Tolerance in the equilibrium	Tol_G	1e-3
Tolerance in the displacements	Tol_D	1e-3
Tolerance in the energy	Tol_W	1e-3
Maximum number of iterations correction phase	I_M	100
Method used in the correction phase	-	Arc-length/Restoring
Initial Arc-length value	Δl_I	0.01
Minimum Bergan value for the switching	B_m	0.4
Maximum Bergan value for the switching	B_M	1.2
Initial increment of load	$\Delta\lambda_I$	1
Final load parameter	λ_F	1
Maximum number of increments	Inc_M	100
Optimum number of iterations correction phase	I_O	50
Update parameters during the incremental procedure	-	No

Table 8.20: Floating bridge submitted to a concentrated load at middle span - Parameters for the nonlinear analysis in an incremental iterative scheme

As explained before, the results will be shown in terms of the vertical displacement

and bending moment mesured in the point where the concentrated load is applied. The depth in the water and the bending moment mesured in te point A are depicted and compared with the rigid model in figures 8.104 and 8.105, respectively.

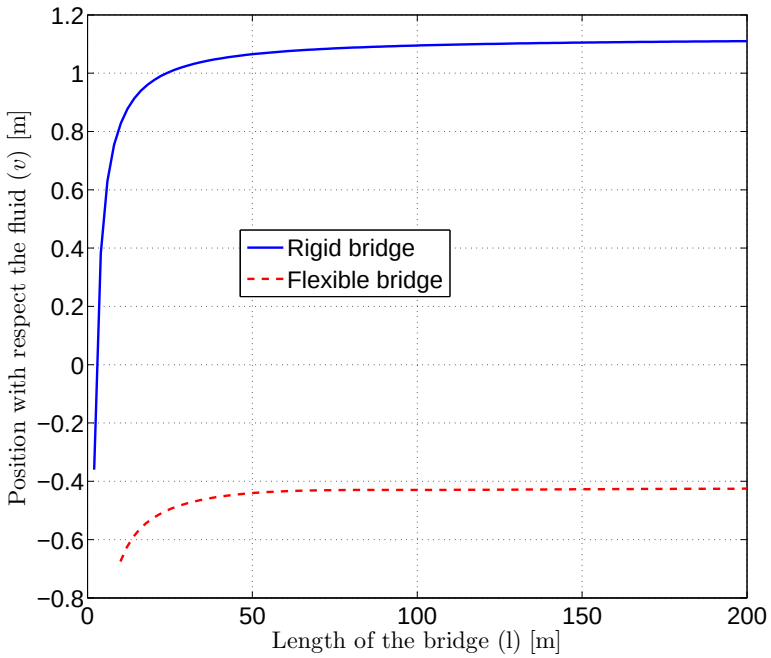

Figure 8.104: Floating bridge submitted to a concentrated load at middle span in the middle - Maximum penetration in the fluid as a function of the length of the bridge considering the bridge rigid and flexible

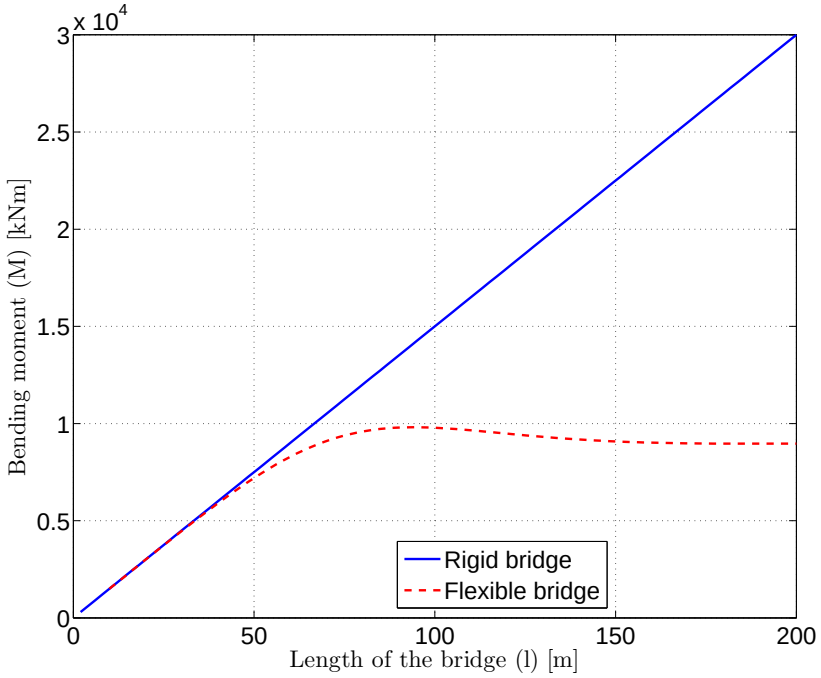

Figure 8.105: Floating bridge submitted to a concentrated load at middle span in the middle - Bending moment at the acting load point as a function of the length of the bridge considering the bridge rigid and flexible

9 Application to a floating box-girder bridge

9.1 Introduction

The proposed formulation is now applied to the structural analysis of a floating box-girder bridge. The considered structure is inspired to the Lacey V. Murrow Memorial Bridge. This structure is a floating bridge that carries the eastbound lanes of Interstate 90 across Lake Washington from Seattle to Mercer Island, Washington. Westbound traffic is carried by the Homer M. Hadley Memorial Bridge running parallel to it. The Lacey V. Murrow Memorial Bridge is the second longest floating bridge on Earth at 6,620 ft (2,020 m), whereas the longest is the Governor Albert D. Rosellini Bridge—Evergreen Point just a few miles to the north on the same lake, built 23 years later. The third longest is the Hood Canal Bridge, also in Washington State, about 30 miles (48 km) to the northwest of the Evergreen Point Floating Bridge.

Along with the east portals of the Mount Baker Ridge Tunnel, the bridge is an official City of Seattle landmark. While the bridge originally had an opening span at the center of the bridge to allow a horizontal opening of 202 feet (62 m) for major waterborne traffic, the only boat passages currently are elevated fixed spans at the ends with 29 feet (8.8 m) of vertical clearance. The situation of the bridge is depicted in figures 9.1, 9.2 and 9.3.

Figure 9.1: Location of the floating bridge referred to the United States of America

Figure 9.2: Location of the floating bridge referred to the Washington state

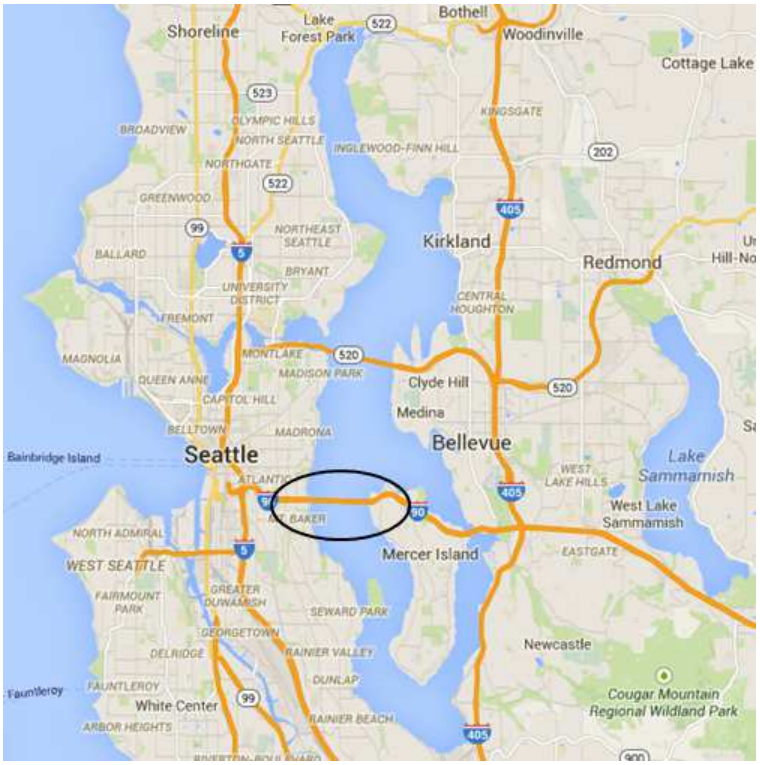

Figure 9.3: Location of the floating bridge in Seattle

9.2 Background and historical context

The bridge was the brainchild of engineer Homer Hadley, who made the first proposal in 1921. Construction began January 1, 1939 and was completed in 1940. The construction cost for the project was on the order of $9,000,000$ $ including approaches. It was partially financed by a bond issue of $4,184,000$ $. Tolls were removed in 1949. It sank in a storm on November 25, 1990, while it was undergoing refurbishing and repair. The current bridge was built in 1993. The eponymous Lacey V. Murrow was the second Director of the Washington State Highway Department and a highly decorated US Air Force officer who served in World War II. He was the oldest brother of CBS commentator Edward R. Murrow.

Formerly known as the "Lake Washington Floating Bridge", the original bridge was built under a 1 1/2-year contract awarded to the Puget Sound Bridge and Dredging Company (the project was led by engineer Peter John Jensen) in the amount of $3,254,000$ $. It included a movable span that could be retracted into a pocket in the center of the fixed span to permit large boats to pass. This design resulted in a roadway "bulge" that required vehicles to swerve twice across polished steel joints as they passed the bulge. A "reversible lane" system, indicated by lighted overhead lane control signals with arrow and 'X' signs, compounded the hazard by putting one lane of traffic on the "wrong" side of the bulge at different times of day in an effort to alleviate rush-hour traffic into or out of Seattle. There were many serious collisions on the bridge. The problems grew worse as the traffic load increased over the years and far outstripped the designed capacity. Reno-

vation or replacement was essential and a parallel bridge, the Homer M. Hadley Memorial Bridge, was completed in 1989.

The Puget Sound region, particularly the urban areas of Seattle and what is commonly known as the "Eastside" – communities east of Lake Washington including Bellevue, Medina, Hunts Point, Yarrow Point, Clyde Hill, Kirkland, Redmond, and many others – was in large part developed because of the numerous deep ports, rivers, and fresh water lakes, which provide connectivity and support maritime commerce. Water is a ubiquitous feature in the region. Inhabitants of the Puget Sound region have long been tasked with crossing and navigating the area's numerous waterways, whether by hand-carved canoes, ferries, pleasure craft, or bridges. The planning and construction of the Lacey V. Murrow memorial Bridge was a mid-century solution to the ongoing challenge of providing an efficient and effective crossing to Lake Washington.

9.2.1 Transportation and Mobility in Western Washington

Water transportation has had a profound impact on the historical development of Western Washington. Multiple bodies of water, including the Pacific Ocean, Puget Sound, and in the Seattle area, Lake Washington and Lake Union, both enhance and restrict transportation. Lake Washington, which is 20 miles long and 4 miles across at its widest point, represents the eastern boundary of Seattle. The Lake is connected to the Puget Sound and ultimately to the Pacific Ocean and beyond, by way of the Lake Washington Ship Canal. The area served by the Evergreen Point Bridge and SR520, from I-5 to the eastern shore of Lake Washington, includes some of the most diverse and complex human and natural landscapes in the Puget Sound region. The geography includes densely developed urban and suburban areas and some of the most critical natural areas and sensitive ecosystems that remain in the urban growth area.

As early as 1859, the territorial legislature unsuccessfully called for the U.S. Congress to build a viable road over Snoqualmie Pass, which would ease the transport across the mountains and would secure Seattle's position as an economic hub. Taking matters into their own hands in 1865, citizens of Seattle explored the Pass and raised 2,500 $ to fund construction of the first wagon road from Ranger's Prairie (now North Bend) over the summit. Passage remained difficult, but momentum for improvements and upgrades continued due to the dedication and hard work of local residents. In 1866, King County and the Territorial Assembly both appropriated funds for the project, and by 1867 travel time over the pass had been substantially reduced. Development continued, though the road remained primitive. In 1909, more than 150 cars travelled over the summit. The Snoqualmie Pass Highway was formally dedicated in 1915, but it was not until the winter of 1930-31 that it remained open during the winter for the first time.

9.2.2 Crossing Lake Washington

In the late nineteenth and early centuries, transport of people and goods across Lake Washington continued to be by water, using canoes, boats, barges, and ferries. These vessels moved everything from people and animals, to gravel and lumber, from one side of the lake to the other. Hundreds of vessels navigated this water body every day. One of the

earliest vessels to make regular runs across the lake was the flat-bottomed steam scow, the Squak, built in 1880. The 41' Squak transported people and goods across the lake until it sank in 1890. Its captain, Frank Curtis, and his sons then commissioned construction of the 60' ship the Elfin, which by 1891 operated between Yarrow Bay, Kirkland, and the base of Madison Street in Seattle.

By the beginning of the 20th century, there were a multitude of boats crossing the lake, including a double-ended public ferry, the King County of Kent, operated by the King County Port Commission. In 1915, the steam ferry Lincoln began service between the base of Madison Street and Kirkland, with a capacity of fifty vehicles. Several regular routes were established as Seattle and the surrounding communities grew; these routes originated in Leschi Park and sailed to Juanita, Houghton, and Kirkland. Other routes carried passengers and cargo between Leschi and East Seattle-Mercer Island, Meydenbauer Bay, and other points eastward.

Although Lake Washington was highly valued as a recreational destination for local residents, it continued to be an obstacle for automobile traffic. There were no bridges to facilitate car travel between Seattle and the Eastside, and cars to and from the city had to travel either north or south of the lake, using local branches of Primary State Highway. This was a slow, circuitous route via the Bothell Branch on the north and the Renton Branch on the south. The southern route alone involved 26 miles of stop-and-go traffic, partially through residential neighborhoods. In 1937, the branches joined to continue over Snoqualmie Pass as one highway.

Meanwhile population growth on the Eastside was gradual, but slow. The area was mostly rural; the towns were small. Farmers grew berries and raised poultry. Industry included the Lake Washington shipyards and a small sash and door establishment. Some residents commuted to Seattle for work. Generally Eastside development centered on the Seattle residents who could afford summer and weekend homes on the lake, boasting impressive views and water access.

It was within this setting that development of the Eastside began to take hold with an eye toward a direct highway connection to Seattle. Several potential bridge crossings were suggested as early as 1926. During the early 1930s, King County and Eastside developers such as Miller Freeman mounted a campaign for bridge construction.

9.2.3 Lacey V. Murrow Bridge

The idea for a bridge across Lake Washington began to take hold during the late 1920s. Proponents of a bridge across the lake had been stymied by several challenges: the width of the lake ($1\frac{1}{2}$ miles across at the narrowest section), the expense of building piers for a bridge of this length, and the soft mud at the bottom of the lake. A young engineer with the Seattle Public School Architect's office, Homer Hadley, first had the idea for a floating pontoon bridge in 1920. His idea—a bridge constructed with hollow concrete barges connected end to end, supporting a deck roadway—would solve several of these challenges.

Figure 9.4: Current situation of the Lacey V. Murrow memorial bridge (right) and the new Homer M. Hadley memorial bridge (left). Photo taken from: USA (Lat: 47.586092, Long: -122.290023)

On October 1, 1921, he presented his idea to a meeting of the American Society of Civil Engineers. However, his proposal was initially considered preposterous and was met with strong resistance for years. Furthermore, his affiliation with the Portland Cement Company, whose motto was "to extend and promote the uses of concrete", both bolstered Hadley's confidence in a concrete bridge and caused some to question his motives. It was not until the creation of the Washington State Toll Bridge Authority, and with the support of Lacey V. Murrow, the Director of the State Highway Department, that Hadley's plan took shape.

Figure 9.5: Current situation of the Lacey V. Murrow memorial bridge (right) and the new Homer M. Hadley memorial bridge (left). Photo taken from: USA (Lat: 47.599284, Long: -122.290674)

Construction on the Lake Washington Floating Bridge, later named the Lacey V. Murrow Bridge, started on January 1, 1939, eighteen years after the idea had first been presented to the American Society of Civil Engineers. The bridge opened on July 2, 1940, to great fanfare, and immediately provided a passable connection between the Eastside and Seattle. With its tied arch approach and the Art Deco-styled east portals of the Mount Baker tunnel, the floating bridge was considered both technologically and architecturally distinctive.

Figure 9.6: Only the central parts of both the Lacey V. Murrow and Homer M. Hadley memorial bridges are floating. The parts that connect the bridges with the coast rest on solid columns anchored to the floor. Photo taken from: USA (Lat: 47.600238, Long: -122.285910)

After opening, the Lacey V. Murrow Bridge soon exceeded its expected capacity of 20,000 cars per day. Removing the tolls in 1949 triggered a rapid upsurge of traffic, from 10,370 vehicles per day in 1948 to 17,884 per day in 1950; this resulted in traffic volumes much higher than the expected 15,000 per day, projected for the first full year of operation. As early as 1949, the Department of Highways—the precursor to the Washington State Department of Transportation – undertook "fact-gathering" studies to determine the need and feasibility for a second bridge across Lake Washington. Between 1950 and 1960, the population of the Eastside's suburbs increased by nearly 88 percent. Additionally, population growth within the Seattle metropolitan area at large experienced an 11 percent growth between 1950 and 1955 alone.

Figure 9.7: The I-90 railway goes from Seattle (top of the picture) to Bellevue (bottom of the picture) passing through the Mercer island (island in the middle of the picture). Photo taken from: USA (Lat: 47.568654, Long: -122.162035)

9.2.4 Construction of the floating bridge

During the project of the Lacey V. Murrow floating bridge, its construction were divided into three different parts. The first one was the construction of the transition zones at both sides of the lake (Coasts of Mercer island and Seattle). This first construction steps are represented in figures 9.8 and 9.9. Later, each floating pontoon was constructed in a floating vessel facility and transported by means of tugboats and connected in the middle of the lake (figure9.9) to the previous floating pontoon using metallic bolts. At

the same time, some concrete blocks were positioned in their corresponding places. When the new pontoon was completely attached to the previous one, the anchorage cables were connected to the concrete blocks and the new pontoon and they were tensioned to the desired stress. This procedure was repeated untill the last pontoons was attached in the at each side of the lake.

Figure 9.8: In the fist stage of construction, the transition zones were built on each side of the bridge and the first floating pontoon positioned in the middle of the lake

Figure 9.9: In the second stage, the new pontoon was attached to the previous one and the block of concrete positioned in the lake's bed

Once the bridge was completely constructed, in July 2 1960, it was open to the public as figure 9.10.

Figure 9.10: The floating bridge of Washington was openned in the 2nd July of 1960

9.3 Analysis of the floating bridge

9.3.1 Geometry of the bridge

The bridge can be divided in two transition zones and one floating structure. The two transition zones go from the Seattle's and Mercer's coasts to one hundred meters inside the lake. The transition zones are composed by two different parts. The first part (called rigid part) is directly anchored to the lake's bed by means of reinforced concrete columns that measure between 10 and 25 meters and the second part (called flexible part) rests on the water's free surface by means of several floaters. In addition, the flexible parts are connected (on each side of the bridge) to the floating structure by flexible connecting joints that allow the relative rotations between both parts. This connections are hydraulic mechanisms and, under the assumption of small relative rotation between the floating structure and the transition zone, its reaction can be assumed proportional to that rotation. Figure 9.11 shows an scheme of the overall structure.

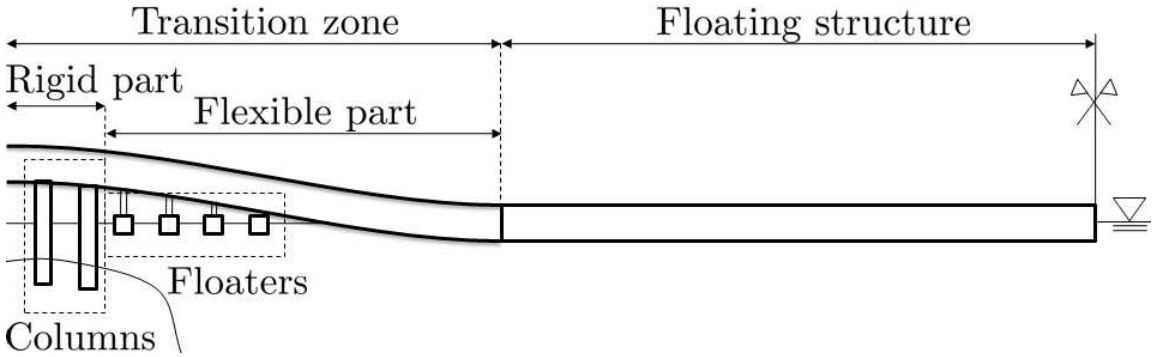

Figure 9.11: Schematic representation of the floating bridge and the transition zones

The floating structure connects both transition zones and is composed by 19 pontoons with approximately 107 meters of length each one. The length of the floating structure is 2020 meters. The connection between two consecutive pontoons is made using clamp bolts and can be considered that there is no relative displacements nor rotations between them (see figure 9.12). It is also anchored to the lake's bed by means of 56 steel cables. The cables go from concrete weights in the lake's bed to each pontoon that compose the floating structure (figure 9.13).

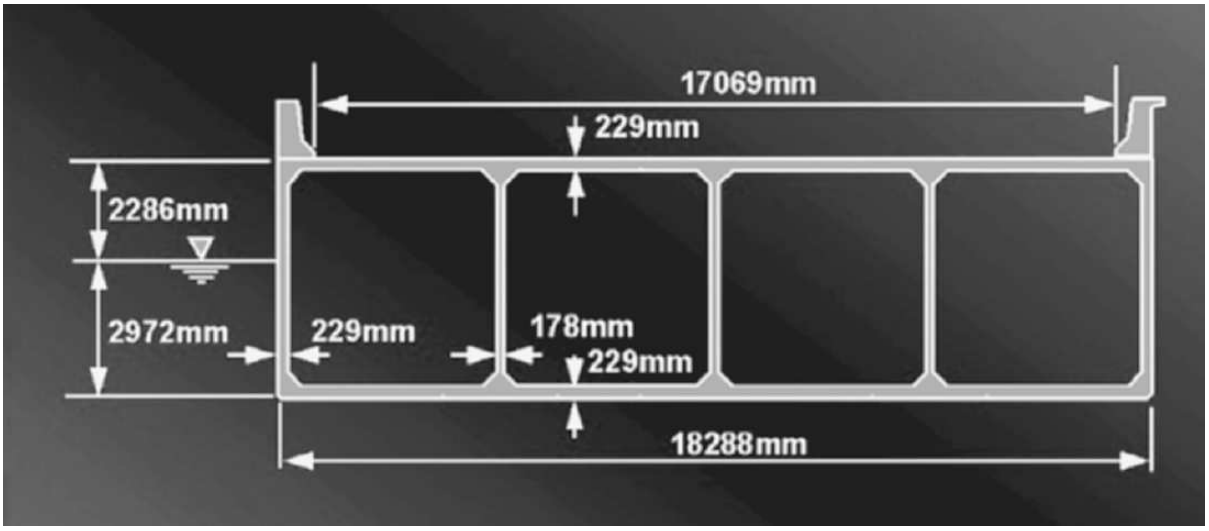

Figure 9.12: Cross-section of the bridge

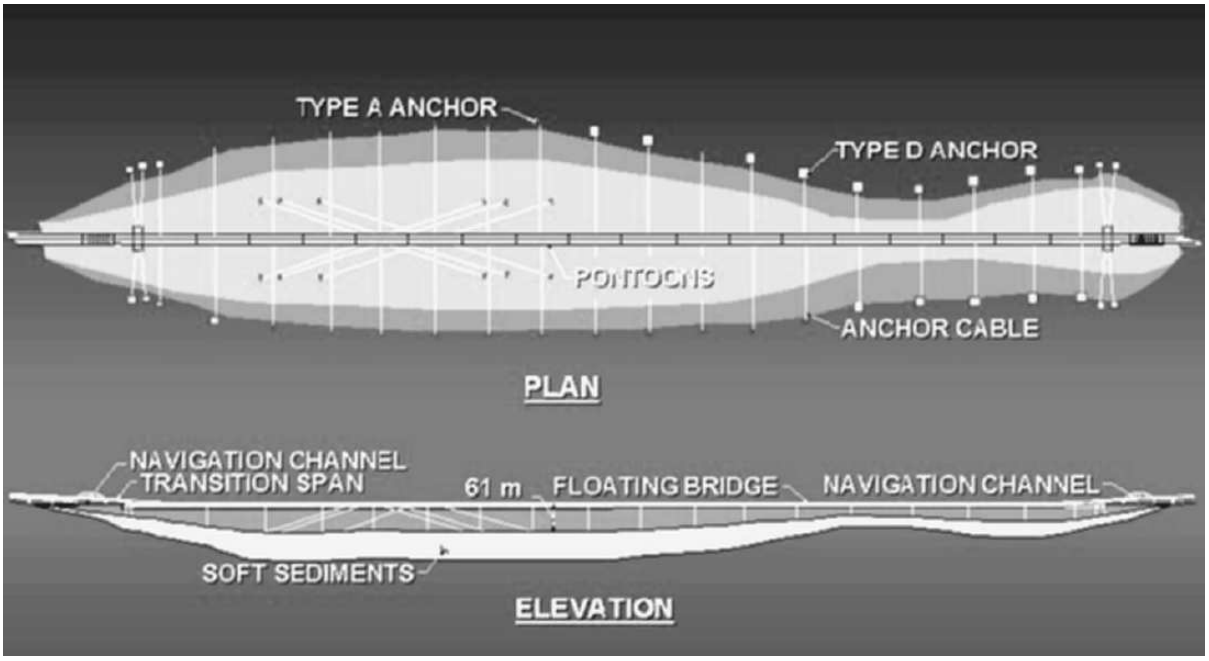

Figure 9.13: The cables provide an horizontal stiffness to the structure attaching the pontoons with the lake's bed

The concrete blocks are partially burried under ground in a soft sediments zone to ensure the stiffness of the anchorage.

9.3.2 Loading conditions

In the following numerical analysis assuming predefined loading cases will be analyzed using the finite element model developed in this thesis. First, the evolutive construction of the floating bridge will be simulated in three steps: positionning and connection of the pontoons (from both coasts), anchorage of the cables to the lake's bed and the pontoons

and the final connection between the two parts of the floating bridge with the last floating pontoon.

In addition, the floating bridge will be subjected to several types of loads following the AASHTO code. First, the behaviour of the bridge completely built will be analysed under its self-weight and the self-weight of the cables. Second, a distributed load in the horizontal plane X-Y along the bridge and orthogonal to the its axis will be applied to model the thrust of the water stream in critical conditions (such as storms). Third, a distributed load will be applied along a certain portion of the axis of the bridge to simulate the pass of a set of trucks.

9.3.3 Analysis of the structure under self-weight

The analysis of the structure completely built under its own self-weight will be shown. The numerical parameters used are reported in table 9.1.

Concept	Symbol	Value
Structural model		
Model for cable structure	M_{cs}	FEM
Model for beam structure	M_{bs}	FEM
Model for flexural behaviour	M_{fb}	Euler-Bernoulli
Model for torsional behaviour	M_{tb}	Saint Venant
Parameters for the analysis		
Tolerance in the equilibrium	Tol_G	1e-3
Tolerance in the displacements	Tol_D	1e-3
Tolerance in the energy	Tol_W	1e-3
Maximum number of iterations correction phase	I_M	500
Method used in the correction phase	-	Arc-length/Restoring
Initial Arc-length value	Δl_I	1.5
Minimum Bergan value for the switching	B_m	0.25
Maximum Bergan value for the switching	B_M	250
Initial increment of load	$\Delta\lambda_I$	1
Final load parameter	λ_F	1
Maximum number of increments	Inc_M	100
Optimum number of iterations correction phase	I_O	500
Update parameters during the incremental procedure	-	No

Table 9.1: Structure under self-weight - Parameters for the nonlinear analysis in an incremental iterative scheme

In the following, the results in terms of efforts are reported in the following figures.

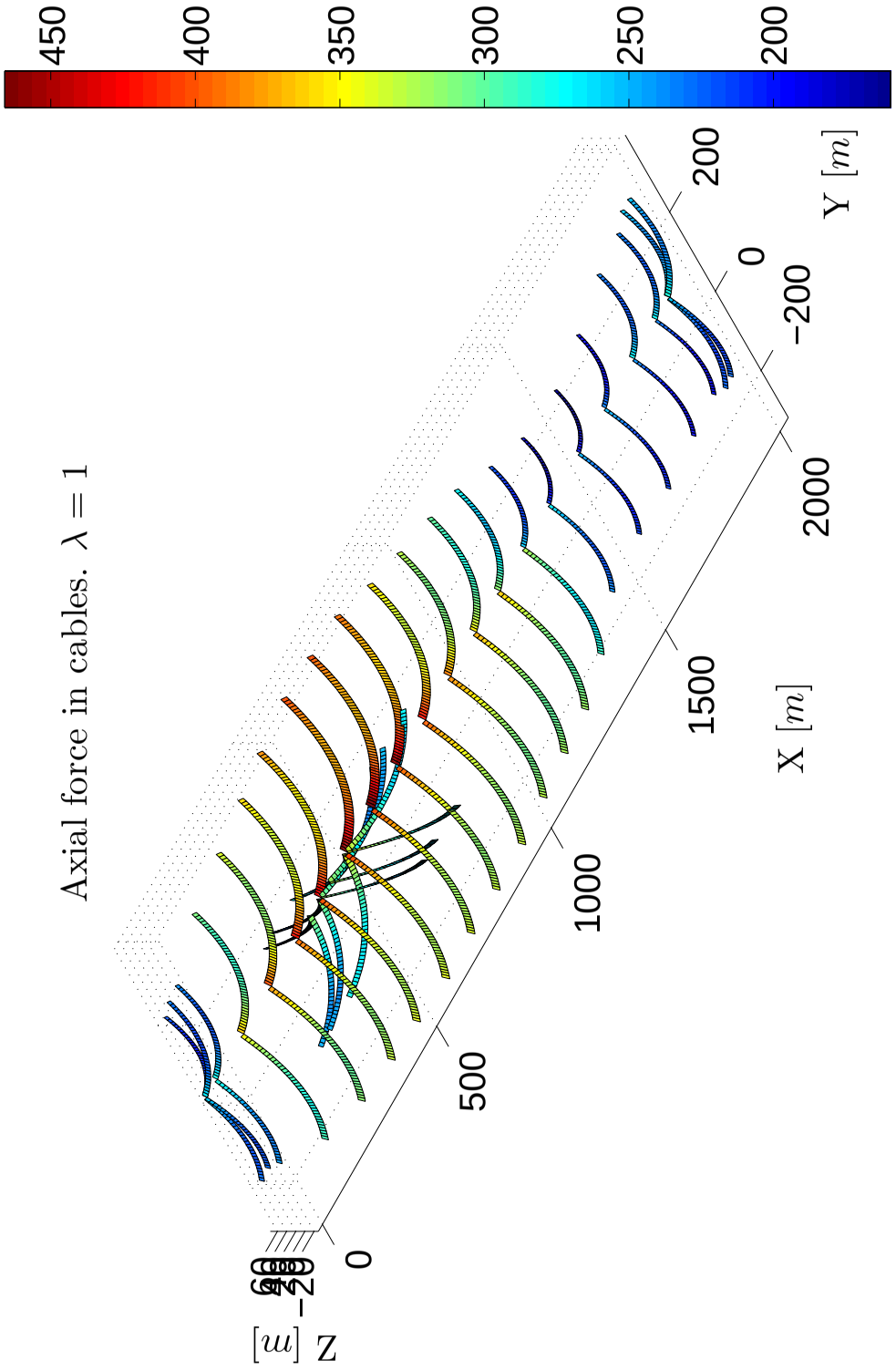

Figure 9.14: Structure under self-weight - Axial force acting on the cables N expressed in $[kN]$

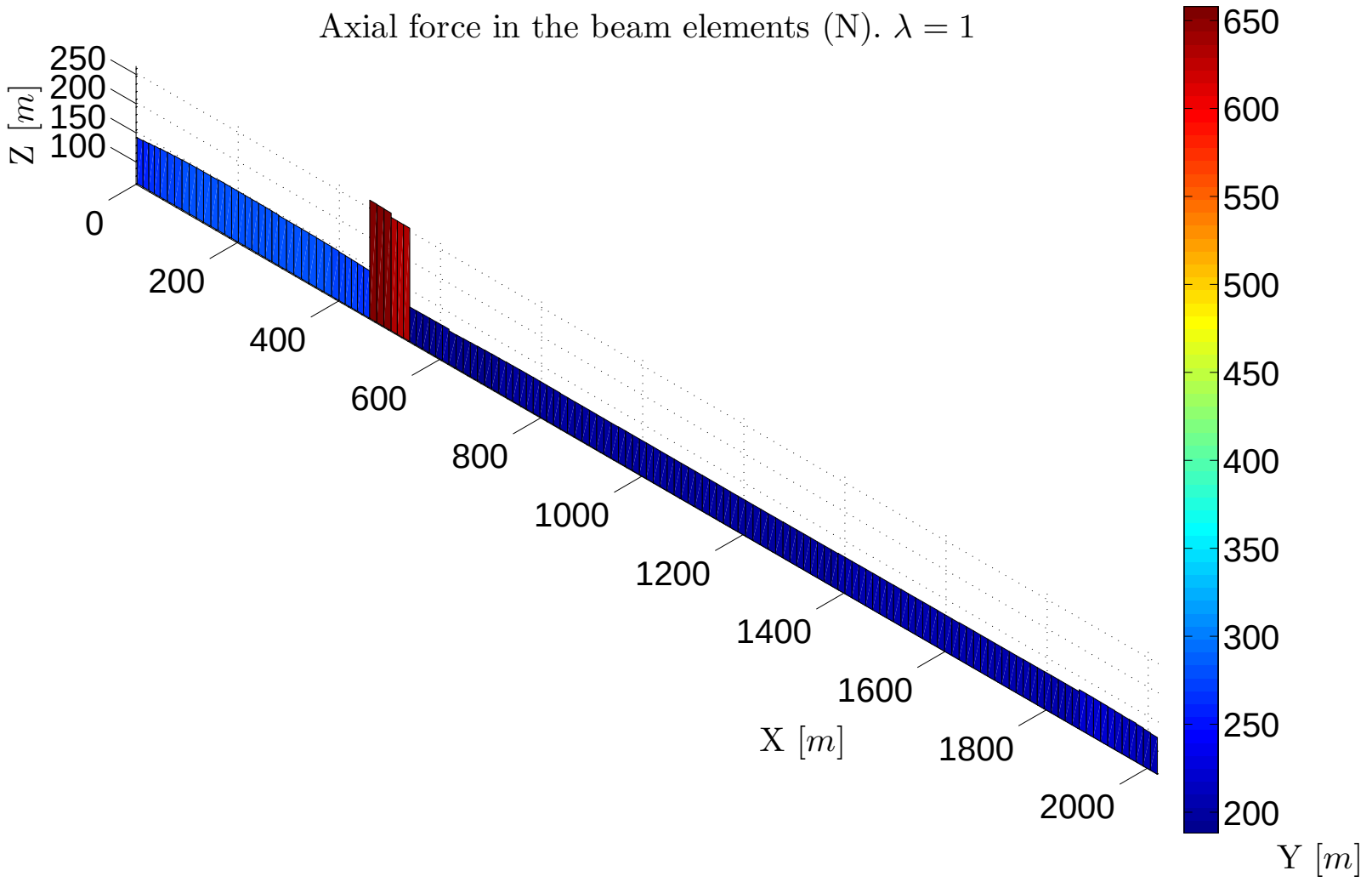

Figure 9.15: Structure under self-weight - Axial force acting on the bridge N expressed in $[kN]$

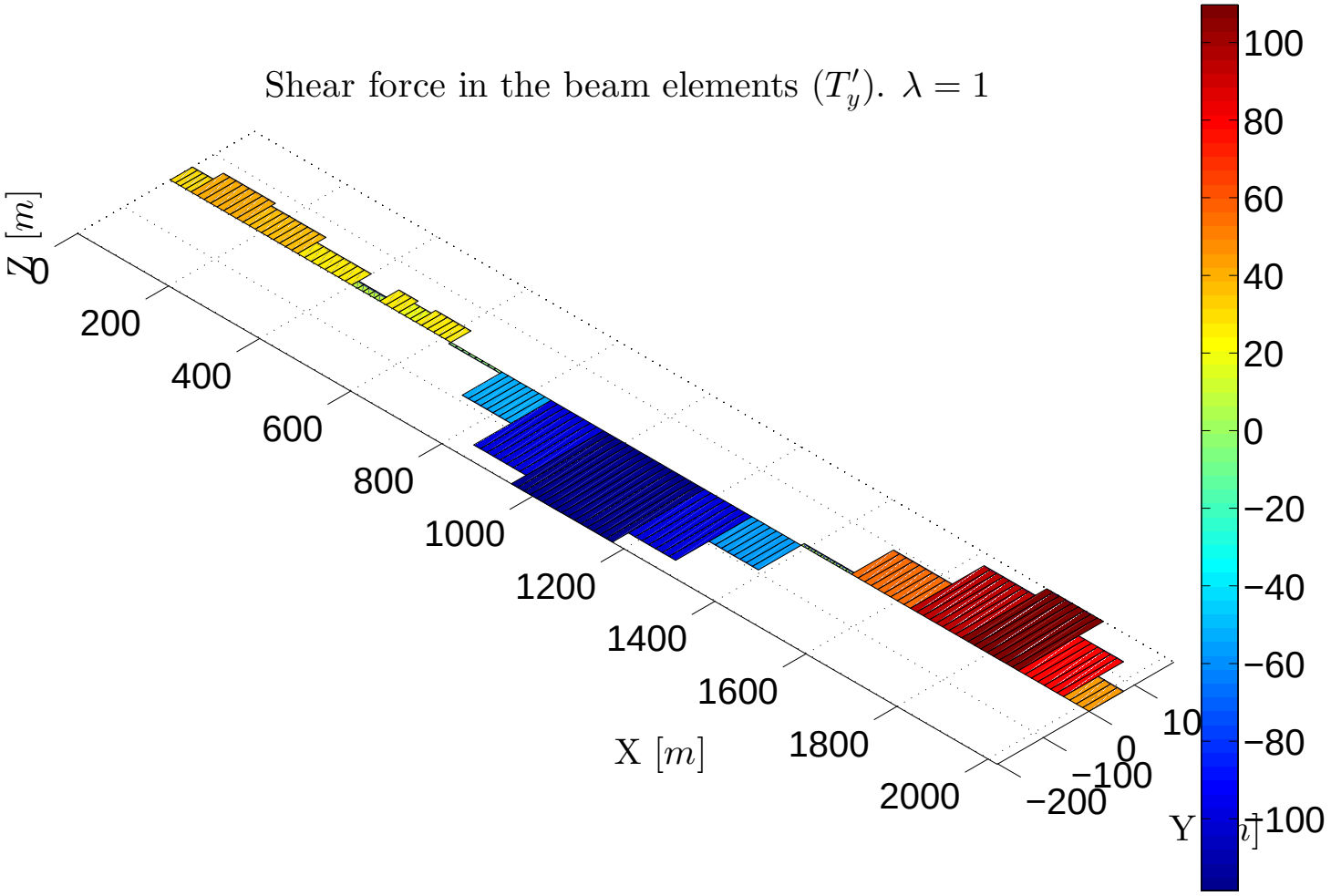

Figure 9.16: Structure under self-weight - Shear force T_y expressed in $[kN]$

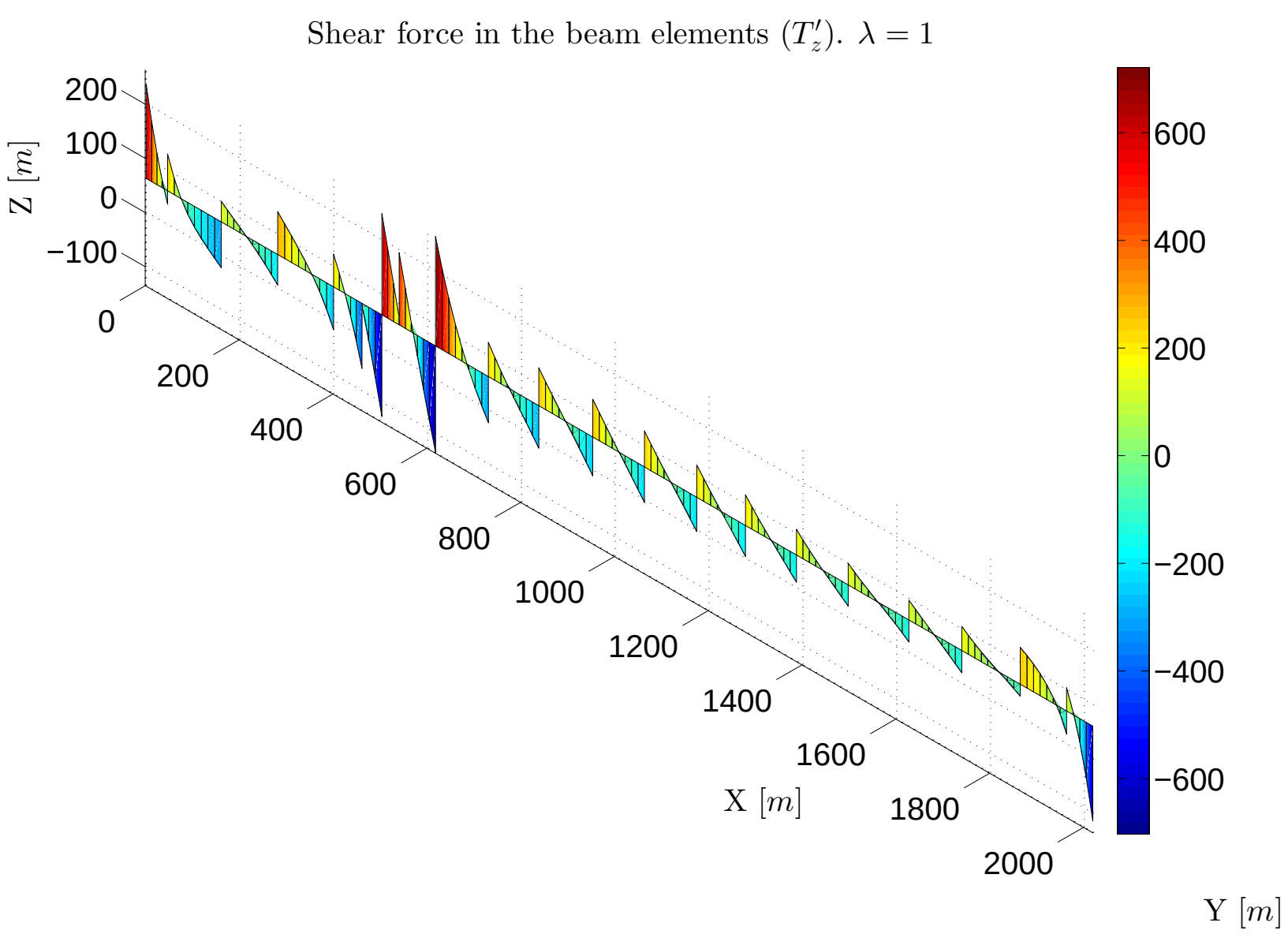

Figure 9.17: Structure under self-weight - Shear force T_z expressed in $[kN]$

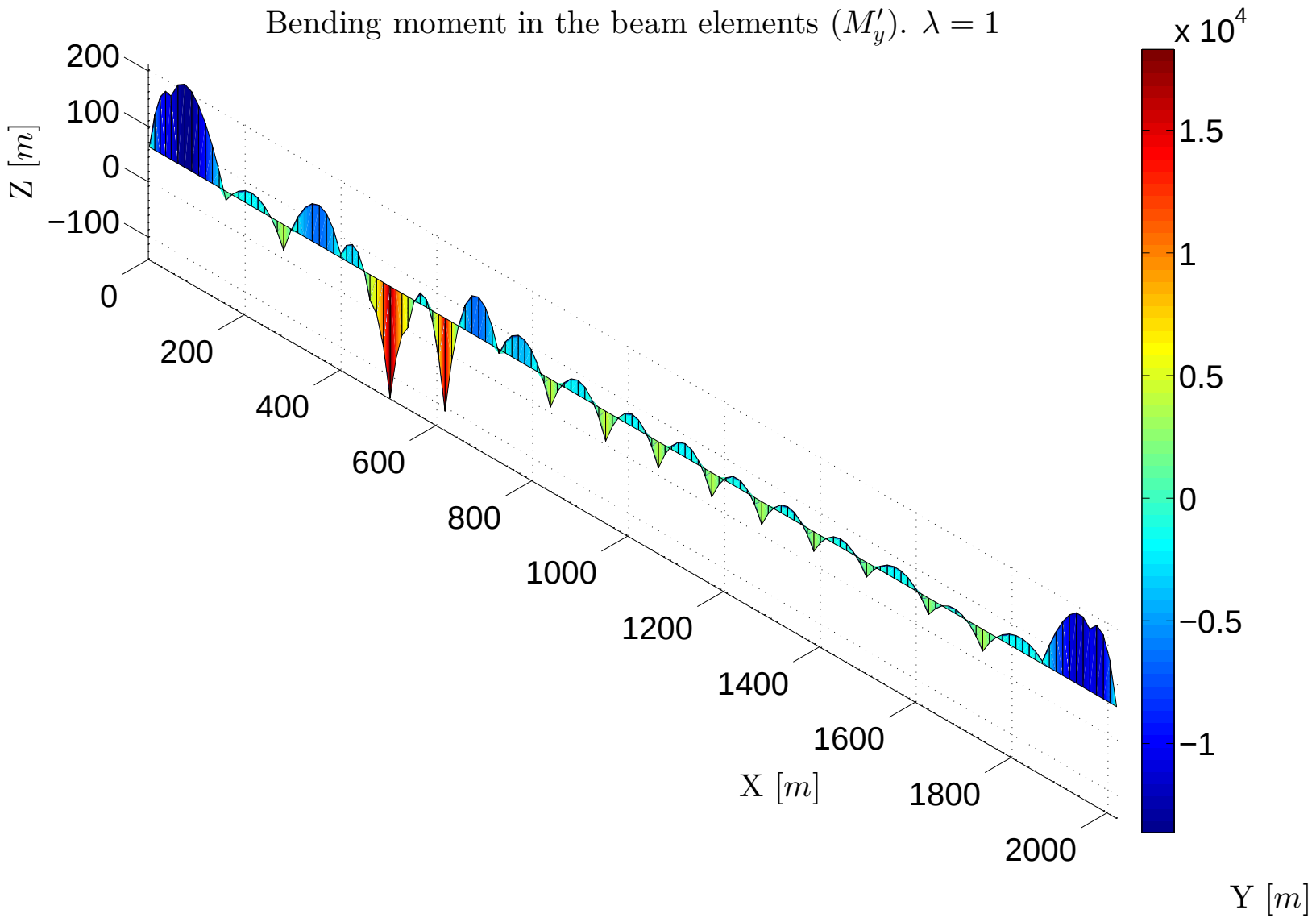

Figure 9.18: Structure under self-weight - Bending moment M_y expressed in $[kN \cdot m]$

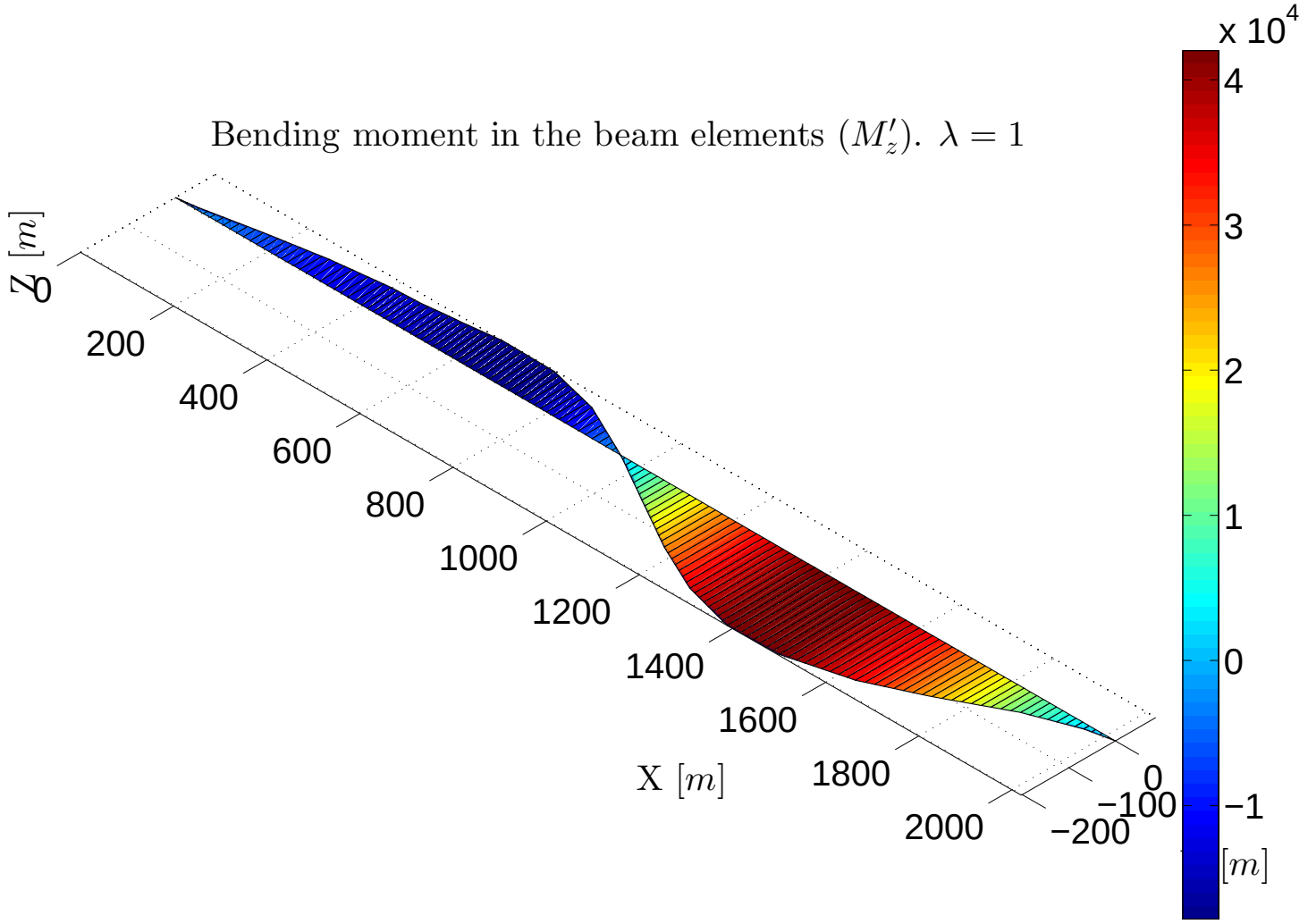

Figure 9.19: Structure under self-weight - Bending moment M_z expressed in $[kN \cdot m]$

The floating bridges has been analyzed under its own self weight and some interesting results has been obtained. Now, some comments about the results will be made.

As the reader can see in figure 9.14 the axial force in the cables is not constant. This result is obtained since the force inside the cable depends (in part) on the length of the cable and looking at the figure, the cables with larger length (cables anchored to the bridge at x coordinate between 450 to 1000 meters) are subjected to larger axial forces.

Figure 9.15 shows us the distribution in the bridge of the axial force. The most important result is the significant change of the axial force occurs approximately between 450 and 500 meters. This is due to the location of the cables, since most of them are not perfectly orthogonal to the bridge and therefore part of their horizontal reaction becomes an axial force within the bridge. It can be seen that the discontinuity of the axial force of the bridge occours exactly where these cables are connected.

Considering now figures 9.16 and 9.19, where the shear force T_y' and the bending moment M_z' are depicted. The results are expected since each discontinuity of the shear force appears at the coordinate where a cable is attached. This can be explained from equilibrium considerations since part of the shear force is absorbed by the cable connected to the bridge. In addition, the variation between two cables of the bending moment is linear since there are no distributed forces applied in the y direction. As a consequence, the variation of the shear force between two consecutive cables is constant.

As a final remark looking at these results, it is expected that the shear force and bending moment in the horizontal plane were almost null in the self weight condition. However, this is not true in general due to the influence of the position, length and prestressing of the cables that anchore the bridge on the lakebed. Indeed, looking at the figures the bridge is under bending in the horizontal plane since the cables are not symmetrically position and their lengths are not exactly the same.

Let us now focus our attention to figures 9.17 and 9.18, where the shear force T_z' and bending moment M_y' are depicted. The results also match with the prediction. Indeed, the discontinuity of the shear force is also located exactly at each point where a cable is connected to the bridge. On the other hand, the maximum values of the bending moment are also located in the same position. In addition, the variation of the shear force between two consecutive cable is almost linear but not in the zones where the effects of the fluid are most important (the ends of the bridge). The same happens with the bending moment. Assuming the model of beam on elastic foundation to analyse the vertical behaviour of the bridge, the variation between two consecutive cables of the bending moment behaves as a negative exponential hyperbolic function (homogeneous solution of the beam on elastic foundation differential equation).

9.3.4 Analysis of the structure under moving trucks

Here the analysis of the structure completely built under its own self-weight and a set of moving trucks will be analysed. Figure 9.20 shows the position of the trucks and the equivalent distributed load used to model their effects.

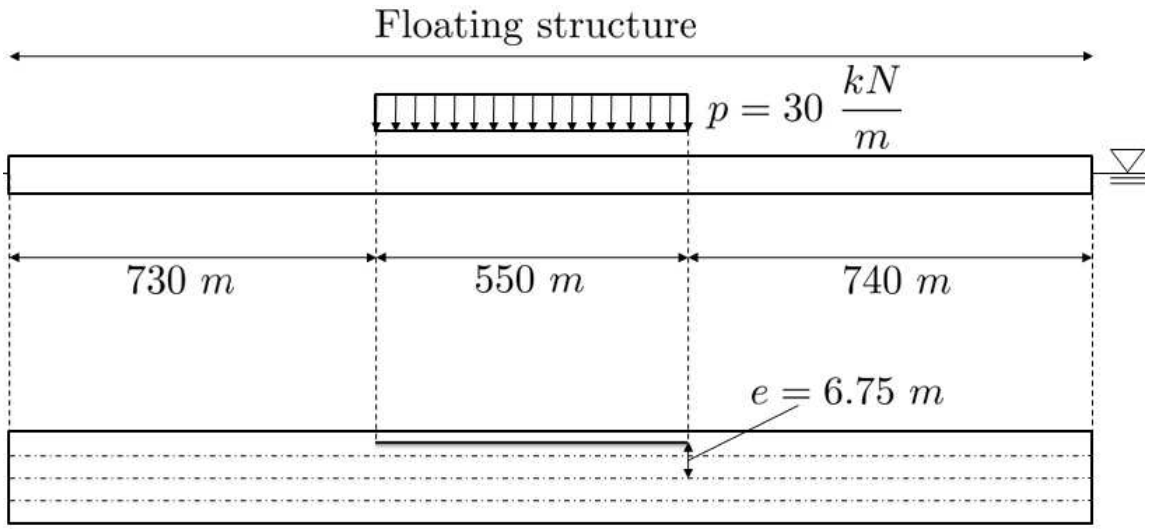

Figure 9.20: The bridge is submitted to a distributed load equal to 30 $\frac{kN}{m}$ with an eccentricity of 6.75 m to simulate 55 trucks, which each one of them weights 30 tones, positioned along 550 m

The numerical parameters used to analysis this case are reported in table 9.1.

Concept	Symbol	Value
Structural model		
Model for cable structure	M_{cs}	FEM
Model for beam structure	M_{bs}	FEM
Model for flexural behaviour	M_{fb}	Euler-Bernoulli
Model for torsional behaviour	M_{tb}	Saint Venant
Parameters for the analysis		
Tolerance in the equilibrium	Tol_G	1e-3
Tolerance in the displacements	Tol_D	1e-3
Tolerance in the energy	Tol_W	1e-3
Maximum number of iterations correction phase	I_M	500
Method used in the correction phase	-	Arc-length/Restoring
Initial Arc-length value	Δl_I	1.5
Minimum Bergan value for the switching	B_m	0.25
Maximum Bergan value for the switching	B_M	250
Initial increment of load	$\Delta\lambda_I$	0.05
Final load parameter	λ_F	1
Maximum number of increments	Inc_M	100
Optimum number of iterations correction phase	I_O	500
Update parameters during the incremental procedure	-	No

Table 9.2: Structure under self weight and a set of moving trucks - Parameters for the nonlinear analysis in an incremental iterative scheme

In the following, the results in terms of efforts are reported in the following figures.

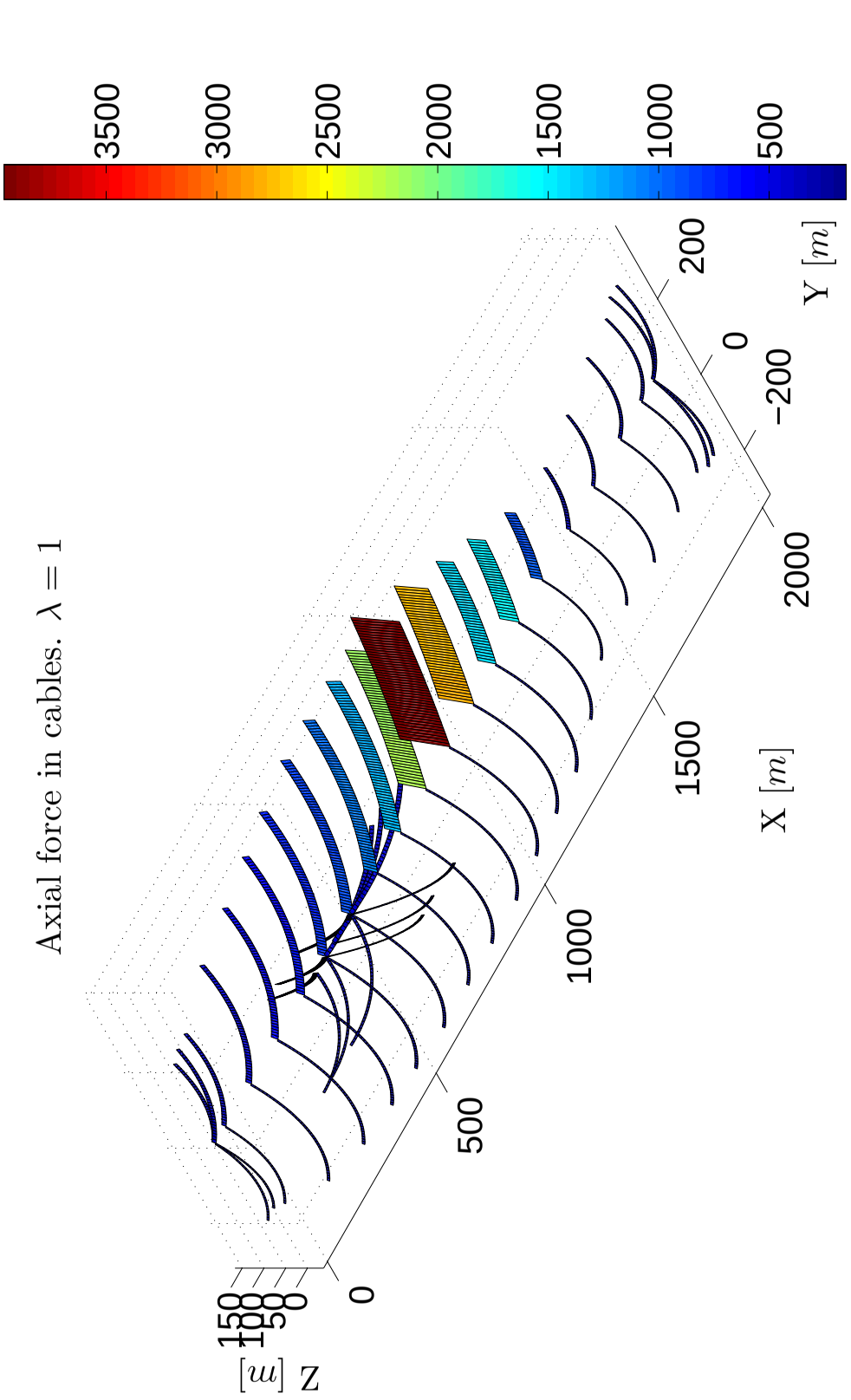

Figure 9.21: Structure under self-weight and a set of moving trucks - Axial force acting on the cables N expressed in $[kN]$

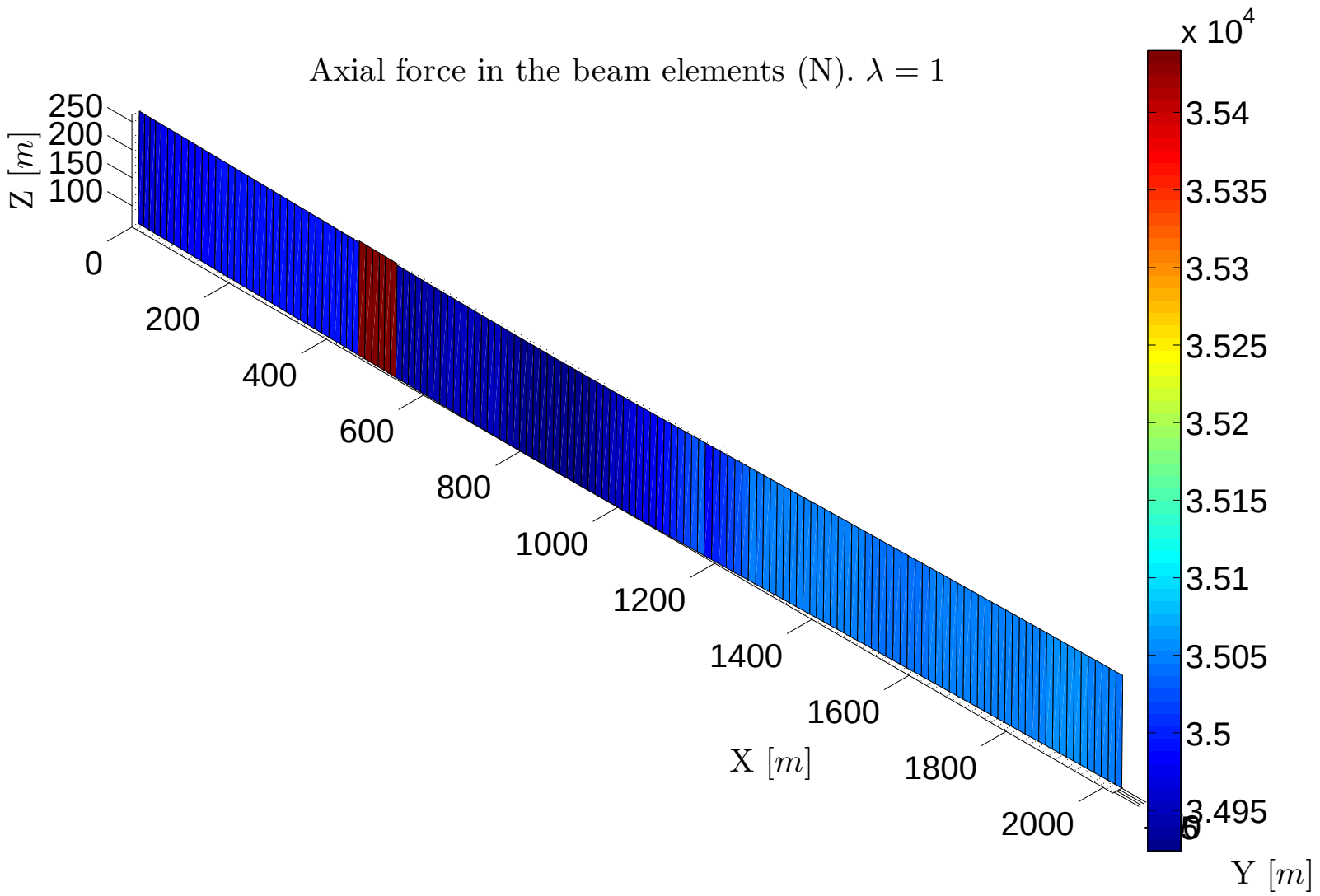

Figure 9.22: Structure under self-weight and a set of moving trucks - Axial force acting on the bridge N expressed in $[kN]$

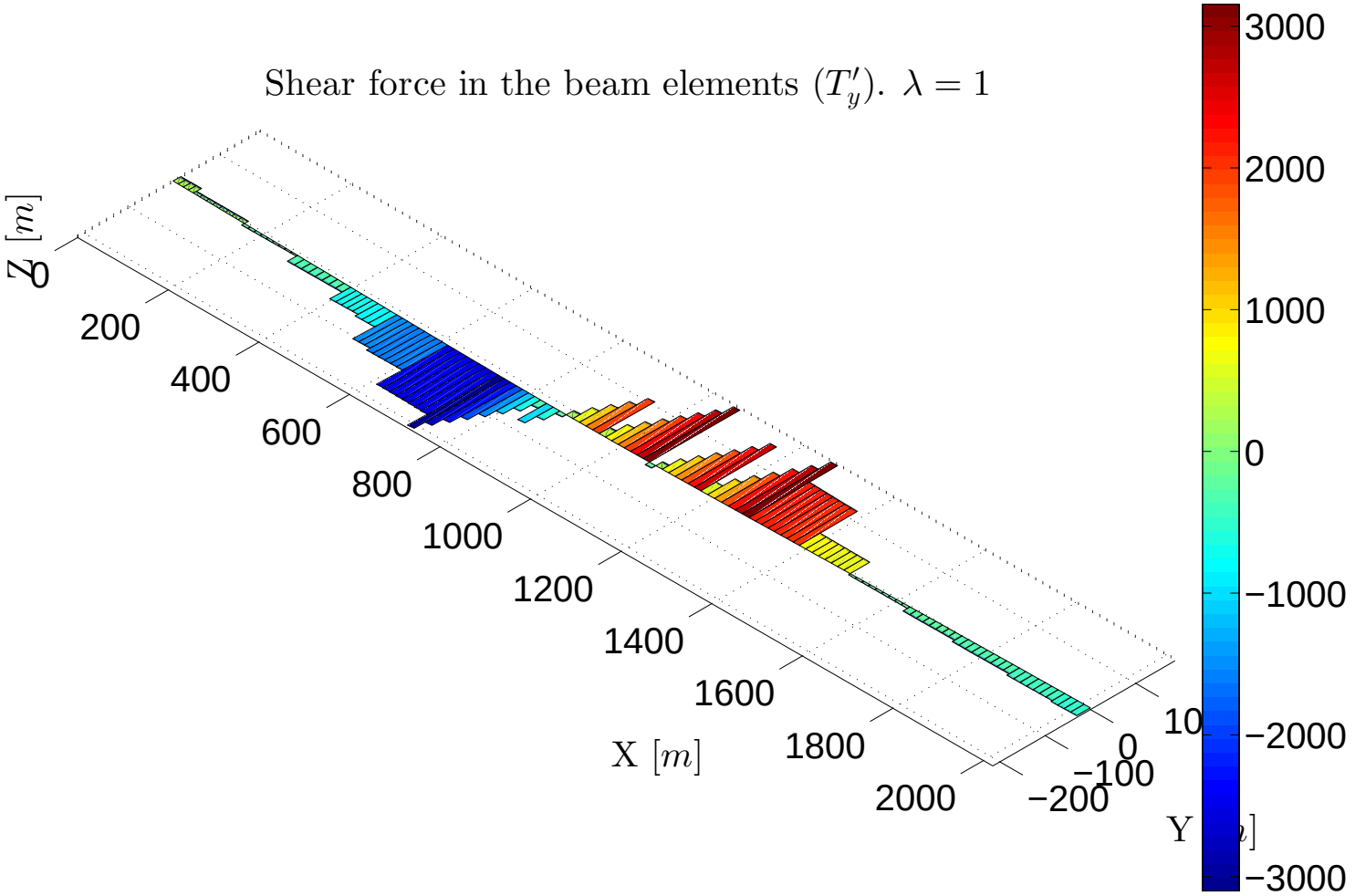

Figure 9.23: Structure under self-weight and a set of moving trucks - Shear force T_y expressed in $[kN]$

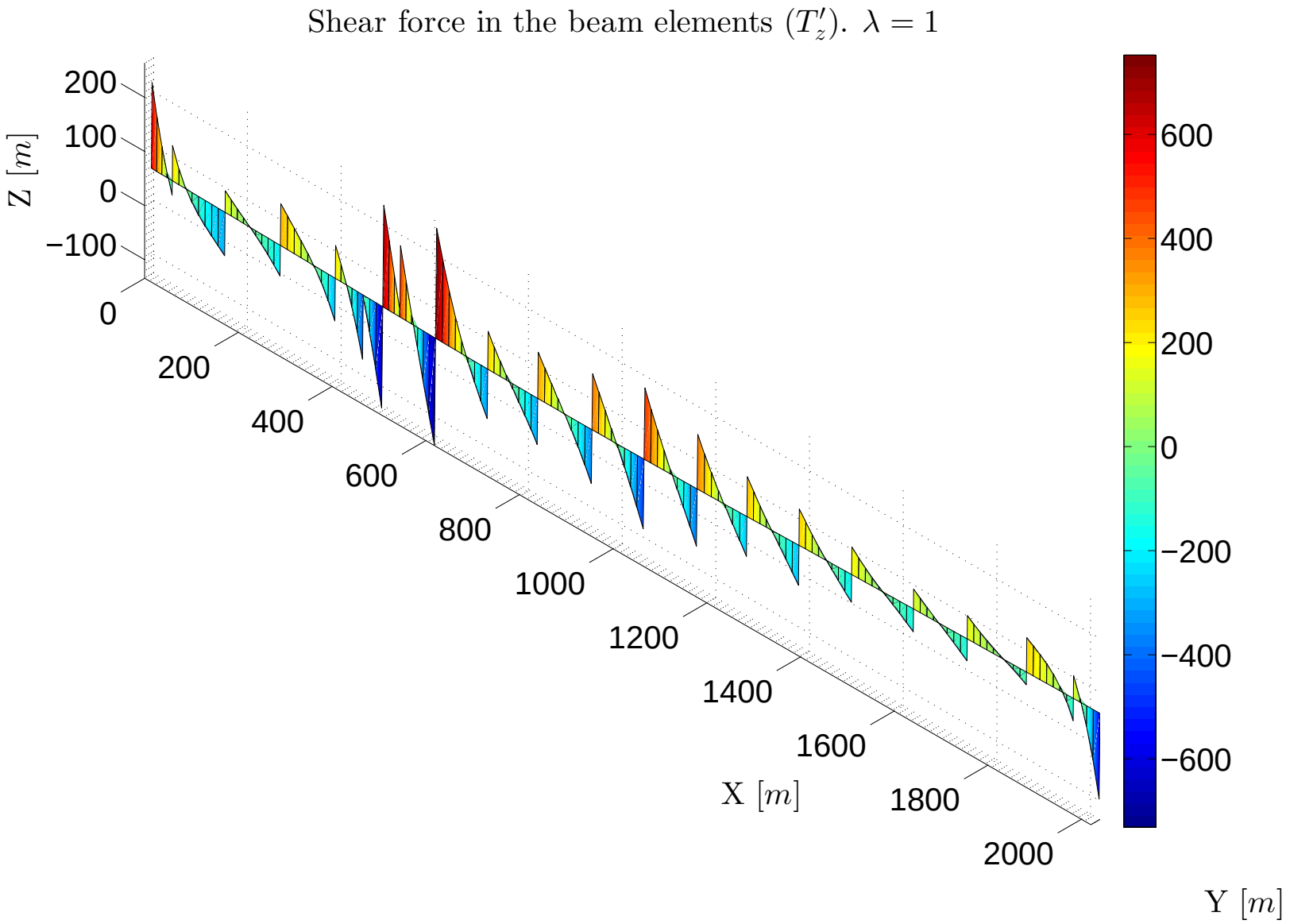

Figure 9.24: Structure under self-weight and a set of moving trucks - Shear force T_z expressed in $[kN]$

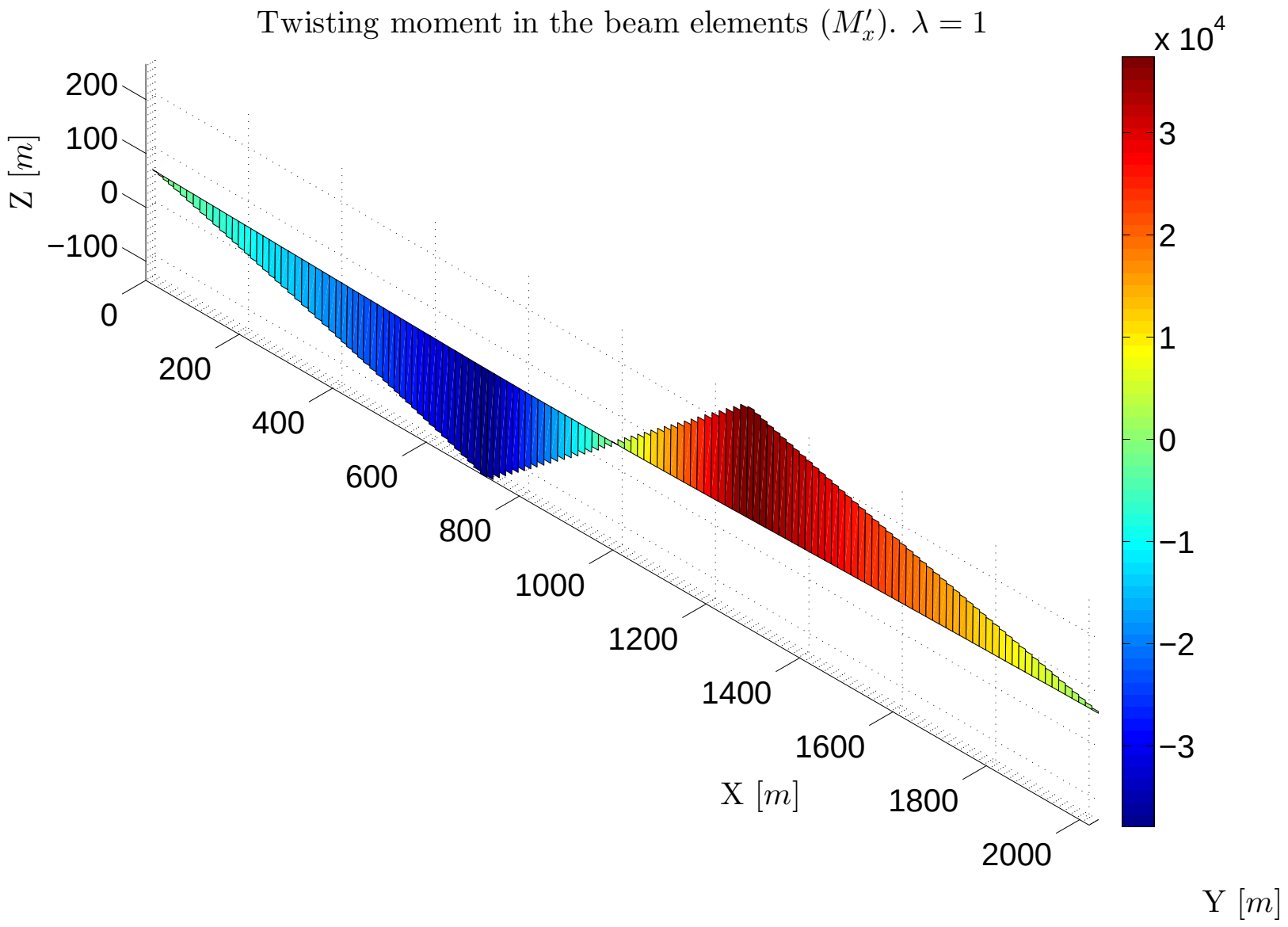

Figure 9.25: Structure under self-weight and a set of moving trucks - Bending moment M_x expressed in $[kN \cdot m]$

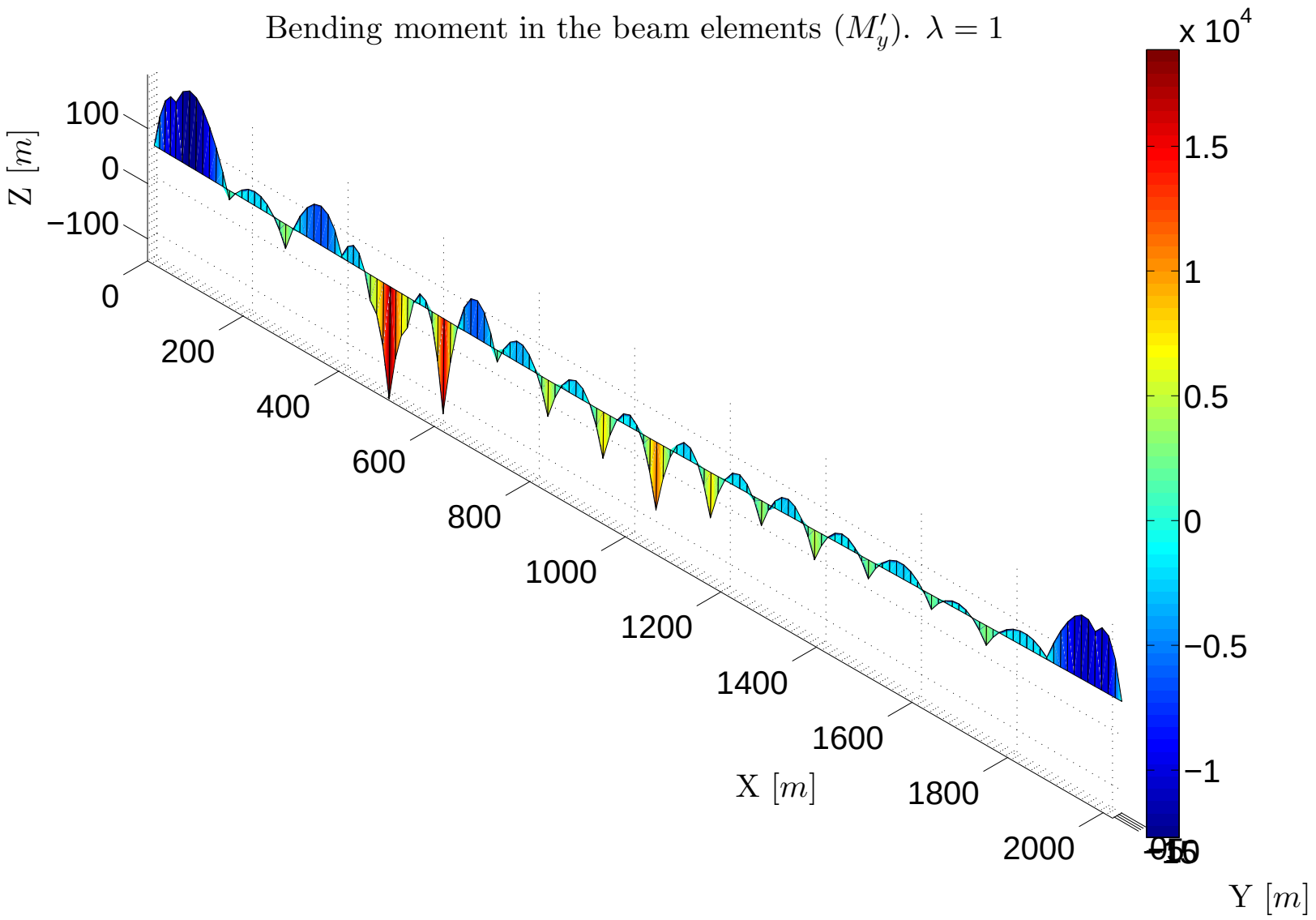

Figure 9.26: Structure under self-weight and a set of moving trucks - Bending moment M_y expressed in $[kN \cdot m]$

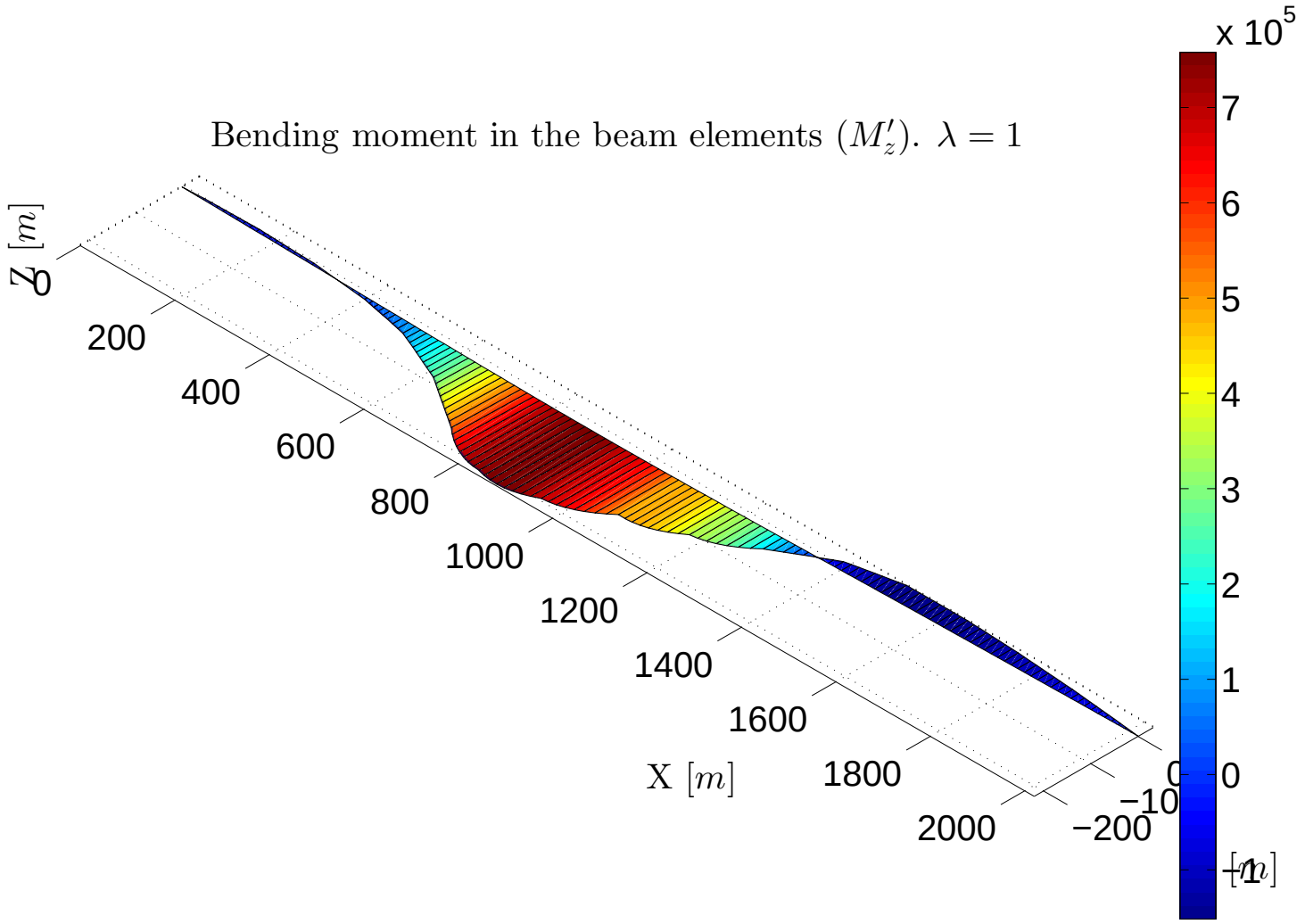

Figure 9.27: Structure under self-weight and a set of moving trucks - Bending moment M_z expressed in $[kN \cdot m]$

The results obtained need some comments.

Considering figure 9.21, where the axial force acting on the cables is plotted, oit is possible to see that the cables placed approximately at $x = 1100\ m$ are subjected to larger axial force. One possible explanation comes the coupling between torsional and bending behaviour, since the bridge moves laterally in the zone where the trucks were positioned. As a consequence, the cables placed in this zone will be subjected to an elongation (cables at positive y coordinates) and the cables on the other side will be subjected to a shortening.

In figure 9.22, the distribution of axial force acting on the beam structure is depicted. It can be seen that, in this case, all the bridge is almost subjected to a constant axial force. Unlike figure 9.15, where the axial force was depicted considering only the self weight, figure 9.22 shows a constant variation of the axial force. This can be considered as a consequence of the final configuration of the bridge. Indeed, in this last analysis the bridge has moved laterally producing an elongation along the span that, in turn, produces an axial force much larger than the one obtained in figure 9.15 ($3.5 \cdot 10^4\ kN$ in contrast with $6 \cdot 10^2\ kN$).

Looking at figures 9.24 and 9.26, the results are very similar compared with the ones obtained in figures 9.17 and 9.18. Indeed, due to the loading condition, the horizontal component of the displacements change basically along the bridge. The behaviour in the vertical direction of the bridge remains almost unchanged. The only remarkable difference occurs near the coordinate $x = 1000\ m$ in figure 9.24, where the shear force increases due to the position of the trucks.

Let us now focus on figure 9.25, where the twisting moment is depicted. It can be seen a linear variation along the bridge. The zone between the two maximum values of the twisting moment (730 and 1280 meters approximately) coincides with the position of the trucks.

Considering now figures 9.23 and 9.27, where the shear force and the bending moment in the horizontal plane are depicted respectively. With respect to the previous situation the displacements in the lateral direction of it's axis due to the coupling between the torsional and bending behaviour has increased the curvature in the y direction and consequently increased the bending moment. In addition, the shear force remains linear between each cable connected to the bridge.

9.3.5 Analysis of the structure under storm conditions

In the following, the effects of a wind storm are qualitatively reproduced by means of a horizontal load applied in one side of the bridge equal to the self-weight of the bridge to simulate the thrust created by the stream of water. The force per unit length is equal to $p = \gamma_m A_s = 223.46\ \dfrac{kN}{m}$. Figure 9.28 shows the situation adopted.

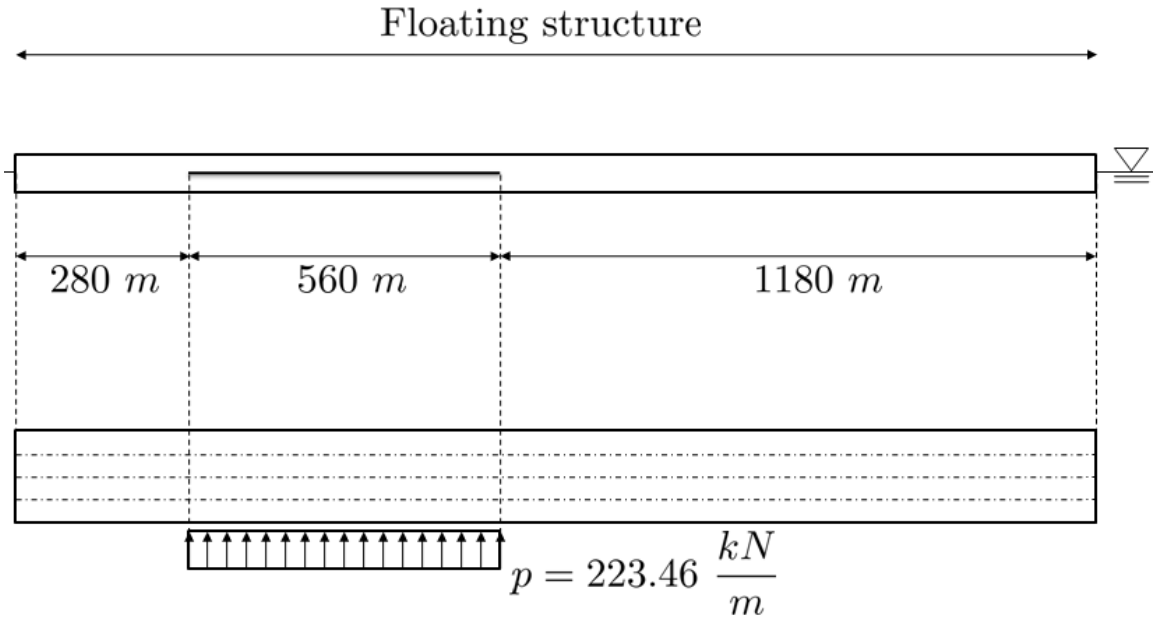

Figure 9.28: The bridge is submitted to a distributed load equal to $p = \gamma_c A_s = 223.46\ \frac{kN}{m}$ to simulate the thrust created by the stream of water

The numerical parameters used to analysis this case are reported in table 9.1.

Concept	Symbol	Value
Structural model		
Model for cable structure	M_{cs}	FEM
Model for beam structure	M_{bs}	FEM
Model for flexural behaviour	M_{fb}	Euler-Bernoulli
Model for torsional behaviour	M_{tb}	Saint Venant
Parameters for the analysis		
Tolerance in the equilibrium	Tol_G	1e-3
Tolerance in the displacements	Tol_D	1e-3
Tolerance in the energy	Tol_W	1e-3
Maximum number of iterations correction phase	I_M	500
Method used in the correction phase	-	Arc-length/Restoring
Initial Arc-length value	Δl_I	1.5
Minimum Bergan value for the switching	B_m	0.25
Maximum Bergan value for the switching	B_M	250
Initial increment of load	$\Delta\lambda_I$	0.05
Final load parameter	λ_F	1
Maximum number of increments	Inc_M	100
Optimum number of iterations correction phase	I_O	500
Update parameters during the incremental procedure	-	No

Table 9.3: Structure under self weight and storm conditions - Parameters for the nonlinear analysis in an incremental iterative scheme

In the following, the results in terms of efforts are reported in the following figures.

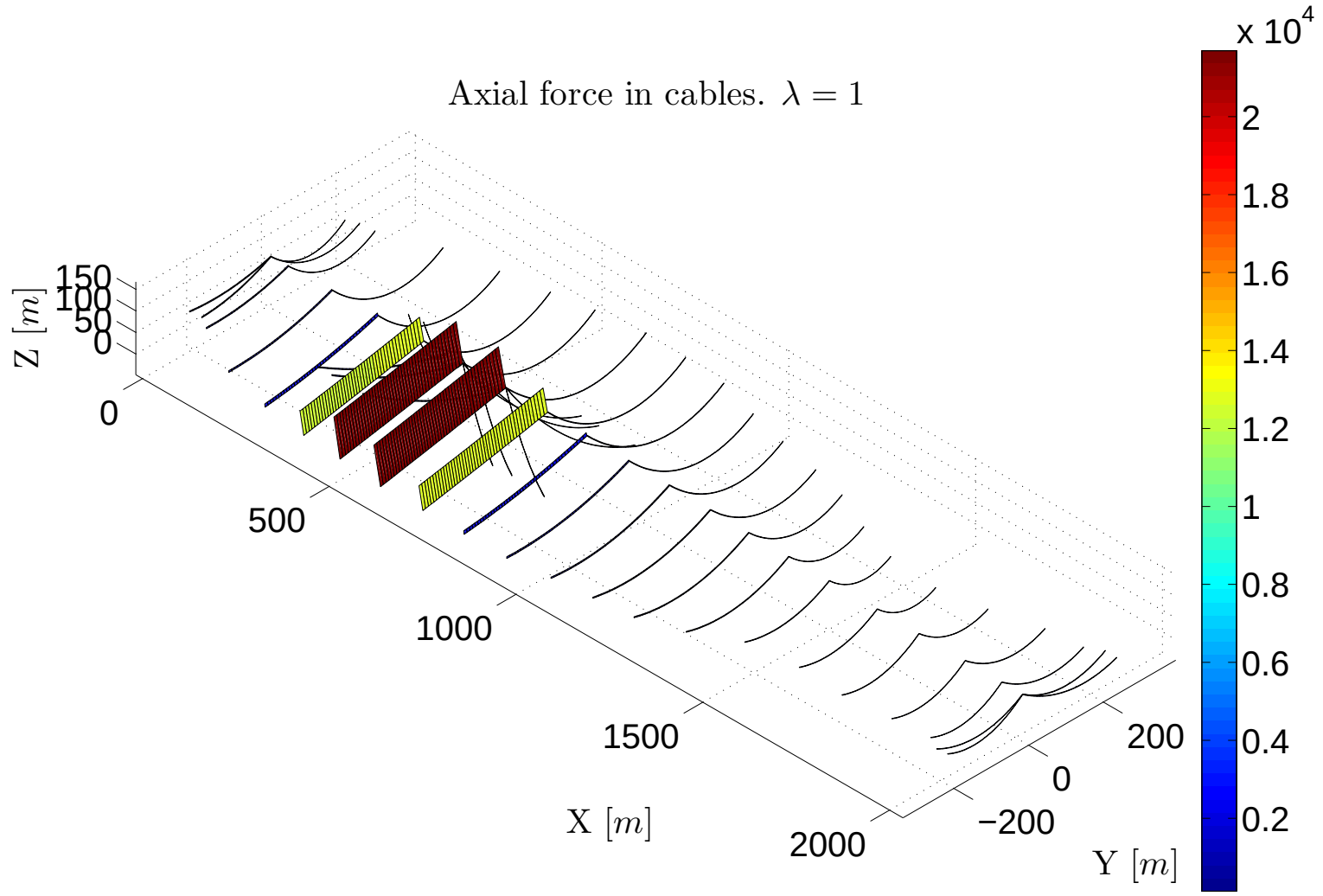

Figure 9.29: Structure under self weight and storm conditions - Axial force acting on the cables N expressed in $[kN]$

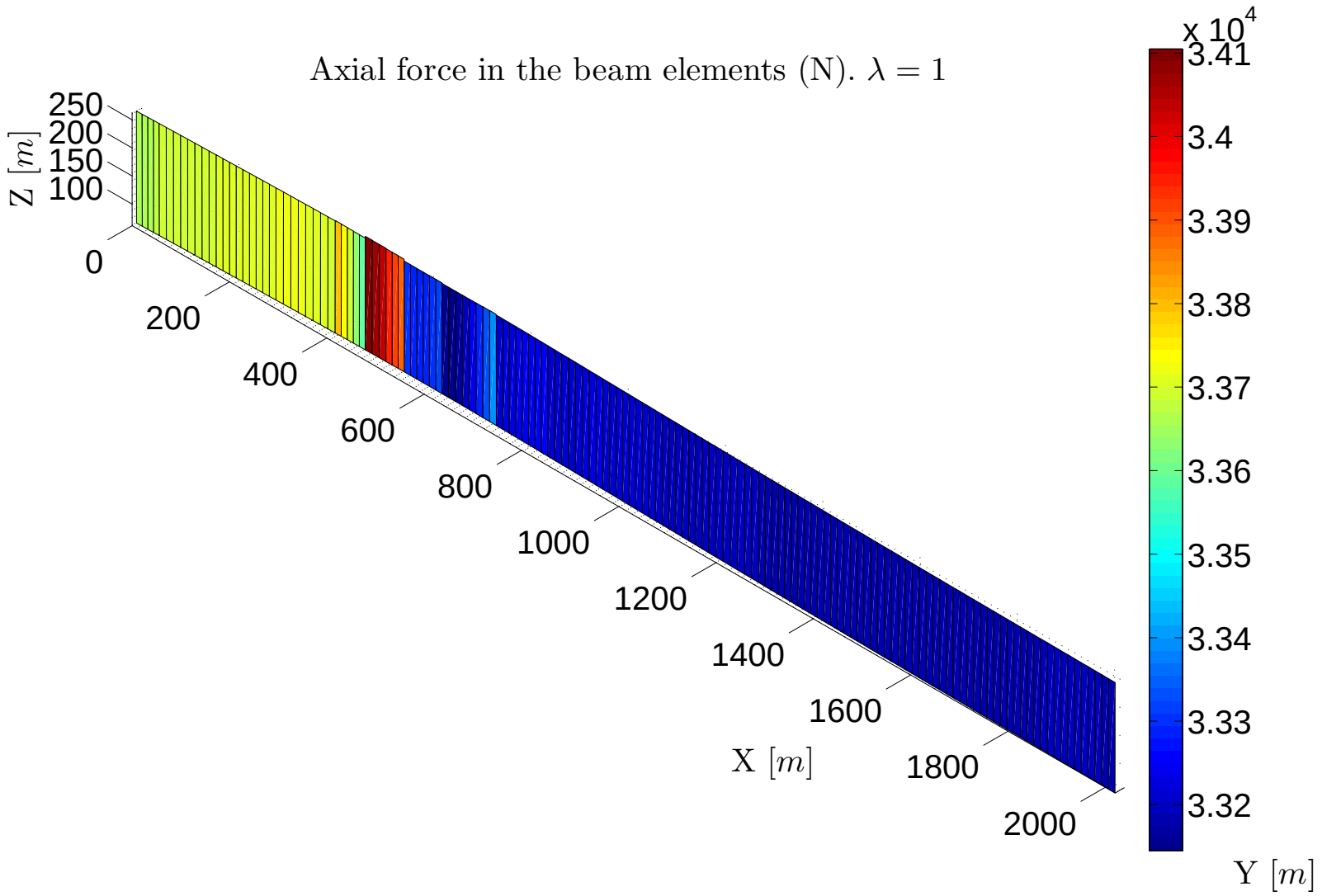

Figure 9.30: Structure under self weight and storm conditions - Axial force acting on the bridge N expressed in $[kN]$

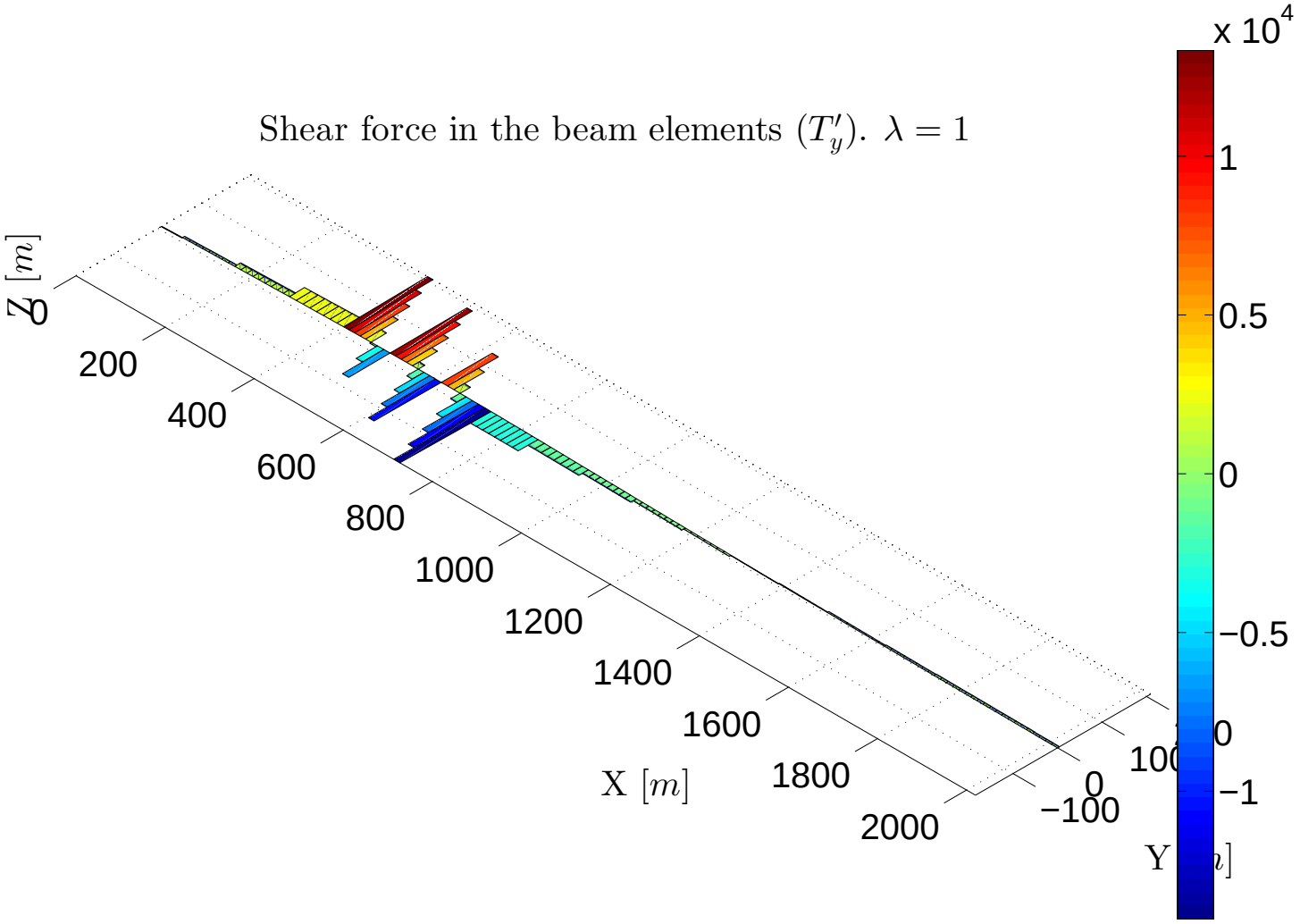

Figure 9.31: Structure under self weight and storm conditions - Shear force T_y expressed in $[kN]$

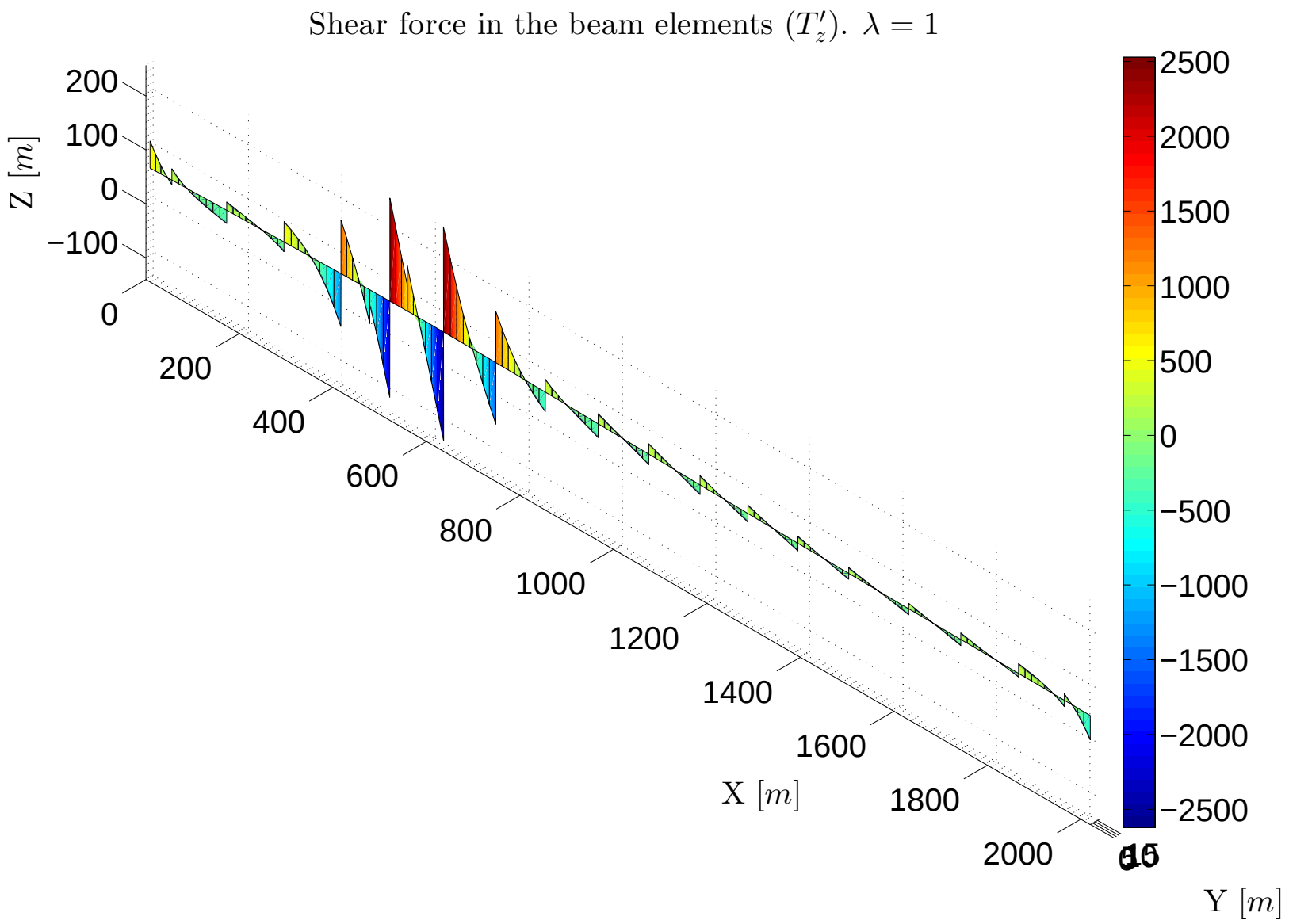

Figure 9.32: Structure under self weight and storm conditions - Shear force T_z expressed in $[kN]$

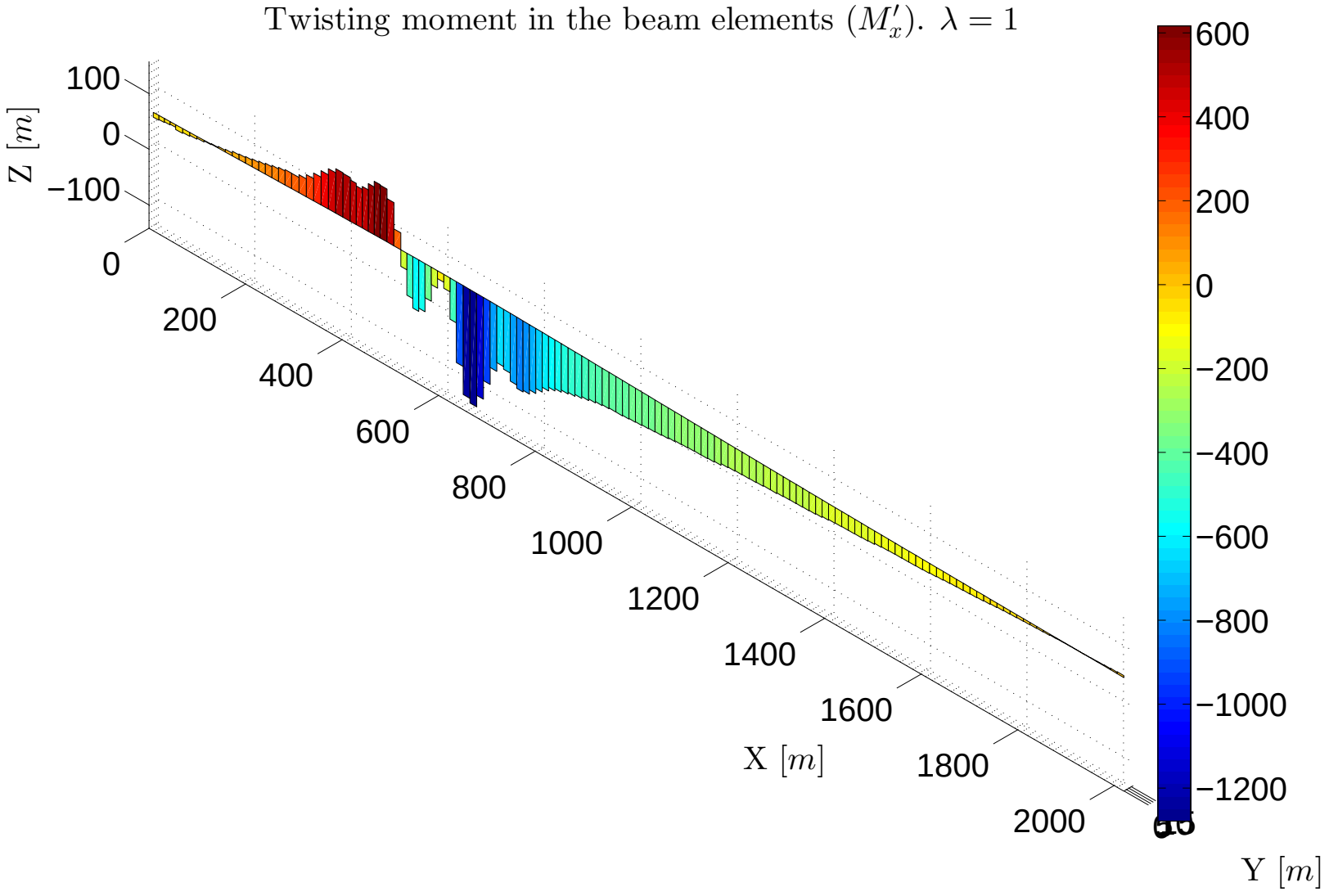

Figure 9.33: Structure under self weight and storm conditions - Bending moment M_x expressed in $[kN \cdot m]$

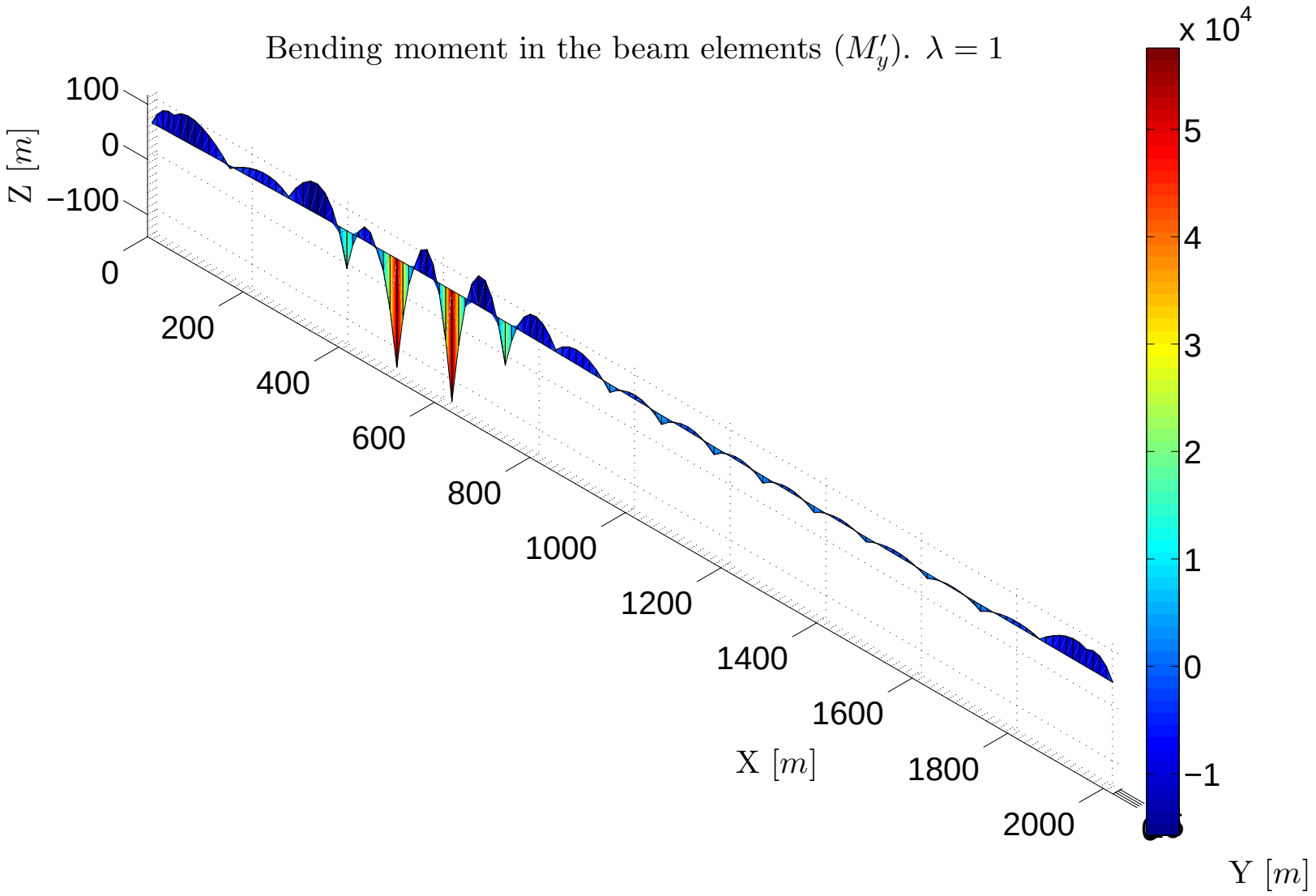

Figure 9.34: Structure under self weight and storm conditions - Bending moment M_y expressed in $[kN \cdot m]$

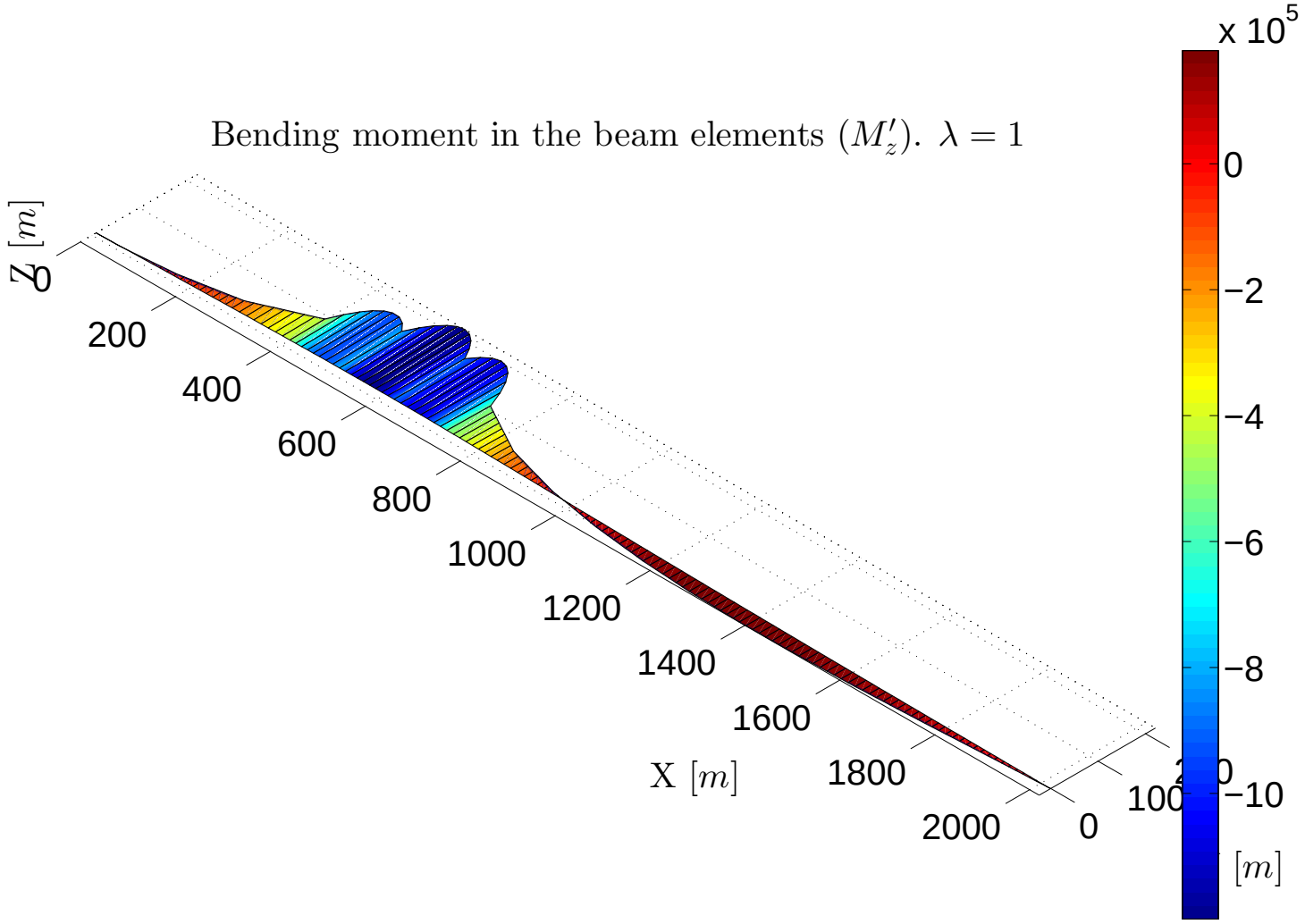

Figure 9.35: Structure under self weight and storm conditions - Bending moment M_z expressed in $[kN \cdot m]$

The analysis of the floating bridge subjected to an horizontal distributed load along its deck has been carried out. Some comments will be breifly summarized.

Let us first focus on figure 9.29, where the axial force acting on the cables is depicted. The results obtained are expected. Indeed, the lateral displacement of the bridge in the zone where the load is applied is directly counteract by the reactions of the cables in that zone (approximately x=500 meters).

Consider now figures 9.31 and 9.35, where the shear force and bending moment in the horizontal plane are depicted. The variation of the shear force is placed in the zone where the horizontal distributed force are applied and maintains the linear variation between two consecutive anchored cables. In addition, the bending moment increases in the zone where the horizontal distributed load are applied and the variation between two consecutive connected cables is parabolic.

Finally, figures 9.32 and 9.34 provide the distribution of shear force and bending moment in the vertical plane. In this case, the difference with respect to the first case considered is not relevant since all the external load is applied in the horizontal plane. In addition, the external loads acting in the vertical plane remain the same as the case where only the self weight has been considered.

9.4 Concluding remarks

In this chapter, the description and analysis of a landmark floating bridge located in the state of Washington under several loads have been carried out. First, an historical introduction about the construction of the bridge was made.

Finally, the bridge has been studied considering several types of loads. The results obtained by the program have proved to catch the physics of the problem and provided reliable results of the behaviour of the bridge.

10 Conclusions

10.1 General Conclusions

This thesis has been devoted to the static analysis of floating structures, with emphasis on floating breakwaters and floating bridges anchored by cables to the seabed. To this purpose, a new finite beam element on elastic foundation, which takes into account the nonlinearities associated with both the fluid-structure interaction and the large displacements due the change of configurations of the anchoring cables has been formulated and subsequently implemented in a code for structural analysis. The problem has been studied considering different levels, from sectional analysis up to the structural analysis. The effects of the nonlinear fluid structure-interaction have been first evaluated at the sectional level by considering arbitrary geometry and loading conditions. In particular, the proposed model allows the integration of the hydrostatic load along the boundary of the section and imposes the equilibrium considering the section as an undeformable body. This new sectional model has been tested and subsequently validated through several case studies.

The cross-sectional formulation has been extended at the structural level based on the principle of virtual displacements to obtain the stiffness matrices and the equivalent nodal force vectors of both the beam finite element on elastic foundation and the cable finite element under large displacements. In addition, a formulation to reproduce the contact effects between cable structures and the seabed has been proposed.

Finally, due to the high nonlinearity involved in the problem, special attention has been devoted to the implementation of advanced numerical techniques for the analysis of nonlinear problems, such as the arc-length and work control procedures.

The accuracy of the proposed formulation has been validated through several benchmarks and applicative examples, and in all cases the framework developed provided reliable and interesting results. The effectiveness and applicability in engineering practice of the presented approach has been demonstrated through the structural analysis of an existing anchored floating bridge under different loading conditions.

10.2 Future Developments

Although the proposed approach provided accurate results in a variety of problems, there are several aspects that need to be further developed and improved, such as:

- Dynamic analysis: The formulations presented in this thesis are limited to the static response of floating breakwaters and floating bridges. The proposed models need to be incorporated in a framework for dynamic nonlinear analysis of the fluid-structure interaction to study the response of floating structures under dynamic loadings, such as waves and moving vehicles. This should be considered as a major need for future developments.

- Kinematic model: The displacement model adopted assumed the Euler-Bernoulli model for bending and axial behavior together with the de Saint Venant model to describe the torsional behavior. As a consequence, the model considers planarity and indeformability of the sections during the deformation of the beam. More accurate displacement models, such as Timoshenko's model to account for the shear deformation and the Wagner-Vlasov's model to consider the torsional warping, can be necessary under large displacements. These improvements will also involve a proper reformulation of the cross-sectional constitutive equations.

- Elements with varying cross sections: The sectional constitutive equations only depend on the shape of the cross-section. However, this is rigorously true only under the assumption of beams with constant cross-section. In the general case of beam elements with varying cross-section, the constitutive equations depend also on the geometry of the beam.

- Material nonlinearity: The analysis performed in this work have been carried out under the hypothesis of linear elastic behavior of the materials. Although this is a reasonable assumption to study the structural behavior of a floating structure under self-weight and service loadings, further developments are required to consider the nonlinear structural behavior at the ultimate or extreme loading conditions, such as the effects of extreme wave loading, impact due to vessels or sudden failure of the isolation systems with penetration of the fluid inside the structure.

- Deterioration effects and life-cycle analysis: Floating structures are generally immersed in an aggressive environment and are prone to deteriorate over the structural lifetime. As an example, in a marine environment reinforced concrete members are exposed to the diffusive attack of aggressive agents, such as chlorides, which may lead over time to corrosion of reinforcement and deterioration of concrete. Further developments towards a life-cycle approach to design and assessment of floating deteriorating structures are therefore needed.

References

P. T. Geiger A. N. Williams and W. G. McDougal. Flexible floating breakwaters. *J. Waterway, Port, Coastal, Ocean Enginnering.*, 117.

B. H. Adee. Analysis of floating breakwater performance. *In Proceedings of Symposium on Modeling Techniques, ASCE*, pages 1585–1602, 1975.

B. H. Adee. Analysis of floating breakwater mooring torces. *Ocean Engineering Mechanics*, pages 77–92, 1977.

B. H. Adee and W. Martin. Theoretical analysis of floating breakwater performance. *Floating Breakwaters Conference Papers, University of Rhode Island*, 24:21–39, 1974.

A.S. Elnashai B.A. Izzuddin. Eulerian formulation for large displacement analysis of space frames.

Markel D. G. Dubose W. G. Carver, R. D. and R. E. Jensen. Sloping float breakwater study, oregon inlet, north carolina. Technical report, U.S. Army Engr. Waterways Experiment Station, Vicksburg, Miss., 2004.

R. D. Carver. Floating breakwater wave-attenuation tests .]or east bay marina olympia harbour, washington. Technical report, US Army Engineer Waterways Experiment Station, Vicksburg, Miss, 1979.

Cui WC Fu SX. Chen XJ, Jensen JJ. Hydroelasticity of a floating plate in multi-directional waves. *Ocean Engineering*, 30(15):1997–2017, 2003a.

Cui WC Tang XF Chen XJ, Wu YS. Nonlinear hydroelastic analysis of a moored floating body. *Ocean Engineering*, 30(8):965–1003, 2003b.

Shi Chunxia. *Problems related to the seismic behaviour of submerged floating tunnels.* PhD thesis, Politecnico di Milano, 2013.

Steele C.R. Beams and shells with moving loads. *International Journal of Solids and Structures*, 7.

Thomas H. Dawson. *Offshore structural engineering.* Prentice-Hall, Inc., 1983.

Remo Magalhães de Souza. *Force-based Finite Element for Large Displacement Inelastic Analysis of Frames.* PhD thesis, UNIVERSITY OF CALIFORNIA, BERKELEY, 2000.

Marco Di Domizio. Analisi non lineare in grandi spostamenti e deformazioni di strutture strallate e sospese. Master's thesis, Politecnico di Milano, 2001-2002.

T. Utsunomiya E. Watanabe, C.M. Wang and T. Moan. Very large floating structures: applications, analysis and design. Technical Report 2, Centre for Offshore Research and Engineering. National University of Singapore, 2004.

Kim JW Demirbilek Z. Ertekin RC, Riggs HR. Hydroelastic analysis of floating bridges in current.

Biondini F. *Notes of the Course on Computational Structural Analysis.* Politecnico di Milano, 2014.

Park SK. Fleischer D. Elastic response analysis method for floating bridges in waves. *Journal of Sound and Vibrations*, 273(3):585–606, 2004.

L. Fry'ba. Vibration of solids and structures under moving loads. Technical report, Research of Institute of Transport, Prague, 1971.

Chen Xujunb Fu Shixiaoa, Cui Weichenga and Wang Conga. Hydroelastic analysis of a nonlinearly connected floating bridge subjected to moving loads. *Marine structures*, 18: 85–107, 2005.

Lin ZM Chen XJ. Fu SX, Cui WC. The effect of gaps on static response of a belt floating bridge. *Journal of Ship Mechanics*, 8(4):86–94, 2004.

V. W. Harms. Design criteria for floating tire breakwater. *J. Wtrway., Port, Coast, and Oc. Div., ASCE*, 105(2):149–170, 1979.

Talbot M Dhatt G. Henchi K, Fafard M. A versatile element for analyzing vehicle-bridge interaction response. *Journal of Sound and Vibrations*, 212(4):663–83, 1998.

Yoshimura T. Hino, J. and N. Ananthanarayana. Vibration analysis of non-linear beam subjected to moving loads by using the galerkin method. *Journal of Sound and Vibration*, 104(2), a.

Yoshimura T. Konishi K. Hino, J. and N. Ananthanarayana. A finite element method predication of the vibration of a bridge subjected to a moving vehicle load. *Journal of Sound and Vibration*, 96(1), b.

Inoue K Oka S Seto H Ueda S Maruyama T. Ikegami K, Kumamoto N. Elastic response of floating bridge in waves. 1989.

Max Irvine. *Cable structures.* Dover publications, Inc., 1992. ISBN 0486671275.

M. Isaacson and S. R. Wu. A numerical study of moored vessel response to beam waves. *Fifth International Offshore and Polar Engineering Conference*, 3:449–506, 1995.

M. Johansson. *Barrier-type breakwaters-Transmission, Reflection and Forces.* PhD thesis, School of Civil Engineering, Chalmers University of Technology, Sweden, 1989.

Lee J.-J. Jones, D. B. and F. Raichlen. A transportable breakwater for nearshore applications. *Proc. Civil Engineering in the Oceans IV, ASCE, New York, N.Y.*, pages 433–456, 1979.

Sollitt C. K. Kerper, D. R. and W. G. McDougal. Theoretical behavior of a compliant wave barrier. *J. Wtrway., Port, Coast, and Oc. Engrg., ASCE*, 1991a.

Sollitt C. K. Kerper, D. R. and W. G. McDougal. Experimental behavior of a compliant wave barrier. *J. Wtrway., Port, Coast, and Oc. Engrg., ASCE*, 1991b.

Fryba L. *Vibration of solids and structures under moving loads.* Thomas Telford, 1999.

McDougal W. G. Leach, P. A. and C. K. Sollitt. A transportable breakwater for nearshore applications. *J. Wtrway., Port, Coast, and Oc. Engrg., ASCE*, 111(5):895–909, 1985.

Sollitt C. K. Lee, C. P. and W. G. McDougal. Mechanically coupled flap type breakwaters: Theory and experiment. *Proc. Twentieth Coastal Engineering Conf, ASCE*, 111(5): 2445–2462, 1986.

M.M. Lwin. Design of the third lake washington floating bridge. *Concrete International: Design and Construction*, 11(2).

P. Malerba. *Appunti del corso di Ponti.* Politecnico di Milano, Dipartimento di Ingegneria Strutturale, 2010.

L. Martinelli and F. Perotti. Numerical analysis of the non-linear dynamic behaviour of suspended cables under turbulent wind excitation. *International Journal of Structural Stability and Dynamics*, 1:207–233, 2001.

Inoue K Ikegami K Seto H Ueda S Maruyama T. Oka S, Kumamoto K. Elastic response analysis method for floating bridges in waves. *Mitsubishi Techn Rev*, 37(2), 2003.

L.N. Vu P. Nanakorn. A 2d field-consistent beam element for large displacement analysis using the total lagrangian formulation. *ScienceDirect*, 42:1240–1247, 2006.

Egil Mollestad Pal G. Bergan and Nils Sandsmark. Non-linear static and dynamic response analysis for floating offshore structures. *Eng. Comput.*, 2, 1985.

Wu YS. Price WG. Structural responses of a swath of multi-hulled vessel traveling in waves. 1985.

Manuel Quagliaroli. Storia della scienza delle costruzioni. evoluzione storica dei sistemi di funi. 2010.

Fausto Saleri Quarteroni, Riccardo Sacco. *Numerical mathematics.* Springer, 2000.

S. Ratnayake and D. Christensen. Floating breakwater behavior: Theory and experiment. *Proc. Ocean Structural Dynamics Symposium '86, ASCE, New York, N.Y.*, pages 700–714, 1986.

V. Sundar S. A. Sannasiraj and R. Sundaravadivelu. Mooring forces and motion reponses of pontoon-type floating breakwaters. Technical report, Ocean Engineering Centre, Indian Institute of Technology, Madras 600 036, India.

P. Betsch S. R. Eugster, C. Hesch and Ch. Glocker. Director-based beam finite elements relying on the geometrically exact beam theory formulated in skew coordinates. *Int. J. Numer. Meth. Engng*, 2013.

Aoki S. Sawaragi, T. and A. Yasui. Tensions on silt curtains and currents in waves. page 13, 1989.

R. J. Seymour and D. M. Hanes. Performance analysis of a tethered float breakwater. *J. Wtrways., Port, Coast., and Oc. Div., ASCE*, 105(3):265–280, 1979.

Z. F. Sheu. The dynamic response of a floating body due to a moving load. Master's thesis, Institute of Naval Architecture and Marine Engineering, National Cheng-Kung University.

Xujun Chena Shixiao Fua, Torgeir Moana and Weicheng Cuib. Hydroelastic analysis of flexible floating interconnected structures. *Ocean Engineering*, 34:1516–1531, 2007.

C.R. Steele. Nonlinear effects in the problem of the beam on a foundation with a moving load. *International Journal of Solids and Structures*, 3, a.

C.R. Steele. The timoshenko beam with a moving load. *Journal of Applied Mechanics, Transactions of the ASME*, 35, b.

A. A. Sutko and E. L. Haden. The effect of surge, heave and pitch on the performance of a floating breakwater. *Floating Breakwaters Conference Papers, University of Rhode Island*, 24:21–39, 1974.

S.I. Suzuki. Dynamic behavior of a finite beam subjected to travelling loads with acceleration. *Journal of Sound and Vibration*, 55(1).

Zhuge Y. Thambiratnam D. Dynamic analysis of beams on an elastic foundation subjected to moving loads. *JSound Vib*, 198(2):149–69, 1996.

Gregory P. Tsinker. *Marine structures engineering: Specialized applications.* Chapman and Hall, 1994. ISBN 0412985713.

Ikegami K Seto H Kumamoto N Inoue K. Ueda S, Maruyama K. Experimental study on the elastic response of a movable floating bridge in waves. 1989.

Kumamoto N Inoue K Oka S. Ueda S, Seto H. Behavior of floating bridge under wind and waves. 1996a.

Kumamoto N Inoue K Seto H. Ueda S, Oka S. Design procedures and computational analysis of motions and deformations of floating bridge subjected to wind and waves. 1996b.

Federico Perotti Vincenzo Gattulli, Luca Martinelli and Fabrizio Vestroni. Nonlinear oscillations of cables under harmonic loading using analytical and finite element models. *Comput. Methods Appl. Mech. Engrg.*, 193:69–85, 2004.

Federico Perotti Vincenzo Gattulli, Luca Martinelli and Fabrizio Vestroni. Dynamics of suspended cables under turbulence loading: Reduced models of wind field and mechanical system. *Journal of Wind Engineering and Industrial Aerodynamics*, 95:187–207, 2007.

Virchis VJ. Prediction of impact factor for military bridges. Technical Report 107, ISVR, 1988.

Eiichi Watanabe and Tomoaki Utsunomiya. Analysis and design of floating bridges. *Prog. Struct. Engng Mater*, 5:127–144, 2003.

Murakoshi J Fumoto K Tanaka H Nagata S Okubo H Itoh K. Watanabe E, Utsunomiya T. Development of dynamic response analysis program for floating bridges subjected to wind and wave loadings. 2003.

A. N. Williams. Wave diffraction by elliptical breakwaters in shallow water. *Ocean Engineering*, 12:25–43, 1985.

A. N. Williams and M. K. Darwiche. Three-dimensional wave scattering by elliptical breakwaters. *Ocean Engineering*, 15:103–118, 1988.

A. N. Williams and P. T. Geiger. Theoretical analysis of flexible floating breakwater. Technical report, Univ. of Houston, Houston, Tex., 1988.

Ronald D. Ziemian Williams McGuire, Richard H. Gallagher. *Matrix structural analysis*. John Wiley and Sons, Inc., 2000. ISBN 0471129186.

Jong-Shyong Wu and Po-Yun Shih. Moving-load-induced vibrations of a moored floating bridge. *Computers and Structures*, 66.

Jong-Shyong Wu and Po-Yun Shih. Moving-load-induced vibrations of a moored floating bridge. *Computers and structures*, 66:435–461, 1998.

J.S. Wu and C.W. Dai. Dynamic response of multi-span nonuniform beam due to moving load. *Journal of Structural Engineering*, 113(3).

Lee M.L. Wu, J.S. and T.S. Lai. The dynamic analysis of a plate under a moving load by the finite element method. *International Journal for Numerical Methods in Engineering*, 24(3).

Cartmell MP. Wu JJ, Whittaker AR. The use of finite element techniques for calculating the dynamic response of structures to moving loads. *Computers and Structures*, 78: 789–99, 2000.

Cartmell MP. Wu JJ, Whittaker AR. Dynamic responses of structures to moving bodies using combined finite element and analytical methods. *IInternational journal of Mechanical Science*, 43:2555–79, 2001.

Sheu JJ. Wu JS. An exact solution for a simplified model of the heave and pitch motions of a ship hull due to a moving load and experimental results. *Journal of Sound and Vibrations*, 192(2):495–520, 1996.

Shih PY. Wu JS. Moving-load-induced vibrations of a moored floating bridge. *Computers and Structures*, 66(4)):435–61, 1998.

T. Yamamoto. Moored floating breakwater response to regular and irregular waves. *Applied Ocean Research*, 3:114–123, 1981.

Yoshida A. Yamamoto, T. and T. Ijima. Dynamics of elastically moored floating objects. *Applied Ocean Research*, 2:85–92, 1980.

Wu YS. Yang YB. A versatile element for analyzing vehicle-bridge interaction response. *Eng Struct*, 23:452–69, 2001.

Shyh-Rong Kuo Yeong-Bin Yang. *Nonlinear framed structures.* Prentice Hall, Inc., 1994. ISBN 0131092243.

Hino J. Yoshimura, T. and N. Ananthanarayana. Vibration analysis of non-linear beam subjected to a moving load using the finite element method. *Journal of Sound and Vibration*, 100(4).

Wu YS. *Hydroelasticity of floating bodies.* PhD thesis, Brunel Univ., UK, 1984.